5-2019

Asteroid Regolith Weathering: A Large-Scale Observational Investigation

Eric Michael MacLennan
University of Tennessee, emaclenn@vols.utk.edu

To the Graduate Council:

I am submitting herewith a dissertation written by Eric Michael MacLennan entitled "Asteroid Regolith Weathering: A Large-Scale Observational Investigation." I have examined the final electronic copy of this dissertation for form and content and recommend that it be accepted in partial fulfillment of the requirements for the degree of Doctor of Philosophy, with a major in Geology.

Joshua P. Emery, Major Professor

We have read this dissertation and recommend its acceptance:

Jeffrey E. Moersch, Harry Y. McSween Jr., Liem T. Tran

Accepted for the Council:

Dixie L. Thompson

Vice Provost and Dean of the Graduate School

(Original signatures are on file with official student records.)

Asteroid Regolith Weathering: A Large-Scale Observational Investigation

A Dissertation Presented for the

Doctor of Philosophy

Degree

The University of Tennessee, Knoxville

Eric Michael MacLennan

May 2019

I would like to dedicate this entire work to my beloved grandparents

Mary, James, Haroldine, and William;

and to my parents, who have given me the ability to achieve my dreams.

Acknowledgments

I am grateful for everyone who has contributed their ideas, advise, and help into making this work possible. Without them, I would not have accomplished what I have in my 6 1/2 years as a graduate student. Firstly, this work would not have been made possible without the help and mentorship of my PhD advisor, Joshua Emery. I am very grateful of the time and energy he has dedicated in training and mentoring me in preparation for my future. The Emery Research Group of Excellence (EMERGE) has included so many exceptional researchers who have fostered a supportive, cooperative, and fun environment to perform research and I am better for having them by my side.

A special thank you to, Michael Lucas and Noemi Pinilla-Alonso, who offered up their valuable IRTF telescope observing time in order to observe some of my targets and for showing me their remote observing skills. In addition, Noemi and Vania Lorenzi arranged time on the TNG for collecting spectra of a few of my target asteroids. I also wish to recognize and acknowledge the very significant cultural role and reverence that the summit of Maunakea has always had within the indigenous Hawaiian community. I am most fortunate to have had the opportunity to conduct remote observations using the IRTF, which lies atop this mountain.

From 2014 to 2017 I was supported by the NASA Earth and Space Sciences Fellowship (NESSF) grant (# NNX14AP21H), which provided a sizable stipend and an allowance that was applied towards miscellaneous supplies, textbooks, computer software, and travel expenses. This dissertation makes use of data products from the Wide-field Infrared Survey Explorer, which is a joint project of the University of California, Los Angeles, and the Jet Propulsion Laboratory/California Institute of Technology, funded by the National Aeronautics and Space Administration.

Abstract

As bodies lacking an atmosphere or significant protection from solar wind particles, asteroids are subject to processes that modify the physical state and spectral properties of their regoliths. By investigating the relevant factors that contribute towards asteroid regolith modification, this work will provide crucial insight into the nature of these processes. I propose and test two major hypotheses: 1) that physical (mechanical) breakdown is caused by both meteoroid bombardment and thermal fatigue cycling, and thus regolith grain size depends on asteroid size and rotation period, and 2) changes in spectral properties (space weathering) are due to solar wind bombardment and depend on an object's mineralogy, sun-distance, and surface age.

I develop and validate a thermophysical modeling (TPM) approach that analyzes multi-epoch (pre- and post-opposition) thermal infrared observations for asteroids without prior shape or spin information, in order to determine various thermophysical properties – chiefly the thermal inertia. This TPM approach is applied to over 250 asteroids to determine their thermal inertia. Combining other thermal inertia datasets with mine, for a total of over 300 objects, a characteristic grain size is estimated for each object. Next, a multiple linear model is used to quantify the grain size dependence on asteroid diameter and rotation period, which are both shown to be statistically-significant model predictors. I also identify grain size differences between spectral groups – namely the M-types, which exhibit 4 times larger regolith grains, on average.

Spectral data from meteorite and irradiated samples, spanning the visible and near-infrared regions, are used to develop an index to quantify the degree of space weathering. This space weathering index is applied to asteroid spectral observations and used in a multi-linear model to determine the predictor variables that increase the perceived amount of

asteroid space weathering. Perihelion distance, diameter, and the average sun distance are found as statistically-significant factors in the multiple linear model. I also present evidence that regolith grains smaller than 0.5 mm enhance the extent of space weathering.

Table of Contents

List of Tables

List of Figures

Nomenclature

Abbreviations, Acronyms, and Initialisms

ALCDB	Asteroid Lightcurve Database
AstDyS	Asteroids - Dynamic Site
ATRAN	Atmospheric Transmission Model
Aub.	Aubrite
BA	Basaltic Achondrite
BAR-Ast	Band Analysis Routine for Asteroids
BIC	Bayesian Information Criterion
CME	Coronal Mass Ejection
DAMIT	Database of Asteroid Models from Inversion Techniques
decl.	Declination
EOC	Equilibrated Ordinary Chondrite
HCM	Hierarchal Clustering Method
HED	Howardite-Eucrite-Diogenite
IPAC	Infrared Processing and Analysis Center
IRAS	Infrared Astronomical Satellite

IRSA	Infrared Science Archive
IRTF	Infrared Telescope Facility
LSST	Large Synoptic Sky Telescope
MBA	Main-Belt Asteroid
MC	Mars-Crossing Asteroid
MPC	Minor Planet Center
NASA	National Aeronautical and Space Administration
NEA	Near-Earth Asteroid
NEAR	Near-Earth Asteroid Rendezvous
NEATM	Near-Earth Asteroid Thermal Model
NEO	Near-Earth Object
NESTM	Night Emission Simulated Thermal Model
NICS	Near Infrared Camera Spectrometer
NIR	Near-Infrared
$npFe^0$	Reduced Nanophase Iron
OC	Ordinary Chondrite
Pan-STARRS	Panoramic Survey Telescope and Rapid Response System
PDS	Planetary Data System
R.A.	Right Ascension
RELAB	Reflectance Experiment Laboratory
s3os2	Small Solar System Object Spectral Survey

SARA	Spectral Analysis Routine for Asteroids
SDSS	Sloan Digital Sky Survey
SED	Spectral Energy Distribution
Sher.	Sergottite
SMASS	Small Main-Belt Asteroid Spectral Survey
SNR	signal-to-noise ratio
STM	Standard Thermal Model
TNG	Telescopio Nazionale Galileo
TPM	Thermophysical Model
UOC	Unequilibrated Ordinary Chondrite
UT	Universal Time
UV	Ultra-Violet
Vis	Visible
WISE	Wide-Field Infrared Survey Explorer
YORP	Yarkovsky-O'Keefe-Radzievskii-Paddack

Model Variables

β^{eclip}	ecliptic latitude of spin vector
Γ	thermal inertia
γ	crater half-opening angle
Δ	difference in value

δ	uncertainty in parameter
ε	emissivity
η	NEATM beaming parameter
Θ	thermal parameter
θ	body-centric longitude
ϑ	surface-normal longitude
$\bar{\theta}$	mean surface slope
Λ	albedo adjustment factor
λ^{eclip}	ecliptic longitude of spin vector
μ	Poisson's ratio
ν	number of degrees of freedom
ξ	specific surface energy of regolith grain
ρ	effective mass density of regolith
ρ_{grain}	mass density of regolith grain
ρ_{bulk}	bulk mass density of object
σ	standard error
ϕ	body-centric latitude
χ^2	chi-squared statistic
ψ	volume filling factor
φ	surface-normal latitude
$\Uparrow$	prograde rotator

$\Downarrow$	retrograde rotator
$\emptyset_p$	regolith porosity
A	bolometric Bond albedo
A_{th}	Bond albedo at thermal wavelengths
a	orbital semimajor axis
a	ellipsoid semi-axis length
B	blackbody flux
B_I, B_{II}	band I and band II
B_IC, $B_{II}C$	band I and II center
B_ID, $B_{II}D$	band I and II depth
B_IS, $B_{II}S$	band I and II slope
BAR	Band Area Ratio
b	ellipsoid semi-axis length
c	ellipsoid semi-axis length
c_s	specific heat capacity
dA	infinitesimal area element
d_g	grain diameter
E	Young's modulus
E_{scat}^{solar}	scattered solar radiation energy
E_{abs}^{therm}	re-radiated thermal energy
E_c	electric field strength

e	orbital eccentricity
F	flux
F_o	observed flux
F_m	modeled flux
$\overline{F}$	lightcurve mean
$\diamondsuit F$	lightcurve peak-to-trough range
f_R	areal surface fraction of craters
G	bulk modulus
g_{eff}	effective gravitational acceleration
H	absolute magnitude
k	thermal conductivity
k_{eff}	effective thermal conductivity
k_{grain}	solid grain thermal conductivity
k_{rad}	radiative thermal conductivity
l_s	thermal skin depth
M, m	mass
$m_{i,j}$	mean of the i^{th} and j^{th} flux measurement
N	number of points
n	number of free model parameters
$\mathbf{n}$	normal vector
P_{rot}	rotation period

p	geometric albedo
Q	aphelion
q	perihelion
$\mathbf{R}$	directional derivative
$\mathbf{r}$	radius vector
r^2_{adj}	adjusted r-squared statistic
r_s	Spearman rank coefficient
$r_{i,j}$	difference between the ith and jth flux measurement
s	shadowing factor
T	temperature variable
T_c	color temperature
$T_{\rm eq}$	equilibrium temperature
T_{ss}	NEATM sub-solar temperature
t, t'	time variable
U, u	velocity
v	visibility factor
x, x'	depth variable
x	X coordinate
y	Y coordinate
z	Z coordinate
b, e, f, k, Ξ, τ, ζ	misc. empirically-derived constants

Mathematical Constants

e_N	Euler's number	2.71828182845 ...
Φ	golden ratio	1.61803398875 ...
π	ratio of a circle's circumference to it's diameter	3.14159265359 ...

Observational Variables

α	solar phase angle
Δ_{AU}	observer-centric distance
R_{AU}	heliocentric distance
$i_{\angle}$	incidence angle
$e_{\angle}$	emission angle
λ	wavelength

Physical and Astronomical Constants

AU	Astronomical Unit	149,597,870,700 m
c_0	speed of light in a vacuum	299,792,458 m s^{-1}
h	Plank constant	$\approx 6.62607004\times 10^{-34}$ m^2 kg s^{-1}
k_b	Boltzmann constant	$\approx 1.38064852\times 10^{-23}$ m^2 kg s^{-2} K^{-1}
$M_{\odot}$	solar mass	$\approx 1.98847\times 10^{30}$ kg
σ_0	Stefan-Boltzmann constant	$\approx 5.67036713\times 10^{-8}$ W m^{-2} K^{-4}
$S_{\odot}$	solar constant	≈ 1367 W m^{-2}

Introduction

Between the orbits of Mars and Jupiter resides the solar system's largest collection of minor planets. Called the main asteroid belt, or simply Main Belt, it houses a reservoir of over 500,000[1] known asteroids. These asteroids, made of leftover planetary material from the early era of solar system formation, exhibit a wide range of sizes, shapes, and spin states, as well as a variety of surface and spectral properties (Michel et al., 2015). Only a handful of the largest asteroids represent a remnant sub-population of planetesimals (Johansen et al., 2015), whereas ∼4.6 Gyr of collisional evolution have produced the remainder of the smaller bodies (Bottke et al., 2015). Asteroid properties are typically derived from observing them using telescopes and in different wavelength regimes. Photometry — the measurement of photons passed through astronomical filters — in the visible is collected in order to estimate an object's absolute brightness (Muinonen et al., 2002), and any time-dependent changes due to shape and spin characteristics of an asteroid (Kaasalainen et al., 2002). Infrared data collected through photometry (Mainzer et al., 2015) can be used to accurately determine the size, albedo, and other surface characteristics (Delbo' et al., 2015). Combined spectroscopic data in the visible (Bus et al., 2002) and near-infrared (DeMeo et al., 2009) regions are used to identify mineral species (Reddy et al., 2015) and define spectral groups (taxa) (DeMeo et al., 2015).

Catastrophic collisions of a larger parent body have produced a number of asteroid families of various ages (Nesvorný et al., 2015). The members of these families — an estimated 1/3 of the total asteroid population — are identified through algorithms designed to identify clusters of asteroids in orbital element space (Bendjoya and Zappalá, 2002), as main-belt orbits are relatively stable over long time periods. Since these family members

[1] https://www.minorplanetcenter.net

originated from a common body (Burbine et al., 2002), they are thought to have similar compositions and spectral properties (Masiero et al., 2015). Asteroid spectral taxonomies, which loosely resemble the broad geochemical variation in the meteorite record (Weisberg et al., 2006), have been developed and can be divided into three broad groups (DeMeo et al., 2015; Scott et al., 2015): primitive (represented by the C- and P-types), heated (S-types), and differentiated (V-, E-, and M-types).

The determinations of asteroid spin rates have revealed that objects 150 m to 10 km in diameter have a rubble-pile structure with a small amount of cohesion, and objects smaller than 150 m are mostly internally coherent monoliths (Pravec et al., 2002). Non-gravitational perturbations (i.e., the Yarkovsky effect; Bottke et al., 2006; Vokrouhlický et al., 2015) dynamically alter the orbits of smaller asteroids such that they can enter orbital resonances with Jupiter (Nesvorný et al., 2002b). Upon reaching these resonances, the orbital eccentricity of these bodies increases enough such that their orbits cross the terrestrial planet region. Meteorites sourced from the Main Belt are delivered to Earth's surface via this process (Morbidelli et al., 2002) and studied in the laboratory in order to gain insight into the geochemical evolution of the solar system (McSween et al., 2006).

Regolith is a term which was originally defined in a terrestrial context by Bates and Jackson (1980) as, "a general term for the layer or mantle of fragmental and unconsolidated rock material, whether residual or transported and of highly varied character, that nearly everywhere forms the surface of the land and overlies or covers bedrock. It includes rock debris of all kinds ...". This term, which the Lunar missions used to describe the Moon's surface, has subsequently been widely adopted for use on all planetary bodies. High-resolution images of asteroid regolith show a mixture of crushed fragments ranging in size from large boulders to fine-grained powder (Sullivan et al., 2002). In general, the regolith of larger bodies is comprised of a higher fraction of finer-grained fragments and a lower fraction of boulders, whereas cobbles and large boulders are more frequent on smaller-sized bodies, such as Eros (Cheng, 2002) and Itokawa (Yoshikawa et al., 2015).

Asteroids show evidence of spectral and albedo surface variation (Clark et al., 2002), which is likely caused by alteration by impactors (micro-meteoroids) or solar-wind ion particles. The processes leading to this alteration are collectively known as space weathering

and result in a reddening of spectral slopes, reduction in absorption band strength, and lowering of albedo (Brunetto et al., 2015). Space weathering is well-studied for the silicate-bearing asteroids, which exhibit mineral absorptions due to olivine and pyroxene (Reddy et al., 2015). Among silicate-bearing asteroid taxonomic groups, S-type spectra exhibit evidence for space weathering whereas Q-type spectra — which are almost exclusively identified within the near-Earth sub-population of asteroids (Binzel et al., 2004) — closely resemble those of the ordinary chondrite meteorites (McFadden et al., 1985; Binzel et al., 1996).

This dissertation is an investigation into the processes that generate, develop, and alter asteroid regolith — both physically (mechanical breakdown) and spectrally (space weathering). Using both photometric infrared survey data and spectral observations in the visible and near-infrared, I will analyze variations in the surface properties of several hundred objects and parameter trends in order to ascertain the root causes of the mechanical breakdown and the space weathering of asteroid regolith.

Chapter 1

Asteroid Thermophysical Modeling

Preamble

This chapter was previously published, in a similar form, in the Astronomical Journal: MacLennan and Emery (2019) under the title "Thermophysical Modeling of Asteroid Surfaces Using Ellipsoid Shape Models".

1.1 Introduction

Multi-wavelength, photometric infrared observations of asteroids provide essential information about the thermophyiscal properties of their surfaces. A handful of both simple thermal models (Lebofsky et al., 1978; Harris, 1998; Lebofsky et al., 1986; Wolters and Green, 2009; Myhrvold, 2016) and more sophisticated themophysical models (TPMs; Spencer et al., 1989; Spencer, 1990; Lagerros, 1996; Delbo' et al., 2007; Mueller, 2007; Rozitis and Green, 2011) have been established as effective means of modeling thermal infrared observations of asteroids. The general purpose of a thermal model is to compute surface temperatures for an object, which are in turn used to calculate the emitted flux at the desired wavelengths (see Delbo' et al., 2015, for a recent review). Thermophysical models, constrained through observational measurements, have proved to be a powerful tool in providing meaningful estimates of an object's size and albedo, as well as granting insight into thermophysical

characteristics of asteroid regoliths (Emery et al., 2014; Rozitis and Green, 2014; Rozitis et al., 2014, 2018; Hanuš et al., 2015, 2018; Landsman et al., 2018).

Most simple thermal models assume an idealized (often spherical) object shape, instead of including *a priori* knowledge of the shape, in order to estimate the diameter and albedo of an object. However, unlike TPMs, simple thermal models lack the ability to estimate geologically relevant thermophysical properties such as the thermal inertia. TPMs require a spin pole — typically sourced from the Database of Asteroid Models from Inversion Techniques (DAMIT[1]; Ďurech, 2010) — and object shape model as input (e.g., Hanuš et al., 2018).

With the recent surge in thermal infrared observations from large-scale surveys, an ever-increasing number of asteroids are being observed across several epochs, building up sets of observations that span both pre- and post-opposition — often at large solar phase angles (Mainzer et al., 2011a). Such observations provide additional constraints and/or allow for more free parameters in data-modeling inversion techniques. However, the rate of thermal infrared observations significantly outpaces the efforts to characterize the shapes of individual asteroids. Advantages of multi-epoch observations have previously been noted (e.g., Spencer, 1990) and they have been used recently to derive thermophysical and spin properties of objects (Müller et al., 2011, 2014, 2017; Ďurech et al., 2017). These studies serve as the foundation on which I build a methodological approach aimed at extracting important thermophysical properties from the large number of asteroids observed at pre- and post-opposition at multiple thermal wavelengths often acquired from thermal infrared surveys.

In chapter 1, I outline and test a TPM approach that utilizes pre- and post-opposition multi-wavelength thermal observations when information about an object is limited. To do so, I use various simple shapes (both spherical and prolate ellipsoids) with varying spin vectors. The goal of this work is to demonstrate and establish the effectiveness of this modeling approach and compare it to previous studies. In section 1.2 I briefly review established thermal modeling techniques and their ability to constrain diameter, albedo, thermal inertia, surface roughness, shape, and spin direction (i.e., prograde or

[1] http://astro.troja.mff.cuni.cz/projects/asteroids3D/web.php

retrograde) — highlighting the use of pre-/post-opposition observing geometries. I describe my thermophysical model and its implementation in section 1.3. In section 1.4, I implement my approach and analyze its effectiveness in relation to that of the previously reviewed works. I then apply my modeling approach and present results for 21 asteroids in section 1.5. In chapter 2, I will supplement the number of objects analyzed with this method by an order of magnitude.

1.2 Thermal Modeling Background

A few simple thermal models and TPMs have been developed to estimate various physical and thermophysical properties of asteroids. Many thermal models attempt to match a disk-integrated flux to a set of telescopic observational data by calculating surface temperatures for a given shape. Simple thermal models model surface temperatures by using closed-form equations (which can be evaluated in a finite number of operations) using the equilibrium surface temperature (T_{eq}), which is calculated via the energy balance between the amount of absorbed insolation and emitted thermal energy:

$$\frac{S_{\odot}(1-A)}{R_{\mathrm{AU}}^2} - \varepsilon_B \sigma_0 T_{eq}^4 = 0. \tag{1.1}$$

In equation (1.1), $S_{\odot}$ is the solar constant[2] (1367 Wm^{-2}; Frölich, 2009), A is the bolometric Bond albedo, R_{AU} is the heliocentric distance in Astronomical Units, ε_B is the bolometric emissivity, and σ_0 is the Stefan-Boltzmann constant. Equation (1.1) implicitly assumes that the spherical body is not rotating with respect to the Sun.

On the other hand, TPMs compute surface temperatures using Fourier's Law of heat diffusion (evaluated numerically). The well-established simple thermal models include the Standard Thermal Model (STM; see Lebofsky et al., 1986, and references within), Near-Earth Asteroid Thermal Model (NEATM; Harris, 1998), and the Fast Rotating Model (FRM; Lebofsky et al., 1978) More recently, the Night Emission Simulated Thermal Model (NESTM; Wolters and Green, 2009) and Generalized FRM (GFRM; Myhrvold, 2016) have been created

[2] $S_{\odot}$ is defined as the solar energy flux measured at 1 AU, per unit surface area.

by modifying the NEATM and FRM, respectively. For reasons of applicability and flexibility, especially when analyzing large datasets, the NEATM has been used most often (Trilling et al., 2010; Mainzer et al., 2011b; Masiero et al., 2011). A brief description and history of the STM, FRM, and NEATM can be found in Harris and Lagerros (2002). The NEATM has been the preferred simple thermal model for multi-wavelength thermal surveys, due to the ease of applying it to single epoch observations of objects for which no shape or spin information exists. However, a TPM is the preferred tool for interpreting the multi-wavelength thermal observations of objects with shape and spin pole information.

1.2.1 Thermophysical Models

Many versions of TPMs, with varying levels of complexity, have been developed throughout the past few decades. Such models explicitly account for the effects that physical attributes of the surface have on the thermal emission (Spencer et al., 1989). Subsurface heat conduction, self-shadowing from direct insolation (incoming solar radiation), multiply scattered insolation, and re-absorbed thermal radiation (i.e., self-heating) are implemented in a multitude of ways. The energy conservation expressed by equation (1.1) is amended to include additional terms that account for these effects:

$$\frac{S_{\odot}(1-A)}{R_{\mathrm{AU}}^2}\cos(i_{\angle})(1-s) + E_{scat}^{solar} + E_{abs}^{therm} + k\frac{dT}{dx}\bigg|_{surf} - \varepsilon_B\sigma_0 T_{surf}^4 = 0. \tag{1.2}$$

Here, k is the *effective* thermal conductivity, x is the depth variable, $i_{\angle}$ is the angle between a surface facet's local zenith and sun-direction (solar incidence angle), and s is a binary factor indicating whether an element is shadowed by another facet ($s = 1$) or not ($s = 0$). The terms E_{scat}^{solar} and E_{abs}^{therm} encompass the contributed energy input from scattered solar radiation and re-radiated thermal photons, respectively, from other surface elements. Additionally, the temperature gradient term accounts for the heat conducted into the subsurface as a function of the surface temperature, $T_{surf} = T(x = 0)$. Rough topography has been modeled as spherical section craters (Spencer, 1990; Emery et al., 1998), random Gaussian surface (Rozitis and Green, 2011), and using fractal geometry (Davidsson and Rickman, 2014). The mathematics and numerical implementations of these features differ somewhat from one

another. For further details, I refer the reader to the primary papers and to Davidsson et al. (2015) for a comparison of the different implementations.

TPMs often use the time-dependent, one-dimensional heat diffusion equation,

$$\frac{\partial T(x,t)}{\partial t} = \frac{k}{\rho c_s} \frac{\partial^2 T(x,t)}{\partial x^2}, \tag{1.3}$$

to model the heat flow into and out from the subsurface as a function of depth and time, t. This presentation of Fourier's Law in equation (1.3) assumes that the *effective* thermophysical factors (thermal conductivity, bulk density, ρ, and specific heat capacity, c_s) do not vary with depth or temperature, $T(x,t)$. One-directional heat flow into the subsurface is also often assumed, but is well-justified by the concept that thermal energy flow is aligned with the temperature gradient — either directly up or down beneath the surface.

In the subsections below, I review and assess how various physical parameters (diameter, albedo, thermal inertia, surface roughness, shape, and spin direction) can be constrained in various observing circumstances. In particular, I highlight the optimal observing configurations and possible biases that may arise from particular viewing geometries.

1.2.2 Diameter and Albedo

One of the primary motivations for developing thermal models was to obtain size estimates of objects from disk-integrated thermal infrared observations (e.g., Allen, 1970; Morrison, 1973), given that thermal flux emission is directly proportional to the object's projected area. A single value of diameter is not uniquely defined for a non-spherical body, so an *effective diameter* (D_{eff}) is given: the diameter of the sphere (Mueller, 2007) having the same projected area as the object. During the span of data collection for a non-spherical body, the projected area will almost never be constant. In this case, D_{eff} is best reported as a time-averaged value, or adjusted using visible lightcurve data obtained simultaneously or proximal in time to the thermal observations (e.g., Lebofsky and Rieke, 1979; Harris and Davies, 1999; Delbo' et al., 2003; Lim et al., 2011). If a detailed shape model is being used, then the rotational phase of the object can be shifted in order to match the time-varying flux (Alí-Lagoa et al., 2014).

The visible geometric albedo (p_V) is calculated directly from D_{eff} and the object's absolute magnitude (H_V) (Russell, 1916; Pravec and Harris, 2007):

$$\sqrt{p_V} = \frac{1329 \text{ km } 10^{-0.2H_V}}{D_{eff}\,[\text{km}]}. \tag{1.4}$$

Some variables used here specifically relate to observations taken using a V-band filter, as denoted by the "V" subscript. Using the definition of the phase integral (q),

$$q \equiv A/p = 0.290 + 0.684 \times G, \tag{1.5}$$

the visible geometric albedo is then converted to the bolometric Bond albedo. In equation (1.5) G is the slope parameter (Bowell et al., 1989), and the approximation $A \approx A_V$ is made within equation (1.1) to solve for p_V.

1.2.3 Thermal Inertia and Surface Roughness

The characteristic ability of a material to resist temperature changes when subject to a change in energy balance is quantified by its thermal inertia ($\Gamma = \sqrt{k\rho c_s}$). Atmosphereless surfaces with low thermal inertia conduct little thermal energy into the subsurface, resulting in dayside temperatures that are close to instantaneous equilibrium with the insolation and extremely high diurnal temperature differences. Surfaces having large thermal inertia store and/or conduct thermal energy in the subsurface during the day, so significant energy is re-radiated during the nighttime hours, which results in a comparatively smaller diurnal temperature change. This influence that thermal inertia has on the surface temperature distribution manifests in the observed spectral energy distribution (SED). Thus, photometry at two wavelengths (e.g., a measurement of the color temperature) can provide a better measure of thermal inertia, compared to that of a single wavelength (Mueller, 2007). Figure 1.1(a) shows the normalized SEDs of surfaces (at opposition) having different thermal inertias, degrees of roughness, and shapes. Surfaces with higher roughness and low thermal inertia exhibit flux enhancement at short wavelengths near opposition, lowering the wavelength location of the peak flux. Data collected that have large wavelength separations,

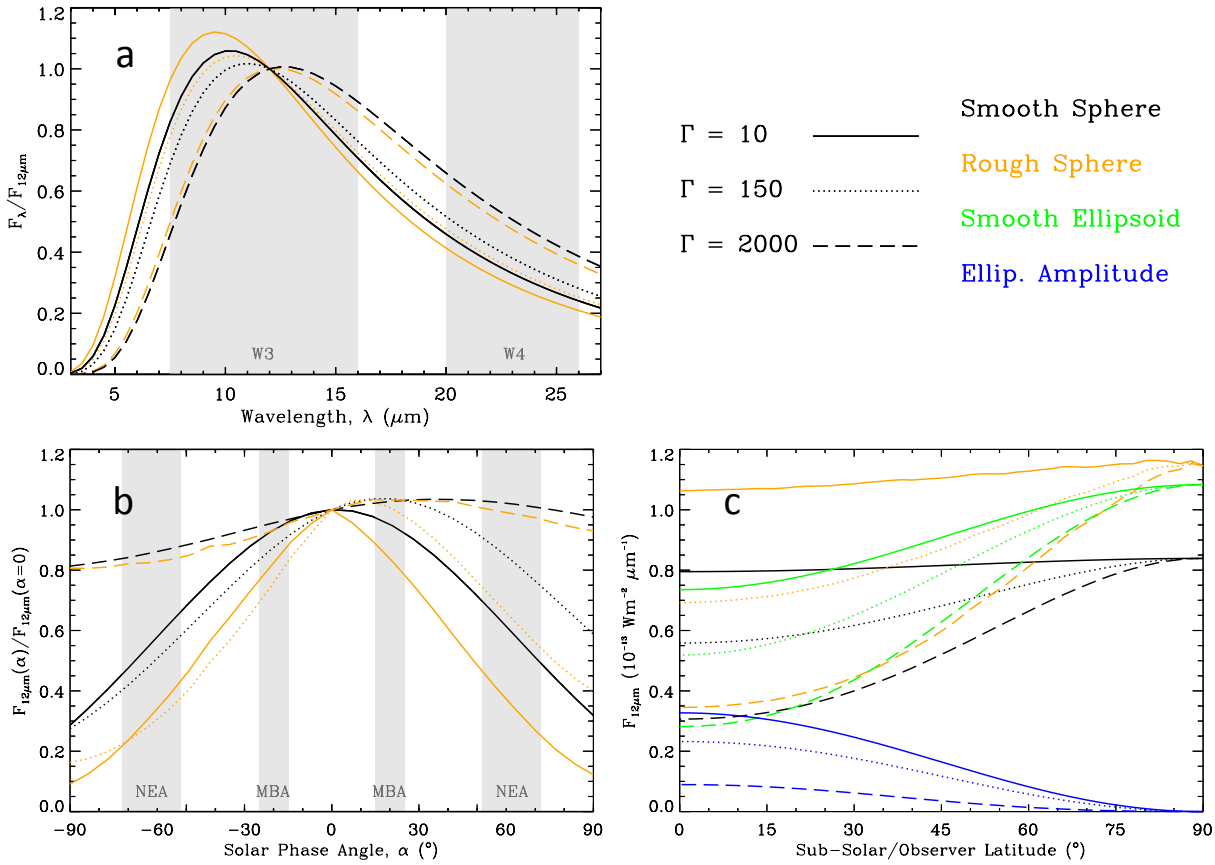

Figure 1.1: Comparison of thermal flux emitted from an object with varying thermophysical properties and shape, as a computed from the TPM described in section 1.3. Panel (a) shows blackbody curves, normalized at 12 μm. Thermal phase curves are shown in (b), and panel (c) shows the flux as a function of the sub-solar/observer latitude. The modeled object has D_{eff} = 1 km, T_{eq} = 300 K, P_{rot} = 10 hr, located 1 AU from the observer and spin axis aligned perpendicular to both the Sun and observer. Within all frames, black curves are for a smooth sphere, orange curves are for a sphere with a mean surface roughness of $\bar{\theta} = 29°$, and green curves are for a prolate ellipsoid with principal axis ratio of a/b = 1.75. Blue curves show the amplitude of the ellipsoid's thermal lightcurve. As indicated in the key, the solid, dotted, and dashed curves in all frames distinguish different values of thermal inertia. I note here that pre-opposition is defined as $\alpha > 0$ (i.e., a positive solar phase angle), in which the afternoon side of a prograde rotator is viewed.

spanning the blackbody peak are most useful because they are sensitive to relatively warmer and cooler portions of the surface — in other words, the overall temperature distribution. Delbo' and Tanga (2009) estimated thermal inertias for 10 main-belt asteroids using multi-wavelength IRAS (Infrared Astronomical Satellite) observations, and Hanuš et al. (2015, 2018) collectively present thermal inertia estimates for 131 objects using Wide-Field infrared Survey Explorer (WISE) data. Harris and Drube (2016) present population trends using over a hundred thermal inertias derived from the NEATM η values of asteroid observed with WISE.

Use of multiple observations at a single wavelength and spanning various solar phase angles (α) — a *thermal phase curve* — has also proven to be a useful method for estimating thermal inertia (e.g., Spencer, 1990). Figure 1.1(b) shows examples of thermal phase curves for 3 different objects, each possessing 5 different thermal inertia values. Müller et al. (2011) and Müller et al. (2017) demonstrated that observations of (162173) 1993 JU_3, Ryugu, taken on one side of opposition but widely spaced in solar phase angle ($\Delta\alpha \sim 30°$) can constrain thermal inertia as they effectively had two points along a thermal phase curve. As seen in figure 1.1(b), this approach can be optimized when the thermal phase curve spans across both sides of opposition. Thus, observing at pre- and post-opposition virtually guarantees that thermal emission information from the warmer afternoon ($\alpha > 0$) and cooler morning sides is gathered (Müller et al., 2014).

Surfaces with large degrees of roughness exhibit warmer dayside temperatures, due both to more of the surface area being pointed toward the sun and to the effects of multiple scattering of reflected and emitted light. The term "beaming effect" is used to describe enhanced thermal flux return in the direction of the sun at low phase angles. As pointed out by Rozitis (2017), the flux enhancement near opposition is highly sensitive to surface roughness. They also demonstrated that telescopic observations at a near pole-on illumination and viewing geometry can be used to effectively constrain the degree of roughness, specifically when $\alpha < 40°$ and the sub-solar latitude is greater than 60° (figure 1.1(b and c)). Figure 1.1(b) shows thermal phase curves of objects with smooth and rough surfaces of varying thermal inertia. Figure 1.1(c) shows the thermal flux emitted as a function of sub-solar latitude and recreates the findings of Rozitis (2017). In general,

estimates of surface roughness for airless bodies are optimally made using data collected at opposition — or better yet, with disk-resolved observations that offer a greater range of viewing geometries. The Rozitis (2017) study shows that the uncertainty in thermal inertia is slightly larger for an object observed at a large phase angle, as a consequence of the difficulty in estimating surface roughness.

1.2.4 Shape and Spin Direction

Disk-integrated flux is also directly affected by the shape and spin pole of an object (Ďurech et al., 2017): if thermal observations sample the entire rotation period, a thermal light curve is useful for constraining these parameters. In particular, the amplitude of the thermal lightcurve is largely affected by the elongation/oblateness and orientation of the spin pole. In principle, constraints can be placed on the spin pole — or spin *direction* — of objects because the temperature distribution is affected by the sub-solar latitude and thus the spin pole (Müller et al., 2011, 2012, 2014). Figure 1.1(c) shows the variation of the flux for an ellipsoid at different viewing geometries. Gathering multiple thermal lightcurves can offer amplitude measurements at different viewing geometries, which can drastically increase the chance of constraining the global shape. Both Morrison (1977) and Hansen (1977b) correctly determine the spin direction by observing the change in diameter estimates for data acquired before and after opposition. The diameter estimate of (1) Ceres, a prograde rotator, before opposition was 5% larger than the diameter estimates from post-opposition observations. Müller et al. (2014) explicitly mentions that observations at either side of opposition are useful indicators of the spin direction. As shown in figure 1.1(a), this effect is due to the flux excess emitted from the hotter afternoon side of a prograde rotator as it is would be observed before opposition (e.g., Lagerros, 1996).

1.2.5 Motivation for this Work

The text and figure above demonstrate how multi-wavelength thermal lightcurve observations that span across an object's blackbody peak region, at both pre- and post-opposition (with $\Delta\alpha > 40°$), contain information directly dependent on an object's physical properties.

Thermal inertia, surface roughness, and spin direction can all be constrained from measurements of an object's thermal phase curve, particularly when observations widely vary in solar phase angle. Additionally, thermal lightcurve amplitude measurements at more than one viewing geometry are a unique indicator of the elongation of a rotating object — in this work, referring to the a/b axis ratio of a prolate ellipsoid. The work described in the rest of this chapter demonstrates and quantifies the effectiveness of using an ellipsoidal TPM to model the thermophysical properties of any given asteroid, given the observation circumstances described above.

1.3 Thermophysical Model Description

The TPM approach described here involves calculating surface temperatures for a spherical and various prolate ellipsoids in order to model and fit pre- and post-opposition multi-wavelength thermal observations. Both a smooth and rough surface TPM were developed for use in the fitting routine.

1.3.1 Smooth TPM

In development of the smooth TPM, I find it particularly useful to parameterize the depth variable in equation (1.3) as $x' = x/l_s$ (Spencer et al., 1989), where l_s is the thermal skin depth, the length scale at which the amplitude of the diurnal temperature variation changes by a factor of $e_N \approx 2.718$:

$$l_s = \sqrt{\frac{k}{\rho c_s}\frac{P_{rot}}{2\pi}}, \tag{1.6}$$

where P_{rot} is the rotation period of the body. This parameterization transforms the temperature gradient term in equation (1.2) as follows:

$$k\frac{dT}{dx}\bigg|_{surf} \Rightarrow \Gamma\sqrt{\frac{2\pi}{P_{rot}}}\frac{dT}{dx'}\bigg|_{surf}. \tag{1.7}$$

In order to further reduce the number of independent input variables, I also parameterize the temperature and time as $T' = T/T_{eq}$ and $t' = 2\pi t/P_{rot}\Theta$. The thermal parameter[3], Θ, is given by:

$$\Theta = \frac{\Gamma}{\varepsilon_B \sigma_0 T_{eq}^3}\sqrt{\frac{2\pi}{P_{rot}}}. \tag{1.8}$$

Spencer et al. (1989) introduced this dimensionless parameter, which accounts for factors that affect the diurnal temperature variation. This parameter was realized by comparing the diurnal rotation of a body to the timescale in which thermal energy is stored and then re-radiated, per unit surface area (Spencer et al., 1989). Ignoring the effects of multiple-scattering and self-heating, this parameterization scheme changes equation (1.2) to

$$\cos(i_\angle) + \Theta \left.\frac{dT'}{dx'}\right|_{surf} - T'^4_{surf} = 0, \tag{1.9}$$

and equation (1.3) to

$$\frac{\partial T'(x',t')}{\partial t'} = \Theta \frac{\partial^2 T'(x',t')}{\partial x'^2}. \tag{1.10}$$

Surface temperatures are calculated across the surface of a sphere by solving equation (1.10), given the upper boundary condition equation (1.9). Because the amplitude of diurnal temperature changes decreases exponentially with depth, the heat flux approaches zero, and the lower boundary becomes:

$$\left.\frac{dT'}{dx'}\right|_{x'\to\infty} = 0. \tag{1.11}$$

Using the parameterized depth, time, and temperature, the number of input variables in this model is effectively reduced to two (the thermal parameter and sub-solar latitude). A finite-difference approach is used to numerically implement equation (1.10), as detailed in appendix A. This spherical, smooth-surface TPM consisted of 13 latitude bins and was run for 46 values of sub-solar latitude (0° to 90° in 2° increments) and 116 values of the thermal parameter (spaced equally in logarithmic space, from 0 to 450) in order to generate the surface temperature look-up tables of T'. These values are chosen because the step sizes

[3]For reference, objects with $\Theta = 0$ exhibit surface temperatures in equilibrium with the insolation, and objects with $\Theta > 100$ have nearly isothermal surface temperatures at each latitude.

allow for the accurate (within 1%) linear interpolation of surface temperatures calculated for these predefined parameters.

1.3.2 Rough TPM

My rough, surface-cratered TPM is similar to that originally presented by Hansen (1977a), which was improved upon by both Spencer (1990) and Emery et al. (1998) to include heat conduction, multiple scattering of insolation, and re-absorption of thermal radiation within spherical craters. Following the procedure of Emery et al. (1998), craters are constructed with $m = 40$ planar elements contained within $k = 4$ rings that are radially symmetric about the crater center. The kth ring outward contains $4k$ elements, all of which are forced to have the same surface area (see Figures 1 and 2 in Emery et al., 1998, for crater depiction). As was mentioned by Spencer (1990), craters with more than four rings significantly increase the overall computational time and do not enhance the model resolution over the four-ringed crater in most cases. The overall geometry of these craters is characterized by the half-opening angle, γ, as measured from the center-line of the crater: the line connecting the center of the spherical crater to its edge — e.g., a hemispherical crater has $\gamma = 90°$. The overall degree of surface roughness is characterized by the mean surface slope ($\bar{\theta}$; Hapke, 1984), which is only a function of γ and the fraction of area covered by craters, f_R (Lagerros, 1996):

$$\tan\bar{\theta} = \frac{2f_R}{\pi}\frac{\sin(\gamma) - \ln[1+\sin(\gamma)] + \ln[\cos(\gamma)]}{\cos(\gamma) - 1}. \tag{1.12}$$

As shown in Emery et al. (1998), the fraction of energy transferred to one crater element from another is (conveniently) equal among all elements. The scattered solar and re-absorbed thermal radiation received by the ith crater facet from the j facet are

$$E^{solar}_{i,scat} = \frac{S_\odot(1-A)}{R^2_{\rm AU}}\frac{A}{1-A\frac{\gamma}{\pi}}\frac{1-\cos(\gamma)}{2m}\sum_{i\neq j}^{m}\cos(i_{\angle j}) \tag{1.13}$$

and

$$E^{therm}_{i,abs} = \frac{1-\cos(\gamma)}{2m}(1-A_{th})\sum_{i\neq j}^{m}\varepsilon_B\sigma_0 T_j^4, \tag{1.14}$$

respectively, in which A_{th} is the Bond albedo at thermal-infrared wavelengths. The energy balance at the surface (equation (1.2)), in my parameterized time, temperature, and depth environment, becomes:

$$\cos(i_\angle)(1-s)+\frac{1-\cos(\gamma)}{2m}\left(\frac{A}{1-A\frac{\gamma}{\pi}}\sum_{i\neq j}^{m}\cos(i_{\angle j})+(1-A_{th})\sum_{i\neq j}^{m}T_j'^4\right)+\Theta\left.\frac{dT'}{dx'}\right|_{surf}-T'^4_{surf}=0. \tag{1.15}$$

Because planetary surfaces are highly absorbing at infrared wavelengths, A_{th} is assumed to be zero. Thus, only singly scattered reaborption of thermal emission within the crater is considered, in contrast to multiple scattering and reabsorption of the insolation. Temperature lookup tables are generated for craters of the same values of sub-solar latitude and thermal parameter as the smooth surface TPM runs. This was done for three sets of craters of varying opening angle, in order to simulate changes in roughness. Unlike the parameterized version of the smooth surface energy balance equation, A is included as an independent input parameter, requiring me to explicitly account for changes in this parameter. Fortunately, it only appears in the solar scattering term, which is not a major contributor to the total energy budget. My spherical, rough-surface TPM consists of 13 different latitude bins and was run for 3 values of $\gamma = \{45°, 68°, 90°\}$, 46 values of sub-solar latitude (0° to 90° in 2° increments), 116 values of the thermal parameter (spread out in logarithmic space, from 0 to 450), and 7 values of $A_{grid} = \{0, 0.1, 0.2, 0.3, 0.4, 0.5, 1\}$[4] to construct this large set of T' lookup tables. Similar to the smooth TPM, these parameters are chosen since they provide sufficient resolution to ensure an accuracy within 1% between the surface temperature values interpolated from the grid and those calculated using the exact model parameters.

1.3.3 Non-spherical Shapes

Shape model facet temperatures are independent of one another in my TPM because global self-heating does not occur on the spherical and ellipsoidal shapes considered here. Because the insolation upon a facet is only dependent on the orientation of the surface normal to the

[4]I omit values of A between 0.5 and 1 because asteroid bond albedos are rarely this large.

sun, it is possible to map, or transform, surface temperatures from one shape to another. I exploit this fact in order to map the surface temperatures from a spherical body to convex DAMIT shape models and ellipsoids. I make use of two kinds of coordinate systems, which are depicted in figure 1.2. The *body-centric* (θ, ϕ) coordinate system defines the latitude and longitude of a facet relative to the center of the shape model. Shape model facets are often described using sets of vectors, $\mathbf{r}$, given in body-centric coordinates. Alternatively, the *surface-normal* coordinates (ϑ, φ) quantify the tilt of a facet relative to the local surface. Both ϑ and φ are calculated using the surface normal vector $\mathbf{n}$ shown in figure 1.2 (for a sphere, the body-centric and facet-normal coordinates are equivalent). For any given facet, on any convex shape model, the temperatures can be equated to a facet on a sphere that has the same surface-normal coordinates. This equivalency holds when equal amounts of small-scale roughness — such as the spherical section crater approximation — are used between the two shape models. In appendix B I derive closed-form analytic expressions to map temperatures from a sphere to the effective coordinates of a triaxial ($\mathsf{a} \geq \mathsf{b} \geq \mathsf{c}$) ellipsoid.

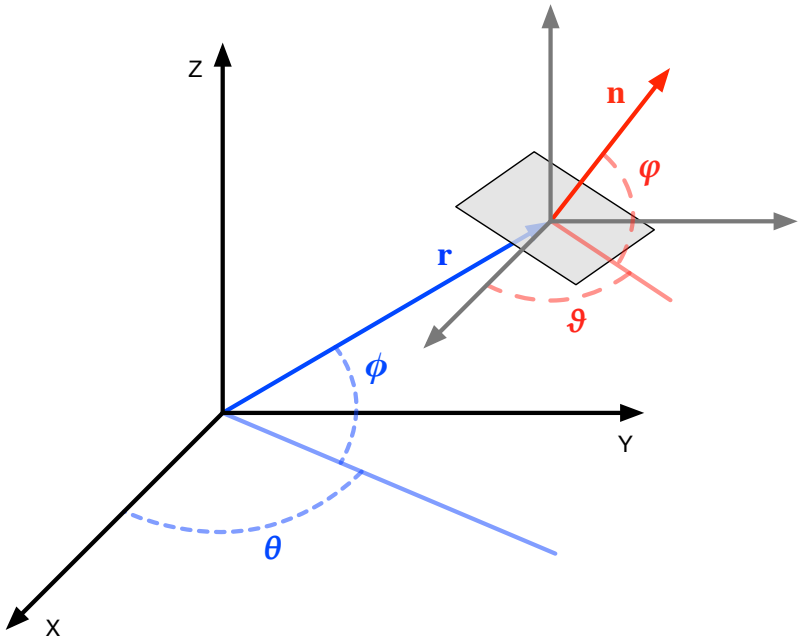

Figure 1.2: The coordinate systems used for a hypothetical planar facet, shown in grey. In blue: body-centric longitude and latitude, θ and ϕ, repsectively. In red: the surface-normal longitude and latitude, ϑ and φ, respectively.

1.3.4 Flux Calculation and Data-fitting Routine

Thermal flux is calculated by a summation of the individual flux contributions from smooth surface and crater elements visible to the observer (i.e., equation (1.18)). To calculate the flux of an object not having exact Θ or sub-solar latitude values included in my lookup temperature tables, I calculate the fluxes for the closest grid points and perform a linear interpolation to compute the fluxes for the desired parameters. Instead of doing the same for A, I calculate the flux for a value from A_{grid} and then multiply by an adjustment factor, Λ. This approach saves time and computational cost by not computing an interpolation across three variables (or dimensions). A similar approach was described by Wolters et al. (2011), in which they calculated fluxes for a perfectly absorbing surface and employed a correction factor based on the desired A. Here, Λ was tested empirically and adjusts the model flux based on the blackbody T_{eq} curves of the desired A and the closest value of A_{grid}:

$$\Lambda(A, A_{grid}) = \frac{1}{2}\left[1 + \left(\frac{B(\lambda, T_{eq}(A_{grid}))}{B(\lambda, T_{eq}(A))}\right)^{2/3}\right]. \tag{1.16}$$

The χ^2 goodness-of-fit statistic is evaluated using the modeled flux points, $F_m(\lambda)$, and the observed flux measurements, $F_o(\lambda)$, with the associated 1σ uncertainty, σ_o, and in general:

$$\chi^2 = \sum \frac{(F_m(\lambda) - F_o(\lambda))^2}{\sigma_o^2}. \tag{1.17}$$

I note here that, instead of individual flux measurements, the modeled and observed fluxes used in equation (1.17) represent only the extracted mean and peak-to-trough range of thermal lightcurve fluxes, along with their uncertainties as calculated via error propagation. As part of the data-fitting routine, the free parameters of the model are varied in order to minimize the goodness-of-fit as described in the following subsection.

A weighted sum of fluxes is used to simulate a surface that is comprised of both smooth and rough surface patches:

$$F(\lambda) = \frac{\varepsilon_\lambda}{\Delta_{\mathrm{AU}}^2} \iint_S \{(1 - f_R)B_{smooth}(\lambda, T(\theta, \phi)) + f_R(1 - v)\Lambda B_{rough}(\lambda, T(\theta, \phi, i_\angle))\} \cos(e_\angle) dA. \tag{1.18}$$

Here, Δ_{AU} is the observer-centric distance in astronomical units and $e_{\angle}$ the angle between a surface facet's local zenith and the direction of the observer (emission angle). The visibility factor, v, is analogous to the shadowing factor; $v = 1$ if a facet is hidden from view, otherwise $v = 0$. Each point on the surface is treated as a blackbody emitter with wavelength-dependent emissivity, ε_λ and temperature, $T = T_{eq}T'$:

$$B(\lambda, T) = \frac{2hc_0{}^2}{\lambda^5} \frac{1}{\exp(hc_0/\lambda k_b T) - 1}, \tag{1.19}$$

with Planck's constant, h, the speed of light, c_0, and Boltzmann's constant, k_b.

At each epoch, both the mean flux and peak-to-trough range of the thermal light curve are extracted and used in the model fitting procedure. As alluded to in section 1.2, these two parameters contain diagnostic information about the object's shape, spin direction, and thermophysical properties; they can be easily extracted from non-dense thermal lightcurve data. In principle, it is just as feasible to fit models to each independent flux point that contributes to an object's infrared lightcurve. Doing so could offer insight into the shape, as departures from a sinusoidal lightcurve can indicate relative topographic lows or highs. However, such an approach works best in cases in which the thermal lightcurve is densely sampled, which is often not the case in untargeted astronomical surveys such as IRAS, Akari, and WISE. In this work, I focus on estimating only the elongation of a body by incorporating the photometric range (peak-to-trough) of the thermal lightcurve. TPM fitting to sparse thermal lightcurves is prone to systematic parameter bias from oversampling and/or heteroscedastic uncertainties across many rotational phases, which can unevenly emphasize certain rotational phases over others, thus skewing the best-fit parameters. An example of this would be a scenario in which peaks of the modeled lightcurve were fit better with the observed lightcurve minima, thus resulting in an overall lower best-fit modeled fluxes. However, the capacity and capability of incorporating thermal lightcurve data into the shape model inversion process, when it is combined with visible lightcurve data, should be explored further (Ďurech et al., 2014, 2015).

In my data-fitting approach, the shape, spin pole (λ_{eclip}, β_{eclip}), roughness, and thermal inertia are left as free parameters that I select from a predefined sample space. I search for

the best-fit D_{eff}, which also uniquely defines a value of p_V using H_V and equation (1.4). A sphere and ellipsoids with b/c = 1 (i.e., prolate) with a/b axis ratios of 1.25, 1.75, 2.5, and 3.5 are used. For each of these shapes, I sample through 25 predefined thermal inertia values, 3 default roughness ($\bar{\theta}$) values, and 235 spin vectors. Following Table 1 in Delbo' and Tanga (2009), each value of γ is paired with a corresponding $f_R = \{1/2, 4/5, 1\}$ value in order to produce default mean surface slopes of $\bar{\theta} = \{10°, 29°, \text{and } 58°\}$. The thermal inertia points are evenly spread in log space from 0 to 3000 J m^{-2} K^{-1} s$^{-1/2}$, and the spin vectors are spread evenly throughout the celestial sphere. For each shape/spin pole/Γ combination, I use a routine to find the D_{eff} value which minimizes χ^2.

The grid of spin vectors are formed by constructing a Fibonacci lattice in spherical coordinates (Swinbank and Purser, 2006). Here, a Fermat spiral is traced along the surface of the celestial sphere, using the golden ratio ($\Phi \approx 1.618$) to determine the turn angle between consecutive points along the spiral. The result is a set of points with near-perfect homogeneous areal coverage across the celestial sphere. This Fibonacci lattice constructed here uses $N = 235$ points, with the lth point ($l \in [0, N-1]$) having an ecliptic latitude and longitude of

$$\beta^l_{eclip} = \arcsin\left(\frac{2l - N + 1}{N - 1}\right) \tag{1.20}$$

and

$$\lambda^l_{eclip} = 2\pi l \Phi^{-1} \bmod 2\pi, \tag{1.21}$$

respectively. The mean flux value and the peak-to-trough range at each wavelength and at each epoch are taken as input to equation (1.17). The Van Wijngaarden-Dekker-Brent minimization algorithm, commonly known as *Brent's Method* (Brent, 1973), combined with the golden section search routine (§10.2 in Press et al., 2007), is used because it does not require any derivatives of the χ^2 function to be known. The algorithm uses three values of χ^2 evaluated at different input diameters to uniquely define a parabola. The algorithm used the minima of these parabolas to iteratively converge on the D_{eff}/A combination that corresponds to the global minimum of χ^2 value to within 0.01%.

The values of D_{eff} and A are linked through equation (1.4) and equation (1.5) for a smooth surface, but the effect of multiple scattering alters the energy balance, and thus

effective albedo (Mueller, 2007)[5], for a cratered surface:

$$A_{crater}(\gamma) = A\frac{1-\sin^2(\gamma/2)}{1-A\sin^2(\gamma/2)}. \tag{1.22}$$

An object having an areal mixture of both smooth and rough topography has an *effective* bond albedo, A_{eff}, which is a weighted average of the albedo of a smooth surface and the bond albedo of a crater A_{crater} (Wolters et al., 2011):

$$A_{\mathit{eff}}(f_R, \gamma) = (1-f_R)A + f_R A_{crater}. \tag{1.23}$$

To place confidence limits on each of the fitted parameters, I use the χ^2 values calculated during the fitting procedure. In general, the χ^2 distribution depends on ν degrees of freedom (three in the present work), which is equal to the number of data points (constraints; eight in this work, as described in section 1.4.1) minus the number of input (free; five in this work) parameters. Because the χ^2 distribution has an expectation value of ν and a standard deviation of $\sqrt{2\nu}$, the best-fit solutions cluster around $\chi^2_{min} = \nu$, and those with $\chi^2 < (\nu + \sqrt{2\nu})$ represent 1σ confidence estimates[6]. However, because of the TPM assumptions (e.g., no global self-heating, homogeneous thermophysical properties), it is often possible for the TPM to not perfectly agree with the data, in which case $\chi^2_{min} > \nu$. In this case, I use $\chi^2/\chi^2_{min} < \nu + \sqrt{2\nu}$ to place 1σ confidence limits. This modification effectively scales the cutoff bounds by a factor of χ^2_{min}, instead of adopting the traditional approach of using a constant χ^2 distance cutoff. This scaling of the χ^2 cutoff bounds is a more conservative approach in quoting parameter uncertainties, as it includes the systematic uncertainties that lead to the larger χ^2_{min} in the reported parameter uncertainties. Using the *reduced* χ^2 statistic ($\tilde{\chi}^2 = \chi^2/\nu$), I can express the solutions within a 1σ range as $\tilde{\chi}^2 < \tilde{\chi}^2_{min}(1 + \sqrt{2\nu}/\nu)$.

In section 1.5, I report TPM results for all of the objects that I analyzed, even those with a high χ^2_{min} (indicating a poor fit to the data), which are considered unreliable and should only be used with caution.

[5]The crater opening angle used in Mueller (2007) is twice that used here.

[6]Consequently, $\chi^2 < (\nu + 2\sqrt{2\nu})$ and $\chi^2 < (\nu + 3\sqrt{2\nu})$ give the respective 2 and 3σ confidence limits.

1.4 Method Testing and Validation

Section 1.2 describes how pre- and post-opposition multi-wavelength thermal observations are able to simultaneously constrain multiple thermophysical (albedo, thermal inertia, and surface roughness) and physical (diameter, shape, and spin direction) properties of an object. In this section, I present results from a proof-of-concept test of the ability to constrain the above parameters with WISE pre- and post-opposition observations. In performing this test, I generate an artificial flux dataset from shape models from DAMIT (Ďurech, 2010) as a benchmark for testing the accuracy and precision of my TPM approach. Specifically, I search for and quantify any biases that may exist among each fit parameter. I also include a comparison to the uncertainty estimates to typical values found in previous works.

1.4.1 Synthetic Flux Data Set

Table 1.1 lists the objects, DAMIT shape models used, the associated rotation periods, and the effective diameter, as computed beforehand via a NEATM fit to the real WISE observations. The observing geometries used in the synthetic model runs are the same as the WISE observations given in section 1.5. I calculate the artificial thermal emission for WISE photometric filters W3 and W4 (12 and 24 μm) for a full rotation of the shape. From these infrared lightcurves, I extract the mean and peak-to-trough flux range for each filter as input into my fitting routine (equation (1.17)). Because I now have these two quantities, observed twice for two wavelengths, there are eight data points to constrain five free parameters: diameter, thermal inertia, surface roughness, shape elongation, and sense of spin. Fluxes for each shape model are calculated using the TPM described here by using the actual WISE observing circumstances described in section 1.5. If an object has two shape models available — a result of ambiguous solutions of the lightcurve inversion algorithm — then both were included in the analysis.

Table 1.1: Shape Models and Properties for Synthetic Data Set

Object	Shape Model	$\mathsf{a/b}^{\text{synth}}$	λ_{eclip}, β_{eclip}	P_{rot} (hr)	$D_{\mathit{eff}}^{\text{synth}}$ (km)	H_V	G_V
(167) Urda	M171	1.31	-69°, 107°	13.06133	43.00	9.131	0.283
	M172	1.30	-68°, 249°				
(183) Istria	M669	1.39	20°, 8°	11.76897	35.48	9.481	0.221
(208) Lacrimosa	M182	1.22	-75°, 20°	14.0769	44.35	9.076	0.232
	M183	1.23	-68°, 176°				
(413) Edburga	M354	1.37	-45°, 202°	15.77149	35.69	9.925	0.296
(509) Iolanda	M521	1.41	24°, 90°	12.29088	60.07	8.476	0.382
	M522	1.32	54°, 248°				
(771) Libera	M250	1.50	-78°, 64°	5.890423	29.52	10.28	0.323
(857) Glasenappia	M609	2.30	34°, 38°	8.20756	15.63	11.29	0.246
	M610	2.32	48°, 227°				
(984) Gretia	M256	1.57	52°, 245°	5.778025	35.76	9.526	0.379
(1036) Ganymed	M261	1.05	-78°, 190°	10.313	37.42	9.236	0.311
(1140) Crimea	M403	1.76	-73°, 12°	9.78693	31.77	9.621	0.207
	M404	1.61	-22°, 175°				
(1188) Gothlandia	M479	1.71	-84°, 334°	3.491820	13.29	11.52	0.254
(1291) Phryne	M409	2.03	35°, 106°	5.584137	27.87	10.29	0.251
	M410	2.30	59°, 277°				
(1432) Ethiopia	M657	1.27	54°, 225°	9.84425	7.510	12.02	0.282
	M658	1.32	44°, 41°				
(1495) Helsinki	M656	1.74	-39°, 355°	5.33131	13.54	11.41	0.359
(1568) Aisleen	M422	2.30	-68°, 109°	6.67597	13.60	11.49	0.131
(1607) Mavis	M477	1.56	70°, 222°	6.14775	15.10	11.32	0.256
	M478	1.93	59°, 0°				
(1980) Tezcatlipoca	M274	1.72	-69°, 324°	7.25226	5.333	13.57	0.186
(2156) Kate	M438	2.15	74°, 49°	5.622153	8.678	4.339	0.186
(4611) Vulkaneifel	M704	1.68	-50°, 197°	3.756356	12.38	11.87	0.268
	M705	1.64	-86°, 5°				
(5625) 1991 AO_2	M682	3.48	-78°, 97°	6.67412	14.25	12.83	0.165
	M683	3.18	-52°, 265°				
(6159) 1991 YH	M757	1.55	67°, 62°	10.65893	5.148	13.38	0.175
	M758	1.65	67°, 266°				

1.4.2 Model Validation Results

The best-fit TPM parameter results for the synthetic dataset are detailed below and depicted in figure 1.3. Overall, using ellipsoid shapes results in more accurate and precise estimates for diameter, thermal inertia, and shape.

Diameter Constraints Figure 1.3 includes model (synthetic) diameters and the best-fit TPM values, along with a linear fit to the data. Diameter uncertainties (not shown in the figure) are calculated by taking the typical WISE signal-to-noise value for these objects. These uncertainties are equal to or larger than the spread in the data points, indicating that the uncertainty introduced by the model assumptions are accurately captured in the parameter uncertainties. The assumption of a spherical shape results in overestimation of diameter of up to 20%, as shown in figure 1.3(a). The TPM performs better when using ellipsoid shapes; at most, diameters are overestimated by 10%. These offsets are particularly pronounced for highly elongated objects with high Θ values and when observed at large sub-solar latitude values. In these cases, the average observed cross-sectional area is particularly large and surface temperatures are, on average, warmer (figure 1.1(c)), since a larger fraction of the surface experiences perpetual daylight. Diameter uncertainties when using ellipsoid shapes are consistent with the $\pm$10% value seen in other thermophysical modeling papers, yet seem to imply a drop in accuracy from the NEATM (Harris, 2005). However, care must be taken when comparing the performance results presented here, which are based on synthetic data generated from shape models with various spin vectors, and those presented by Harris (2005), which uses an idealized synthetic dataset generated from spherical shapes with no obliquity. The work of Wright (2007), who included rough spheres in their performance test of NEATM, shows diameter accuracy of the NEATM to be on par with TPM works, such as this one.

Thermal Inertia/Parameter Constraints I transform thermal inertia estimates into thermal parameter space equation (1.14), because the rotation periods of synthetic objects affect the temperature distribution and must be taken into account. Panels (c) and (d) in figure 1.3 show the estimated Θ values for the spherical and best-fit ellipsoidal shape,

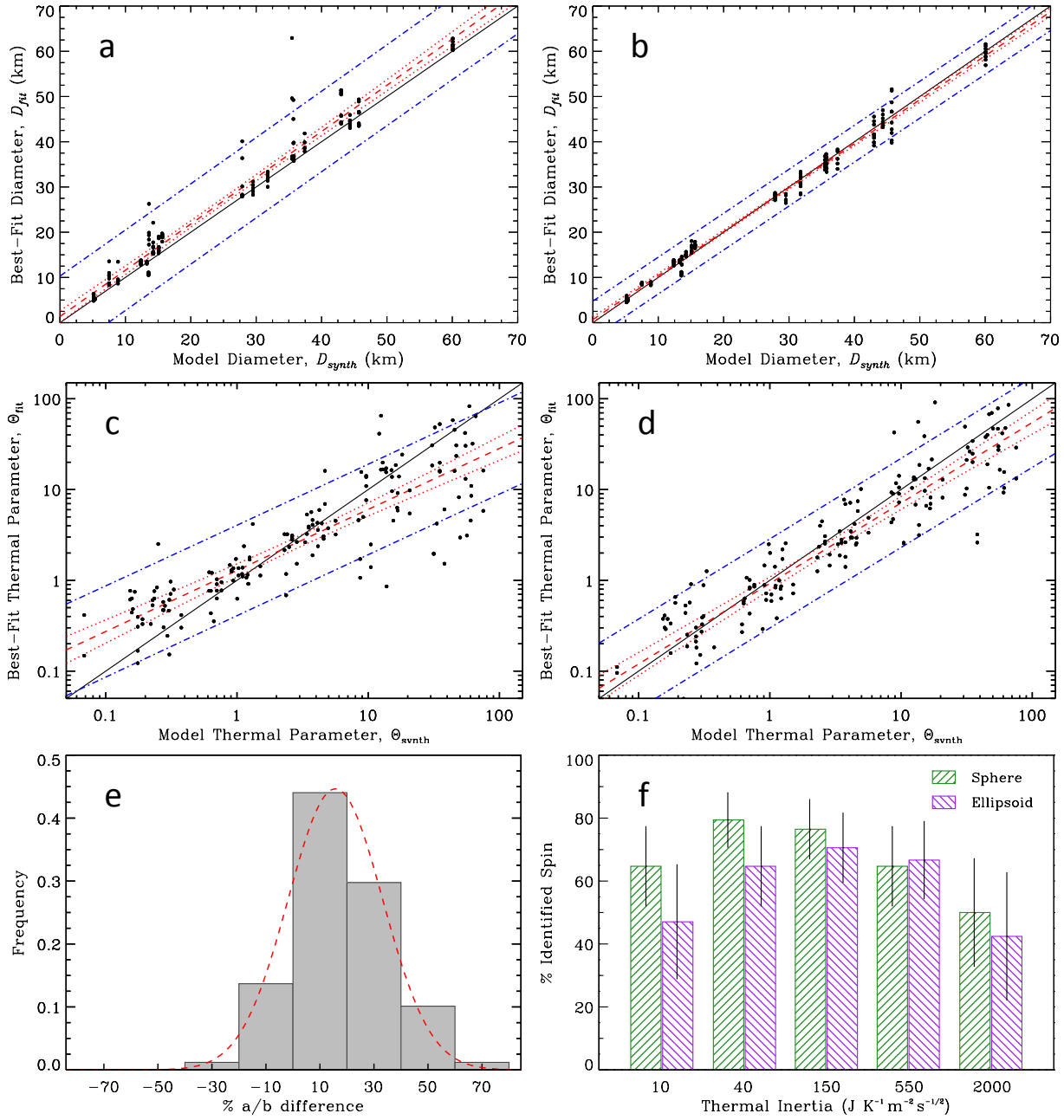

Figure 1.3: The best-fit diameter vs. model diameter for spherical (a) and ellipsoidal (b) TPM shape. Panels (c) and (d) show the same for Θ. The red dashed and dotted lines show the best fit to the data and the corresponding 95% confidence interval. Blue, dashed-dotted lines show the 68% prediction interval. Panel (e) shows the fractional difference in DAMIT area-equivalent a/b to the best fit ellipsoid, expressed as a percentage. Lastly, the percentage of TPM solutions that correctly identifiy the spin direction is given in panel (f).

respectively, against the synthetic values. When a sphere is used for a TPM, thermal inertia is overestimated at low values and underestimated at large Θ values. At either extreme of Θ, this offset is systematically different by a factor of $\sim$4. Ellipsoidal shapes do a much better job matching the input Θ, with systematic offsets of less than 25% (red dashed line in figure 1.3(d)). I investigate this discrepancy further in section 1.4.3, but note here that the estimated uncertainties (not shown), calculated from WISE signal-to-noise ratios for each object, are far larger than the systematic offset, indicating that the assumptions in my TPM fitting do not contribute significantly to the overall uncertainty in thermal inertia and the χ^2-based errors values reasonably reflect the overall precision in my TPM.

Shape Constraints To assess how well my method is able to constrain the shape (elongation) of an object, I compare the best-fit ellipsoid $\mathsf{a/b}$ to that of the area-equivalent $\mathsf{a/b}$ ratio of the DAMIT shape model. Because I use a sparse grid of possible $\mathsf{a/b}$ values, placing meaningful confidence bars based on χ^2 values is not practical. Instead, in figure 1.3 I plot the frequency distribution of the percent-difference between the $\mathsf{a/b}$ of the preferred ellipsoid solution ($\mathsf{a/b}_{\mathrm{ellip}}$) to the equivalent $\mathsf{a/b}$ of the projected cross-sectional area of the DAMIT shape model ($\mathsf{a/b}_{\mathrm{DAMIT}}$): $\mathsf{a/b} = \left(\frac{\mathsf{a/b}_{\mathrm{ellip}}}{\mathsf{a/b}_{\mathrm{DAMIT}}} - 1\right) \times 100\%$. Fitting a Gaussian function (16%, with a standard deviation of 18%) to the distribution shows that the assumptions within the model, most likely the use of a prolate ellipsoid ($\mathsf{b/c} = 1$), result in a slight overestimation of the $\mathsf{a/b}$ axis. The standard deviation of this distribution is not reflective of the uncertainty in the mean offset in the shape accuracy, but rather of the inherent model uncertainties that arise from assuming an ellipsoid shape. Accounting for this discrepancy, I shift the TPM best-fit shape result downward by 16% and assign an uncertainty of 18%.

Spin Constraints I also investigated the ability to constrain the spin direction of an object (i.e., retrograde or prograde rotation). In total, the ellipsoid TPM correctly identified the spin direction for $58.3 \pm 6.5\%$ of the occurrences, compared to $67.1 \pm 5.7\%$ for the spherical TPM. In section 1.2.4, I pointed out that thermal inertia is a significant factor when constraining spin direction. Thus, I break down my results into the thermal inertia bins assigned for the artificial dataset. Figure 1.3(f) shows the percentage of best-fit solutions, broken down

by sphere/ellipsoid shape assumption, in which spin direction was correctly identified for a given thermal inertia. It is clear that intermediate values of thermal inertia provide more reliable constraints on the spin direction, which can be explained by the increased asymmetry of thermal phase curves at intermediate values of thermal inertia. More extreme (low and high) values of thermal inertia result in more symmetric thermal phase curves, which make it difficult to distinguish morning and afternoon hemispheres — and thus spin direction (figure 1.1(a)). One caveat to point out here is that rotation period plays a secondary role to the thermal inertia in determining this asymmetry. For example, using the definition of the thermal parameter, one can deduce that a doubling of the thermal inertia has the same effect on the diurnal temperature curve (and by extension, the thermal phase curve) as does quadrupling the rotation period.

1.4.3 Parameter Bias Analysis

I performed a linear multiple linear (multi-linear) regression analysis on the percent diameter and Θ difference ($\%\Delta D_{\mathit{eff}}$ and $\%\Delta\Theta_{\mathit{eff}}$, between the synthetic and TPM estimates) to distinguish which factors, if any, bias the estimates. The predictor variables chosen were $\log_{10}(\Theta)$, the sub-solar latitude (s-s lat.; relevant to Θ) or sub-observer latitude (s-o lat.; relevant to D_{eff}), and the elongation of the shape model ($\mathsf{a/b}^{\mathrm{synth}}$), because they are the most likely to affect the response variable (section 1.2). The regression models the response variable — the percent difference in diameter or Θ — as being linearly-dependent on the sum of any number of independent predictor variables — in this case four. For each predictor, the regression model computes a slope coefficient that represents the change in that variable when all others are held constant. An intercept term, quantifying the value of the response when all predictors are zero, is also computed. Table 1.2 shows the slope coefficients, intercepts, and the associated p-values that indicate the statistical significance of each predictor variable in the multi-linear regression model. I use $p < .05$, representing a 95% confidence level, to identify predictor variables that affect the response variable (p-values that are larger than this cutoff indicate that the predictor variable has little-to-no statistically relevant effect on the response variable).

Table 1.2: Multi-linear Regression Results

	$\%\Delta D_{eff}$		$\%\Delta\Theta$	
	coefficient	p-value	coefficient	p-value
D_{eff}^{synth}	-0.0009 ± 0.0004	.02	0.0012 ±0.0017	.48
$\log_{10}(\Theta^{synth})$	-0.0037 ± 0.0067	.59	-0.1390 ± 0.0292	$< .01$
s-s lat.^{synth}	—	—	-0.0036 ± 0.0024	.12
s-o lat.^{synth}	0.0024 ± 0.0005	$< .01$	—	—
a/b^{synth}	0.0085 ± 0.0119	.48	0.0573 ± 0.0507	.26
intercept	-0.0264 ± 0.0319	.41	-0.0621 ± 0.1357	.65

The diameters calculated from my approach are overestimated when observations occur at high sub-observer latitudes ($p < .01$) and for small diameters ($p = .02$) as marked in grey in table 1.2. From the multi-linear regression results performed on Θ, the only predictor that explains the variance in response variable is Θ^{synth}, marked in table 1.2 with grey: the negative sign represents an overestimation for small Θ and/or underestimation at large Θ. A re-examination of panel (d) in figure 1.3 shows that this dependency is apparent for $\Theta > 6$. For lower values of Θ, the best-fit line is likely skewed upward due to the underestimation at the larger end. Thus, I employ a formulation to correct objects for which $\Theta > 6$:

$$\Theta_{corr} = 10^{\left(\frac{b_1}{1+b_2}\right)}\Theta^{\left(\frac{1}{1+b_2}\right)}. \tag{1.24}$$

To determine the correction factor, I fit a line to objects with $\Theta > 4$ (shown by the purple-dotted line in figure 1.4) and compute $b_1 = 0.026$ and $b_2 = -0.136$. This fit provides a means of removing the systematic underestimation in thermal parameter, and by proxy, thermal inertia. The bias seen in panel (d) of figure 1.3 vanishes; as shown by the red best-line in figure 1.4 re-computed after using equation (1.24) to adjust the $\Theta^{synth} > 6$ values. Objects with thermal parameters this large can more often found for objects with unusually high thermal inertia and/or rotate very slowly — or for icy bodies with low surface temperatures in the outer solar system (e.g., Table 1 in Spencer et al., 1989).

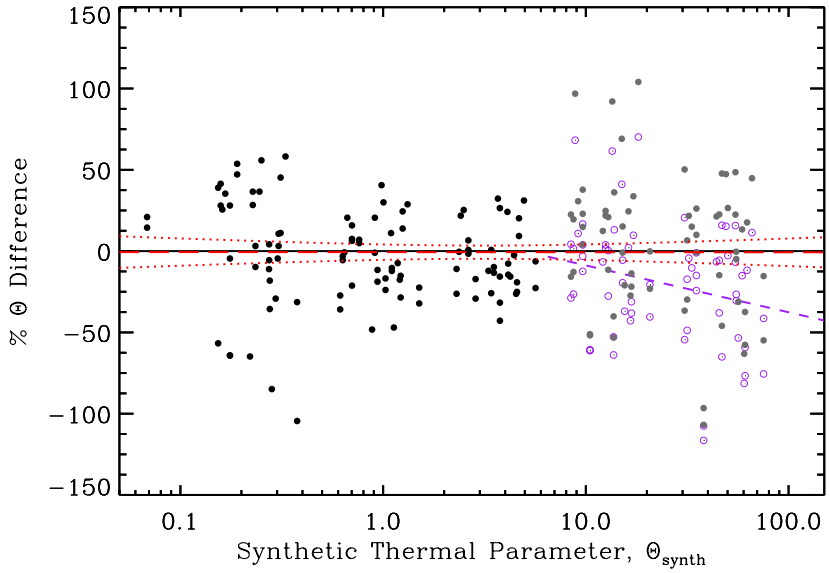

Figure 1.4: Percent difference between synthetic and best-fit Θ as a function of the synthetic (known) value. For $\Theta > 6$, I derive a formula to adjust the underestimation (open purple circles) such that the corrected values (grey dots) are symmetric about zero percent difference, represented by the black horizontal line. The red best-fit line to the black and grey dots has a slope of nearly zero and shows no evidence for a bias at either Θ extreme.

1.4.4 Other Possible Sources of Bias

Upon closer inspection of the multi-linear regression results, I see that the skew at small sizes is due to particular objects being observed at high latitudes rather than by the intrinsic diameter of the object. The effect that the viewing geometry has on the size estimation can be explained by the fact that the thermal lightcurve-averaged flux does not properly represent the effective diameter. For the extreme case of observations taken from a "pole-on" geometry, the thermal flux represents the largest feasible cross-sectional area, which would result in the overestimation of diameters, regardless of the shape used in the TPM.

In some of the largest publications of independently derived thermal inertias (Delbo' and Tanga, 2009; Hanuš et al., 2015, 2018), convex shape models were used in the TPM approach. One critique of using convex shape models is that actual asteroids can potentially harbor shape concavities, which raises potential concern as to whether or not large deviations from a spherical shape will bias the temperature distribution in any significant way (Rozitis and Green, 2013). Radar observations of the near-Earth asteroid (NEA) (341843) 2008 EV_5 showed a large concavitiy, and thermal observations were analyzed in detail by Alí-Lagoa

et al. (2014). They found no evidence that the concavity influenced the results, as its effects on the thermal emission (i.e., shadowing and global self-heating) were likely below the signal-to-noise of the observations. Using a larger set of shape models with concavities, Rozitis and Green (2013) demonstrated that the effects of global self-heating and shadowing have negligible effects on the temperature distribution, compared to those of thermal inertia and surface roughness; this is consistent with the findings of Lagerros (1997), who investigated the effect using random Gaussian shapes. All of these studies justify the use of convex, prolate ellipsoid studies in my TPM approach.

Although not the case here, thermal inertia bias could arise if the size is fixed during the fitting procedure. For example, diameters that are estimated from radar observations can suffer from an overestimated z-axis if the object is observed at near-equatorial view, yielding a higher thermal inertia (Rozitis and Green, 2014). Some studies have investigated how changes in shape and spin pole can affect the value of thermal inertia. Using both a spherical and radar shape model for the asteroid (101955) Bennu, Emery et al. (2014) found that the radar shape model gave a lower thermal inertia result compared to a spherical shape with the same spin pole. The lower thermal inertia is explained by the oblateness of Bennu, as surface facets are systematically tilted away from the sun-direction, cooling the surface temperatures relative to that of a sphere and requiring a lower model thermal inertia to compensate. As briefly mentioned before, my use of prolate ellipsoids may likely be the cause of overestimation of the elongation of objects. For example: if I were to make $b/c = 1.1$, the average orientation of the shape facets would be directed away from the sun and effectively lower the modeled surface temperatures. By lengthening the b semi-axis, there is less need to lengthen the a semi-axis in order to match the surface temperature.

It is becoming increasingly common for thermal infrared observations to be used to refine the detailed shape models created from the delay-Doppler radar and/or the visible lightcurve inversion techniques Ďurech et al. (2017). Shape models from these methodologies can sometimes yield an incorrect z-axis if the object is observed nearly equator-on (Rozitis et al., 2013; Rozitis and Green, 2014). In short, thermal data constrain the effective diameter — and by extension, the z-axis dimension — if the x- and y-axis dimensions were known to great accuracy from the observations. Additionally, Hanuš et al. (2015) utilized thermal

infrared data to refine convex shape models derived from lightcurve inversion. They varied a convex shape model within the uncertainty of the photometric errors to generate a set of shapes that were used to generate thermal fluxes from a TPM, which were then fit to WISE observations. Although not much work has been done to derive new shapes from only disk-integrated thermal emission data, approaches that combine thermal observations with optical lightcurves (Ďurech et al., 2012, 2014) and other telescopic observations (e.g., stellar occultations, optical interferometry, and delay-Doppler radar; see Ďurech et al., 2015, 2017) have been employed in order to refine pre-existing shape models. Generally, the refined shape models appear smoother (Ďurech et al., 2012; Hanuš et al., 2015), which is likely in part due to the thermal emission being sensitive to large-scale curvature, especially at lower thermal inertia values (Lagerros, 1996).

1.5 Application to WISE Observations

In this section, I apply my multi-epoch TPM approach to WISE observations of asteroids that were used in my synthetic dataset. The TPM implementation on the WISE data is the same as described in section 1.3.4 except that I incorporate surface roughness in order to account for surface topography effects. I step through three default roughness values ($\bar{\theta} = 10°,\ 29°,\ 58°$) that Delbo' and Tanga (2009) used for IRAS observations.

1.5.1 Data Description

The WISE mission, an astrophysics mission designed to map the entire sky, operated in its fully cryogenic mode from 2010 January 14 to August 5 at wavelengths centered near 3.4, 4.6, 12, and 22 μm, denoted W1, W2, W3, and W4 (Wright et al., 2010). A data-processing enhancement called NEOWISE (Mainzer et al., 2011a) detected moving solar system objects, most of which were asteroids in the Main Belt and in near-Earth orbits. During each grouping of observations (an epoch), a moving object is typically detected around 10 to 20 times, in $\approx$1.6 hr multiples — the orbital period of the spacecraft. Therefore, depending on the object's range of motion on the sky, each epoch of observations can potentially span up to 36 hr.

NEOWISE reports each moving object detection to the Minor Planet Center (MPC[7]), where the start time, R.A. and decl. of each observation can be retrieved. The set of times and locations are used to parse the WISE All-Sky Single Exposure (L1b) catalog on the Infrared Science Archive (IRSA) maintained by the Infrared Processing and Analysis Center (IPAC[8]). I select detections reported to within 10″ and 10 s of those reported to the MPC. These constraints are "relaxed" relative to the accuracy of the telescope's astrometric precision, to guarantee that IPAC returns flux information for each reported MPC observation. These criteria also return many spurious detections: I discuss my method of rejecting spurious sources returned from these generous search criteria two paragraphs below.

According to the WISE Explanatory Supplement (Cutri et al., 2012), photometric profile fits are unreliable for W3 $<$ -3 mag or W4 $<$ -4 mag, due to saturation of the detector. Because non-linearity is present for sources with W3 $<$ 3.6 mag and W4 $<$ -0.6 mag, I increase the magnitude uncertainty to 0.2 mag for objects brighter than these values (Mainzer et al., 2011b). I shift the isophotal wavelengths and zero magnitude point of W3 and W4 to account for the red-blue calibrator discrepancy described in the Explanatory Supplement. The raw magnitudes that are reported were calibrated assuming that the flux across each filter was that of Vega's spectrum. Thus, a color-correction must be made to account for the discrepancy between the spectrum of the object and that of Vega (Wright et al., 2010; Cutri et al., 2012). For each individual observation, NEATM was used to calculate the flux spectrum across the full bandpass for each WISE band for use in the color correction, which ranged from 0.87 to 1.0 for W3 and was nearly constant at 0.98 for W4. Based on an analysis of asteroid flux uncertainties in consecutive frames by Hanuš et al. (2015), I increase the flux error in W3 and W4 by factors of 1.4 and 1.3, respectively.

In order to filter out bad observations of an asteroid — for example, in a situation where it passes near a background star or when the query returns a detection of an unwanted object — I employ "Peirce's criterion"[9] (Peirce, 1852; Gould, 1855) as outlined and demonstrated

[7] http://www.minorplanetcenter.net/

[8] http://irsa.ipac.caltech.edu/Missions/wise.html

[9] This procedure for rejecting outlier data points uses a criterion based on Gaussian statistics. In short, rejection of a data point occurs when the probability of the deviation from the mean obtained by retaining the data in question is less than that of the deviation from the mean obtained by their rejection, multiplied by the probability of making as many, and no more, outlier observations. The motivation for using this relatively obscure procedure is due to the fact that it makes no arbitrary assumptions about the cutoff

by Ross (2003). I flag spurious observations using this algorithm based on W4−W3, since it will identify and remove sources of an anomalous color temperature. Using color, rather than raw flux, avoids the possibility of removing seemingly anomalous observations of the minimum or maximum flux of a highly elongated object. This rejection method is a simpler alternative to that implemented by Alí-Lagoa et al. (2014) and Hanuš et al. (2015, 2018) on WISE data, in which the WISE inertial source catalog was checked explicitly for possible flux contamination of stars.

Mean fluxes, denoted as $\overline{F_{\mathrm{W3}}}$ and $\overline{F_{\mathrm{W4}}}$, were calculated by simply taking the error-weighted mean of all observations. The photometric range for each band, denoted as $\diamondsuit W3$ and $\diamondsuit W4$, was calculated by subtracting the minimum and maximum fluxes. Table 1.3 tabulates the observing circumstances and calculated lightcurve mean and range for WISE observations of the asteroids studied in this chapter. Standard error propagation was used to estimate 1σ uncertainties for each of these parameters, and then input as σ_o in equation (1.17). These bright, slow-moving objects with $P_{\mathrm{rot}} < 36$ hr have sufficient coverage in rotational phase to provide estimates of these parameters. However, some objects may have only been detected a handful of times, which could only sparsely sample the rotational phases. In chapter 2, I will develop and present a more rigorous method for accurately estimating the flux mean and range, with associated errors, from sparse lightcurve coverage.

1.5.2 Results and Discussion

A summary of my TPM fits and corresponding 1σ uncertainties for 19 main-belt asteroids (MBAs) and 2 NEAs are given in table 1.4. For diameter, albedo, and thermal inertia, uncertainties are based on the χ^2 values calculated during the fitting routine. In some cases, two values of roughness could not be distinguished with respect to one being better than the other, so both values are reported. In the case of (6159) Andreseloy, all roughness values tried provided statistically indistinguishable fits to the data. The spin direction reported for each object here reflects the preferred spin pole. Often, many spin pole solutions lie within the 1σ uncertainty bounds, so reporting a single solution would not be meaningful. The spin

for outliers and can be used to simultaneously identify multiple outliers. Peirce's criterion is rigorous and generalized in its applicability, when compared to William Chauvenet's criterion (Taylor, 1997).

Table 1.3: WISE Observation Circumstances and Fluxes

Object	UT Date[a]	$\Delta t_{\rm obs}$[b]	N[c]	$R_{\rm AU}$[d]	$\Delta_{\rm AU}$[e]	α (°)[f]	$\overline{F_{\rm W3}}$[g]	$\diamondsuit F_{\rm W3}$[h]	$\overline{F_{\rm W4}}$[g]	$\diamondsuit F_{\rm W4}$[h]
(167) Urda	9 Feb 2010	1.257	13	2.840	2.647	20.33	451.8 ± 5.2	141.6 ± 10.3	1224 ± 26	350.2 ± 65.8
	2 Aug 2010	1.257	12	2.787	2.510	−21.27	601.1 ± 7.2	185.9 ± 13.8	1559 ± 30	480.7 ± 51.1
(183) Istria	4 Feb 2010	3.772	22	3.718	3.580	15.38	87.65 ± 1.27	36.88 ± 2.57	322.7 ± 9.0	119.9 ± 16.1
	21 Jul 2010	1.257	13	3.765	3.562	−15.62	70.84 ± 1.19	43.98 ± 2.23	274.7 ± 8.0	160.0 ± 14.9
(208) Lacrimosa	10 Feb 2010	0.595	9	2.888	2.700	19.98	508.2 ± 5.7	119.8 ± 10.6	1358 ± 28	344.8 ± 57.3
	8 Aug 2010	1.257	10	2.913	2.645	−20.30	442.4 ± 4.9	97.78 ± 9.89	1269 ± 25	255.1 ± 48.3
(413) Edburga	10 Feb 2010	1.257	14	3.180	3.009	18.08	164.9 ± 2.2	72.85 ± 3.98	534.7 ± 11.5	208.9 ± 24.1
	26 Jul 2010	1.257	15	2.701	2.427	−22.01	478.4 ± 5.8	180.3 ± 11.6	1219 ± 25	410.4 ± 42.0
(509) Iolanda	18 Jan 2010	0.596	8	3.342	3.164	17.11	440.3 ± 5.1	230.6 ± 9.9	1405 ± 30	594.3 ± 67.6
	3 Jul 2010	1.257	15	3.327	3.080	−17.72	470.5 ± 6.0	216.4 ± 12.2	1461 ± 24	649.9 ± 40.7
(771) Libera	29 Jan 2010	1.257	10	2.764	2.593	20.88	223.7 ± 2.8	74.50 ± 5.24	618.4 ± 15.4	223.4 ± 28.7
	16 Jul 2010	3.903	22	3.111	2.847	−18.97	146.2 ± 2.1	75.75 ± 4.31	474.6 ± 11.2	223.2 ± 19.7
(857) Glasenappia	19 Jan 2010	1.125	14	2.329	2.085	24.99	180.8 ± 2.4	70.40 ± 5.26	373.4 ± 9.3	127.4 ± 23.6
	11 Jul 2010	1.389	17	2.172	1.823	−27.75	279.2 ± 3.5	80.68 ± 6.9	527.0 ± 12.7	164.6 ± 21.7
(984) Gretia	31 Jan 2010	1.125	9	3.324	3.188	17.24	161.3 ± 2.2	76.53 ± 4.46	531.1 ± 11.0	214.3 ± 19.9
	21 Jul 2010	1.125	10	3.159	2.920	−18.71	192.6 ± 2.5	81.18 ± 5.08	604.3 ± 14.8	258.7 ± 32.8
(1036) Ganymed	15 Jan 2010	0.860	9	3.897	3.729	14.61	72.50 ± 1.10	12.50 ± 2.16	294.7 ± 7.0	39.25 ± 14.02
	22 Jun 2010	1.125	14	3.463	3.241	−17.02	141.3 ± 2.1	27.94 ± 4.14	494.8 ± 12.1	81.66 ± 24.09
(1140) Crimea	13 Feb 2010	1.125	11	3.075	2.900	18.73	184.4 ± 2.4	77.33 ± 4.85	524.7 ± 12.0	201.6 ± 26.8
	1 Aug 2010	1.124	11	2.990	2.725	−19.76	220.7 ± 2.9	110.0 ± 5.1	624.5 ± 12.6	290.7 ± 24.4
(1188) Gothlandia	18 Jan 2010	0.992	10	2.580	2.354	22.41	59.19 ± 1.11	41.00 ± 2.05	158.7 ± 6.3	99.88 ± 12.78
	2 Jul 2010	1.389	16	2.521	2.222	−23.68	88.37 ± 1.40	58.34 ± 2.47	214.4 ± 6.8	129.9 ± 11.8
(1291) Phryne	21 Jan 2010	0.992	8	3.210	3.038	17.85	117.5 ± 1.8	122.0 ± 3.6	367.8 ± 9.7	350.8 ± 18.2
	8 Jul 2010	1.257	14	3.090	2.825	−19.12	131.0 ± 2.1	142.4 ± 4.3	393.8 ± 11.4	386.3 ± 18.9
(1432) Ethiopia	4 Feb 2010	3.771	23	2.699	2.511	21.43	15.44 ± 0.60	4.102 ± 1.217	43.91 ± 3.48	17.13 ± 8.23
	28 Jul 2010	1.389	15	2.307	1.992	−26.02	32.16 ± 0.76	7.282 ± 1.496	78.34 ± 3.84	14.90 ± 7.49
(1495) Helsinki	8 Feb 2010	4.301	19	2.490	2.284	23.33	90.81 ± 1.46	42.36 ± 3.0	208.3 ± 6.6	81.53 ± 12.85
	5 Aug 2010	1.125	10	2.267	1.940	−26.47	140.6 ± 2.0	87.26 ± 4.38	299.8 ± 8.3	154.2 ± 16.5
(1568) Aisleen	24 Jan 2010	1.125	12	2.950	2.776	19.50	27.39 ± 0.68	14.91 ± 1.37	82.59 ± 3.85	51.08 ± 7.46
	7 Jul 2010	1.257	14	3.100	2.550	−21.04	52.16 ± 0.90	21.74 ± 1.84	135.1 ± 4.8	63.58 ± 9.57
(1607) Mavis	21 Jan 2010	0.993	10	3.285	3.116	17.43	28.51 ± 0.71	20.45 ± 1.44	94.41 ± 4.53	63.07 ± 8.75
	4 Jul 2010	1.125	12	3.039	2.778	−19.47	35.16 ± 0.73	14.46 ± 1.44	107.9 ± 3.9	48.81 ± 8.31

Table 1.3 — continued

Object	UT Date[a]	Δt_{obs}[b]	N[c]	R_{AU}[d]	Δ_{AU}[e]	α (°)[f]	$\overline{W3}$[g]	$\diamondsuit W3$[h]	$\overline{W4}$[g]	$\diamondsuit W4$[h]
(1980) Tezcatlipoca	23 Jan 2010	0.992	11	2.333	2.109	24.96	13.79 ± 0.53	5.748 ± 1.041	34.52 ± 2.83	22.68 ± 5.61
	30 Jun 2010	1.257	8	2.064	1.716	−29.39	29.65 ± 0.73	18.61 ± 1.54	65.74 ± 3.46	42.50 ± 6.61
(2156) Kate	25 Jan 2010	0.992	9	2.688	2.502	21.49	23.82 ± 0.68	16.42 ± 1.38	64.43 ± 3.85	34.34 ± 8.27
	11 Jul 2010	1.126	11	2.625	2.322	−22.67	24.93 ± 0.66	15.41 ± 1.29	66.16 ± 3.66	37.33 ± 7.50
(4611) Vulkaneifel	25 Jan 2010	0.993	10	3.103	2.944	18.50	21.82 ± 0.66	10.80 ± 1.36	72.11 ± 3.44	31.03 ± 7.05
	11 Jul 2010	1.257	13	3.100	2.834	−19.05	25.08 ± 0.65	13.63 ± 1.25	81.09 ± 3.86	40.84 ± 7.26
(5625) 1991 AO_2	28 Jan 2010	0.993	11	3.180	3.032	18.04	28.80 ± 0.72	19.98 ± 1.43	91.72 ± 4.18	49.67 ± 8.86
	14 Jul 2010	1.125	13	3.168	2.900	−18.61	34.55 ± 0.83	31.91 ± 1.63	107.8 ± 4.3	100.6 ± 7.7
(6159) 1991 YH	3 Feb 2010	4.301	19	2.341	2.124	24.91	13.21 ± 0.84	11.16 ± 1.49	31.40 ± 3.64	27.42 ± 7.01
	30 Jul 2010	1.389	11	2.424	2.120	−24.67	14.90 ± 0.59	11.15 ± 1.17	36.87 ± 3.36	27.63 ± 6.68

Notes. All mean flux and range values are in units of mJy = 10^{-29} Wm^{-2} Hz^{-1}.

[a]UT date of the first observation.

[b]Time spanned by observations (days).

[c]Number of observations used.

[d]Mean Heliocentric distance.

[e]Mean WISE-centric distance.

[f]Mean solar phase angle.

[g]Lightcurve-averaged mean flux.

[h]Photometric range of lightcurve.

Table 1.4: WISE Data TPM Results

Object	D_{eff} (km)	p_V	Γ[a]	$\bar{\theta}(^\circ)$	a/b[b]	Spin[c]	$\tilde{\chi}^2_{min}$	MBA/NEA
(167) Urda	39.48 ± 0.89	$0.252^{+0.010}_{-0.019}$	51^{+20}_{-16}	38 ± 13	1.51 ± 0.27	$\Downarrow$	1.27	MBA
(183) Istria	31.43 ± 2.92	$0.288^{+0.029}_{-0.033}$	21^{+12}_{-10}	47 ± 13	1.51 ± 0.27	$\Uparrow$	5.16	MBA
(208) Lacrimosa	40.44 ± 1.37	$0.253^{+0.012}_{-0.014}$	77^{+31}_{-22}	41 ± 13	1.51 ± 0.27	$\Uparrow$	1.66	MBA
(413) Edburga	33.44 ± 1.75	$0.169^{+0.012}_{-0.022}$	41^{+19}_{-10}	9 ± 6	1.51 ± 0.27	$\Downarrow$	1.98	MBA
(509) Iolanda	54.39 ± 3.86	$0.243^{+0.019}_{-0.027}$	$8.6^{+12.2}_{-8.6}$	18 ± 7	1.51 ± 0.27	$\Uparrow$	3.01	MBA
(771) Libera[d]	29.23 ± 2.10	$0.160^{+0.013}_{-0.019}$	61^{+34}_{-26}	53 ± 39	1.51 ± 0.27	$\Downarrow$	13.50	MBA
(857) Glasenappia	13.62 ± 0.84	$0.297^{+0.013}_{-0.021}$	58^{+30}_{-24}	< 20	2.16 ± 0.39	$\Uparrow$	1.52	MBA
(984) Gretia	34.72 ± 1.18	$0.227^{+0.012}_{-0.023}$	28^{+8}_{-7}	53 ± 10	1.51 ± 0.27	$\Uparrow$	1.81	MBA
(1036) Ganymed	35.85 ± 1.95	$0.278^{+0.017}_{-0.027}$	15^{+22}_{-15}	40 ± 32	1.08 ± 0.19	—	0.55	NEA
(1140) Crimea	30.13 ± 1.18	$0.276^{+0.020}_{-0.028}$	23^{+15}_{-23}	23 ± 21	1.51 ± 0.27	$\Downarrow$	1.50	MBA
(1188) Gothlandia	13.52 ± 0.84	$0.238^{+0.019}_{-0.022}$	38^{+21}_{-13}	41 ± 27	1.51 ± 0.27	$\Downarrow$	0.43	MBA
(1291) Phryne	27.03 ± 1.65	$0.186^{+0.014}_{-0.017}$	20^{+16}_{-6}	45 ± 17	2.16 ± 0.39	$\Uparrow$	1.78	MBA
(1432) Ethiopia	7.15 ± 0.67	$0.535^{+0.058}_{-0.070}$	71^{+180}_{-65}	—	1.51 ± 0.27	$\Uparrow$	0.56	MBA
(1495) Helsinki	13.31 ± 0.59	$0.271^{+0.017}_{-0.033}$	19^{+13}_{-13}	12 ± 8	1.51 ± 0.27	$\Uparrow$	0.52	MBA
(1568) Aisleen	11.66 ± 1.01	$0.328^{+0.034}_{-0.038}$	51^{+41}_{-22}	46 ± 38	2.16 ± 0.39	$\Downarrow$	2.74	MBA
(1607) Mavis[d]	14.52 ± 1.72	$0.249^{+0.032}_{-0.037}$	37^{+42}_{-25}	58 ± 50	1.51 ± 0.27	$\Uparrow$	21.45	MBA
(1980) Tezcatlipoca	5.68 ± 0.58	$0.205^{+0.035}_{-0.040}$	170^{+170}_{-110}	57 ± 39	1.51 ± 0.27	$\Downarrow$	1.67	NEA
(2156) Kate	8.04 ± 0.45	$0.294^{+0.021}_{-0.025}$	56^{+23}_{-23}	49 ± 32	2.16 ± 0.39	$\Uparrow$	0.39	MBA

Table 1.4 — continued

Object	D_{eff} (km)	p_V	Γ[a]	$\bar{\theta}(^\circ)$	a/b[b]	Spin[c]	$\tilde{\chi}^2_{min}$	MBA/NEA
(4611) Vulkaneifel	12.10 ± 1.12	$0.216^{+0.023}_{-0.028}$	32^{+23}_{-32}	< 53	1.51 ± 0.27	$\Downarrow$	1.01	MBA
(5625) Jamesferguson	14.46 ± 0.86	$0.062^{+0.005}_{-0.006}$	52^{+14}_{-15}	> 36	2.16 ± 0.39	$\Downarrow$	2.46	MBA
(6159) Andreseloy	5.65 ± 1.37	$0.247^{+0.061}_{-0.061}$	60^{+177}_{-60}	—	1.51 ± 0.27	$\Downarrow$	0.19	MBA

Notes. [a]Thermal inertia values are in SI units (J m^{-2} K^{-1} s$^{-1/2}$).

[b]a/b values are adjusted downward by 16% to account for the overestimation as described in section 1.4.2.

[c]Indicates either prograde ($\Uparrow$) or retrograde ($\Downarrow$) spin direction.

[d]TPM results with $\chi^2_{min} > 8$ and thus should be used with caution.

direction of (1036) Ganymed could not be independently determined here, which is likely due to the nearly spherical shape of the object combined with its low thermal inertia reducing the asymmetry of the thermal phase curve, as demonstrated in figure 1.1(b).

Comparing the diameter estimates from NEATM fits presented by the WISE team (i.e., Mainzer et al., 2011b; Masiero et al., 2011) to the values obtained here, I observe agreement (within ± 15% of another) between the two sets of results. However, for objects ≈40 km and above, TPM diameter estimates are systematically higher. The objects in question (Urda, Lacrimosa, and Iolanda) did not saturate, nor were they bright enough to lie in the non-linear regime of the WISE detectors. This discrepancy may be due to one the flux corrections described above or from the model differences between my TPM approach and the NEATM used by the WISE team.

When comparing to other previous works, my results are consistent with the thermal inertias reported: (771) Libera and (1980) Tezcatlipoca have thermal inertia estimates of 65 +85/-35 and 220 +380/-204 J m^{-2} K^{-1} $s^{-1/2}$, respectively, made by Hanuš et al. (2015), though the reader should take note that the large χ^2 values indicate that my fits for Libera were relatively poor, contributing to the relatively high parameter uncertainties. Ganymed has several thermal inertia estimates: 24 ± 8 (Rozitis et al., 2018), 35 +65/-29 (Hanuš et al., 2015), and 214 ± 80 J m^{-2} K^{-1} $s^{-1/2}$ (Rivkin et al., 2017)[10]. The higher estimates are approximately an order of magnitude greater than the smallest estimates, and can be explained by the thermal inertia dependency on temperature (e.g., Vasavada et al., 1999). My thermal inertia estimate for Ganymed was based on data collected at $R_{\mathrm{AU}} = 3.5$ and 3.8, and is thus consistent with similar estimates at the same distance.

Eleven objects in this study have been analyzed by the recent work of Hanuš et al. (2018), in which the varied-shape TPM was used to derive thermophysical properties from the WISE dataset. A comparison of the thermal inertias for each of these objects in shown in the bottom panel of figure 1.5. Some objects have two estimates presented in Hanuš et al. (2018) due to ambiguous shape models that produce equivalent fits to the data. For 7 out of these 11 objects, there is very good agreement (i.e., the estimates are within the

[10]Instead of a TPM analysis, this work employed an approach pioneered by Harris and Drube (2016) in which the NEATM η value is used to indirectly determine the thermal inertia.

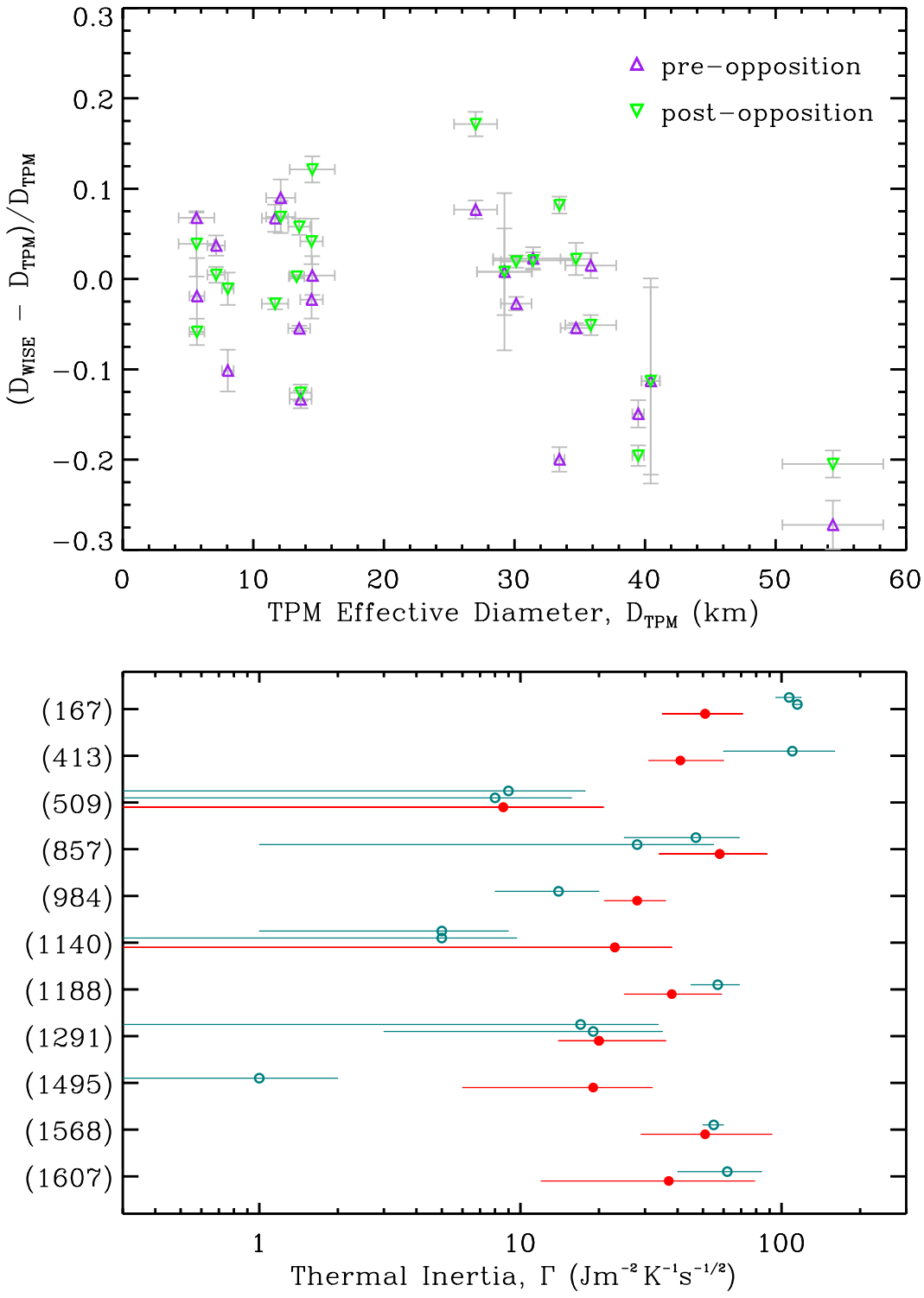

Figure 1.5: Top: comparison of the effective diameter values obtained by Masiero et al. (2011) and Mainzer et al. (2011b) to my reported TPM values. Purple, upward-facing and green, downward-facing triangles represent data collected at pre- and post-opposition, respectively. Bottom: comparison of thermal inertia estimates for 11 objects by Hanuš et al. (2018), in teal open circles, to mine, in red filled circles.

1σ uncertainties) between the estimates from their work and mine. I note that my model fit for (1607) Mavis was noticeably inaccurate, as indicated by the large $\tilde{\chi}^2_{min}$ in table 1.4, for which I note the error bars for each parameter are noticeably large[11] and consistent with Hanuš et al. (2018). For two objects, (413) Edburga and (984) Gretia, the 1σ error bars just barely miss overlapping, and two others, (167) Urda and (1495) Helsinki, have very different estimates. The two thermal inertia estimates Hanuš et al. (2018) present for (167) Urda are just over twice as large as mine and have very small reported uncertainties of $\pm$ 5 $Jm^{-2}K^{-1}s^{-1/2}$. Hanuš et al. (2018) report a thermal inertia just over zero for (1495) Helsinki, also with a very small uncertainty. For each of these objects, my 2σ uncertainty bounds encompass the Hanuš et al. (2018) estimates and both works overall appear to deliver no systematically different estimates from another.

With the combination of my TPM results with the subset compiled by Delbo' et al. (2015) and the large dataset of Hanuš et al. (2018), I note that the number of known thermal inertias of objects in the 5–50 km size range increases by 20. Restricting my analysis to the compiled thermal inertias from Delbo' et al. (2015), I detect a negative correlation with diameter (figure 1.6) evidenced by the Spearman's rank coefficient of r_s = -0.55; this correlation remains when including the ∼120 thermal inertias of Hanuš et al. (2018). From the findings of Rozitis et al. (2018), however, thermal inertia should be adjusted to account for its dependency on heliocentric distance by using the formula: $\Gamma = \Gamma_0 R_{\rm AU}^{\zeta}$. Doing this allows for a better comparison of hot, small NEAs and cool, larger MBAs because the effects of temperature are partially taken into account. I use $\zeta = 3/4$ here, which was suggested previously by Delbo' et al. (2015) and Mueller et al. (2010). Even when performing the adjustment on asteroid thermal inertias, the correlation remains statistically significant (with r_s = -0.41 and $p < .001$) as shown in the right panel of figure 1.6. However, this correlation becomes insignificant if I use $\zeta = 4/3$, which is large but well within the range of empirically derived values from analyzing individual objects (i.e., Ganymed and 2002 CE_{26}; Rozitis et al., 2018). While the purpose of this work is not to investigate this dependency, I plan a follow-up

[11] As a reminder, parameter uncertainties are scaled by $\tilde{\chi}^2_{min}$ values in order to account for best-fit TPM fluxes that deviate from the measured fluxes.

work to increase the number thermal inertia estimates of small main-belt asteroids, combine my results with Hanuš et al. (2018), and revisit this dependency in much greater detail.

The prograde/retrograde spin directions reported here are in agreement with those from DAMIT (table 1.1) with the exception of three objects: (208) Lacrimosa, (1495) Helsinki, and (6159) Andreseloy. Incorporating the ambiguous spin direction for Ganymed, this means that 17 out of 21 (81 ± 9%) objects matched the spin vectors in the DAMIT shape models. Comparing this result to the findings of my proof-of-concept study in section 1.4.2, there is a noticeable difference. Assuming the DAMIT shape models are 100% accurate, there is much improvement in the percent of synthetic objects in which the spin direction was correctly identified (approximately 58% and 67% for ellipsoids and a sphere, respectively). When broken down by thermal inertia, as in panel (f) of figure 1.3, these results are comparable to the best-case scenario (spherical shape for $\Gamma = 40$ $\mathrm{Jm^{-2}K^{-1}s^{-1/2}}$) and outperform each situation in which an ellipsoid shape is used. A reasonable explanation for this discrepancy is the inclusion of roughness in the real-world application of the TPM, which adds to the asymmetry of the thermal phase curve — particularly for asteroids in the Main Belt (e.g., figure 1.1(b)).

1.6 Summary and Future Work

The opportunity to constrain diagnostic thermophysical properties of asteroids by constraining the multi-wavelength phase curves will become more common with the advent of more thermal infrared survey telescopes. In this chapter, I have demonstrated the accuracy and precision of estimating various asteroid parameters using only pre- and post-opposition multi-wavelength thermal observations for an object, without the aid of a known shape model. By varying the a/b axis of a prolate ellipsoid shape model and sampling from a grid of several spin vectors, unique solutions for diameter/albedo, thermal inertia, and the elongation of an object can be ascertained. A small correction to the best-estimate a/b axis is applied to account for the overestimation of the elongation of the body. Constraints on surface roughness and sense of spin direction are more difficult to obtain, most likely due to the relatively low number of data points compared to the number of free parameters I used

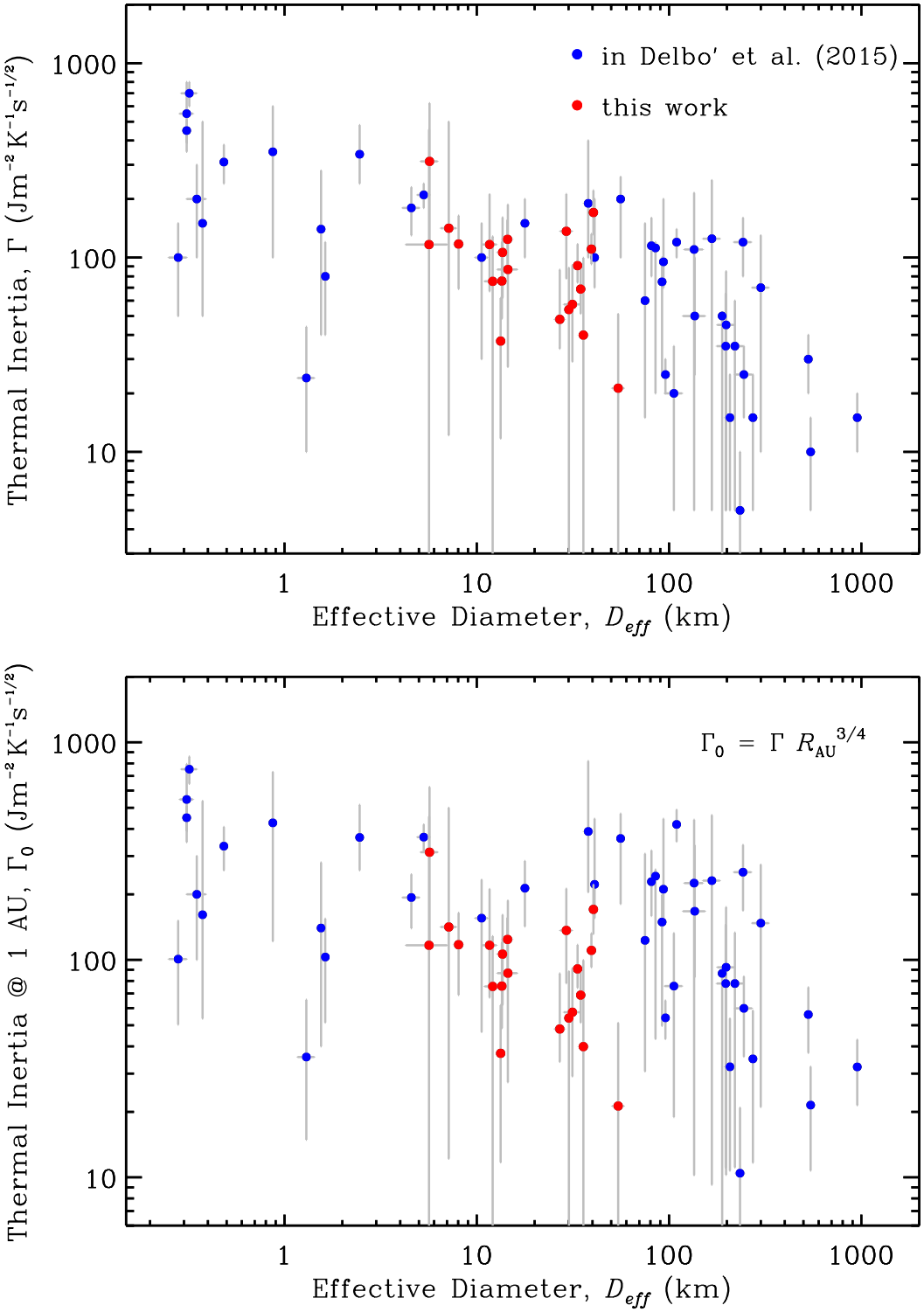

Figure 1.6: Thermal inertia vs. diameter values from this work compared along with previous estimates. The bottom panel shows the thermal inertias in the top panel scaled at a heliocentric distance of 1 AU, as per the text and Rozitis et al. (2018).

in the TPM approach. Additional multi-wavelength observations taken close to opposition would increase the precision of the surface roughness estimate, as the flux beaming effect from surface topography is most pronounced in this configuration. Spin axis estimates would also benefit from additional sets of observations taken at another observing geometry. The strong correlation between the peak-to-trough flux range and the sub-solar latitude can be exploited in this case to increase the accuracy and precision of the spin axis orientation.

The TPM approach outlined here was applied to 21 asteroids: 19 MBAs and 2 NEAs (table 1.3). Chapter 2 features diameter, albedo, thermal inertia, and roughness estimates for over 200 asteroids that were observed by WISE. Results pertaining to surface roughness, shape, and spin sense are also be provided. Future work will focus on investigating and improving upon the accuracy and precision of shape and spin using ellipsoids and multi-epoch thermal observations. With the release of WISE/NEOWISE survey data and large-scale visible surveys, for example the Large Synoptic Survey Telescope (LSST) and the Panoramic Survey Telescope and Rapid Response System, it is important that appropriate models are developed alongside the releases of these data sets. In particular, sensitive surveys will discover and observe smaller-sized objects and may be the only available observations for newly discovered, faint asteroids. Thus, models that can make use of these survey observations in order to derive asteroid physical properties will be valuable.

Chapter 2

Mechanical Weathering of Regolith

2.1 Introduction

The characterization and origin of regolith — the unconsolidated, heterogeneous, rocky material covering the surface of other planetary bodies — has, and will continue to be, an important subject for researchers and explorers of the solar system. The Apollo astronauts discovered a Lunar surface that was abundant in a fine-grained powder ranging in size from 40 to 800 μm, with a bulk of the powder consisting of 60 to 80 μm grains (McKay et al., 1991). The lunar regolith has been remotely characterized using thermal emission observations and thermophysical modeling to map thermal inertia — a measurement of the resistance to temperature change — and estimate the abundance of blocky material on the surface (e.g., Winter and Saari, 1969; Bandfield et al., 2011; Vasavada et al., 2012; Hayne et al., 2017).

Similarly, regoliths on asteroids have been characterized for a few dozen remotely-observed asteroids and from spacecraft visits to a handful of objects. The largest asteroids in the solar system — (1) Ceres, (2) Pallas, and (4) Vesta — possess thermal inertias comparable to the Moon ($\approx$50 J m^{-2} K^{-1} s$^{-1/2}$; Wesselink, 1948; Cremers, 1975; Mueller and Lagerros, 1998; Capria et al., 2014). The small asteroids (433) Eros and (25143) Itokawa have estimated thermal inertias of $\approx$150 J m^{-2} K^{-1} s$^{-1/2}$ and $\approx$700 J m^{-2} K^{-1} s$^{-1/2}$, respectively (Mueller, 2007). Spacecraft images of these asteroids (figure 2.1) reveal that Eros' regolith consists of both fine grains and small boulders (Robinson et al., 2002) and the surface of Itokawa is mostly blocky with patches of coarse-grained regolith (Mazrouei et al., 2014). The Vestan surface,

however, is covered in fine-grained regolith (Schröder et al., 2013) that is similar to the Moon's. Interestingly, the ≈250 km diameter M-type asteroid (16) Psyche has a thermal inertia of ≈120 $J\,m^{-2}\,K^{-1}\,s^{-1/2}$, more than three times greater than similar sized asteroids (Figure 5 in Matter et al., 2013). M-types are thought to be metal rich, which would lead to a high thermal conductivity, possibly explaining to Psyche's high thermal inertia. Overall, the study of asteroid thermophysical properties is integral in developing our understanding of the processes that produce and cultivate regolith.

The observed correlation of thermal inertia with size (Delbo' et al., 2015; Hanuš et al., 2018; Rozitis et al., 2018) suggests that only larger asteroids harbor a "lunar-like" regolith, whereas smaller asteroid regoliths are comprised of course sand or a higher fraction of blocky material. Though there is evidence of a trend in thermal inertia with size, exceptions exist, and the low number of objects in the current dataset precludes the separation of different effects, making it impossible to deduce how size, along with rotation period, age, and composition determine regolith grain size outcomes. In this work, I hypothesize two mechanisms for regolith development: meteoroid impact degradation and thermal fatigue cycling. These processes have been proposed as relevant for the formation and development

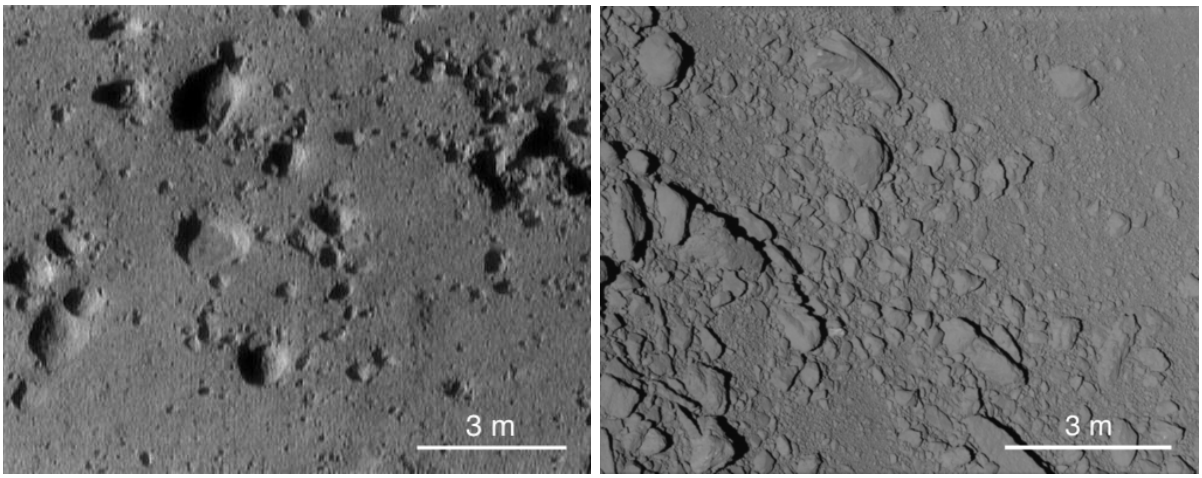

(a) Eros (b) Itokawa

Figure 2.1: Spacecraft images of the regolith on Eros and Itokawa taken by the NEAR spacecraft and Hayabusa, respectively, at approximately the same scale.

of regolith on asteroid surfaces. Currently, the knowledge ascertained from remote and in-situ studies of observed asteroid regoliths have yet to provide confirmation of the effectiveness of these processes.

Here, I propose and evaluate two tests aimed at investigating the effectiveness of the two hypothesized regolith weathering mechanisms: 1) larger-sized asteroids exhibit well-developed regoliths, quantified by smaller grain sizes, and 2) slowly spinning asteroids have a poorly-developed regolith, characterized by larger grain sizes and boulders/blocks. The relevance of each weathering mechanism can be examined by comparing the relative correlation between regolith grain size and diameter or rotation period. If regolith is chiefly generated from the micrometeoroid impacts then a strong correlation with asteroid diameter is expected and if thermal cycling is effective, then I should observe a correlation with the rotation period. Additionally, I investigate how the compositional properties of asteroids affect the development of their regoliths and attempt to establish a mechanical weathering timescale by using members of asteroid families (which have varying ages). By performing statistical comparison tests between the grain size distributions of different spectral groups and families I infer compositional dependencies and weathering rate, respectively.

In this work I present new thermal inertias for a large set (230+) of asteroids and use them in a thermal conductivity model in order to estimate a characteristic regolith grain size for each object. I also include objects for which estimates of thermal inertia already exist, and use this large grain size database to investigate factors that influence the regoliths of these small bodies. Section 2.2 is a brief overview of the hypothesized formation mechanisms that act to generate regolith on asteroid surfaces and introduces how I will test their relative impact on the development of regolith. I describe my thermophysical model in section 2.3 and present those results in section 2.3.4. Next, the thermal conductivity model used to estimate a characteristic grain size is given in section 2.5. Section 2.7 contains the statistical analysis performed on the set of grain sizes, and section 2.8 discusses the results in the context of both regolith formation mechanisms and possible relevant grain ejection, or loss, processes.

2.2 Background: Regolith Formation Mechanisms

Meteoroid Impacts When a meteoroid strikes an asteroid surface, a large amount of energy is concentrated into a small area. Some of the energy from an impact is partitioned into altering the near-surface material of the target body, albeit the exact fraction of energy that goes into fracturing or mechanically weakening the target material is very uncertain. Some of the energy is channeled into excavating material, called ejecta, at various initial velocities that are dependent on the proximity to the impact site and the properties of the impactor and target. If the target object is large enough, and/or if the kinetic energy of the impactor is low enough, most of the ejecta is retained as regolith. Other factors, such as the target strength and porosity, also play relevant, yet relatively underconstrained roles in the production of craters and of regolith. However, Housen and Holsapple (2003) found a clear inverse relationship between the ejecta-to-impactor mass ratio and porosity of the target. Impacts that excavate into relatively undisturbed, but possibly fractured, bedrock of an asteroid will throw up a thick blanket of boulders/blocks. After a few large impacts a mega-regolith forms, in which the portion of fractured bedrock extends down to tens or hundreds of meters beneath the surface; such is the case on Earth's moon (Hartmann, 1973). Asteroids that repeatedly survive high-energy impacts should have heavily fractured interiors and will develop a regolith that is continuously overturned, or gardened.

Thermal Cycling Internal stresses caused by differential thermal expansion within a thermochemically heterogeneous rock, brought on by the repeated heating and cooling, result in the formation and further breakdown of regolith on large timescales. The effectiveness of this thermal cycling process has been extensively simulated under the thermal environments of airless solar system bodies (e.g., Molaro and Byrne, 2012) and its feasibility has been demonstrated on meteorite samples (Delbo' et al., 2014). Although rapidly rotating asteroids should exhibit global, latitudinally-isothermal temperatures, Delbo' et al. (2014) showed that a cycling period of 2.2 hr is still sufficient to create and propagate thermal cracks. The process is thought to act across several spatial scales, complicating attempts to characterize crack growth and breakdown and to estimate a timescale on which it acts, although Molaro and Byrne (2012) predict that asteroid surfaces experiencing short thermal cycles facilitate larger

spatial thermal gradients. A small amount of heterogeneity within the material structure (from mineralogical differences or pores of empty space) can increase the nominal peak stress (ranging across 10s of MPa, depending on the composition) by at least a factor of 3 (Molaro et al., 2015). These micro-cracks originate near mineral grain boundaries, prefer to grow perpendicular to the local surface, and ultimately join with other micro-cracks to reach sizes of several centimeters (Delbo' et al., 2014; Molaro et al., 2015). The propagation of the thermal wave within a boulder initiates cracks at the microscale throughout the interior throughout the diurnal cycle. Growth of large-scale cracks occur in the direction of the heat flow throughout the boulder, and are thus able to transverse a rock that is several times larger than the initial fracture. Molaro et al. (2015) studied the sensitivity of their micro-stress model to changes in the material properties of the rock and found the thermal expansion coefficient and Young's modulus (E; which describes tensile elasticity) to be the most influential, and that thermal conductivity, surprisingly, does not significantly affect the rate of crack growth.

2.3 Observations & Thermophysical Modeling

I use data from the Wide-field Infrared Survey Explorer (WISE) and the thermophysical modeling (TPM) approach presented in chapter 1, and re-summarized below. Absolute magnitude (H_V) and slope parameter (G_V) from Oszkiewicz et al. (2011), and P_{rot} from the Asteroid Lightcurve Database (ALCDB; Warner et al., 2009) are used as TPM input values for each object (table 2.1) along with mean and peak-to-trough fluxes calculated from sparse lightcurve data. In section 1.5 I describe that the mean and peak-to-trough flux quantities were extracted from the thermal light curve via simple geometric average and subtracting the maximim and minimum values, respectively. Although those simplistic calculations are useful for dense lightcurve data, they can be problematic when used on sparsely sampled lightcurves for reasons discussed in section 2.3.2. The results of the TPM implementation on these fluxes are given in section 2.3.4. For reference, I include the results from table 1.4 separated in the topmost section of the table.

Table 2.1: Absolute Magnitudes, Slope Parameters, and Rotation Periods used as TPM Input

Object	H_V	G_V	P_{rot} (hr)	Object	H_V	G_V	P_{rot} (hr)	Object	H_V	G_V	P_{rot} (hr)
(91) Aegina	8.795	0.200	6.0250[†]	(1759) Kienle	13.01	0.277	29.25	(4908) Ward	13.61	0.206	10.96
(155) Scylla	10.87	0.087	7.9597	(1768) Appenzella	12.33	0.056	5.1839	(5035) Swift	12.25	0.236	9.4752
(271) Penthesilea	9.724	0.134	18.787	(1807) Slovakia	12.25	0.162	308.0	(5052) Nancyruth	14.21	0.134	17.204
(295) Theresia	9.841	0.185	10.730	(1896) Beer	13.69	0.251	3.3278	(5080) Oja	12.64	0.280	7.2220
(322) Phaeo	8.986	0.211	17.5845	(1936) Lugano	11.41	0.046	19.651	(5088) Tancredi	12.51	0.181	5.0591
(343) Ostara	11.51	0.148	109.87	(1979) Sakharov	13.63	0.485	7.5209	(5104) Skripnichenko	11.93	0.162	2.8270[†]
(444) Gyptis	7.837	0.193	6.214	(2005) Hencke	12.10	0.224	10.186	(5226) Pollack	13.12	0.284	2.725
(463) Lola	11.43	0.105	6.206	(2072) Kosmodemyanskaya	12.69	0.343	4.4	(5333) Kanaya	12.86	0.066	3.8022
(464) Megaira	9.586	0.119	12.726	(2106) Hugo	12.18	0.096	6.9297	(5378) Ellyett	13.68	0.207	47.32
(493) Griseldis	10.72	0.183	51.940	(2111) Tselina	10.48	0.283	6.563	(5427) Jensmartin	13.65	0.287	5.810
(500) Selinur	9.316	0.316	8.0111	(2123) Vltava	11.46	0.170	34.0	(5527) 1991 UQ_3	13.57	0.209	4.2554
(520) Franziska	10.49	0.252	14.0	(2140) Kemerovo	11.24	0.143	9.2	(5574) Seagrave	12.29	0.319	4.6629
(538) Friederike	9.342	0.085	46.728	(2144) Marietta	11.16	0.254	5.489	(5592) Oshima	11.68	0.119	12.54
(558) Carmen	9.065	0.354	11.387	(2177) Oliver	11.84	0.226	6.1065	(5604) 1992 FE	17.35	0.309	5.3375
(562) Salome	9.870	0.188	6.351	(2203) van Rhijn	11.52	0.201	30.55	(5682) Beresford	13.54	0.238	3.769
(567) Eleutheria	9.047	0.263	7.717	(2204) Lyyli	11.93	0.141	11.063	(5712) Funke	12.75	0.217	3.950
(583) Klotilde	9.009	0.143	9.2116	(2214) Carol	11.55	0.082	4.987	(6091) Mitsuru	13.08	0.074	5.853
(651) Antikleia	9.952	0.229	20.299	(2239) Paracelsus	10.92	0.344	6.101	(6121) Plachinda	13.29	0.266	4.0863
(656) Beagle	9.833	0.145	7.035	(2268) Szmytowna	11.51	0.119	11.260	(6139) Naomi	12.18	0.284	21.35
(662) Newtonia	10.40	0.402	16.46	(2275) Cuitlahuac	12.46	0.208	6.2891	(6170) Levasseur	13.44	0.357	2.6529
(668) Dora	11.81	0.123	22.914	(2297) Daghestan	11.28	0.203	7.75	(6185) Mitsuma	12.90	0.087	21.05
(670) Ottegebe	9.362	0.255	10.045	(2306) Bauschinger	12.05	0.110	21.64	(6261) Chione	14.07	0.218	5.3334
(688) Melanie	10.58	0.120	18.87	(2332) Kalm	10.85	0.180	22.8	(6361) Koppel	13.18	0.230	9.1122
(734) Benda	9.888	0.285	7.110	(2347) Vinata	11.21	0.175	4.4835	(6572) Carson	12.41	0.125	2.8235
(735) Marghanna	9.558	0.151	15.95	(2365) Interkosmos	11.29	0.218	6.1548	(6838) Okuda	12.07	0.287	8.983
(793) Arizona	10.03	0.376	7.399	(2375) Radek	10.35	0.168	16.875	(6870) 1991 OM_1	13.85	0.240	4.487
(826) Henrika	11.34	0.083	5.9846	(2446) Lunacharsky	12.91	0.134	3.613	(6901) Roybishop	13.27	0.084	4.682
(829) Academia	10.77	0.107	7.891	(2463) Sterpin	11.87	0.324	13.44	(6905) Miyazaki	11.47	0.180	2.7418

Table 2.1 — continued

Object	H_V	G_V	P_{rot} (hr)	Object	H_V	G_V	P_{rot} (hr)	Object	H_V	G_V	P_{rot} (hr)
(883) Matterania	12.50	0.228	5.64	(2500) Alascattalo	12.49	0.254	2.754	(6911) Nancygreen	14.02	0.233	59.1
(906) Repsolda	9.244	0.180	15.368	(2556) Louise	13.23	0.308	3.809	(7476) Ogilsbie	11.37	0.104	3.92
(918) Itha	10.58	0.310	3.4739†	(2567) Elba	11.69	0.148	9.7785	(7783) 1994 JD	14.23	0.265	31.83
(972) Cohnia	9.436	0.137	18.472	(2687) Tortali	11.82	0.207	21.75	(7829) Jaroff	14.50	0.560	4.398
(977) Philippa	9.672	0.107	15.405	(2786) Grinevia	11.95	0.352	2.911	(7832) 1993 FA_{27}	13.74	0.183	8.295
(987) Wallia	9.430	0.240	10.0813	(2855) Bastian	12.95	0.102	3.5160	(7949) 1992 SU	12.25	0.038	17.91
(998) Bodea	11.35	0.152	8.574	(2870) Haupt	12.78	0.135	274.0	(8213) 1995 FE	13.56	0.237	2.911
(1018) Arnolda	11.01	0.373	14.617	(2947) Kippenhahn	12.58	0.163	10.5	(8862) Takayukiota	12.76	0.150	3.2549
(1047) Geisha	11.87	0.241	25.62	(2985) Shakespeare	11.94	0.144	6.06	(8887) Scheeres	12.62	0.253	2.9827
(1051) Merope	9.935	0.172	27.2	(3036) Krat	10.14	0.061	9.61	(9297) Marchuk	12.17	0.102	18.09
(1076) Viola	12.05	0.215	7.336	(3051) Nantong	12.22	0.080	3.690	(10936) 1998 FN_{11}	12.50	0.123	25.70
(1077) Campanula	12.18	0.194	3.8508†	(3144) Brosche	13.86	0.181	3.300	(11549) 1992 YY	12.07	0.289	2.671
(1083) Salvia	12.06	0.273	4.23	(3162) Nostalgia	11.29	0.185	6.412	(11780) Thunder Bay	12.82	0.134	295.0
(1095) Tulipa	10.27	0.193	2.7872†	(3249) Musashino	13.40	0.241	4.5527†	(12376) Cochabamba	13.28	0.238	6.3206†
(1109) Tata	9.861	0.161	8.277	(3267) Glo	12.73	0.166	6.8782	(12753) Povenmire	12.61	0.177	12.854
(1123) Shapleya	11.51	0.220	52.92	(3305) Ceadams	12.19	0.238	2.729	(13474) V'yus	13.59	0.167	6.587
(1125) China	11.52	0.156	5.367	(3411) Debetencourt	13.37	0.197	9.93	(13856) 1999 XZ_{105}	12.84	0.133	4.4475
(1136) Mercedes	10.93	0.207	24.64	(3438) Inarradas	11.69	0.183	24.82	(14342) Iglika	12.31	0.154	3.9867
(1142) Aetolia	10.18	0.273	10.730	(3483) Svetlov	14.02	0.465	6.790	(14950) 1996 BE_2	13.59	0.183	3.2791†
(1152) Pawona	11.13	0.349	3.4154	(3509) Sanshui	12.17	0.254	13.68	(15362) 1996 ED	13.54	0.199	31.4
(1162) Larissa	9.594	0.490	6.516	(3536) Schleicher	13.85	0.243	5.79	(15430) 1998 UR_{31}	14.04	0.162	2.5273†
(1224) Fantasia	11.43	0.233	4.995	(3544) Borodino	12.32	0.186	5.442	(15499) Cloyd	12.77	0.128	6.878
(1258) Sicilia	10.44	0.065	13.500	(3554) Amun	15.58	0.181	2.5300†	(15914) 1997 UM_3	14.08	0.210	12.8
(1281) Jeanne	11.43	0.114	15.2	(3560) Chenqian	10.86	0.257	18.79	(16681) 1994 EV_7	14.34	0.337	5.3147
(1288) Santa	11.23	0.143	8.28	(3628) Boznemcova	12.71	0.198	3.3354†	(16886) 1998 BC_{26}	13.04	0.233	5.9908
(1296) Andree	11.60	0.194	5.1836†	(3751) Kiang	11.56	0.175	8.2421	(17681) Tweedledum	14.53	0.496	75.2
(1299) Mertona	11.48	0.364	4.977	(3823) Yorii	12.91	0.171	6.669	(17822) 1998 FM_{135}	13.52	0.220	4.613
(1310) Villigera	11.49	0.229	7.830	(3907) Kilmartin	11.74	0.224	3.841	(18487) 1996 AU_3	12.63	0.188	6.512
(1316) Kasan	12.93	0.246	5.82	(3915) Fukushima	11.96	0.082	9.418	(19251) Totziens	13.41	0.124	18.446

Table 2.1 — continued

Object	H_V	G_V	P_{rot} (hr)	Object	H_V	G_V	P_{rot} (hr)	Object	H_V	G_V	P_{rot} (hr)
(1325) Inanda	12.13	0.236	20.52	(3935) Toatenmongakkai	11.86	0.236	106.3	(20378) 1998 KZ_{46}	12.84	0.243	5.14
(1335) Demoulina	12.74	0.301	74.86	(3936) Elst	12.89	0.219	6.6322	(20932) 2258 T-1	13.33	0.144	4.3239
(1352) Wawel	11.07	0.233	16.97	(4003) Schumann	11.10	0.149	5.7502	(21594) 1998 VP_{31}	13.08	0.091	5.5865
(1375) Alfreda	11.45	0.320	19.14	(4006) Sandler	12.55	0.183	3.40	(23200) 2000 SH_3	12.97	0.156	16.22
(1412) Lagrula	12.24	0.272	5.9176	(4008) Corbin	12.94	0.110	6.203	(23276) 2000 YT_{101}	14.26	0.045	3.661
(1443) Ruppina	10.97	0.287	5.880	(4029) Bridges	12.65	0.241	3.5746	(24101) Cassini	12.89	0.167	3.986
(1452) Hunnia	11.94	0.122	17.2	(4142) Dersu-Uzala	13.18	0.272	140.0	(27851) 1994 VG_2	13.64	0.125	7.733
(1501) Baade	11.86	0.217	15.132	(4150) Starr	12.70	0.240	4.5179	(28126) Nydegger	15.13	0.154	3.783
(1517) Beograd	10.98	0.147	6.943	(4255) Spacewatch	13.08	0.268	20.0	(30470) 2000 OR_{19}	13.85	0.153	23.02
(1536) Pielinen	12.57	0.308	66.22	(4264) Karljosephine	13.33	0.180	30.96	(32802) 1990 SK	13.87	0.223	2.427
(1542) Schalen	10.46	0.316	7.516	(4294) Horatius	12.62	0.135	12.499	(33916) 2000 LF_{19}	14.39	0.138	4.4099
(1565) Lemaitre	12.71	0.321	11.403	(4352) Kyoto	11.62	0.245	21.9352	(41044) 1999 VW_6	13.12	0.146	2.734
(1567) Alikoski	9.550	0.152	16.405	(4359) Berlage	13.47	0.135	7.413	(41223) 1999 XD_{16}	13.43	0.066	32.52
(1573) Vaisala	12.23	0.249	252.0	(4363) Sergej	13.29	0.233	13.04	(41288) 1999 XD_{107}	14.19	0.154	4.36
(1577) Reiss	12.65	0.397	4.5050	(4383) Suruga	13.08	0.332	3.4069	(42265) 2001 QL_{69}	13.24	0.157	8.6
(1628) Strobel	10.01	0.107	9.52	(4528) Berg	12.03	0.271	3.5163	(42946) 1999 TU_{95}	13.67	0.202	3.42
(1644) Rafita	11.41	0.321	6.800	(4565) Grossman	12.77	0.255	4.7429	(44892) 1999 VJ_8	12.83	0.259	5.872
(1651) Behrens	12.13	0.364	34.34	(4569) Baerbel	12.13	0.209	2.737	(45436) 2000 AD_{176}	14.22	0.105	18.47
(1655) Comas Sola	10.96	0.243	20.456	(4613) Mamoru	11.61	0.165	5.388	(68216) 2001 CV_{26}	16.38	0.244	2.4290
(1702) Kalahari	10.92	0.238	21.153	(4713) Steel	13.29	0.339	5.199	(69350) 1993 YP	15.29	0.293	31.79
(1723) Klemola	10.04	0.257	6.2545	(4771) Hayashi	12.48	0.122	9.801	(72675) 2001 FP_{54}	14.38	0.067	2.50
(1734) Zhongolovich	11.50	0.111	7.171	(4898) Nishiizumi	14.21	0.421	3.289	(90698) Kosciuszko	14.17	0.196	5.014
(1741) Giclas	11.45	0.324	2.943	(4899) Candace	12.75	0.209	40.7				

Note. †Indicates a P_{rot} value that has been truncated from the reported value at four decimal places.

2.3.1 Data Description

In 2010, WISE mapped the entire sky, from an Earth orbit, in four photometric filters: 3.4, 4.6, 12, and 22 μm, respectively referred to as W1, W2, W3, and W4 (Wright et al., 2010). WISE was designed as an astrophysics all-sky mapping mission, but its infrared sensors could serendipidously detect the thermal emission from warm asteroids in the inner solar system. A data-processing enhancement (NEOWISE; Mainzer et al., 2011a) to the nominal pipeline was thus designed and implemented to identify and measure the emission from these solar system objects. Since this mapping survey did not target moving objects, the asteroids were only observed for a relatively brief (typically less than a couple days) period of time, referred to as an epoch. Each epoch of observations nominally yielded 10 to 20 individual measurements that were separated by ≈1.6 hr — the orbital period of WISE. NEOWISE stores the extracted flux data at the Infrared Processing and Analysis Center[1] (IPAC) and reports each detection of a moving solar system object to the Minor Planet Center[2] (MPC), where the information regarding the sky position and time of observation can be retrieved. In downloading the data, I used the MPC observation file to parse the WISE All-Sky Single Exposure (L1b) catalog on IPAC's Infrared Science Archive (IRSA) and select detections acquired within 10 s of that reported to the MPC, with a search cone of 10″. I shift the isophotal wavelengths of the filters and perform a color-correction to the fluxes (Wright et al., 2010), as per the recommendation of the WISE Explanatory supplement Cutri et al. (2012). Since the criteria used to parse IPAC can potentially return contaminated (i.e., by a background star or galaxy) or unwanted (non-asteroid) infrared sources from the catalog, I employ Peirce's Criterion (Peirce, 1852; Gould, 1855) on the infrared color, W4–W3, as detailed in chapter 1, to ensure inclusion of only uncontaminated observations of asteroids.

2.3.2 Sparse Lightcurve Sampling

Due to the nature of the orbit and observing cadence of WISE, any given asteroid will be visited an average of a dozen times, with each instance separated by ≈1.6 hours. This sparse sampling does not allow for the construction of a well-characterized rotational lightcurve.

[1] http://irsa.ipac.caltech.edu/Missions/wise.html
[2] http://www.minorplanetcenter.net/

Since observations are taken at irregularly-spaced rotational phases — depending both on the number of observations and the object's rotation period — infrared photometry may be missing for crucial points of an object's lightcurve, such as the minima and maxima. The WISE orbital cadence may over-sample certain rotational phases, which poses a challenge for extracting scientifically-important characteristics such as the mean and peak-to-trough range of the lightcurve. I present here a technique for extracting these parameters from a small photometric set of observations, given an object's rotation period. Applying this approach to the objects analyzed in chapter 1 does not significantly change those previously-determined flux estimates tabulated in table 1.3. The WISE fluxes computed from this method, along with observing circumstances, are detailed in table 2.2 and denoted as W3 and W4.

First, I step through each possible pair of flux measurement points and compute their average and difference so that for the ith and jth point the mean and range (absolute difference) are m_{ij} and r_{ij}, respectively. The flux uncertainties (δf) are summed in quadrature, so that the errors in each mean (δm_{ij}) and range (δr_{ij}) are given by:

$$2\delta m_{ij} = \delta r_{ij} = \sqrt{\delta f_i^2 + \delta f_j^2} \tag{2.1}$$

Note the factor of 2 associated with the mean, as per the rules of error propagation. Proceeding, I calculate a weighting factor, s_{ij}, based on the separation in rotational phase (normalized to 2π radians) of the two points, $\phi_i - \phi_j$. In this weighting scheme, pairs that sample around the same rotational phase or half a turn ($\phi_i - \phi_j = 0, 1/2$), are given a weight of $s_{ij} = 0$, and pairs separated by a quarter turn ($\phi_i - \phi_j = 1/4, 3/4$) have $s_{ij} = 1$ (top left panel of figure 2.2).

The weighted flux mean ($\overline{F}$) and error ($\delta\overline{F}$) are then given by:

$$\overline{F} = \frac{\sum_i \sum_{j>i} m_{ij} \delta m_{ij}{}^{-2} s_{ij}^2}{\sum_i \sum_{j>i} \delta m_{ij}{}^{-2} s_{ij}^2} \tag{2.2}$$

and

$$\delta\overline{F} = \sqrt{\sum_i \sum_{j>i} \delta m_{ij}{}^{2} s_{ij}^2 \Big/ \sum_i \sum_{j>i} s_{ij}^2}. \tag{2.3}$$

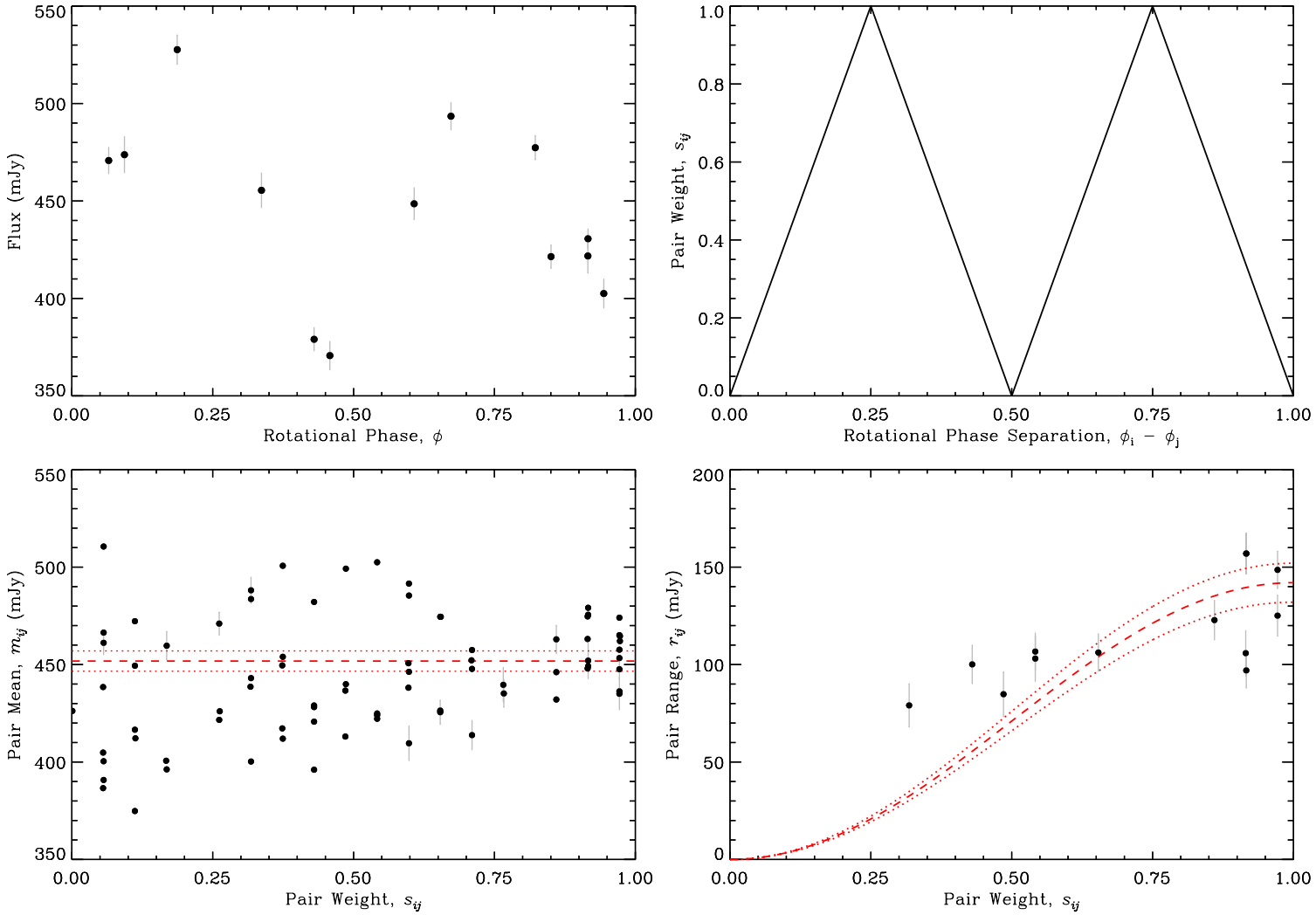

Figure 2.2: Graphical depiction of applying Equation 2.2 and Equation 2.4 toward computing the mean (lower left) and flux range (lower right) of W3 data for 167 (Urda). The upper left panels shows the W3 fluxes and upper right shows the weights applied to pairs as a function of phase separation. The red dashed line and dotted lines give the best-fit and 1σ uncertainty for the mean and amplitude of $\overline{F} = 451.8 \pm 5.2$ mJy and $\diamondsuit F = 142 \pm 10$ mJy.

Table 2.2: WISE Observation Circumstances and Fluxes

Object	UT Date[a]	$\Delta t_{\rm obs}$[b]	N[c]	$R_{\rm AU}$[d]	$\Delta_{\rm AU}$[e]	α (°)[f]	$\overline{F_{\rm W3}}$[g]	$\diamondsuit F_{\rm W3}$[h]	$\overline{F_{\rm W4}}$[g]	$\diamondsuit F_{\rm W4}$[h]
(91) Aegina	17 Jan 2010	1.125	12	2.604	2.376	22.19	8604 ± 1238	2721 ± 2350	129200 ± 260	3602 ± 442
	5 Jul 2010	1.258	12	2.772	2.491	-21.43	5539 ± 797	1289 ± 1590	10360 ± 230	2003 ± 393
(155) Scylla	30 Jan 2010	1.125	12	2.860	2.694	20.14	599.0 ± 6.9	155.2 ± 14.7	1388 ± 27	363.3 ± 55.6
	16 Jul 2010	3.902	20	3.252	2.999	-18.12	299.1 ± 3.7	92.30 ± 7.06	858.8 ± 19.0	241.3 ± 36.9
(271) Penthesilea	20 Jan 2010	0.992	10	3.278	3.104	17.46	849.2 ± 9.2	152.4 ± 18.5	2411 ± 45	341.6 ± 73.0
	6 Jul 2010	1.258	15	3.306	3.056	-17.83	789.9 ± 9.3	169.0 ± 18.8	2296 ± 41	493.3 ± 76.6
(295) Theresia	31 Jan 2010	1.125	11	3.122	2.977	18.39	198.6 ± 2.6	22.02 ± 5.41	547.7 ± 12.6	46.63 ± 24.87
	22 Jul 2010	0.992	12	3.257	3.023	-18.12	155.2 ± 2.2	16.47 ± 4.28	457.0 ± 10.0	46.24 ± 19.72
(322) Phaeo	25 Jan 2010	0.992	8	3.445	3.302	16.60	605.1 ± 6.8	188.3 ± 13.3	1858 ± 38	467.2 ± 76.5
	10 Jul 2010	1.121	10	3.281	3.022	-17.95	880.6 ± 9.8	225.6 ± 19.3	2389 ± 46	601.7 ± 109.3
(343) Ostara	12 Jan 2010	0.992	11	2.678	2.443	21.51	165.1 ± 2.3	62.98 ± 4.39	359.4 ± 9.6	234.7 ± 16.7
	25 Jun 2010	1.254	14	2.916	2.656	-20.33	139.0 ± 1.9	51.18 ± 3.62	343.3 ± 9.2	122.7 ± 18.3
(444) Gyptis	30 Jan 2010	1.125	9	3.150	3.005	18.22	7659 ± 1114	3179 ± 2370	14500 ± 2050	2603 ± 4636
	20 Jul 2010	1.258	12	2.925	2.673	-20.27	15060 ± 2180	3594 ± 4736	21640 ± 3100	2781 ± 6289
(463) Lola	7 Jan 2010	0.598	6	2.904	2.659	19.73	182.6 ± 2.5	28.24 ± 4.94	435.4 ± 11.2	40.06 ± 21.72
	14 Jun 2010	1.254	12	2.903	2.616	-20.36	149.7 ± 2.0	28.69 ± 3.88	380.1 ± 9.2	65.19 ± 17.67
(464) Megaira	9 Jan 2010	0.465	6	3.371	3.162	16.92	1033 ± 11	74.80 ± 21.49	3016 ± 39	181.1 ± 60.3
	17 Jun 2010	3.504	26	3.320	3.071	-17.73	1148 ± 149	148.0 ± 285.4	3254 ± 65	369.4 ± 137.7
(493) Griseldis	13 Jan 2010	0.727	9	3.487	3.298	16.36	235.4 ± 2.9	76.84 ± 5.77	737.4 ± 14.5	268.0 ± 33.0
	26 Jun 2010	0.992	9	3.621	3.399	-16.25	199.6 ± 2.5	44.93 ± 4.97	656.6 ± 15.0	153.2 ± 29.1
(500) Selinur	7 Feb 2010	1.258	9	2.951	2.764	19.52	446.7 ± 5.0	115.8 ± 9.4	1218 ± 27	232.3 ± 56.3
	27 Jul 2010	1.125	11	2.785	2.514	-21.30	718.3 ± 8.1	121.6 ± 15.8	1724 ± 28	202.7 ± 58.5
(520) Franziska	19 Jan 2010	0.859	11	3.207	3.029	17.86	107.1 ± 1.7	72.43 ± 3.39	330.1 ± 7.9	189.5 ± 15.5
	5 Jul 2010	1.254	13	3.305	3.056	-17.83	105.0 ± 1.5	58.25 ± 3.30	335.1 ± 8.3	167.9 ± 19.0
(538) Friederike	15 Feb 2010	1.125	12	3.586	3.439	15.99	595.8 ± 6.8	109.7 ± 13.7	1862 ± 43	391.4 ± 104.5
	3 Aug 2010	0.992	11	3.403	3.160	-17.27	840.1 ± 9.4	164.7 ± 17.9	2448 ± 40	396.7 ± 77.0
(558) Carmen	3 Feb 2010	3.906	23	2.937	2.769	19.60	1058 ± 83	444.3 ± 245.3	2514 ± 44	565.0 ± 113.1
	27 Jul 2010	1.258	16	3.000	2.746	-19.71	1048 ± 108	306.9 ± 265.2	2580 ± 44	582.9 ± 80.2

Table 2.2 — continued

Object	UT Date[a]	$\Delta t_{\rm obs}$[b]	N[c]	$R_{\rm AU}$[d]	$\Delta_{\rm AU}$[e]	α (°)[f]	$\overline{W3}$[g]	$\diamondsuit W3$[h]	$\overline{W4}$[g]	$\diamondsuit W4$[h]
(562) Salome	22 Jan 2010	0.992	13	3.225	3.061	17.76	186.7 ± 2.4	54.54 ± 5.04	591.6 ± 13.7	152.9 ± 24.1
	10 Jul 2010	1.258	15	3.095	2.828	-19.07	246.5 ± 3.4	74.90 ± 7.48	707.0 ± 15.9	199.2 ± 31.9
(567) Eleutheria	20 Jan 2010	0.992	10	2.835	2.637	20.30	3218 ± 465	940.2 ± 901.3	6781 ± 101	1590 ± 188
	10 Jul 2010	1.254	14	2.871	2.588	-20.62	2654 ± 386	1029 ± 802	5886 ± 107	2048 ± 231
(583) Klotilde	26 Jan 2010	0.992	8	2.771	2.595	20.81	2968 ± 426	530.1 ± 876.2	6325 ± 117	1104 ± 165
	21 Jul 2010	0.992	10	3.016	2.769	-19.63	1625 ± 233	278.2 ± 478.3	4226 ± 90	812.8 ± 219.9
(651) Antikleia	29 Jan 2010	1.125	11	3.312	3.172	17.30	162.5 ± 2.1	43.80 ± 4.03	510.6 ± 13.8	117.9 ± 31.7
	17 Jul 2010	3.902	20	3.306	3.059	-17.82	187.1 ± 2.4	52.87 ± 4.69	559.9 ± 12.7	154.1 ± 22.3
(656) Beagle	31 Jan 2010	1.258	12	2.824	2.661	20.42	813.7 ± 132.2	1275 ± 281	2342 ± 49	1780 ± 124
	27 Jul 2010	1.125	14	3.031	2.779	-19.50	554.2 ± 7.5	426.9 ± 15.4	1593 ± 29	1303 ± 62
(662) Newtonia	17 Jan 2010	0.992	10	2.681	2.462	21.51	214.6 ± 2.8	122.5 ± 6.1	498.4 ± 11.8	242.7 ± 26.3
	7 Jul 2010	1.391	18	2.289	1.961	-26.24	532.2 ± 7.0	395.5 ± 14.3	1029 ± 21	478.6 ± 38.8
(668) Dora	17 Jan 2010	0.992	9	3.219	3.033	17.78	104.8 ± 1.5	42.35 ± 2.97	291.0 ± 8.4	107.8 ± 16.5
	2 Jul 2010	1.258	15	2.895	2.626	-20.47	156.6 ± 2.1	84.84 ± 3.96	384.6 ± 11.2	203.1 ± 24.4
(670) Ottegebe	26 Jan 2010	0.996	9	3.332	3.187	17.18	183.5 ± 2.5	40.37 ± 5.03	593.0 ± 12.3	112.4 ± 26.2
	12 Jul 2010	1.125	13	3.206	2.942	-18.38	207.0 ± 2.6	53.42 ± 5.45	638.6 ± 13.6	175.1 ± 23.9
(688) Melanie	25 Jan 2010	0.992	11	2.808	2.629	20.52	645.9 ± 7.4	224.3 ± 15.7	1461 ± 30	571.7 ± 55.9
	15 Jul 2010	4.301	25	2.566	2.269	-23.22	964.6 ± 11.2	291.0 ± 22.2	2012 ± 35	569.2 ± 72.7
(734) Benda	13 Jan 2010	0.727	8	3.237	3.038	17.66	949.1 ± 11.2	310.2 ± 22.8	2624 ± 47	594.0 ± 90.8
	28 Jun 2010	0.992	12	3.363	3.125	-17.53	755.5 ± 8.3	281.2 ± 16.1	2189 ± 45	752.8 ± 99.7
(735) Marghanna	3 Feb 2010	3.770	20	3.313	3.156	17.31	864.6 ± 10.7	173.1 ± 25.5	2374 ± 46	390.9 ± 91.0
	23 Jul 2010	0.594	8	2.873	2.616	-20.64	2161 ± 310	270.2 ± 622.6	4391 ± 78	731.5 ± 175.8
(793) Arizona	1 Feb 2010	0.992	10	3.046	2.897	18.87	159.7 ± 2.2	31.25 ± 4.63	451.8 ± 11.8	76.92 ± 21.93
	23 Jul 2010	1.125	13	2.871	2.613	-20.65	210.8 ± 2.7	22.51 ± 5.66	557.4 ± 13.0	52.99 ± 24.17
(826) Henrika	16 Jan 2010	0.859	8	2.547	2.314	22.70	268.7 ± 3.9	87.78 ± 8.22	594.5 ± 18.9	213.4 ± 44.8
	10 Jul 2010	1.387	14	2.230	1.889	-26.96	491.2 ± 5.9	145.5 ± 11.1	970.3 ± 19.6	249.1 ± 38.7
(829) Academia	17 Jan 2010	0.992	9	2.797	2.587	20.58	654.8 ± 7.9	295.5 ± 15.2	1498 ± 29	598.2 ± 52.8
	3 Jul 2010.	1.258	12	2.835	2.561	-20.92	695.0 ± 8.3	238.3 ± 15.4	1578 ± 32	522.5 ± 59.5

Table 2.2 — continued

Object	UT Date[a]	$\Delta t_{\rm obs}$[b]	N[c]	$R_{\rm AU}$[d]	$\Delta_{\rm AU}$[e]	α (°)[f]	$\overline{W3}$[g]	$\diamondsuit W3$[h]	$\overline{W4}$[g]	$\diamondsuit W4$[h]
(883) Matterania	16 Jan 2010	0.992	8	2.571	2.341	22.47	27.42 ± 0.79	12.08 ± 1.64	63.19 ± 4.22	29.54 ± 8.82
	3 Jul 2010	1.121	14	2.261	1.933	-26.60	43.37 ± 0.90	26.01 ± 1.80	91.33 ± 4.19	51.78 ± 8.21
(906) Repsolda	13 Feb 2010	1.125	13	3.000	2.821	19.21	1146 ± 158	323.3 ± 310.1	3026 ± 49	478.9 ± 83.8
	3 Aug 2010	1.258	12	2.864	2.589	-20.65	1840 ± 264	350.0 ± 546.8	4302 ± 66	1088 ± 104
(918) Itha	25 Jan 2010	0.992	8	3.286	3.136	17.43	52.28 ± 0.97	14.68 ± 1.94	182.9 ± 5.8	41.91 ± 11.12
	12 Jul 2010	1.125	10	3.058	2.786	-19.31	102.4 ± 1.6	24.24 ± 3.13	306.8 ± 7.5	78.31 ± 13.81
(972) Cohnia	16 Feb 2010	1.125	9	3.662	3.519	15.65	670.6 ± 7.6	101.1 ± 15.4	2081 ± 34	340.1 ± 68.1
	4 Aug 2010	1.125	11	3.426	3.184	-17.14	916.9 ± 10.1	197.6 ± 17.7	2677 ± 53	575.4 ± 120.3
(977) Philippa	19 Jan 2010	0.992	12	3.038	2.850	18.88	1088 ± 137	462.3 ± 279.3	2976 ± 57	1028 ± 149
	7 Jul 2010	1.125	12	3.072	2.809	-19.23	1158 ± 167	510.8 ± 326.7	3285 ± 53	1150 ± 117
(987) Wallia	15 Feb 2010	1.125	11	3.365	3.210	17.07	344.4 ± 4.4	64.07 ± 8.82	1088 ± 19	122.3 ± 42.4
	5 Aug 2010	0.859	6	2.992	2.723	-19.72	737.4 ± 8.6	53.58 ± 17.37	1810 ± 33	64.21 ± 65.66
(998) Bodea	7 Feb 2010	1.125	8	3.727	3.578	15.34	71.80 ± 1.21	43.08 ± 2.29	258.6 ± 6.8	148.0 ± 14.7
	25 Jul 2010	0.992	10	3.560	3.338	-16.52	105.6 ± 1.6	63.93 ± 2.88	354.5 ± 8.6	211.5 ± 16.0
(1018) Arnolda	10 Feb 2010	0.992	10	2.858	2.668	20.20	69.15 ± 1.15	27.09 ± 2.17	190.7 ± 6.3	74.98 ± 13.27
	3 Jul 2010	1.387	10	2.439	2.136	-24.49	151.5 ± 2.1	91.37 ± 3.85	347.0 ± 9.0	183.8 ± 18.6
(1047) Geisha	17 Jan 2010	0.992	12	2.651	2.429	21.77	52.48 ± 0.99	19.88 ± 2.07	122.7 ± 4.8	46.02 ± 9.21
	1 Jul 2010	1.391	14	2.637	2.350	-22.58	50.23 ± 0.97	23.05 ± 1.92	120.2 ± 4.9	50.83 ± 8.98
(1051) Merope	26 Jan 2010	0.859	11	3.396	3.254	16.85	587.6 ± 6.4	93.96 ± 13.64	1701 ± 30	320.3 ± 57.5
	13 Jul 2010	1.258	14	3.259	3.000	-18.08	724.2 ± 7.7	134.1 ± 14.7	2024 ± 42	349.1 ± 102.6
(1076) Viola	24 Jan 2010	0.992	10	2.503	2.295	23.15	334.8 ± 4.0	36.84 ± 8.26	677.5 ± 14.0	39.52 ± 29.06
	13 Jul 2010	1.258	14	2.729	2.431	-21.74	247.7 ± 3.1	41.02 ± 5.88	535.4 ± 12.7	76.71 ± 23.36
(1077) Campanula	22 Jan 2010	0.992	10	2.850	2.662	20.19	23.19 ± 0.68	10.91 ± 1.30	69.82 ± 4.21	38.68 ± 8.96
	8 Jul 2010	1.258	11	2.678	2.386	-22.20	28.91 ± 0.70	13.18 ± 1.39	82.05 ± 4.02	31.76 ± 7.44
(1083) Salvia	7 Jan 2010	0.992	11	2.018	1.692	29.08	141.8 ± 2.0	94.99 ± 4.03	264.5 ± 6.8	168.3 ± 14.1
	29 Jun 2010	0.992	13	2.361	2.048	-25.40	86.86 ± 1.39	34.85 ± 2.93	183.5 ± 5.6	68.22 ± 11.41
(1095) Tulipa	12 Jan 2010	0.992	10	2.951	2.733	19.44	215.3 ± 2.7	50.85 ± 5.76	599.9 ± 12.7	140.7 ± 25.3
	29 Jun 2010	1.254	16	2.970	2.709	-19.93	180.1 ± 2.4	53.84 ± 5.06	530.7 ± 12.7	141.0 ± 23.6

Table 2.2 — continued

Object	UT Date[a]	$\Delta t_{\rm obs}$[b]	N[c]	$R_{\rm AU}$[d]	$\Delta_{\rm AU}$[e]	α (°)[f]	$\overline{W3}$[g]	$\diamondsuit W3$[h]	$\overline{W4}$[g]	$\diamondsuit W4$[h]
(1109) Tata	10 Feb 2010	1.125	12	2.987	2.804	19.29	1318 ± 190	351.9 ± 388.2	3058 ± 59	350.0 ± 111.7
	4 Aug 2010	1.125	8	2.894	2.620	-20.42	1581 ± 227	233.2 ± 464.1	3405 ± 65	722.5 ± 152.6
(1123) Shapleya	9 Feb 2010	1.258	13	2.566	2.352	22.61	71.23 ± 1.28	35.78 ± 3.05	161.9 ± 5.39	66.59 ± 11.27
	29 Jul 2010	1.258	12	2.518	2.223	-23.68	80.40 ± 1.25	43.53 ± 2.43	175.4 ± 6.2	89.60 ± 13.11
(1125) China	12 Feb 2010	1.125	10	3.187	3.017	18.04	111.0 ± 1.5	55.77 ± 3.09	344.5 ± 9.5	168.6 ± 17.8
	1 Aug 2010	0.992	11	3.500	3.263	-16.78	86.05 ± 1.29	36.15 ± 2.67	293.0 ± 7.5	136.1 ± 17.0
(1136) Mercedes	4 Feb 2010	3.770	22	3.079	2.917	18.67	157.2 ± 2.1	54.11 ± 4.11	418.9 ± 10.3	116.9 ± 21.3
	24 Jul 2010	1.121	12	2.745	2.475	-21.64	359.3 ± 4.2	66.54 ± 8.61	780.4 ± 17.3	154.0 ± 29.5
(1142) Aetolia	27 Jan 2010	1.125	10	2.944	2.780	19.54	136.5 ± 1.8	24.48 ± 3.62	369.7 ± 10.7	63.15 ± 21.98
	23 Jul 2010	1.258	11	2.900	2.642	-20.44	149.4 ± 2.0	50.21 ± 4.38	390.6 ± 10.1	114.1 ± 22.8
(1152) Pawona	16 Jan 2010	0.992	12	2.324	2.068	25.02	206.7 ± 2.9	37.61 ± 6.43	440.2 ± 12.4	102.1 ± 26.6
	9 Jul 2010	1.391	14	2.344	2.019	-25.56	243.1 ± 3.2	41.58 ± 6.18	519.9 ± 11.2	87.69 ± 26.02
(1162) Larissa	28 Jan 2010	1.254	12	3.610	3.480	15.83	183.2 ± 2.4	68.91 ± 5.02	607.7 ± 14.2	214.9 ± 33.2
	22 Jul 2010	1.258	10	3.514	3.292	-16.75	224.2 ± 2.9	36.96 ± 5.92	725.8 ± 16.2	121.3 ± 30.9
(1224) Fantasia	8 Feb 2010	0.594	8	2.761	2.563	20.93	83.37 ± 1.31	12.65 ± 2.68	195.8 ± 5.6	29.47 ± 11.26
	26 Jul 2010	0.992	10	2.652	2.372	-22.42	85.89 ± 1.46	14.52 ± 2.79	216.1 ± 6.6	29.33 ± 12.08
(1258) Sicilia	27 Jan 2010	1.125	9	3.303	3.160	17.34	367.0 ± 4.6	55.84 ± 9.12	1073 ± 25	212.8 ± 46.0
	16 Jul 2010	3.902	22	3.283	3.036	-17.95	373.0 ± 7.9	70.47 ± 33.76	1100 ± 35	259.0 ± 139.7
(1281) Jeanne	14 Jan 2010	1.125	12	2.567	2.329	22.51	422.1 ± 5.1	94.81 ± 10.48	851.7 ± 19.6	156.1 ± 37.3
	6 Jul 2010	1.391	15	2.195	1.856	-27.45	698.3 ± 8.4	248.8 ± 15.8	1299 ± 29	402.6 ± 55.7
(1288) Santa	22 Jan 2010	0.992	8	3.052	2.875	18.81	241.4 ± 3.1	177.7 ± 5.6	623.0 ± 15.7	417.9 ± 29.3
	11 Jul 2010	0.992	12	2.993	2.719	-19.75	336.5 ± 4.4	172.9 ± 8.7	827.8 ± 18.7	418.7 ± 40.2
(1296) Andree	20 Jan 2010	0.992	10	2.310	2.069	25.20	720.9 ± 8.4	223.9 ± 14.8	1363 ± 24	361.0 ± 50.6
	10 Jul 2010	1.387	13	2.571	2.266	-23.16	363.2 ± 4.3	108.8 ± 8.5	827.5 ± 18.1	200.9 ± 32.0
(1299) Mertona	19 Jan 2010	0.992	8	3.006	2.815	19.09	51.62 ± 1.00	23.62 ± 2.06	146.1 ± 5.3	63.74 ± 11.01
	4 Jul 2010	0.992	12	3.230	2.980	-18.26	31.51 ± 0.75	18.40 ± 1.44	103.5 ± 4.2	50.74 ± 7.51
(1310) Villigera	19 Jan 2010	0.992	10	2.170	1.910	26.95	213.3 ± 2.7	63.98 ± 5.28	385.6 ± 11.2	121.8 ± 19.6
	2 Jul 2010	1.125	12	2.778	2.503	-21.38	61.41 ± 1.08	15.08 ± 2.17	158.6 ± 5.0	41.43 ± 10.28

Table 2.2 — continued

Object	UT Date[a]	$\Delta t_{\rm obs}$[b]	N[c]	$R_{\rm AU}$[d]	$\Delta_{\rm AU}$[e]	α (°)[f]	$\overline{W3}$[g]	$\diamondsuit W3$[h]	$\overline{W4}$[g]	$\diamondsuit W4$[h]
(1316) Kasan	14 Jan 2010	0.992	9	3.022	2.818	18.97	13.30 ± 0.52	1.927 ± 1.058	32.35 ± 3.00	6.024 ± 5.970
	23 Jun 2010	1.125	10	3.175	2.938	-18.61	11.43 ± 0.51	1.818 ± 1.017	30.25 ± 3.05	10.60 ± 6.30
(1325) Inanda	18 Jan 2010	0.996	13	3.145	2.957	18.22	26.52 ± 0.68	10.39 ± 1.32	74.42 ± 3.66	32.24 ± 6.95
	1 Jul 2010	1.258	13	2.915	2.649	-20.33	30.42 ± 0.76	17.80 ± 1.52	81.33 ± 4.22	59.72 ± 8.96
(1335) Demoulina	8 Jan 2010	0.727	9	2.560	2.300	22.54	28.74 ± 0.72	16.68 ± 1.43	64.39 ± 3.65	38.53 ± 7.52
	21 Jun 2010	1.391	14	2.565	2.284	-23.27	22.71 ± 0.70	26.55 ± 1.32	53.77 ± 3.65	65.49 ± 7.00
(1352) Wawel	1 Feb 2010	1.125	11	2.951	2.797	19.50	97.17 ± 1.41	32.99 ± 2.84	281.2 ± 7.9	95.20 ± 15.20
	25 Jul 2010	0.992	13	2.950	2.693	-20.07	92.12 ± 1.51	48.37 ± 2.98	275.4 ± 7.8	147.9 ± 15.3
(1375) Alfreda	30 Jan 2010	1.258	11	2.501	2.310	23.19	100.9 ± 1.6	21.40 ± 2.82	234.7 ± 7.7	55.63 ± 14.53
	24 Jul 2010	1.258	12	2.599	2.317	-22.93	97.46 ± 1.46	18.57 ± 2.83	235.6 ± 6.9	47.80 ± 13.60
(1412) Lagrula	23 Jan 2010	0.992	12	2.258	2.022	25.83	53.52 ± 1.35	47.35 ± 3.69	111.0 ± 4.3	93.99 ± 8.55
	13 Jul 2010	1.254	11	2.427	2.102	-24.61	52.74 ± 0.94	31.90 ± 1.93	113.7 ± 4.6	82.07 ± 8.25
(1443) Ruppina	11 Feb 2010	1.125	12	3.029	2.851	19.01	52.19 ± 0.98	25.00 ± 1.80	161.9 ± 5.9	71.18 ± 12.14
	3 Aug 2010	0.992	9	2.933	2.666	-20.15	60.26 ± 1.02	20.21 ± 2.26	183.3 ± 5.9	58.84 ± 12.80
(1452) Hunnia	23 Jan 2010	0.996	11	2.849	2.663	20.21	152.4 ± 2.3	97.22 ± 4.84	354.2 ± 10.2	163.4 ± 19.8
	11 Jul 2010	1.254	11	3.183	2.921	-18.52	84.56 ± 1.33	52.23 ± 2.65	247.5 ± 7.3	149.4 ± 16.7
(1501) Baade	17 Feb 2010	1.258	9	3.142	2.977	18.33	16.69 ± 0.65	5.537 ± 1.308	55.98 ± 3.59	17.40 ± 6.76
	5 Aug 2010	0.398	5	2.962	2.691	-19.93	25.35 ± 0.66	7.139 ± 1.298	75.87 ± 3.57	23.11 ± 7.11
(1517) Beograd	30 Jan 2010	0.859	9	2.718	2.545	21.24	657.0 ± 8.1	95.67 ± 15.35	1456 ± 34	186.3 ± 61.5
	25 Jul 2010	1.258	13	2.645	2.366	-22.50	741.0 ± 8.8	139.9 ± 17.9	1576 ± 37	311.5 ± 90.9
(1536) Pielinen	17 Jan 2010	0.992	9	2.634	2.412	21.92	25.52 ± 0.70	21.03 ± 1.41	61.29 ± 3.33	52.30 ± 6.64
	2 Jul 2010	1.391	16	2.534	2.236	-23.55	37.30 ± 0.86	26.51 ± 1.71	82.11 ± 3.85	61.70 ± 8.21
(1542) Schalen	21 Jan 2010	0.996	10	3.439	3.279	16.62	298.4 ± 4.1	154.9 ± 8.6	899.9 ± 17.2	445.2 ± 32.8
	7 Jul 2010	1.254	12	3.406	3.157	-17.28	337.2 ± 4.168	156.4 ± 8.062	991.6 ± 19.96	416.9 ± 40.93
(1565) Lemaitre	20 Feb 2010	0.992	12	3.092	2.927	18.65	14.22 ± 0.56	3.013 ± 1.117	38.54 ± 3.27	7.218 ± 6.449
	4 Aug 2010	1.258	11	2.690	2.403	-22.05	30.19 ± 0.74	3.058 ± 1.446	66.17 ± 3.53	9.524 ± 7.161
(1567) Alikoski	16 Jan 2010	0.992	11	2.951	2.745	19.45	1790 ± 258	385.6 ± 531.5	3970 ± 64	611.1 ± 108.1
	3 Jul 2010	0.727	8	3.027	2.763	-19.53	1619 ± 232	273.7 ± 478.8	3789 ± 78	613.6 ± 160.5

Table 2.2 — continued

Object	UT Date[a]	$\Delta t_{\rm obs}$[b]	N[c]	$R_{\rm AU}$[d]	$\Delta_{\rm AU}$[e]	α (°)[f]	$\overline{W3}$[g]	$\diamondsuit W3$[h]	$\overline{W4}$[g]	$\diamondsuit W4$[h]
(1573) Vaisala	4 Feb 2010	3.773	21	2.901	2.729	19.87	23.46 ± 0.74	16.20 ± 1.41	61.87 ± 3.71	44.56 ± 7.75
	21 Jul 2010	1.258	17	2.704	2.437	-22.01	40.71 ± 0.87	27.40 ± 1.69	94.12 ± 3.84	82.24 ± 8.28
(1577) Reiss	8 Feb 2010	0.992	10	2.599	2.388	22.30	12.12 ± 0.59	5.103 ± 1.189	31.64 ± 3.49	14.16 ± 7.78
	28 Jul 2010	0.594	6	2.516	2.228	-23.72	10.80 ± 0.54	6.998 ± 1.078	26.82 ± 3.13	4.533 ± 6.230
(1628) Strobel	26 Jan 2010	0.992	10	2.983	2.820	19.27	872.0 ± 9.6	221.8 ± 20.5	2158 ± 43	519.6 ± 107.9
	14 Jul 2010	0.664	9	3.093	2.819	-19.07	890.3 ± 11.3	148.7 ± 21.7	2318 ± 48	370.9 ± 100.8
(1644) Rafita	19 Jan 2010	1.125	11	2.394	2.160	24.25	155.3 ± 2.2	37.28 ± 4.27	310.8 ± 9.1	57.83 ± 16.32
	9 Jul 2010	1.391	13	2.676	2.383	-22.21	117.9 ± 1.7	14.21 ± 3.28	252.6 ± 7.0	34.16 ± 15.97
(1651) Behrens	24 Jan 2010	1.258	11	2.041	1.785	28.83	156.3 ± 2.2	86.55 ± 4.50	259.0 ± 8.5	134.0 ± 20.2
	27 Jul 2010	1.523	15	2.147	1.813	-28.12	105.6 ± 1.6	79.34 ± 3.11	197.0 ± 6.5	182.6 ± 12.3
(1655) Comas Sola	22 Jan 2010	0.992	12	2.951	2.771	19.48	419.4 ± 4.9	75.71 ± 9.21	1039 ± 21	169.0 ± 36.3
	8 Jul 2010	1.125	11	3.258	3.003	-18.09	249.8 ± 3.0	63.90 ± 6.30	707.2 ± 15.6	144.6 ± 35.0
(1702) Kalahari	26 Jan 2010	0.996	13	3.182	3.027	18.02	242.0 ± 3.1	82.62 ± 6.17	660.2 ± 15.8	164.2 ± 41.6
	13 Jul 2010	1.125	13	3.009	2.732	-19.63	384.6 ± 4.6	149.2 ± 9.3	944.4 ± 21.6	257.4 ± 42.6
(1723) Klemola	1 Feb 2010	1.258	15	2.919	2.762	19.72	301.7 ± 3.7	102.7 ± 7.5	809.2 ± 16.3	265.4 ± 38.4
	26 Jul 2010	1.254	16	2.990	2.736	-19.79	339.9 ± 4.38	94.55 ± 8.98	888.4 ± 18.0	207.2 ± 37.2
(1734) Zhongolovich	5 Feb 2010	3.770	16	3.345	3.189	17.14	107.1 ± 1.7	27.52 ± 3.61	331.2 ± 9.4	80.04 ± 18.30
	25 Jul 2010	0.992	11	3.112	2.865	-18.98	200.9 ± 2.8	37.73 ± 5.28	522.1 ± 12.6	93.76 ± 24.87
(1741) Giclas	14 Feb 2010	1.258	12	3.082	2.910	18.69	26.54 ± 0.71	4.530 ± 1.426	86.16 ± 4.08	16.84 ± 8.32
	5 Aug 2010	1.258	10	3.050	2.785	-19.33	43.04 ± 0.89	9.065 ± 1.767	118.1 ± 4.9	27.52 ± 10.04
(1759) Kienle	31 Jan 2010	1.125	11	3.387	3.253	16.91	5.260 ± 0.534	3.971 ± 1.069	15.57 ± 3.60	23.29 ± 6.90
	16 Jul 2010	3.902	21	3.079	2.810	-19.17	11.24 ± 0.58	6.387 ± 1.162	33.22 ± 3.50	24.74 ± 7.19
(1768) Appenzella	16 Feb 2010	0.859	8	2.886	2.706	20.01	128.3 ± 1.9	33.28 ± 3.97	313.4 ± 6.7	72.51 ± 13.66
	4 Aug 2010	0.992	12	2.766	2.484	-21.41	143.8 ± 2.1	45.99 ± 3.85	341.9 ± 9.5	113.6 ± 17.5
(01807) Slovakia	28 Jan 2010	1.125	13	2.622	2.437	22.05	42.82 ± 0.89	29.57 ± 1.67	97.08 ± 4.58	101.0 ± 10.4
	16 Jul 2010	4.168	21	2.511	2.202	-23.74	44.36 ± 1.02	41.55 ± 2.35	94.07 ± 4.35	89.33 ± 9.19
(1896) Beer	24 Jan 2010	1.125	10	2.872	2.692	20.04	3.668 ± 0.551	2.372 ± 1.110	12.89 ± 3.43	8.372 ± 6.634
	10 Jul 2010	1.121	10	2.674	2.377	-22.22	5.898 ± 0.544	2.684 ± 1.109	18.74 ± 3.16	8.696 ± 6.395

Table 2.2 — continued

Object	UT Date[a]	$\Delta t_{\rm obs}$[b]	N[c]	$R_{\rm AU}$[d]	$\Delta_{\rm AU}$[e]	α (°)[f]	$\overline{W3}$[g]	$\diamondsuit W3$[h]	$\overline{W4}$[g]	$\diamondsuit W4$[h]
(1936) Lugano	29 Jan 2010	1.258	12	2.357	2.152	24.70	847.6 ± 10.4	84.61 ± 20.44	$1510. \pm 24.79$	115.8 ± 56.66
	28 Jul 2010	1.254	11	2.577	2.290	-23.11	754.0 ± 8.8	72.25 ± 16.44	1375 ± 24	99.09 ± 48.34
(1979) Sakharov	3 Feb 2010	0.598	9	2.542	2.362	22.80	11.48 ± 0.61	3.270 ± 1.205	27.33 ± 3.41	18.20 ± 6.96
	27 Jul 2010	1.258	13	2.611	2.327	-22.80	7.480 ± 0.530	2.513 ± 1.069	18.85 ± 3.27	9.564 ± 6.457
(2005) Hencke	13 Feb 2010	1.125	9	3.055	2.880	18.86	12.46 ± 0.53	2.008 ± 1.088	39.10 ± 3.33	9.072 ± 6.557
	1 Aug 2010	0.992	9	3.019	2.759	-19.56	15.26 ± 0.56	2.762 ± 1.138	48.41 ± 3.43	11.77 ± 6.98
(2072) Kosmodemyanskaya	29 Jan 2010	1.254	13	2.695	2.517	21.43	4.511 ± 0.524	1.488 ± 1.040	14.38 ± 3.28	7.749 ± 6.683
	20 Jul 2010	1.254	9	2.840	2.582	-20.90	3.577 ± 0.501	0.955 ± 0.958	11.22 ± 4.04	6.158 ± 8.638
(2106) Hugo	15 Feb 2010	0.992	11	2.964	2.785	19.46	58.76 ± 1.13	34.10 ± 2.25	170.1 ± 5.0	83.51 ± 9.25
	5 Aug 2010	1.125	14	2.931	2.661	-20.15	60.07 ± 1.08	38.61 ± 2.44	175.1 ± 6.0	100.3 ± 11.0
(2111) Tselina	26 Jan 2010	0.730	9	3.273	3.124	17.50	68.31 ± 1.19	11.95 ± 2.38	232.0 ± 6.7	39.98 ± 14.02
	13 Jul 2010	1.125	12	3.294	3.034	-17.87	86.34 ± 1.31	24.99 ± 2.48	277.9 ± 8.6	80.77 ± 15.53
(2123) Vltava	8 Jan 2010	0.859	9	3.067	2.836	18.65	46.95 ± 0.95	12.40 ± 2.04	138.5 ± 5.3	34.81 ± 10.32
	21 Jun 2010	1.125	12	3.069	2.824	-19.27	52.23 ± 0.99	10.11 ± 1.83	146.8 ± 5.3	27.80 ± 11.82
(2140) Kemerovo	28 Jan 2010	1.125	12	3.144	2.994	18.25	279.8 ± 3.5	20.75 ± 7.63	717.6 ± 14.5	93.83 ± 32.56
	20 Jul 2010	0.992	10	3.145	2.907	-18.79	270.5 ± 3.6	31.82 ± 7.83	709.8 ± 14.1	49.88 ± 31.83
(2144) Marietta	31 Jan 2010	1.258	11	3.014	2.861	19.07	49.88 ± 0.97	18.84 ± 2.01	153.7 ± 4.6	53.90 ± 8.90
	24 Jul 2010	1.125	12	3.049	2.800	-19.39	42.64 ± 0.91	23.29 ± 1.80	144.5 ± 4.7	70.93 ± 9.01
(2177) Oliver	12 Feb 2010	0.992	10	3.259	3.093	17.63	46.64 ± 0.92	23.89 ± 1.83	165.9 ± 5.3	64.19 ± 9.76
	3 Aug 2010	1.258	12	3.101	2.843	-19.01	55.87 ± 1.01	33.25 ± 2.02	192.1 ± 5.9	91.41 ± 11.73
(2203) van Rhijn	31 Jan 2010	1.125	12	3.673	3.554	15.55	38.53 ± 0.84	19.77 ± 1.72	149.3 ± 5.0	69.59 ± 9.86
	21 Jul 2010	1.125	9	3.575	3.357	-16.46	55.17 ± 0.96	24.76 ± 1.80	195.9 ± 5.6	76.99 ± 10.89
(2204) Lyyli	17 Jan 2010	0.992	11	2.289	2.035	25.44	657.6 ± 8.4	210.4 ± 15.4	1187 ± 25	354.1 ± 44.3
	30 Jun 2010	1.258	15	2.974	2.717	-19.91	232.8 ± 3.0	56.45 ± 5.58	571.9 ± 14.6	158.8 ± 31.2
(2214) Carol	14 Feb 2010	1.258	13	3.187	3.021	18.05	129.9 ± 1.8	81.35 ± 4.11	360.0 ± 10.0	206.7 ± 23.3
	5 Aug 2010	0.598	7	2.744	2.457	-21.58	284.6 ± 3.6	151.5 ± 6.4	678.5 ± 11.3	319.6 ± 21.3
(2239) Paracelsus	8 Jan 2010	0.859	11	3.482	3.273	16.36	164.4 ± 2.4	93.39 ± 4.80	538.5 ± 12.8	311.7 ± 24.4
	21 Jun 2010	1.125	13	3.516	3.296	-16.75	154.5 ± 2.2	73.53 ± 4.70	512.6 ± 11.3	203.7 ± 23.8

Table 2.2 — continued

Object	UT Date[a]	$\Delta t_{\rm obs}$[b]	N[c]	$R_{\rm AU}$[d]	$\Delta_{\rm AU}$[e]	α (°)[f]	$\overline{W3}$[g]	$\diamondsuit W3$[h]	$\overline{W4}$[g]	$\diamondsuit W4$[h]
(2268) Szmytowna	16 Jan 2010	0.992	10	3.137	2.944	18.26	37.24 ± 0.81	8.993 ± 1.600	112.5 ± 4.5	31.58 ± 9.50
	2 Jul 2010	1.258	16	3.246	2.997	-18.18	34.87 ± 0.78	8.080 ± 1.519	105.0 ± 4.5	28.15 ± 9.16
(2275) Cuitlahuac	4 Feb 2010	4.035	21	2.596	2.400	22.31	16.23 ± 0.66	16.04 ± 1.33	42.98 ± 3.39	37.89 ± 6.64
	28 Jul 2010	1.387	12	2.329	2.017	-25.74	35.38 ± 0.81	28.83 ± 1.65	77.37 ± 3.82	51.59 ± 7.38
(2297) Daghestan	13 Jan 2010	1.125	12	2.870	2.650	20.02	229.3 ± 3.0	115.5 ± 6.0	611.7 ± 14.8	233.6 ± 29.5
	4 Jul 2010	1.258	14	2.749	2.467	-21.61	248.6 ± 3.1	110.0 ± 6.2	645.1 ± 15.3	242.5 ± 27.8
(2306) Bauschinger	22 Jan 2010	0.992	10	2.872	2.683	20.03	102.4 ± 1.6	83.73 ± 2.96	252.9 ± 7.6	197.5 ± 14.6
	10 Jul 2010	1.258	13	2.793	2.504	-21.23	142.1 ± 2.1	92.85 ± 4.21	343.7 ± 9.0	204.0 ± 19.4
(2332) Kalm	13 Jan 2010	1.125	12	3.149	2.947	18.18	210.9 ± 2.8	128.3 ± 5.2	625.8 ± 16.4	378.9 ± 37.4
	29 Jun 2010	1.258	16	3.055	2.800	-19.36	229.4 ± 3.2	145.0 ± 6.7	656.6 ± 16.3	442.1 ± 35.3
(2347) Vinata	27 Jan 2010	0.992	7	3.701	3.573	15.43	47.96 ± 0.87	15.21 ± 1.75	185.8 ± 5.8	59.58 ± 13.13
	13 Jul 2010	0.992	9	3.741	3.501	-15.68	38.39 ± 0.78	17.74 ± 1.58	165.7 ± 4.8	56.78 ± 9.16
(2365) Interkosmos	21 Jan 2010	1.121	11	2.351	2.120	24.73	167.2 ± 2.4	46.32 ± 4.76	350.4 ± 9.2	97.27 ± 21.20
	14 Jul 2010	1.391	11	2.561	2.250	-23.24	113.4 ± 1.59	33.54 ± 3.06	268.9 ± 7.1	59.80 ± 14.15
(2375) Radek	20 Jan 2010	1.125	13	2.537	2.320	22.81	751.2 ± 8.5	202.3 ± 14.8	1481 ± 29	315.1 ± 55.0
	21 Jul 2010	1.254	15	2.528	2.244	-23.62	806.1 ± 10.0	306.6 ± 19.6	1549 ± 31	514.5 ± 84.2
(2446) Lunacharsky	25 Jan 2010	1.125	10	2.255	2.027	25.89	139.5 ± 2.0	96.00 ± 4.22	291.9 ± 8.4	187.6 ± 15.5
	29 Jul 2010	1.523	14	1.997	1.639	-30.43	355.2 ± 4.2	181.7 ± 9.1	616.2 ± 14.4	289.7 ± 27.0
(2463) Sterpin	24 Jan 2010	0.730	8	2.672	2.478	21.61	50.35 ± 0.96	12.70 ± 1.89	120.9 ± 5.4	33.40 ± 10.00
	11 Jul 2010	1.258	12	2.895	2.613	-20.44	39.80 ± 0.78	6.104 ± 1.561	107.5 ± 3.8	26.57 ± 7.30
(2500) Alascattalo	26 Jan 2010	1.258	13	2.029	1.777	29.03	76.01 ± 1.24	20.93 ± 2.50	141.8 ± 4.8	37.22 ± 9.02
	1 Aug 2010	1.656	15	2.076	1.726	-29.14	62.26 ± 1.13	18.50 ± 2.53	126.2 ± 4.9	30.63 ± 10.05
(2556) Louise	12 Jan 2010	1.121	13	2.119	1.827	27.61	38.05 ± 0.88	20.09 ± 2.02	79.13 ± 3.62	35.15 ± 7.29
	5 Jul 2010	1.391	16	2.192	1.854	-27.50	42.36 ± 0.89	19.98 ± 1.85	83.88 ± 4.23	49.38 ± 8.94
(2567) Elba	14 Jan 2010	1.125	11	3.058	2.850	18.74	56.35 ± 1.08	15.83 ± 2.13	166.1 ± 6.1	40.24 ± 12.44
	28 Jun 2010	1.258	16	2.894	2.629	-20.49	85.75 ± 1.36	20.47 ± 3.05	228.6 ± 6.6	57.51 ± 11.63
(2687) Tortali	18 Jan 2010	0.992	12	2.644	2.427	21.83	66.15 ± 1.12	27.69 ± 2.37	171.8 ± 5.4	60.79 ± 10.84
	8 Jul 2010	1.258	15	2.424	2.109	-24.67	138.6 ± 2.0	44.23 ± 3.73	305.5 ± 8.0	77.63 ± 17.20

Table 2.2 — continued

Object	UT Date[a]	$\Delta t_{\rm obs}$[b]	N[c]	$R_{\rm AU}$[d]	$\Delta_{\rm AU}$[e]	α (°)[f]	$\overline{W3}$[g]	$\diamondsuit W3$[h]	$\overline{W4}$[g]	$\diamondsuit W4$[h]
(2786) Grinevia	15 Jan 2010	0.992	11	2.998	2.791	19.13	18.59 ± 0.64	7.540 ± 1.257	59.42 ± 3.66	24.17 ± 7.41
	28 Jun 2010	1.258	12	3.063	2.810	-19.31	19.32 ± 0.61	8.310 ± 1.213	61.06 ± 3.48	24.38 ± 6.88
(2855) Bastian	12 Jan 2010	0.992	12	2.431	2.174	23.82	54.29 ± 0.99	8.973 ± 2.048	111.4 ± 4.0	13.21 ± 7.68
	28 Jun 2010	1.391	15	2.706	2.429	-21.98	27.58 ± 0.74	6.113 ± 1.468	68.10 ± 3.55	18.17 ± 6.75
(2870) Haupt	31 Jan 2010	1.258	12	2.862	2.700	20.13	78.11 ± 1.32	90.06 ± 2.87	181.0 ± 6.0	174.9 ± 11.2
	22 Jul 2010	1.125	11	2.639	2.363	-22.56	109.9 ± 1.7	200.6 ± 3.4	240.4 ± 6.7	415.1 ± 14.1
(2947) Kippenhahn	8 Feb 2010	1.258	12	2.392	2.161	24.35	50.12 ± 1.014	20.06 ± 1.85	97.59 ± 4.03	32.89 ± 8.38
	3 Jul 2010	1.125	13	2.562	2.269	-23.24	29.47 ± 0.74	16.39 ± 1.54	69.13 ± 3.83	29.81 ± 7.83
(2985) Shakespeare	15 Jan 2010	0.992	10	2.912	2.702	19.72	25.56 ± 0.69	13.41 ± 1.34	73.05 ± 3.93	40.02 ± 8.02
	3 Jul 2010	1.258	15	2.843	2.569	-20.86	32.71 ± 0.76	19.86 ± 1.53	93.22 ± 4.21	59.42 ± 9.41
(3036) Krat	29 Jan 2010	0.992	10	3.428	3.293	16.70	248.9 ± 3.2	70.68 ± 6.13	805.1 ± 14.5	216.2 ± 24.1
	16 Jul 2010	0.594	8	3.303	3.040	-17.81	364.4 ± 4.1	55.13 ± 8.37	1118 ± 21	170.4 ± 45.5
(3051) Nantong	9 Feb 2010	1.258	11	3.210	3.041	17.90	34.05 ± 0.74	8.057 ± 1.565	112.7 ± 4.6	26.73 ± 9.64
	27 Jul 2010	1.125	10	2.969	2.712	-19.93	52.54 ± 0.95	17.92 ± 1.90	162.4 ± 5.4	52.63 ± 11.51
(3144) Brosche	1 Feb 2010	1.258	13	2.554	2.373	22.69	8.326 ± 0.561	4.752 ± 1.118	19.95 ± 3.23	11.03 ± 6.81
	26 Jul 2010	1.391	11	2.197	1.871	-27.42	15.55 ± 0.62	11.67 ± 1.24	36.06 ± 3.35	25.31 ± 6.91
(3162) Nostalgia	20 Jan 2010	0.992	13	3.229	3.057	17.74	159.0 ± 2.1	53.49 ± 4.12	497.5 ± 12.2	168.8 ± 22.9
	6 Jul 2010	1.258	16	3.444	3.204	-17.10	100.3 ± 1.54	55.76 ± 2.89	358.6 ± 8.6	183.4 ± 17.3
(3249) Musashino	23 Jan 2010	0.992	11	2.898	2.717	19.85	4.707 ± 0.529	2.929 ± 1.062	17.00 ± 3.25	20.34 ± 6.79
	7 Jul 2010	1.258	14	2.890	2.614	-20.49	5.565 ± 0.515	3.013 ± 1.063	18.80 ± 3.27	14.11 ± 6.51
(3267) Glo	14 Jan 2010	1.125	15	2.505	2.264	23.10	27.12 ± 0.68	8.897 ± 1.297	61.87 ± 3.31	20.61 ± 6.73
	25 Jun 2010	1.387	15	2.882	2.628	-20.59	15.33 ± 0.54	4.989 ± 1.044	38.84 ± 3.04	12.64 ± 6.21
(3305) Ceadams	17 Jan 2010	1.125	12	2.540	2.310	22.77	38.17 ± 0.86	14.24 ± 1.67	97.26 ± 3.98	43.10 ± 8.79
	8 Jul 2010	1.391	15	2.286	1.955	-26.27	88.30 ± 1.39	26.51 ± 2.77	185.5 ± 5.64	55.21 ± 9.96
(3411) Debetencourt	13 Jan 2010	1.258	13	2.062	1.766	28.44	41.86 ± 0.89	15.87 ± 1.75	74.06 ± 3.88	24.00 ± 7.97
	6 Jul 2010	1.520	17	2.289	1.961	-26.23	21.55 ± 0.67	12.87 ± 1.38	44.50 ± 3.53	24.07 ± 7.42
(3438) Inarradas	30 Jan 2010	1.125	7	3.512	3.384	16.28	62.88 ± 1.01	30.53 ± 2.06	204.9 ± 6.8	99.42 ± 13.96
	17 Jul 2010	3.902	19	3.274	3.026	-18.00	108.1 ± 1.6	61.82 ± 3.62	320.8 ± 8.6	168.0 ± 13.9

Table 2.2 — continued

Object	UT Date[a]	$\Delta t_{\rm obs}$[b]	N[c]	$R_{\rm AU}$[d]	$\Delta_{\rm AU}$[e]	α (°)[f]	$\overline{W3}$[g]	$\diamondsuit W3$[h]	$\overline{W4}$[g]	$\diamondsuit W4$[h]
(3483) Svetlov	27 Jan 2010	1.258	14	2.172	1.944	26.95	3.713 ± 0.493	1.402 ± 1.024	10.10 ± 3.24	7.199 ± 6.372
	17 Jul 2010	4.562	31	2.043	1.689	-29.68	7.883 ± 0.556	4.366 ± 1.214	17.52 ± 3.28	14.94 ± 6.46
(3509) Sanshui	25 Jan 2010	0.992	9	2.972	2.804	19.34	22.41 ± 0.67	2.700 ± 1.285	62.35 ± 3.50	11.10 ± 7.33
	12 Jul 2010	1.125	14	2.830	2.541	-20.93	25.73 ± 0.69	5.474 ± 1.376	72.92 ± 3.48	15.84 ± 6.78
(3536) Schleicher	28 Jan 2010	1.258	10	2.354	2.145	24.73	6.651 ± 0.548	4.957 ± 1.088	13.61 ± 3.47	8.149 ± 6.769
	24 Jul 2010	1.391	10	2.436	2.139	-24.55	7.737 ± 0.547	6.560 ± 1.108	17.74 ± 3.30	13.40 ± 6.83
(3544) Borodino	19 Jan 2010	1.125	12	2.485	2.259	23.31	28.95 ± 0.78	21.15 ± 1.44	72.49 ± 3.72	50.44 ± 7.26
	12 Jul 2010	1.391	17	2.065	1.701	-29.32	96.77 ± 1.55	67.70 ± 3.20	186.1 ± 5.7	125.2 ± 10.7
(3554) Amun	13 Jan 2010	1.125	13	1.081	0.423	65.40	326.4 ± 3.9	32.85 ± 7.64	487.2 ± 11.0	55.47 ± 21.07
	4 May 2010	1.391	15	1.219	0.606	-55.47	163.9 ± 2.08	22.62 ± 4.25	227.6 ± 6.6	25.38 ± 13.63
(3560) Chenqian	9 Feb 2010	0.992	10	3.362	3.198	17.06	89.43 ± 1.40	23.33 ± 2.83	261.1 ± 7.8	59.87 ± 15.99
	29 Jul 2010	1.125	13	3.296	3.056	-17.88	83.81 ± 1.32	25.49 ± 2.72	260.9 ± 6.8	65.88 ± 12.07
(3628) Boznemcova	14 Jan 2010	0.859	8	3.215	3.019	17.79	6.446 ± 0.522	1.830 ± 1.047	24.54 ± 3.15	6.930 ± 6.136
	26 Jun 2010	1.125	11	2.923	2.663	-20.28	12.63 ± 0.54	3.554 ± 1.079	36.71 ± 3.75	18.92 ± 6.79
(3751) Kiang	3 Feb 2010	3.508	19	3.072	2.914	18.71	129.0 ± 1.8	42.73 ± 3.85	365.4 ± 8.8	121.0 ± 16.1
	28 Jul 2010	1.125	12	2.920	2.658	-20.27	136.9 ± 1.9	64.81 ± 3.82	384.9 ± 8.0	152.2 ± 15.4
(3823) Yorii	10 Feb 2010	1.125	12	2.779	2.583	20.79	49.46 ± 0.94	13.25 ± 1.90	127.9 ± 4.5	41.89 ± 8.49
	3 Jul 2010	1.258	12	3.201	2.951	-18.41	27.60 ± 0.68	5.931 ± 1.314	87.56 ± 3.69	23.22 ± 7.53
(3907) Kilmartin	15 Jan 2010	0.992	8	3.126	2.930	18.32	5.885 ± 0.466	2.361 ± 0.940	20.80 ± 3.14	12.48 ± 6.26
	30 Jun 2010	1.258	11	3.096	2.844	-19.09	5.257 ± 0.494	1.349 ± 0.989	24.74 ± 3.05	9.624 ± 6.331
(3915) Fukushima	25 Jan 2010	1.125	13	2.491	2.287	23.27	300.7 ± 4.0	208.9 ± 8.0	597.0 ± 15.1	403.9 ± 29.5
	16 Jul 2010	4.434	29	2.419	2.110	-24.73	406.4 ± 5.2	334.3 ± 12.5	798.6 ± 16.8	536.0 ± 32.7
(3935) Toatenmongakkai	24 Jan 2010	0.992	8	3.016	2.846	19.05	33.96 ± 0.75	13.93 ± 1.47	87.38 ± 4.24	31.12 ± 7.45
	9 Jul 2010	1.125	11	3.130	2.866	-18.85	21.76 ± 0.63	12.57 ± 1.28	61.19 ± 3.73	41.06 ± 8.15
(3936) Elst	17 Jan 2010	0.730	9	2.430	2.190	23.87	13.10 ± 0.57	2.377 ± 1.124	28.45 ± 3.18	8.861 ± 6.194
	10 Jul 2010	1.391	16	2.200	1.856	-27.36	23.03 ± 0.68	6.897 ± 1.396	47.59 ± 3.32	18.13 ± 6.57
(4003) Schumann	2 Feb 2010	1.125	11	3.388	3.258	16.91	198.2 ± 2.6	17.49 ± 5.11	608.6 ± 14.0	86.85 ± 26.49
	27 Jul 2010	0.992	11	3.236	2.993	-18.22	237.4 ± 3.1	31.78 ± 5.92	684.8 ± 11.4	92.83 ± 23.05

Table 2.2 — continued

Object	UT Date[a]	$\Delta t_{\rm obs}$[b]	N[c]	$R_{\rm AU}$[d]	$\Delta_{\rm AU}$[e]	α (°)[f]	$\overline{W3}$[g]	$\diamondsuit W3$[h]	$\overline{W4}$[g]	$\diamondsuit W4$[h]
(4006) Sandler	9 Feb 2010	1.125	11	2.904	2.715	19.85	64.50 ± 1.13	12.84 ± 2.37	176.4 ± 6.5	39.92 ± 11.75
	28 Jul 2010	0.859	8	2.976	2.718	-19.87	71.91 ± 1.33	16.76 ± 2.38	201.7 ± 6.1	29.41 ± 12.53
(4008) Corbin	20 Jan 2010	1.125	13	1.967	1.684	30.00	56.17 ± 1.11	8.653 ± 2.043	97.93 ± 4.21	14.80 ± 9.03
	12 Jul 2010	1.520	19	2.357	2.038	-25.43	29.72 ± 0.71	4.143 ± 1.376	65.33 ± 3.26	13.30 ± 6.68
(4029) Bridges	23 Jan 2010	0.996	11	2.261	2.026	25.80	42.03 ± 0.94	12.01 ± 1.93	86.08 ± 4.00	29.35 ± 8.48
	26 Jul 2010	1.391	15	2.202	1.876	-27.36	64.65 ± 1.15	21.69 ± 2.34	126.3 ± 4.8	38.47 ± 10.49
(4142) Dersu-Uzala	20 Jan 2010	1.520	17	1.709	1.381	35.14	123.8 ± 1.8	54.08 ± 3.60	180.4 ± 5.2	75.45 ± 10.90
	12 Jul 2010	1.387	14	2.020	1.647	-30.03	77.67 ± 1.28	20.18 ± 2.52	125.2 ± 4.9	42.65 ± 10.45
(4150) Starr	12 Jan 2010	0.859	9	2.509	2.257	23.04	29.67 ± 0.75	7.640 ± 1.519	65.79 ± 3.67	24.41 ± 7.31
	28 Jun 2010	1.387	16	2.244	1.920	-26.83	42.35 ± 0.94	20.17 ± 1.85	86.43 ± 4.17	50.59 ± 9.20
(4255) Spacewatch	2 Feb 2010	0.996	11	3.532	3.407	16.20	37.30 ± 0.81	6.879 ± 1.630	110.6 ± 4.3	21.65 ± 9.13
	27 Jul 2010	1.254	13	3.389	3.153	-17.37	44.81 ± 0.85	8.374 ± 1.660	128.7 ± 5.0	25.72 ± 10.56
(4264) Karljosephine	8 Jan 2010	0.727	6	2.980	2.748	19.22	7.801 ± 0.531	2.536 ± 1.049	24.18 ± 3.34	14.50 ± 6.90
	16 Jun 2010	1.258	14	3.104	2.829	-18.98	5.458 ± 0.506	3.895 ± 1.015	16.24 ± 3.28	22.71 ± 6.80
(4294) Horatius	20 Jan 2010	0.992	7	2.861	2.666	20.11	27.32 ± 0.70	3.314 ± 1.406	63.28 ± 3.59	10.76 ± 6.91
	9 Jul 2010	1.121	13	2.850	2.567	-20.78	29.54 ± 0.73	3.008 ± 1.478	70.75 ± 3.68	16.80 ± 7.64
(4352) Kyoto	9 Feb 2010	1.125	11	3.226	3.056	17.81	24.46 ± 0.67	8.892 ± 1.351	75.66 ± 4.03	28.66 ± 8.01
	27 Jul 2010	1.125	10	3.306	3.068	-17.82	19.25 ± 0.60	8.777 ± 1.258	62.06 ± 3.53	25.29 ± 7.73
(4359) Berlage	22 Jan 2010	0.992	10	2.502	2.288	23.15	8.399 ± 0.553	6.148 ± 1.109	19.48 ± 3.31	15.73 ± 6.96
	10 Jul 2010	1.258	13	2.342	2.014	-25.59	15.79 ± 0.61	15.57 ± 1.19	35.92 ± 3.58	27.31 ± 7.56
(4363) Sergej	14 Feb 2010	1.125	10	2.877	2.694	20.07	6.078 ± 0.529	5.389 ± 1.071	16.62 ± 3.24	16.32 ± 6.72
	2 Aug 2010	0.859	10	2.638	2.347	-22.52	12.88 ± 0.59	4.870 ± 1.241	32.20 ± 3.52	15.26 ± 6.99
(4383) Suruga	28 Jan 2010	1.258	13	2.554	2.365	22.68	19.62 ± 0.66	4.328 ± 1.316	48.79 ± 3.42	18.51 ± 7.05
	22 Jul 2010	1.391	13	2.575	2.295	-23.16	15.83 ± 0.61	3.655 ± 1.180	40.31 ± 3.44	18.18 ± 7.15
(4528) Berg	12 Jan 2010	0.727	8	2.331	2.059	24.92	70.31 ± 1.12	21.56 ± 2.27	146.4 ± 5.5	44.33 ± 11.93
	1 Jul 2010	1.258	16	2.571	2.279	-23.19	48.99 ± 0.92	12.52 ± 1.85	112.5 ± 4.2	28.01 ± 9.16
(4565) Grossman	15 Jan 2010	0.992	11	2.281	2.017	25.51	35.05 ± 0.85	17.22 ± 1.76	76.72 ± 3.62	34.40 ± 7.65
	10 Jul 2010	1.520	16	2.253	1.919	-26.68	49.35 ± 0.96	29.84 ± 2.04	103.4 ± 4.0	52.14 ± 9.26

Table 2.2 — continued

Object	UT Date[a]	$\Delta t_{\rm obs}$[b]	N[c]	$R_{\rm AU}$[d]	$\Delta_{\rm AU}$[e]	α (°)[f]	$\overline{W3}$[g]	$\diamondsuit W3$[h]	$\overline{W4}$[g]	$\diamondsuit W4$[h]
(4569) Baerbel	15 Jan 2010	1.125	10	2.490	2.249	23.25	63.22 ± 1.13	17.11 ± 2.45	140.9 ± 5.1	44.79 ± 11.46
	5 Jul 2010	1.391	16	2.425	2.114	-24.67	50.45 ± 1.00	21.14 ± 2.33	122.3 ± 4.6	50.47 ± 10.07
(4613) Mamoru	20 Jan 2010	0.992	10	3.307	3.137	17.31	13.48 ± 0.57	5.676 ± 1.127	48.24 ± 3.37	24.84 ± 7.12
	3 Jul 2010	1.125	14	3.464	3.225	-17.00	11.81 ± 0.52	4.811 ± 1.029	45.53 ± 3.31	22.44 ± 6.58
(4713) Steel	20 Jan 2010	1.523	18	1.885	1.589	31.45	83.95 ± 1.35	34.06 ± 2.64	139.5 ± 4.7	47.43 ± 9.36
	29 Jul 2010	1.785	20	1.784	1.389	-34.53	103.3 ± 1.6	33.78 ± 2.94	172.2 ± 5.7	41.74 ± 11.41
(4771) Hayashi	30 Jan 2010	1.125	10	2.919	2.761	19.72	27.99 ± 0.71	7.902 ± 1.465	92.22 ± 3.92	22.59 ± 7.29
	23 Jul 2010	1.258	15	2.663	2.387	-22.35	59.64 ± 1.07	25.86 ± 2.28	159.5 ± 5.3	63.37 ± 9.97
(4898) Nishiizumi	15 Jan 2010	1.258	16	1.801	1.469	33.07	11.49 ± 0.60	4.730 ± 1.172	20.19 ± 3.17	9.890 ± 6.578
	12 Jul 2010	1.258	9	1.940	1.558	-31.41	6.246 ± 0.495	2.801 ± 0.943	13.36 ± 3.17	10.74 ± 6.56
(4899) Candace	22 Jan 2010	1.125	10	2.212	1.969	26.42	50.63 ± 0.97	9.938 ± 1.986	92.27 ± 3.93	15.03 ± 7.60
	22 Jul 2010	1.652	20	1.946	1.594	-31.37	89.15 ± 1.40	27.86 ± 2.74	146.0 ± 4.6	41.90 ± 10.10
(4908) Ward	26 Jan 2010	0.992	9	2.657	2.468	21.74	8.856 ± 0.554	7.540 ± 1.116	20.58 ± 3.23	20.30 ± 6.76
	12 Jul 2010	1.258	14	2.384	2.057	-25.09	16.35 ± 0.63	14.56 ± 1.18	35.72 ± 3.20	33.65 ± 6.48
(5035) Swift	22 Jan 2010	1.125	13	2.501	2.287	23.17	44.13 ± 0.91	18.75 ± 1.95	100.8 ± 4.5	35.19 ± 8.73
	11 Jul 2010	0.992	10	2.774	2.482	-21.38	32.33 ± 0.74	10.53 ± 1.50	83.23 ± 4.04	23.79 ± 8.90
(5052) Nancyruth	13 Jan 2010	0.992	8	2.700	2.469	21.33	8.125 ± 0.544	8.112 ± 1.080	17.57 ± 3.32	23.64 ± 6.77
	26 Jun 2010	1.258	12	2.618	2.336	-22.77	9.601 ± 0.548	7.922 ± 1.075	21.06 ± 3.16	19.02 ± 6.51
(5080) Oja	23 Jan 2010	1.125	11	2.324	2.097	25.05	52.95 ± 1.02	11.17 ± 2.19	104.9 ± 4.4	22.06 ± 8.96
	13 Jul 2010	1.391	12	2.491	2.175	-23.94	36.35 ± 0.82	6.510 ± 1.715	80.15 ± 3.52	18.21 ± 7.03
(5088) Tancredi	22 Jan 2010	0.859	9	3.133	2.959	18.31	34.74 ± 0.79	19.44 ± 1.59	117.1 ± 4.3	61.54 ± 8.90
	9 Jul 2010	1.125	11	3.363	3.111	-17.51	27.59 ± 0.68	15.11 ± 1.42	102.9 ± 4.1	51.63 ± 8.20
(5104) Skripnichenko	16 Jan 2010	0.996	9	2.345	2.092	24.77	60.30 ± 1.10	12.00 ± 2.23	141.7 ± 5.1	30.49 ± 10.36
	9 Jul 2010	1.391	15	2.332	2.005	-25.71	73.28 ± 1.20	22.82 ± 2.37	160.8 ± 5.38	48.53 ± 9.54
(5226) Pollack	11 Feb 2010	1.125	13	2.416	2.192	24.10	14.31 ± 0.60	6.051 ± 1.203	34.15 ± 3.33	15.58 ± 6.33
	2 Aug 2010	1.125	11	2.532	2.233	-23.52	14.75 ± 0.60	5.527 ± 1.221	37.38 ± 3.23	15.56 ± 6.41
(5333) Kanaya	25 Jan 2010	0.992	11	1.980	1.716	29.80	340.1 ± 4.0	91.72 ± 7.99	556.7 ± 13.0	151.6 ± 22.6
	27 Jul 2010	1.523	15	2.272	1.954	-26.45	180.8 ± 2.4	54.87 ± 4.55	349.7 ± 9.8	91.73 ± 19.76

Table 2.2 — continued

Object	UT Date[a]	$\Delta t_{\rm obs}$[b]	N[c]	$R_{\rm AU}$[d]	$\Delta_{\rm AU}$[e]	α (°)[f]	$\overline{W3}$[g]	$\diamondsuit W3$[h]	$\overline{W4}$[g]	$\diamondsuit W4$[h]
(5378) Ellyett	2 Feb 2010	4.828	22	1.936	1.670	30.59	11.43 ± 0.56	5.344 ± 1.095	20.25 ± 3.16	16.05 ± 6.42
	30 Jul 2010	1.520	14	2.076	1.729	-29.14	9.506 ± 0.554	8.635 ± 1.149	18.62 ± 3.24	19.97 ± 6.42
(5427) Jensmartin	17 Jan 2010	1.125	12	1.995	1.704	29.53	9.567 ± 0.533	3.948 ± 1.100	20.36 ± 2.98	8.761 ± 5.900
	9 Jul 2010	1.523	17	1.844	1.444	-33.27	16.79 ± 0.60	9.563 ± 1.198	32.63 ± 3.15	18.66 ± 6.04
(5527) 1991 UQ_3	18 Jan 2010	1.125	10	2.247	1.993	25.95	23.42 ± 0.71	8.223 ± 1.476	47.27 ± 3.56	23.64 ± 7.00
	14 Jul 2010	1.520	18	2.007	1.629	-30.23	45.66 ± 1.44	49.15 ± 6.15	75.11 ± 4.04	83.95 ± 9.06
(5574) Seagrave	14 Jan 2010	0.992	11	2.425	2.175	23.90	50.49 ± 0.95	16.70 ± 1.90	115.9 ± 4.2	33.77 ± 7.41
	5 Jul 2010	1.391	15	2.613	2.322	-22.80	38.57 ± 0.79	7.978 ± 1.718	94.05 ± 4.01	17.90 ± 8.29
(5592) Oshima	21 Jan 2010	0.992	11	3.302	3.133	17.33	70.28 ± 1.24	18.47 ± 2.41	225.6 ± 6.6	73.64 ± 13.26
	8 Jul 2010	1.254	15	3.215	2.957	-18.34	92.71 ± 1.42	28.09 ± 2.97	271.5 ± 7.6	61.14 ± 13.38
(5604) 1992 FE	2 Feb 20103	1.125	10	1.238	0.746	53.03	6.043 ± 0.579	3.292 ± 1.169	8.307 ± 3.503	3.237 ± 7.276
	27 Jun 2010	0.594	8	1.068	0.259	-71.61	57.71 ± 1.04	6.040 ± 2.055	79.07 ± 3.95	11.19 ± 8.10
(5682) Beresford	13 Jan 2010	0.992	10	2.965	2.752	19.34	4.540 ± 0.523	2.370 ± 1.048	14.55 ± 3.32	13.36 ± 6.93
	24 Jun 2010	1.258	15	2.736	2.466	-21.73	8.383 ± 0.536	2.392 ± 1.083	22.11 ± 3.29	9.685 ± 6.515
(5712) Funke	14 Jan 2010	0.992	8	3.158	2.956	18.13	6.310 ± 0.523	2.952 ± 1.067	22.51 ± 3.11	14.58 ± 6.37
	29 Jun 2010	1.258	16	2.967	2.705	-19.96	10.70 ± 0.56	5.643 ± 1.109	32.64 ± 3.16	15.93 ± 6.12
(6091) Mitsuru	18 Jan 2010	1.125	10	2.314	2.069	25.14	23.53 ± 0.69	13.35 ± 1.44	45.77 ± 3.51	33.25 ± 6.81
	13 Jul 2010	1.258	12	1.869	1.470	-32.73	48.73 ± 0.95	40.28 ± 1.89	83.16 ± 4.04	70.19 ± 8.81
(6121) Plachinda	2 Feb 2010	1.254	12	2.655	2.481	21.78	10.79 ± 0.61	5.256 ± 1.221	28.58 ± 3.69	17.50 ± 7.37
	24 Jul 2010	1.258	13	2.433	2.136	-24.58	14.98 ± 0.60	7.243 ± 1.200	38.79 ± 3.22	21.05 ± 7.16
(6139) Naomi	29 Jan 2010	1.125	11	2.255	2.040	25.89	87.33 ± 1.36	25.92 ± 2.79	169.2 ± 5.1	44.10 ± 10.06
	1 Aug 2010	1.254	16	2.401	2.091	-24.89	90.34 ± 1.33	16.73 ± 2.73	175.9 ± 6.1	47.60 ± 10.08
(6170) Levasseur	25 Jan 2010	1.125	13	1.881	1.600	31.55	47.34 ± 0.99	6.329 ± 2.035	87.13 ± 4.22	20.99 ± 9.08
	13 Jul 2010	1.387	12	2.497	2.184	-23.88	17.92 ± 0.60	2.443 ± 1.196	42.32 ± 3.12	8.030 ± 6.088
(6185) Mitsuma	16 Jan 2010	1.258	14	2.145	1.871	27.28	117.5 ± 1.7	36.81 ± 3.43	215.0 ± 6.4	70.24 ± 12.45
	7 Jul 2010	1.258	14	2.472	2.161	-24.17	68.60 ± 1.17	17.42 ± 2.15	148.9 ± 5.4	32.82 ± 10.70
(6261) Chione	27 Jan 2010	1.125	13	2.120	1.882	27.66	12.49 ± 0.78	9.822 ± 1.247	24.10 ± 3.19	25.35 ± 6.68
	13 Jul 2010	1.258	14	2.735	2.447	-21.71	4.981 ± 0.485	3.476 ± 0.967	13.99 ± 3.02	7.591 ± 5.965

Table 2.2 — continued

Object	UT Date[a]	$\Delta t_{\rm obs}$[b]	N[c]	$R_{\rm AU}$[d]	$\Delta_{\rm AU}$[e]	α (°)[f]	$\overline{W3}$[g]	$\diamondsuit W3$[h]	$\overline{W4}$[g]	$\diamondsuit W4$[h]
(6361) Koppel	19 Jan 2010	1.125	13	2.087	1.815	28.11	9.189 ± 0.551	8.545 ± 1.075	20.97 ± 3.24	19.32 ± 6.63
	26 Jul 2010	1.520	15	2.059	1.713	-29.44	14.57 ± 0.62	5.572 ± 1.245	30.59 ± 3.33	11.00 ± 6.59
(6572) Carson	19 Jan 2010	0.992	12	2.998	2.808	19.15	11.94 ± 0.56	4.093 ± 1.114	35.55 ± 3.41	11.44 ± 6.32
	4 Jul 2010	1.258	15	2.610	2.317	-22.82	32.51 ± 0.79	9.702 ± 1.577	79.19 ± 3.99	26.95 ± 8.37
(6838) Okuda	27 Jan 2010	1.258	11	2.378	2.171	24.46	105.5 ± 1.6	18.25 ± 3.07	201.2 ± 6.6	35.31 ± 14.35
	22 Jul 2010	0.992	13	2.694	2.422	-22.08	40.19 ± 0.84	12.70 ± 1.61	107.9 ± 4.3	32.61 ± 8.37
(6870) 1991 OM_1	26 Jan 2010	1.258	15	2.114	1.873	27.76	4.320 ± 0.534	2.513 ± 1.077	10.12 ± 3.33	5.285 ± 6.667
	16 Jul 2010	4.832	34	2.122	1.786	-28.51	5.289 ± 0.485	4.814 ± 0.937	12.35 ± 3.10	20.77 ± 6.39
(6901) Roybishop	15 Jan 2010	1.258	10	2.046	1.758	28.71	31.04 ± 0.75	4.250 ± 1.488	60.13 ± 3.45	8.725 ± 6.569
	4 Jul 2010	1.652	14	2.158	1.823	-27.99	28.92 ± 0.72	4.024 ± 1.402	58.32 ± 3.12	12.75 ± 6.00
(6905) Miyazaki	10 Feb 2010	1.125	13	2.992	2.810	19.25	52.93 ± 1.01	4.188 ± 1.979	136.2 ± 4.7	26.14 ± 9.42
	29 Jul 2010	1.125	9	2.719	2.441	-21.83	86.22 ± 1.25	4.627 ± 2.556	210.7 ± 5.6	14.07 ± 10.69
(6911) Nancygreen	12 Feb 2010	0.992	10	2.103	1.844	27.99	5.084 ± 0.589	4.853 ± 1.208	16.13 ± 3.49	15.10 ± 8.14
	2 Aug 2010	1.520	17	1.996	1.639	-30.44	12.24 ± 0.53	2.597 ± 1.064	20.43 ± 2.97	12.93 ± 5.96
(7476) Ogilsbie	24 Jan 2010	1.258	13	2.440	2.226	23.78	184.9 ± 2.4	56.39 ± 4.60	441.9 ± 9.0	140.7 ± 17.0
	21 Jul 2010	1.391	14	2.496	2.210	-23.95	107.3 ± 1.6	41.45 ± 3.24	302.7 ± 8.6	101.1 ± 16.8
(7783) 1994 JD	8 Jan 2010	1.258	15	1.830	1.484	32.42	9.217 ± 0.566	8.680 ± 1.088	19.34 ± 3.03	20.95 ± 6.55
	4 Jul 2010	1.785	17	1.990	1.629	-30.58	8.147 ± 0.507	8.284 ± 1.000	16.07 ± 3.00	12.76 ± 6.13
(7829) Jaroff	3 Feb 2010	4.832	24	1.965	1.697	30.10	5.225 ± 0.521	3.737 ± 1.025	12.30 ± 3.27	8.342 ± 6.952
	2 Aug 2010	1.125	10	2.087	1.737	-28.95	5.165 ± 0.558	3.201 ± 1.125	12.01 ± 3.35	10.83 ± 6.81
(7832) 1993 FA_{27}	10 Feb 2010	1.387	12	2.430	2.205	23.96	7.306 ± 0.548	3.404 ± 1.108	13.99 ± 3.58	10.91 ± 7.47
	5 Aug 2010	0.859	9	2.013	1.647	-30.09	16.65 ± 0.62	2.196 ± 1.224	31.07 ± 3.33	12.56 ± 6.56
(7949) 1992 SU	31 Jan 2010	1.125	14	3.284	3.145	17.46	73.15 ± 1.22	8.732 ± 2.361	201.3 ± 5.4	20.66 ± 12.20
	17 Jul 2010	3.902	26	3.595	3.364	-16.35	42.64 ± 0.86	10.15 ± 1.69	134.8 ± 5.1	37.94 ± 10.93
(8213) 1995 FE	13 Feb 2010	1.391	10	2.095	1.838	28.12	20.94 ± 0.68	10.48 ± 1.33	41.95 ± 3.22	20.21 ± 6.65
	5 Aug 2010	0.465	6	2.506	2.205	-23.76	11.72 ± 0.56	12.21 ± 1.08	28.59 ± 2.99	22.57 ± 6.05
(8862) Takayukiota	25 Jan 2010	0.859	10	3.105	2.944	18.48	5.661 ± 0.534	9.779 ± 1.056	22.68 ± 3.27	48.90 ± 7.03
	11 Jul 2010	1.125	13	3.038	2.766	-19.44	7.192 ± 0.514	6.474 ± 1.038	25.97 ± 3.14	18.76 ± 6.21

Table 2.2 — continued

Object	UT Date[a]	$\Delta t_{\rm obs}$[b]	N[c]	$R_{\rm AU}$[d]	$\Delta_{\rm AU}$[e]	α (°)[f]	$\overline{W3}$[g]	$\diamondsuit W3$[h]	$\overline{W4}$[g]	$\diamondsuit W4$[h]
(8887) Scheeres	18 Jan 2010	0.992	12	2.717	2.503	21.22	18.43 ± 0.60	7.322 ± 1.170	49.72 ± 3.18	19.43 ± 6.38
	6 Jul 2010	1.387	15	2.495	2.192	-23.94	31.15 ± 0.71	9.841 ± 1.492	75.11 ± 3.50	21.97 ± 7.08
(9297) Marchuk	18 Jan 2010	0.992	8	2.540	2.313	22.78	59.62 ± 1.02	3.412 ± 2.019	127.6 ± 5.0	26.20 ± 10.21
	11 Jul 2010	1.387	14	2.318	1.984	-25.86	95.54 ± 1.51	9.372 ± 2.749	178.5 ± 5.5	20.18 ± 10.73
(10936) 1998 FN_{11}	20 Jan 2010	0.594	8	3.063	2.878	18.73	26.78 ± 0.70	10.65 ± 1.35	73.49 ± 3.33	30.24 ± 6.57
	2 Jul 2010	1.258	13	3.079	2.822	-19.20	25.75 ± 0.69	11.25 ± 1.34	73.55 ± 4.03	31.29 ± 8.02
(11549) 1992 YY	28 Jan 2010	1.391	12	2.352	2.144	24.74	58.82 ± 0.99	11.14 ± 1.93	129.9 ± 4.6	23.26 ± 9.48
	28 Jul 2010	1.391	11	2.311	1.996	-25.96	106.8 ± 1.6	12.68 ± 2.93	211.4 ± 6.1	24.19 ± 11.53
(11780) Thunder Bay	4 Feb 2010	3.773	19	3.193	3.036	17.98	8.406 ± 0.576	4.809 ± 1.267	25.13 ± 3.32	15.68 ± 6.76
	23 Jul 2010	1.258	15	2.941	2.686	-20.14	9.865 ± 0.523	12.38 ± 1.04	26.26 ± 3.02	39.95 ± 5.84
(12376) Cochabamba	9 Jan 2010	0.859	6	2.111	1.807	27.69	28.01 ± 0.74	15.44 ± 1.50	60.31 ± 3.17	26.64 ± 6.26
	19 Jul 2010	1.785	21	1.961	1.609	-31.11	46.08 ± 0.96	20.08 ± 1.93	84.25 ± 4.09	33.62 ± 8.21
(12753) Povenmire	16 Jan 2010	1.125	13	2.269	2.008	25.67	44.33 ± 0.87	45.86 ± 1.70	89.20 ± 4.13	86.18 ± 7.79
	13 Jul 2010	1.523	17	2.273	1.934	-26.41	53.90 ± 1.03	46.73 ± 2.06	108.6 ± 4.4	86.52 ± 8.40
(13474) V'yus	14 Jan 2010	0.992	8	3.359	3.170	17.01	3.968 ± 0.510	2.708 ± 0.990	15.88 ± 3.35	10.08 ± 6.93
	26 Jun 2010	1.125	7	3.158	2.912	-18.70	6.015 ± 0.518	2.656 ± 1.036	20.15 ± 3.12	6.408 ± 6.123
(13856) 1999 XZ_{105}	25 Jan 2010	0.992	9	3.172	3.014	18.08	38.65 ± 0.86	12.37 ± 1.65	111.5 ± 4.1	43.64 ± 8.51
	11 Jul 2010	1.125	10	3.138	2.871	-18.80	36.35 ± 0.79	15.33 ± 1.64	107.0 ± 4.4	45.06 ± 9.62
(14342) Iglika	18 Feb 2010	0.992	11	3.500	3.354	16.40	24.87 ± 0.64	15.85 ± 1.27	85.08 ± 3.70	54.86 ± 7.42
	4 Aug 2010	0.992	12	3.237	2.985	-18.18	36.10 ± 0.79	24.83 ± 1.59	109.8 ± 4.4	74.95 ± 9.81
(14950) 1996 BE_2	12 Jan 2010	0.465	5	2.034	1.725	28.85	45.35 ± 0.94	28.75 ± 1.89	84.25 ± 3.49	55.54 ± 6.95
	9 Jul 2010	1.523	17	2.130	1.779	-28.35	53.34 ± 1.01	17.01 ± 2.06	98.47 ± 4.37	27.07 ± 9.47
(15362) 1996 ED	25 Jan 2010	0.992	10	2.393	2.181	24.29	14.99 ± 0.61	7.519 ± 1.249	31.96 ± 3.21	18.14 ± 6.44
	14 Jul 2010	1.121	13	2.597	2.287	-22.90	10.31 ± 0.56	5.461 ± 1.134	27.12 ± 3.37	18.29 ± 6.71
(15430) 1998 UR_{31}	21 Jan 2010	1.258	16	1.985	1.709	29.71	13.89 ± 0.66	3.658 ± 1.334	28.99 ± 3.19	10.17 ± 6.60
	3 Aug 2010	1.656	13	1.863	1.474	-32.82	27.48 ± 0.75	5.109 ± 1.470	45.91 ± 3.36	9.144 ± 6.666
(15499) Cloyd	31 Jan 2010	1.125	13	3.151	3.007	18.22	14.68 ± 0.60	3.882 ± 1.159	44.52 ± 3.39	14.21 ± 7.30
	23 Jul 2010	1.258	14	3.249	3.014	-18.16	11.91 ± 0.53	2.456 ± 1.038	39.45 ± 3.28	13.30 ± 6.76

Table 2.2 — continued

Object	UT Date[a]	$\Delta t_{\rm obs}$[b]	N[c]	$R_{\rm AU}$[d]	$\Delta_{\rm AU}$[e]	α (°)[f]	$\overline{W3}$[g]	$\diamondsuit W3$[h]	$\overline{W4}$[g]	$\diamondsuit W4$[h]
(15914) 1997 UM_3	17 Jan 2010	0.859	9	2.634	2.412	21.92	4.122 ± 0.561	2.081 ± 1.097	11.95 ± 3.77	10.91 ± 7.38
	2 Jul 2010	1.258	11	2.829	2.554	-20.97	4.402 ± 0.534	3.669 ± 1.106	11.16 ± 3.41	9.538 ± 6.748
(16681) 1994 EV_7	25 Jan 2010	0.280	9	1.984	1.723	29.76	14.62 ± 0.62	13.98 ± 1.25	27.96 ± 3.26	26.19 ± 6.60
	18 Jul 2010	2.110	21	2.005	1.657	-30.35	20.68 ± 0.63	17.65 ± 1.24	38.47 ± 3.10	41.70 ± 6.39
(16886) 1998 BC_{26}	27 Jan 2010	0.992	12	1.983	1.722	29.75	14.61 ± 0.62	13.97 ± 1.25	27.95 ± 3.26	26.18 ± 6.60
	13 Jul 2010	1.125	13	2.005	1.657	-30.35	20.67 ± 0.63	17.64 ± 1.24	38.46 ± 3.10	41.70 ± 6.39
(17681) Tweedledum	15 Jan 2010	1.387	15	1.823	1.500	32.62	8.785 ± 0.524	8.873 ± 1.010	17.65 ± 3.05	19.37 ± 6.28
	8 Jul 2010	1.656	18	1.875	1.484	-32.66	9.788 ± 0.545	9.385 ± 1.067	17.69 ± 3.18	17.64 ± 6.74
(17822) 1998 FM_{135}	11 Feb 2010	0.992	11	3.394	3.233	16.90	8.588 ± 0.533	3.819 ± 1.058	35.76 ± 3.29	17.78 ± 6.43
	1 Aug 2010	1.258	10	3.206	2.953	-18.37	10.11 ± 0.57	7.016 ± 1.125	40.97 ± 3.44	21.69 ± 7.41
(18487) 1996 AU_3	28 Jan 2010	1.125	13	2.893	2.727	19.90	11.33 ± 0.56	5.905 ± 1.104	34.19 ± 3.16	17.80 ± 6.29
	17 Jul 2010	4.297	29	2.595	2.301	-22.95	25.49 ± 0.71	16.21 ± 1.52	63.00 ± 3.62	38.62 ± 7.07
(19251) Totziens	17 Jan 2010	0.727	10	3.319	3.135	17.22	5.190 ± 0.514	1.550 ± 1.046	16.63 ± 3.29	21.65 ± 6.37
	28 Jun 2010	1.125	13	3.066	2.814	-19.29	7.170 ± 0.502	3.314 ± 1.014	19.58 ± 3.13	10.54 ± 6.36
(20378) 1998 KZ_{46}	17 Jan 2010	0.992	7	2.850	2.645	20.18	15.38 ± 0.57	4.956 ± 1.144	42.17 ± 3.24	13.92 ± 6.37
	3 Jul 2010	1.258	14	2.905	2.637	-20.40	11.08 ± 0.53	4.326 ± 1.059	33.74 ± 3.07	15.09 ± 5.98
(20932) 2258 T-1	27 Jan 2010	1.125	12	2.999	2.840	19.16	4.276 ± 0.543	1.721 ± 1.090	14.18 ± 3.39	12.10 ± 6.77
	13 Jul 2010	1.121	13	2.746	2.449	-21.60	8.242 ± 0.543	1.509 ± 1.071	24.43 ± 3.30	11.10 ± 6.15
(21594) 1998 VP_{31}	15 Jan 2010	1.125	12	2.324	2.065	25.01	101.9 ± 1.6	25.05 ± 2.88	195.0 ± 6.0	48.84 ± 10.75
	14 Jul 2010	1.520	14	2.145	1.786	-28.11	128.9 ± 1.8	35.81 ± 3.57	236.1 ± 6.7	62.09 ± 12.85
(23200) 2000 SH_3	14 Feb 2010	0.992	12	2.899	2.717	19.91	10.19 ± 0.59	5.215 ± 1.149	28.83 ± 3.54	24.12 ± 7.76
	29 Jul 2010	1.254	11	2.713	2.438	-21.89	17.49 ± 0.59	5.435 ± 1.247	41.90 ± 3.21	16.93 ± 6.66
(23276) 2000 YT_{101}	18 Feb 2010	1.258	16	3.053	2.885	18.88	9.133 ± 0.536	2.327 ± 1.080	26.64 ± 3.18	10.89 ± 6.42
	5 Aug 2010	1.254	13	2.841	2.564	-20.82	13.05 ± 0.56	3.746 ± 1.119	33.64 ± 3.28	15.59 ± 7.06
(24101) Cassini	12 Feb 2010	1.125	11	3.177	3.007	18.10	7.619 ± 0.521	1.978 ± 1.065	26.03 ± 3.13	9.564 ± 6.221
	28 Jul 2010	1.258	15	3.418	3.186	-17.22	5.375 ± 0.473	2.015 ± 0.935	16.95 ± 3.19	10.82 ± 7.14
(27851) 1994 VG_2	12 Feb 2010	1.125	11	2.439	2.218	23.87	72.08 ± 1.21	33.75 ± 2.32	144.3 ± 5.0	65.09 ± 9.48
	29 Jul 2010	1.258	16	2.713	2.436	-21.89	45.48 ± 0.91	17.59 ± 1.66	102.5 ± 4.43	37.68 ± 9.27

Table 2.2 — continued

Object	UT Date[a]	$\Delta t_{\rm obs}$[b]	N[c]	$R_{\rm AU}$[d]	$\Delta_{\rm AU}$[e]	α (°)[f]	$\overline{W3}$[g]	$\diamondsuit W3$[h]	$\overline{W4}$[g]	$\diamondsuit W4$[h]
(28126) Nydegger	12 Jan 2010	1.125	12	2.183	1.899	26.73	5.353 ± 0.538	1.819 ± 1.098	11.64 ± 3.42	10.97 ± 7.14
	2 Jul 2010	1.387	15	2.387	2.074	-25.10	3.473 ± 0.561	2.717 ± 1.123	8.427 ± 3.483	4.742 ± 7.075
(30470) 2000 OR_{19}	21 Jan 2010	0.992	11	2.879	2.689	19.99	17.86 ± 0.65	18.34 ± 1.38	50.23 ± 3.73	47.43 ± 7.29
	13 Jul 2010	1.254	15	2.550	2.237	-23.36	44.44 ± 0.91	33.35 ± 1.73	100.7 ± 4.4	75.48 ± 8.27
(32802) 1990 SK	3 Feb 2010	3.773	13	2.884	2.710	19.98	3.279 ± 0.569	1.359 ± 1.124	10.75 ± 3.51	9.590 ± 7.345
	20 Jul 2010	1.125	10	2.664	2.393	-22.36	7.376 ± 0.927	12.24 ± 2.79	16.13 ± 3.50	14.01 ± 6.97
(33916) 2000 LF_{19}	18 Jan 2010	0.992	12	2.582	2.357	22.38	8.188 ± 0.594	3.047 ± 1.185	19.98 ± 3.43	16.95 ± 7.08
	5 Jul 2010	1.387	15	2.129	1.783	-28.38	20.21 ± 0.66	10.88 ± 1.30	37.56 ± 3.30	21.97 ± 6.83
(41044) 1999 VW_6	3 Feb 2010	3.641	25	3.024	2.857	19.02	4.948 ± 0.550	5.743 ± 1.205	16.10 ± 3.38	15.95 ± 6.87
	24 Jul 2010	1.258	15	2.833	2.572	-20.94	9.724 ± 0.515	2.008 ± 1.034	27.86 ± 3.07	12.29 ± 6.15
(41223) 1999 XD_{16}	16 Jan 2010	0.992	11	3.616	3.441	15.77	11.49 ± 0.54	4.047 ± 1.07	42.23 ± 3.43	17.29 ± 7.48
	26 Jun 2010	1.125	13	3.417	3.186	-17.24	14.63 ± 0.57	7.231 ± 1.159	45.49 ± 3.28	20.30 ± 6.55
(41288) 1999 XD_{107}	21 Jan 2010	0.465	7	2.450	2.226	23.67	6.753 ± 0.496	1.614 ± 0.990	15.83 ± 3.04	4.988 ± 6.510
	11 Jul 2010	1.391	15	2.249	1.910	-26.72	14.80 ± 0.60	7.317 ± 1.19	29.64 ± 3.25	19.04 ± 6.64
(42265) 2001 QL_{69}	28 Jan 2010	1.258	11	2.980	2.821	19.30	8.709 ± 0.561	8.867 ± 1.140	24.45 ± 3.50	33.65 ± 7.05
	22 Jul 2010	1.258	11	2.910	2.654	-20.36	11.54 ± 0.56	5.215 ± 1.121	33.46 ± 3.33	12.31 ± 6.90
(42946) 1999 TU_{95}	1 Feb 2010	1.258	11	2.380	2.180	24.45	11.44 ± 0.59	2.488 ± 1.162	25.16 ± 3.64	10.31 ± 6.60
	3 Jul 2010	1.254	14	2.449	2.145	-24.38	11.03 ± 0.56	4.083 ± 1.123	26.30 ± 3.19	11.11 ± 6.39
(44892) 1999 VJ_8	12 Feb 2010	0.992	7	3.148	2.975	18.27	10.07 ± 0.53	4.346 ± 1.125	31.40 ± 3.18	32.40 ± 6.12
	3 Jul 2010	1.258	11	2.912	2.646	-20.31	12.30 ± 0.54	2.464 ± 1.083	33.34 ± 3.15	8.932 ± 6.319
(45436) 2000 AD_{176}	28 Jan 2010	1.523	16	2.252	2.034	25.93	12.08 ± 0.60	8.163 ± 1.183	24.66 ± 3.49	20.57 ± 6.98
	3 Jul 2010	0.465	5	2.455	2.148	-24.31	7.309 ± 0.520	5.159 ± 1.056	17.28 ± 3.18	12.32 ± 6.22
(68216) 2001 CV_{26}	23 Jan 2010	0.992	13	1.102	0.486	63.28	48.96 ± 0.97	8.693 ± 2.139	68.47 ± 3.52	14.70 ± 7.31
	25 Jun 2010	1.520	16	1.698	1.287	-36.64	6.617 ± 0.561	2.597 ± 1.115	11.23 ± 3.46	7.553 ± 7.134
(69350) 1993 YP	10 Feb 2010	1.520	17	2.076	1.813	28.38	5.645 ± 0.529	4.560 ± 1.071	13.47 ± 3.15	10.29 ± 6.37
	4 Aug 2010	1.652	17	1.939	1.574	-31.43	12.33 ± 0.54	10.29 ± 1.09	24.20 ± 2.96	16.48 ± 6.00
(72675) 2001 FP_{54}	17 Jan 2010	0.992	10	2.533	2.301	22.83	5.848 ± 0.577	2.085 ± 1.179	14.92 ± 3.30	6.007 ± 6.648
	8 Jul 2010	1.391	11	2.571	2.269	-23.17	6.495 ± 0.534	0.983 ± 1.059	14.79 ± 3.15	5.238 ± 6.434

Table 2.2 — continued

Object	UT Date[a]	$\Delta t_{\rm obs}$[b]	N[c]	$R_{\rm AU}$[d]	$\Delta_{\rm AU}$[e]	α (°)[f]	$\overline{W3}$[g]	$\diamondsuit W3$[h]	$\overline{W4}$[g]	$\diamondsuit W4$[h]
(90698) Kosciuszko	27 Jan 2010	1.258	10	1.970	1.714	29.98	21.99 ± 0.68	5.908 ± 1.336	34.16 ± 3.21	7.188 ± 6.564
	24 Jul 2010	1.391	13	2.470	2.185	-24.21	6.606 ± 0.502	2.078 ± 1.021	14.66 ± 3.09	13.31 ± 6.12

Notes. All mean flux and range values are in units of mJy = 10^{-29} $\mathrm{Wm^{-2}\ Hz^{-1}}$.

[a]UT date of the first observation.

[b]Time spanned by observations (days).

[c]Number of observations used.

[d]Mean Heliocentric distance.

[e]Mean WISE-centric distance.

[f]Mean solar phase angle.

[g]Lightcurve-averaged mean flux.

[h]Photometric range of lightcurve.

In order to formulate the lightcurve range ($\diamondsuit F$) and error ($\delta\diamondsuit F$) I employ a slightly different approach than that used for the mean. For the i*th* point, I iterate across every combination of differences between points, to select the j*th* point that which maximizes the range between the two: $r_{\widehat{ij}}$. Difference pairs that are separated by a quarter-turn of the asteroid are given more weight based off the pair weight, s_{ij}, from above (i.e., the factor $(1-\cos(4\pi s_{\widehat{ij}}))^2$):

$$\diamondsuit F = 2\,\frac{\sum r_{\widehat{ij}}\delta r_{\widehat{ij}}{}^{-2}(1-\cos(4\pi s_{\widehat{ij}}))}{\sum \delta r_{\widehat{ij}}{}^{-2}(1-\cos(4\pi s_{\widehat{ij}}))^2} \tag{2.4}$$

and

$$\delta\diamondsuit F = \sqrt{\sum \delta r_{\widehat{ij}}{}^{2} s_{\widehat{ij}}^2 \Big/ \sum s_{\widehat{ij}}^2} \tag{2.5}$$

The factor, $1-\cos(4\pi s_{\widehat{ij}})$, is used to scale the $s_{\widehat{ij}}$ factor in equation (2.4) in order to create a weight function based off a sinusoid (plotted in the top right panel of figure 2.2); this factor is not used in equation (2.5) since I am not interested in how well the data resembles a sine function, yet I still wish to add weights to the errors as in equation (2.3).

2.3.3 TPM Implementation

The TPM approach taken here is similar to that presented in chapter 1 and is summarized here for reader convenience. First, the surface temperatures are modeled across the surface of a spherical object constructed of discrete facets. This is done by numerically solving the one-dimensional heat transfer equation (Fourier's Law) and using the estimated insolation (incoming solar radiation) as the energy input. The discrete facets are characterized as planar faces and divided into latitude bins. A diurnal cycle is simulated by rotating the facets about the object's spin axis. Two types of surfaces are modeled: a perfectly smooth surface in which only direct insolation is considered, and a rough surface that is comprised of spherical-section craters, for which direct and multiply-scattered insolation and thermally re-radiated energy from other facets are calculated. Surface roughness is characterized by the mean surface slope ($\bar{\theta}$; Hapke, 1984), which is varied by differing both the opening angle of the crater (γ) and the proportion of surface area that is covered by those craters (f_R); the latter is implemented when calculating the flux contribution of rough and smooth surfaces.

I use parameterized forms of the energy balance equation and heat diffusion equation, which reduces the number of TPM variables that are necessary to calculate a unique surface temperature distribution, in order to construct temperature reference tables and reduce the computational time. In this scheme, the necessary information required for rough surface temperature calculation is the bond albedo (A), thermal parameter ($\Theta \propto \Gamma$), and spin obliquity (sub-solar latitude); whereas the smooth surface only requires the thermal parameter and sub-solar latitude. The surface temperatures stored in the reference tables are expressed as: $T' = T/T_{\rm eq}$, the fraction of the theoretical sub-solar temperature for a surface facing towards and in direct equilibrium with the insolation — i.e., equation (1.1). The smooth-surface TPM was run for 46 values of sub-solar latitude (0° to 90° in 2° increments) and 116 values of the thermal parameter (spaced equally in $\log_{10}$ space, from 0 to 450) whereas the rough-surface TPM was iterated across 3 values of $\gamma = \{45°, 68°, 90°\}$ and run for 46 values of sub-solar latitude (0° to 90° in 2° increments), 116 values of the thermal parameter (spread out in $\log_{10}$ space, from 0 to 450), and 7 values of $A_{grid} = \{0, 0.1, 0.2, 0.3, 0.4, 0.5, 1\}$. These parameters are chosen since they provide sufficient resolution to ensure an accuracy within 1% between the surface temperature values interpolated from the grid and those calculated using the exact model parameters.

Temperatures calculated for spheres are mapped to prolate ellipsoids ($\mathsf{b/c} = 1$, where $\mathsf{a} \geq \mathsf{b} \geq \mathsf{c}$) using simple, closed-form algebraic expressions (appendix B) in order to model elongated bodies of differing $\mathsf{a/b}$ axis ratio. Fluxes are calculated for the given observing circumstances by interpolation of the flux calculated using the tabulated temperatures. The flux calculated from the interpolated grid are within 1% of the flux calculated by running the TPM with the exact thermophysical and observing parameters. Finally, thermal flux is calculated by a summation of the individual flux contributions, using a grey-body approximation, with wavelength-dependent emissivity (ε_λ), from smooth surface and crater elements (with discrete area element dA) visible to the observer:

$$F(\lambda) = \frac{\varepsilon_\lambda}{\Delta_{\rm AU}^2} \iint_S \{(1 - f_R) B_{smooth}(\lambda, T(\theta, \phi)) + f_R (1 - v) \Lambda B_{rough}(\lambda, T(\theta, \phi, i_\angle))\} \cos(e_\angle) dA. \tag{2.6}$$

In my data fitting approach, the shape, spin vector (λ_{eclip}, β_{eclip}), roughness, and thermal inertia are left as free parameters that I select from a pre-defined sample space, and I search for the best-fit D_{eff}. A sphere and prolate ellipsoids with a/b axis ratios of 1.25, 1.75, 2.5, and 3.5 are used. For each of these shapes, I sample 25 predefined thermal inertia values, 3 default roughness (mean surface slope; $\bar{\theta}$) values, and 235 spin vectors. Each individual value of γ is paired with a corresponding $f_R = \{1/2, 4/5, 1\}$ value in order to produce default mean surface slopes of $\bar{\theta} = \{10°, 29°, \text{and } 58°\}$. The thermal inertia points are evenly spread in log space from 0 to 3000 J m^{-2} K^{-1} s$^{-1/2}$, and the spin vectors are spread evenly throughout the celestial sphere, which is achieved by constructing a Fibonacci lattice in spherical coordinates (e.g., Swinbank and Purser, 2006). For each shape/spin vector/Γ combination I use a routine to find the D_{eff} value which minimizes χ^2. To place confidence limits on each of the fitted parameters, I use the reduced χ^2 statistic ($\tilde{\chi}^2 = \chi^2/\nu$) to express the solutions within a 1σ range as $\tilde{\chi}^2 < \tilde{\chi}^2_{min}(1 + \sqrt{2\nu}/\nu)$.

2.3.4 TPM Results

The TPM was run for 239 objects: 3 near-Earth asteroids (NEAs), 2 Mars-crossers (MCs), and 234 main-belt asteorids (MBAs). Table 2.3 shows the best-fit and 1σ uncertainties for the effective diameter (D_{eff}), geometric albedo (p_V), thermal inertia (Γ), surface roughness ($\bar{\theta}$), elongation (a/b; prolate ellipsoid axis ratio), and sense of spin ($\Uparrow$ for prograde and $\Downarrow$ for retrograde) for all 239 objects, with the results of the 21 object from chapter 1 included at the top. Diameter errors for $D_{\mathit{eff}} > 10$ km are below 15% of the diameter value, but can be as high as 40% for objects smaller than 10 km. Upper and lower thermal inertia uncertainties are, on average, 180% and 67% of the reported value, respectively. Surface roughness could only be estimated for 97 of the 239 (41%) objects and sense of spin could be constrained for all but 17 of the 239 (93%). In some cases, TPM fits only allowed for a lower or upper bound on the surface roughness.

Table 2.3: TPM Results

Object	D_{eff} (km)	p_V	Γ[a]	$\bar{\theta}(^\circ)$	a/b[b]	Spin[c]
(167) Urda	39.48 ± 0.89	$0.252^{+0.010}_{-0.019}$	51^{+20}_{-16}	38 ± 13	1.51 ± 0.27	$\Downarrow$
(183) Istria	31.43 ± 2.92	$0.288^{+0.029}_{-0.033}$	21^{+12}_{-10}	47 ± 13	1.51 ± 0.27	$\Uparrow$
(208) Lacrimosa	40.44 ± 1.37	$0.253^{+0.012}_{-0.014}$	77^{+31}_{-22}	41 ± 13	1.51 ± 0.27	$\Uparrow$
(413) Edburga	33.44 ± 1.75	$0.169^{+0.012}_{-0.022}$	41^{+19}_{-10}	9 ± 6	1.51 ± 0.27	$\Downarrow$
(509) Iolanda	54.39 ± 3.86	$0.243^{+0.019}_{-0.027}$	$8.6^{+12.2}_{-8.6}$	18 ± 7	1.51 ± 0.27	$\Uparrow$
(771) Libera[d]	29.23 ± 2.10	$0.160^{+0.013}_{-0.019}$	61^{+34}_{-26}	53 ± 39	1.51 ± 0.27	$\Downarrow$
(857) Glasenappia	13.62 ± 0.84	$0.297^{+0.013}_{-0.021}$	58^{+30}_{-24}	< 20	1.51 ± 0.27	$\Uparrow$
(984) Gretia	34.72 ± 1.18	$0.227^{+0.012}_{-0.023}$	28^{+8}_{-7}	53 ± 10	1.51 ± 0.27	$\Uparrow$
(1036) Ganymed	35.85 ± 1.95	$0.278^{+0.017}_{-0.027}$	15^{+22}_{-15}	40 ± 32	1.08 ± 0.19	—
(1140) Crimea	30.13 ± 1.18	$0.276^{+0.020}_{-0.028}$	23^{+15}_{-23}	23 ± 21	1.51 ± 0.27	$\Downarrow$
(1188) Gothlandia	13.52 ± 0.84	$0.238^{+0.019}_{-0.022}$	38^{+21}_{-13}	41 ± 27	1.51 ± 0.27	$\Downarrow$
(1291) Phryne	27.03 ± 1.65	$0.186^{+0.014}_{-0.017}$	20^{+16}_{-6}	45 ± 17	2.16 ± 0.39	$\Uparrow$
(1432) Ethiopia	7.15 ± 0.67	$0.535^{+0.058}_{-0.070}$	71^{+180}_{-65}	—	1.51 ± 0.27	$\Uparrow$
(1495) Helsinki	13.31 ± 0.59	$0.271^{+0.017}_{-0.033}$	19^{+13}_{-13}	12 ± 8	1.51 ± 0.27	$\Uparrow$
(1568) Aisleen	11.66 ± 1.01	$0.328^{+0.034}_{-0.038}$	51^{+41}_{-22}	46 ± 38	2.16 ± 0.39	$\Downarrow$
(1607) Mavis[d]	14.52 ± 1.72	$0.249^{+0.032}_{-0.037}$	37^{+42}_{-25}	58 ± 50	1.51 ± 0.27	$\Uparrow$
(1980) Tezcatlipoca	5.68 ± 0.58	$0.205^{+0.035}_{-0.040}$	170^{+170}_{-110}	57 ± 39	1.51 ± 0.27	$\Downarrow$
(2156) Kate	8.04 ± 0.45	$0.294^{+0.021}_{-0.025}$	56^{+23}_{-23}	49 ± 32	2.16 ± 0.39	$\Uparrow$
(4611) Vulkaneifel	12.10 ± 1.12	$0.216^{+0.023}_{-0.028}$	32^{+23}_{-32}	< 53	1.51 ± 0.27	$\Downarrow$
(5625) Jamesferguson	14.46 ± 0.86	$0.062^{+0.005}_{-0.006}$	52^{+14}_{-15}	> 36	2.16 ± 0.39	$\Downarrow$
(6159) Andreseloy	5.65 ± 1.37	$0.247^{+0.061}_{-0.061}$	60^{+177}_{-60}	—	1.51 ± 0.27	$\Downarrow$
(91) Aegina	101.40 ± 13.85	$0.052^{+0.007}_{-0.007}$	19^{+31}_{-19}	17 ± 12	1.08 ± 0.19	$\Uparrow$
(155) Scylla	38.41 ± 0.54	$0.054^{+0.002}_{-0.003}$	16^{+15}_{-5}	34 ± 22	1.51 ± 0.27	$\Uparrow$
(271) Penthesilea	65.05 ± 2.30	$0.054^{+0.003}_{-0.003}$	16^{+33}_{-16}	16 ± 4	1.51 ± 0.27	$\Uparrow$
(295) Theresia	30.50 ± 1.23	$0.220^{+0.013}_{-0.013}$	24^{+38}_{-17}	45 ± 20	1.08 ± 0.19	$\Uparrow$
(322) Phaeo	59.66 ± 1.29	$0.126^{+0.004}_{-0.009}$	12^{+11}_{-7}	—	2.16 ± 0.39	$\Downarrow$
(343) Ostara	19.65 ± 1.38	$0.113^{+0.009}_{-0.010}$	140^{+120}_{-60}	—	1.51 ± 0.27	$\Downarrow$
(444) Gyptis	162.3 ± 22.9	$0.049^{+0.007}_{-0.008}$	74^{+74}_{-74}	—	1.08 ± 0.19	$\Downarrow$
(463) Lola	20.27 ± 1.48	$0.115^{+0.009}_{-0.010}$	70^{+30}_{-30}	44 ± 15	2.16 ± 0.39	$\Uparrow$
(464) Megaira	69.56 ± 6.38	$0.053^{+0.006}_{-0.006}$	120^{+120}_{-120}	15 ± 11	2.16 ± 0.39	—
(493) Griseldis	40.86 ± 1.13	$0.054^{+0.003}_{-0.004}$	56^{+25}_{-32}	—	1.51 ± 0.27	—

Table 2.3 — continued

Object	D_{eff} (km)	p_V	Γ^a	$\bar{\theta}(^\circ)$	a/b[b]	Spin[c]
(500) Selinur	41.15 ± 0.37	$0.196^{+0.004}_{-0.017}$	16^{+7}_{-8}	—	1.51 ± 0.27	⇓
(520) Franziska	27.42 ± 1.00	$0.149^{+0.008}_{-0.011}$	12^{+24}_{-5}	—	1.51 ± 0.27	—
(538) Friederike	66.45 ± 1.42	$0.073^{+0.003}_{-0.003}$	35^{+12}_{-11}	—	1.51 ± 0.27	—
(558) Carmen	59.71 ± 3.15	$0.117^{+0.007}_{-0.011}$	$7.7^{+26.9}_{-7.7}$	—	1.08 ± 0.19	⇓
(562) Salome	36.99 ± 1.90	$0.145^{+0.009}_{-0.011}$	23^{+12}_{-20}	19 ± 10	1.08 ± 0.19	⇑
(567) Eleutheria	87.45 ± 7.81	$0.056^{+0.005}_{-0.007}$	19^{+30}_{-11}	—	1.08 ± 0.19	⇑
(583) Klotilde	80.78 ± 6.25	$0.067^{+0.006}_{-0.006}$	30^{+12}_{-19}	49 ± 35	1.08 ± 0.19	⇑
(651) Antikleia	34.07 ± 1.92	$0.159^{+0.010}_{-0.014}$	37^{+16}_{-26}	48 ± 40	1.08 ± 0.19	⇓
(656) Beagle	55.14 ± 3.02	$0.068^{+0.005}_{-0.004}$	32^{+14}_{-14}	—	1.51 ± 0.27	⇑
(662) Newtonia	24.04 ± 1.41	$0.211^{+0.014}_{-0.022}$	35^{+23}_{-25}	47 ± 39	1.51 ± 0.27	⇓
(668) Dora	23.18 ± 0.48	$0.062^{+0.004}_{-0.003}$	52^{+8}_{-8}	52 ± 8	1.51 ± 0.27	⇑
(670) Ottegebe	35.08 ± 0.76	$0.258^{+0.009}_{-0.018}$	44^{+14}_{-18}	46 ± 10	1.51 ± 0.27	⇑
(688) Melanie	38.44 ± 2.49	$0.070^{+0.006}_{-0.007}$	41^{+44}_{-19}	45 ± 13	1.51 ± 0.27	⇑
(734) Benda	66.30 ± 2.75	$0.045^{+0.002}_{-0.003}$	13^{+8}_{-13}	17 ± 11	1.51 ± 0.27	⇑
(735) Marghanna	65.09 ± 3.93	$0.063^{+0.004}_{-0.005}$	17^{+88}_{-17}	48 ± 29	1.51 ± 0.27	⇑
(793) Arizona	26.94 ± 1.33	$0.237^{+0.013}_{-0.020}$	32^{+16}_{-13}	50 ± 24	1.08 ± 0.19	⇑
(826) Henrika	23.11 ± 0.97	$0.096^{+0.006}_{-0.005}$	45^{+16}_{-21}	29 ± 24	1.08 ± 0.19	⇑
(829) Academia	37.20 ± 1.49	$0.063^{+0.003}_{-0.004}$	15^{+7}_{-15}	23 ± 17	2.16 ± 0.39	⇓
(883) Matterania	7.60 ± 0.81	$0.304^{+0.034}_{-0.038}$	36^{+37}_{-24}	—	1.51 ± 0.27	⇑
(906) Repsolda	71.08 ± 6.05	$0.070^{+0.007}_{-0.007}$	47^{+115}_{-28}	—	1.08 ± 0.19	⇓
(918) Itha	21.59 ± 0.37	$0.222^{+0.009}_{-0.017}$	37^{+10}_{-10}	—	1.51 ± 0.27	⇓
(972) Cohnia	73.12 ± 0.79	$0.055^{+0.002}_{-0.003}$	19^{+38}_{-13}	40 ± 12	1.51 ± 0.27	⇑
(977) Philippa	76.87 ± 6.35	$0.040^{+0.004}_{-0.004}$	27^{+84}_{-21}	—	1.08 ± 0.19	⇓
(984) Gretia	34.72 ± 1.18	$0.227^{+0.012}_{-0.023}$	29^{+8}_{-7}	56 ± 16	1.51 ± 0.27	⇑
(987) Wallia	43.05 ± 1.91	$0.161^{+0.009}_{-0.012}$	46^{+64}_{-46}	—	2.16 ± 0.39	⇓
(998) Bodea	31.14 ± 1.87	$0.052^{+0.004}_{-0.005}$	20^{+16}_{-7}	—	1.08 ± 0.19	⇓
(1018) Arnolda	16.31 ± 1.74	$0.260^{+0.029}_{-0.037}$	43^{+47}_{-43}	—	1.51 ± 0.27	⇑
(1047) Geisha	10.53 ± 0.41	$0.283^{+0.015}_{-0.024}$	35^{+58}_{-14}	31 ± 10	1.51 ± 0.27	⇑
(1051) Merope	53.46 ± 1.81	$0.066^{+0.004}_{-0.006}$	48^{+81}_{-25}	—	2.16 ± 0.39	⇑
(1076) Viola	22.22 ± 1.49	$0.054^{+0.004}_{-0.005}$	24^{+44}_{-24}	—	1.51 ± 0.27	⇓
(1077) Campanula	10.12 ± 0.80	$0.230^{+0.020}_{-0.022}$	56^{+40}_{-34}	56 ± 31	1.51 ± 0.27	⇑
(1083) Salvia	11.22 ± 1.12	$0.209^{+0.024}_{-0.029}$	54^{+17}_{-30}	16 ± 10	1.51 ± 0.27	⇓

Table 2.3 — continued

Object	D_{eff} (km)	p_V	Γ^a	$\bar{\theta}(^\circ)$	a/b[b]	Spin[c]
(1095) Tulipa	31.05 ± 1.36	$0.143^{+0.008}_{-0.010}$	23^{+13}_{-13}	—	1.08 ± 0.19	⇑
(1109) Tata	64.10 ± 2.59	$0.049^{+0.003}_{-0.002}$	10^{+46}_{-10}	—	1.08 ± 0.19	⇑
(1123) Shapleya	11.97 ± 0.55	$0.304^{+0.019}_{-0.027}$	14^{+33}_{-14}	16 ± 14	1.51 ± 0.27	—
(1125) China	26.87 ± 1.09	$0.060^{+0.004}_{-0.004}$	34^{+8}_{-7}	54 ± 24	1.51 ± 0.27	⇓
(1136) Mercedes	24.66 ± 1.81	$0.123^{+0.010}_{-0.012}$	54^{+81}_{-34}	—	2.16 ± 0.39	⇓
(1142) Aetolia	23.91 ± 1.28	$0.260^{+0.018}_{-0.022}$	$8.0^{+29.7}_{-8.0}$	37 ± 25	1.08 ± 0.19	⇑
(1152) Pawona	17.47 ± 0.90	$0.203^{+0.012}_{-0.017}$	26^{+35}_{-14}	—	1.08 ± 0.19	⇓
(1162) Larissa	41.15 ± 2.27	$0.152^{+0.011}_{-0.014}$	19^{+15}_{-19}	52 ± 44	1.51 ± 0.27	⇑
(1224) Fantasia	13.65 ± 0.22	$0.252^{+0.013}_{-0.022}$	58^{+16}_{-12}	64 ± 8	1.51 ± 0.27	⇑
(1258) Sicilia	44.05 ± 2.62	$0.060^{+0.004}_{-0.004}$	61^{+76}_{-31}	—	1.51 ± 0.27	⇑
(1281) Jeanne	24.38 ± 0.94	$0.079^{+0.004}_{-0.004}$	90^{+44}_{-25}	53 ± 27	1.51 ± 0.27	⇑
(1288) Santa	30.68 ± 1.27	$0.060^{+0.004}_{-0.003}$	15^{+23}_{-5}	33 ± 28	2.16 ± 0.39	⇓
(1296) Andree	23.28 ± 2.12	$0.074^{+0.007}_{-0.008}$	40^{+74}_{-12}	—	2.16 ± 0.39	⇑
(1299) Mertona	15.22 ± 1.18	$0.194^{+0.017}_{-0.024}$	15^{+29}_{-8}	—	1.51 ± 0.27	⇑
(1310) Villigera	14.63 ± 1.28	$0.209^{+0.021}_{-0.026}$	40^{+23}_{-30}	50 ± 31	1.08 ± 0.19	⇑
(1316) Kasan	6.54 ± 0.50	$0.277^{+0.033}_{-0.041}$	10^{+34}_{-10}	51 ± 26	1.51 ± 0.27	⇓
(1325) Inanda	11.42 ± 1.57	$0.189^{+0.027}_{-0.030}$	76^{+50}_{-36}	61 ± 21	2.16 ± 0.39	⇑
(1335) Demoulina	7.65 ± 0.78	$0.241^{+0.027}_{-0.031}$	130^{+90}_{-100}	—	2.16 ± 0.39	⇑
(1352) Wawel	21.72 ± 1.68	$0.139^{+0.012}_{-0.012}$	97^{+28}_{-71}	—	1.51 ± 0.27	⇑
(1375) Alfreda	14.46 ± 0.55	$0.222^{+0.012}_{-0.022}$	30^{+48}_{-18}	< 42	1.08 ± 0.19	⇓
(1412) Lagrula	9.13 ± 0.50	$0.267^{+0.019}_{-0.027}$	37^{+23}_{-9}	—	1.51 ± 0.27	⇓
(1443) Ruppina	16.68 ± 1.03	$0.259^{+0.018}_{-0.020}$	40^{+18}_{-14}	—	1.51 ± 0.27	⇑
(1452) Hunnia	21.22 ± 1.99	$0.065^{+0.007}_{-0.008}$	24^{+34}_{-20}	—	1.51 ± 0.27	⇑
(1501) Baade	11.48 ± 0.88	$0.240^{+0.020}_{-0.022}$	34^{+48}_{-34}	—	1.08 ± 0.19	⇓
(1517) Beograd	34.21 ± 2.25	$0.061^{+0.004}_{-0.004}$	19^{+55}_{-5}	—	1.51 ± 0.27	⇑
(1536) Pielinen	8.53 ± 0.19	$0.225^{+0.013}_{-0.019}$	74^{+23}_{-35}	23 ± 36	1.51 ± 0.27	—
(1542) Schalen	46.48 ± 1.54	$0.053^{+0.003}_{-0.004}$	10^{+15}_{-10}	38 ± 19	1.51 ± 0.27	⇓
(1565) Lemaitre	8.44 ± 0.96	$0.204^{+0.026}_{-0.033}$	24^{+53}_{-24}	48 ± 30	1.08 ± 0.19	⇑
(1567) Alikoski	71.15 ± 4.24	$0.053^{+0.004}_{-0.005}$	$7.2^{+73.4}_{-7.2}$	45 ± 38	1.08 ± 0.19	⇓
(1573) Vaisala	10.31 ± 0.64	$0.213^{+0.022}_{-0.033}$	130^{+120}_{-80}	46 ± 28	1.51 ± 0.27	⇓
(1577) Reiss	5.72 ± 0.57	$0.468^{+0.052}_{-0.066}$	25^{+36}_{-20}	—	1.51 ± 0.27	⇑
(1628) Strobel	53.71 ± 1.20	$0.060^{+0.003}_{-0.005}$	47^{+12}_{-30}	51 ± 36	1.51 ± 0.27	⇓

Table 2.3 — continued

Object	D_{eff} (km)	p_V	Γ[a]	$\bar{\theta}(^\circ)$	a/b[b]	Spin[c]
(1644) Rafita	13.49 ± 0.84	$0.263^{+0.019}_{-0.031}$	28^{+25}_{-14}	48 ± 15	1.51 ± 0.27	$\Downarrow$
(1651) Behrens	10.09 ± 0.46	$0.242^{+0.015}_{-0.025}$	59^{+29}_{-19}	43 ± 36	1.51 ± 0.27	$\Uparrow$
(1655) Comas Sola	35.09 ± 1.30	$0.059^{+0.003}_{-0.005}$	40^{+37}_{-30}	14 ± 7	1.51 ± 0.27	$\Uparrow$
(1702) Kalahari	34.16 ± 1.23	$0.065^{+0.003}_{-0.006}$	28^{+40}_{-9}	46 ± 8	1.51 ± 0.27	$\Downarrow$
(1723) Klemola	33.77 ± 0.91	$0.148^{+0.007}_{-0.011}$	30^{+11}_{-10}	37 ± 10	1.51 ± 0.27	$\Downarrow$
(1734) Zhongolovich	25.33 ± 0.71	$0.069^{+0.004}_{-0.004}$	35^{+31}_{-10}	42 ± 28	2.16 ± 0.39	$\Downarrow$
(1741) Giclas	13.17 ± 0.56	$0.266^{+0.093}_{-0.015}$	33^{+20}_{-10}	—	1.51 ± 0.27	$\Downarrow$
(1759) Kienle	7.73 ± 1.17	$0.184^{+0.029}_{-0.030}$	52^{+88}_{-52}	—	1.51 ± 0.27	$\Downarrow$
(1768) Appenzella	18.91 ± 0.59	$0.058^{+0.004}_{-0.003}$	31^{+18}_{-12}	—	1.51 ± 0.27	$\Uparrow$
(1807) Slovakia[d]	9.83 ± 1.19	$0.229^{+0.030}_{-0.033}$	200^{+240}_{-50}	—	1.51 ± 0.27	$\Uparrow$
(1896) Beer	5.07 ± 0.96	$0.229^{+0.045}_{-0.045}$	80^{+335}_{-80}	—	1.51 ± 0.27	$\Uparrow$
(1936) Lugano	24.03 ± 0.27	$0.083^{+0.005}_{-0.007}$	120^{+70}_{-80}	49 ± 13	2.94 ± 0.53	—
(1979) Sakharov	4.69 ± 0.77	$0.282^{+0.048}_{-0.062}$	58^{+269}_{-27}	—	1.51 ± 0.27	$\Uparrow$
(2005) Hencke	8.99 ± 0.95	$0.315^{+0.037}_{-0.046}$	40^{+48}_{-34}	—	1.08 ± 0.19	$\Downarrow$
(2072) Kosmodemyanskaya	4.74 ± 1.44	$0.657^{+0.201}_{-0.207}$	19^{+129}_{-19}	—	1.08 ± 0.19	$\Uparrow$
(2106) Hugo	16.15 ± 1.50	$0.091^{+0.009}_{-0.010}$	22^{+36}_{-9}	—	1.51 ± 0.27	$\Uparrow$
(2111) Tselina	24.05 ± 2.19	$0.195^{+0.020}_{-0.026}$	47^{+36}_{-24}	46 ± 13	1.51 ± 0.27	$\Downarrow$
(2123) Vltava	16.05 ± 0.68	$0.179^{+0.011}_{-0.010}$	56^{+37}_{-22}	—	1.08 ± 0.19	$\Downarrow$
(2140) Kemerovo	33.56 ± 2.05	$0.050^{+0.004}_{-0.005}$	20^{+39}_{-14}	46 ± 13	1.08 ± 0.19	$\Uparrow$
(2144) Marietta	17.26 ± 0.45	$0.203^{+0.009}_{-0.010}$	53^{+10}_{-8}	39 ± 14	1.51 ± 0.27	$\Uparrow$
(2177) Oliver	19.52 ± 0.50	$0.085^{+0.005}_{-0.003}$	42^{+10}_{-10}	< 18	1.51 ± 0.27	$\Uparrow$
(2203) van Rhijn	22.31 ± 1.08	$0.087^{+0.005}_{-0.005}$	55^{+55}_{-27}	—	2.16 ± 0.39	$\Downarrow$
(2204) Lyyli	25.05 ± 0.95	$0.047^{+0.003}_{-0.004}$	90^{+36}_{-50}	49 ± 22	2.16 ± 0.39	$\Downarrow$
(2214) Carol	26.28 ± 1.60	$0.061^{+0.005}_{-0.005}$	21^{+15}_{-9}	42 ± 31	1.51 ± 0.27	$\Uparrow$
(2239) Paracelsus	37.53 ± 2.48	$0.054^{+0.004}_{-0.006}$	18^{+7}_{-18}	—	1.51 ± 0.27	$\Uparrow$
(2268) Szmytowna	15.18 ± 1.46	$0.190^{+0.020}_{-0.019}$	30^{+32}_{-30}	—	1.08 ± 0.19	$\Downarrow$
(2275) Cuitlahuac	7.29 ± 0.19	$0.342^{+0.017}_{-0.028}$	13^{+24}_{-13}	< 13	1.51 ± 0.27	$\Downarrow$
(2297) Daghestan	25.06 ± 0.89	$0.086^{+0.005}_{-0.004}$	58^{+23}_{-18}	34 ± 25	2.16 ± 0.39	$\Uparrow$
(2306) Bauschinger	19.24 ± 0.97	$0.072^{+0.005}_{-0.005}$	18^{+14}_{-10}	15 ± 8	1.51 ± 0.27	$\Downarrow$
(2332) Kalm	36.52 ± 2.55	$0.060^{+0.005}_{-0.005}$	77^{+15}_{-48}	—	1.51 ± 0.27	$\Uparrow$
(2347) Vinata	23.63 ± 1.27	$0.103^{+0.008}_{-0.008}$	35^{+20}_{-14}	12 ± 11	2.16 ± 0.39	$\Uparrow$
(2365) Interkosmos	16.62 ± 1.41	$0.195^{+0.018}_{-0.021}$	41^{+10}_{-41}	—	1.08 ± 0.19	$\Uparrow$

Table 2.3 — continued

Object	D_{eff} (km)	p_V	Γ[a]	$\bar{\theta}(^\circ)$	a/b[b]	Spin[c]
(2375) Radek	32.19 ± 1.60	$0.123^{+0.008}_{-0.010}$	11^{+14}_{-11}	45 ± 15	1.51 ± 0.27	⇓
(2446) Lunacharsky	12.43 ± 0.31	$0.078^{+0.003}_{-0.004}$	33^{+12}_{-10}	< 21	2.16 ± 0.39	⇓
(2463) Sterpin	11.93 ± 0.69	$0.221^{+0.016}_{-0.023}$	17^{+43}_{-17}	—	1.08 ± 0.19	⇓
(2500) Alascattalo	7.99 ± 0.27	$0.278^{+0.013}_{-0.020}$	41^{+18}_{-28}	33 ± 20	1.08 ± 0.19	⇑
(2556) Louise	5.96 ± 0.55	$0.252^{+0.025}_{-0.031}$	61^{+37}_{-33}	—	2.16 ± 0.39	⇓
(2567) Elba	18.40 ± 1.27	$0.110^{+0.008}_{-0.009}$	50^{+11}_{-36}	—	1.08 ± 0.19	⇓
(2687) Tortali	14.91 ± 0.21	$0.148^{+0.005}_{-0.011}$	59^{+16}_{-10}	< 27	1.08 ± 0.19	⇓
(2786) Grinevia	11.07 ± 0.98	$0.237^{+0.023}_{-0.029}$	12^{+19}_{-12}	< 23	1.08 ± 0.19	⇓
(2855) Bastian	8.78 ± 0.57	$0.151^{+0.012}_{-0.012}$	17^{+42}_{-7}	< 41	1.08 ± 0.19	⇑
(2870) Haupt[d]	15.51 ± 2.28	$0.057^{+0.009}_{-0.009}$	130^{+180}_{-130}	—	2.94 ± 0.53	—
(2947) Kippenhahn	7.80 ± 0.29	$0.267^{+0.014}_{-0.017}$	32^{+18}_{-11}	> 28	1.51 ± 0.27	⇑
(2985) Shakespeare	10.64 ± 0.92	$0.260^{+0.025}_{-0.024}$	41^{+49}_{-13}	—	2.16 ± 0.39	⇓
(3036) Krat	41.41 ± 1.28	$0.090^{+0.006}_{-0.005}$	15^{+57}_{-9}	< 43	2.16 ± 0.39	⇓
(3051) Nantong	16.79 ± 1.60	$0.081^{+0.008}_{-0.009}$	27^{+28}_{-14}	< 38	1.08 ± 0.19	⇑
(3144) Brosche	4.80 ± 0.53	$0.219^{+0.026}_{-0.027}$	59^{+56}_{-45}	—	1.51 ± 0.27	⇑
(3162) Nostalgia	28.88 ± 1.48	$0.064^{+0.005}_{-0.006}$	29^{+51}_{-15}	—	3.49 ± 0.63	⇑
(3249) Musashino	6.44 ± 1.22	$0.185^{+0.036}_{-0.036}$	93^{+132}_{-73}	—	1.51 ± 0.27	⇓
(3267) Glo	7.37 ± 1.28	$0.262^{+0.049}_{-0.053}$	23^{+43}_{-13}	43 ± 29	1.08 ± 0.19	⇓
(3305) Ceadams	10.37 ± 0.12	$0.218^{+0.007}_{-0.013}$	21^{+6}_{-3}	> 26	1.08 ± 0.19	⇓
(3411) Debetencourt	5.18 ± 0.21	$0.294^{+0.017}_{-0.020}$	22^{+83}_{-12}	14 ± 13	1.51 ± 0.27	⇑
(3438) Inarradas	25.18 ± 0.68	$0.058^{+0.003}_{-0.003}$	54^{+15}_{-15}	49 ± 11	1.51 ± 0.27	⇓
(3483) Svetlov	2.96 ± 0.48	$0.496^{+0.107}_{-0.114}$	110^{+400}_{-50}	—	1.51 ± 0.27	⇓
(3509) Sanshui	9.93 ± 0.84	$0.243^{+0.023}_{-0.028}$	62^{+27}_{-34}	—	1.08 ± 0.19	⇑
(3536) Schleicher	3.67 ± 1.14	$0.375^{+0.118}_{-0.119}$	32^{+182}_{-10}	—	1.51 ± 0.27	⇓
(3544) Borodino	9.29 ± 0.81	$0.241^{+0.024}_{-0.027}$	72^{+14}_{-45}	—	1.51 ± 0.27	⇓
(3554) Amun	2.71 ± 0.02	$0.140^{+0.027}_{-0.028}$	1400^{+700}_{-200}	< 14	1.08 ± 0.19	⇓
(3560) Chenqian	22.84 ± 0.56	$0.152^{+0.007}_{-0.011}$	44^{+22}_{-10}	50 ± 7	1.51 ± 0.27	⇑
(3628) Boznemcova	8.07 ± 0.80	$0.223^{+0.023}_{-0.024}$	32^{+23}_{-32}	—	1.08 ± 0.19	⇓
(3751) Kiang	22.38 ± 0.68	$0.083^{+0.005}_{-0.007}$	62^{+20}_{-16}	35 ± 6	2.46 ± 0.44	⇑
(3823) Yorii	13.66 ± 1.47	$0.064^{+0.007}_{-0.008}$	49^{+22}_{-49}	—	1.08 ± 0.19	⇓
(3907) Kilmartin	8.16 ± 1.12	$0.530^{+0.076}_{-0.083}$	26^{+47}_{-26}	—	1.08 ± 0.19	⇑
(3915) Fukushima	22.18 ± 0.39	$0.059^{+0.004}_{-0.003}$	22^{+13}_{-7}	41 ± 18	1.51 ± 0.27	⇓

Table 2.3 — continued

Object	D_{eff} (km)	p_V	Γ^a	$\bar{\theta}(^\circ)$	a/b[b]	Spin[c]
(3935) Toatenmongakkai	12.02 ± 0.82	$0.219^{+0.017}_{-0.021}$	120^{+90}_{-60}	51 ± 27	1.51 ± 0.27	⇑
(3936) Elst	5.00 ± 0.68	$0.490^{+0.069}_{-0.074}$	22^{+56}_{-22}	—	1.08 ± 0.19	⇓
(4003) Schumann	31.92 ± 0.41	$0.063^{+0.003}_{-0.002}$	32^{+35}_{-11}	—	2.16 ± 0.39	⇑
(4006) Sandler	16.89 ± 0.64	$0.059^{+0.003}_{-0.003}$	36^{+7}_{-11}	47 ± 14	1.08 ± 0.19	⇓
(4008) Corbin	6.18 ± 0.31	$0.307^{+0.025}_{-0.035}$	67^{+37}_{-25}	39 ± 15	1.08 ± 0.19	⇓
(4029) Bridges	7.87 ± 0.62	$0.246^{+0.021}_{-0.025}$	32^{+26}_{-18}	46 ± 25	1.08 ± 0.19	⇓
(4142) Dersu-Uzala	6.31 ± 0.52	$0.236^{+0.048}_{-0.049}$	110^{+140}_{-30}	—	1.08 ± 0.19	⇓
(4150) Starr	6.93 ± 0.39	$0.304^{+0.021}_{-0.024}$	29^{+16}_{-14}	—	1.51 ± 0.27	⇑
(4255) Spacewatch	15.71 ± 0.45	$0.042^{+0.003}_{-0.002}$	24^{+22}_{-17}	42 ± 19	1.51 ± 0.27	⇑
(4264) Karljosephine	6.37 ± 1.83	$0.202^{+0.059}_{-0.059}$	110^{+300}_{-110}	—	1.51 ± 0.27	—
(4294) Horatius	8.07 ± 0.66	$0.242^{+0.023}_{-0.023}$	12^{+77}_{-12}	—	1.51 ± 0.27	—
(4352) Kyoto	11.33 ± 1.31	$0.308^{+0.038}_{-0.041}$	47^{+64}_{-32}	—	2.16 ± 0.39	⇑
(4359) Berlage	4.98 ± 0.69	$0.289^{+0.042}_{-0.042}$	40^{+71}_{-26}	—	1.51 ± 0.27	⇓
(4363) Sergej	5.48 ± 0.48	$0.282^{+0.026}_{-0.031}$	27^{+94}_{-27}	—	1.51 ± 0.27	⇓
(4383) Suruga	6.79 ± 1.03	$0.223^{+0.035}_{-0.040}$	37^{+53}_{-17}	—	1.08 ± 0.19	⇑
(4528) Berg	10.45 ± 0.96	$0.247^{+0.024}_{-0.033}$	26^{+20}_{-26}	—	1.08 ± 0.19	⇓
(4565) Grossman	7.57 ± 0.37	$0.240^{+0.017}_{-0.022}$	51^{+36}_{-12}	53 ± 35	1.51 ± 0.27	⇓
(4569) Baerbel	9.21 ± 0.73	$0.292^{+0.026}_{-0.028}$	48^{+45}_{-9}	49 ± 17	2.16 ± 0.39	⇑
(4613) Mamoru	11.96 ± 1.48	$0.280^{+0.036}_{-0.037}$	$9.4^{+22.6}_{-9.4}$	< 22	1.08 ± 0.19	⇓
(4713) Steel	6.58 ± 0.18	$0.196^{+0.025}_{-0.037}$	40^{+28}_{-13}	—	1.08 ± 0.19	⇑
(4771) Hayashi	13.32 ± 0.96	$0.101^{+0.008}_{-0.008}$	61^{+37}_{-29}	—	1.08 ± 0.19	⇓
(4898) Nishiizumi	2.46 ± 0.22	$0.600^{+0.073}_{-0.103}$	34^{+445}_{-34}	—	1.26 ± 0.23	⇑
(4899) Candace	7.17 ± 0.57	$0.271^{+0.028}_{-0.039}$	79^{+104}_{-60}	—	1.08 ± 0.19	⇑
(4908) Ward	4.91 ± 0.71	$0.262^{+0.040}_{-0.042}$	12^{+68}_{-12}	—	1.51 ± 0.27	—
(5035) Swift	10.22 ± 1.06	$0.211^{+0.023}_{-0.025}$	26^{+35}_{-20}	—	1.08 ± 0.19	⇓
(5052) Nancyruth	4.66 ± 0.78	$0.167^{+0.029}_{-0.032}$	10^{+72}_{-10}	—	1.51 ± 0.27	—
(5080) Oja	7.98 ± 0.53	$0.243^{+0.018}_{-0.026}$	26^{+50}_{-17}	—	1.08 ± 0.19	⇑
(5088) Tancredi	16.17 ± 1.02	$0.066^{+0.005}_{-0.005}$	40^{+12}_{-19}	—	1.51 ± 0.27	⇓
(5104) Skripnichenko	9.49 ± 0.48	$0.329^{+0.021}_{-0.026}$	41^{+31}_{-22}	—	1.51 ± 0.27	⇓
(5226) Pollack	5.74 ± 1.03	$0.303^{+0.056}_{-0.062}$	24^{+51}_{-18}	—	1.08 ± 0.19	⇓
(5333) Kanaya	13.86 ± 1.32	$0.066^{+0.007}_{-0.007}$	23^{+32}_{-7}	—	1.08 ± 0.19	⇑
(5378) Ellyett	2.77 ± 0.25	$0.776^{+0.095}_{-0.119}$	75^{+455}_{-62}	—	2.16 ± 0.39	⇓

Table 2.3 — continued

Object	D_{eff} (km)	p_V	Γ^a	$\bar{\theta}(^\circ)$	a/b[b]	Spin[c]
(5427) Jensmartin	3.13 ± 0.14	$0.622^{+0.055}_{-0.084}$	19^{+76}_{-19}	—	1.08 ± 0.19	⇓
(5527) 1991 UQ_3	5.30 ± 0.56	$0.233^{+0.026}_{-0.029}$	120^{+130}_{-80}	—	2.16 ± 0.39	⇓
(5574) Seagrave	9.72 ± 1.05	$0.225^{+0.027}_{-0.032}$	34^{+34}_{-34}	—	1.08 ± 0.19	⇓
(5592) Oshima	23.91 ± 1.16	$0.065^{+0.004}_{-0.005}$	34^{+23}_{-27}	—	1.08 ± 0.19	⇓
(5604) 1992 FE	0.67 ± 0.01	$0.447^{+0.077}_{-0.086}$	1100^{+2200}_{-600}	—	1.51 ± 0.27	⇑
(5682) Beresford	5.37 ± 1.83	$0.233^{+0.080}_{-0.082}$	29^{+152}_{-29}	—	1.08 ± 0.19	⇓
(5712) Funke	7.22 ± 1.60	$0.269^{+0.061}_{-0.062}$	33^{+50}_{-33}	—	1.51 ± 0.27	⇓
(6091) Mitsuru	4.94 ± 0.75	$0.423^{+0.068}_{-0.070}$	45^{+25}_{-13}	62 ± 36	2.46 ± 0.44	⇑
(6121) Plachinda	5.83 ± 0.82	$0.250^{+0.036}_{-0.038}$	56^{+63}_{-34}	—	1.51 +- 0.27	⇑
(6139) Naomi	10.68 ± 0.36	$0.207^{+0.014}_{-0.025}$	66^{+31}_{-36}	53 ± 32	1.08 ± 0.19	⇓
(6170) Levasseur	5.57 ± 0.63	$0.238^{+0.031}_{-0.040}$	76^{+161}_{-56}	—	1.08 ± 0.19	⇓
(6185) Mitsuma	10.36 ± 1.00	$0.113^{+0.012}_{-0.013}$	66^{+61}_{-45}	41 ± 16	1.08 ± 0.19	⇓
(6261) Chione	3.91 ± 0.56	$0.270^{+0.046}_{-0.052}$	41^{+52}_{-41}	—	1.51 ± 0.27	⇓
(6361) Koppel	3.59 ± 0.19	$0.728^{+0.049}_{-0.062}$	20^{+172}_{-20}	—	1.51 ± 0.27	⇓
(6572) Carson	8.56 ± 1.21	$0.262^{+0.038}_{-0.038}$	21^{+33}_{-15}	—	1.08 ± 0.19	⇓
(6838) Okuda	11.88 ± 0.28	$0.185^{+0.010}_{-0.014}$	47^{+13}_{-10}	53 ± 16	1.08 ± 0.19	⇑
(6870) 1991 OM_1	2.80 ± 0.66	$0.647^{+0.180}_{-0.193}$	59^{+330}_{-59}	—	1.51 ± 0.27	⇓
(6901) Roybishop	5.05 ± 0.44	$0.337^{+0.054}_{-0.058}$	59^{+83}_{-40}	—	1.08 ± 0.19	⇓
(6905) Miyazaki	14.30 ± 0.73	$0.222^{+0.015}_{-0.019}$	26^{+66}_{-26}	43 ± 36	1.08 ± 0.19	⇑
(6911) Nancygreen	2.90 ± 0.32	$0.515^{+0.068}_{-0.081}$	210^{+1220}_{-180}	—	1.51 ± 0.27	⇓
(7476) Ogilsbie[d]	18.41 ± 1.21	$0.146^{+0.013}_{-0.015}$	70^{+30}_{-20}	—	1.08 ± 0.19	⇑
(7783) 1994 JD	2.78 ± 0.33	$0.461^{+0.098}_{-0.104}$	170^{+190}_{-110}	—	1.51 ± 0.27	⇓
(7829) Jaroff	2.55 ± 0.50	$0.430^{+0.117}_{-0.133}$	32^{+176}_{-32}	—	1.08 ± 0.19	⇓
(7832) 1993 FA_{27}	3.55 ± 0.53	$0.444^{+0.070}_{-0.073}$	46^{+160}_{-46}	—	1.08 ± 0.19	⇑
(7949) 1992 SU	18.26 ± 1.36	$0.066^{+0.006}_{-0.006}$	37^{+28}_{-27}	32 ± 29	1.51 ± 0.27	⇑
(8213) 1995 FE[d]	4.80 ± 1.02	$0.287^{+0.063}_{-0.068}$	36^{+167}_{-18}	—	1.51 ± 0.27	⇓
(8862) Takayukiota	7.76 ± 2.35	$0.229^{+0.070}_{-0.070}$	43^{+195}_{-43}	10 ± 10	2.16 ± 0.39	⇑
(8887) Scheeres	7.56 ± 0.81	$0.275^{+0.032}_{-0.037}$	21^{+52}_{-21}	< 43	1.51 ± 0.27	⇑
(9297) Marchuk	9.55 ± 0.57	$0.260^{+0.019}_{-0.020}$	22^{+120}_{-22}	39 ± 27	1.08 ± 0.19	⇑
(10936) 1998 FN_{11}	11.75 ± 0.50	$0.127^{+0.008}_{-0.010}$	13^{+22}_{-13}	< 5	1.08 ± 0.19	⇑
(11549) 1992 YY	10.30 ± 0.44	$0.247^{+0.017}_{-0.030}$	30^{+18}_{-5}	—	1.08 ± 0.19	⇓
(11780) Thunder Bay	7.82 ± 2.43	$0.214^{+0.067}_{-0.067}$	130^{+450}_{-130}	—	1.51 ± 0.27	⇑

Table 2.3 — continued

Object	D_{eff} (km)	p_V	Γ^a	$\bar{\theta}(^\circ)$	a/b[b]	Spin[c]
(12376) Cochabamba	5.93 ± 0.97	$0.245^{+0.041}_{-0.046}$	120^{+60}_{-110}	—	1.51 ± 0.27	⇓
(12753) Povenmire	8.00 ± 0.19	$0.249^{+0.015}_{-0.027}$	17^{+23}_{-11}	< 8	1.51 ± 0.27	⇓
(13474) V'yus	6.63 ± 1.41	$0.146^{+0.032}_{-0.033}$	64^{+123}_{-44}	—	1.26 ± 0.23	—
(13856) 1999 XZ_{105}	14.79 ± 1.23	$0.059^{+0.005}_{-0.006}$	20^{+12}_{-10}	—	1.08 ± 0.19	⇑
(14342) Iglika	16.22 ± 1.11	$0.079^{+0.006}_{-0.007}$	24^{+8}_{-14}	—	1.51 ± 0.27	⇑
(14950) 1996 BE_2	6.66 ± 1.01	$0.145^{+0.023}_{-0.024}$	54^{+49}_{-34}	—	1.51 ± 0.27	⇓
(15362) 1996 ED	4.95 ± 1.01	$0.275^{+0.058}_{-0.058}$	110^{+120}_{-110}	—	1.51 ± 0.27	⇑
(15430) 1998 UR_{31}	3.78 ± 0.43	$0.297^{+0.037}_{-0.039}$	72^{+127}_{-63}	—	1.08 ± 0.19	⇓
(15499) Cloyd	9.67 ± 1.25	$0.146^{+0.020}_{-0.020}$	33^{+36}_{-33}	—	1.08 ± 0.19	⇑
(15914) 1997 UM_3	4.20 ± 0.95	$0.234^{+0.054}_{-0.054}$	88^{+188}_{-72}	—	1.51 ± 0.27	⇓
(16681) 1994 EV_7	3.94 ± 0.34	$0.209^{+0.037}_{-0.038}$	63^{+74}_{-30}	—	1.51 ± 0.27	⇓
(16886) 1998 BC_{26}	7.11 ± 0.78	$0.211^{+0.025}_{-0.027}$	33^{+49}_{-18}	49 ± 33	1.08 ± 0.19	—
(17681) Tweedledum	2.48 ± 0.31	$0.441^{+0.071}_{-0.098}$	130^{+320}_{-110}	—	1.51 ± 0.27	⇓
(17822) 1998 FM_{135}	10.92 ± 1.43	$0.058^{+0.008}_{-0.008}$	79^{+53}_{-52}	—	1.51 ± 0.27	⇑
(18487) 1996 AU_3	7.78 ± 0.79	$0.259^{+0.030}_{-0.035}$	46^{+36}_{-26}	—	1.51 ± 0.27	⇓
(19251) Totziens	6.24 ± 2.14	$0.196^{+0.068}_{-0.069}$	32^{+121}_{-32}	—	1.08 ± 0.19	⇑
(20378) 1998 KZ_{46}	7.78 ± 0.80	$0.212^{+0.026}_{-0.035}$	34^{+23}_{-14}	—	1.08 ± 0.19	⇑
(20932) 2258 T-1	5.76 ± 1.32	$0.247^{+0.057}_{-0.058}$	41^{+111}_{-41}	—	1.08 ± 0.19	⇓
(21594) 1998 VP_{31}	10.30 ± 0.26	$0.097^{+0.005}_{-0.005}$	44^{+16}_{-12}	50 ± 17	1.08 ± 0.19	⇑
(23200) 2000 SH_3	7.20 ± 1.10	$0.219^{+0.035}_{-0.037}$	17^{+66}_{-17}	—	1.08 ± 0.19	⇓
(23276) 2000 YT_{101}	7.01 ± 0.96	$0.071^{+0.010}_{-0.010}$	27^{+30}_{-27}	—	1.08 ± 0.19	⇑
(24101) Cassini	7.40 ± 1.43	$0.224^{+0.045}_{-0.045}$	15^{+38}_{-15}	—	1.08 ± 0.19	—
(27851) 1994 VG_2	10.43 ± 0.98	$0.057^{+0.006}_{-0.006}$	11^{+14}_{-11}	< 20	1.08 ± 0.19	—
(28126) Nydegger	2.63 ± 0.76	$0.226^{+0.066}_{-0.067}$	33^{+205}_{-33}	—	1.08 ± 0.19	—
(30470) 2000 OR_{19}	9.42 ± 0.28	$0.057^{+0.004}_{-0.004}$	45^{+43}_{-22}	< 11	1.51 ± 0.27	⇓
(32802) 1990 SK	4.27 ± 1.76	$0.273^{+0.114}_{-0.116}$	20^{+162}_{-20}	—	1.51 ± 0.27	⇓
(33916) 2000 LF_{19}	4.08 ± 0.41	$0.185^{+0.020}_{-0.020}$	38^{+51}_{-38}	—	1.51 ± 0.27	⇑
(41044) 1999 VW_6	5.79 ± 1.58	$0.297^{+0.082}_{-0.083}$	14^{+157}_{-14}	—	1.51 ± 0.27	⇓
(41223) 1999 XD_{16}	11.61 ± 1.15	$0.055^{+0.006}_{-0.006}$	23^{+43}_{-23}	—	1.08 ± 0.19	⇑
(41288) 1999 XD_{107}	4.22 ± 0.98	$0.207^{+0.050}_{-0.051}$	41^{+86}_{-34}	—	1.08 ± 0.19	⇓
(42265) 2001 QL_{69}	7.07 ± 1.35	$0.177^{+0.035}_{-0.036}$	25^{+89}_{-25}	—	1.51 ± 0.27	⇓
(42946) 1999 TU_{95}	4.74 ± 0.79	$0.266^{+0.046}_{-0.047}$	37^{+60}_{-37}	—	1.08 ± 0.19	⇓

Table 2.3 — continued

Object	D_{eff} (km)	p_V	Γ^a	$\bar{\theta}(^\circ)$	a/b[b]	Spin[c]
(44892) 1999 VJ_8	7.80 ± 1.66	$0.213^{+0.046}_{-0.048}$	32^{+93}_{-32}	—	1.08 ± 0.19	⇑
(45436) 2000 AD_{176}	3.89 ± 1.54	$0.240^{+0.098}_{-0.099}$	75^{+482}_{-75}	—	1.51 ± 0.27	⇑
(68216) 2001 CV_{26}	1.24 ± 0.05	$0.322^{+0.022}_{-0.030}$	430^{+1210}_{-280}	—	1.08 ± 0.19	⇓
(69350) 1993 YP	2.87 ± 0.69	$0.162^{+0.041}_{-0.044}$	240^{+490}_{-150}	—	1.51 ± 0.27	⇓
(72675) 2001 FP_{54}	3.77 ± 1.32	$0.219^{+0.078}_{-0.078}$	29^{+367}_{-29}	—	1.08 ± 0.19	⇓
(90698) Kosciuszko	3.55 ± 0.25	$0.298^{+0.028}_{-0.034}$	16^{+49}_{-16}	—	1.08 ± 0.19	⇑

[a]Thermal inertia values are in SI units (J m^{-2} K^{-1} $s^{-1/2}$).

[b]a/b values are adjusted downward by 16% to account for the overestimation as described in section 1.4.2.

[c]Indicates either prograde (⇑) or retrograde (⇓) spin direction.

[d]TPM results with $\chi^2_{min} > 8$ and thus should be used with caution.

2.3.5 Comparison to Previous Works

Diameters The diameter estimates from NEATM fits presented by the WISE team (i.e., Mainzer et al., 2011b; Masiero et al., 2011) are separately reported for the pre- and post-opposition epochs. I present a comparison of these diameter pairs (D_{eff}^{WISE}) to the diameter values (one per object; D_{eff}^{TPM}) obtained here, and plot them (colored by observing geometry) in figure 2.3. There is a general agreement of within ± 15% between the two datasets, with a few important notes. Firstly, for objects ∼30 km and above, my TPM diameters are slightly higher than the NEATM model estimates of the WISE team. This discrepancy is likely due to the inherent model differences between my TPM approach and the NEATM used by the WISE team. Secondly, objects smaller than 20 km exhibit, on average, 5% lower diameters from my TPM analysis than from the WISE NEATM analysis.. Lastly, I highlight an interesting trend seen in figure 2.3 for different observing geometries: pre-opposition (upright triangles) NEATM diameters are more similar to the TPM-derived diameters for objects smaller than 8 km while the post-opposition (downward triangles) diameters remain consistently offset from my TPM diameters at smaller sizes. From this result I can conclude that the majority (over 50%) of small diameter asteroids are retrograde rotators — which is in good agreement with my sense of spin results section 2.4.2. Additionally, the results show that the diameter estimates at post-opposition (i.e., observation of the warmer side of a retrograde rotator) are larger for smaller sizes — due to the shifting of the longitude of the maximum surface temperature farther from the sub-solar point (e.g., Spencer et al., 1989).

Thermal Inertias Combined with the results from chapter 1, I have increased the number of asteroids with thermal inertia by 239, an approximate doubling over the tally of literature values (185; Delbo' et al., 2015; Hanuš et al., 2018). This increase is mostly among objects in the 5–50 km size range (figure 2.4). Overall, there is a negative correlation between thermal inertia and diameter, as evidenced by the Spearman's rank coefficient of r_s = -0.26 ($p < .001$). From the findings of Rozitis et al. (2018), however, thermal inertia should be adjusted to account for its dependence on heliocentric distance, caused by temperature changes by using the power-law formula: $\Gamma = \Gamma_0 \cdot R_{\mathrm{AU}}^{\zeta}$. This adjustement partially compensates for the effects of temperature on the thermal inertia, and allows for a better comparison of hot, small NEAs

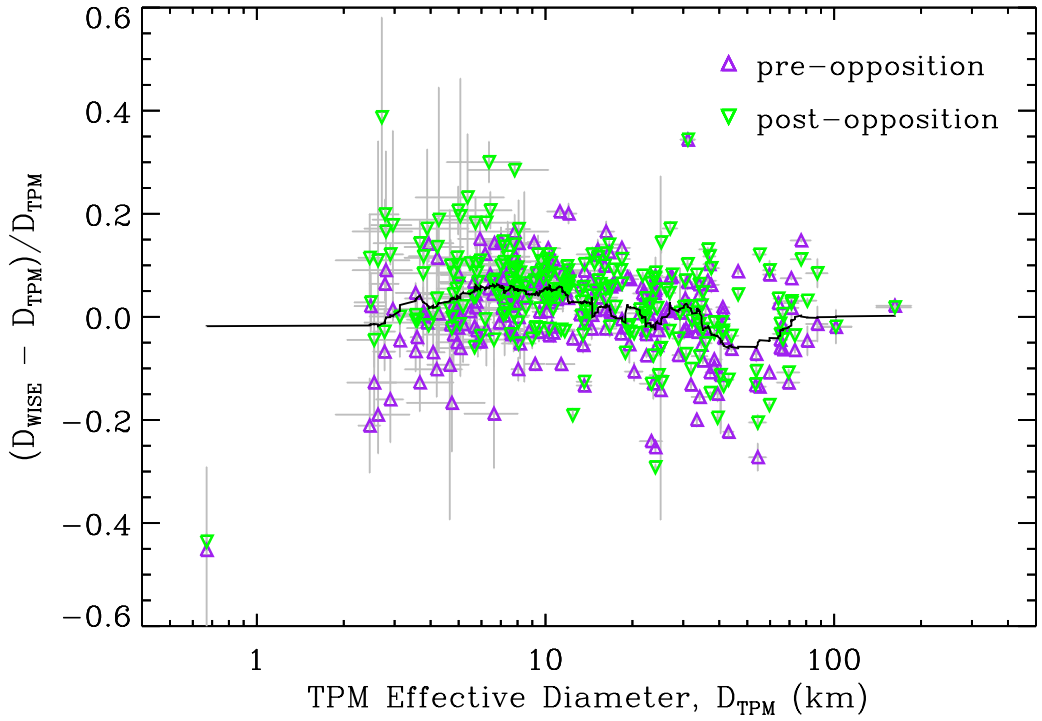

Figure 2.3: Comparison of the effective diameter values obtained by Masiero et al. (2011) and Mainzer et al. (2011b) to my reported TPM values. I plot the difference between the individual pre- and post-opposition diameters of the WISE team and my TPM diameter as a function of the diameter from my TPM. Purple, upward-facing and green, downward-facing triangles are data collected at pre- and post-opposition, respectively, and a running mean of the relative diameter difference is given by the black line.

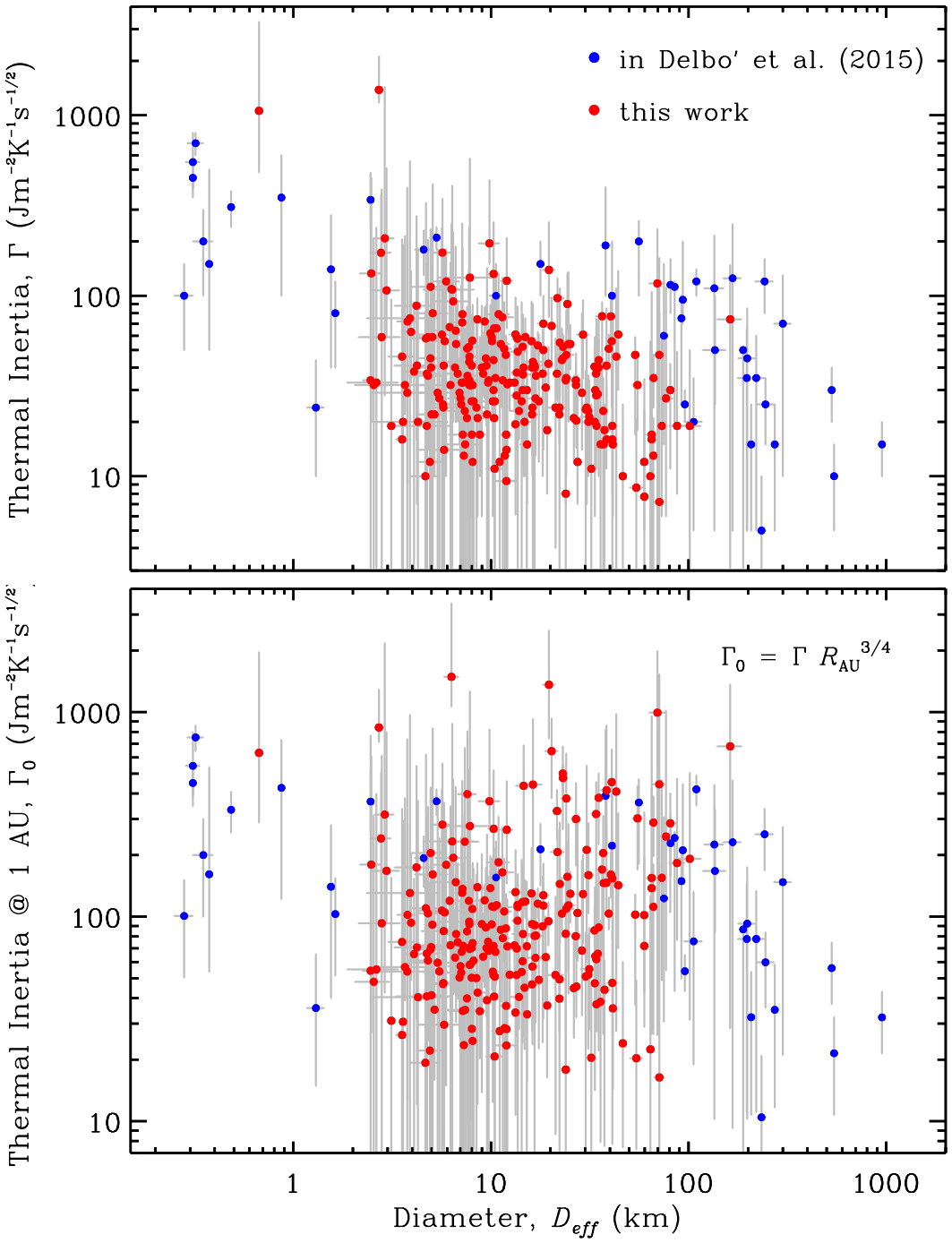

Figure 2.4: Thermal inertia versus object diameter values from this work along with previous estimates. The bottom panel shows the thermal inertias from the top panel scaled at a heliocentric distance of 1 AU, as described in the text and Rozitis et al. (2018).

and cool, larger MBAs. I use $\zeta = 3/4$ here, which was suggested by Delbo' et al. (2015) and Mueller et al. (2010). Performing the adjustment on this larger set if asteroid thermal inertias removes the size correlation, with $r_s = 0.06$ and $p = .32$. This result is different from that of chapter 1, and is most likely caused by the addition of objects in the 3–30 km size range. In the next subsection, I directly model the thermal inertia dependence on temperature, which is more physically appropriate.

2.4 TPM Analysis

2.4.1 Thermal Inertia Dependence on Diameter and Temperature

A forward stepwise multivariate regression model (Draper and Smith, 1998) was implemented on the large dataset of TPM results in an attempt to discern the major factors that control the thermal inertia. Object diameter, rotation period, and color temperature (an approximation of the surface temperature; section 2.5.2) were all transformed into $\log_{10}$ space and used as independent factors in this model. The forward stepwise regression model permits a factor to enter when there the relationship with the dependent variable is statistically-significant (i.e., if $p < .05$). The regression model selected both diameter and temperature (figure 2.5) as necessary explanatory variables, given by:

$$\Gamma = 10^{-2.05 \pm 0.97} - D_{eff}^{0.213 \pm 0.036} + T_c^{1.66 \pm 0.41}. \tag{2.7}$$

The uncertainty of the calculated temperature exponent is consistent with the temperature dependence of thermal conductivity, as detailed in subsection 2.5.2 ($k \propto T^3$), which theoretically predicts $\Gamma \propto T^{3/2}$.

This multivariate regression model does not select rotation period as a statistically significant independent variable, which runs counter to the claim of Harris and Drube (2016), who did not consider the temperature dependence of thermal inertia. Harris and Drube (2016) used an indirect method of thermal inertia determination to investigate its dependence on rotation period and found a strong positive correlation, which they attributed primarily to the increase in thermal skin depth equation (1.6) — indicating that the thermal

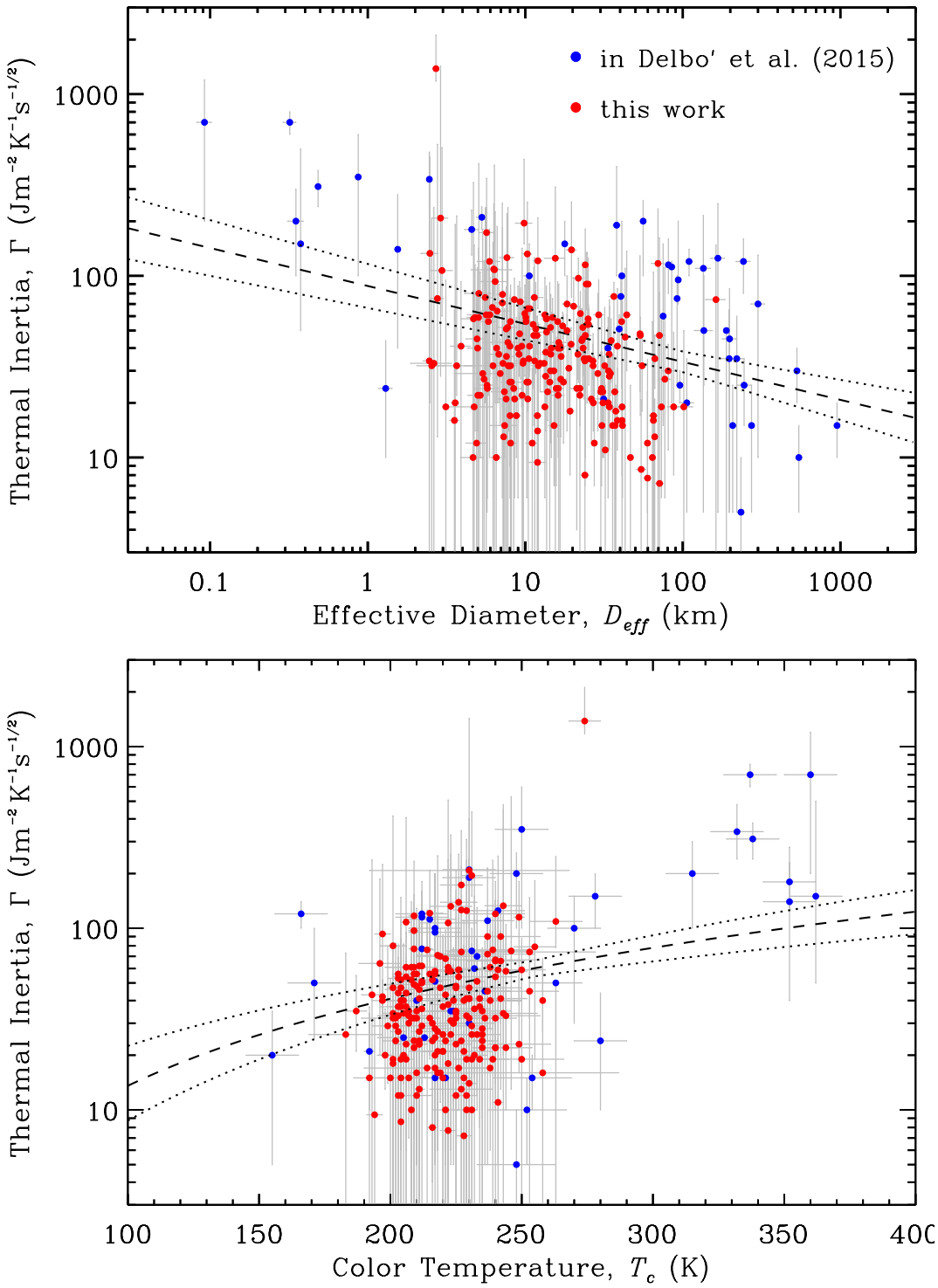

Figure 2.5: Thermal inertia dependence on object diameter and the surface (color) temperature. The black lines show the best-fit multivariate regression model to the data (dashed) and 1σ uncertainty (dotted).

wave penetrates deeper into the subsurface. Following their logic, the correlation between thermal inertia and skin depth ($l_s = \sqrt{kP_{rot}/2\pi\rho c_s}$) was used to indicate an increase in the grain size at greater depths. Even if I ignore my null result for a test of thermal inertia dependence on rotation period, there are a few issues with the logic of Harris and Drube (2016). Firstly, both thermal inertia and thermal skin depth have the exact same square-root thermal conductivity dependence, which is the controlling factor (c.f., heat capacity and density) for asteroid surfaces. Thus I expect that thermal inertia and skin depth should *always* exhibit strong correlations independent of any variation in the subsurface structure of regoliths. Secondly, if grain size, or packing fraction, do indeed increase with depth then it would inherently be very difficult to detect the effects on disk-integrated daytime thermal emission data. The trouble here arises when one realizes that the thermal wave is more heavily influenced by the thermophysical properties of the material closer to the surface (nearest the upper boundary) during daytime hours. If a hypothetical conducting slab of bare rock was overlain with a regolith layer, the daytime temperatures would still be mostly affected by the uppermost layers, since the downward heat flow has not encountered the slab — as if it were non-existent. Once the heat flow reaches this hypothetical slab, most of the thermal energy has already been stored within the overlying regolith, and thermal conductivity increase at depth would not be great enough to recursively influence the daytime surface temperatures. I thus conclude that changes in the thermal inertia seen here, and estimated elsewhere from TPM modeling of disk-integrated thermal emission, are primarily a consequence of the thermophysical properties across the surface and not structural changes from beneath the surface.

2.4.2 Spin Dependency on Size

Based on the TPM results, I observe a correlation between the retrograde/prograde ratio and asteroid size. I bin my objects by diameter in figure 2.6 and assign the uncertainty (shown as vertical lines) of the bins to be the number of objects with undetermined spins in that diameter bin. Horizontal lines that transect some of the spin/diameter bins indicate the number of near-Earth asteroids in that bin. Asteroids in the 16–30 km and $>$ 30 km bins show an excess of prograde spins. The retrograde and prograde numbers are roughly

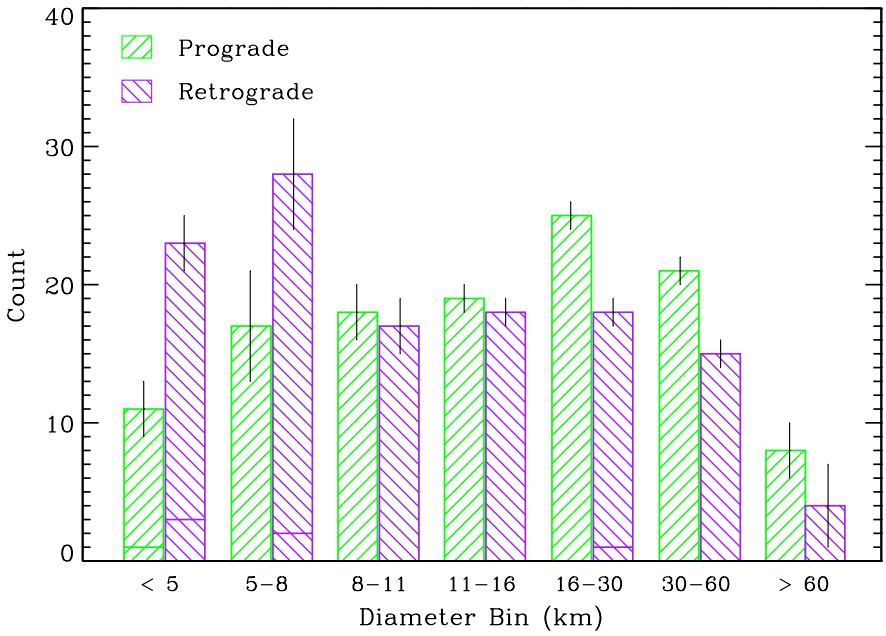

Figure 2.6: Number of prograde and retrograde rotators as a function of diameter bin. Vertical lines indicte the number of objects with indetermined sense of spin within that size range; if there are none I fix the uncertainty to be one.

equal within my sample for diameters between 8 and 16 km and retrograde rotators are more represented at small sizes ($D_{\mathit{eff}} < 8$ km).

My result showing prograde spin excess at larger sizes is generally consistsent with previous findings of spin vector distributions estimated from lightcurve inversion methods (Kryszczynska et al., 2007; Hanuš et al., 2011; Ďurech et al., 2016). However, the precise diameter cutoff at which the excess in prograde rotators disappears is unclear as the latter two in this list both show that the prograde excess exists for asteroids larger than 60 km, and disappears among 30–60 km objects. Here, I show an excess of prograde rotators within the 30–60 km and $>$ 60 km bins — although I have few objects and large spin ambiguity for the $>$ 60 km bin. The prograde excess at larger sizes is likely a remnant of the primordial spins of large protoplanets due to the accretion direction of pebbles into planetesimals, and the nature of momentum conservation (Johansen and Lacerda, 2010). Spina et al. (2004) identified a larger fraction of retrograde rotators among NEAs, and attributed the cause for this to be a dynamical selection effect in which these retrograde main-belt asteroids

more efficiently enter resonances with Jupiter via Yarkovsky orbital drift. My results show an overabundance of retrograde rotators at small sizes inherent in small main-belt objects. This result, if true, removes the need for any selection effect for main-belt asteroids that are transferred to NEA orbits. The question now becomes: what mechanisms are at play in the Main Belt that result in an excess of asteroids spinning in the retrograde sense? Answering this question is beyond the scope of this work, but I suspect that modeling of YORP spin obliquity alteration and the spin states of collisional fragments can be used to investigate this problem.

2.5 Methods: Grain Size Estimation

Using the results of my TPM analysis, I employ a regolith thermal conductivity model devloped by Gundlach and Blum (2013) to estimate a characteristic regolith grain size for each asteroid. This model requires compositional information about each individual asteroid I must infer this knowledge using spectral characteristics, when possible. In the 88 cases where spectral type is not available, however, I infer the composition from the derived albedo. In all cases in which an asteroid belongs to a dynamical family, I cross-check the spectral type with that of the family. I discuss this strategy for inferring composition in section 2.5.1 in the context of meteorite analogs. I wish to best capture the uncertainties in the meteorite material properties and propagate them through the thermal conductivity model, so I employ a Monte Carlo approach for estimating the regolith grain sizes for each object (section 2.5.2).

2.5.1 Asteroid-Meteorite Connections

Establishing a meteorite analog to an asteroid can be most reliably be made for objects for which I have well-characterized spectra. Various taxonomic systems have been defined based on combining albedo information with photometric colors (Tholen, 1984), or absorption features with spectral slopes of Vis-NIR reflectance spectra (DeMeo et al., 2009). Groups within these taxonomies capture a wide range of compositions seen in the meteorite record, although featureless spectra across many meteorite groups introduce ambiguity in

establishing appropriate analogs for featureless asteroid spectra. Band parameter analyses of S-complex spectra can refine the estimated composition and associated meteorite analogs (Reddy et al., 2015, and references therein).

For the asteroids in my sample that possess identifiable and distinct NIR absorption features, I can make specific associations to meteorite sub-types such as the H/L/LL types within the ordinary chondrites. It is not possible to associate an asteroid with a specific meteorite sub-type if only the visible spectrum (or colors) and albedo are known. In these cases, only a broad meteorite association is made using whatever data are available. For example, if an asteroid only has sufficient color or visible wavelength coverage to be broadly defined as S-complex, the full range of the silicate-dominated asteroids, as given in the top line of table 2.6, are used. Visible spectra and color information can be used to distinguish between the S-complex, C-complex, and X-complex. Objects falling within the X-complex are further divided into meteorite analog groups by using my albedo results and the work of Tholen (1984). E-type (from colors; Tholen, 1984) and Xe-type (from Vis/NIR spectra DeMeo et al., 2009) objects have $p_V \gtrsim 0.425$, M-types have $0.12 < p_V < 0.425$, and P-types have $p_V \lesssim 0.12$. The uncertainty in p_V for individual asteroids creates ambiguity along the M- and P-type cutoff criterion. Thus, care is taken to distinguish these objects using a thermal inertia cutoff of $\Gamma \gtrsim 250$ to distinguish M-types from P-types as noted by a the Γ superscript in table 2.7. Many asteroids in my sample have no previous color or spectral information available, and I am left to infer the meteorite analog based on the albedo alone. An albedo cutoff at 0.12 is used to distinguish between high albedo S-types and low-albedo C-types, and albedos above 0.425 are assigned to the E-types. A two panel summary figure of these selection criteria can be found in figure 2.7. It is interesting to note here that the overall trend (across taxonomic groups) is a positive correlation between p_V and G_V. However, within each taxonomic group there is an absence or slight negative relationship between these two variables. Such a scenario is an example of Simpson's statistical paradox[3] (Simpson, 1951; Yule, 1903). I briefly note this paradox here for future works that may investigate the complex relationship between p_V, G_V, and regolith grain-scale size and

[3]This phrase describes a dataset that exhibit correlations across the entire sample that are statistically distinguishable from the within-group correlations.

roughness across different spectral/compositonal groups. The albedo-based classification described here neglects the possibility that M-types and P-types could be misclassified as S-types and C-types, respectively. However, I see no reason to re-assign any of these S-types to the M-type group, as the thermal inertias are consistent with a silicate-dominated material with low thermal conductivity. Although some P-types might be misclassified as C-types, having no currently available spectral information, the difference in assumed material properties that I use is not large and would not alter the reported grain size by more than a few percent. I do however change the classification of (4003) Schumann from C-type to P-type, based on its location in the outer part of the Main Belt ($R_{\rm AU}$ = 3.4 AU) where P-types outnumber C-types (DeMeo and Carry, 2013, 2014).

Table 2.6 shows the different spectral types and associated meteorite analog with the thermophysical and mechanical properties that will be used in the thermal conductivity model: thermal conductivity (k_{grain}), heat capacity (c_s), mass density (ρ_{grain}), Young's modulus, E, and Poisson's ratio, μ. I also distinguish between the low emissivity of metal-rich materials and higher emissivity of silicates and carbonaceous materials. Below I briefly describe how these properties differ for each meteorite analog and analyze data from many sources, when appropriate, to account for temperature and porosity effects.

Conductivity

Thermal conductivity measurements reveal a strong dependence on the porosity, $\emptyset_p$, of the meteorite being studied and the ambient temperature of the laboratory conditions. In their review paper of thermal conductivites, Flynn et al. (2017) note that laboratory measurements of thermal conductivity do not change significantly in the temperature range from 100 and 300 K, but drop off to zero at 0 K. Within a granular material, such as asteroid regolith, void spaces can significantly impede solid-state heat flow between grains and the grain temperatures controls the efficiency of radiative heat transfer within the pore space (section 2.5.2). To account for porosity effects, I estimate the thermal conductivity for zero porosity using data collected at 200 K as measured by other works. A similar analysis was performed by Flynn et al. (2017), but they chose to fit the dataset to $\log(\emptyset_p)$, which becomes meaningless as $\emptyset_p$ approaches zero.

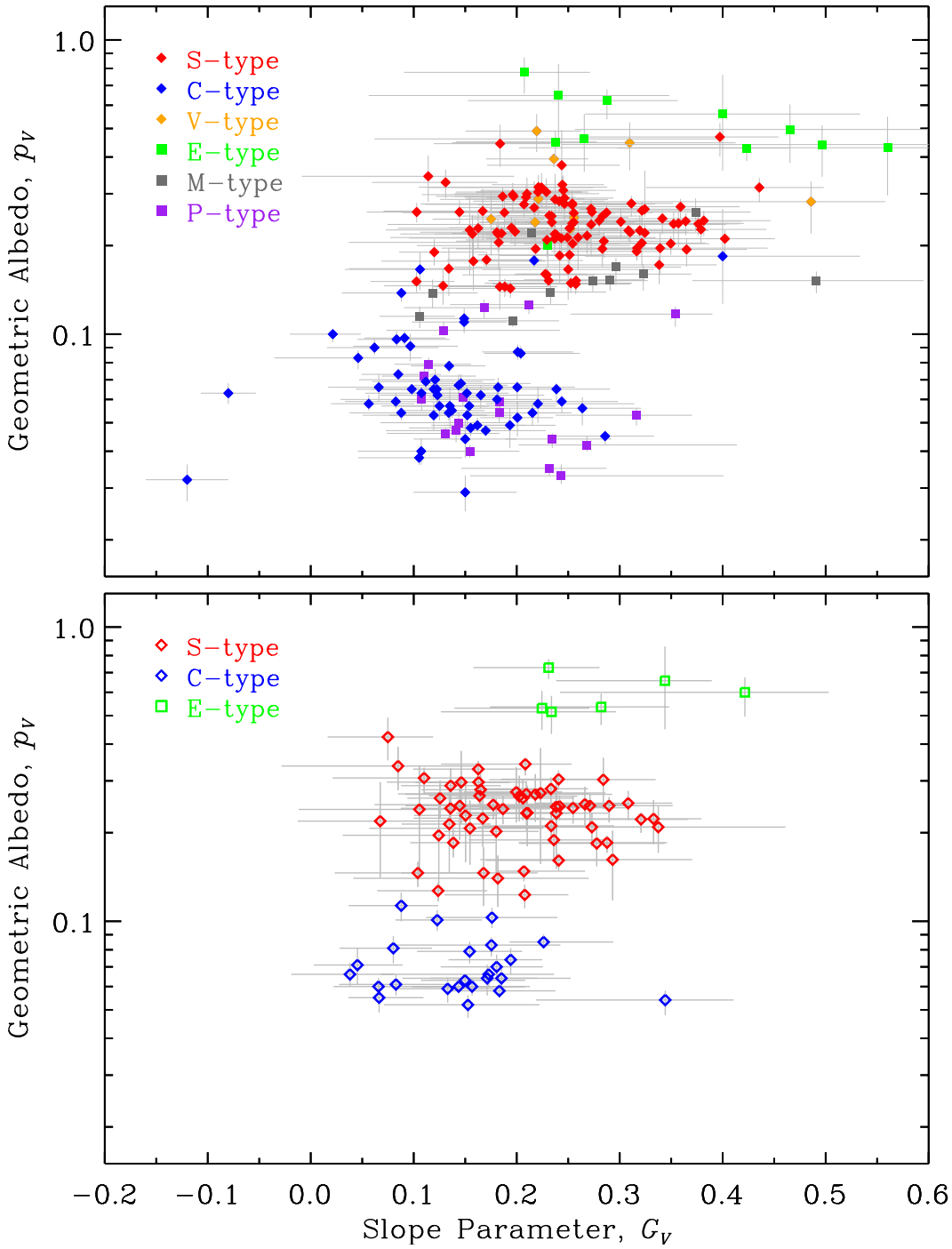

Figure 2.7: Geometric albedos and slope parameters for asteroids in this study. The top panel, consisting only of filled symbols, shows the objects classified on the basis of spectral or color data and family membership, when applicable. The bottom panel, consisiting of open symbols, are the 88 objects classified only on the basis of albedo.

Table 2.4: Meteorite Thermal Conductivity Measurements @ $T_{\rm lab}$ = 200 K

Sample	Group	$\emptyset_p$ [a]	k_{eff} [b]	Source
ALH 77288	H6	2.0	3.53	Yomogida and Matsui (1983)
Arapahoe	L5	2.5	2.31	Yomogida and Matsui (1983)
Bath Furnace 1	L6	4.3	2.26	Opeil et al. (2012)
Bath Furnace 2	L6	4.3	2.72	Opeil et al. (2012)
Bath Furnace 3	L6	4.3	3.15	Opeil et al. (2012)
Bruderheim	L6	8.0	1.03	Yomogida and Matsui (1983)
Farmington	L5	5.5	2.14	Yomogida and Matsui (1983)
Gilgoin Station	H5	5.0	3.60	Yomogida and Matsui (1983)
Gladstone	H5	5.0	2.16	Yomogida and Matsui (1983)
Holbrook 1	L6	10.4	0.45	Opeil et al. (2012)
Holbrook 2	L6	10.4	1.15	Opeil et al. (2012)
Kunashak	L6	5.2	1.86	Yomogida and Matsui (1983)
Leedey,A	L6	10.4	0.40	Yomogida and Matsui (1983)
Leedey,B	L6	10.6	0.47	Yomogida and Matsui (1983)
Los Angeles	Sher*	8.1	0.77	Opeil et al. (2012)
MET 78003	L6	7.8	1.54	Yomogida and Matsui (1983)
Monroe	H4	5.9	2.35	Yomogida and Matsui (1983)
New Concord	L6	9.2	0.78	Yomogida and Matsui (1983)
Pultusk	H5	7.5	1.25	Opeil et al. (2012)
Wellman	H5	6.1	3.85	Yomogida and Matsui (1983)
Y-74156	H4	9.2	1.54	Yomogida and Matsui (1983)
Y-74191	L3	10.3	1.24	Yomogida and Matsui (1983)
Y-74647	H4.5	9.1	1.15	Yomogida and Matsui (1983)
Y-75097	L4	10.3	0.97	Yomogida and Matsui (1983)
Abee	EH6	3.0	5.33	Opeil et al. (2010)
Pillistfer	EL6	2.4	5.51	Opeil et al. (2012)
Campo del Cielo	IAB	1.2	22.4	Opeil et al. (2010)

Notes. *Shergottite meteorite group (Martian origin).
[a]Sample porosity, given in percent.
[b]Effective thermal conductivity, given in W m^{-1} K^{-1}.

In order to estimate thermal conductivity at $\phi_p = 0$, lines are fit to meteorite samples with porosities less than 12% from the literature (table 2.4), as shown in figure 2.8. Since the carbonaceous chondrites with measured k_{eff} had porosities exceeding this cutoff, I did not use any for my analysis. I found that enstatite chondrites have a larger thermal conductivity than the ordinary chondrite samples (and one Shergottite), likely due to the small amounts of metal contained within them. The y-intercept of the best-fit lines give the thermal conductivity at zero porosity of 4.05 ± 0.35 and 6.23 for ordinary chondrites and enstatite chondrites, respectively. Opeil et al. (2012) showed that the thermal conductivities of ordinary and carbonaceous chondrites greatly overlap; thus I assume the same thermal conductivity at zero porosity for both groups. I used the same line slope to extrapolate a single measurement of thermal conductivity (Opeil et al., 2010) of the iron-nickel meteorite Campo del Cielo to estimate the y-intercept. These calculated thermal conductivities at zero-porosity are used in the thermal conductivity model to compute grain size.

Heat Capacity

The ability of material to store thermal energy per unit mass is quantified by its specific heat capacity, c_s. Heat capacity is quantified by the amount of energy required to cause a temperature change of 1 K, per unit mass, when heated or cooled — without undergoing a phase change. Laboratory heat capacity measurements of meteorites reveal a non-negligible dependence on temperature (Beech et al., 2009; Opeil et al., 2012; Szurgot et al., 2012; Consolmagno et al., 2013; Wach et al., 2013). I account for this dependency by performing an analysis, similar to the one performed for thermal conductivity, in which I use literature data on meteorite heat capacities measured at various ambient temperatures (shown in table 2.5). I find that two groups with distinct trends emerge: a group with all the iron-nickel meteorites, and a non-metallic group, comprised of all chondritic and achondritic meteorites (figure 2.8). Flynn et al. (2017) use similar data, but present fits for temperatures of 75–200 K which does not cover the full range of asteroid surface at temperatures relevant to my sample of asteroids. Thus I compute the fits to this dataset for a temperature range of 175 to 300 K and with a y-intercept fixed at zero. The best-fit heat capacity equations (and coefficient uncertainties) for non-metallic and metallic meteorites at different temperatures are given

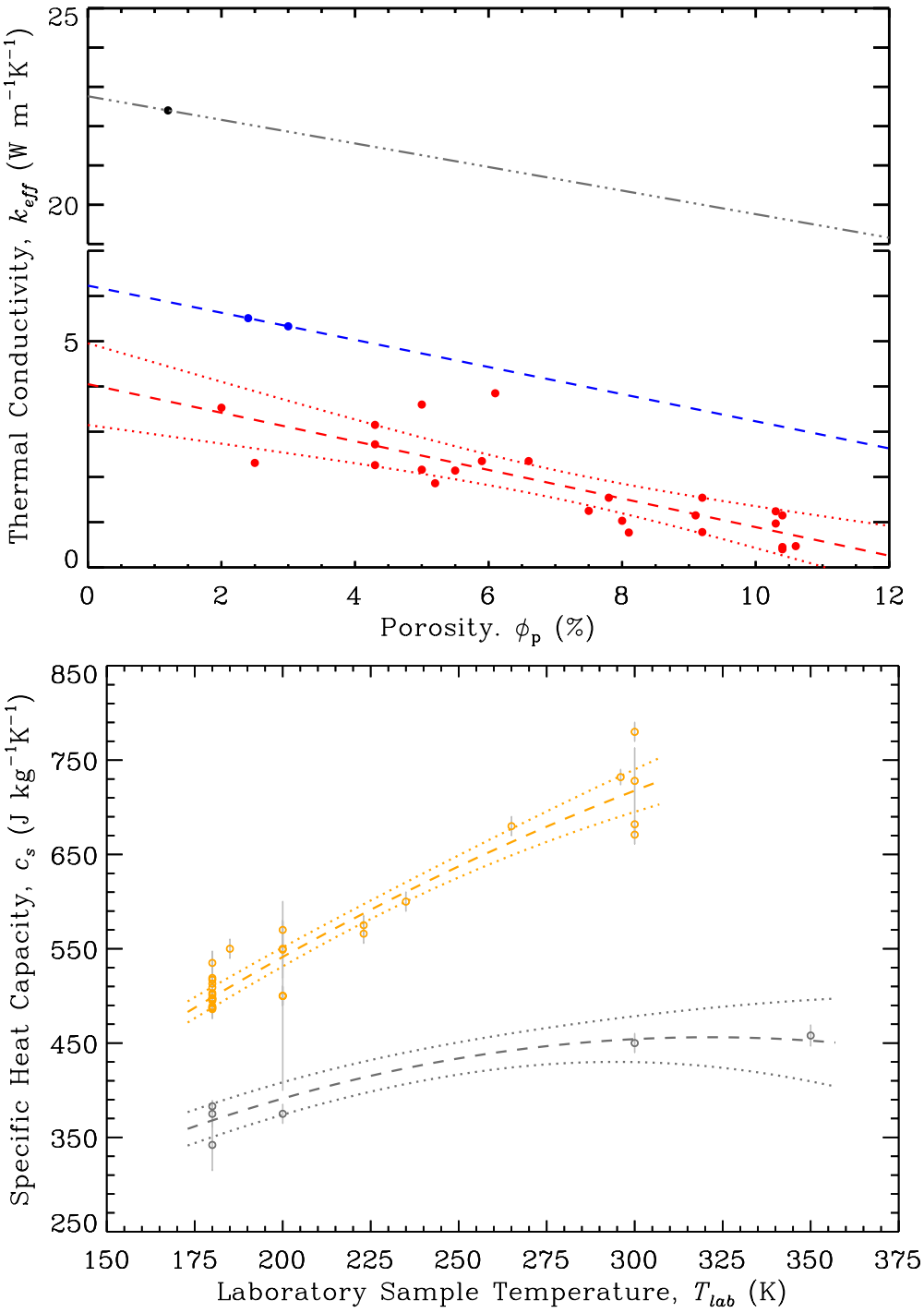

Figure 2.8: Meteorite thermal conductivity as a function of porosity (top) and specific heat capacity as a function of temperature (bottom). Dashed lines show linear fits in the top panel, and parabola fits through the origin in the bottom panel, with dotted lines representing 95% confidence intervals. The dashed-dotted line through the Campo del Cielo datum assumes a slope of 0.3.

by c_s = -0.0031 ($\pm$ 0.0004)$\times T^2$ + 3.34 ($\pm$ 0.10)$\times T$ and c_s = -0.0044 ($\pm$ 0.0004)$\times T^2$ + 2.84 ($\pm$ 0.11)$\times T$, respectively.

Mechanical Properties

Young's modulus (E) and Poisson's ratio (μ) are used in the thermal conductivity model to calculate the contact area between grains within a regolith. In particular, these two quantities are used to describe the tendancy for certain materials to become deformed along the axis of an applied force and the amount of longitudinal deformation of the material, respectively. For M-type asteroids, I use the values of these properties measured for iron-nickel alloys, which are similar to iron meteorites, by Ledbetter and Reed (1973). Ibrahim (2012) reports Young's and Bulk Modulus (G) for many ordinary and carbonaceous chondrite meteorites. I calculate Poisson's Ratio using the relationship between the three variables: $\mu = \frac{E}{2G} - 1$. This equation assumes an isotropic material and it also used to propagate the reported uncertainties presented in Ibrahim (2012). The values for E-types are assumed to be that of S-types, as indicated by italics in table 2.6.

Density and Porosity

Meteorite specimens, while not regolith, still contain small pores that affect the bulk density of an un-ground sample (e.g., Cadenhead and Stetter, 1975). Typical meteorite porosities, $\emptyset_p$, range from 4% to 10%, but can be as high as 20% for weathered finds and low as 2% for iron meteorites. The density of individual grains, or grain density (ρ_{grain}), is the relevant density for input to the thermal conductivity model as it avoids the effect of porosity. I primarily use grain density data collected by Macke (2010), who measured the porosities of individual meteorites with various compositions and computed the grain densities. Table 2.6 lists grain densities for many specific meteorite sub-types (e.g., H chondrite), which are used for asteroids that I can tie to a specific meterorite analog. But, as mentioned in section 2.5.1, specific meteorite sub-type connections can't be made for an S-type asteroid if only the visible spectrum (or colors) or albedo is known. In this scenario, I assume the full range of grain densities across all sub-types for the object (i.e., a uniform distribution of ρ_{grain} is used instead of a normal distribution) as input to the thermal conductivity model.

Table 2.5: Meteorite Heat Capacity Measurements at Different Ambient Temperatures

Sample	Group	T_{lab} (K)	c_s (J kg^{-1} K^{-1})	Source
Allende	CV	180	501 ± 21	Consolmagno et al. (2013)
Bilanga	Di.	180	509 ± 26	Consolmagno et al. (2013)
Bori	L6	180	495 ± 8	Consolmagno et al. (2013)
Cumberland	Aub.†	180	513 ± 14	Consolmagno et al. (2013)
Hedjaz	L3.7-6	180	488 ± 12	Consolmagno et al. (2013)
Holbrook	L6	180	486 ± 9	Consolmagno et al. (2013)
Ness Country	L6	180	517 ± 6	Consolmagno et al. (2013)
NWA 2086	CV	180	519 ± 28	Consolmagno et al. (2013)
NWA 4293	H6	180	498 ± 7	Consolmagno et al. (2013)
Ornans	CO	180	497 ± 7	Consolmagno et al. (2013)
Pipe Creek	H6	180	489 ± 10	Consolmagno et al. (2013)
Pultusk	H5	180	496 ± 8	Consolmagno et al. (2013)
Renazzo	CR	180	535 ± 12	Consolmagno et al. (2013)
Thuathe	H4-5	180	487 ± 9	Consolmagno et al. (2013)
Warrenton	CO	180	503 ± 16	Consolmagno et al. (2013)
Gao-Guenie	H5	296	732 ± 8	Beech et al. (2009)
Soltmany	L6	200	549 ± 30	Szurgot et al. (2012)
Soltmany	L6	300	728 ± 35	Szurgot et al. (2012)
Los Angeles	Sher.⋆	185	550 ± 10	Opeil et al. (2012)
Los Angeles	Sher.⋆	300	780 ± 10	Opeil et al. (2012)
Los Angeles	Sher.⋆	235	600 ± 10	Opeil et al. (2012)
Los Angeles	Sher.⋆	265	680 ± 10	Opeil et al. (2012)
Soltmany	L6	223	575 ± 10	Wach et al. (2013)
Soltmany	L6	300	671 ± 10	Wach et al. (2013)
NWA 4560	LL3.2	223	566 ± 10	Wach et al. (2013)
NWA 4560	LL3.2	300	682 ± 10	Wach et al. (2013)
Cronstad	H5	200	550 ± 10	Yomogida and Matsui (1983)
Abee	E4	200	500 ± 10	Yomogida and Matsui (1983)
Cold Bokkeveld	CM2	200	500 ± 100	Yomogida and Matsui (1983)
Lumpkin	L6	200	570 ± 10	Yomogida and Matsui (1983)
NWA 5515	CK4	200	500 ± 10	Yomogida and Matsui (1983)
Campo del Cielo	IAB	200	375 ± 10	Opeil et al. (2010)
Campo del Cielo	IAB	300	450 ± 10	Opeil et al. (2010)
Auggustinovka	IIIAB	180	375 ± 13	Consolmagno et al. (2013)
Pirapora	IIIAB	180	342 ± 27	Consolmagno et al. (2013)
Sikhote-Alin	Fe IIAB	350	458 ± 11	Beech et al. (2009)
Estherville	Meso‡	180	383 ± 6	Consolmagno et al. (2013)

Notes. ⋆Shergottite meteorite group (Martian origin).
†Aubrite meteorite group.
‡Mesosiderite meteorite group.

Table 2.6: Material Properties of Meteorite Groups

Spectral Type	Meteorite Analog(s)	k_{grain}	ρ_{grain} (kg m^{-3})	c_s [a]	ϵ_g	E (GPa)	μ [b]
S-complex		4.05 ± 0.35	3180–3710	-0.0033×T^2 + 3.39×T	0.9	28.8 ± 2.4[i]	0.23 ± 0.04[c]
S-type	H chondrite	" "	3710 ± 10[m]	" "	" "	" "	" "
	L chondrite	" "	3580 ± 10[m]	" "	" "	" "	" "
	LL chondrite	" "	3520 ± 10[m]	" "	" "	" "	" "
V-type		" "	3180–3440	" "	" "	" "	" "
	Howardite	" "	3260 ± 20[m]	" "	" "	" "	" "
	Eucrite	" "	3190 ± 10[m]	" "	" "	" "	" "
	Diogenite	" "	3430 ± 10[m]	" "	" "	" "	" "
X-complex							
E/Xe-type	EH/EL chondrite	4.76 + ^{287}/T	3635 ± 35[m]	-0.0033×T^2 + 3.39×T	0.9	*28.8 ± 2.4*	*0.23 ± 0.04*[c]
M-type	FeNi metal-rich	12.4 + 0.05×T	7500 ± 200[c]	-0.0042×T^2 + 2.77×T	0.66	169–209[l]	0.27–0.37[l]
P-type	CI/CM chondrite	0.26 + 0.0013×T	2690 ± 40[m]	-0.0033×T^2 + 3.39×T	0.9	18.9 ± 3.7[i]	0.14 ± 0.06[d]
C-complex	carb. chondrite	4.05 ± 0.35	3520 ± 130[m]	-0.0033×T^2 + 3.39×T	0.9	18.9 ± 3.7[i]	0.14 ± 0.06[c]

Notes. [a]Heat capacity, calculated using the polynomial fits shown in figure 2.8, in units of J kg^{-1} K^{-1}.

[b]Poisson's ratio.

[c]Average using data from: Consolmagno et al. (2008); Opeil et al. (2010); Szurgot et al. (2012).

[d]Calculated from E and G values presented in Ibrahim (2012).

[f]Flynn et al. (2017)

[i]Ibrahim (2012)

[l]Ledbetter and Reed (1973)

[m]Macke (2010)

2.5.2 Regolith Thermal Conductivity Model

Thermal inertia can be used as a first-order estimate for different asteroid regolith grain sizes. In general, low thermal inertia ($\Gamma < 100$ J m^{-2}K^{-1}s$^{-1/2}$) indicates a fine-grained (lunar-like) regolith and $\Gamma > 2500$ J m^{-2}K^{-1}s$^{-1/2}$ represents a bare rock surface or one that is nearly void of fine grained regolith (Jakosky, 1986). A few recent works have developed more sophisticated, quantitative relationships between Γ and grain size, by modeling k_{eff} within a granular material. Since, for planetary regoliths, Γ is influenced mostly by changes in thermal conductivity (Presley, 2010; Presley and Christansen, 2010), a few experiments have empirically studied the effect of particle size on k_{eff} (Presley and Christansen, 1997; Presley and Craddock, 2006). Generally speaking, k_{eff} has a solid-state component that describes heat conduction through grains and across grain contacts, and a radiative component that describes heat radiated within pore spaces (e.g., Piqueux and Christensen, 2009):

$$k_{eff} = k_{solid} + k_{rad} = k_1 + k_2 T^3. \tag{2.8}$$

The k_1 and k_2 coefficients in equation (2.8) are dependent on the material properties of the regolith, such as grain size, packing fraction, and amount of contact between the grains (Watson, 1964). If these coefficients are accurately approximated, then measurements of Γ (combined with the compositional information about the asteroid, as discussed in the previous subsection) can be used to estimate the grain size for an asteroid.

Most recently, Gundlach and Blum (2013) presented a simple, yet physically realistic, technique for deriving regolith grain sizes for asteroids from measured Γ values. Their approach includes acquired laboratory measurements of regolith (Chan and Tien, 1973; Gundlach and Blum, 2012) and uses lunar regolith samples as a calibration tool for estimating coefficients within a semi-empirical model. Gundlach and Blum (2013) present an equation for k_{eff} that is similar in form to the rightmost side of equation (2.8), but includes more explicitly defined k_1 and k_2 coefficients (equation (2.9) and equation (2.10), below). I employ their procedure, detailed here, in a Monte Carlo approach in order to reasonably estimate an average grain radius (r_g) for the objects in my asteroid thermal inertia dataset.

The solid thermal conductivity component, k_{solid}, is modeled by Gundlach and Blum (2013) by computing the efficiency of heat transfer within a network of particles, via the

contacts between them:

$$k_1 = k_{grain}\left[\frac{9\pi}{4}\frac{1-\mu^2}{E}\frac{\xi(T)}{r_g}\right]^{1/3}(f_1\ exp([f_2\psi]))\ \Xi. \tag{2.9}$$

k_{grain} is the thermal conductivity of a grain of the material having zero porosity, μ is Poisson's ratio, E is Young's Modulus, $\xi(T) = T \cdot 6.67 \times 10^5$ J m^{-2} is the specific surface energy of each grain — a measure for the adhesive bonding strength between grains. The empirically-derived constants $f_1 = (5.18 \pm 3.45) \times 10^2$ and $f_2 = 5.26 \pm 0.94$ encapsulate information about the path of regolith contact chains (Gundlach and Blum, 2012). The factors contained within brackets in equation (2.9) simulate adhesive forces between regolith grains, which dominate over gravity on small bodies, to estimate the contact area between them. Gundlach and Blum (2013) use Apollo 11 & 12 heat conductivity measurements and grain size as a calibrator to estimate $\Xi = 0.41 \pm 0.02$, which incorporates and accounts for the irregular shapes of the particles and heterogeneity of regolith on the whole.

The radiative thermal conductivity (k_{rad}) coefficient is calculated by Gundlach and Blum (2013) to be:

$$k_2 = 8\sigma_0\epsilon\left[e_1\frac{1-\psi}{\psi}r_g\right], \tag{2.10}$$

with the empirical coefficient $e_1 = 1.34 \pm 0.01$ (Dullien, 1979; Gundlach and Blum, 2012). The bracketed term in equation (2.10) represents the mean free path of a photon, which is dependent on the volume filling factor, $\psi = 1 - \phi_p$ and directly proportional to the grain size. Given values of c_s, ρ_{grain} and Γ for each object, an estimate of the thermal conductivity, k_{eff}^{obs}, is made. Assuming some value for the regolith porosity, this observed thermal conductivity is equated to the modeled thermal conductivity in order to obtain an estimated regolith grain size. As discussed in section 2.5.3, this quantity should not be thought of as the average of a regolith comprised of grains of varying sizes, but rather a *thermally-characteristic* grain size. In fact, Presley and Craddock (2006) modeled the thermal conductivity of known granular mixtures and deduced that the modeled grain size is most representative of the larger regolith grains (larger than 85% – 95%), rather than the mean or modal grain size.

Temperature Estimation The temperature of the asteroid regolith at the time of observation(s) is another important input to the thermal conductivity model. Calculating a single value for the characteristic surface temperature of an asteroid, which exhibits wide temperature variations across the surface, can be approached in a few different ways. One approach is to rely on the estimation of the sub-solar temperature, based on the theoretical energy balance formulation (equation (1.1)). This approach has two problems: the assumptions made in the energy balance equation will often lead to the overestimation of the true sub-solar temperature, and there is a low likelihood that the sub-observer point is close to the sub-solar point.

In order to overcome these possible problems I calculate the color temperature, T_c, by independently fitting (via least-squares minimization) a blackbody curve to the asteroid's thermal fluxes in W3 and W4. Using the temperature of the best-fit blackbody curve bypasses any issues related to model theory and partially implicitly accounts for the spatial variation in surface temperatures. The blackbody assumption of $\varepsilon = 1$ does not introduce uncertainty in the temperature, as any non-zero value would not shift the peak of a blackbody emission curve, which is related to the temperature through Wein's Law. Fitting a blackbody function to my WISE dataset is straightforward, but retroactively applying this approach to thermal inertias found in the literature is difficult. To estimate T_c for asteroids with previous reported value of thermal inertia, I calculate the relationship between the NEATM sub-solar temperature T_{ss} and T_c for my set of asteroids: $T_{ss} = 0.777 \times T_c^{1.063(\pm 0.005)}$. This best-fit equation is depicted in figure 2.9 by the dotted red line and blue dot-dash lines showing the 1σ uncertainty bounds in the exponent. This relationship is inverted and used on TPM results from previous works, since it is seldom that this quantity is reported alongside the thermal inertia. For these objects section 2.5.2 is used, assuming $\eta = 1.1$ (the approximate mean for main-belt objects Mainzer et al., 2011b), to compute T_{ss} and subsequently T_c:

$$T_{ss} = \left[\frac{S_\odot(1-A)}{\eta \varepsilon_B \sigma_0 R_{\mathrm{AU}}^2}\right]^4. \tag{2.11}$$

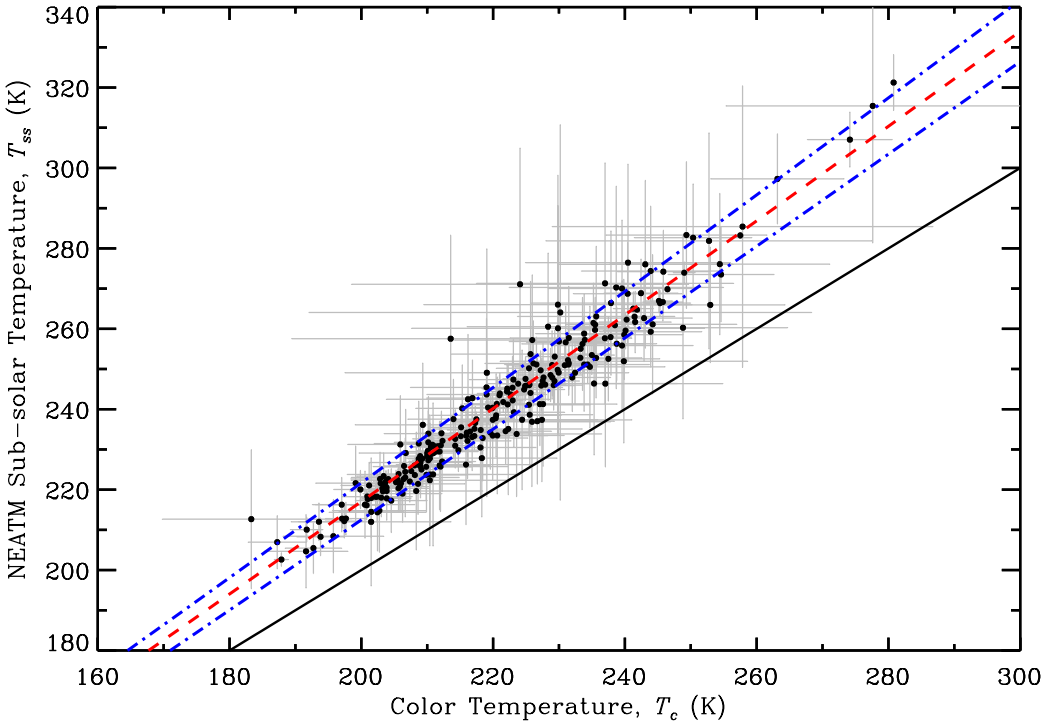

Figure 2.9: NEATM T_{ss} as a function of color temperature, fit by the red dashed line (equation given in the text) with the blue dash-dot lines showing the 1σ uncertainty in the fit parameters. The black solid line shows the identity function.

Monte Carlo Implementation For each object, the thermal conductivity model is implemented 1,000,000 times in a Monte Carlo approach, to appropriately account for both the uncertainties in the input parameters and model assumptions. Each input/model variable is taken from a random distribution that is generated based on the uncertainty of the parameter given in table 2.6 and mentioned in the above text. Most parameters have associated 1σ uncertainties from which I generate Gaussian probability distributions, except a uniform random distribution from 0.276 to 0.876 is used for the porosity[4] and a few select input variables that appear as a range in table 2.6 (e.g., S-type ρ_{grain}). For each iteration, a single grain size is produced, ultimately constructing a distributed set of 1,000,000 grain sizes. This output distribution does not necessarily, or typically, represent a normal distribution of output grains sizes. Thus, I report the median of this distribution as the best-fit grain size, and report (asymmetric) uncertainties based off of the grain sizes that encompass one standard deviation from the median value. Since it is necessary to compute the thermal conductivity within the model, the thermal skin depth (l_s) is also computed for each iteration and the median and standard deviation, as similarly done for grain size, is extracted from the output distribution. An example output distribution of r_g and l_s are shown in figure 2.10 for a hypothetical S-type asteroid with $\Gamma = 150 \pm 50$ J m^{-2}K^{-1}s$^{-1/2}$, $T_c = 300 \pm 10$ K, and $P_{rot} = 10$ hr.

2.5.3 Data and Model Limitations

Before discussing my results, I highlight here some of the implicit limitations of the data and modeling approaches that must be considered when interpreting and using the grain sizes and thermal inertias reported below. Since the flux of thermally emitted photons is strongly temperature dependent ($\propto T^4$), the fluxes modeled here in the thermal infrared heavily represent the warmest portions of the surface with little contribution from cooler portions. Thus, the grain size estimates are biased toward the hotter areas of the surface (on average, the sunlit equatorial region of an asteroid) and less representative of cooler areas (on average, the polar regions) of an asteroid.

[4]The lower value is the porosity of close-hexagonal packing scheme and the upper value represents the hypothesized porosity of cometary regolith.

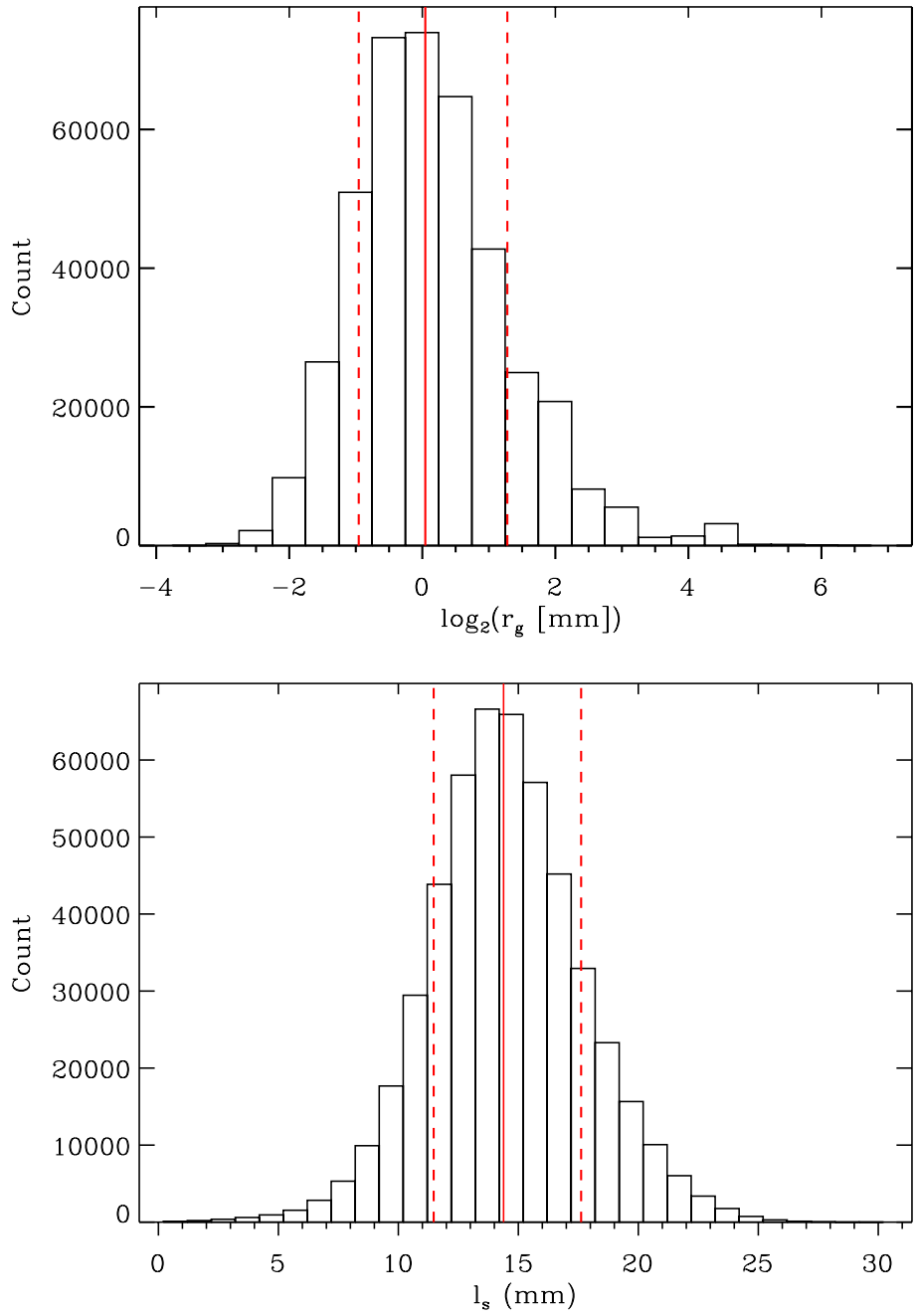

Figure 2.10: Example output of the Monte Carlo thermal conductivity model. Model output is shown for a hypothetical S-type asteroid with $\Gamma = 150 \pm 50$ J m^{-2}K^{-1}s$^{-1/2}$, $T_c = 300 \pm 10$ K, and $P_{rot} = 10$ hr. The red verticle lines show the mean (solid) and 1σ range (dashed) for the grain size (top) and skin depth (bottom).

For many asteroids in my sample it is likely that the material properties indirectly inferred from spectroscopy, color, or albedo data are incorrect. For example, the assumption that an asteroid is a metallic M-type, when it is actually comprised of silicate S-type material would prove to be a cause for concern. To understand how this could potentially shift the grain size estimate for such an object I re-ran my thermal conductivity model for (22) Kalliope, which is spectrally classified as an M-type, however may resemble a silicate-rich body instead of having a metal-dominated surface. Switching the classification to an S-type increased the grain size by a factor of ∼8%, which is far below the typical $d_{g\phi}$ uncertainty reported for most asteroids in section 2.6. I can reasonably assume that uncertainty in the assumed material properties do not significantly contribute to any systematic bias in grain sizes.

Both the thermal conductivity model (Gundlach and Blum, 2013) and my TPM assume constant thermophysical properties throughout the subsurface (down to $\sim 3l_s$) and a regolith consisting of a single grain size. This assumption is certainly not the case for *any* asteroid. Many spacecraft missions have revealed surfaces that are heterogeneous and display processes that sort grain sizes both vertically and spatially. Yet, since telescopic observations do not provide spatially resolved images of my targets, my TPM implementation cannot properly constrain the thermophysical properties of a surface in which thermal inertia and albedo are not constant. Overall, most asteroid regoliths are expected to be heterogeneous, and the assumption of a single grain size and homogeneous regolith is an oversimplification. The series of experiments performed by Presley and Craddock (2006) showed that grain sizes derived from thermal inertia measurements are close to the actual maximum grain size, rather than a mean, median, or modal of the grain size distribution.

Additionally, some individual regolith grains may become fused together in a glassy matrix to form an agglutinate particle (Hörz and Schaal, 1981). Agglutination would result in raising the overall grain size estimate. Although agglutinate formation is common on the Moon (Noble et al., 2005), micrometeoroid impacts on asteroid surfaces are less likely to produce the heat required to produce an extensive agglutinate sample in asteroid regoliths (Noble et al., 2010). In fact, petrographic studies of regolith breccias indicate that agglutinates are not common on asteroid surfaces (Bischoff et al., 2006). In summary, these grain sizes from the thermal inertia and the thermal conductivity model might not represent

a strictly average or median grain size, but rather a thermally-relevant grain size that can effectively be utilized to compare regolith trends across and within asteroid populations, despite the high probability that asteroid regoliths exhibit grain sizes spanning many orders of magnitude.

2.6 Grain Size Modeling Results

I report modeled estimates of grain size and thermal skin depth in table 2.7, along with the model input parameters (with associated uncertainties) for each object — Γ, T_c and spectral type. Grain sizes are transformed into $d_{g\phi}$, which is a $\log_2$ scale developed by Krumbein and Aberdeen (1937) to compare sediment sizes across many orders of magnitude. The output grain size from the Gundlach and Blum (2013) model, $d_g = 2r_g$, is transformed into this scale with:

$$d_{g\phi} = -2 \log_2(d_g[\text{mm}]). \tag{2.12}$$

By using the Krumbien Scale in this case, the 1σ uncertainty estimates in the grain size can be reported with one number, as the probability distribution of output grain sizes is approximately symmetric in $\log_2$ space (figure 2.10). The 44 objects at the top of the table, before the double line break, are objects with previously determined Γ from the compilation in Delbo' et al. (2015).

2.6.1 Notes on Individual Objects

Three objects in this study have estimated grain sizes which are $\sim$3 times greater than the thermal skin depth. Since the thermal skin depth represents a characteristic depth at which thermophysical properties can be ascertained, the grain sizes calculated for these objects actually give a lower limit for $d_{g\phi}$.

(3554) Amun Discovered in 1986, (3554) Amun is in the Aten orbital group of near-Earth asteroids (and a Venus-crosser) and has an estimated size of $D_{\mathit{eff}} = 2.71 \pm 0.02$ km. Its rotation period of 2.53 hr places it close to the theoretical spin barrier limit, and near-infrared reflectance observations show a red and featureless spectrum yielding an ambiguous

Table 2.7: Grain Size Model Inputs and Results

Object	Γ[a]	T_c (K)	Spec.	$d_{g\phi}$	l_s (mm)	Family
(1) Ceres	15^{+5}_{-5}	254 ± 15	C[s]	$2.3^{+1.9}_{-2.3}$	$6.0^{+1.3}_{-1.2}$	
(2) Pallas	10^{+5}_{-5}	252 ± 15	C[s]	$2.1^{+2.0}_{-2.3}$	$4.5^{+1.3}_{-1.4}$	
(3) Juno	5^{+5}_{-4}	248 ± 15	S[s]	$2.3^{+1.9}_{-2.2}$	$3.4^{+1.3}_{-1.4}$	
(4) Vesta	30^{+10}_{-10}	230 ± 10	V[s]	$2.2^{+0.8}_{-1.4}$	$7.1^{+1.6}_{-1.4}$	
(16) Psyche	120^{+40}_{-40}	212 ± 10	M[p,s]	$-2.0^{+1.1}_{-1.0}$	$9.4^{+2.1}_{-1.9}$	
(21) Lutetia	25^{+5}_{-5}	205 ± 10	M[p,s]	$0.5^{+1.8}_{-2.4}$	$6.0^{+1.1}_{-0.8}$	
(22) Kalliope	125^{+125}_{-120}	241 ± 10	M[p,s]	$-2.7^{+1.8}_{-1.4}$	$9.4^{+3.9}_{-4.2}$	
(32) Pomona	112^{+8}_{-92}	215 ± 10	L[b,s]	$-0.9^{+1.6}_{-0.9}$	10^{+3}_{-4}	
(41) Daphne	< 50[u]	263 ± 10	C[s]	$2.5^{+1.1}_{-1.8}$	$6.1^{+2.0}_{-2.7}$	
(44) Nysa	115^{+45}_{-35}	212 ± 10	E[p,s]	$-2.2^{+1.2}_{-1.0}$	15^{+3}_{-3}	Nysa-Polana
(45) Eugenia	45^{+40}_{-40}	236 ± 10	C[s]	$0.2^{+1.7}_{-1.3}$	$8.6^{+3.4}_{-3.7}$	
(65) Cybele	15^{+10}_{-10}	217 ± 10	P[p,s]	$2.8^{+1.3}_{-1.2}$	$6.5^{+2.2}_{-2.5}$	
(87) Sylvia	70^{+60}_{-60}	233 ± 10	P[p,s]	$-1.3^{+1.9}_{-1.5}$	13^{+5}_{-5}	Sylvia
(107) Camilla	25^{+10}_{-10}	213 ± 10	P[p,s]	$1.9^{+1.2}_{-1.0}$	$7.6^{+1.8}_{-1.8}$	
(110) Lydia	95^{+105}_{-25}	217 ± 10	M[p,s]	$-2.8^{+1.6}_{-1.3}$	17^{+5}_{-4}	Padua
(115) Thyra	75^{+25}_{-50}	231 ± 10	S[s]	$-0.1^{+1.4}_{-1.1}$	11^{+3}_{-4}	
(121) Hermione	35^{+25}_{-30}	224 ± 10	C[s]	$0.9^{+1.5}_{-1.2}$	$7.4^{+2.8}_{-3.2}$	
(130) Elektra	35^{+30}_{-30}	223 ± 10	C[s]	$0.6^{+1.5}_{-1.2}$	$7.5^{+2.9}_{-3.2}$	
(277) Elvira	190^{+210}_{-90}	230 ± 10	H[c,f]	$-4.2^{+1.9}_{-1.5}$	46^{+15}_{-14}	Koronis
(283) Emma	110^{+105}_{-105}	237 ± 10	P[p,s]	$-2.5^{+2.2}_{-1.6}$	18^{+7}_{-8}	Emma
(306) Unitas	200^{+60}_{-100}	248 ± 10	C[s]	$-2.6^{+1.5}_{-1.1}$	20^{+5}_{-6}	
(382) Dodona	60^{+90}_{-45}	232 ± 10	M[p,s]	$-1.7^{+1.7}_{-1.4}$	$7.8^{+3.1}_{-3.2}$	
(433) Eros	150^{+50}_{-50}	278 ± 10	LL[s,b]	$-1.4^{+1.1}_{-1.0}$	14^{+3}_{-3}	
(532) Herculina	15^{+10}_{-10}	221 ± 10	L/H[s,b]	$2.3^{+1.5}_{-2.3}$	$6.5^{+2.2}_{-2.5}$	
(617) Patroclus	20^{+15}_{-15}	155 ± 10	P[c,p]	$0.1^{+1.6}_{-1.3}$	$7.4^{+2.7}_{-3.0}$[e]	
(694) Ekard	120^{+20}_{-20}	166 ± 10	C[c,p]	$-3.4^{+0.7}_{-0.7}$	17^{+3}_{-2}	
(720) Bohlinia	100^{+100}_{-30}	217 ± 10	L[s,f]	$-2.7^{+1.6}_{-1.4}$	20^{+6}_{-5}	Koronis
(956) Elisa	100^{+50}_{-70}	270 ± 10	V[s]	$-0.7^{+1.6}_{-1.1}$	20^{+6}_{-8}	Flora
(1173) Anchises	50^{+50}_{-25}	171 ± 10	P[c,p]	$-2.3^{+1.8}_{-1.5}$	22^{+7}_{-7}	
(1580) Betulia	180^{+50}_{-50}	352 ± 10	C[c]	$-0.6^{+1.1}_{-0.9}$	15^{+3}_{-3}	
(1620) Geographos	340^{+140}_{-100}	332 ± 10	LL[s,b]	$-3.1^{+1.2}_{-1.0}$	20^{+4}_{-4}	
(1862) Apollo	140^{+140}_{-100}	352 ± 10	LL[s,b]	$-1.0^{+1.9}_{-1.4}$	10^{+4}_{-4}	

Table 2.7 — continued

Object	Γ^a	T_c (K)	Spec.	$d_{g\phi}$	l_s (mm)	Family
(2867) Steins	210^{+30}_{-30}	230 ± 10	E[p,s]	$-3.3^{+0.6}_{-0.6}$	19^{+3}_{-2}	
(25143) Itokawa	700^{+100}_{-100}	337 ± 10	LL[s,b]	$-4.9^{+0.6}_{-0.7}$	41^{+7}_{-5}	
(29075) 1950 DA	24^{+20}_{-14}	280 ± 10	E[p,s]	$2.3^{+1.4}_{-1.8}$	4^{+1}_{-1}	
(33342) 1998 WT_{24}	200^{+100}_{-100}	315 ± 10	E[p,s]	$-1.8^{+1.5}_{-1.2}$	12^{+3}_{-4}	
(54509) YORP	700^{+500}_{-500}	360 ± 10	S[s]	$-4.9^{+2.2}_{-1.5}$	$5.3^{+1.9}_{-2.1}$	
(99942) Apophis	150^{+350}_{-100}	362 ± 10	S[s]	$-2.6^{+2.3}_{-1.7}$	44^{+18}_{-17}	
(101955) Bennu	310^{+70}_{-70}	338 ± 10	C[s]	$-2.5^{+0.9}_{-0.8}$	16^{+3}_{-3}	
(162173) Ryugu	350^{+250}_{-250}	250 ± 10	C[s]	$-4.8^{+2.1}_{-1.4}$	27^{+9}_{-11}	
(175706) 1996 FG3	80^{+40}_{-40}	328 ± 15	C[s]	$1.0^{+1.3}_{-1.1}$	$7.7^{+2.1}_{-2.3}$	
(308635) 2005 YU_{55}	550^{+250}_{-200}	325 ± 10	C[s]	$-4.6^{+1.4}_{-1.1}$	47^{+11}_{-10}	
(341843) 2008 EV_5	450^{+60}_{-60}	321 ± 15	C[s]	$-3.9^{+0.6}_{-0.7}$	19^{+4}_{-2}	
2002 NY_{40}	100^{+50}_{-50}	363 ± 15	LL[s,b]	$0.9^{+1.5}_{-1.1}$	20^{+5}_{-6}	
(91) Aegina	19^{+31}_{-19}	250 ± 16	C[s]	$1.5^{+1.7}_{-1.5}$	$6.6^{+3.0}_{-3.0}$	Astraea
(155) Scylla	16^{+15}_{-5}	219 ± 12	C[c]	$1.9^{+1.5}_{-1.7}$	$7.4^{+2.1}_{-1.8}$	
(167) Urda	51^{+10}_{-8}	217 ± 3	H[s,b]	$0.9^{+0.8}_{-0.8}$	14^{+3}_{-2}	Koronis
(183) Istria	21^{+13}_{-11}	192 ± 2	Di[s,b]	$1.5^{+1.5}_{-1.4}$	10^{+3}_{-3}	
(208) Lacrimosa	77^{+23}_{-18}	212 ± 4	H[s,b]	$-0.8^{+1.0}_{-0.8}$	18^{+4}_{-3}	Koronis
(271) Penthesilea	16^{+33}_{-16}	210 ± 1	C[s]	$0.5^{+1.6}_{-1.3}$	13^{+6}_{-6}	
(295) Theresia	24^{+38}_{-17}	211 ± 3	S[s]	$0.2^{+1.6}_{-1.4}$	12^{+5}_{-5}	
(322) Phaeo	12^{+11}_{-7}	210 ± 6	D[s]	$2.7^{+1.3}_{-1.2}$	11^{+4}_{-4}	Phaeo
(343) Ostara	140^{+120}_{-60}	226 ± 7	C[c]	$-3.1^{+1.7}_{-1.4}$	75^{+23}_{-22}	
(413) Edburga	40^{+12}_{-7}	210 ± 12	M[p,s]	$0.7^{+1.2}_{-2.0}$	11^{+2}_{-2}	
(444) Gyptis	74^{+74}_{-74}	253 ± 25	C[s]	$-1.0^{+1.9}_{-1.5}$	11^{+5}_{-5}	
(463) Lola	68^{+30}_{-28}	221 ± 4	M[c,p]	$-0.4^{+1.2}_{-1.1}$	$8.5^{+2.1}_{-2.1}$	
(464) Megaira	120^{+120}_{-120}	209 ± 2	C[s]	$-3.2^{+2.0}_{-1.5}$	23^{+9}_{-10}	
(493) Griseldis	56^{+25}_{-32}	203 ± 2	P[p,s]	$-0.7^{+1.5}_{-1.2}$	36^{+10}_{-12}	
(500) Selinur	16^{+7}_{-8}	218 ± 7	S[s]	$2.3^{+1.6}_{-2.3}$	$6.2^{+1.7}_{-1.9}$	
(509) Iolanda	$8.6^{+12.2}_{-8.6}$	204 ± 1	S[s]	$2.2^{+1.6}_{-2.3}$	$6.9^{+3.0}_{-3.0}$	
(520) Franziska	12^{+24}_{-5}	204 ± 2	S[c,p,f]	$1.2^{+1.5}_{-1.4}$	11^{+4}_{-4}	Eos
(538) Friederike	35^{+12}_{-11}	207 ± 3	C[p,f]	$1.3^{+1.1}_{-1.1}$	23^{+5}_{-5}	Hygiea
(558) Carmen	$7.7^{+26.9}_{-7.7}$	222 ± 3	P[p,s]	$1.5^{+1.7}_{-1.4}$	10^{+5}_{-5}	
(562) Salome	23^{+12}_{-20}	206 ± 5	S[s,f]	$1.8^{+1.3}_{-1.6}$	$6.4^{+2.3}_{-2.7}$	Eos
(567) Eleutheria	19^{+30}_{-11}	234 ± 4	C[c,p]	$1.2^{+1.5}_{-1.4}$	$8.3^{+3.1}_{-3.0}$	

Table 2.7 — continued

Object	Γ^a	T_c (K)	Spec.	$d_{g\phi}$	l_s (mm)	Family
(583) Klotilde	30^{+12}_{-19}	224 ± 11	C[c,p]	$1.9^{+1.4}_{-1.5}$	$8.4^{+2.5}_{-3.1}$	
(651) Antikleia	37^{+16}_{-26}	206 ± 2	S[s,f]	$1.0^{+1.3}_{-1.1}$	15^{+5}_{-6}	Eos
(656) Beagle	32^{+14}_{-14}	210 ± 1	C[p,f]	$1.3^{+1.2}_{-1.2}$	$8.5^{+2.2}_{-2.2}$	Beagle
(662) Newtonia	35^{+23}_{-25}	235 ± 11	S[s]	$1.2^{+1.5}_{-1.2}$	13^{+4}_{-5}	
(668) Dora	52^{+8}_{-8}	216 ± 7	C[s]	$0.9^{+0.9}_{-0.8}$	19^{+4}_{-2}	Dora
(670) Ottegebe	44^{+14}_{-18}	203 ± 2	H[s,b]	$0.8^{+1.1}_{-1.0}$	11^{+3}_{-3}	
(688) Melanie	41^{+44}_{-19}	230 ± 6	C[s]	$-0.1^{+1.6}_{-1.3}$	18^{+6}_{-5}	
(734) Benda	13^{+8}_{-13}	211 ± 2	C[s]	$2.0^{+1.7}_{-2.5}$	$5.0^{+1.9}_{-2.2}$	
(735) Marghanna	17^{+88}_{-17}	214 ± 24	C[s]	$-1.5^{+2.0}_{-1.6}$	18^{+9}_{-9}	
(771) Libera	61^{+34}_{-26}	206 ± 8	M[c,p]	$-0.7^{+1.3}_{-1.2}$	$8.4^{+2.2}_{-2.2}$	
(793) Arizona	32^{+16}_{-13}	215 ± 4	H[s,b]	$1.4^{+1.4}_{-1.2}$	$8.5^{+2.2}_{-2.1}$	
(826) Henrika	45^{+16}_{-21}	237 ± 8	C[s]	$1.4^{+1.2}_{-1.2}$	$8.4^{+2.1}_{-2.3}$	
(829) Academia	15^{+7}_{-15}	228 ± 1	C[p,s]	$2.1^{+1.9}_{-2.4}$	$5.1^{+1.9}_{-2.3}$	
(857) Glasenappia	58^{+30}_{-24}	244 ± 8	S[c,p]	$0.4^{+1.3}_{-1.1}$	12^{+3}_{-3}	
(883) Matterania	36^{+37}_{-24}	232 ± 6	LL[s,b]	$0.4^{+1.7}_{-1.3}$	$8.5^{+3.1}_{-3.3}$	Matterania
(906) Repsolda	47^{+115}_{-28}	225 ± 9	C[p]	$-2.1^{+2.0}_{-1.6}$	22^{+9}_{-8}	
(918) Itha	37^{+10}_{-10}	203 ± 7	S[s]	$1.2^{+1.0}_{-1.0}$	$6.6^{+1.4}_{-1.1}$	Itha
(972) Cohnia	19^{+38}_{-13}	206 ± 3	C[s]	$0.2^{+1.6}_{-1.4}$	15^{+6}_{-6}	
(977) Philippa	27^{+84}_{-21}	211 ± 3	C[c,p]	$-1.6^{+2.0}_{-1.5}$	18^{+8}_{-8}	
(984) Gretia	29^{+8}_{-7}	202 ± 2	S[s]	$1.7^{+1.2}_{-1.2}$	$7.7^{+1.5}_{-1.2}$	
(987) Wallia	46^{+64}_{-46}	211 ± 13	S[p]	$-1.3^{+1.9}_{-1.5}$	14^{+6}_{-6}	
(998) Bodea	20^{+16}_{-7}	198 ± 3	C[p]	$1.3^{+1.3}_{-1.4}$	$8.7^{+2.4}_{-2.1}$	
(1018) Arnolda	43^{+47}_{-43}	221 ± 10	M[c,p]	$-0.5^{+1.4}_{-1.3}$	11^{+5}_{-5}	
(1036) Ganymed	15^{+22}_{-15}	192 ± 6	H[s,b]	$1.0^{+1.7}_{-1.4}$	$8.2^{+3.6}_{-3.7}$	
(1047) Geisha	35^{+58}_{-14}	225 ± 1	S[s]	$-0.5^{+1.8}_{-1.4}$	23^{+8}_{-7}	Flora
(1051) Merope	48^{+81}_{-25}	210 ± 2	C[p]	$-1.8^{+1.9}_{-1.4}$	27^{+10}_{-9}	Alauda
(1076) Viola	24^{+44}_{-24}	235 ± 4	C[s]	$0.5^{+1.6}_{-1.4}$	$8.8^{+4.0}_{-4.0}$	
(1077) Campanula	56^{+40}_{-34}	209 ± 3	H[s,b]	$-0.6^{+1.5}_{-1.3}$	$8.3^{+2.7}_{-3.0}$	
(1083) Salvia	54^{+17}_{-30}	240 ± 8	S[p]	$1.1^{+1.4}_{-1.1}$	$7.4^{+2.0}_{-2.5}$	
(1095) Tulipa	23^{+13}_{-13}	211 ± 3	S[p,f]	$1.8^{+1.3}_{-1.5}$	$4.6^{+1.4}_{-1.5}$	Eos
(1109) Tata	10^{+46}_{-10}	229 ± 4	C[c]	$0.5^{+1.8}_{-1.4}$	$9.0^{+4.3}_{-4.3}$	Hygiea
(1123) Shapleya	14^{+33}_{-14}	230 ± 3	S[s]	$1.1^{+1.6}_{-1.4}$	21^{+10}_{-9}	Flora
(1125) China	34^{+8}_{-7}	201 ± 4	C[p]	$1.3^{+1.0}_{-1.0}$	$7.9^{+1.5}_{-1.1}$	

Table 2.7 — continued

Object	Γ^a	T_c (K)	Spec.	$d_{g\phi}$	l_s (mm)	Family
(1136) Mercedes	54^{+81}_{-34}	226 ± 12	S[p]	$-1.5^{+1.9}_{-1.5}$	25^{+10}_{-9}	
(1140) Crimea	23^{+15}_{-23}	211 ± 1	H[s,b]	$1.8^{+1.4}_{-1.5}$	$7.5^{+2.9}_{-3.3}$	
(1142) Aetolia	$8.0^{+29.7}_{-8.0}$	216 ± 2	S[s,b]	$1.2^{+1.6}_{-1.4}$	$8.8^{+4.2}_{-4.1}$	
(1152) Pawona	26^{+35}_{-14}	233 ± 1	L[s,b]	$0.8^{+1.5}_{-1.3}$	$6.2^{+2.2}_{-2.1}$	
(1162) Larissa	19^{+15}_{-19}	201 ± 1	P[c,p]	$1.6^{+1.5}_{-1.2}$	$7.7^{+3.0}_{-3.4}$	
(1188) Gothlandia	38^{+22}_{-13}	222 ± 7	LL[p,b,f]	$1.0^{+1.3}_{-1.2}$	$6.8^{+1.7}_{-1.5}$	Flora
(1224) Fantasia	58^{+16}_{-12}	222 ± 4	S[s]	$0.3^{+1.0}_{-0.8}$	$9.7^{+1.9}_{-1.5}$	
(1258) Sicilia	61^{+76}_{-31}	209 ± 1	C[p]	$-1.9^{+1.8}_{-1.4}$	20^{+7}_{-6}	
(1281) Jeanne	90^{+44}_{-25}	242 ± 5	P[p,s]	$-1.5^{+1.2}_{-1.1}$	25^{+6}_{-5}	
(1288) Santa	15^{+23}_{-5}	220 ± 3	C[s,f]	$1.5^{+1.4}_{-1.4}$	$8.3^{+2.8}_{-2.3}$	
(1291) Phryne	20^{+16}_{-6}	205 ± 2	S[p]	$1.6^{+1.4}_{-1.4}$	$7.1^{+1.9}_{-1.6}$	Eos
(1296) Andree	40^{+74}_{-12}	238 ± 12	C[p]	$-0.9^{+1.7}_{-1.5}$	11^{+4}_{-3}	
(1299) Mertona	15^{+29}_{-8}	207 ± 7	S[s]	$0.8^{+1.5}_{-1.3}$	$7.0^{+2.7}_{-2.5}$	
(1310) Villigera	40^{+23}_{-30}	224 ± 26	H[s,b]	$0.9^{+1.6}_{-1.3}$	$8.8^{+3.1}_{-3.6}$	
(1316) Kasan	10^{+34}_{-10}	221 ± 5	S[s]	$1.0^{+1.6}_{-1.4}$	$6.8^{+3.2}_{-3.2}$	
(1325) Inanda	76^{+50}_{-36}	214 ± 3	S[p]	$-1.4^{+1.5}_{-1.3}$	24^{+7}_{-7}	
(1335) Demoulina	130^{+90}_{-100}	227 ± 3	H[p,f]	$-2.5^{+1.9}_{-1.3}$	50^{+18}_{-21}	Koronis
(1352) Wawel	97^{+28}_{-71}	209 ± 2	M[p,s]	$-1.2^{+1.3}_{-1.0}$	15^{+5}_{-6}	
(1375) Alfreda	30^{+48}_{-18}	224 ± 2	S[p]	$-0.1^{+1.6}_{-1.4}$	17^{+7}_{-6}	
(1412) Lagrula	37^{+23}_{-9}	234 ± 2	LL[s,b]	$1.2^{+1.2}_{-1.2}$	$8.8^{+2.1}_{-1.7}$	Flora
(1432) Ethiopia	71^{+180}_{-65}	218 ± 8	E[p]	$-3.4^{+2.1}_{-1.7}$	21^{+9}_{-9}	
(1443) Ruppina	40^{+18}_{-14}	205 ± 1	H[s,b]	$0.6^{+1.3}_{-1.0}$	$8.7^{+2.1}_{-1.9}$	Koronis
(1452) Hunnia	24^{+34}_{-20}	216 ± 12	C[p,f]	$0.5^{+1.6}_{-1.4}$	13^{+6}_{-6}	Meliboea
(1495) Helsinki	19^{+13}_{-13}	229 ± 5	S[p,f]	$2.2^{+1.4}_{-1.8}$	$5.5^{+1.9}_{-2.2}$	Eunomia
(1501) Baade	34^{+48}_{-34}	205 ± 5	Di[s,b]	$-0.7^{+1.7}_{-1.4}$	15^{+7}_{-7}	
(1517) Beograd	19^{+55}_{-5}	231 ± 3	P[p,s]	$-0.2^{+2.0}_{-1.6}$	12^{+5}_{-4}	
(1536) Pielinen	74^{+23}_{-35}	227 ± 5	S[s]	$-0.2^{+1.2}_{-1.0}$	36^{+9}_{-10}	
(1542) Schalen	10^{+15}_{-10}	208 ± 1	D[s]	$2.3^{+1.4}_{-1.3}$	$7.0^{+3.1}_{-3.2}$	
(1565) Lemaitre	24^{+53}_{-24}	227 ± 14	H[s,b]	$0.0^{+1.8}_{-1.5}$	12^{+5}_{-5}	
(1567) Alikoski	$7.2^{+73.4}_{-7.2}$	228 ± 3	C[s]	$-0.5^{+1.7}_{-1.6}$	16^{+8}_{-7}	Ursula
(1568) Aisleen	51^{+41}_{-22}	212 ± 8	S[p,f]	$-0.7^{+1.5}_{-1.2}$	12^{+4}_{-3}	Phocaea
(1573) Vaisala	130^{+120}_{-80}	223 ± 8	S[s]	$-3.2^{+1.9}_{-1.4}$	110^{+40}_{-40}	Phocaea
(1577) Reiss	25^{+36}_{-20}	217 ± 4	S[s]	$0.4^{+1.7}_{-1.4}$	$7.1^{+2.9}_{-3.0}$	Flora

Table 2.7 — continued

Object	Γ^a	T_c (K)	Spec.	$d_{g\phi}$	l_s (mm)	Family
(1607) Mavis	37^{+42}_{-25}	204 ± 4	Ho^{s,b}	$-0.5^{+1.6}_{-1.4}$	10^{+4}_{-4}	
(1628) Strobel	47^{+12}_{-30}	219 ± 3	P^{p,s}	$0.7^{+1.4}_{-0.9}$	12^{+4}_{-5}	
(1644) Rafita	28^{+25}_{-14}	235 ± 4	S^{s}	$1.4^{+1.5}_{-1.3}$	$8.4^{+2.7}_{-2.6}$	
(1651) Behrens	59^{+29}_{-19}	250 ± 9	S^{s}	$0.5^{+1.2}_{-1.1}$	25^{+6}_{-5}	Flora
(1655) Comas Sola	40^{+37}_{-30}	215 ± 7	C^{s}	$-0.1^{+1.5}_{-1.3}$	17^{+6}_{-7}	
(1702) Kalahari	28^{+40}_{-9}	217 ± 6	C^{s}	$0.1^{+1.5}_{-1.3}$	18^{+6}_{-5}	
(1723) Klemola	30^{+11}_{-10}	216 ± 1	S^{s}	$1.9^{+1.6}_{-1.3}$	$7.8^{+1.8}_{-1.6}$	Eos
(1734) Zhongolovich	35^{+31}_{-10}	210 ± 9	C^{s}	$0.2^{+1.4}_{-1.3}$	11^{+3}_{-2}	Dora
(1741) Giclas	33^{+20}_{-10}	207 ± 8	H^{s,b}	$0.8^{+1.6}_{-1.1}$	$5.9^{+1.5}_{-1.3}$	Koronis
(1759) Kienle	52^{+88}_{-52}	208 ± 1	S^{p}	$-2.0^{+1.8}_{-1.5}$	27^{+12}_{-12}	
(1768) Appenzella	31^{+18}_{-12}	223 ± 2	C^{s}	$1.4^{+1.2}_{-1.2}$	$7.4^{+1.9}_{-1.8}$	Hertha
(1807) Slovakia	200^{+240}_{-50}	231 ± 4	S^{s}	$-4.7^{+1.5}_{-1.4}$	170^{+50}_{-40}	Flora
(1896) Beer	80^{+335}_{-80}	201 ± 5	S^{p,f}	$-5.2^{+2.6}_{-1.8}$	17^{+8}_{-8}	Hertha
(1936) Lugano	120^{+70}_{-80}	249 ± 2	C^{s}	$-1.5^{+1.5}_{-1.2}$	24^{+8}_{-9}	Aedeona
(1979) Sakharov	58^{+269}_{-27}	223 ± 3	V^{p,f}	$-4.1^{+2.4}_{-1.8}$	23^{+10}_{-9}	Vesta
(1980) Tezcatlipoca	170^{+170}_{-110}	227 ± 8	LL^{s,b}	$-3.9^{+2.0}_{-1.5}$	21^{+8}_{-8}	
(2005) Hencke	40^{+48}_{-34}	204 ± 1	S^{p,f}	$-0.7^{+1.8}_{-1.4}$	13^{+5}_{-6}	Eunomia
(2072) Kosmodemyanskaya	19^{+129}_{-19}	204 ± 1	E^{p}	$-2.7^{+2.0}_{-1.6}$	11^{+5}_{-5}	
(2106) Hugo	22^{+36}_{-9}	209 ± 1	C^{s}	$0.3^{+1.6}_{-1.3}$	$9.5^{+3.3}_{-2.9}$	
(2111) Tselina	47^{+36}_{-24}	201 ± 2	S^{s}	$-0.6^{+1.5}_{-1.3}$	11^{+3}_{-3}	Eos
(2123) Vltava	56^{+37}_{-22}	210 ± 2	H^{s,b}	$-0.5^{+1.4}_{-1.2}$	26^{+7}_{-6}	Koronis
(2140) Kemerovo	20^{+39}_{-14}	217 ± 1	P^{p,s}	$0.2^{+1.9}_{-1.5}$	12^{+5}_{-5}	
(2144) Marietta	53^{+10}_{-8}	203 ± 4	H^{s,b}	$0.4^{+0.8}_{-0.7}$	$9.5^{+1.7}_{-1.2}$	Koronis
(2156) Kate	56^{+23}_{-23}	215 ± 1	LL^{s,b}	$0.4^{+0.6}_{-0.7}$	$9.5^{+1.7}_{-1.2}$	
(2177) Oliver	42^{+10}_{-10}	197 ± 1	C^{p}	$0.9^{+1.0}_{-1.0}$	$9.4^{+1.8}_{-1.4}$	
(2203) van Rhijn	55^{+55}_{-27}	194 ± 4	C^{p,f}	$-1.6^{+1.7}_{-1.3}$	28^{+9}_{-9}	Themis
(2204) Lyyli	90^{+36}_{-50}	237 ± 20	P^{p,s}	$-1.1^{+1.6}_{-1.2}$	19^{+6}_{-6}	
(2214) Carol	21^{+15}_{-9}	220 ± 8	C^{p}	$1.9^{+1.2}_{-1.6}$	$6.2^{+1.8}_{-1.7}$	
(2239) Paracelsus	18^{+7}_{-18}	201 ± 1	C^{p}	$1.9^{+1.6}_{-2.3}$	$5.2^{+1.9}_{-2.3}$	
(2268) Szmytowna	30^{+32}_{-30}	207 ± 1	H^{s,b}	$0.3^{+1.6}_{-1.3}$	10^{+4}_{-5}	Koronis
(2275) Cuitlahuac	13^{+24}_{-13}	227 ± 12	S^{p}	$1.6^{+1.4}_{-1.5}$	$6.2^{+2.9}_{-2.9}$	
(2297) Daghestan	58^{+23}_{-18}	217 ± 1	C^{p,f}	$0.0^{+1.1}_{-1.0}$	12^{+3}_{-2}	Themis
(2306) Bauschinger	18^{+14}_{-10}	222 ± 1	P^{p,s}	$2.2^{+1.3}_{-1.2}$	14^{+5}_{-5}	Padua

Table 2.7 — continued

Object	Γ^a	T_c (K)	Spec.	$d_{g\phi}$	l_s (mm)	Family
(2332) Kalm	77^{+15}_{-48}	209 ± 2	C[s]	$-0.4^{+1.3}_{-0.9}$	20^{+6}_{-8}	Themis
(2347) Vinata	35^{+20}_{-14}	187 ± 4	C[p]	$0.2^{+1.3}_{-1.1}$	$8.0^{+2.1}_{-2.0}$	
(2365) Interkosmos	41^{+10}_{-41}	234 ± 9	S[s]	$1.9^{+1.3}_{-1.2}$	$6.9^{+2.4}_{-3.0}$	Astraea
(2375) Radek	11^{+14}_{-11}	241 ± 2	D[p,c]	$3.0^{+1.3}_{-1.3}$	$9.7^{+4.2}_{-4.3}$	
(2446) Lunacharsky	33^{+12}_{-10}	244 ± 13	C[s]	$2.2^{+1.2}_{-1.4}$	$5.8^{+1.3}_{-1.1}$	Nysa-Polana
(2463) Sterpin	17^{+43}_{-17}	217 ± 7	LL[s,b]	$0.3^{+1.7}_{-1.4}$	12^{+6}_{-5}	Eunomia
(2500) Alascattalo	41^{+18}_{-28}	242 ± 6	S[p,f]	$1.5^{+1.3}_{-1.2}$	$5.2^{+1.7}_{-2.0}$	Flora
(2556) Louise	61^{+37}_{-33}	238 ± 3	S[p]	$-0.1^{+1.4}_{-1.2}$	$8.4^{+2.5}_{-2.7}$	
(2567) Elba	50^{+11}_{-36}	212 ± 5	C[s]	$0.9^{+1.3}_{-1.0}$	10^{+3}_{-4}	
(2687) Tortali	59^{+16}_{-10}	226 ± 10	S[p]	$0.3^{+0.8}_{-0.9}$	20^{+4}_{-3}	
(2786) Grinevia	12^{+19}_{-12}	203 ± 1	S[p,f]	$1.5^{+1.4}_{-1.5}$	$4.1^{+1.9}_{-1.8}$	Eunomia
(2855) Bastian	17^{+42}_{-7}	226 ± 12	S[s]	$0.5^{+1.8}_{-1.5}$	$6.6^{+2.5}_{-2.2}$	
(2870) Haupt	130^{+180}_{-130}	229 ± 3	C[p,f]	$-3.5^{+2.1}_{-1.6}$	120^{+50}_{-50}	Nysa-Polana
(2947) Kippenhahn	32^{+18}_{-11}	236 ± 12	S[p]	$1.6^{+1.3}_{-1.2}$	11^{+3}_{-2}	
(2985) Shakespeare	41^{+49}_{-13}	211 ± 1	H[p,f]	$-0.6^{+1.6}_{-1.3}$	11^{+3}_{-3}	Koronis
(3036) Krat	15^{+57}_{-9}	204 ± 2	C[s]	$-0.7^{+1.7}_{-1.5}$	12^{+5}_{-5}	Alauda
(3051) Nantong	27^{+28}_{-14}	203 ± 3	C[p]	$0.4^{+1.4}_{-1.2}$	$6.7^{+2.2}_{-2.1}$	
(3144) Brosche	59^{+56}_{-45}	226 ± 2	S[p,f]	$-1.0^{+1.8}_{-1.3}$	$8.2^{+3.1}_{-3.4}$	Flora
(3162) Nostalgia	29^{+51}_{-15}	199 ± 6	C[p]	$-0.8^{+1.6}_{-1.4}$	11^{+4}_{-4}	
(3249) Musashino	93^{+132}_{-73}	197 ± 3	L[s]	$-3.4^{+2.1}_{-1.6}$	14^{+6}_{-6}	Nysa-Polana
(3267) Glo	23^{+43}_{-13}	225 ± 6	S[s]	$0.3^{+1.6}_{-1.4}$	$9.5^{+3.7}_{-3.4}$	Phocaea
(3305) Ceadams	21^{+6}_{-3}	228 ± 11	S[p,f]	$2.6^{+1.3}_{-2.3}$	$4.4^{+0.8}_{-0.6}$	Eunomia
(3411) Debetencourt	22^{+83}_{-12}	244 ± 10	S[p,f]	$-0.7^{+1.9}_{-1.5}$	14^{+6}_{-5}	Flora
(3438) Inarradas	54^{+15}_{-15}	206 ± 5	C[p]	$0.2^{+1.0}_{-0.9}$	21^{+4}_{-4}	Inarradas
(3483) Svetlov	110^{+400}_{-50}	222 ± 11	E[p,f]	$-5.2^{+2.4}_{-1.8}$	26^{+11}_{-10}	Hungaria
(3509) Sanshui	62^{+27}_{-34}	212 ± 1	S[p]	$-0.3^{+1.5}_{-1.1}$	16^{+5}_{-5}	
(3536) Schleicher	32^{+182}_{-10}	230 ± 8	S[s]	$-2.9^{+2.2}_{-1.7}$	16^{+7}_{-6}	
(3544) Borodino	72^{+14}_{-45}	237 ± 18	S[p]	$0.5^{+1.3}_{-1.0}$	$9.0^{+2.6}_{-3.4}$	
(3554) Amun	1400^{+700}_{-200}	274 ± 6	M[p, t]	$-8.7^{+0.9}_{-1.0}$	33^{+7}_{-6}	
(3560) Chenqian	44^{+22}_{-10}	206 ± 3	S[p,f]	$0.2^{+1.1}_{-1.1}$	18^{+4}_{-3}	Eos
(3628) Boznemcova	32^{+23}_{-32}	201 ± 12	S[s]	$0.5^{+1.6}_{-1.2}$	$5.8^{+2.3}_{-2.5}$	
(3751) Kiang	62^{+20}_{-16}	211 ± 1	C[p]	$-0.1^{+1.1}_{-0.9}$	13^{+3}_{-2}	
(3823) Yorii	49^{+22}_{-49}	209 ± 10	C[p]	$0.2^{+1.5}_{-1.1}$	$8.9^{+3.3}_{-3.9}$	

Table 2.7 — continued

Object	Γ^a	T_c (K)	Spec.	$d_{g\phi}$	l_s (mm)	Family
(3907) Kilmartin	26^{+47}_{-26}	183 ± 14	E[p]	$-1.1^{+1.7}_{-1.4}$	$7.4^{+3.4}_{-3.4}$	
(3915) Fukushima	22^{+13}_{-7}	240 ± 1	C[s]	$2.3^{+1.4}_{-1.8}$	$8.3^{+2.1}_{-1.8}$	
(3935) Toatenmongakkai	120^{+90}_{-60}	215 ± 5	S[s]	$-2.8^{+1.6}_{-1.3}$	70^{+21}_{-20}	
(3936) Elst	22^{+56}_{-22}	235 ± 3	V[p,f]	$-0.1^{+1.8}_{-1.5}$	$9.6^{+4.5}_{-4.4}$	Vesta
(4003) Schumann	32^{+35}_{-11}	208 ± 3	P[p,o]	$-0.3^{+1.6}_{-1.3}$	12^{+4}_{-3}	
(4006) Sandler	36^{+7}_{-11}	212 ± 1	P[p,s]	$1.3^{+1.0}_{-0.8}$	$7.3^{+1.5}_{-1.3}$	
(4008) Corbin	67^{+37}_{-25}	240 ± 16	S[p]	$-0.3^{+1.4}_{-1.2}$	12^{+3}_{-3}	
(4029) Bridges	32^{+26}_{-18}	240 ± 3	S[p]	$1.2^{+1.4}_{-1.2}$	$6.2^{+2.0}_{-2.1}$	
(4142) Dersu-Uzala	110^{+140}_{-30}	263 ± 10	S[s]	$-2.4^{+1.7}_{-1.5}$	82^{+25}_{-21}	
(4150) Starr	29^{+16}_{-14}	231 ± 6	S[p]	$1.8^{+1.4}_{-1.3}$	$6.4^{+1.8}_{-1.9}$	
(4255) Spacewatch	24^{+22}_{-17}	209 ± 2	P[p,f]	$0.9^{+1.6}_{-1.3}$	16^{+6}_{-6}	Schubart
(4264) Karljosephine	110^{+300}_{-110}	206 ± 2	S[p]	$-4.9^{+2.5}_{-1.8}$	49^{+23}_{-23}	
(4294) Horatius	12^{+77}_{-12}	225 ± 2	S[p]	$-0.8^{+1.9}_{-1.6}$	15^{+7}_{-7}	
(4352) Kyoto	47^{+64}_{-32}	204 ± 2	S[s]	$-1.5^{+1.8}_{-1.4}$	23^{+9}_{-9}	
(4359) Berlage	40^{+71}_{-26}	228 ± 1	S[p]	$-1.0^{+1.8}_{-1.5}$	12^{+5}_{-5}	
(4363) Sergej	27^{+94}_{-27}	218 ± 5	S[p]	$-1.6^{+2.0}_{-1.6}$	17^{+8}_{-8}	
(4383) Suruga	37^{+53}_{-17}	220 ± 1	S[p]	$-0.6^{+1.8}_{-1.3}$	$8.1^{+2.8}_{-2.5}$	
(4528) Berg	26^{+20}_{-26}	231 ± 6	S[p]	$1.7^{+1.4}_{-1.4}$	$5.0^{+2.0}_{-2.2}$	
(4565) Grossman	51^{+36}_{-12}	233 ± 3	S[p,f]	$0.00^{+1.3}_{-1.1}$	$9.7^{+2.4}_{-2.0}$	Eunomia
(4569) Baerbel	48^{+45}_{-9}	225 ± 5	S[p,f]	$-0.5^{+1.4}_{-1.3}$	$7.8^{+2.1}_{-1.6}$	Maria
(4611) Vulkaneifel	32^{+23}_{-32}	202 ± 1	S[s]	$0.61^{+1.26}_{-1.26}$	$6.1^{+2.4}_{-2.7}$	Eunomia
(4613) Mamoru	$9.4^{+22.6}_{-9.4}$	194 ± 3	S[p]	$1.1^{+1.5}_{-1.5}$	$5.9^{+2.8}_{-2.8}$	
(4713) Steel	40^{+28}_{-13}	258 ± 1	S[s]	$1.3^{+1.6}_{-1.2}$	$8.3^{+2.2}_{-1.9}$	
(4771) Hayashi	61^{+37}_{-29}	208 ± 10	C[p]	$-0.8^{+1.6}_{-1.2}$	14^{+4}_{-4}	
(4898) Nishiizumi	34^{+445}_{-34}	243 ± 13	E[p]	$-4.8^{+2.5}_{-1.9}$	16^{+8}_{-8}	
(4899) Candace	79^{+104}_{-60}	255 ± 8	S[p]	$-1.6^{+1.9}_{-1.5}$	34^{+14}_{-14}	
(4908) Ward	12^{+68}_{-12}	229 ± 4	S[p]	$-0.4^{+1.7}_{-1.5}$	13^{+6}_{-6}	
(5035) Swift	26^{+35}_{-20}	223 ± 7	S[p,f]	$0.5^{+1.6}_{-1.3}$	10^{+4}_{-4}	Eunomia
(5052) Nancyruth	10^{+72}_{-10}	231 ± 1	S[p,f]	$-0.5^{+1.9}_{-1.5}$	16^{+8}_{-8}	Flora
(5080) Oja	26^{+50}_{-17}	235 ± 7	S[p,f]	$0.2^{+1.8}_{-1.5}$	10^{+4}_{-4}	Matterania
(5088) Tancredi	40^{+12}_{-19}	197 ± 4	C[p,f]	$0.9^{+1.1}_{-1.1}$	$7.8^{+1.9}_{-2.2}$	Themis
(5104) Skripnichenko	41^{+31}_{-22}	229 ± 4	S[p]	$0.5^{+1.4}_{-1.3}$	$6.3^{+2.0}_{-2.0}$	
(5226) Pollack	24^{+51}_{-18}	221 ± 3	S[p]	$-0.2^{+1.8}_{-1.4}$	$6.2^{+2.6}_{-2.6}$	

Table 2.7 — continued

Object	Γ^a	T_c (K)	Spec.	$d_{g\phi}$	l_s (mm)	Family
(5333) Kanaya	23^{+32}_{-7}	249 ± 12	C^{s}	$1.4^{+1.5}_{-1.4}$	$6.4^{+2.0}_{-1.7}$	
(5378) Ellyett	75^{+455}_{-62}	246 ± 7	E^{p,f}	$-4.9^{+2.5}_{-1.8}$	64^{+30}_{-29}	Hungaria
(5427) Jensmartin	19^{+76}_{-19}	239 ± 6	E^{p,f}	$-0.6^{+1.8}_{-1.5}$	$9.3^{+4.4}_{-4.4}$	Hungaria
(5527) 1991 UQ$_3$	120^{+130}_{-80}	254 ± 17	S^{p}	$-2.4^{+1.9}_{-1.5}$	13^{+5}_{-5}	
(5574) Seagrave	34^{+34}_{-34}	225 ± 3	S^{p,f}	$0.4^{+1.7}_{-1.3}$	$7.2^{+3.0}_{-3.2}$	Eunomia
(5592) Oshima	34^{+23}_{-27}	206 ± 4	C^{s}	$0.6^{+1.1}_{-1.2}$	11^{+4}_{-5}	Veritas
(5604) 1992 FE	1100^{+2200}_{-600}	281 ± 1	V^{s}	$-9.2^{+2.4}_{-1.8}$	55^{+21}_{-20}	
(5625) Jamesferguson	52^{+14}_{-15}	204 ± 1	C^{p,f}	$0.34^{+1.00}_{-0.87}$	11^{+2}_{-2}	Adeona
(5682) Beresford	29^{+152}_{-29}	212 ± 10	S^{p}	$-2.9^{+2.2}_{-1.7}$	12^{+6}_{-6}	
(5712) Funke	33^{+50}_{-33}	202 ± 7	S^{p,f}	$-0.8^{+1.8}_{-1.4}$	$7.8^{+3.5}_{-3.5}$	Gefion/Minerva
(6091) Mitsuru	45^{+25}_{-13}	253 ± 11	S^{p}	$1.1^{+1.3}_{-1.1}$	$9.2^{+2.2}_{-1.9}$	
(6121) Plachinda	56^{+63}_{-34}	217 ± 1	S^{p}	$-1.3^{+1.7}_{-1.4}$	$9.9^{+3.5}_{-3.6}$	
(6139) Naomi	66^{+31}_{-36}	242 ± 1	S^{s}	$0.0^{+1.6}_{-1.0}$	19^{+6}_{-6}	
(6159) Andreseloy	61^{+177}_{-61}	222 ± 2	V^{p,f}	$-3.2^{+2.2}_{-1.7}$	22^{+10}_{-10}	Vesta
(6170) Levasseur	76^{+161}_{-56}	239 ± 16	S^{p,f}	$-2.7^{+2.1}_{-1.7}$	11^{+4}_{-4}	Phocaea
(6185) Mitsuma	66^{+61}_{-45}	240 ± 11	C^{p}	$-0.9^{+1.7}_{-1.3}$	21^{+8}_{-8}	
(6261) Chione	41^{+52}_{-41}	230 ± 22	S^{p}	$-0.3^{+1.9}_{-1.5}$	$9.0^{+4.0}_{-4.0}$	
(6361) Koppel	20^{+172}_{-20}	232 ± 5	E^{p}	$-2.7^{+2.1}_{-1.7}$	17^{+8}_{-8}	
(6572) Carson	21^{+33}_{-15}	218 ± 11	S^{p}	$0.6^{+1.7}_{-1.3}$	$5.4^{+2.2}_{-2.2}$	
(6838) Okuda	47^{+13}_{-10}	230 ± 20	S^{p,h}	$1.1^{+1.1}_{-0.9}$	12^{+2}_{-2}	
(6870) 1991 OM$_1$	59^{+330}_{-59}	226 ± 1	E^{p,f}	$-4.5^{+2.4}_{-1.8}$	17^{+8}_{-8}	Hungaria
(6901) Roybishop	59^{+83}_{-40}	241 ± 3	S^{p}	$-1.3^{+1.8}_{-1.4}$	11^{+4}_{-4}	
(6905) Miyazaki	26^{+66}_{-26}	220 ± 3	S^{p,f}	$-0.8^{+2.0}_{-1.5}$	$6.7^{+3.1}_{-3.1}$	Eunomia
(6911) Nancygreen	210^{+1220}_{-180}	230 ± 38	E^{p}	$-7.9^{+3.0}_{-2.1}$	120^{+60}_{-60}	
(7476) Ogilsbie	70^{+30}_{-20}	219 ± 9	S^{p}	$-0.6^{+1.1}_{-1.0}$	$9.8^{+2.2}_{-1.9}$	
(7783) 1994 JD	170^{+190}_{-110}	237 ± 4	E^{p,f}	$-3.8^{+1.9}_{-1.5}$	44^{+16}_{-16}	Hungaria
(7829) Jaroff	32^{+176}_{-32}	225 ± 1	E^{p,f}	$-3.0^{+2.1}_{-1.6}$	13^{+6}_{-6}	Hungaria
(7832) 1993 FA$_{27}$	46^{+160}_{-46}	245 ± 2	S^{p,f}	$-2.4^{+2.2}_{-1.7}$	17^{+8}_{-8}	Flora
(7949) 1992 SU	37^{+28}_{-27}	209 ± 7	C^{p}	$0.3^{+1.5}_{-1.2}$	15^{+5}_{-5}	
(8213) 1995 FE	36^{+167}_{-18}	228 ± 12	S^{p,f}	$-2.8^{+2.2}_{-1.7}$	11^{+5}_{-4}	Phocaea
(8862) Takayukiota	43^{+195}_{-43}	193 ± 4	S^{p}	$-4.0^{+2.4}_{-1.8}$	13^{+6}_{-6}	Astraea
(8887) Scheeres	21^{+52}_{-21}	220 ± 6	S^{p,f}	$-0.1^{+1.7}_{-1.5}$	$6.2^{+2.9}_{-2.9}$	Maria
(9297) Marchuk	22^{+120}_{-22}	240 ± 9	S^{p,f}	$-1.7^{+2.1}_{-1.6}$	21^{+10}_{-10}	Eunomia

Table 2.7 — continued

Object	Γ^a	T_c (K)	Spec.	$d_{g\phi}$	l_s (mm)	Family
(10936) 1998 FN_{11}	13^{+22}_{-13}	212 ± 2	S^p	$1.5^{+1.3}_{-1.5}$	13^{+6}_{-6}	
(11549) 1992 YY	30^{+18}_{-5}	236 ± 7	S^p	$1.7^{+1.1}_{-1.2}$	$5.5^{+1.3}_{-1.0}$	
(11780) Thunder Bay	130^{+450}_{-130}	212 ± 6	S^p	$-5.7^{+2.6}_{-1.9}$	180^{+90}_{-90}	
(12376) Cochabamba	120^{+61}_{-110}	240 ± 11	S^p	$-1.7^{+1.8}_{-1.3}$	13^{+5}_{-6}	
(12753) Povenmire	17^{+23}_{-11}	238 ± 1	S^p	$1.8^{+1.6}_{-1.4}$	$9.6^{+3.6}_{-3.7}$	
(13474) V'yus	64^{+123}_{-44}	196 ± 8	S^p	$-3.1^{+2.1}_{-1.6}$	17^{+7}_{-7}	
(13856) 1999 XZ_{105}	20^{+12}_{-10}	209 ± 1	C^p	$1.9^{+1.3}_{-1.9}$	$5.5^{+1.6}_{-1.7}$	Aedeona
(14342) Iglika	24^{+8}_{-14}	202 ± 5	C^p	$2.0^{+1.3}_{-2.1}$	$5.2^{+1.4}_{-1.8}$	Chloris
(14950) 1996 BE_2	54^{+49}_{-34}	246 ± 1	$S^{p,f}$	$-0.1^{+1.4}_{-1.3}$	$7.6^{+2.7}_{-2.8}$	Flora
(15362) 1996 ED	110^{+120}_{-110}	226 ± 12	$S^{p,h}$	$-2.8^{+2.0}_{-1.5}$	35^{+15}_{-15}	
(15430) 1998 UR_{31}	72^{+127}_{-63}	249 ± 16	S^p	$-2.0^{+2.1}_{-1.6}$	$8.9^{+3.9}_{-3.9}$	
(15499) Cloyd	33^{+36}_{-33}	203 ± 4	$S^{p,f}$	$-0.1^{+1.7}_{-1.3}$	$9.3^{+4.0}_{-4.1}$	Eos
(15914) 1997 UM_3	88^{+188}_{-72}	214 ± 7	S^p	$-3.7^{+2.3}_{-1.7}$	26^{+11}_{-11}	Hertha
(16681) 1994 EV_7	63^{+74}_{-30}	245 ± 2	S^p	$-1.0^{+1.7}_{-1.4}$	12^{+4}_{-4}	
(16886) 1998 BC_{26}	33^{+49}_{-18}	220 ± 3	S^p	$-0.3^{+1.6}_{-1.4}$	10^{+4}_{-3}	
(17681) Tweedledum	130^{+320}_{-110}	243 ± 7	$E^{p,f}$	$-4.3^{+2.3}_{-1.7}$	72^{+32}_{-32}	Merxia
(17822) 1998 FM_{135}	79^{+53}_{-52}	188 ± 1	$C^{p,f}$	$-2.1^{+1.7}_{-1.3}$	12^{+4}_{-4}	Hygeia
(18487) 1996 AU_3	46^{+36}_{-26}	216 ± 11	$S^{p,f}$	$-0.2^{+1.5}_{-1.3}$	10^{+3}_{-4}	Eunomia
(19251) Totziens	32^{+121}_{-32}	209 ± 8	S^p	$-2.4^{+2.1}_{-1.7}$	24^{+11}_{-11}	
(20378) 1998 KZ_{46}	34^{+23}_{-14}	210 ± 5	$S^{p,f}$	$0.7^{+1.5}_{-1.2}$	$8.2^{+2.3}_{-2.1}$	Maria
(20932) 2258 T-1	41^{+111}_{-41}	206 ± 6	S^p	$-2.4^{+2.2}_{-1.7}$	11^{+5}_{-5}	
(21594) 1998 VP_{31}	44^{+16}_{-12}	246 ± 3	$C^{p,f}$	$1.6^{+0.9}_{-1.1}$	$8.4^{+1.8}_{-1.5}$	Chloris
(23200) 2000 SH_3	17^{+66}_{-17}	220 ± 10	$S^{p,f}$	$-0.7^{+1.9}_{-1.5}$	16^{+8}_{-7}	Phocaea
(23276) 2000 YT_{101}	27^{+30}_{-27}	214 ± 6	C^p	$0.6^{+1.7}_{-1.2}$	$5.9^{+2.5}_{-2.6}$	
(24101) Cassini	15^{+38}_{-15}	200 ± 4	S^p	$0.1^{+1.7}_{-1.5}$	$6.5^{+3.0}_{-3.0}$	
(27851) 1994 VG_2	11^{+14}_{-11}	234 ± 7	$C^{p,l}$	$2.2^{+1.5}_{-2.3}$	$5.4^{+2.4}_{-2.4}$	
(28126) Nydegger	33^{+205}_{-33}	229 ± 7	S^s	$-3.2^{+2.3}_{-1.7}$	13^{+6}_{-6}	Flora
(30470) 2000 OR_{19}	45^{+43}_{-22}	224 ± 13	$C^{p,f}$	$-0.2^{+1.5}_{-1.3}$	20^{+6}_{-6}	Gefion
(32802) 1990 SK	20^{+162}_{-20}	219 ± 22	S^p	$-2.8^{+2.3}_{-1.8}$	$9.4^{+4.6}_{-4.5}$	
(33916) 2000 LF_{19}	38^{+51}_{-38}	240 ± 19	S^p	$-0.1^{+1.8}_{-1.4}$	$7.8^{+3.5}_{-3.5}$	
(41044) 1999 VW_6	14^{+157}_{-14}	209 ± 7	S^p	$-2.9^{+2.2}_{-1.8}$	10^{+5}_{-5}	
(41223) 1999 XD_{16}	23^{+43}_{-23}	201 ± 8	C^p	$-0.3^{+1.8}_{-1.4}$	20^{+9}_{-9}	
(41288) 1999 XD_{107}	41^{+86}_{-34}	234 ± 10	S^p	$-1.2^{+1.9}_{-1.5}$	$9.8^{+4.3}_{-4.3}$	

Table 2.7 — continued

Object	Γ^a	T_c (K)	Spec.	$d_{g\phi}$	l_s (mm)	Family
(42265) 2001 QL_{69}	25^{+89}_{-25}	210 ± 2	$S^{p,f}$	$-1.7^{+2.0}_{-1.6}$	14^{+7}_{-7}	Eos
(42946) 1999 TU_{95}	37^{+60}_{-37}	227 ± 5	S^{p}	$-0.6^{+1.7}_{-1.4}$	$7.4^{+3.3}_{-3.3}$	
(44892) 1999 VJ_8	32^{+93}_{-32}	210 ± 7	$S^{p,f}$	$-1.9^{+2.0}_{-1.6}$	12^{+6}_{-5}	Eunomia
(45436) 2000 AD_{176}	75^{+482}_{-75}	231 ± 9	S^{p}	$-5.3^{+2.7}_{-1.9}$	44^{+21}_{-21}	
(68216) 2001 CV_{26}	430^{+1210}_{-280}	278 ± 22	$L^{s,b}$	$-7.2^{+2.7}_{-1.9}$	24^{+10}_{-10}	
(69350) 1993 YP	240^{+490}_{-150}	235 ± 13	S^{p}	$-5.8^{+2.4}_{-1.8}$	66^{+27}_{-25}	
(72675) 2001 FP_{54}	29^{+367}_{-29}	223 ± 6	S^{p}	$-4.7^{+2.6}_{-1.9}$	14^{+7}_{-7}	
(90698) Kosciuszko	16^{+49}_{-16}	258 ± 29	$S^{p,f}$	$0.8^{+1.7}_{-1.5}$	$7.1^{+3.4}_{-3.3}$	Phocaea

Notes. [a]Thermal inertia values are in SI units (J $m^{-2}K^{-1}s^{-1/2}$).

[b]Band parameters are used (chapter 3).

[c]Colors from (Tholen, 1984) are used.

[e]The mutual eclipse duration of 4 hr was used to compute thermal skin depth.

[f]Family association is used Table 2.11.

[h]High albedo not consistent with C-type Themis family identification of PDS.

[l]Low albedo not consistent with Phocaea family identification of AstDyS.

[o]Orbital location in the outer main-belt is used to infer P-type.

[p]Albedo Figure 2.7 is used to infer meteorite connection.

[s]Reflectance spectrum is used from DeMeo et al. (2009) or Lazzaro et al. (2004).

[t]High thermal inertia is used to distinguish an M-type from a P-type.

[u]A uniform, rather than a Gaussian, distribution from 0 to 50 was used for the thermal inertia.

classification as a X- or D-type (Thomas et al., 2014). The moderate albedo ($p_V \approx 0.241$) of this object and its very high thermal inertia, however, are suggestive of a metal-rich surface and thus can be re-classified as belonging to the M-type taxonomy.

(5604) 1992 FE The V-type near-Earth asteroid (5604) 1992 FE is also an Aten and has been flagged as a Potentially Hazardous Asteroid (PHA) by the MPC. This sub-kilometer object has a very high thermal inertia, but with large error bars, resulting in relatively large uncertainty in the grain size estimates. Its high optical albedo and radar circular polarization ratio are consistent with its V-type taxonomic classification and having a surface similar to the large differentiated asteroid, Vesta.

(68216) 2001 CV_{26} With a size of ∼1.24 km and an Apollo NEA, 2001 CV_{26} has been classified as an S-/Sq-type. This spectral classification indicates that the surface has been space weathered to some extent. The band parameter analysis in chapter 3 points toward a meteorite analog of L chondrites of the ordinary chondrite group.

2.7 Analysis

My aim here is to investigate statistically-relevant physical factors and quantify their influence on the regolith grain size for my sub-sample of the asteroid population. As stated in my hypothesis in section 2.2, I test whether or not grain sizes are negatively correlated with asteroid diameter — indicating impact driven processes — and if grain size is positively correlated with rotation period — due to thermal fracturing processes. Various multiple linear (hereafter, multi-linear) regression models are fit to the main-belt asteroids to identify and characterize the dependencies of these factors (section 2.7.2). In order to quantify the grain size dependence, if any, on asteroid size and spin rate a multi-linear regression analysis is performed. The multi-linear model residuals are used as input to an analysis of variance routine, to determine if the compositional groups have characteristically different grain sizes (Section 2.7.3). Finally, an attempt at defining and estimating a weathering timescale will be made using grain sizes and approximating the surface age of the objects within the dataset using objects within asteroid families.

Although the NEAs in this work offer insight into the regolith of very small asteroids, the chaotic nature of changes in their orbital parameters makes it difficult to hold other factors constant — such as thermal environment and impact flux — potentially complicating the multi-linear analysis. Thus, I perform a statistical analyses on them separate from the MBAs in section 2.7.5.

2.7.1 Thermal Skin Depth

The thermal skin depth is an important quantity to consider when using infrared data and interpreting thermophysical modeling results. Rotation period is an important influence on the skin depth, as it controls the timescale of the diurnal thermal cycle, and it is more useful to analyze the skin depth in the context of different rotation periods (figure 2.11). Diurnal temperature changes occur mainly in the upper regions of regolith — down to $\sim 3l_s$. From these values I can infer that, since l_s ranges from 5 mm up to several centimeters, thermal inertia is indicative of the bulk properties of regolith down to these depths.

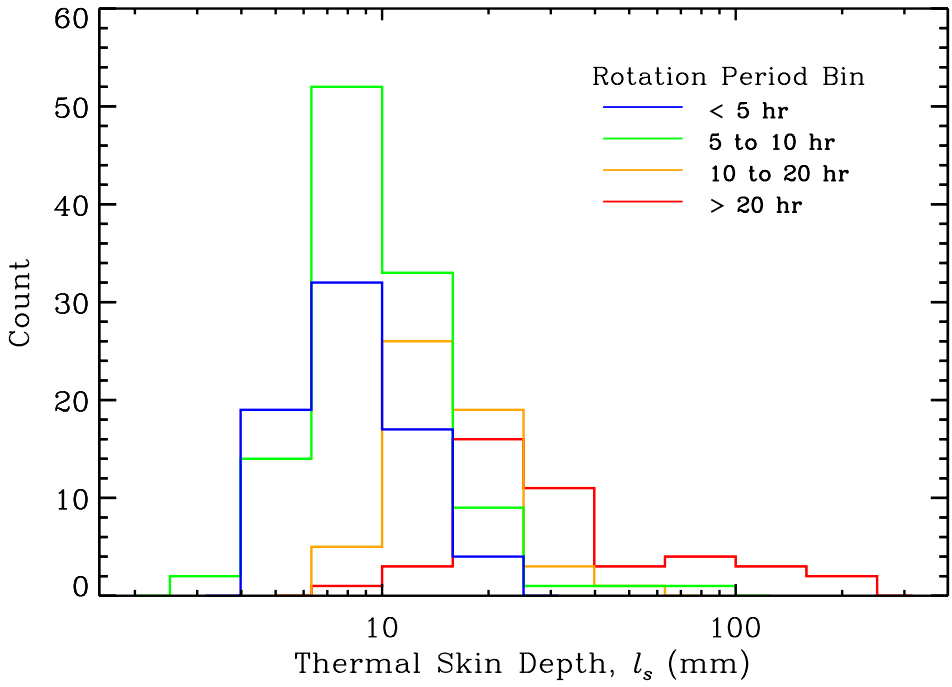

Figure 2.11: Thermal skin depth for objects in my sample for different rotation period bins.

2.7.2 Multi-linear Regression

As breifly described in section 1.4.3, multi-linear linear regression is a method that attempts to model a dependent variable (the grain size, $d_{g\phi}$) as a linear combination of several independent variables — in my case, diameter and rotation period. The multi-linear regression model reports the slope, or coefficient, of each independent variable and a y-intercept, along with 1σ uncertainties for each of these parameters. I also consider segmented, or piece-wise, multi-linear regression models for both independent variables as listed here:

- *M-1*: Multi-linear regression with no breakpoints
- *M-2*: Multi-linear regression with one diameter breakpoint
- *M-3*: Multi-linear regression with one rotation period breakpoint
- *M-4*: Multi-linear regression with one breakpoint for each variable

This class of model-fitting allows each independent variable to be partitioned into several intervals in which a different line is fit to the data. I consider only one breakpoint per variable, which divides the linear regression into two linear regression functions. The location and uncertainty of the breakpoints are estimated, in addition to the slope of the lines, in the segmented multi-linear regression models. Finally, I mention here that, henceforth, the diameter and rotation period are transformed by taking the $\log_{10}$ and square root, respectively, before used in the multi-linear regression models. This variable transformation is done to best capture the wide variance in D_{eff} and P_{rot}, which each span at least 2 orders of magnitude.

The r^2_{adj} (adjusted r-squared) statistic and Bayesian Information Criterion (BIC) for all models are compared to determine which most accurately fits the relationship between grain size and the diameter and rotation period. The r^2_{adj} is a determination of the degree to which the model explains the variance in the dependent variable. Higher values indicate a better fit, while accounting for the number of predictor parameters in the model. The BIC is used to indicate which model maximizes the likelihood of matching the data while minimizing the

Table 2.8: Comparison of Multi-linear Regression Models

Model	n	r^2_{adj}	BIC
M-1	4	0.234	1078
M-2	6	0.425	1007
M-3	6	0.247	1082
M-4	8	0.427	1015

number of necessary model parameters. For each model, table 2.8 gives the r^2_{adj} and BIC and number of (free) model parameters, n[5].

The highest r^2_{adj} are seen for both *M-2* and *M-4*, indicating that the breakpoint in the diameter dimension is a useful addition to the models. Raw values of the BIC have little meaning and the more practical use of this statistic is choosing between two or more model fits by computing the BIC difference (a $\Delta BIC > 2$ is desirable when preferring one fit to another; Kass and Raftery, 1995). The BIC of *M-2* is lower than for *M-4*, with $\Delta BIC = 8$, giving strong indication (ΔBIC of 6–10 indicates a strong preference for the model with a lower BIC) that the additional breakpoint in the rotation period does not meaningfully increase the robustness of the model fit[6]. I therefore choose *M-2* as the preferred model for capturing the grain size dependency on diameter and rotation period. The estimated intercept, linear coefficients (slopes), and breakpoint (D_b), along with the associated uncertainties are given in table 2.9. Note that the model intercept value represents the predicted $d_{g\phi}$ for an asteroid with $D_{eff} = 1$ km and $P_{rot} = 1$ hr.

Diameter Dependence For asteroids larger than ∼10 km there is no significant relationship with $d_{g\phi}$, as seen in figure 2.12. On average, the diameter of regolith on > 10 km bodies is just below 1 mm, with many asteroids having $d_{g\phi} \sim$ 150–200 μm. However, a strong negative relationship for sub-10 km bodies is apparent in which the average grain

[5]The number of free parameters is calculated from the total number of fitted variables and each of their y-intercepts. Although they are added together and reported as a single intercept, they independently contribute to the number of free parameters. Adding a breakpoint to one independent variable effectively creates another line, thus increasing m by 2.

[6]Employing the Davies Test (Davies, 2002) here, which tests for a non-zero slope change in a predictor variable, supports this claim with a p-value = .45.

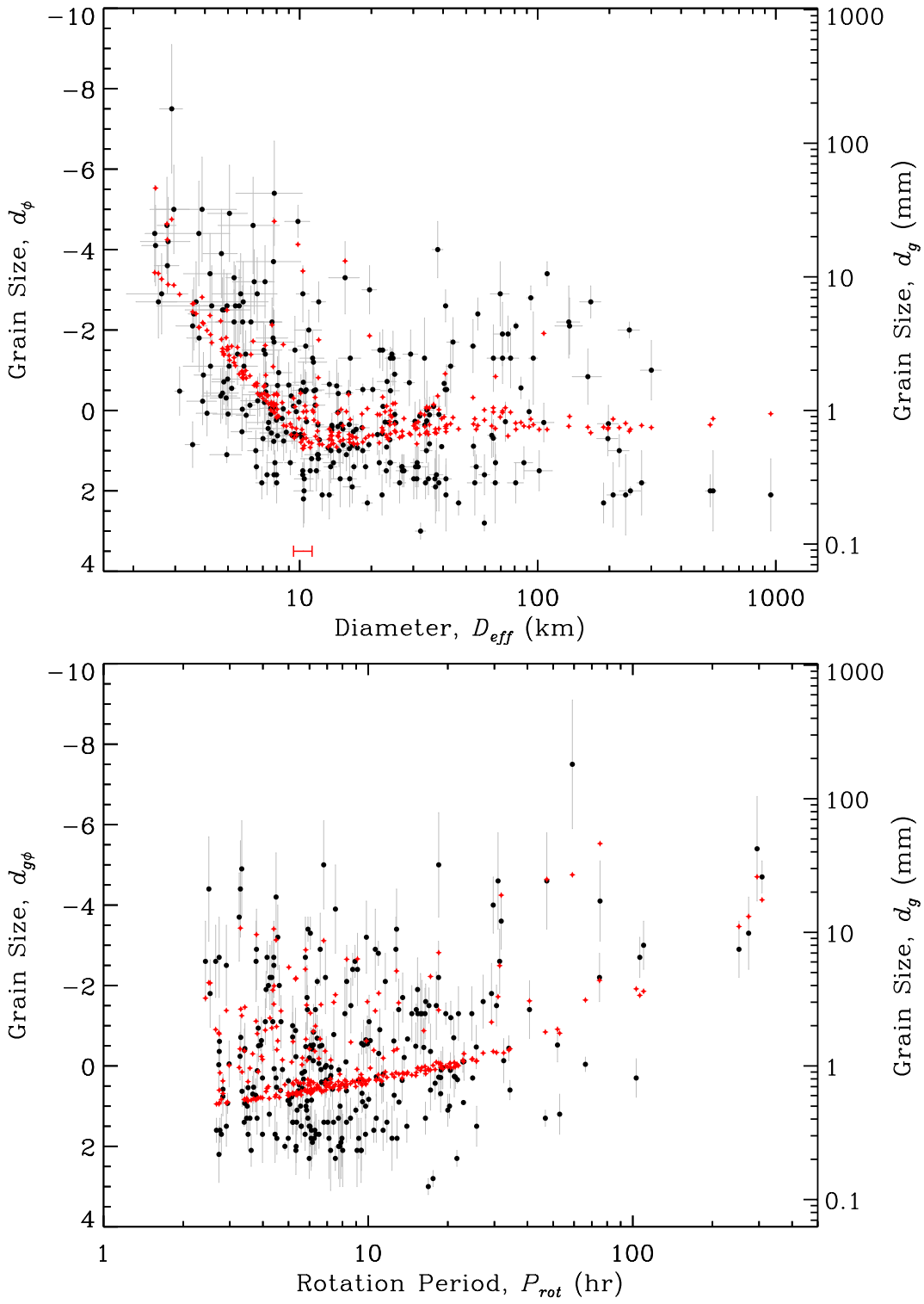

Figure 2.12: Multi-linear model fit (*M-2*), given by red stars, and the grain size dataset, shown by black dots, as a function of asteroid diameter (top) and rotation period (bottom). The red bar in the left panel indicates the 1σ range in uncertainty in the breakpoint between the two segments.

Table 2.9: Linear Coefficients and Intercept for *M-2*

Parameter	Estimate	1σ Uncertainty	p-value
intercept $[d_{g\phi}]$	5.58	$\pm$ 0.64	$< .001$
D_b [km]	10.3	+1.0/-0.9	$< .001$
P_{rot}^{slope}	0.31	$\pm$ 0.04	$< .001$
D_{eff}^{slope} $(< D_b)$	6.95	$\pm$ 0.80	$< .001$
D_{eff}^{slope} $(> D_b)$	0.22	$\pm$ 0.26	.42

size is a factor of ten-fold larger than (underdeveloped) surfaces represented by ∼100 mm grain size estimates — essentially bare rock. For an order of magnitude change in asteroid diameter (below ∼10 km), the multi-linear regression model predicts a change in regolith grain size by a factor of ∼50. This can be graphically deduced by extrapolating the data in figure 2.12 to a ∼1 km sized asteroid, for which there should be ≈25 mm grains, compared to a ∼10 km asteroid with ≈0.5 mm grains.

Rotation Period Dependence My preferred multi-linear model predicts that objects with longer rotation periods have larger grain sizes. For asteroids with longer rotation periods, the positive correlation with grain size is clear, and the multi-linear regression captures this relationship well. In figure 2.12 the fast rotating asteroids can be seen to exhibit a wide range of grain sizes, although the model predicts that most of these objects have a ∼0.5 mm regolith. The spread in grain sizes for fast rotators can partly be caused by the range of asteroid sizes below 10 km, for which there is a strong grain size dependency.

2.7.3 Compositional Groups

Here, I investigate if, and how much, the grain sizes vary/depend on the surface composition of an asteroid. Simply comparing the means of the grain size distributions between the compositions is not appropriate, as some of the independent predictor variables are correlated grain size: for example, primitive C-complex and P-type bodies are more represented at

larger sizes, and the E/Xe-types are largely represented in the lower size range[7]. Instead, I perform Welch's t-tests between the compositional groups, using the model residuals from *M-2* as plotted in figure 2.13. Since the multi-linear analysis was performed without regard to the compositional group, a difference in the mean model residuals of a group from the entire sample would indicate a disparity in regolith grain size for that particular group.

I apply Welch's t-test[8] (Welch, 1947) in a series of trials between each possible pairing of compositional group, as well as between each group and the remainder of the entire sample (with that group removed). The null hypothesis that is tested is that the means between the groups do not differ. The resulting p-values of these trials are tabulated in table 2.10: lower p-values indicate a higher probability that the null hypothesis is not supported.

The model residual distributions, grouped by composition, along with model residuals plotted against the explanatory variables are shown in figure 2.13. Compared to the mean of the remainder of the sample, the M-type asteroids have a statistically significant ($p < .001$) different mean grain size, which remains true even when M-type residuals are included as part of the entire sample. On average, the M-types exhibit regolith grain sizes 4 $\times$ larger than asteroids of the same diameter and rotation period. I interpret this result as an indication that one of the thermophysical or material properties of the M-types is affecting the efficiency of one or both of the regolith degradation processes and discuss this point further in section 2.8. The mean grain sizes of M-types and V-types are, in statistical terms, not significantly different from each other (table 2.10), which is not true for other groups and the M-types. The S-types statistically show a smaller mean grain size compared to the remainder of the sample ($p = .03$). The E-types themselves show a greater likelihood of having a larger grain size than the S-types ($p = .05$), C-types ($p = .10$), and the sample as a whole ($p = .10$). Lastly, there is an 85% probability that P-types have a smaller average grain size than the rest of the sample ($p = .15$). Potential explanations for these differences between the grain sizes of compositional groups is discussed in section 2.8.

[7]Similar relationships are apparent between spectral classes and heliocentric distance (DeMeo and Carry, 2013).

[8]Welch's t-test, as opposed to the Student's t-test, as it does not assume that the two groups have equal variance or sample size.

Table 2.10: Residual grain size statistics and Welch's t-test results for compositional groups

		Spectral Group					
		S	C	V	E	M	P
$\Delta d_{g\phi}$	mean	-0.19	-0.12	0.36	0.25	2.07	-0.53
	std. dev.	1.19	1.32	1.57	1.71	0.72	1.66
p-value	all excl.	.03	.71	.63	.10	$< .001$	.15
	S	—	.40	.50	.05	$< .001$	.40
	C		—	.60	.10	$< .001$	.24
	V			—	.80	.13	.34
	E				—	$< .01$	.33
	M					—	$< .001$
	P						—

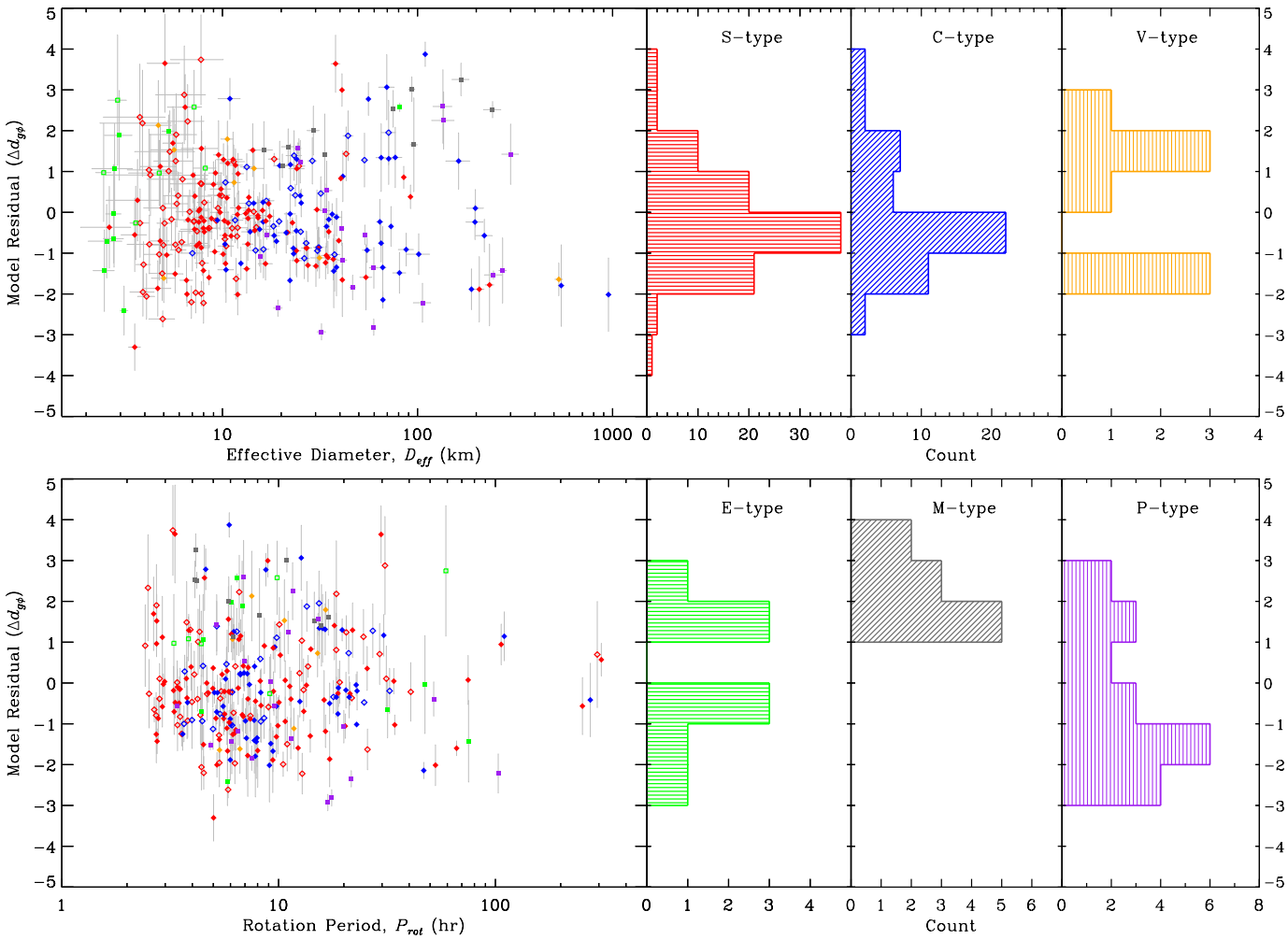

Figure 2.13: Grain size model residual distributions for different compositional groups. The plots on the left show the model residuals for *M-2* as a function of effective diameter (top) and rotation period (bottom). The histograms on the top show the grain size model residual distributions for S, C, and V-types, with the bottom histograms showing the same for E, M, and P-types.

2.7.4 Asteroid Families and Weathering Timescale

The identification of asteroid families — orbital groups of asteroids of a common origin — has been at one of the foci of orbital dynamical modeling for around 100 years. The first work used an algorithm called the Hierarchal Clustering Method (HCM; Zappala et al., 1990) to identify three asteroid clusters within orbital element space. Since then, several works have used the HCM and developed other family-finding algorithms, resulting in the expansion of the number of unique asteroid families to 122 (Nesvorný et al., 2015). The size of the orbits of family members become increasingly dispersed throughout time, as a result of the Yarkovsky effect: a drift in the semimajor axis due to small thermal forces acting on astronomical timescales (Bottke et al., 2001). The rate of this orbital drift allows an estimate of the timing of the original collision to be made, providing a useful approximation for the surface age of the asteroid members.

Within an asteroid family, the Yarkovsky effect is more relevant for smaller asteroids, as they have less mass and approximately the same magnitude of thermal forces acting to alter their orbital semimajor axis (Bottke et al., 2001). This orbital drift of family members leads to a characteristic "V-shape" that is seen on a size (often expressed as the absolute magnitude, H_V) vs. semimajor axis plot (Nesvorný et al., 2003). The method in which family age estimates are calculated relies on the ability to characterize the slope of the lines which define the envelope of the V-shape (e.g., Bolin et al., 2018, and references therein); the older the family, the shallower the slope is (i.e., a wider V-shape). Unfortunately, it is inherently difficult to constrain the ages of very young and very old families because the borders of the V are not well defined. Members of young families have not had long enough time to have experienced significant semimajor axis drift (Nesvorný et al., 2002a), and families as old as the solar system are so widely dispersed that they are hard to distinguish from the background asteroid population (Bolin et al., 2018). Another complication arises when a collision produces a family near a strong mean-motion resonance with Jupiter or Saturn. In these cases the resonances truncate the family when members are delivered to other regions of the solar system. Nevertheless, the ages of a few dozen asteroid families have been estimated by a several authors and are included in table 2.11.

Table 2.11: Asteroid Family Properties

PDS Family ID	AstDyS Family ID	Spec.	Collision Type[1]	Age (Myr)	Count[2]
609 Veritas	(490) Veritas	Ch		8.3 ± 0.5^{m}	1
620 Beagle	(656) Beagle	C		$< 10^{k}$	1
403 Baptistina	(883) Matterania	S		175 ± 40^{a}	2
003 Hungaria	(434) Hungaria	Xe	Fragmentation	210 ± 70^{n}	6
507 Padua	(110) Padua	X		$270 \pm 150^{i,j}$	1
—	(135) Hertha	S		300 ± 55^{f}	3
—	(5) Astraea	?	Cratering	330 ± 100^{i}	2
—	(808) Merxia	S	Fragmentation	$360 \pm 170^{j,m,n}$	1
512 Dora	(668) Dora	Ch	Fragmentation	$500 \pm 175^{j,n}$	2
604 Meliboea	—	Ch		640 ± 10^{d}	1
902 Alauda	—	?		640 ± 50^{d}	2
509 Chloris	(410) Chloris	C		700 ± 400^{j}	2
505 Adeona	(145) Aedeona	?		$750 \pm 380^{i,j}$	3
403 Flora	—	S		$955 \pm 370^{e,j}$	14
401 Vesta	(4) Vesta	V	Cratering	$965 \pm 240^{c,g,n}$	3
516 Gefion	(93) Minerva	S		$1150 \pm 400^{j,l,n}$	2
701 Phocaea	(25) Phocaea	S		1190 ± 320^{i}	7
606 Eos	(221) Eos	K	Fragmentation	$1490 \pm 420^{h,m}$	10
633 Itha	—	S		$< 1500^{c}$	1
601 Hygiea	(10) Hygeia	C	Cratering	$1607 \pm 820^{j,n}$	3
002 Schubart	(1911) Schubart	P	Fragmentation	1700 ± 700^{b}	1
502 Eunomia	(15) Eunomia	S	Cratering	$2020 \pm 600^{d,j,n}$	13
605 Koronis	(158) Koronis	S(H*)	Fragmentation	$2050 \pm 1570^{d,n}$	11
602 Themis	(24) Themis	C	Fragmentation	$2360 \pm 1420^{d,j,n}$	4
506 Maria	(170) Maria	S		$2465 \pm 940^{j,n}$	3
902 Alauda	—	?		$< 3500^{d}$	2
—	(375) Ursula	?		$3500 \pm 1000^{d,n}$	1

Notes. *Koronis members are associated with H chondrites (Vernazza et al., 2014).

[1]Collisional type definitions from Milani et al. (2015).

[2]Number of asteroid family members present in this study.

[a]Bottke et al. (2007)
[b]Brož and Vokrouhlický (2008)
[c]Broz et al. (2013)
[d]Carruba et al. (2016)
[e]Dykhuis et al. (2014)
[f]Dykhuis and Greenberg (2015)
[g]Marchi et al. (2012)
[h]Milani et al. (2014)
[i]Milani et al. (2015)
[j]Nesvorný et al. (2005)
[k]Nesvorný et al. (2008)
[l]Nesvorný et al. (2009)
[m]Nesvorný et al. (2015)
[n]Spoto et al. (2015)

Here, the surface ages of the members of asteroids within families are assumed to be concordant with the age of the family of which they are a member. Only a fraction of the objects in the study were identified to be part of a family, and some families do not have a current age estimate. Table 2.11 lists the ages of families used in this study. I re-ran the multi-linear regression model *M-2* including only the subset of objects that exist within families (table 2.7) and considering the additional predictor variable of family age as model input (this new model will be referred to as *M-2t*). This reanalysis of the multi-linear model accounts for any colinearity between diameter and surface age, which is especially relevant because larger asteroids are less likely to have experienced a catastrophic collision — thus possess older surfaces — and smaller asteroids are statistically younger, on average.

I found that incorporating the surface age did not result in a statistically measurable difference in the multi-linear model. This null-result may be due to the level of uncertainty associated with grain size estimates, which drown out any small potential differences between asteroids of different ages. If, for this dataset, there actually was no dependence on the surface age, it would indicate that the weathering timescale was shorter than the age of the youngest families included here (< 10 Myr). As further discussed in section 2.8, a small mechanical weathering timescale would mean that most surfaces of main-belt asteroids > 1 km are in a steady state between regolith production and loss (section 3.8.4).

2.7.5 Near-Earth Asteroids

In section 2.7.2 I removed non main-belt asteroids (NEAs and Mars Crossers) from my analysis in order to remove the effect of different thermal and impact environments. These groups show a wide range of orbit types (varying in both semimajor axis, a, and eccentricity, e) as there are asteroids with aphelia (Q) in the Main Belt and many with orbits completely nested within Earth's. Here, I analyze the grain sizes (section 2.6) calculated for the NEAs with previously determined thermal inertia measurements ($N = 15$) and those estimated in this work ($N = 7$). With grain sizes for these 22 asteroids, I can potentially identify regolith dependencies on orbital factors.

Here, I performed a multi-linear regression model, similar to the one performed in section 2.7. I did not consider segmented linear fits as there are not enough to determine any

significant breakpoints (in other words, I conservatively avoid overfitting the small number of objects). The independent predictor variables I include here are the diameter and rotation period, logarithmically transformed as before, but I also include the orbital semimajor axis (a), perihelion (q), and aphelion distance (Q).

The NEA multi-linear regression model only selected Q as the statistically significant variable. The grain sizes of the NEAs (table 2.7) do not follow the same trends with the diameter and rotation period that exist among main-belt objects. On further inspection, potential co-linearity between D_{eff} and Q could raises some doubt of the significance of this result. Re-running the multi-linear model restricted to only these two variables, however, did not change the result — Q is thus a better predictor of grain size than diameter and rotation period among NEAs. The grain sizes as a function of aphelion, diameter, and rotation period are shown in figure 2.14. The grain sizes of objects with q within ~0.1 AU of Earth's orbit are somewhat higher than the asteroids that orbit just outside. The higher grain size regoliths are among the asteroids with perihelia interior to Earth's orbit, although some of these objects also have more fine-grained surfaces, like that of the largest main-belt objects. Asteroids with spin rates near the spin barrier ($P_{rot} \approx 2.12$ hr) exhibit a range spanning 3 orders of magnitude, which mimics the grain size span for the entire Main Belt sample.

2.8 Discussion

2.8.1 Regolith Weathering

Meteoroid Impacts

Repeated impacts of smaller asteroids or meteoroids into the surface of an asteroid will create ejecta — some of which is retained at the surface as regolith. The general relationship between the mass of the ejecta (M) above a certain velocity (u), as a function of impactor mass and velocity (m & U) is:

$$\frac{M}{m} \propto \left(\frac{u}{U}\right)^{-3\tau} \tag{2.13}$$

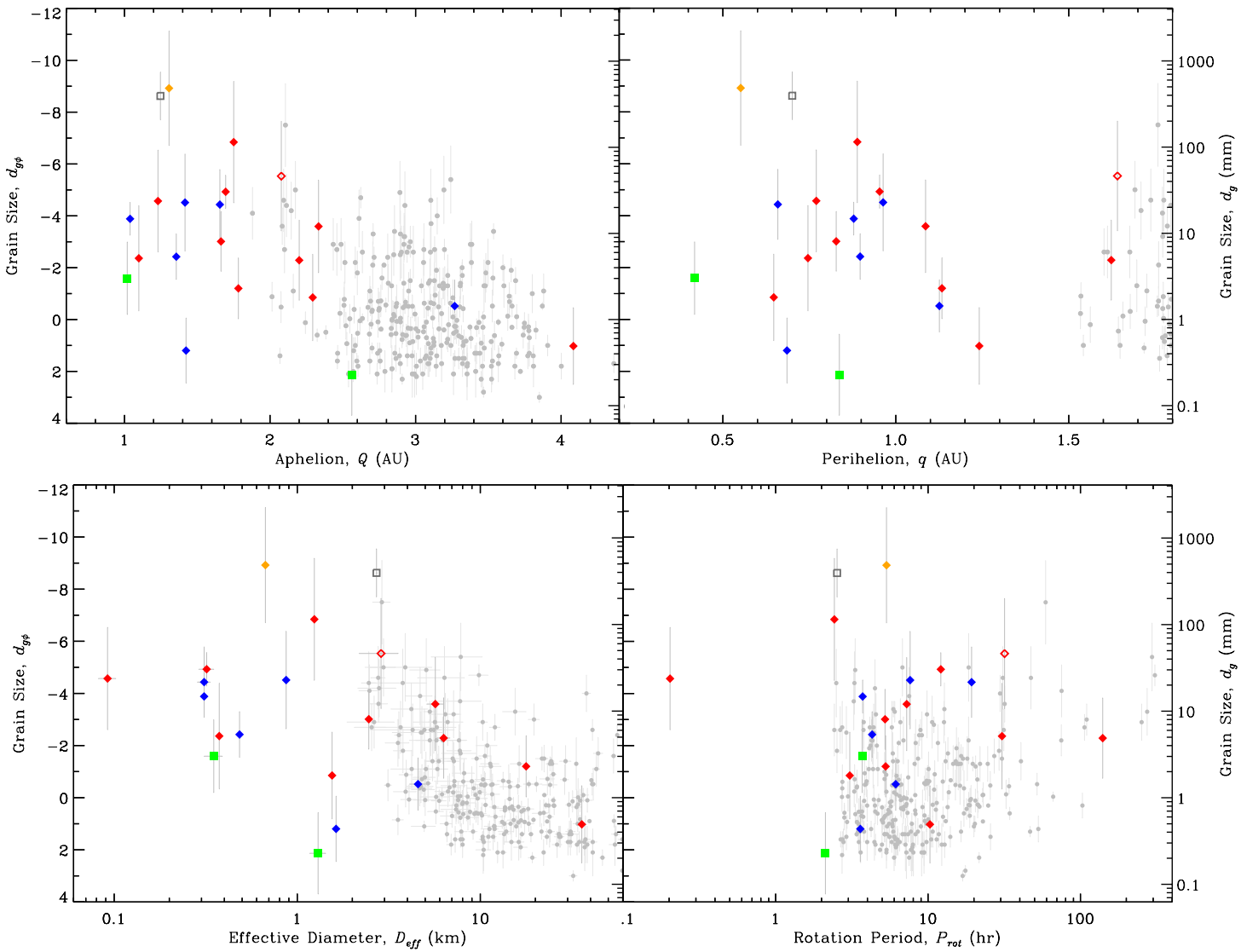

Figure 2.14: Regolith grain sizes of NEAs as a function of aphelion and perihelion distance, diameter, and rotation period. Red, orange, green, grey, and blue symbols represent S, V, E, M, and C-types, respectively. The open symbols are objects with an inferred composition based on the albedo (i.e., figure 2.7) and grey symbols with error bars are MBAs.

where τ, an empirically-derived exponent, is taken as 0.41 — the value for sand (Housen and Holsapple, 2011). For reference, the probability distribution of relative velocities between asteroids in the Main Belt, which is roughly Maxwellian, has a mode of 4.3 km s^{-1} and a mean value of 5.3 km s^{-1} (Farinella and Davis, 1992; Bottke et al., 1994). The velocities of incoming meteorioids are mostly independent of the size of target body (due to the extremely small gravitational attraction of an asteroid) which leaves the relative size of the impactor to the target asteroid as the dominant factor in equation (2.13). It is interesting to note that laboratory experiments show that lower velocity impacts can actually transfer more kinetic energy into the ejecta (10–20%), than high velocity impacts (Waza et al., 1985). Additionally, the mechanical and structural properties of the impacted asteroid play a small but non-negligible role in determining the outcome of ejecta. For non-porous asteroids, the upper limit of the ejected dust velocity can often be 0.1% to 0.5% of the impactor velocity (Nakamura and Fujiwara, 1991; Nakamura et al., 1994), but the velocity of the smallest ejected particles can greatly exceed this range (Asada, 1985). Nakamura and Fujiwara (1991) report a power law dust size and velocity with a slope of -1/6 for basalt, indicating that smaller ejecta travel much faster, and farther, than larger blocks and boulders, which are more likely to remain in the original impact crater (Thomas et al., 2001).

Other factors, such as the target body porosity can have a noticeable effect on the mass of the ejecta from an impact (Housen and Holsapple, 2003). Energy from the impact is concentrated near the impact site and worked into crushing the surface material, instead of ejecting it at high velocities. Holsapple et al. (2002) points out that if the porosity of the target region is greater than 50%, only 10% of the crater mass is ejected, as most of the energy is partitioned into compacting the material. Additionally, material strength of the target plays a vital role in the ejecta outcome. In general, stronger asteroids produce more ejecta, which can escape the gravitational well of the body more easily than an asteroid comprised of weaker material. A higher than average strength could partly explain the larger average grain sizes for M-types, which are all $>$ 10 km in my sample. The fact that my multi-linear model could not completely capture the entire variance in grain sizes for my sample might be exploited to indicate broad differences in porosity and strength properties

of asteroids. For example, ∼100 km objects that exhibit lower than expected regolith grains could be stronger and/or less porous than the average main-belt asteroid.

The discovery and study of meteorite impact breccias — fragmented samples from a variety of parent bodies (Burbine and Binzel, 2002) — offers a connection to the state of asteroid regolith. Impact breccias are formed from the lithification of near-surface material from the heat and pressure of an impact and classified by their texture and presence/absence of clasts (Bischoff et al., 2006). A direct connection to asteroid regolith can be made if they are rich in solar-wind gases, identified isotopically (McKay et al., 1989). Clasts found within identified regolith breccias range in size from several hundred microns up to many centimeters have been found in HEDs, carbonaceous, ordinary, and enstatite chondrites, and other stony meteorites (Bischoff et al., 2006, and references within). Interestingly, Bischoff et al. (2006) note that some aubrites are known to contain large enstatite clasts up to 10 cm in size, as well as metal grains up to 1 cm in size. If the aubrite parent body is matched by an E-type spectrum, then these systematically-larger clasts and grains are well-matched to the finding that E-types have atypically large regolith grains.

Asteroids larger than ∼10 km exhibit regoliths that are similar to the largest bodies, whereas the grain sizes of some asteroids of diameter ∼2 km approach the limit for what is considered a "bare rock" or bedrock surface. The break in main-belt asteroid grain sizes around 10 km could indicate a change in either the nature of regolith generation, or be a result of lower gravitational retention of smaller regolith grains. Using crater scaling laws, Housen et al. (1979) predict that asteroids in the 1–10 km range should harbor a $\ll 1$ mm thick regolith due to a decrease in *both* the strength and gravitational field of bodies of this size.

My results show that the differences in grain size for near-Earth and Mars-crossing asteroids are mostly controlled by their orbital parameters, which may be explained by the increase in meteoroid flux in the Main Belt at distances > 2.2 AU. The aphelion velocity of an NEA with an orbit that extends into the Main Belt will be less than the typical orbital velocity of a main-belt asteroid. For this reason, the relative impact velocity between a main-belt meteoroid with an NEA will be greater than a meteoroid impact with another

main-belt asteroid. This combination of a higher impactor flux and velocity would likely result in a faster impact weathering rate for NEAs with $Q \gtrsim 2.2$ AU.

Using the measured meteorite flux at 1 AU, Basilevsky et al. (2013) calculated a characteristic lunar boulder survival lifetime using boulder size counts on crater rims with known ages. They calculated that it takes 25–50 Myr to destroy 50% of a typical 1 m-sized boulder. They predict with their model that the fraction of boulders remaining exponentially decreases with time, and after 190–300 Myr, more than 99 % of boulders should be completely destroyed. Basilevsky et al. (2015) extrapolated the lunar timescale to Ceres and Vesta assuming that boulders are broken down exclusively via impact weathering. On these large MBAs the boulder weathering timescale is 3% of the lunar value (i.e., 750 kyr–1.5 Myr), which is mainly a consequence of the meteorite flux being ∼2 orders of magnitude greater in the Main Belt than at 1 AU.

This timescale is significantly shorter than the ages of the families studied in this work, and consistent with my multi-linear regression result of not finding any relationship between grain size and surface age. A few recently-formed families with ages less than 1 Myr have been identified (e.g., Table 1 in Nesvorný et al., 2015) in the Main Belt. Members of these families can, in principle, be used to track the progression of regolith weathering across time. A caveat, however, is the fact that young families are comprised of very small members, which are more likely to lose regolith either by impacts or other means (section 2.8.2). Statistically speaking, a 1-km asteroid is likely to experience around 5 catastrophic breakups every 1 Myr (Holsapple et al., 2002), or once every ∼200 kyr. This timescale is shorter than the boulder survival timescale (750 kyr–1.5 Myr), so I expect that a main-belt asteroid at this size would not survive long enough to have much of a developed regolith. Main-belt asteroids smaller than 1 km have even shorter timescales for a catastrophic breakup, so should not have surfaces old enough to develop much regolith at all, nor have the gravitational forces necessary to retain boulders or blocks at the surface. A typical 10 km main-belt asteroid, on the other hand, will survive ∼80 times longer (16 Myr) before experiencing a breakup event — much longer than the expected boulder destruction timescale (Basilevsky et al., 2013).

Thermal Fatigue Weathering

The cyclic heating and cooling of an asteroid surface, as a consequence of time-varying insolation, can result in spatial thermal gradients (∇T) within regolith grains a few times larger than the thermal skin depth. This *thermal fatigue cycling* creates heterogeneous thermal stress gradients (expansion and contraction) across mineral grain boundaries of a rock (Molaro et al., 2015). The structural weakening of the material ultimately results in the mechanical failure and breakdown of the rock and formation of asteroid regolith. It has been debated whether or not thermal fracturing is a significant weathering mechanism for terrestrial rocks (e.g., Molaro and McKay, 2010, and references within), but convincing evidence from the Moon and Mars (Eppes et al., 2015) indicates that thermal shock (rapid timescale) and/or fatigue (long timescale) efficiently operates in these environments. Recently, Delbo' et al. (2014) experimentally demonstrated the effectiveness of this process on a chip of the Murchison (CM2 carbonaceous chondrite) and Sahara 97210 (L/LL 3.2 ordinary chondrite) meteorites.

The surfaces of airless bodies are the most susceptible to thermal fatigue, as their lack of a thermally-insulating atmosphere exposes them to extreme insolation forcing. Molaro and Byrne (2012) attempted to numerically simulate the amount of internal stress experienced by a rock on Vesta, Mercury, and the Moon's surface. In particular, they estimated the amount of temperature change, per unit time ($^{\Delta T}/_{\Delta t}$) and compared to the temperature gradient ∇T within rocks having orientations at different latitudes on the surface. They found that while a rock on Vesta experienced the largest temporal temperature change, it also had the lowest ∇T. This case is opposite to that of the Moon and Mercury, in which ∇T and $^{\Delta T}/_{\Delta t}$ were highly correlated. The modeling efforts of Molaro and Byrne (2012) demonstrated that greater thermal stresses were experienced for rocks experiencing faster sunrises (i.e., shorter rotation periods). The stresses were more pronounced for airless solar system bodies farther from the Sun and on rock faces that were angled closer toward the morning sun. Daytime shadowing, especially when occurring just after local sunrise or before local sunset, was also a major contributor to increasing the temperature gradients. The authors also predict that

pre-existing cracks would contribute even more to the growth rate and shorten weathering timescales.

As noted by Molaro and Byrne (2012), the highest rates of temperature change occur on quickly rotating bodies. In the analysis of my large asteroid grain size dataset, the rotation period was a significant factor, as it correlates positively with increasing grain size. This coincides with the findings of Molaro and Byrne (2012), as they predicted greater influence of thermal fatigue for objects with more thermal cycles and faster sunrise times. For asteroids rotating more slowly than Earth, there is a particular dearth of regoliths with smaller average grain sizes (< 0.5 mm) and, in figure 2.13, a visual uptick of the minimum grain size at $P_{rot} = 10$–20 hr. This uptick could indicate a subtle turning point related to the thermal fatigue mechanism, in which asteroids with $P_{rot} < 10$ hr are susceptible to a greater number of high-rate thermal cycling. Despite the long solar days for the Moon, corresponding to thermal fatigue weathering inefficiency, the lunar regolith is one of the most well-developed in the Solar System. The fine-grained lunar regolith is consistent with an impact dominated weathering mechanism, rather than thermal fatigue (Basilevsky et al., 2015).

The thermal parameter (Θ; equation (1.8)) may intuitively seem to be useful in predicting the effectiveness of thermal fatigue on asteroid surfaces, as it can be used as a proxy for the amplitude of the diurnal temperature range. However, its formulation doesn't capture the essential information regarding the heating and cooling rates of a boulder/rock at the surface. Regolith on bodies that are very slow rotators will experience slow sunrises. As the disk of the sun creeps above the local horizon the surface temperatures slowly reach equilibrium with the insolation and a boulder would not be subject to a large rate of temperature change. This may seem paradoxical if one were only to examine the thermal parameter for a hypothetical slow rotator: for larger values of P_{rot}, Θ becomes smaller and the diurnal temperature swings are maximized. However, because this hypothetical object is slowly rotating, a point on the surface does not experience a large temporal temperature change, and the insolation change during the long sunrises and sunsets does not cause large enough spatial temperature gradients.

The grain size of M-type asteroids are, on average, 4 times higher than asteroids of the same diameter and rotation period (figure 2.13), suggesting that either regolith is not

efficiently broken down, or that smaller regolith grains are preferentially lost via one of the mechanisms in section 2.8.2. High values of Young's modulus were shown by Molaro et al. (2015) to significantly increase the efficiency of the thermal fatigue process, because stiffer materials are less able to accommodate the thermal expansion of grains. Iron-nickel meteorites, which are compositionally homogeneous could serve as an analog for M-type asteroids. Mesosiderites, a silicate-metal mixture, could prove as a heterogeneous alternative that would be more susceptible to thermal stress buildup surrounding silicate grains. Iron-nickel metal's extremely high Young's modulus, combined with possible grain heterogeneity of a metal-rich regolith should make these surfaces more susceptible to thermal cycling. By following this logic, and assuming that thermal cycling is the dominant weathering process, it would stand to reason that asteroids that are composed of metal-silicate mixtures should have fine-grained surfaces and pure metal surfaces should not have fine-grained regoliths. Since my results show that M-types harbor coarse-grained regoliths it could indicate that M-types are comprised of pure-metal surfaces. Alternatively, M-type regoliths could be silicate-metal mixtures that are subject to a process or processes that remove the fine-grained portion of regolith. Impact ejection seems the most likely, as metal targets should have a much higher strength, which would increase the overall velocities of ejecta particles relative to weaker targets (i.e., S and C-types).

2.8.2 Regolith Retention & Loss

Once formed, the regolith layer of an asteroid is held by gravitational and cohesive forces. For a spherical asteroid the force of gravity experienced at the surface decreases by a factor proportional to the diameter of the object (while holding other factors, such as the rotation period and bulk density, constant). If the object were not rotating at all, the effective gravitational potential would be homogeneous across the surface. Centrifugal forces, which are greatest at the equator of a rotating object, counteract the effective downward gravitational force at a magnitude proportional to the spin rate equation (2.15).

For a typical main-belt asteroid, the cohesive (e.g., van der Waals) forces between regolith grains smaller than $\sim$1 cm have theoretically (Scheeres et al., 2010) and experimentally (Murdoch et al., 2015) been shown to dominate over gravitational, solar radiation pressure,

and electrostatic forces. Evidence for non-zero cohesive forces acting on an asteroid surface was found by Rozitis et al. (2014) for the 1.3 km NEA (29075) 1950 DA. They calculated the strength of cohesion to be at least 64^{+12}_{-20} Pa. Cohesive forces are inversely dependent on the surface area of the regolith gains (Scheeres et al., 2010) which indicates that a regolith comprised of smaller grains may be stronger than one comprised of larger grains. The cohesive forces within a regolith alters the effectiveness and behavior of potential loss mechanisms. Regolith grains lacking cohesion could incrementally be lost at a steady rate, but the addition of these inter-particle forces makes the regolith more susceptible to large-scale structural failure — since planes of weakness will preferentially form around massive clumps of grains, after plastic deformation has occurred. As these grain structures are held in a higher energy state, even a small force exceeding the yield stress could trigger a landslide, potentially resulting in a catastrophic loss of regolith (Scheeres et al., 2010).

Several potential mechanisms can conceivably remove regolith from the surface of asteroids. Below, I review each mechanism and the effects that each has on altering the grain size distribution of an asteroid's regolith, as well as the scenarios in which each is predicted to dominate over other removal processes, if applicable. In each case, a particle is ejected from the surface when it exceeds the escape velocity, given by:

$$u_{\text{esc}} \approx \sqrt{\frac{2GM}{D_{\mathit{eff}}}}, \tag{2.14}$$

where G is the universal gravitational constant and M is the mass of the body.

Impact Ejection In addition to mechanically weathering regolith, the process of multiple meteoroid impacts may also *eject* regolith grains from an asteroid surface. Energy from a meteoroid impact upon an asteroid surface is partly transferred to individual regolith grains, resulting in a velocity distribution that depends on the size of the grains. Ejecta grains traveling at a velocity that exceeds the escape velocity of the object are permanently ejected from the surface and ultimately become interplanetary dust. The other factors, impactor mass and target mass, thus can be varied in order to predict the mass fraction of ejecta that is retained as a function of velocity (equation (2.13)).

An impact event is the most likely cause of the brightening seen for (596) Scheila, a main-belt asteroid, in December of 2010 (Ishiguro et al., 2011a). This 113 km asteroid was struck by a 35–80 m meteoroid (Bodewits et al., 2011; Jewitt et al., 2011), which produced a 10^7 to 10^9 kg cone of debris consisiting of 1–100 μm particles (Ishiguro et al., 2011b; Hsieh et al., 2012). Earlier the same year, the ∼120 m object P/2010 A2 was also observed to exhibit dust activity, as a tail of dust particles slowly drifted away for a time period exceeding several months. Both Snodgrass et al. (2010) and Jewitt et al. (2010) calculate the impact to have occurred in January or February of 2009 and the dust trail to consist of large (millimeter to centimeter) sized particles that were slow to be dispersed by radiation pressure. However, rotational instability (discussed below) via YORP spin-up could still explain the long-lived dust tail (Jewitt, 2012), but the rotation period of P/2010 A2 remains unknown.

These two observations of regolith escaping asteroid surfaces in real-time provide important knowledge about the nature of impact ejection. Knowing the size of the dust grains that were visibly detected provide an upper size limit for the regolith that was removed from the surface of Scheila, since larger grains are not traveling faster than the body's escape velocity. I can expect that the area on the surface that was struck by a meteoroid to retain 0.1 mm-sized regolith grains. This grain size is at the lower size limit that the thermal conductivity model will produce for $\Gamma \rightarrow 0$. In fact this grain size is what I calculate for the asteroids with $\Gamma < 50$ J m^{-2} K^{-1} s$^{-1/2}$. Future observations of impact ejecta events of sub-10 km asteroids should exhibit larger grains in the cloud of debris as the size of the object decreases.

Centrifugal Ejection The effective surface gravity at the equator is lower than at the poles of a spinning spherical body (e.g., Scheeres et al., 2010), because the rotating frame of reference causing a centrifugal "force" directed away from the axis of rotation:

$$g_{eff} \approx 2\pi D_{eff} \left(\frac{\pi cos^2 \phi}{P_{rot}^2} - \frac{G\rho_{eff}}{3} \right), \tag{2.15}$$

where ϕ is the latitude, in radians, and ρ_{eff} is the effective bulk density of the sphere-shaped asteroid. Regolith grains exist in a steady-state on the surface of a fast-rotator,

and a small perturbation can transfer enough energy to cause the ejection of equatorial grains where the effective gravity is near-zero (Guibout and Scheeres, 2003). It is difficult to theoretically predict whether this kind of mass-loss occurs incrementally, on a grain-by-grain basis, or catastrophically, with large chunks ejected at a time (Scheeres, 2015). Equating the gravitational and centrifugal forces at the equator of a rotating spherical body allows us to derive a critical rotational period, below which material at the equator experiences negative effective gravity:

$$P_{\rm crit} \approx \mathsf{a}/\mathsf{b}\left(\frac{3\pi}{G\rho_{\mathit{eff}}}\right)^{1/2}, \tag{2.16}$$

where, a/b is the axis ratio of a prolate ellipsoid. In the special case of a sphere, $\mathsf{a}/\mathsf{b} = 1$ and the equation (2.16) becomes an exact calculation (i.e., the "≈" is replaced by a "=") Jewitt (2012). The existence of the "spin barrier", an observed dearth of asteroids with $P_{rot} \lesssim 2.12$ hr and larger than a few hundred meters in diameter (Harris, 1996), indicates that gravitationally bound asteroids rotating more rapidly than this rate are not stable and break apart (Pravec and Harris, 2000). The mechanism known as YORP (Yarkovsky-O'Keefe-Radzievskii-Paddack; Bottke et al., 2006, and references therein) can increase the rotation rate of an asteroid enough such that $g_{\mathit{eff}} \approx 0$ across most of the surface (Yu et al., 2018).

Dust activity surrounding P/2013 P5, including multiple dust tails as observed in September 2013, is thought to originate from rotational instability (Jewitt et al., 2013). The multiple dust tails of P/2013 P5, which are comprised of particles ranging in size from 10 to 100 μm, are roughly co-planar and amount to 10^{-4}–10^{-3} of the total mass of the body ($D_{\mathit{eff}} \approx 240$ m if $p_V = 0.29$). Although the rotational period of P/2013 P5 is undetermined, the morphology and slow ejection speed (i.e., comparable to its escape velocity, ∼0.3 ms^{-1}; Jewitt et al., 2013) of the dust activity points to excess centrifugal forces ejecting the regolith (Jewitt et al., 2013). Increased observations of the of dust activity for all active asteroids can support efforts in placing limits on the frequency of centrifugal ejection and the amount of dust (and size distribution) that is lost via this mechanism.

Rapidly rotating asteroids (with $P_{rot} \approx 2.2$ hr) are most at-risk for centrifugal regolith ejection. These objects are likely to have been spun up by thermal torques via YORP, rather

than being born at a high spin rate (Pravec et al., 2008). Ejection of surface material has been observed for P/2015 P5 to occur incrementally over several months and attributed to rotational instability of regolith (Hainaut et al., 2014). The existance of cohesion on asteroids with short rotation periods has important implications for the failure criterion and nature of mass shedding events. Large-scale chunks of material held together by cohesion are thought to discretely de-laminate off the asteroid as a result of chains of structural failure at depth.

Two fast rotators in my sample, 1950 DA and Amun, posses regolith characteristics at completely opposite ends of the observable range of my sample. Amun, which is possibly completely void of regolith, may have always been as such. Another possibility is that Amun had been part of a 1950 DA-like body in the past, in which it was a rubble pile held together by cohesive forces, and was subsequently and periodically spun-up such that all the loose granular material was shed as a consequence. In this scenario, I might expect 1950 DA to lose a portion of its regolith as its rotation rate incrementally increases and structural failure occurs. In the future, thermal inertia estimates of these rapid rotators may provide insight as to the efficiency of centrifugal ejection and the cohesive strength of rubble pile asteroids.

Electrostatic Levitation/Ejection Regolith grains can potentially become charged via heterogeneous exposure to ionized solar wind particles. As one side of the grain is positively charged from solar wind particles an electric field differential could build up enough to exceed the cohesive forces of other grains. Ignoring cohesive forces, a grain with radius on the order of $r_g^{E_c}$ experiences electrostatic levitation when the electric field, E_c, is strong enough to liberate it from the surface, where it is kept by gravity (Lee, 1996):

$$r_g^{E_c} \sim \frac{2qE_c}{3\pi g_{eff}\rho_{grain}}, \tag{2.17}$$

in which g_{eff} is defined in equation (2.15). Regolith grains can become charged by a global electric field or via local terminator passage. On Eros, the latter is the preferred method of charging — due to its high spin obliquity, the equatorial regions experience high rates of change in the illumination conditions.

The NEAR spacecraft mission to (433) Eros offered spatially resolved images of regolith "ponds", which were later interpreted to consist of smal grains that collected in low lying topographical areas of greater (negative) gravitational potential (Robinson et al., 2001; Dombard et al., 2010). More disk-resolved images of NEAs having differing illumination conditions will provide invaluable insight into the nature of electrostatic levitations. Jewitt (2012) notes that no clear example of active asteroid losing regolith dust via electrostatic forces has been identified, which could be attributed to possible slow and incremental (uniformitarian) nature of the process that would theoretically generate dust ejection that is undetectable on faint asteroids.

Radiation Pressure Sweeping The momentum imparted by many solar photons absorbed by a regolith grain could be enough to lift it from an asteroid surface and result in ejection. Jewitt (2012) calculated the maximum size of a grain, in μm, that could theoretically be removed from resting on a flat asteroid surface as a function of D_{eff}, ρ_{eff}, and $R_{\rm AU}$ (equation (2.18)). Using $\rho_{eff} = 2000$ kg m^{-3} as a nominal effective bulk density, it can be shown that a 1 km asteroid at 3 AU should be void of grains smaller than about 1 μm:

$$r_g^{\beta} < \frac{GM_{\odot}}{g_{eff} R_{\rm AU}^2}. \tag{2.18}$$

The nature of a regolith layer most likely means that individual regolith grains are wedged between other grains, and/or cohesive forces act such that grains are stuck to the surface and must be "plucked" before ejection via radiation pressure takes over. In this scenario, electrostatic forces can aid and may even be necessary to isolate and levitate a grain as it is carried away. Generally, the asteroid must be close to the Sun and, as stated above, levitation is most likely to happen for grains close to the terminator where electric field gradients are stronger.

2.9 Conclusions

At the beginning of this chapter I had hypothesized that both meteoroid impacts and thermal cycling were relevant processes that act to mechanically weather asteroid regolith.

In section 2.7.2 I presented results of an analysis as part of my test to determine whether asteroid size and rotation period were important factors in affecting regolith grain size. I determined that both factors were statistically relevant and thus am able to support the hypothesis that both the above mechanisms are relevant for regolith degradation.

Chapter 3

Regolith Space Weathering

3.1 Introduction

High-energy particles, such as solar wind ions and micrometeoroids, alter the surfaces of asteroids and other airless Solar System bodies (Hapke, 2001; Pieters and Noble, 2016). Evidence for space weathering on Earth's moon can readily be observed: Tycho crater, a large impact feature in the southern hemisphere, features recently excavated bright material that contrasts against the darker surroundings (Gold, 1955). However, the concept of space weathering surfaced after the Apollo missions returned samples of the lunar regolith (e.g., Conel and Nash, 1970; McCord and Johnson, 1970) and remote sensing of the spectral properties become more sophisticated (Pieters et al., 2000; Taylor et al., 2001). The "lunar style" of space weathering is characterized by darkening, spectral reddening, and decrease in absorption band strength (Adams and McCord, 1971). The exact amount of observed variance in these band parameters is distinct between the anorthositic highlands and basaltic Mare (Pieters et al., 2000), and is specifically dependent on the amount of FeO in the regolith/rock (Morris, 1978; Lucey et al., 1998). The source of these spectral effects has been identified as sub-micron or nano-phase iron ($npFe^0$) particles that exist in the altered rims of regolith grains, formed by the condensation of vapor from solar wind and/or micrometeorite irradiation (Taylor et al., 2001; Hapke, 2001). This space weathering mechanism, and its spectral effects, were subsequently used to explain a mismatch between meteorite and asteroid spectra.

Spacecraft visits to a small number of asteroids have provided evidence for space weathering on their surfaces. On October 29, 1991, the spacecraft Galileo flew by the asteroid (951) Gaspra, taking images of its surface from within 1,600 km (figure 3.1). From these images of Gaspra's surface, which is dominated by silicates, Helfenstein et al. (1994) showed that bright, spectrally less-red (fresh) regolith concentrated on crater ridges and darker, spectrally redder (weathered) material occurred mostly on downslope areas. The spectrally weathered regolith also exhibited up to 30% reduction in spectral contrast, compared to fresh surfaces. Similarly, the Galileo mission flew by main-belt asteroid (243) Ida on August 28, 1993, and collected images that revealed a space weathered surface Sullivan et al. (1996). Veverka et al. (1996) characterized two different-colored terrains: one darker (by 1%) and redder, with weaker absorption bands (in low-lying areas) and a brighter, less-red terrain that had 5% stronger absorption bands (e.g., Azzura crater, other impact sites, and their associated ejecta). Near-earth asteroid (433) Eros, the primary target of the NEAR-Shoemaker mission, was seen to have large variations in albedo and subtle color variations across the surface (Murchie et al., 2002; Bell et al., 2002). Clark et al. (2001) showed that the northern slopes of the Psyche crater contained much of the brighter material and could be partly, but not fully, explained by variations in grain size or mineralogy, leading them to posit that a space weathering reddening effect occurred before brightness changes. Ishiguro et al. (2007) mapped the entire surface of the NEA (25143) Itokawa from images gathered by the sample-return mission, Hayabusa, and managed to correlate brighter, bluer areas with steeper surface slopes, which are associated with recent regolith mobilization and/or impact events. These bright regolith patches are less common than the weathered regolith (Hiroi et al., 2006).

Ever since astronomers have been characterizing the colors and spectra of asteroids, there has been an apparent mismatch between the most common taxa of asteroid, the S-type, and the most common meteorite group, the ordinary chondrites (OCs; see Chapman, 1996, for a comprehensive review). This discrepancy was resolved after the discovery and classification of Q-types, which exhibit spectral slopes and absorption bands that resemble those of the OCs. These Q-type asteroids were seen only to exist in either near-Earth space or Mars-crossing orbits. Binzel et al. (2010) used this observation to hypothesize that Q-types are

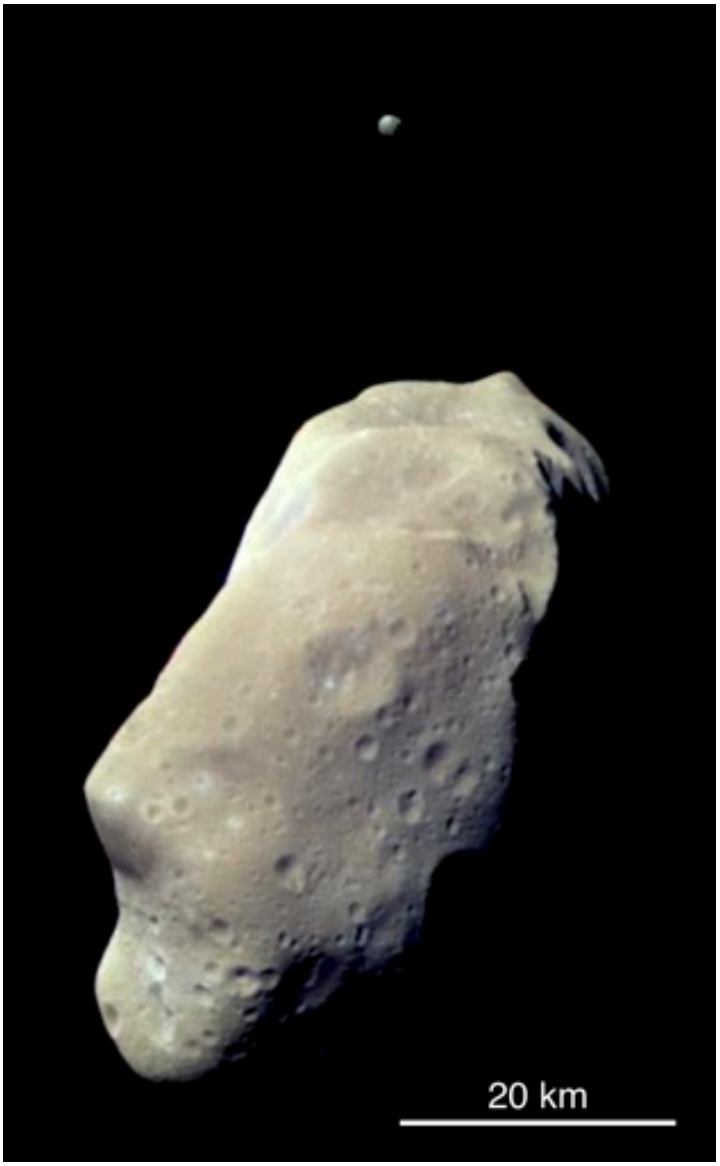

(a) Ida and Dactyl

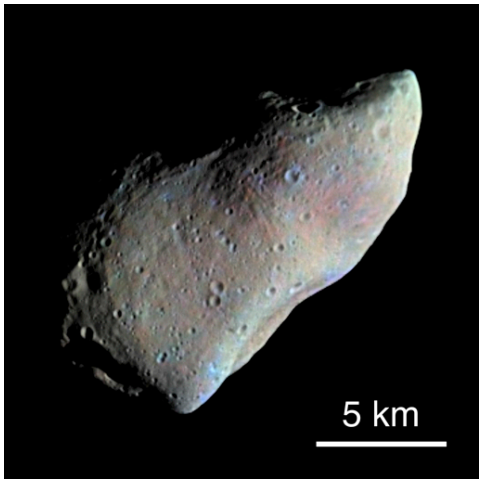

(b) Gaspra

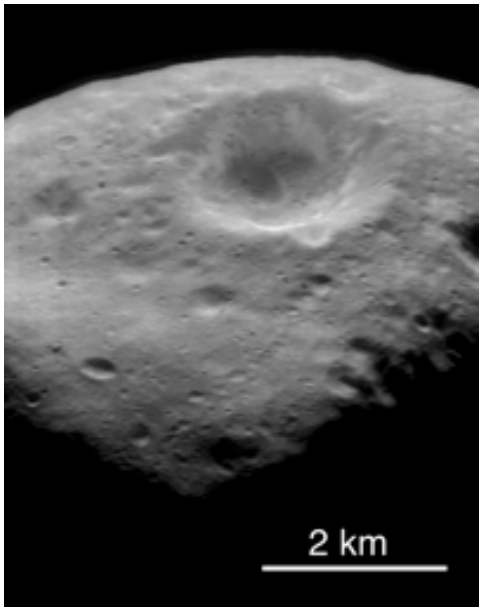

(c) Eros

Figure 3.1: False-color images of Ida, its moon Dactyl (a) and Gaspra (b) from the Galileo orbiter and a greyscale image of Eros (c) from the NEAR mission.

evolved S-types that have had significant resurfacing via tidal interactions during close-Earth encounters. S-complex asteroids, as opposed to the C-/X-complex asteroids[1] (Bus and Binzel, 2002b; DeMeo et al., 2009), have remained the focus of most space weathering studies due to diagnostic spectral features that allow for distinguishing several sub-types and the mineralogical interpretation of individual objects. Thus, mineralogic interpretations of asteroid spectra must be studied with regard to space weathering in order to be understood more completely.

In this work, I build upon the current knowledge of space weathering while utilizing large spectral datasets of both meteorites and asteroids, in order to characterize the alteration caused by space weathering on silicate-dominated asteroids. I am to construct a procedure for quantifying the degree of alteration seen in asteroid reflectance spectra at the population level, and use it to investigate influential factors that determine the effectiveness of space weathering. Following an approach in Moroz et al. (1996), I track spectral changes from meteorites to asteroids using two band parameters diagnostic of space weathering: spectral slope and band depth. A quantitative approach to measuring the degree of alteration due to space weathering of an asteroid, called the Space Weathering Index (SWI), is developed and applied to spectral data for several hundred objects. This index is used in replication of past studies, with use taxonomic classification of asteroids, to quantify the dependence of space weathering on various factors. I aslo perform an analysis of the albedo variation among the objects in my dataset, since space weathering is also known to progressively darken surfaces. Factors that have been shown to be relevant to space weathering, such as the estimated solar wind exposure, perihelion distance of NEAs, and composition, are considered in a multi-linear fitting model with the SWI as the dependent variable. I also investigate the potential influence of grain size on the SWI. Finally, I attempt to reconcile previous estimates of the timescale for which space weathering acts, by using members of asteroid families with age estimates.

[1]The C-/X-complex asteroids are unlike the S-complex in this sense because of the complex nature of establishing mineralogical ground-truth due to their mostly featureless spectra.

3.2 Space Weathering Background

3.2.1 Laboratory Studies

Starting in the mid-1990's, laboratory experiments were designed to mimic the environment and mechanism of space weathering by irradiating samples with high-energy lasers (Moroz et al., 1996). Since then, several irradiation (laser and ion) experiments have been conducted on both meteorite and terrestrial silicate samples (e.g., Yamada et al., 1999; Marchi et al., 2005; Brunetto et al., 2006; Vernazza et al., 2006; Lazzarin et al., 2006; Fulvio et al., 2012). The spectral changes of laser irradiated olivine and pyroxene (enstatite) samples closely resemble the spectral changes occurring on the Moon (Sasaki et al., 2001) and asteroids (Hiroi and Sasaki, 2001). Microscopic images of these samples indicate that spectral changes are caused by the growth of npFe^0 particles (Sasaki et al., 2003) and are produced more effectively in olivine than in pyroxene (Sasaki et al., 2002). An experiment to perform the controlled growth of npFe^0 particles was sucessfully carried out by Kohout et al. (2014): in which terrestrial olivine powders were subject to a two-step heating procedure. While this approach may not simulate the exact mechanism that plays out on asteroid surfaces, the formation of npFe0 in these olivine samples additionally supports the idea that these particles are directly connected with the optical changes associated with space weathering (Hapke, 2001).

Material on an asteroid surface or in the laboratory is said to reach optical maturity after a characteristic timescale in which there are no further measurable changes in its reflectance properties (Gaffey, 2010; Shestopalov et al., 2013). An optical maturity timescale for micrometeoroid impacts and solar wind irradiation was estimated for laboratory samples — $\sim$1 Gyr and $<$ 1 Myr, respectively (Sasaki et al., 2001; Brunetto and Strazzulla, 2005). However, surface processes such as impact gardening (Shestopalov et al., 2013) may reveal fresh material from beneath, which mitigates the perceived disk-integrated spectral changes of space weathering and lengthens the effective maturation timescale.

Transmission election micoscope images of returned lunar grains show npFe^0 in the size range 1–10 nm within depositional rims and sub-microscopic particles in agglutinates (Pieters et al., 2000; Keller and Clemett, 2001). Samples returned from Itokawa by the

Hayabusa spacecraft showed regolith grains containing np(Fe,Mg)S particles in a 30–60 nm-thick composition rim (Noguchi et al., 2014). The sizes of these nanophase particles ranged from 1–4 nm, which is very similar to the ranges found in the lunar samples (Noble et al., 2005). Using synthesized analog soils Noble et al. (2007) showed that smaller (< 10 nm) npFe^0 particles will darken and redden Vis-NIR spectra, whereas larger (> 40 nm) npFe^0 particles will only darken. This finding may explain the different space weather styles described for the asteroids visited by spacecraft (i.e., Gaffey, 2010).

3.2.2 Asteroid Observational Studies

Observations of asteroid families, which exhibit a wide range of dynamical ages, offer a novel way to quantify the rates of space weathering and compare them to the estimated timescales from lab experiments. In particular, Sloan Digital Sky Survey (SDSS) colors of family members have been used to track spectral slope changes across time (Jedicke et al., 2004). The strong correlation between the average color of a family and its dynamical age has been used to calculate a space weathering timescale of over 2000 Myr (Jedicke et al., 2004) and a reddening rate of 0.01 $\mu m^{-1} \times \log_{10} t$ (Nesvorný et al., 2005). Further studies used very young asteroid clusters (< 10 Myr) to re-calculate timescales of 570 ± 220 Myr (Willman et al., 2008) and 960 ± 160 Myr (Willman et al., 2010), using differing models that partly account for regolith gardening, causing the overturn of unweathered regolith via small impacts. However, using photometric colors, it is difficult to isolate the effect of composition on asteroid colors in order to isolate the effect that space weathering has on the color (Jedicke et al., 2004).

Several investigatiors have used average spectral slope over visible wavelengths to study the space weathering effects on reddening for S-type asteroids. Marchi et al. (2006a) identified a positive trend, among MBAs, between the spectral slope and the amount of solar wind exposure (using the time-averaged heliocentric distance as a proxy). Their follow-up study identified the trend between the perihelion distance of NEAs and the ratio of Sq- and Q- to S-type asteroids (Marchi et al., 2006b), which widely vary in spectral slope. Using average spectral slopes of families, Vernazza et al. (2009) inferred a two-step process consisting of 1 Myr of rapid reddening due to solar wind bombardment and 2000 Myr of gradual

reddening via micrometeoroid bombardment. They also used spectral band analysis to show that a greater olivine abundance corresponded to higher spectral reddening. However, these analyses did not account for the observed variation in spectral slope with both phase angle (i.e., phase reddening; Sanchez et al., 2012) and grain size Adams and Filice (1967). Generally, non-compositional effects should be accounted for when interpreting spectral slopes in the context of space weathering.

An inverse trend between size and absorption band depth for asteroids smaller than 100 km was observed by Gaffey et al. (1993). Smaller asteroids have statistically shorter collisional lifetimes (Bottke et al., 2005), leading Clark et al. (2002) to postulate that this inverse trend of band depth with size was due to the alteration of surfaces from space weathering. However, the grain size of silicate powders is also known to influence the band depth (Adams and Filice, 1967), as smaller grains have weaker absorption bands. Thus, the correlation of band depth with asteroid size (see chapter 2) can cause similar changes in band depth. Additionally, there is a known inverse relationship between grain size and albedo for < 0.5 mm silicate grains (Adams and Filice, 1967) that is comparable to the changes in albedo due to space weathering. Studies that have analyzed albedo and spectral slope (Gaffey et al., 1993; Binzel et al., 2004; Rivkin et al., 2011; Thomas et al., 2011, 2012) attribute changes in these parameters to space weathering without accounting for grain size effects. For example, Thomas et al. (2011) and Thomas et al. (2012) noted a decrease in spectral slope for small (< 5 km) Koronis family members, which is close to the diameter (≈ 10 km) at which regolith grain size is known to increase with decreasing object size (chapter 2) — thus, one would expect smaller asteroids to be made redder from the presence of larger-sized regolith grains.

3.3 Methodology

My study consists of analyses that can be loosely broken into four steps:

1. I calculate and use diagnostic space weathering band parameters (spectral slope and band depth) of meteorites to represent values for "un-weathered" asteroid spectra.

2. I identify space weathering "pathways" in spectral slope and band depth parameter space from the spectral measurements of laboratory-irradiated samples (meteorites and terrestrial minerals).

3. For a large set of asteroids, I calculate an object's location along these pathways from the unweathered band parameters as a measurement of the degree of space weathering — which I call the space weathering index (SWI).

4. Finally, I investigate potentially important factors that contribute to increased space weathering on asteroids using my SWI dataset.

I focus the analyses on asteroid and meteorite groups that represent three distinct mineralogies: olivine-rich, pyroxene-dominated, and ordinary chondrite meteorites (roughly equal amounts of olivine and pyroxene). In the near-infrared, both of these minerals exhbit overlapping absorbtion bands around 1 μm (B_I), with pyroxene showing an additional absorption band (B_{II}) at 2 μm (Burns, 1993). The band area ratio, or BAR, (defined as the

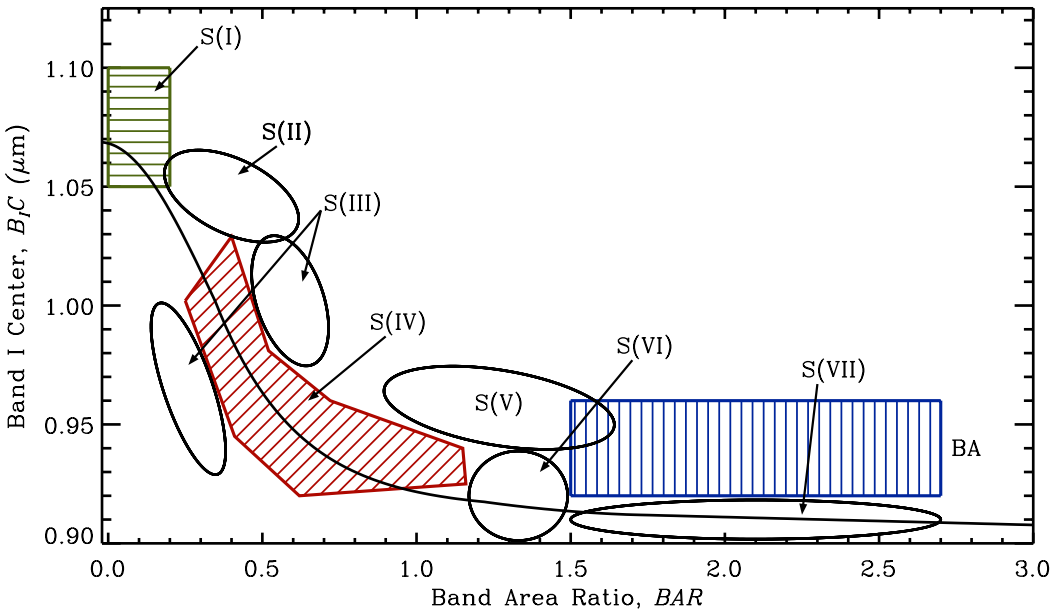

Figure 3.2: Band parameter selection criteria of the three mineralogical groups used in this study. The boxes with hatches define the Gaffey et al. (1993) sub-types that represent olivine-rich (S(I); green), ordinary chondrite (S(IV); red), and basaltic achondrite (BA; blue) meteorite analogs. The solid curve shows the olivine-orthopyroxene mixing line from Cloutis et al. (1986).

area of B_{II} divided by the B_I area) is thus useful in approximating the relative abundance of olivine and pyroxene. Gaffey et al. (1993) used BAR and the center wavelength of B_I (B_IC) to define asteroid sub-types that were associated with distinct mineralogy. Olivine-rich asteroid spectra, which exhibit shallow or no B_{II}, have small BAR values and B_IC approaching 1.1 μm, whereas pyroxene-dominated spectra generally have $BAR > 1.5$ and $B_IC \sim 0.94$ μm (figure 3.2). Olivine-rich mineralogies are often associated with A-type asteroid taxa Sunshine et al. (2007), but I also take care to select any asteroid with band parameters that fall within the S(I) sub-region, which may include objects not classified as A-types. Pyroxene-dominated asteroid spectra are very well known to be associated with the V-type taxa, named as such in order to relate to the minor planet (4) Vesta. Many V-type asteroids are found within the Vesta dynamical family, yet many have been discovered outside the region of the Main Belt in which Vesta resides (Moskovitz et al., 2010; Hardersen et al., 2018). Nevertheless, all V-types exhibit very strong pyroxene absorption bands that have band parameters that fall within the "BA" sub-field defined by (Gaffey et al., 1993). Gaffey et al. (1993) also defined a "boot" shape, shown as the red region in figure 3.2, that represents the band parameters of ordinary chondrite meteorite group.

My spectroscopic analysis described below is focused within the visible and near-infrared (0.4–2.5 μm) wavelength range. This spectral region contains both B_I and B_{II} absorption features and also records spectral slope changes due to space weathering (and the other effects described in section 3.2). Recent work has identified UV slope changes that are particularly sensitive to space weathering, but the UV region does not capture the absorption features. I incorporate visible wavelengths in my analysis, when available, since the widely used Bus-DeMeo taxonomy requires information at these wavelengths in order to classify a spectrum.

3.3.1 Telescopic Survey

Fifty-one asteroids from chapter 2 that exhibit silicate absorption features are targeted here in order to obtain diagnostic band parameters of objects for which I have regolith grain size estimates. Near-infrared spectra were acquired using SpeX and the Near Infrared Camera Spectrometer (NICS) instruments on the 3-meter NASA Infrared Telescope Facility (IRTF; Mauna Kea, Hawaii) and 3.6-meter Telescopio Nazionale Galileo (TNG; La Palma, Spain),

respectively. SpeX is a medium resolution spectrograph that operates in the ∼0.7–2.5 μm wavelength range with a resolving power of $\frac{\lambda}{\Delta\lambda} \approx 200$ (Rayner et al., 2003) in Prism mode. Similarly, NICS observes in the ∼0.7–2.5 μm wavelength range, with $\frac{\lambda}{\Delta\lambda} \approx 500$ using the Amici dispersers[2].

Observations Each observing run targeted objects that were bright enough to achieve high signal and, optimally, could be observed near the local meridian at some time that night. In addition to these asteroids, solar-type stars (G dwarfs with solar-like colors: B-V ≈ 0.62 and V-K ≈ 1.49) that were located near (often within 2°) the asteroid were targeted for observation. For each object the spectroscopic slit was aligned with the the angle between the great circle through a celestial object and the zenith. This is done in order to ensure that the direction of atmospheric dispersion is aligned with (parallel to) the slit, measured at 0.8" x 15". The telescope is nodded in order to move the target (asteroid or star) between two slit positions (A and B), separated by 7.5", in succession (A to B then B to A, etc.). At least 3 A-B pairs are taken per target visit, in order to mitigate random effects during the reduction steps (Rayner, 2017). Asteroid exposure times are calculated before an observing run, based on the visible brightness, to achieve a minimum signal-to-noise ratio (SNR) of 100 across absorption features. Individual exposure times are limited to less than 120 s to limit the effect of atmospheric variability. In order to bracket the asteroid observations, stellar spectra were taken proximate in time (within 16 min), before and after each visit. These solar analog spectra were used to correct for the Sun's spectrum and absorption by Earth's atmosphere using the reduction procedure described below. If a faint asteroid required more than 16 total minutes of integration (∼30 minutes of real time), these time blocks were broken up such that the solar analog was visited within a half hour of any given asteroid integration. Observational information, integration times, and solar analog stars used for all spectra are given in table 3.1.

Extraction/Reduction All raw spectra from images were reduced using SpeXTool v4.1 (Spectral EXtraction TOOL; Cushing et al., 2004), which prepares calibration frames

[2] http://www.tng.iac.es/instruments/nics/spectroscopy.html

Table 3.1: Observing Information for EMM Spectral Survey

Object	Obs. Date	UT Start	$R_{\rm AU}$	α (°)	t_f (sec)	# Frames	Airmass	Star
(80) Sappho	02-Feb-2016	10:56:25	2.60	6.0	20	8	1.055	SAO 117473
(167) Urda	12-Aug-2016	14:56:12	2.78	11.8	30	8	1.326	SAO 42627
(183) Istria	04-Jul-2016	13:46:52	2.81	9.9	20	8	1.249	SAO 156960
(270) Anahita	02-Feb-2016	14:08:48	2.52	6.9	30	8	1.272	SAO 119865
(295) Theresia	04-Jul-2016	13:20:25	2.95	11.6	20	6	1.206	SA 102-1081
(349) Dembowska	12-Aug-2016	10:52:44	2.77	4.5	6	8	1.455	SA 102-1081
(376) Geometria	25-Nov-2015	14:40:36	2.68	13.3	60	8	1.104	SAO 76348
(391) Ingeborg	02-Feb-2016	12:05:31	2.88	13.2	90	8	1.313	SAO 78941
(487) Venetia	12-Aug-2016	14:40:35	2.48	19.6	20	8	1.120	BD+24 1873
(509) Iolanda	22-Feb-2015	11:00:30	3.33	9.2	120	6	1.260	SAO 93914
(562) Salome	22-Feb-2015	12:30:50	3.27	12.2	120	8	1.068	HD 283682
(651) Antikleia	15-Mar-2015	15:10:12	3.31	8.6	90	6	1.448	SAO 75241
(670) Ottegebe	12-Aug-2016	14:23:21	2.33	11.1	30	8	1.330	SAO 187733
(793) Arizona	31-Oct-2016	05:30:15	2.50	10.8	40	12	1.539	SAO 147941
(876) Scott	12-Aug-2016	05:40:27	3.03	18.9	120	8	1.148	SAO 190520
(883) Matterania	02-Feb-2016	11:17:44	2.66	1.3	90	8	1.023	HD 211064
(918) Itha	12-Aug-2016	13:42:51	2.33	9.5	30	8	1.264	HD 217340
(1077) Campanula	25-Nov-2015	11:34:48	2.12	4.9	120	8	1.069	SAO 146870
(1140) Crimea	12-Aug-2016	14:05:21	2.48	21.3	30	8	1.153	SAO 165755
(1142) Aetolia	15-Mar-2015	11:08:56	3.10	6.4	120	6	1.136	HD 198395
(1152) Pawona[a]	26-Jan-2017	07:40:48	2.38	1.9	120	8	1.284	HD 174941
(1188) Gothlandia	02-Feb-2016	15:24:15	2.43	9.7	30	8	1.424	SAO 146484
(1224) Fantasia	02-Feb-2016	10:21:33	2.28	6.8	120	8	1.033	SAO 160549
(1291) Phryne	12-Aug-2016	06:39:58	2.82	17.3	30	8	1.179	SAO 164559
(1299) Mertona	12-Aug-2016	08:53:56	3.08	11.2	120	10	1.249	SAO 146153
(1310) Villigera	27-Nov-2016	13:57:22	1.54	36.7	30	8	1.310	SA 110 361
(1412) Lagrula	25-Nov-2015	15:07:58	1.97	24.7	60	8	1.026	SAO 141647
(1443) Ruppina	12-Aug-2016	11:05:15	2.76	1.0	30	4	1.195	SAO 146888
(1536) Pielinen	02-Feb-2016	14:26:18	2.48	7.5	120	8	1.305	SAO 129163
(1553) Bauersfelda	12-Aug-2016	07:29:17	3.18	10.7	120	15	1.375	SAO 187292
(1577) Reiss	02-Feb-2016	15:52:12	2.36	11.0	120	4	1.579	SAO 163482
(1644) Rafita	31-Oct-2016	06:43:40	2.41	6.7	90	12	1.181	SAO 118036
(1723) Klemola	22-Feb-2015	14:57:09	2.91	15.9	120	5	1.100	HD 121935
	04-Jul-2016	12:41:58	3.10	4.0	120	7	1.360	BD+13 2289
(1741) Giclas	12-Aug-2016	11:25:19	2.80	4.2	30	8	1.224	SAO 118036
(1762) Russell	12-Aug-2016	12:25:45	2.77	5.6	30	4	1.183	BD+23 2150
(1802) Zhang	12-Aug-2016	09:30:21	2.91	6.7	90	8	1.289	TYC 1401-234
(2110) Moore-Sitterly	02-Feb-2016	12:42:22	2.57	2.5	120	15	1.100	HD 80653
(2111) Tselina	12-Aug-2016	06:13:10	3.16	16.3	75	7	1.160	BD+10 2130
(2123) Vltava	12-Aug-2016	06:59:45	2.79	12.9	90	8	1.408	BD+10 2221
(2144) Marietta	12-Aug-2016	09:56:05	2.90	2.7	30	8	1.246	SAO 144137

Table 3.1 – continued

Object	Obs. Date	UT Start	$R_{\rm AU}$	α (°)	t_f (sec)	# Frames	Airmass	Star
(2156) Kate	02-Feb-2016	14:56:55	2.36	5.0	90	8	1.552	HD 178489
(2855) Bastian	27-Nov-2016	13:23:45	2.04	15.0	60	10	1.084	SAO 191552
(2912) Lapalma	12-Aug-2016	12:42:23	2.43	11.3	90	8	1.990	SAO 164224
(3249) Musashino	25-Nov-2015	12:07:02	1.85	2.7	120	8	1.084	SAO 59046
(3536) Schleicher	25-Nov-2015	10:15:30	2.26	10.7	120	20	1.120	SAO 27446
(3726) Johnadams	12-Aug-2016	13:12:39	2.65	12.4	105	8	1.121	BD+16 128
(4352) Kyoto	04-Jul-2016	14:35:30	2.72	18.1	120	8	1.336	BD+16 128
(4611) Vulkaneifel[a]	23-Jan-2017	07:37:15	2.25	22.7	120	8	1.073	BD+22 1932
(4628) Laplace	15-Jun-2015	11:09:19	2.78	11.8	120	6	1.393	SAO 163208
(4713) Steel	22-Feb-2015	08:33:10	1.97	17.9	90	6	1.117	BD+16 128
(28126) Nydegger	25-Nov-2015	12:42:14	2.00	4.9	120	36	1.134	SA 98-978

[a]Data acquired with the TNG telescope.

(combines and normalizes flatfield exposures and creates an arc image suitable for wavelength calibration) and extracts spectra (extracts and wavelength calibrates asteroid and standard star spectra). Pairs of spectra taken in the A and B positions are extracted together, in order to remove (by subtraction) the sky brightness. The star and asteroid spectra are divided (star/asteroid) in order to reveal the spectral reflectance (in percentage) of the asteroid. As the telescope moves between the solar analog star and asteroid, small instrument flexures cause non-negligable shifts of the spectra on the detector. Thus it is necessary to perform sub-pixel scale spectrum shifts in order to properly match the wavelength values; failing to do so results in spurious spikes in the final spectral reflectance spectrum (e.g., § 2.2 in Gaffey et al., 2002). Specifically, the shift is calculated by minimizing the residual difference between the raw stellar and asteroid spectra for the wavelength region around 1.32 μm, where there is a steep flux drop-off due to the 1.4 μm telluric absorption.

Telluric Feature Removal During observations, care is taken to ensure that star and asteroid frames are taken at similar airmass — which minimizes any differences in the atmospheric conditions between the two celestial objects. However, if left uncorrected, large variations in atmospheric water vapor often produce very noticeable differences in the output reflectance values. I minimize this effect by using modelled transmission spectra of Earth's atmosphere (ATRAN; Lord, 1992) for varying amounts of precipitable water. Following the approach of Clark et al. (2004), I minimize the residual difference between the ATRAN spectrum and stellar/asteroid spectrum in the telluric regions (notably at ∼1.4 μm and ∼1.85 μm) by iterating across different values of precipitable water. The best-fit ATRAN spectrum is used to divide the stellar and asteroid spectra before the final reflectance is calculated: i.e., (star/ATRAN)/(asteroid/ATRAN). Final, reduced spectra are plotted in panels (a) and (b) of figure 3.3.

3.3.2 Other Data Sources

Data from large asteroid spectral surveys are mined, including half a dozen sets of published spectra that can be accessed using NASA's Planetary Data System. Unpublished near-infrared (NIR; ∼0.7–2.5 μm) spectra, taken with the SpeX instrument on the IRTF (Rayner

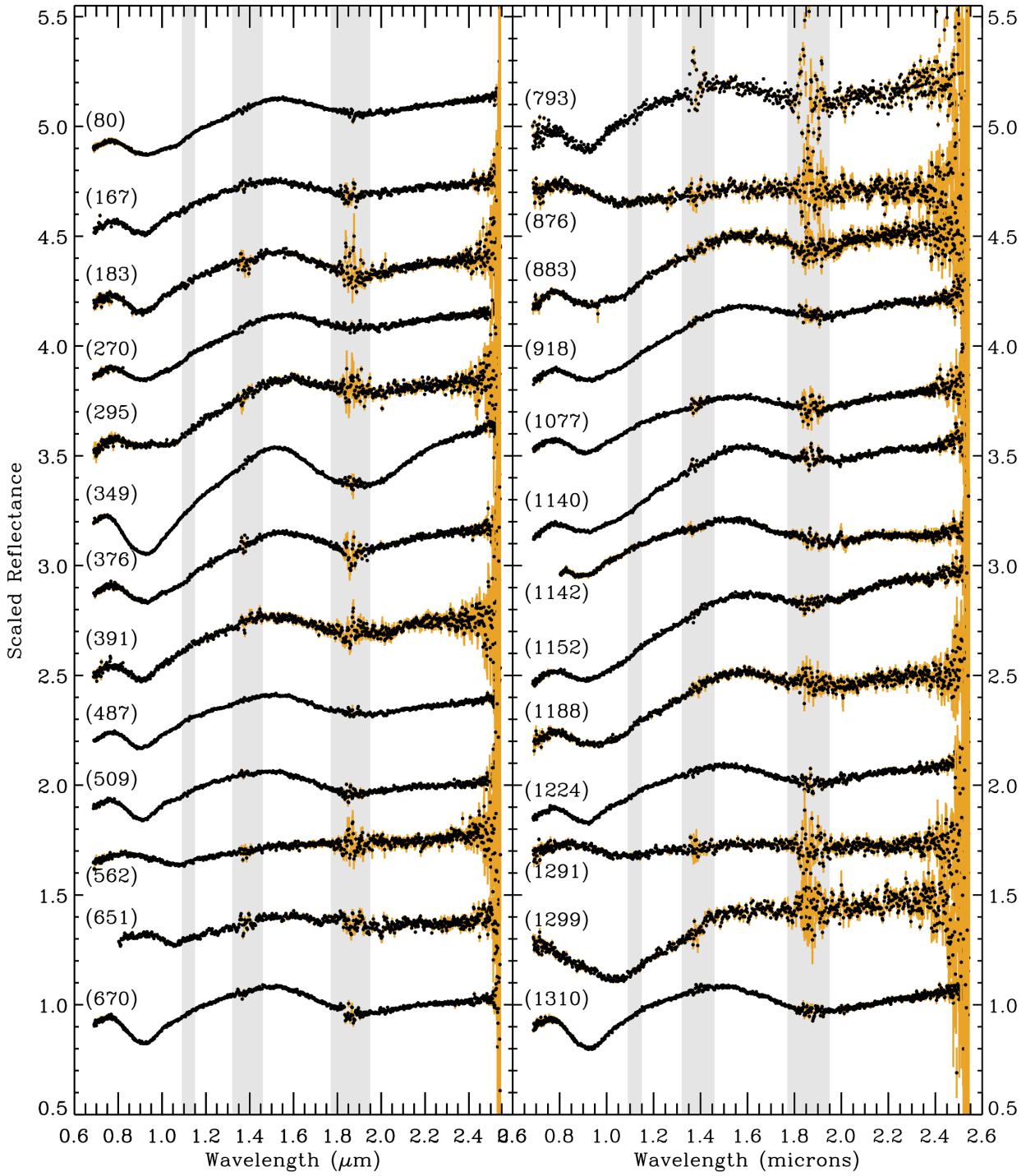

(a)

Figure 3.3: Near-infrared reflectance spectra of 49 asteroids acquired with the IRTF and 2 with the TNG, as part of this study (table 3.1). The black points and orange bars show the reflectance value and the 1σ uncertainty. Grey vertical areas mark the telluric water regions, in which the SNR is often reduced.

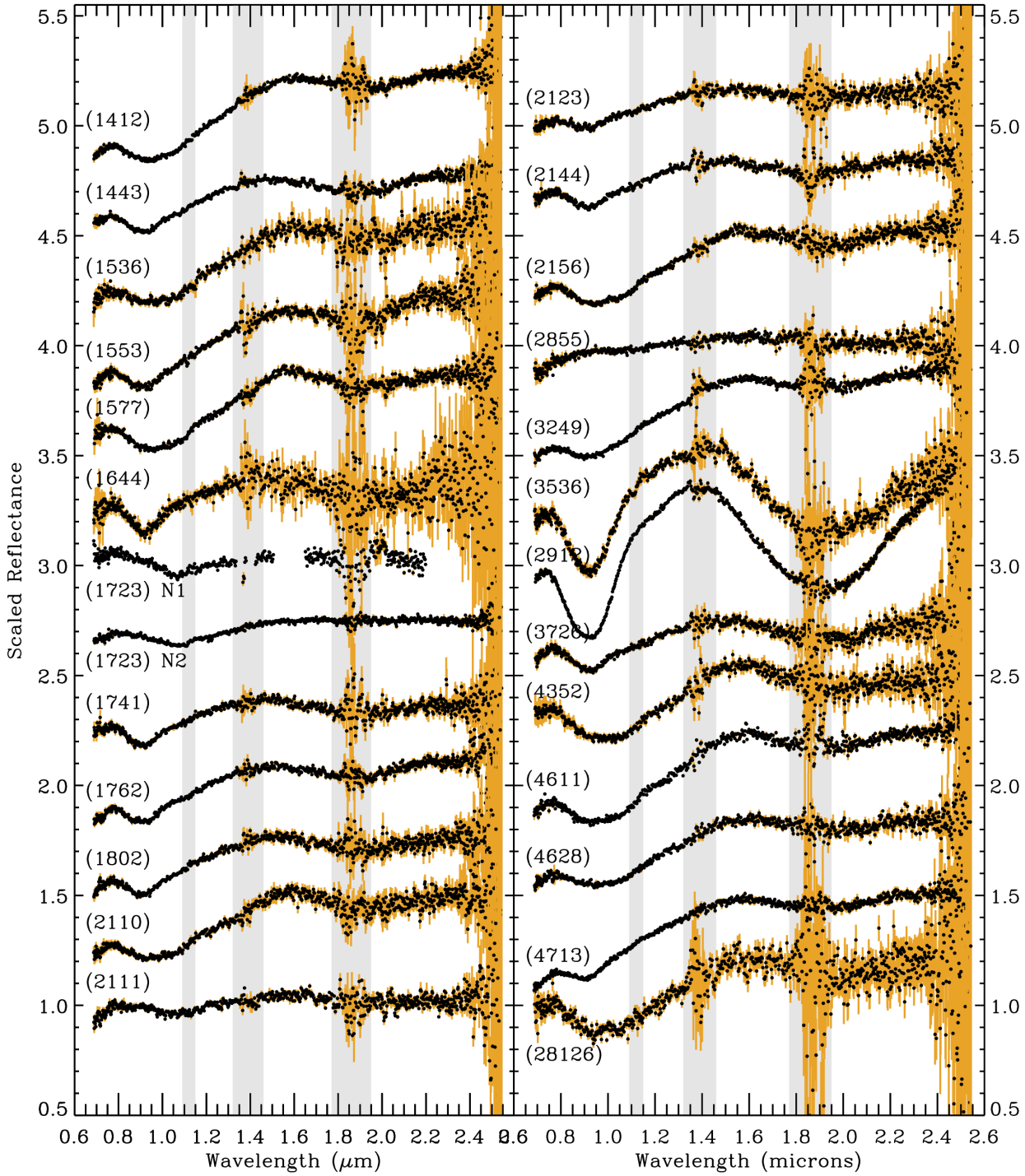
Scaled Reflectance
Wavelength (μm)
Wavelength (microns)
(1412)
(1443)
(1536)
(1553)
(1577)
(1644)
(1723) N1
(1723) N2
(1741)
(1762)
(1802)
(2110)
(2111)
(2123)
(2144)
(2156)
(2855)
(3249)
(3536)
(2912)
(3728)
(4352)
(4611)
(4628)
(4713)
(28126)

(b)

et al., 2003), are publicly available through the MIT-UH-IRTF Joint Campaign for NEO Reconnaissance (Binzel et al., 2006) for both main-belt and near-Earth asteroids.

SMASS The two phases of the Small Main-belt Asteroid Spectral Survey (SMASS I and II; Xu et al., 1995; Bus and Binzel, 2002a) contain the largest single collection (1870 objects) of visible (Vis; ∼0.44–0.92 μm) asteroid spectra available.

NEOSpec Also referred to as MITHNEOs in other works, the MIT-UH-IRTF Joint Campaign for Spectral Reconnaisance (Binzel et al., 2006, http://smass.mit.edu/minus.html), houses unpublished NIR spectra for hundreds of asteroids. All spectra are taken using the IRTF's SpeX instrument and are combined with SMASS visible spectra, when applicable. These spectra are named here using the convention found on the MIT website (spXX).

PDS: Small Bodies Node Scientists with observations of asteroidal bodies can publish them at the NASA Planetary Data System Small Bodies Node (http://pdssbn.astro.umd.edu). The Small Solar System Objects Spectroscopic Survey (s3os2; Lazzaro et al., 2004) contains visible spectra and taxonomic classification of 620 additional asteroids not found in SMASSI/II.

RELAB A vast archive of meteorite and terrestrial sample spectra has been accrued at the KECK/NASA Reflectance Experiment Laboratory Pieters and Hiroi (2004). The facility houses a spectrometer capable of gathering bidirectional reflectance measurements in the UV-Vis-NIR ($\lambda \sim 0.32$–2.55 μm) wavelength range at high resolution ($\lambda/\delta\lambda \approx 50$–$250$). Because the facility makes its services available to others, several hundred meteorite and mineral samples have been sent by investigators for analysis and are subsequently posted in an online database[3]. In section 3.4, I make use of the RELAB database in providing (both irradiated and non-altered) olivine, pyroxene, and meteorite spectra for which the accompanying file identification is specified for each spectrum used.

[3] http://www.planetary.brown.edu/relab/

3.3.3 Band Parameter Analysis

Here I describe the Band Analysis Routine for Asteroids (BAR-Ast), an algorithm designed to identify and quantify various characteristic band parameters of absorption features, to allow me to compare to other asteroid spectra and laboratory meteorite spectra. In the current version of BAR-Ast, B_I and B_{II} are characterized by the center wavelength of the band minimum, band depth at the center, spectral slope of a continuum across the band, and the area enclosed by the continuum and reflectance values (figure 3.4). A brief description of the algorithm, which is based on the Spectral Analysis Routine for Asteorids (SARA; Lindsay et al., 2015), is given below. Since BAR-Ast utilizes a non-parametric smoothing algorithm there are no assumptions made in regard to the shape of the spectral features. This approach overcomes the subjectivity associated with many other band analysis routines that make use of nth-degree polynomial functions fit to the data across a preset wavelength range. Another advantage of this algorithm is its robustness in the wavelength regions in which telluric absorption features decrease the SNR, notably near 1.4 and 1.85 μm (see figure 3.3).

Step1: The reflectance values are smoothed using a locally weighted scatterplot smoothing (LOWESS) algorithm, which fits a polynomial function to localized subset of data via a least-squares minimization. The smoothed function is a super-sample of the native spectrum (i.e., I set the wavelength resolution to $\Delta\lambda \sim 0.0001$) and it's calculated using the closest few reflectance points[4], weighted by the inverse of the 1σ uncertainty. The local polynomial smoothing functions are $5th$ and $2nd$ order for B_I and B_{II}, respectively, in order to account for the different shapes of the bands[5].

Step 2: The short wavelength (blue) and long wavelength (red) "edges" of both bands are determined:

B_I: For the 1-μm band, the blue edge is initially identified as the maximum reflectance value in the 0.7–0.8 μm range. Next, a set of hypothetical linear continua are

[4]This local weighting of the polynimial fits differs from fitting them to a significant portion of the entire band.

[5]Because B_I can often be an overlapping combination of olivine and pyroxene absorptions a higher degree polynomial matches subtle "shoulder" features, and is thus more appropriate.

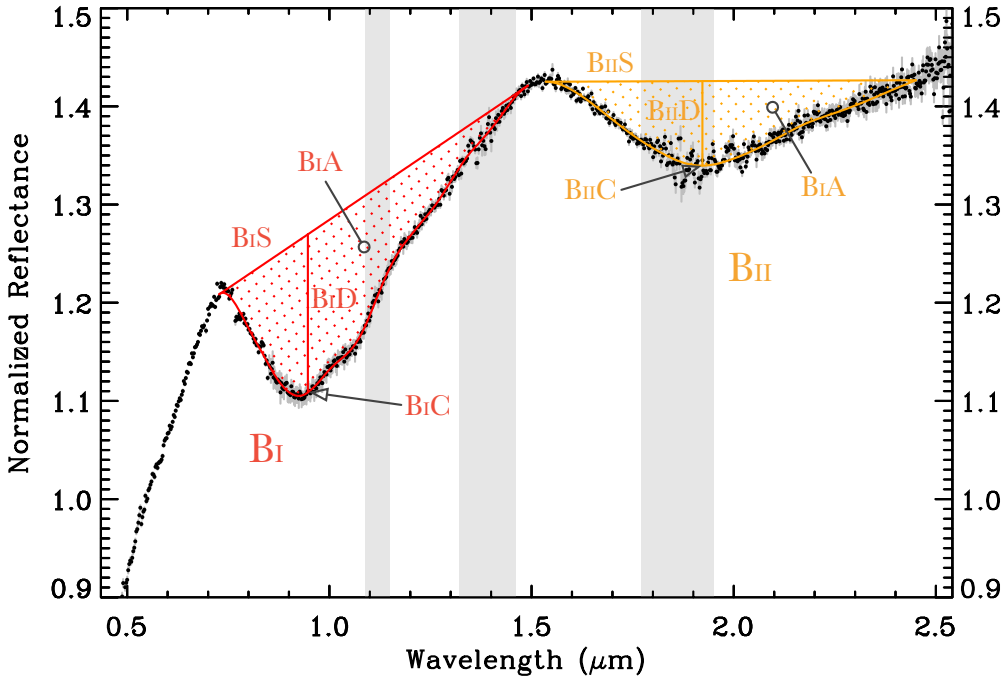

Figure 3.4: Depiction of a few band parameters for a spectrum of (80) Sappho, calculated with BARAst for B_I (red) and B_{II} (gold). The wavelength regions marked in grey show Earth's atmospheric water absorption features.

generated for each point in the spectrum, with the blue edge as an anchor. The red edge is identified as the point that maximizes the slope of the continuum across B_I. The red edge often lies in the 1.3–1.7 μm range, depending on the nature of the spectrum.

B_{II}: The red-edge of the B_{II} is held fixed during the entire procedure at 2.45 μm[6]. In similar fashion to B_I, several hypothetical linear continua are generated with the red edge serving as the anchor point. The blue edge of the B_{II} is chosen that minimizes the continuum slope.

Step 3: The reflectance values within each band are divided by the continuum values, effectively removing the overall slope across each band. The band centers (B_IC and $B_{II}C$) are identified as the wavelength of the minimum reflectance value, after the continuum division. I technically note that $B_{II}C$ is likely not the true "center" of B_{II} since the

[6]Due to instrument NIR wavelength coverage at many astronomical facilities the spectral noise is overwhelming at $\lambda > 2.45$ μm.

model red edge cutoff is at 2.45 μm — shortward of the true edge of the absorption feature, which lies beyond 2.55 μm.

Step 4: Band depths (B_ID and $B_{II}D$) are calculated using the continuum at the wavelength of the center, R_c, and the reflectance at the center wavelength, R_b: $B_xD = \frac{R_c - R_b}{R_c}$.

Step 5: The width of each band is calculated by measuring the distance, in microns, at "half minimum" — in which the continuum-divided reflectance value is halfway to the minimum value.

Step 6: Band areas are computed by integrating the region enclosed between the reflectance and the continuum, and the B_IA is divided into $B_{II}A$ to define the band area ratio, BAR.

In order to assess the uncertainty in each parameter appropriately, the BAR-Ast algorithm is implemented as part of a Monte Carlo simulation to produce a probability distribution for each parameter: for 10,000 iterations the reflectance values at each wavelength are randomly sampled, based on a normal distribution characterized by the individual 1σ errors at each wavelength value. The output parameter distributions closely resemble normal distributions and thus parameter values can appropriately be reported using mean and standard deviation statistics.

3.4 Results: Meteorites and Irradiated Samples

Here I estimate the spectral band parameters of meteorite samples collected and analyzed in the lab. In the following subsections I parse through the appropriate meteorite analogs that correspond to the three compositional groups (olivine-rich, pyroxene-dominated, and ordinary chondrite meteorites). My analysis is focused on two sets of band parameters: B_IS and B_ID — which are the most indicative of space weathering — as well as B_IC, $B_{II}C$, and BAR — which are primarily used as parameters diagnostic of mineralogy (Gaffey, 2001). All meteorite band parameters are reported without explicit uncertainties, since the high-quality laboratory spectra have very high SNR. Individual reflectance measurement uncertainties are

on the order of the smallest decimal place, which are very small compared to the variation from one sample to another. Trends and variations in $B_I S$ and $B_I D$ within each meteorite group are considered here to be caused by secondary effects such as differences in grain size, petrologic type (a measure of thermal alteration, or metamorphism, experienced shortly after the formation of chondritic meteorites), and mineral chemistry (for example, Fo#: the amount of MgO in olivine) of the samples. Chondritic meteorites with a petrologic type of 3 are the least altered, whereas type 6 have been heated to just short of partial-melting temperatures (Huss et al., 2006). As explained below, relationships between $B_I S$ and $B_I D$ can be leveraged to provide population level estimates of petrologic type for ordinary-chondrite-like asteroids.

3.4.1 Ordinary Chondrites

I analyzed and determined band parameters for over 200 spectra from the RELAB database; results for the space weathering parameters ($B_I S$ and $B_I D$) and mineralogic parameters ($B_I C$, $B_{II} C$, and BAR) are tabulated in table 3.2. Although the overall variation in space weathering band parameters are small, I found that the $B_I D$ to be affected by the petrologic type of the meteorite and $B_I S$ to be affected by the grain size of the powder. In addition, the BAR exhibits a strong correlation with grain size. Spectra of both individual meteorites and group distributions are used to support these claims, as further detailed below. Table 3.3 shows that the average $B_I D$ and $B_I S$ of H, L, and LL chondrites are not statistically distinguishable from one another and are thus independent of these sub-types.

Nine OC meteorites with spectra measured in RELAB had been ground and sorted into the following size bins: < 75 μm, < 125 μm, < 150 μm, and 125–500 μm. These samples comprise a spectral suite that can be used to study the effects of grain size on spectral parameters. The $B_I S$, $B_I D$, and BAR for each of these series are plotted by grain size bin in figure 3.5. Each sample is colored by its sub-type except Burnwell, shown by black symbols, which has been classified as an HH-type due to its anomalously high metal content. The top panel shows a systematic decrease in $B_I S$ for the largest grain size bin with the notable exception being Hamlet (LL4), which exhibits no clear trend between grain size bin and $B_I S$. Differences in $B_I S$ between the < 125 μm and < 150 μm size fractions are minimal, likely due

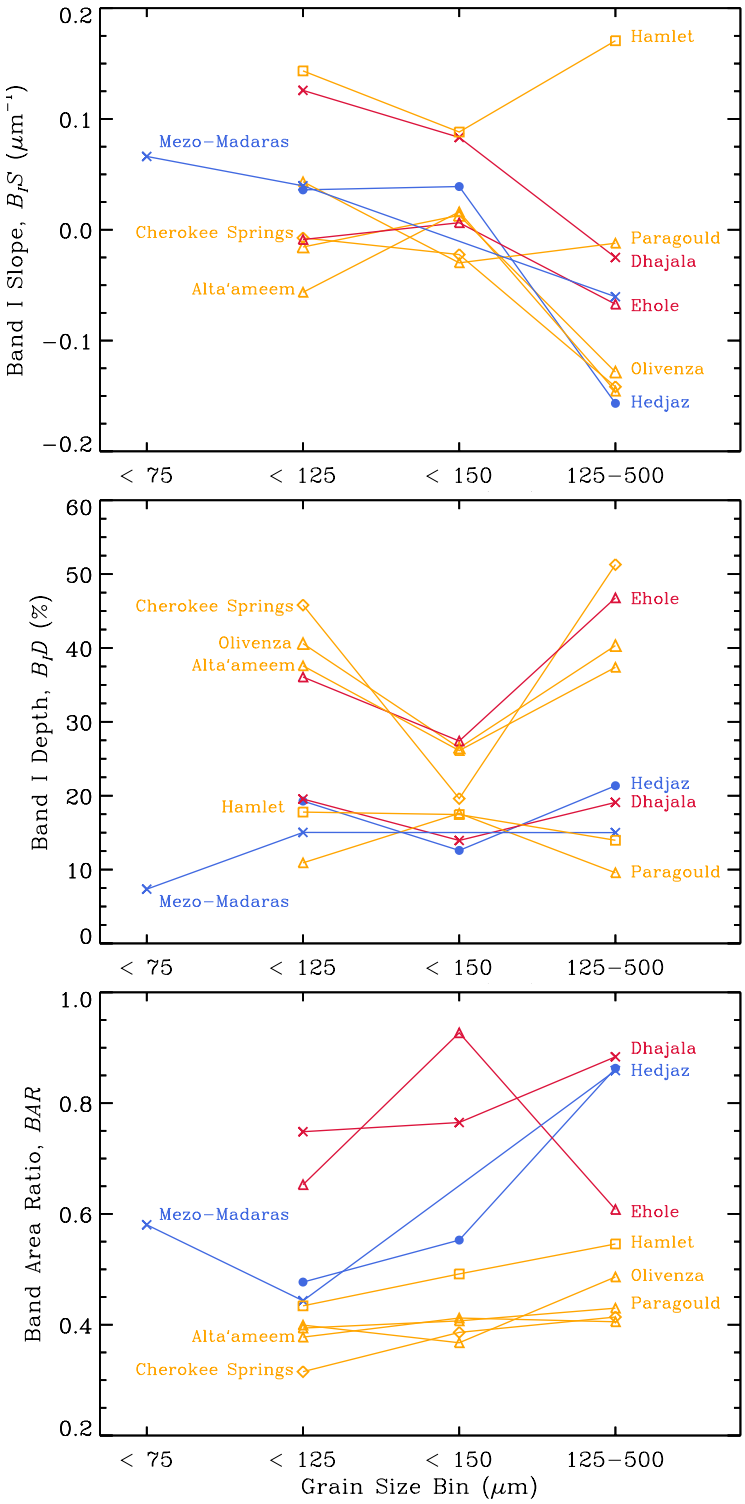

Figure 3.5: Band slope and band depth of individual ordinary chondrites across many grain size bins. Gold, blue, and red colors show LL, L, and H sub-types, respectively. The x, square, triangle, diamond sybmbols denote a petrologic type of 6, 5, 4 and 3-3.9, respectively. Hedjaz, shown as filled circles, is classified as 3.7-6, as it is an impact breccia comprised of petrologic types in that range.

Table 3.2: Band Parameters of Ordinary Chondrites

Meteorite	Type	Grain Size	RELAB ID	B_IC (μm)	B_IS (μm^{-1})	B_ID (%)	$B_{II}C$ (μm)	BAR
ALH85121,11	H3.7	$<$ 45 μm	MT-PFV-154-A	0.920	0.026	0.124	1.952	0.666
ALHA77299,91	H3.7	$<$ 45 μm	MT-PFV-157-A	0.921	0.049	0.094	1.947	0.567
Allegan	H5	—	MR-MJG-028	0.925	0.088	0.331	1.911	0.959
Allegan	H5	—	TB-TJM-104	0.922	0.025	0.237	1.898	1.045
Allegan	H5	$<$ 150 μm	TB-TJM-125	0.924	0.038	0.232	1.879	0.776
Andura	H6	$<$ 75 μm	TB-TJM-088	0.914	0.088	0.168	1.899	0.799
Avanhandav	H4	$<$ 150 μm	TB-TJM-066	0.921	0.027	0.146	1.916	0.811
BTN00301,7	H3.3	$<$ 45 μm	MT-PFV-167-A	0.933	0.035	0.082	1.982	0.365
BTN00302,5	H3.3	$<$ 45 μm	MT-PFV-132-A	0.930	0.036	0.095	1.959	0.390
Barwise	H5	—	MR-MJG-036	0.918	0.136	0.113	1.926	0.819
Burnwell	HH4	$<$ 150 μm	TB-TJM-068	0.919	0.025	0.123	1.917	0.712
Butsura	H6	$<$ 150 μm	TB-TJM-069	0.920	-0.013	0.146	1.910	0.754
Canon City	H6	$<$ 150 μm	TB-TJM-131	0.933	0.031	0.441	1.923	0.693
Castalia	H5	—	MR-MJG-029	0.921	-0.060	0.175	1.901	1.014
Chela	H4	$<$ 150 μm	TB-TJM-071	0.913	0.128	0.256	1.918	0.920
Chiang Khan	H6	$<$ 150 μm	TB-TJM-132	0.928	0.007	0.288	1.907	0.812
Collescipo	H5	—	MR-MJG-030	0.922	0.005	0.218	1.916	0.871
DOM03219,6	H3.8	$<$ 45 μm	MT-PFV-176-A	0.927	0.274	0.068	1.935	0.462
Dhajala	H3.8	$<$ 125 μm	OC-TXH-020-C	0.927	0.126	0.195	1.934	0.748
Dhajala	H3.8	$<$ 150 μm	TB-TJM-091	0.926	0.083	0.139	1.926	0.765
Dhajala	H3.8	125–500 μm	OC-TXH-020-B	0.921	-0.024	0.190	1.941	0.883
Dwaleni	H4 to 6	$<$ 150 μm	TB-TJM-073	0.929	-0.050	0.189	1.899	0.625
EET83248,20	H3.5	$<$ 45 μm	MT-PFV-172-A	0.915	0.027	0.082	1.958	0.455
EET83267,11	H3.6	$<$ 45 μm	MT-PFV-174-A	0.920	0.036	0.123	1.949	0.581
Ehole	H5	$<$ 125 μm	OC-TXH-006-C	0.930	-0.009	0.361	1.903	0.653
Ehole	H5	$<$ 150 μm	TB-TJM-074	0.923	0.006	0.274	1.945	0.926
Ehole	H5	125–500 μm	OC-TXH-006-B	0.937	-0.067	0.468	1.914	0.608
Farmville	H4	$<$ 150 μm	TB-TJM-128	0.920	0.013	0.167	1.920	0.704
Forest City	H5	—	MR-MJG-031	0.924	-0.017	0.188	1.911	1.033
Forest Vale	H4	$<$ 75 μm	TB-TJM-093	0.929	0.043	0.135	1.893	0.556
GRA95208,20	H3.7	$<$ 45 μm	MT-PFV-158-A	0.922	0.049	0.128	1.948	0.515
GRA98023,7	H3.8	$<$ 45 μm	MT-PFV-164-A	0.922	0.030	0.134	1.939	0.619
Grüneberg	H4	—	MR-MJG-040	0.925	-0.015	0.209	1.924	0.972
Guareña	H6	$<$ 150 μm	TB-TJM-094	0.919	-0.009	0.350	1.889	0.696
Ipiranga	H6	$<$ 150 μm	TB-TJM-135	0.924	0.029	0.197	1.907	0.785
Itapicuru-Mirim	H5	$<$ 150 μm	TB-TJM-097	0.923	0.011	0.211	1.894	0.775
Kabo	H4	$<$ 150 μm	TB-TJM-136	0.924	0.018	0.157	1.907	0.825
LAR04382,5	H3.4	$<$ 45 μm	MT-PFV-171-A	0.948	0.078	0.093	1.963	0.370
Lancon	H6	—	MR-MJG-033	0.929	0.006	0.264	1.916	0.697
Lancon	H6	—	MR-MJG-033	0.941	-0.132	0.305	1.920	0.514
Lost City	H5	$<$ 150 μm	TB-TJM-129	0.924	-0.001	0.175	1.919	0.788
MAC88174,17	H3.5	$<$ 45 μm	MT-PFV-146-A	0.921	0.047	0.086	1.950	0.406
MET00506,11	H3.4	$<$ 45 μm	MT-PFV-143-A	0.952	0.097	0.082	1.960	0.218
MET00607,8	H3.4	$<$ 45 μm	MT-PFV-144-A	0.932	0.108	0.089	1.955	0.181
MET01182,7	H3.8	$<$ 45 μm	MT-PFV-159-A	0.930	0.040	0.098	1.950	0.358
Magombedze	H3 to 5	$<$ 150 μm	TB-TJM-108	0.924	0.000	0.288	1.920	0.804
Marilia	H4	$<$ 150 μm	TB-TJM-078	0.920	0.034	0.179	1.939	0.769
Monroe	H4	$<$ 125 μm	OC-TXH-005-C	0.922	0.030	0.173	1.939	0.664
Monroe	H4	125–500 μm	OC-TXH-005-B	0.927	-0.112	0.160	1.939	0.961
Nanjemoy	H6	—	MR-MJG-034	0.933	0.029	0.266	1.904	1.088
Nanjemoy	H6	—	MR-MJG-034	0.929	0.045	0.303	1.913	0.849
Nulles	H6	$<$ 125 μm	OC-TXH-018-C	0.934	0.001	0.308	1.924	0.559
Nulles	H6	125–500 μm	OC-TXH-018-B	0.932	-0.161	0.356	1.919	0.733
Ochansk	H4	—	MR-MJG-027	0.922	0.012	0.191	1.926	0.964
Ochansk	H4	$<$ 125 μm	OC-TXH-008-C	0.922	-0.031	0.200	1.939	0.732
Ochansk	H4	125–500 μm	OC-TXH-008-B	0.928	-0.139	0.238	1.929	0.870
Olmedilla de Alarcón	H5	—	MR-MJG-075	0.927	-0.044	0.260	1.908	1.057

Table 3.2 — continued

Meteorite	Type	Grain Size	RELAB ID	$B_I C$ (μm)	$B_I S$ (μm^{-1})	$B_I D$ (%)	$B_{II} C$ (μm)	BAR
Olmedilla de Alarcón	H5	< 125 μm	OC-TXH-019-C	0.931	0.017	0.202	1.939	0.644
Olmedilla de Alarcón	H5	125–500 μm	OC-TXH-019-B	0.931	-0.179	0.241	1.929	0.772
Pantar	H5	—	MR-MJG-032	0.918	-0.014	0.148	1.911	0.871
Pribram	H5	< 150 μm	TB-TJM-143	0.925	0.054	0.197	1.893	0.750
Pulsora	H5	< 150 μm	TB-TJM-120	0.926	-0.004	0.157	1.923	0.742
Queen's Mercy	H6	—	MR-MJG-035	0.934	-0.093	0.226	1.911	0.662
Queen's Mercy	H6	—	MR-MJG-035	0.924	-0.009	0.239	1.926	0.764
Quenggouk	H4	—	MR-MJG-042	0.972	-0.025	0.281	1.951	0.331
RKPA80205,29	H3.8	< 45 μm	MT-PFV-160-A	0.916	0.027	0.116	1.942	0.663
São Jose do Rio Preto	H4	< 150 μm	TB-TJM-082	0.920	0.021	0.178	1.880	0.958
Schenectady	H5	< 150 μm	TB-TJM-083	0.920	0.102	0.267	1.922	0.699
Sitathali	H5	< 150 μm	TB-TJM-123	0.927	-0.006	0.185	1.908	0.736
Suwahib (Buwah)	H3.8	< 150 μm	TB-TJM-124	0.920	0.050	0.124	1.920	0.782
Uberaba	H5	< 150 μm	TB-TJM-085	0.932	0.036	0.191	1.922	0.794
WSG95300,64	H3.3	< 45 μm	MT-PFV-134-A	0.925	0.072	0.073	1.977	0.267
Zhovtnevyi	H6	—	MR-MJG-041	0.917	0.006	0.268	1.895	0.700
Aïr	L6	< 150 μm	TB-TJM-063	0.931	0.023	0.162	1.935	0.511
ALH84086,27	L3.8	< 45 μm	MT-PFV-161-A	0.927	0.083	0.171	1.942	0.558
ALH84120,15	L3.8	< 45 μm	MT-PFV-162-A	0.924	0.057	0.169	1.945	0.539
ALH85045,25	L3.8	< 45 μm	MT-PFV-163-A	0.929	0.087	0.144	1.954	0.494
ALH85070,8	L3.6	< 45 μm	MT-PFV-178-A	0.931	0.078	0.153	1.959	0.472
ALH85155,7	L3.7	< 45 μm	MT-PFV-155-A	0.935	0.046	0.114	1.964	0.421
Alfianello	L6	—	MR-MJG-051	0.943	0.057	0.413	1.932	0.564
Andover	L6	—	MR-MJG-052	0.941	0.014	0.341	1.924	0.514
Apt	L6	< 150 μm	TB-TJM-064	0.936	0.029	0.315	1.936	0.463
Atarra	L4	< 150 μm	TB-TJM-065	0.920	-0.002	0.267	1.923	0.638
Aumale	L6	—	MR-MJG-053	0.955	-0.100	0.382	1.936	0.371
Aumale	L6	< 150 μm	TB-TJM-101	0.934	0.045	0.301	1.939	0.554
Ausson	L5	—	MR-MJG-047	0.940	0.054	0.339	1.933	0.623
Ausson	L5	< 150 μm	MT-HYM-084	0.921	0.027	0.249	1.913	0.981
Bald Mountain	L4	—	MR-MJG-044	0.918	0.053	0.184	1.917	0.732
Blackwell	L5	< 150 μm	MT-HYM-081	0.932	0.144	0.124	1.950	0.485
Bruderheim	L6	—	MR-MJG-054	0.929	0.024	0.270	1.916	0.507
Buschof	L6	—	MR-MJG-055	0.941	0.014	0.408	1.924	0.482
Buschof	L6	—	MR-MJG-055	0.944	0.094	0.369	1.935	0.459
Chantonnay	L6	< 150 μm	TB-TJM-070	0.928	0.031	0.120	1.889	0.444
Cilimus	L5	< 150 μm	MT-HYM-082	0.927	0.040	0.207	1.923	0.488
Colby (Wisconsin)	L6	—	MR-MJG-057	0.961	-0.103	0.338	1.952	0.334
Colby (Wisconsin)	L6	—	MR-MJG-057	0.939	0.030	0.281	1.929	0.404
Cranganore	L6	< 150 μm	TB-TJM-133	0.938	0.021	0.326	1.909	0.479
Denver	L6	< 150 μm	TB-TJM-072	0.937	0.007	0.164	1.949	0.546
Drake Creek	L6	—	MR-MJG-058	0.958	0.012	0.478	1.946	0.445
EET90161,20	L3	< 45 μm	MT-PFV-179-A	0.940	0.133	0.074	1.949	0.321
EET90628,11	L3.4	< 45 μm	MT-PFV-180-A	0.951	0.146	0.060	1.955	0.246
Elenovka	L5	—	MR-MJG-066	0.936	-0.020	0.348	1.930	0.517
Farmington	L5	—	MR-MJG-077	0.911	-0.003	0.165	1.920	0.784
Farmington	L5	—	MR-MJG-077	0.917	0.043	0.134	1.909	0.951
GRO06054,11	L3.6	< 45 μm	MT-PFV-153-A	0.969	0.102	0.068	1.945	0.217
GRO95502,31	L3.2	< 45 μm	MT-PFV-139-A	0.927	0.070	0.105	1.950	0.453
GRO95504,20	L3.5	< 45 μm	MT-PFV-148-A	0.930	0.075	0.078	1.960	0.340
GRO95536,18	L3.3	< 45 μm	MT-PFV-140-A	0.935	0.057	0.105	1.960	0.378
GRO95542,9	L3.5	< 45 μm	MT-PFV-149-A	0.927	0.067	0.088	1.963	0.371
GRO95544,36	L3.2	< 45 μm	MT-PFV-133-A	0.925	0.074	0.080	1.960	0.442
GRO95550,6	L3.5	< 45 μm	MT-PFV-150-A	0.931	0.049	0.106	1.954	0.397
Girgenti	L6	—	MR-MJG-059	0.947	0.043	0.375	1.933	0.482
Girgenti	L6	< 150 μm	TB-TJM-103	0.937	0.033	0.390	1.937	0.476
Guibga	L5	< 150 μm	TB-TJM-134	0.932	0.027	0.260	1.926	0.586
Harleton	L6	< 125 μm	OC-TXH-003-C	0.946	0.043	0.331	1.957	0.384

Table 3.2 — continued

Meteorite	Type	Grain Size	RELAB ID	B_IC (μm)	B_IS (μm^{-1})	B_ID (%)	$B_{II}C$ (μm)	BAR
Harleton	L6	125–500 μm	OC-TXH-003-B	0.95	-0.120	0.399	1.942	0.527
Hedjaz	L3.7 to 6	$<$ 125 μm	OC-TXH-016-C	0.940	0.036	0.193	1.950	0.477
Hedjaz	L3.7 to 6	$<$ 150 μm	TB-TJM-095	0.930	0.039	0.125	1.889	0.552
Hedjaz	L3.7 to 6	125–500 μm	OC-TXH-016-B	0.932	-0.157	0.214	1.960	0.863
Homestead	L5	—	MR-MJG-048	0.934	0.114	0.242	1.926	0.724
Karkh	L6	$<$ 150 μm	TB-TJM-137	0.937	0.003	0.143	1.916	0.371
Khohar	L3.6	$<$ 150 μm	TB-TJM-138	0.933	0.051	0.113	1.959	0.377
Kunashak	L6	$<$ 150 μm	TB-TJM-139	0.942	0.047	0.302	1.937	0.479
Kuttippura	L6	$<$ 75 μm	TB-TJM-098	0.930	0.014	0.233	1.904	0.506
Kyushu	L6	$<$ 75 μm	TB-TJM-140	0.94	0.102	0.317	1.929	0.496
L'Aigle	L6	$<$ 150 μm	TB-TJM-141	0.929	-0.012	0.169	1.946	0.757
LEW85339,10	L3.4	$<$ 45 μm	MT-PFV-181-A	0.932	0.098	0.132	1.959	0.400
LEW86018,71	L3.1	$<$ 45 μm	MT-PFV-130-A	0.930	0.103	0.152	1.954	0.565
LEW86127,8	L3.3	$<$ 45 μm	MT-PFV-135-A	0.93	0.059	0.114	1.954	0.392
LEW86505,9	L3.4	$<$ 45 μm	MT-PFV-142-A	0.925	0.071	0.106	1.959	0.364
LEW87284,16	L3.6	$<$ 45 μm	MT-PFV-182-A	0.927	0.034	0.106	1.934	0.350
Leedey	L6	—	MR-MJG-060	0.943	-0.004	0.268	1.936	0.458
MAC88199,7	L3.3	$<$ 45 μm	MT-PFV-183-A	0.935	0.070	0.102	1.955	0.327
MET00489,12	L3.6	$<$ 45 μm	MT-PFV-151-A	0.943	0.102	0.119	1.959	0.347
MET96503,25	L3.6	$<$ 45 μm	MT-PFV-152-A	0.932	0.086	0.090	1.955	0.240
Mabwe-Khoywa	L5	$<$ 150 μm	TB-TJM-107	0.928	0.019	0.227	1.935	0.658
Malakal	L5	$<$ 150 μm	TB-TJM-109	0.929	0.057	0.207	1.950	0.568
Maryville	L6	$<$ 150 μm	TB-TJM-110	0.942	-0.011	0.387	1.929	0.645
Messina	L5	$<$ 75 μm	TB-TJM-099	0.930	0.018	0.189	1.927	0.533
Mezö-Madaras	L3.7	—	MR-MJG-043	0.926	0.052	0.156	1.901	0.713
Mezö-Madaras	L3.7	$<$ 125 μm	OC-TXH-004-C	0.933	0.040	0.150	1.951	0.443
Mezö-Madaras	L3.7	125–500 μm	OC-TXH-004-B	0.939	-0.060	0.150	1.948	0.858
Mirzapur	L5	$<$ 150 μm	TB-TJM-111	0.925	0.124	0.192	1.933	0.661
Nejo	L6	$<$ 150 μm	TB-TJM-112	0.939	0.071	0.404	1.928	0.515
Nerft	L6	—	MR-MJG-061	0.940	0.008	0.346	1.932	0.463
New Concord	L6	$<$ 150 μm	TB-TJM-130	0.934	0.021	0.316	1.924	0.546
PRE95401,13	L3.5	$<$ 45 μm	MT-PFV-145-A	0.933	0.066	0.088	1.960	0.422
Paranaiba	L6	$<$ 75 μm	TB-TJM-142	0.930	0.109	0.121	1.943	0.401
Patrimonio	L6	$<$ 150 μm	TB-TJM-113	0.933	0.023	0.265	1.942	0.615
Rio Negro	L4	$<$ 150 μm	TB-TJM-081	0.925	0.064	0.234	1.894	0.706
Rupota	L4 to 6	$<$ 150 μm	TB-TJM-121	0.931	-0.003	0.103	1.958	0.582
Shelburne	L5	—	MR-MJG-050	0.941	0.018	0.325	1.936	0.594
Shelburne	L5	$<$ 150 μm	TB-TJM-122	0.933	0.016	0.290	1.932	0.614
St. Michel	L6	—	MR-MJG-062	0.944	0.038	0.422	1.931	0.501
St. Michel	L6	—	MR-MJG-062	0.952	-0.013	0.360	1.936	0.563
Tourinnes-la-Grosse	L6	—	MR-MJG-063	0.940	-0.001	0.367	1.931	0.517
Utrecht	L6	—	MR-MJG-064	0.940	-0.011	0.391	1.933	0.562
Valdinizza	L6	$<$ 150 μm	TB-TJM-087	0.924	0.087	0.285	1.932	0.499
Vouill	L6	$<$ 150 μm	TB-TJM-086	0.923	0.055	0.182	1.879	0.515
Vouill	L6	—	MR-MJG-125	0.980	0.031	0.266	1.951	0.405
Wethersfield (1982)	L6	$<$ 150 μm	TB-TJM-147	0.939	-0.014	0.434	1.916	0.542
Zavid	L6	—	MR-MJG-065	0.943	-0.090	0.327	1.935	0.540
Zavid	L6	—	MR-MJG-065	0.935	0.032	0.300	1.926	0.557
ALH83007,34	LL3.35	$<$ 45 μm	MT-PFV-136-A	0.935	0.045	0.102	1.950	0.386
ALH83010,40	LL3.3	$<$ 45 μm	MT-PFV-138-A	0.925	0.066	0.142	1.950	0.364
ALH84126,21	LL3.4	$<$ 45 μm	MT-PFV-170-A	1.014	0.087	0.120	1.979	0.380
ALHA76004,41	LL3.3	$<$ 45 μm	MT-PFV-137-A	0.937	0.033	0.108	1.946	0.433
ALHA77278,111	LL3.7	$<$ 45 μm	MT-PFV-156-A	0.945	0.091	0.136	1.96	0.425
ALHA78119,35	LL3.5	$<$ 45 μm	MT-PFV-147-A	0.930	0.064	0.104	1.964	0.402
Aldsworth	LL5	$<$ 150 μm	MT-HYM-077	0.935	0.052	0.167	1.953	0.523
Alta'ameem	LL5	$<$ 125 μm	OC-TXH-010-C	0.985	-0.056	0.375	1.949	0.377
Alta'ameem	LL5	$<$ 150 μm	MT-HYM-078	0.948	0.016	0.261	1.947	0.412
Alta'ameem	LL5	125–500 μm	OC-TXH-010-B	0.975	-0.145	0.373	1.953	0.405

Table 3.2 — continued

Meteorite	Type	Grain Size	RELAB ID	$B_I C$ (μm)	$B_I S$ (μm^{-1})	$B_I D$ (%)	$B_{II} C$ (μm)	BAR
Bandong	LL6	< 150 μm	TB-TJM-067	0.989	0.025	0.212	1.976	0.250
Benares (a)	LL4	< 150 μm	MT-HYM-083	1.018	0.106	0.198	1.969	0.462
Cherokee Springs	LL6	< 125 μm	OC-TXH-001-C	0.969	-0.007	0.458	1.936	0.315
Cherokee Springs	LL6	< 150 μm	TB-TJM-090	0.953	-0.022	0.196	1.929	0.386
Cherokee Springs	LL6	125–500 μm	OC-TXH-001-B	0.968	-0.141	0.512	1.962	0.413
Chicora	LL6	< 125 μm	OC-TXH-014-C	1.010	-0.037	0.272	1.964	0.188
Chicora	LL6	125–500 μm	OC-TXH-014-B	0.991	-0.181	0.264	1.953	0.235
EET83213,76	LL3.7	< 45 μm	MT-PFV-175-A	0.931	0.127	0.161	1.954	0.433
Ensisheim	LL6	< 150 μm	TB-TJM-092	0.951	-0.039	0.160	1.939	0.251
GRO95596,6	LL3.8	< 45 μm	MT-PFV-177-A	0.935	0.067	0.144	1.952	0.444
GRO95658,17	LL3.3	< 45 μm	MT-PFV-141-A	0.936	0.112	0.090	1.960	0.392
Greenwell	LL4	< 150 μm	TB-TJM-075	0.95	0.068	0.272	1.949	0.446
Hamlet #1	LL4	—	MR-MJG-069	0.955	-0.031	0.240	1.959	0.624
Hamlet #1	LL4	—	MR-MJG-069	0.936	0.112	0.192	1.960	0.597
Hamlet	LL4	< 125 μm	OC-TXH-002-C	0.945	0.143	0.178	1.983	0.434
Hamlet	LL4	< 150 μm	MT-HYM-075	0.934	0.088	0.174	1.964	0.491
Hamlet	LL4	125–500 μm	OC-TXH-002-B	0.943	0.171	0.140	1.960	0.546
Jelica	LL6	—	MR-MJG-072	0.967	0.063	0.229	1.954	0.414
Karatu	LL6	< 75 μm	TB-TJM-077	1.000	0.005	0.200	1.959	0.288
LAR06301,8	LL3.8	< 45 μm	MT-PFV-165-A	0.933	0.047	0.118	1.949	0.459
LAR06469,4	LL3	< 45 μm	MT-PFV-166-A	0.930	0.025	0.085	1.959	0.362
LEW87254,16	LL3.5	$45 - 125\mu$m	MT-PFV-173-A	0.975	0.040	0.092	1.96	0.350
Manbhoom	LL6	—	MR-MJG-073	0.990	-0.007	0.380	1.956	0.278
Olivenza	LL5	—	MR-MJG-071	1.006	0.097	0.307	1.960	0.339
Olivenza	LL5	< 125 μm	OC-TXH-009-C	0.983	-0.015	0.405	1.957	0.399
Olivenza	LL5	< 150 μm	MT-HYM-085	1.010	0.013	0.264	1.959	0.367
Olivenza	LL5	125–500 μm	OC-TXH-009-B	0.975	-0.128	0.403	1.956	0.486
Paragould	LL5	—	MR-MJG-076	0.940	0.211	0.054	1.946	0.486
Paragould	LL5	< 125 μm	OC-TXH-007-C	0.961	0.043	0.109	1.975	0.394
Paragould	LL5	< 150 μm	MT-HYM-079	0.954	-0.029	0.176	1.959	0.407
Paragould	LL5	125–500 μm	OC-TXH-007-B	0.975	-0.012	0.096	1.930	0.430
Parnallee	LL3.6	—	MR-MJG-068	0.937	0.016	0.224	1.940	0.720
Parnallee	LL3.6	—	MR-MJG-068	0.940	0.021	0.199	1.951	1.006
Soko-Banja	LL4	—	MR-MJG-070	0.952	0.064	0.258	1.954	0.535
Soko-Banja	LL4	—	MR-MJG-070	0.946	0.073	0.223	1.961	0.633
Soko-Banja	LL4	—	MR-MJG-070	0.939	0.062	0.142	1.962	1.076
Soko-Banja	LL4	< 125 μm	OC-TXH-017-C	0.975	0.041	0.309	1.970	0.403
Soko-Banja	LL4	125–500 μm	OC-TXH-017-B	0.968	-0.084	0.374	1.966	0.564
TIL82408,31	LL3.3	< 45 μm	MT-PFV-131-A	0.952	0.147	0.079	1.955	0.352
Tuxtuac	LL5	< 150 μm	MT-HYM-080	1.038	0.068	0.338	1.968	0.270
Vavilovka	LL6	—	MR-MJG-074	1.007	0.035	0.353	1.961	0.345
Witsand Farm	LL4	< 150 μm	MT-HYM-076	1.024	0.078	0.159	1.979	0.416

Table 3.3: Average Band Depth and Spectral Slope for Ordinary Chondrite sub-types

	B_ID (%)	B_IS (μm^{-1})
H	18 ± 8	0.025 ± 0.071
L	19 ± 10	0.050 ± 0.047
LL	22 ± 12	0.017 ± 0.080

to the significant overlap between the grain size bins. The middle panel shows varied changes among the B_ID values across each grain size bin, strongly suggesting that there is no clear correlation between the two parameters. There appears to be a dichotomy in B_ID between higher and lower petrologic types, which is further investigated in the next paragraph. The BAR of all the samples, with the exception of Ehole (H5), shows a systematic upward trend going from the < 125 μm to 125–500 μm size fractions. Mezö-Madaras (L3.7) also appears to contradict this trend with the large BAR for < 75 μm grains, but this grain size bin contains no other samples, so a comparison to other meteorites is not possible. Despite the two anomalous samples, I observe a strong correlation between BAR and grain size of ordinary chondrites.

Next, I incorporate the band parameter dataset calculated from all 200+ spectra. Within the overall population, the trend between B_IS and grain size observed among the individual samples is also apparent. The mean and variance of the B_ID distribution for different petrologic types are interconnected, as discussed in the next paragraph. The top panel of figure 3.6 (a) shows that smaller, blue (negative) spectral slopes are represented among the largest grain sizes (125–250 μm). When grouped by petrologic type in (b), the mean B_IS values overlap significantly and show no discernible trend. Yet, the meteorites below petrologic type 4 show a slight positive offset. This offset may likely be an effect of grain size just mentioned — most of these less-altered samples were ground and sieved into the $<$ 45 μm grain size bin featured in the "MT-PFV-XXX" RELAB series.

In the bottom panels of figure 3.6 (a & b), B_ID values are shown; grouped by sample grain size and meteorite petrologic type. The B_ID values exhibit an increase in both the mean and standard deviation values with greater thermal alteration. The systematically lower B_ID seen for the < 45 μm grain size bin may be an effect of the petrologic type, since

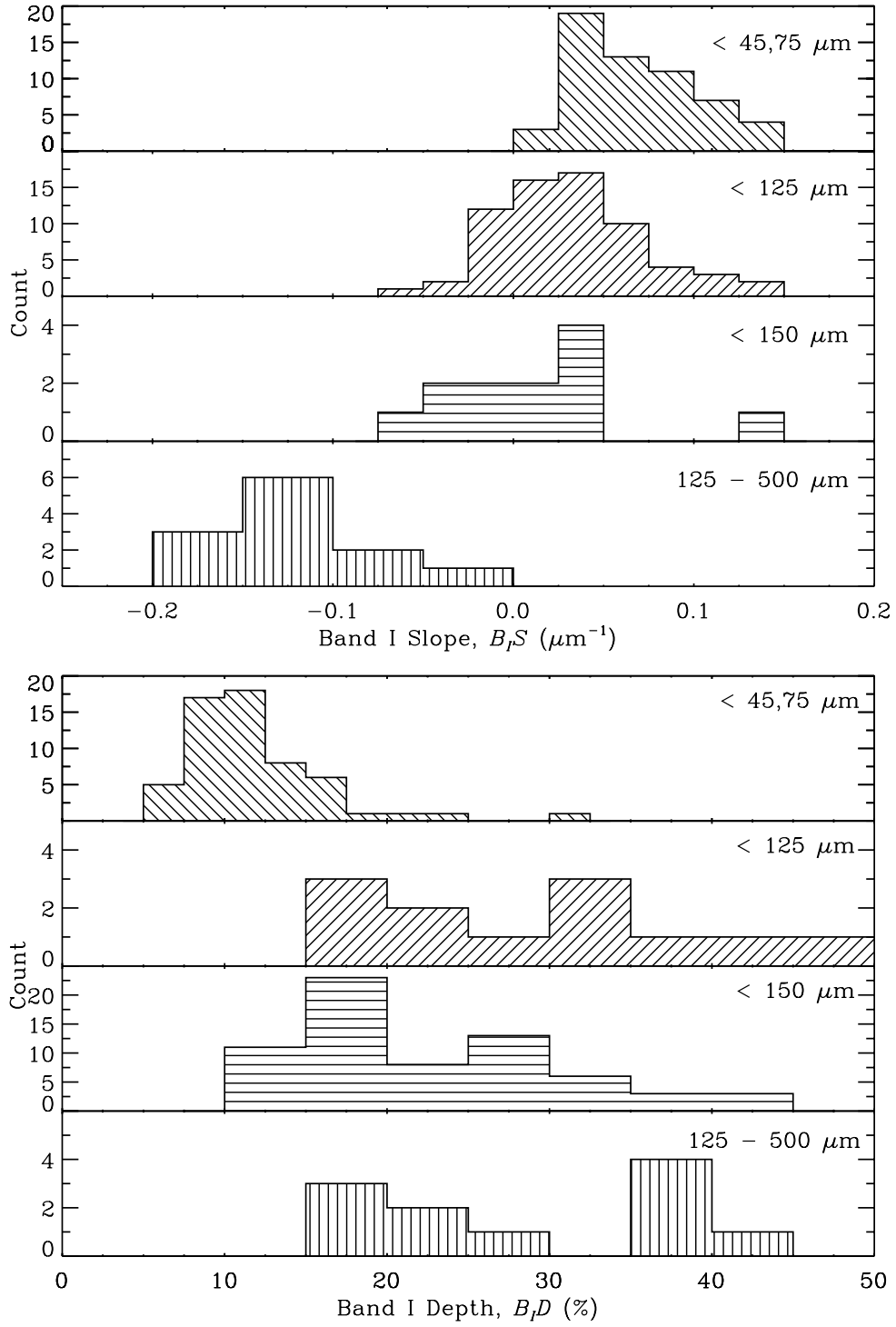

(a) grain size bin

Figure 3.6: B_IS and B_ID of the 1 μm absorption of ordinary chondrites, grouped by grain size bin and petrologic type.

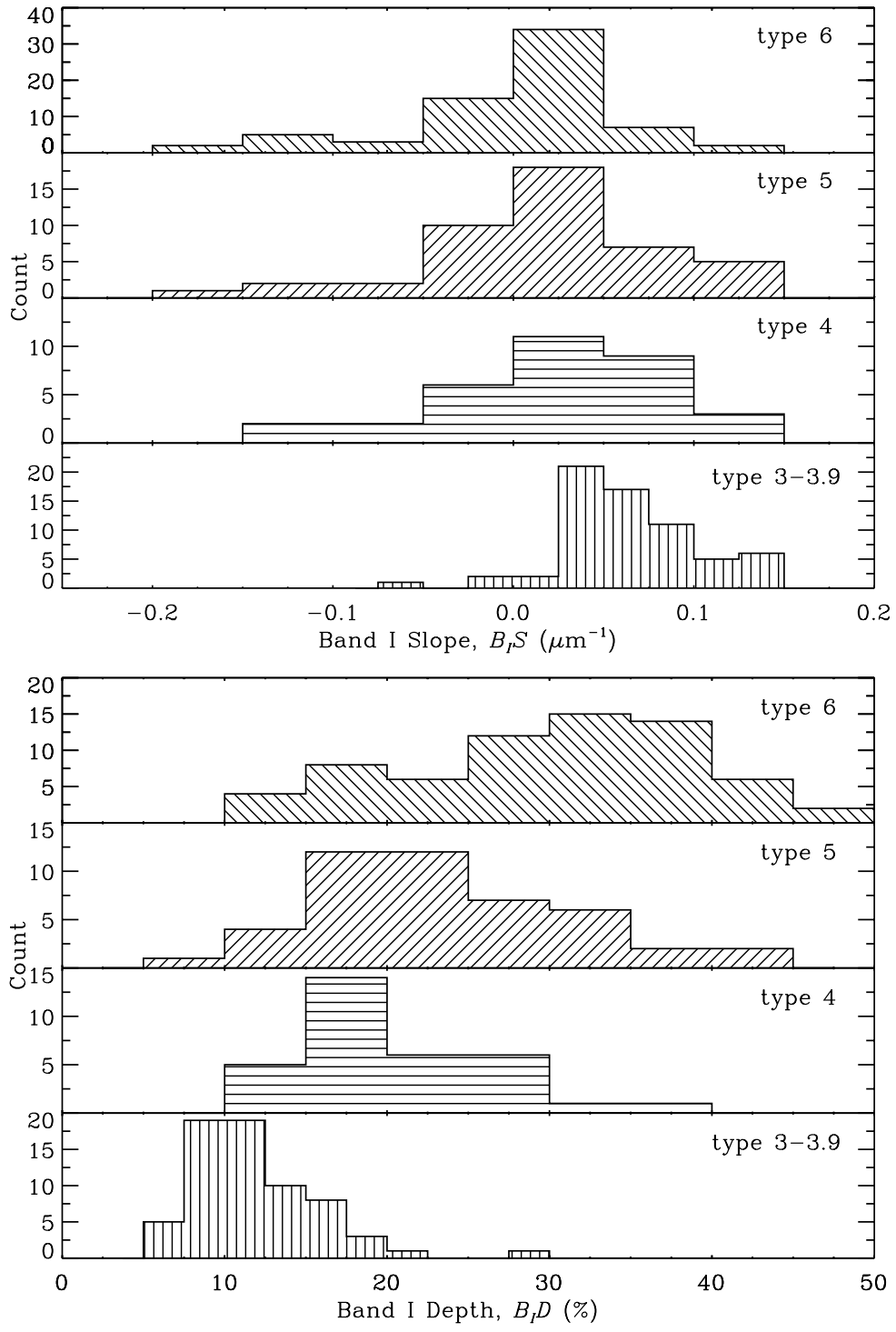

(b) As in panel(a), but grouped by petrologic type

the low (<4) petrologic types group exclusively populates this size bin; in this dataset, it appears that no identifiable relationship between grain size and $B_I D$ exists. If is I exclude the samples in the < 45 μm grain size bin, then the proposed $B_I D$ trend with petrologic type is still apparent. If I exclusively analyze the $B_I D$ distributions among the low (<4) petrologic type meteorite samples, the same trend is evident and significant at the $p < .001$ level (figure 3.7). Although no clear trend in in the $B_I D$ and grain size is apparent in the top right panel, I notice that the lower end of the band depth distribution for the 3–3.9 types (5%) is around half that of the 4, 5, and 6 petrologic types (10%). The significant overlap between the groups in the top right panel could suggest that grain size is not a sufficient factor in explaining the overall variance in the $B_I D$ distribution.

In order to robustly characterize the relationships described above I performed a multiple-linear regression analysis on this database. This multi-linear regression models a dependent variable ($B_I D$ or $B_I S$) as a function of the summation of two independent variables (grain

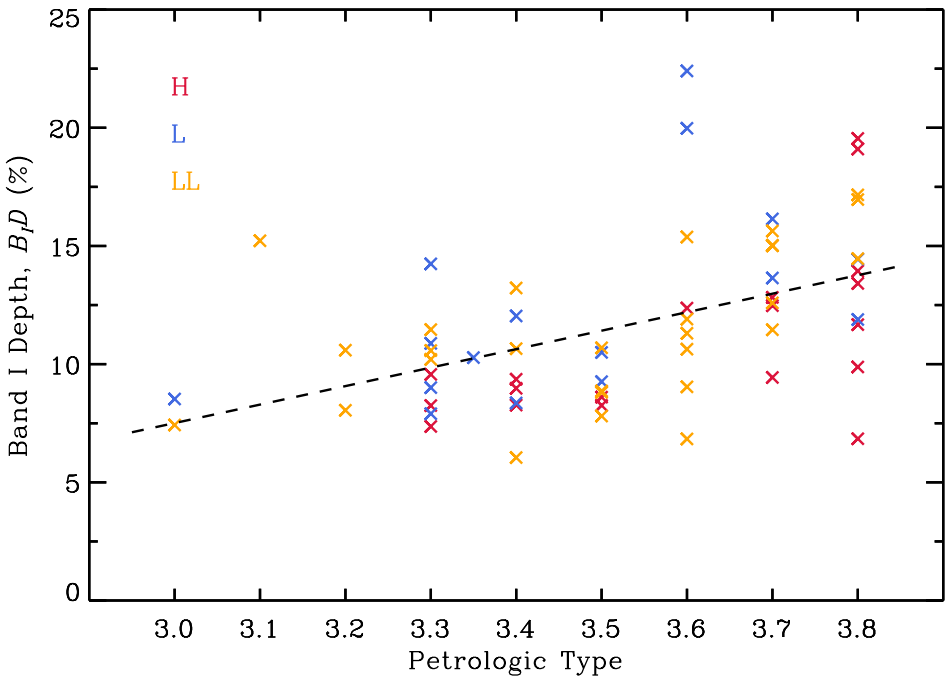

Figure 3.7: $B_I D$ for ordinary chondrites with petrologic types 3-3.8. I cut off the x-axis at 3.8 since no petrologic type 3.9 exist in my sample. A straight line (p-value $< .01$) is fit to all these points demonstrating the increase in mean $B_I D$ with petrologic type. The spread in points around the line also increases with increasing petrologic type, indicating the increase in band depth variance with thermal alteration.

size and petrologic type). The results of running this model indicate that $B_I D$ is dependent on the petrologic type (but not grain size), and $B_I S$ is not dependent on either petrologic type or grain size. A complication of this approach is that samples were not sorted into distinct size bins, which would be appropriate in identifying any small effect(s) that grain size has on any of the band parameters studies here. I suggest and encourage future research into investigating the effect of grain size of OC meteorites on various band parameters.

Space Weathering Parameters

I analyze the Vis-NIR reflectance spectra of spectra twelve ordinary chondrite samples that have been subjected to space weathering laboratory simulation experiments performed by others (table 3.4). Band parameters of these samples, which were used for laser and ion irradiated experiments, as estimated using BAR-Ast are given in table 3.4. As indicated, a total of ten of these samples come from RELAB and two from other independent works (Strazzulla et al., 2005; Kanuchova et al., 2015). Several samples were not ground into particulates and remained as "chips" during the simulation experiment. As a consequence, the $B_I S$ of these samples are somewhat shifted to smaller (negative) values (figure 3.8). As with the analyzed un-weathered samples, the unaltered spectra exhibit most variation in $B_I D$. Characteristic changes in the spectra after irradiation are mostly often with $B_I S$ (up to 40% change) and a decrease in the $B_I D$ exceed 10% in some cases (top panels in figure 3.6). The bottom two panels indicate that the changes in band depth and spectral slope are non-linearly correlated with the irradiation exposure. In particular, the largest changes occur at the onset of irradiation and decrease with increasing irradiation.

3.4.2 HEDs

The howardite-eucrite-diogenite (HED) meteorite group, the most abundant class of achondrites, represents material originating from a differentiated body — most likely, Vesta (McCord et al., 1970; McSween et al., 2013). Generally speaking, HEDs represent magmatic material — primarily composed of pyroxene and plaigioclase — which cooled quickly near the surface (eucrites, the most common of the three), slowly beneath the surface (diogenites),

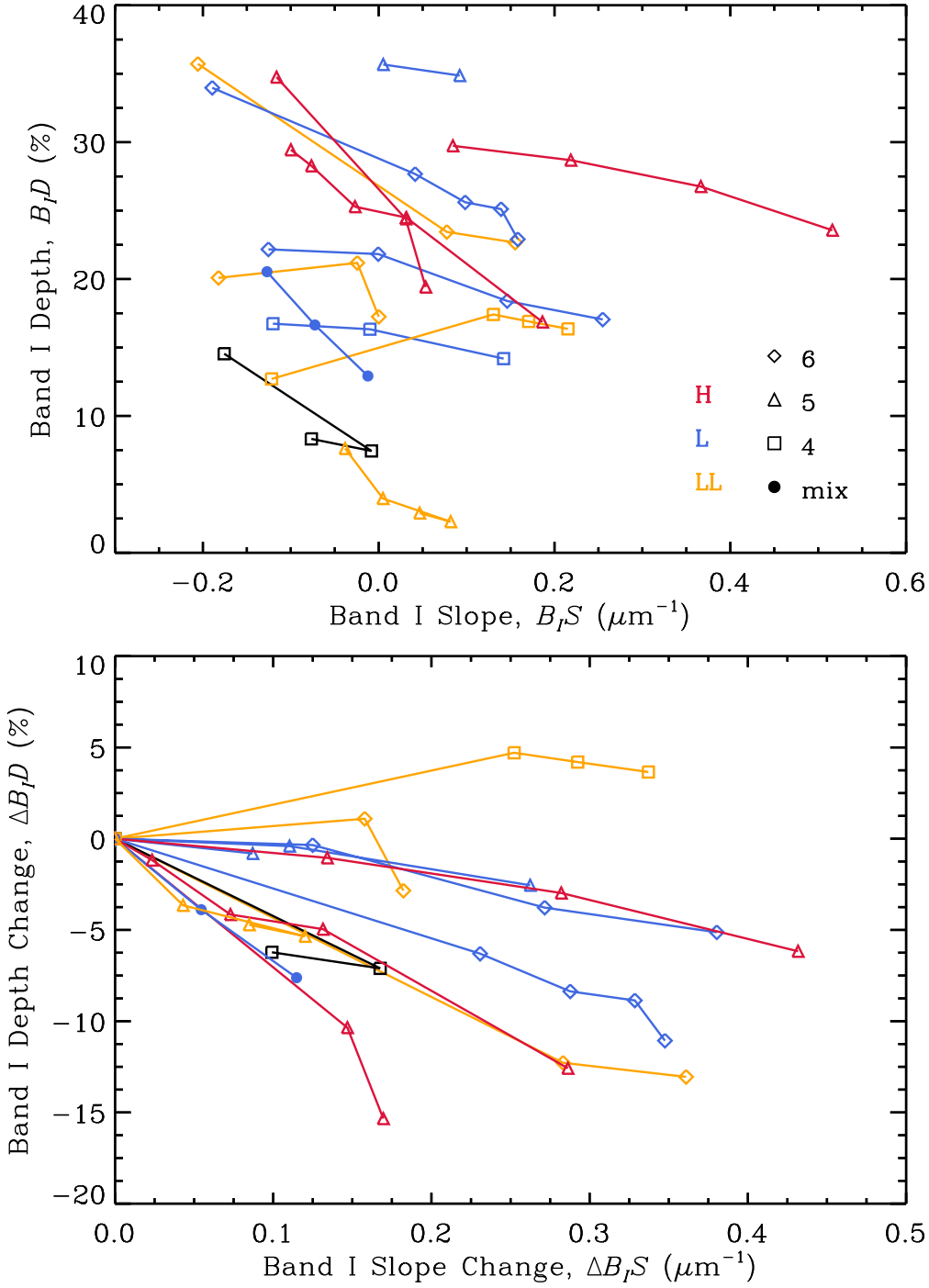

Figure 3.8: Space weathering band parameters (B_IS and B_ID) of ordinary chondrites.

Table 3.4: Band Parameters of Laser and Ion-irradiated Ordinary Chondrites

Meteorite	Type	Grain Size	RELAB ID/Work	Energy	B_IC (μm)	B_IS (μm^{-1})	B_ID (%)	$B_{II}C$ (μm)	BAR	$\Delta B_ID/\Delta B_IS$
Appley Bridge	LL6	chip	OC-TXH-012-A	—	1.010	0.206	0.357	1.954	0.252	38.1
			OC-TXH-012-A20	20 mJ	0.998	0.078	0.234	1.940	0.261	
			OC-TXH-012-A40	40 mJ	1.002	0.155	0.227	1.934	0.263	
Athens	LL6	$<$ 125 μm pellet	OC-TXH-013-D	—	1.020	0.182	0.201	1.938	0.278	7.5
			OC-TXH-013-D05	5 mJ	0.998	0.024	0.212	1.949	0.240	
			OC-TXH-013-D15	5 + 10 mJ	1.020	0.000	0.172	1.952	0.227	
Burnwell	HH4	chip	OC-TXH-021-A	—	0.980	0.176	0.145	1.945	0.506	43.9
			OC-TXH-021-A20	20 mJ	0.898	0.008	0.074	1.930	0.488	
			OC-TXH-021-A40	40 mJ	0.905	0.077	0.083	1.933	0.726	
Chateau Renard	L6	chip	OC-TXH-011-A	—	0.960	0.189	0.340	1.960	0.309	29.7
			OC-TXH-011-A20	20 mJ	0.975	0.042	0.277	1.965	0.292	
			OC-TXH-011-A40	40 mJ	0.964	0.098	0.256	1.932	0.277	
			OC-TXH-011-A60	60 mJ	0.955	0.139	0.251	1.940	0.290	
			OC-TXH-011-A80	80 mJ	0.983	0.158	0.229	1.939	0.293	
		$<$ 125μm pellet	OC-TXH-011-D	—	0.950	0.125	0.222	1.928	0.435	14.7
			OC-TXH-011-D05	5 mJ	0.946	0.001	0.218	1.928	0.413	
			OC-TXH-011-D15	5 + 10 mJ	0.944	0.146	0.184	1.930	0.398	
			OC-TXH-011-D35	5 + 10 + 20 mJ	0.936	0.255	0.170	1.930	0.380	
Cynthiana	L4	$<$ 125 μm pellet	OC-TXH-015-D	—	0.940	0.120	0.167	1.945	0.541	10.0
			OC-TXH-015-D05	5 mJ	0.935	0.010	0.163	1.938	0.531	
			OC-TXH-015-D15	5 + 10 mJ	0.930	0.142	0.142	1.930	0.486	
Ehole	H5	chip	OC-TXH-006-A	—	0.927	0.116	0.348	1.903	0.716	83.3
			OC-TXH-006-A20	20 mJ	0.933	0.031	0.244	1.899	0.837	
			OC-TXH-006-A40	40 mJ	0.938	0.053	0.194	1.915	0.579	
Elenovka	L5	$<$ 75 μm pellet	MS-CMP-041-A	—	0.936	0.005	0.357	1.928	0.536	9.3
			MS-CMP-041-B	1.5 KW	0.939	0.092	0.349	1.924	0.511	
Epinal	H5	bulk powder	Strazzulla et al. (2005)	—	0.932	0.084	0.297	1.893	0.533	14.2
				1.3e15	0.932	0.219	0.287	1.906	0.548	
				4.3e15	0.932	0.366	0.268	1.922	0.543	
				1.7e16	0.930	0.516	0.236	1.895	0.571	
Hamlet	LL4	chip	OC-TXH-002-A	—	1.053	0.122	0.127	1.985	0.496	12.8
			OC-TXH-002-A20	20 mJ	1.040	0.130	0.174	1.973	0.395	
			OC-TXH-002-A40	40 mJ	1.037	0.171	0.169	1.968	0.356	
			OC-TXH-002-A60	60 mJ	1.040	0.215	0.164	1.955	0.336	
Hedjaz	L3-6	chip	OC-TXH-016-A	—	0.921	0.127	0.205	1.935	0.906	66.3
			OC-TXH-016-A20	20 mJ	0.916	0.073	0.166	1.905	0.764	
			OC-TXH-016-A40	40 mJ	0.910	0.012	0.129	1.940	0.779	
Kosice	H5	bulk powder	Kanuchova et al. (2015)	—	0.927	0.100	0.294	1.896	0.781	42.7
				2.7e14	0.938	0.076	0.283	1.893	0.822	
				4.0e15	0.938	0.027	0.253	1.888	0.738	
				1.0e16	0.935	0.032	0.245	1.890	0.874	
				5.0e16	0.928	0.186	0.169	1.902	0.951	
Paragould	LL5	chip	OC-TXH-007-A	—	0.965	0.038	0.076	2.020	0.097	43.1
			OC-TXH-007-A20	20 mJ	1.078	0.005	0.040	2.045	0.109	
			OC-TXH-007-A40	40 mJ	0.960	0.082	0.023	1.990	1.035	
			OC-TXH-007-A60	60 mJ	1.326	0.047	0.029	2.045	0.068	

or reflect impact breccias that are a mixture of both (howardites; McSween et al., 2013). I analyzed over 150 spectra within RELAB and tabulate some of the diagnostic space weathering and mineralogical band parameters (B_IC, B_IS, B_ID, $B_{II}C$, and BAR) in table 3.5. The samples listed in table 3.5 are grouped by meteorite sub-type. Here, I make the additional distinction between monomict (of a single lithology) and polymict (of multiple lithologies) eucrites.

Duffard et al. (2005) studied and found a positive correlation between BAR and the grain size of HED powders. Following them, I select meteorites in RELAB which contain samples sorted into discrete grain size bins (figure 3.9). In agreement with Duffard et al. (2005), I note that B_ID non-monotonically varies with grain size and peaks when the grain size is around 45–75 μm, with a range as great as 10%. As I will discuss shortly, this complicates the use of B_ID in interpreting the space weathering band parameters of asteroids. The top panel of figure 3.9 shows a variety of B_IS trends with grain size. Notably, the eucrite Juvinas shows B_IS changes of more than 0.6 μm^{-1} for grain size bins $<$ 25 μm to 75–125 μm.

Space Weathering Parameters

I analyze the spectra of laser and ion-irradiated HED meteorites and terrestrial orthopyroxene (OPx) in order to characterize the change in B_IS and B_ID caused by space weathering. Figure 3.10 shows the B_IS and B_ID for the values listed in table 3.6, colored by meteorite type with symbols depicting the type of irradiation (laser or ion). I compute the average change in B_IS and B_ID by fitting lines to the parameters calculated for each sample. Compared to the irradiated ordinary chondrites, the pyroxene and HED samples show greater spectral reddening, but a similar decrease in B_ID for similar irradiation exposure. There is a notable increase in B_ID with increased dosage for the eucrite Millbillillie, which adds to the overall dispersion in the space weathering paths. The HEDs average change in band depth per unit of spectral slope is $\Delta B_ID/\Delta B_IS$ = -14.3 %μm^{-1} which I use in section 3.6 to compare the average space weathering parameters of HEDs to asteroids of similar composition.

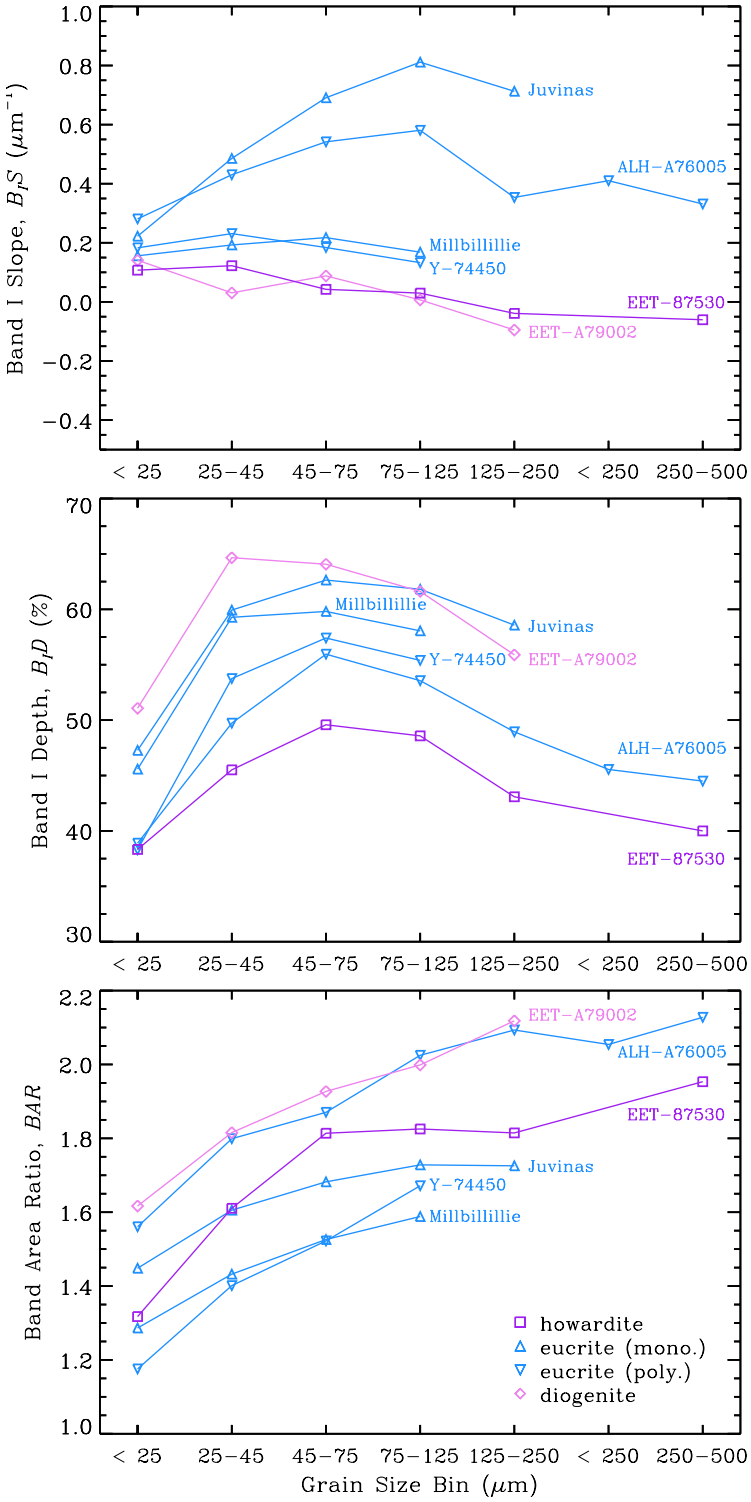

Figure 3.9: Band parameters of individual HED samples as a function of grain size bin. Purple squares, blue triangles, and pink diamonds are, respectively, howardite, eucrite, and diogenites. Upward-facing triangles are monomict eucrites and downward-facing triangles are ploymict eucrites.

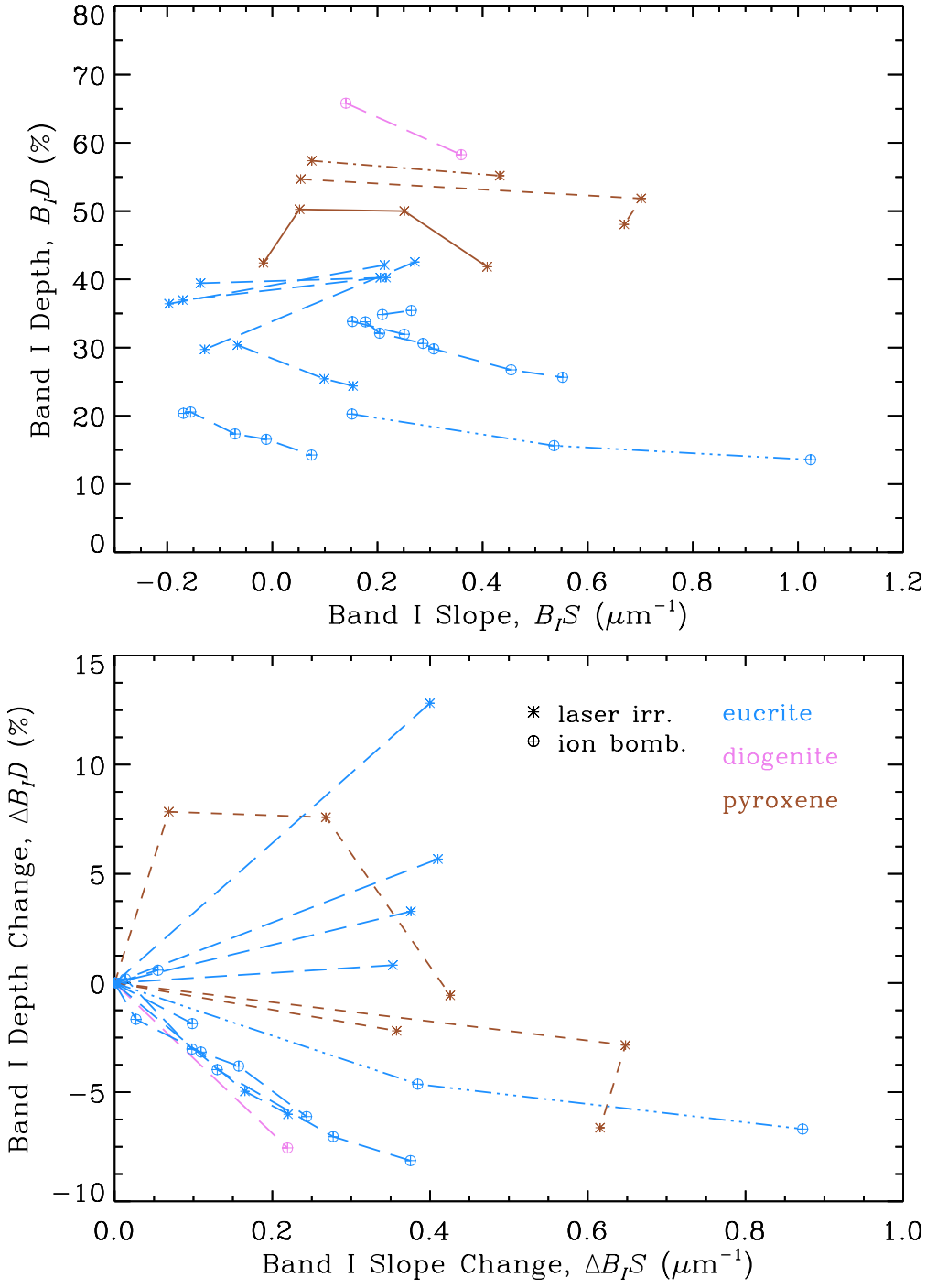

Figure 3.10: Space weathered band parameters of HEDs and terrestrial pyroxene. Colors indicate the type of sample: brown for terrestrial pyroxene, blue for eucrites, and pink for the diogenite. Circles with crosses indicate samples that have been ion bombarded and asterisks indicate laser irradiattion.

Table 3.5: Band Parameters of HEDs

Meteorite	Type	Grain Size	RELAB ID	B_IC (μm)	B_IS (μm^{-1})	B_ID (%)	$B_{II}C$ (μm)	BAR
A-87272,96	eu (mono.)	< 25 μm	MP-TXH-094-A	0.941	0.104	0.553	1.989	1.253
Bereba	eu (mono.)	< 25 μm	MP-TXH-089-A	0.940	0.341	0.421	2.011	1.423
Bouvante	eu (mono.)	< 25 μm	MP-TXH-090-A	0.943	0.745	0.457	2.001	1.744
Bouvante	eu (mono.)	< 44 μm	TB-TJM-118	0.946	0.958	0.514	1.984	2.047
Bouvante	eu (mono.)	bulk	TB-RPB-029	0.947	0.358	0.408	1.988	2.228
EET92003,15	eu (mono.)	< 125 μm	MP-TXH-118	0.933	0.184	0.577	1.992	1.610
Jonzac	eu (mono.)	< 25 μm	MP-TXH-091-A	0.938	0.321	0.545	1.996	1.597
Juvinas	eu (mono.)	—	MB-TXH-070-1	0.941	0.372	0.570	1.976	1.610
Juvinas	eu (mono.)	—	MB-TXH-070-2	0.940	0.284	0.567	1.990	1.610
Juvinas	eu (mono.)	< 25 μm	MB-TXH-070-A	0.936	0.222	0.472	1.989	1.448
Juvinas	eu (mono.)	$25 - 45$ μm	MB-TXH-070-B	0.940	0.485	0.599	1.984	1.605
Juvinas	eu (mono.)	$45 - 75$ μm	MB-TXH-070-C	0.944	0.690	0.626	1.977	1.682
Juvinas	eu (mono.)	$75 - 125$ μm	MB-TXH-070-D	0.948	0.811	0.618	1.969	1.728
Juvinas	eu (mono.)	$125 - 250$ μm	MB-TXH-070-E	0.950	0.712	0.585	1.964	1.725
Juvinas	eu (mono.)	—	MR-MJG-091	0.943	0.577	0.551	1.954	1.549
Juvinas	eu (mono.)	—	MR-MJG-091	0.943	0.576	0.549	1.956	1.552
Juvinas	eu (mono.)	< 250 μm	TB-RPB-153	0.945	0.722	0.625	1.972	1.741
Millbillillie	eu (mono.)	—	MS-JTW-050	0.948	0.007	0.425	1.978	1.626
Millbillillie	eu (mono.)	—	MS-JTW-050	0.946	0.033	0.243	1.978	1.790
Millbillillie	eu (mono.)	< 25 μm	MB-TXH-069-A	0.937	0.155	0.455	2.000	1.286
Millbillillie	eu (mono.)	$25 - 45$ μm	MB-TXH-069-B	0.938	0.192	0.592	1.996	1.432
Millbillillie	eu (mono.)	$45 - 75$ μm	MB-TXH-069-C	0.941	0.217	0.598	1.997	1.526
Millbillillie	eu (mono.)	$75 - 125$ μm	MB-TXH-069-D	0.941	0.168	0.580	1.996	1.588
Stannern	eu (mono.)	bulk	MR-MJG-092-P	0.946	0.561	0.406	1.976	2.114
Stannern	eu (mono.)	bulk	MR-MJG-092-P	0.944	0.570	0.428	1.976	1.989
Y-791186-90	eu (mono.)	bulk	TB-RPB-009	0.948	0.180	0.407	1.969	1.587
Y-792510-140	eu (mono.)	bulk	TB-RPB-007	0.943	0.024	0.511	1.983	1.504
ALH-78132,61	eu (poly.)	< 25 μm	MB-TXH-072-A	0.932	0.292	0.429	1.953	1.683
ALH-78132,61	eu (poly.)	$25 - 45$ μm	MB-TXH-072-B	0.933	0.460	0.586	1.954	1.816
ALH-78132,61	eu (poly.)	$45 - 75$ μm	MB-TXH-072-C	0.935	0.495	0.622	1.956	1.927
ALHA76005,85	eu (poly.)	< 25 μm	MB-TXH-066-A	0.934	0.280	0.388	1.972	1.560
ALHA76005,85	eu (poly.)	$25 - 45$ μm	MB-TXH-066-B	0.937	0.430	0.497	1.974	1.799
ALHA76005,85	eu (poly.)	$45 - 75$ μm	MB-TXH-066-C	0.940	0.541	0.559	1.972	1.870
ALHA76005,85	eu (poly.)	$75 - 125$ μm	MB-TXH-066-D	0.941	0.580	0.535	1.978	2.024
ALHA76005,85	eu (poly.)	$125 - 250$ μm	MB-TXH-066-E	0.941	0.353	0.489	1.969	2.093
ALHA76005,85	eu (poly.)	$250 - 500$ μm	MB-TXH-066-F	0.941	0.331	0.444	1.962	2.127
ALHA76005	eu (poly.)	bulk	TB-RPB-023	0.942	0.191	0.400	1.972	2.080
ALHA76005	eu (poly.)	< 250 μm	TB-RPB-024	0.942	0.410	0.455	1.969	2.054
ALHA81011,83	eu (poly.)	bulk	TB-RPB-013	0.961	-0.040	0.371	2.049	1.241
ALHA81011,85	eu (poly.)	< 125 μm	MP-TXH-122	0.950	0.252	0.471	2.026	1.166
EET83251	eu (poly.)	bulk	TB-RPB-022	0.937	0.208	0.439	1.959	1.813
EETA79005	eu (poly.)	< 250 μm	TB-RPB-026	0.936	0.283	0.491	1.959	1.865
EETA79005,99	eu (poly.)	< 25 μm	MP-TXH-072-A	0.934	0.343	0.469	1.964	1.705
EETA79006,66	eu (poly.)	< 125 μm	MP-TXH-123	0.935	0.263	0.479	1.968	1.801
EETA790B	eu (poly.)	bulk	TB-RPB-025	0.937	0.115	0.454	1.949	1.853
LEW 86001-21	eu (poly.)	< 75 μm	MT-D2M-251-A	0.943	0.287	0.493	1.996	1.480
LEW 87004-25	eu (poly.)	< 75 μm	MT-D2M-209-A	0.933	0.245	0.412	1.969	1.577
LEW87004	eu (poly.)	bulk	TB-RPB-019	0.937	0.145	0.448	1.964	1.655
LEW87004-23	eu (poly.)	< 25 μm	MP-TXH-079-A	0.934	0.327	0.433	1.969	1.419
Macibini Clast 3	eu (poly.)	< 63 μm	TB-RPB-027	0.940	0.316	0.467	1.983	1.501
Pasamonte	eu (poly.)	< 25 μm	MP-TXH-087-A	0.939	0.280	0.495	1.996	1.347
Pasamonte	eu (poly.)	—	MR-MJG-090	0.936	0.171	0.406	1.994	1.317
Petersburg	eu (poly.)	< 25 μm	MP-TXH-070-A	0.936	0.222	0.472	1.989	1.448
Petersburg:53	eu (poly.)	bulk	MR-MJG-097	0.936	0.350	0.483	1.955	1.965
Petersburg:55	eu (poly.)	bulk	MR-MJG-097	0.936	0.350	0.482	1.955	1.965
Y-75011-107	eu (poly.)	bulk	TB-RPB-008	0.946	-0.080	0.280	1.996	1.296

Table 3.5 — continued

Meteorite	Type	Grain Size	RELAB ID	B_IC (μm)	B_IS (μm^{-1})	B_ID (%)	$B_{II}C$ (μm)	BAR
Y-74450,92	eu (poly.)	< 25 μm	MB-TXH-071-A	0.934	0.183	0.383	1.974	1.175
Y-74450,92	eu (poly.)	$25 - 45$ μm	MB-TXH-071-B	0.936	0.231	0.537	1.964	1.401
Y-74450,92	eu (poly.)	$45 - 75$ μm	MB-TXH-071-C	0.937	0.184	0.574	1.971	1.522
Y-74450,92	eu (poly.)	$75 - 125$ μm	MB-TXH-071-D	0.938	0.132	0.553	1.975	1.671
A-881526-90	di	< 25 μm	MP-TXH-095-A	0.920	0.093	0.646	1.891	1.720
ALH 85015-10	di	< 45 μm	RM-REM-122-A	0.923	0.120	0.461	1.929	1.552
ALH 85015-10	di	bulk	RM-REM-122-P	0.921	-0.210	0.455	1.918	1.869
ALHA 77256-34	di	< 45 μm	RM-REM-123-A	0.920	0.106	0.547	1.893	1.805
ALHA 77256-34	di	bulk	RM-REM-123-P	0.917	0.056	0.722	1.889	2.141
EET 83246-29	di	< 45 μm	RM-REM-127-A	0.920	0.197	0.612	1.899	1.910
EET 83246-29	di	bulk	RM-REM-127-P	0.923	0.378	0.775	1.882	2.352
EETA79002,146	di	< 25 μm	MB-TXH-067-A	0.919	0.141	0.510	1.889	1.616
EETA79002,146	di	$25 - 45$ μm	MB-TXH-067-B	0.920	0.030	0.646	1.892	1.815
EETA79002,146	di	$45 - 75$ μm	MB-TXH-067-C	0.920	0.088	0.640	1.889	1.927
EETA79002,146	di	$75 - 125$ μm	MB-TXH-067-D	0.920	0.006	0.616	1.897	1.998
EETA79002,146	di	$125 - 250$ μm	MB-TXH-067-E	0.921	-0.090	0.559	1.907	2.118
EETA79002,146	di	$250 - 500$ μm	MB-TXH-067-F	0.921	-0.060	0.537	1.901	2.188
GRA 98108-26	di	< 45 μm	RM-REM-125-A	0.921	-0.010	0.487	1.908	1.253
GRA 98108-26	di	bulk	RM-REM-125-P	0.921	-0.260	0.815	1.910	1.788
GRA98108	di	< 45 μm	MT-AWB-169-A	0.921	0.119	0.630	1.890	1.826
GRA98108	di	bulk	MT-AWB-169	0.920	0.085	0.678	1.889	1.926
Johnstown	di	< 25 μm	MB-TXH-095-A	0.917	0.045	0.448	1.884	1.439
Johnstown	di	$25 - 45$ μm	MB-TXH-095-B	0.917	0.037	0.629	1.884	1.736
Johnstown	di	bulk	MR-MJG-098-P	0.926	0.412	0.698	1.881	2.305
Johnstown	di	bulk	MR-MJG-098-P	0.926	0.354	0.733	1.887	2.174
LAP 02216-19	di	< 45 μm	RM-REM-129-A	0.920	0.026	0.540	1.904	1.734
LAP 02216-19	di	bulk	RM-REM-129-P	0.918	0.000	0.685	1.900	2.158
LAP 03979-11	di	< 45 μm	RM-REM-131-A	0.925	0.069	0.543	1.920	1.649
LAP 03979-11	di	bulk	RM-REM-131-P	0.927	0.081	0.832	1.910	2.107
LAP91900,27	di	< 25 μm	MP-TXH-077-A	0.922	0.070	0.625	1.904	1.744
LEW 88008-23	di	< 45 μm	RM-REM-128-A	0.918	0.087	0.601	1.890	1.753
LEW 88008-23	di	bulk	RM-REM-128-P	0.920	0.162	0.690	1.885	2.116
MET 01084-11	di	< 45 μm	RM-REM-132-A	0.921	0.040	0.523	1.904	1.571
MET 01084-11	di	bulk	RM-REM-132-P	0.920	-0.13	0.711	1.893	2.094
MIL 03368-14	di	< 45 μm	RM-REM-121-A	0.921	0.141	0.571	1.912	1.804
MIL 03368-14	di	bulk	RM-REM-121-P	0.922	0.090	0.681	1.909	2.093
MIL 03443-19	di	< 45 μm	RM-REM-126-A	1.058	0.006	0.310	1.999	0.120
MIL 03443-19	di	bulk	RM-REM-126-P	1.060	-0.040	0.502	2.014	0.070
MIL07001	di	< 45 μm	MT-AWB-168-A	0.921	0.115	0.602	1.894	1.830
MIL07001	di	bulk	MT-AWB-168	0.920	0.115	0.620	1.895	1.943
PCA 02008-12	di	< 45 μm	RM-REM-130-A	0.923	0.051	0.425	1.924	1.510
PCA 02008-12	di	bulk	RM-REM-130-P	0.923	0.002	0.502	1.920	1.599
QUE 99050-7	di	< 45 μm	RM-REM-120-A	0.919	0.143	0.573	1.893	1.842
QUE 99050-7	di	bulk	RM-REM-120-P	0.918	0.180	0.828	1.886	2.281
Tatahouine	di	< 25 μm	MP-TXH-088-A	0.920	0.087	0.634	1.894	1.676
Tatahouine	di	bulk	MR-MJG-100-P	0.916	0.174	0.759	1.884	2.017
Y-74013,HR	di	< 25 μm	MB-TXH-073-A	0.923	0.095	0.422	1.916	1.684
Y-74013,HR	di	$25 - 45$ μm	MB-TXH-073-B	0.922	0.077	0.604	1.908	1.881
Y-75032,HR	di	< 25 μm	MB-TXH-074-A	0.927	0.192	0.519	1.937	1.481
Y-75032,HR	di	$25 - 45$ μm	MB-TXH-074-B	0.927	0.207	0.664	1.938	1.685
CRE 01400-12	how	< 75 μm	MT-D2M-200-A	0.922	0.276	0.561	1.916	1.827
EET 83376-16	how	< 75 μm	MT-D2M-242-A	0.930	0.318	0.519	1.953	1.826
EET 87503-166	how	< 75 μm	MT-D2M-243-A	0.931	0.156	0.423	1.959	1.590
EET 87509-109	how	< 75 μm	MT-D2M-201-A	0.931	0.285	0.469	1.964	1.758
EET 87513-134	how	< 75 μm	MT-D2M-244-A	0.931	0.166	0.428	1.956	1.619
EET 87518-10	how	< 75 μm	MT-D2M-245-A	0.935	0.323	0.474	1.967	1.750

Table 3.5 — continued

Meteorite	Type	Grain Size	RELAB ID	$B_I C$ (μm)	$B_I S$ (μm^{-1})	$B_I D$ (%)	$B_{II} C$ (μm)	BAR
EET 99400-11	how	< 75 μm	MT-D2M-247-A	0.932	0.308	0.493	1.960	1.849
EET 99408-12	how	< 75 μm	MT-D2M-204-A	0.932	0.298	0.476	1.965	1.727
EET 87503-97	how	< 25 μm	MB-TXH-068-A	0.929	0.107	0.383	1.948	1.317
EET 87503-97	how	$25 - 45$ μm	MB-TXH-068-B	0.929	0.122	0.455	1.949	1.610
EET 87503-97	how	$45 - 75$ μm	MB-TXH-068-C	0.930	0.042	0.495	1.948	1.813
EET 87503-97	how	$75 - 125$ μm	MB-TXH-068-D	0.932	0.029	0.485	1.960	1.825
EET 87503-97	how	$125 - 250$ μm	MB-TXH-068-E	0.933	-0.030	0.430	1.966	1.814
EET 87503-97	how	$250 - 500$ μm	MB-TXH-068-F	0.934	-0.060	0.400	1.968	1.953
GRO 95535-13	how	< 75 μm	MT-D2M-248-A	0.929	0.158	0.465	1.944	1.655
GRO 95574-14	how	< 75 μm	MT-D2M-205-A	0.928	0.172	0.434	1.944	1.646
GRO 95581-11	how	< 75 μm	MT-D2M-249-A	0.929	0.156	0.453	1.942	1.659
GRO 95602-7	how	< 75 μm	MT-D2M-206-A	0.929	0.167	0.415	1.951	1.633
GRO95574-9	how	< 125 μm	MP-TXH-125	0.929	0.150	0.485	1.943	1.685
Kapoeta	how	bulk	MP-TXH-053	0.931	0.027	0.552	1.935	1.928
Kapoeta	how	< 25 μm	MP-TXH-053-A	0.929	0.123	0.408	1.947	1.242
LAP 04838-8	how	< 75 μm	MT-D2M-250-A	0.935	0.353	0.437	1.963	1.524
LAP 04838-9	how	< 75 μm	MT-D2M-207-A	0.934	0.390	0.415	1.962	1.539
Le Teilleul	how	< 25 μm	MP-TXH-093-A	0.928	0.260	0.560	1.937	1.758
LEW 85313-39	how	< 75 μm	MT-D2M-208-A	0.930	0.195	0.425	1.956	1.553
MET 00423-7	how	< 75 μm	MT-D2M-210-A	0.932	0.180	0.386	1.969	1.622
MET 96500-17	how	< 75 μm	MT-D2M-252-A	0.932	0.188	0.426	1.957	1.595
MET 96500-19	how	< 75 μm	MT-D2M-211-A	0.930	0.236	0.448	1.950	1.666
PCA 02009-19	how	< 40 μm	MT-AWB-238	0.923	0.062	0.469	1.921	1.582
PCA 02013-6	how	< 40 μm	MT-AWB-239	0.922	0.090	0.357	1.921	1.535
PCA 02014-7	how	< 40 μm	MT-AWB-240	0.928	0.061	0.340	1.945	1.399
PCA 02015-11	how	< 40 μm	MT-AWB-241	0.936	0.055	0.258	1.969	1.216
PCA 02066-8	how	< 75 μm	MT-D2M-253-A	0.936	0.053	0.395	1.959	1.281
PRA 04401-7	how	< 75 μm	MT-D2M-254-A	0.922	0.141	0.221	1.945	1.263
QUE 94200-29	how	< 75 μm	MT-D2M-255-A	0.923	0.250	0.560	1.916	1.921
QUE 97001-39	how	< 75 μm	MT-D2M-256-A	0.924	0.236	0.551	1.917	1.915
QUE 97001-40	how	< 75 μm	MT-D2M-212-A	0.922	0.272	0.563	1.912	1.960
QUE 97002-28	how	< 75 μm	MT-D2M-257-A	0.938	0.266	0.368	1.976	1.613
QUE 97002-29	how	< 75 μm	MT-D2M-213-A	0.936	0.233	0.339	1.974	1.557
QUE 99033-14	how	< 75 μm	MT-D2M-214-A	0.922	0.306	0.560	1.915	2.000
QUE97001-28	how	< 125 μm	MP-TXH-126	0.925	0.274	0.577	1.924	1.995
SAN 03472-9	how	< 75 μm	MT-D2M-258-A	0.929	0.215	0.476	1.955	1.935
SCO 06040-8	how	< 75 μm	MT-D2M-215-A	0.930	0.130	0.371	1.961	1.475
Y-7308-142	how	< 25 μm	MP-TXH-097-A	0.927	0.118	0.578	1.936	1.674
Y-790727-144	how	< 25 μm	MP-TXH-098-A	0.931	0.372	0.492	1.949	1.675
Y-791573-145	how	< 25 μm	MP-TXH-099-A	0.927	0.208	0.470	1.939	1.695

Table 3.6: Band Parameters of Laser and Ion-irradiated Pyroxenes and HEDs

Work	Sample	Grain Size	Energy	B_IC (μm)	B_IS (μm^1)	B_ID	$B_{II}C$ (μm)	BAR	$\Delta B_ID/\Delta B_IS$
Yamada et al. (1999)	OPx	$<$ 75 μm pellet	—	0.921	-0.017	0.424	1.869	1.821	-4.5
			30 mJ	0.918	0.052	0.503	1.887	1.698	
			300 mJ	0.921	0.251	0.500	1.880	1.774	
			600 mJ	0.925	0.409	0.418	1.892	1.640	
Marchi et al. (2005)	OPx	100 – 200 μm	—	0.913	0.075	0.574	1.853	2.204	-6.1
			200 keV	0.915	0.433	0.552	1.853	2.273	
Brunetto et al. (2006)	OPx	$\sim$ 200 μm	—	0.912	0.054	0.547	1.852	2.199	-7.3
			43 Jcm^{-2}	0.914	0.702	0.518	1.858	2.337	
			86 Jcm^{-2}	0.915	0.669	0.481	1.857	2.240	
MS-JTW-049-A	Johnstown (D)	10 – 100 μm pellet	—	0.921	0.140	0.658	1.887	2.016	-34.4
MS-JTW-049-B			?	0.922	0.359	0.583	1.890	2.052	
MS-JTW-049-C			?	0.924	0.166	0.354	1.905	1.414	
MS-JTW-052-1	Millbillillie (Eu)	$<$ 75 μm	—	0.943	0.216	0.403	1.990	1.497	
MS-JTW-052-3				0.950	-0.137	0.394	1.979	0.527	
MS-JTW-052-4				0.943	0.206	0.403	1.993	1.477	
MS-JTW-052-6				0.962	-0.170	0.370	1.973	0.393	
MS-JTW-052-7				0.943	0.214	0.421	1.991	1.491	
MS-JTW-052-9				0.963	-0.196	0.364	1.972	0.345	
Vernazza et al. (2006)	Béréba (Eu)	10 – 100 μm	—	0.933	0.151	0.203	2.024	1.332	-7.5
			1.6e15 Ar^{++}	0.936	0.536	0.156	2.047	1.567	
			6.6e15 Ar^{++}	0.944	1.024	0.136	2.065	1.016	
Fulvio et al. (2012)	Béréba	10 – 100 μm pellet	—	0.934	-0.066	0.304	2.018	1.587	-28.0
			4.35e17 Ar$^+$ cm^{-2}	0.945	0.099	0.254	2.019	1.724	
			3.5e15 C$^+$ cm^{-2}	0.948	0.154	0.244	2.020	1.785	
	Béréba	10 – 100 μm pellet	—	0.945	-0.169	0.204	2.017	1.566	-26.0
			5e16 Ar$^+$ cm^{-2}	0.946	-0.155	0.206	2.017	1.566	
			3e15 C$^+$ cm^{-2}	0.949	-0.071	0.173	2.019	1.430	
			8e15 C$^+$ cm^{-2}	0.950	-0.012	0.166	2.037	1.684	
			2.3e16 C$^+$ cm^{-2}	0.954	0.075	0.143	2.052	1.762	
	Dar Al Gani 684 (E)	10 – 100 μm pellet	—	0.946	0.152	0.338	2.016	1.805	-18.9
			8e16 Ar$^+$ cm^{-2}	0.949	0.251	0.320	2.020	1.810	
	Dar Al Gani 684	10 – 100 μm pellet	—	0.949	0.209	0.349	1.969	1.607	10.7
			2e17 Ar$^+$ cm^{-2}	0.949	0.209	0.349	1.984	1.559	
	Dar Al Gani 684	10 – 100 μm pellet	—	0.945	0.177	0.338	1.988	1.801	-21.0
			5e16 Ar$^+$ cm^{-2}	0.948	0.204	0.321	2.020	1.760	
			3e15 C$^+$ cm^{-2}	0.957	0.287	0.306	2.013	1.718	
			2e16 Ar$^+$ cm^{-2}	0.955	0.307	0.298	2.017	1.735	
			8e15 C$^+$ cm^{-2}	0.958	0.454	0.267	2.019	1.803	
			1.3e16 Ar$^+$ cm^{-2}	0.962	0.552	0.256	2.021	1.816	

3.4.3 Olivine-Rich Meteorites

The selected meteorite groups for this study that are mineralogically and spectrally dominated by olivine include the brachinites, pallasites, R and CK chondrites. Despite their spectral commonalities, these meteorite groups represent different geochemical histories and compositions. Brachinites are primitive achondrites (most likely partial melt residues) with high amounts of olivine, up to 15% of clinopyroxene, and minor amounts of other minerals such as plagioclase and chromite, and trace amounts of metal (Keil, 2014). Large olivine crystals embedded in a metal matrix characterize pallasite meteorites, which are thought to represent the core-mantle regions of differentiated planetary bodies (Chabot and Haack, 2006). R (Rumuruti type) chondrites contain high amounts of iron-rich olivine and can be distinguished from other chondrites by their high matrix fraction, greater sulfide content, and low amounts of Ni-Fe metal due to the highly oxidizing formation conditions (Bischoff et al., 2011). CK (Karoonda-like) chondrites contain highly oxidized primitive solar system material with large (0.7–1 mm), high-FeO chondrules (Fa29–33) and are nearly absent of any metallic Fe or Ni (Greenwood et al., 2010). Both R and CK chondrites can exhibit varying degrees of metamorphism, reflected in the petrologic type sub-classification number ranging from 3 (least altered) to 6 (most altered), which I take care to include with every sample in my analysis.

Diogenites from Vesta, which may represent a shallow mantle origin or plutonic rocks from within the crust (Ammannito et al., 2013), can contain amounts of olivine exceeding 90% (MIL 03443; Beck and McSween, 2010) of cumulate (not mantle) origin. Since this meteorite type is a rarity in meteorite collections, I exclude it from further consideration. Other olivine-rich meteorites in RELAB, such as the ureilite group, other olivine diogenites, and CV/CO chondrites were considered, but had band centers less than 1.05 μm and/or BAR greater than 0.2, and thus plot outside the S(I) box in figure 3.2.

The band parameters derived from RELAB spectra of several samples from these meteorite groups are given in table 3.7. Space weathering band parameters (B_IS and B_ID) of olivein-rich meteorites and terrestrial olivine samples are plotted in figure 3.11. A large variance in the B_ID (2%–65%) is apparent among the meteorite dataset. In a study of

Table 3.7: Band Parameters of Olivine-rich Meteorites

Meteorite	Fo#	Type	RELAB/USGS ID	Grain Size	B_IC (μm)	B_IS (μm^1)	B_ID (%)	$B_{II}C$ (μm)	BAR
Brachnia	70	brach.	MT-TXH-049-A	$<$ 45	1.052	0.267	0.396	—	—
Eagle's Nest	68	brach.	MT-TXH-050-A	$<$ 45 μm	1.055	0.418	0.392	—	—
EET 99402,44	65	brach.	MT-JMS-088	bulk powder	1.063	0.029	0.289	—	—
		brach.	TB-TJM-058	$<$ 125 μm	1.070	0.102	0.483	—	—
Hughes 026	66	brach.	MT-TXH-051-A	$<$ 45 μm	1.060	0.100	0.295	—	—
Reid 013	66	brach.	MT-TXH-052-A	$<$ 45 μm	1.062	0.056	0.201	—	—
Esquel	89	PMG	MB-TXH-043	slab	1.196	0.544	0.643	—	—
Imilac	87	PMG	MB-TXH-041	slab	1.066 $\pm$ 0.014	-0.020 $\pm$ 0.079	0.445 $\pm$ 0.147	—	—
Marjalahti	86	PMG ol	MS-CMP-005-C	100 – 200 μm	1.056	0.169	0.647	—	—
			MS-CMP-005-F	40 – 100 μm	1.057	0.187	0.360	—	—
			MS-CMP-005-X	$<$ 40 μm	1.051	0.180	0.147	—	—
Thiel Mountains	88	PMG ol	MT-TJM-027	$<$ 74 μm	1.055	0.097	0.420	—	—
ALH85002,25	71	CK4	MB-TXH-081-A	$<$ 25 μm	1.061	-0.016	0.124	—	—
		CK4	MB-TXH-081-B	25 – 45 μm	1.075	-0.088	0.129	—	—
		CK4	MB-TXH-081-C	45 – 75 μm	1.064	-0.172	0.187	—	—
		CK4	MB-TXH-081-D	75 – 125 μm	1.070	-0.231	0.133	—	—
ALH85002	71	CK4	PH-D2M-035	$<$ 75 μm	1.065	-0.068	0.101	—	—
EET83311	69	CK5	PH-D2M-047	$<$ 75 μm	1.066	-0.081	0.107	—	—
EET87507,27	71	CK5	MB-TXH-092	$<$ 500 μm	1.059	-0.126	0.135	—	—
EET87526,11	71	CK5	LM-LAM-019	bulk powder	1.062	-0.138	0.105	—	—
EET87860,5	72	CK5-6	LM-LAM-018	bulk powder	1.060	-0.094	0.108	—	—
LEW87009,28	69	CK6	MB-TXH-088	$<$ 500 μm	1.060	0.007	0.309	—	—
LEW87009,4	69	CK6	LM-LAM-017	bulk powder	1.060	-0.030	0.245	—	—
PCA91470	67	CK4	PH-D2M-046	$<$ 75 μm	1.068	-0.043	0.144	—	—
Y-693	71	CK4-5	MB-TXH-077	$<$ 125 μm	1.067	-0.130	0.132	—	—
A-881988,70	66	R4	MP-TXH-059	$<$ 125 μm	1.095	-0.009	0.016	1.970	1.044
LAP04840,16	62	R6 olivine	DD-AHT-109	$<$ 45 μm	1.054	0.096	0.343	1.975	0.048
LAP04840,16	62	R6	DD-AHT-107	$<$ 125 μm	1.031	0.239	0.365	1.970	0.053
MET01149	61	R3	PH-D2M-045	$<$ 75 μm	1.065	0.085	0.130	2.068	0.140
			DD-AHT-108	$<$ 45 μm	1.045	0.148	0.269	1.970	0.074
PCA91002,13	61	R3.8-6	MB-TXH-065	$<$ 125 μm	1.059	-0.055	0.113	2.135	0.147
			MB-TXH-065-A	$<$ 63 μm	1.064	0.043	0.123	2.140	0.127
			MB-TXH-065-B	63 – 125 μm	1.062	-0.124	0.156	2.091	0.194
PRE95411,5	61	R3	MT-TXH-045	$<$ 125 μm	1.065	0.154	0.141	1.995	0.191
Rumuruti	61	R3.8-6	MT-TJM-013	$<$ 150 μm	1.067	0.089	0.285	2.121	0.050

Table 3.8: Band Parameters of Olivine Samples

Sample ID	Locality	Fo#	Grain Size (μm)	B_IC (μm)	B_IS (μm^1)	B_ID (%)
GDS70.a	South Point, Hawaii USA	89	150 – 250 (165)	1.062	0.415	0.820
GDS70.b	”	”	104 – 150 (115)	1.060	0.319	0.768
GDS70.c	”	”	60 – 104 (70)	1.054	0.303	0.709
GDS70.d	”	”	< 60	1.058	0.110	0.406
GDS70.e	”	”	< 30	1.060	0.220	0.552
GDS71.a	Twin Sisters Peak, WA USA	91	60 – 104 (70)	1.051	0.117	0.701
GDS71.b	”	”	< 60	1.044	0.086	0.343
KI3188	Kiglapait Intrusive, Labrador Canada	51	< 60	1.074	0.203	0.581
KI3189	”	60	< 60	1.069	0.205	0.620
KI4143	”	41	< 60	1.079	0.266	0.576
KI3291	”	29	< 60	1.089	0.455	0.718
KI3377	”	18	< 60	1.089	0.420	0.571
KI3005	”	11	< 60	1.094	0.480	0.620
PO-52	Rome, Italy	97	< 45	1.059	0.045	0.133
PO-76	Fort Defiance, AZ USA	92	< 45	1.057	0.061	0.200
PO-60	Twin Sisters Peak, WA USA	92	< 45	1.060	0.082	0.204
GSB	Green Sand Beach, HI USA	89	< 60	1.063	0.113	0.291
PO-64	Stillwater, MT USA	86	< 45	1.061	0.116	0.319
PO-31	Volcano National Park, HI USA	84	< 45	1.066	0.108	0.326
PO-74	Rustanburg, South Africa	42	< 45	1.080	0.097	0.393
PO-72	Franklin, NJ USA	36	< 45	1.089	0.091	0.448

the spectral effects of varying olivine and metal mixtures in band parameters Cloutis et al. (2015) remark that greater band depths can be a consequence of increasing either or both the grain size of olivine and fraction of metal in the sample, as well as the Fo#. As shown in table 3.7, R and CK chondrites typically have band depths below 35% and as low as a few percent, whereas brachinite and pallasite band depths extend up to ∼50% and ∼65%, respectively. The largest band depths are found among the pallasites, which contain the most metal out of these four groups, supporting the idea that increasing the metal content results in spectral reddening. The band depth effects from changing the olivine grain size can be easily seen for the pallasite Marjalahti and, to a lesser extent, the brachinite EET 99402. With the small number of samples that are available, there appears to be a similar positive trend between petrologic type and band depth within the R chondrites, similar to what was seen among the ordinary chondrites: the two R6 olivines and two CK6 meteorites exhibit systematically higher band depths (∼35% and ∼30%, respectively) compared to the lower grade petrologic types (R3-4/CK4; ∼15%). I also note that the $B_I D$ range of R chondrites, which that contain chondrules with a wide range of thermal alteration, fall within the range of 15–35%.

Grain size variations for the R chondrites LAP04840 and PCA91002,13 mainly contribute to spectral slope changes, which also mimics the trend seen among ordinary chondrites. Furthermore, the degree of slope change with grain size is consistent with that of ordinary chondrites, which is on the order of 0.15 μm^{-1} for grain sizes bins varying from < 45 μm up to < 125 μm among the R chondrites. The CK chondrite ALH85002 exhibits a very similar trend, although there is a somewhat systematic downward shift in spectral slope for CK chondrites compard to R chondrites. It is not clear what the cause of spectral slope differences among the pallasites is, although variation in the fraction of metal to olivine and the amount of FeO in the olivine is known to influence the slope. As noted by Cloutis et al. (2015) increasing FeO in olivine and the metal increases the spectral slope in a similar fashion. The singular fact that pallasites contain much more metal than brachnites, however, doesn't explain the considerable overlap in spectral slope between these two groups. Thus, the competing interplay between both the metal content and olivine FeO on spectral slope may be the reason for the overlap between the pallasites and brachinites.

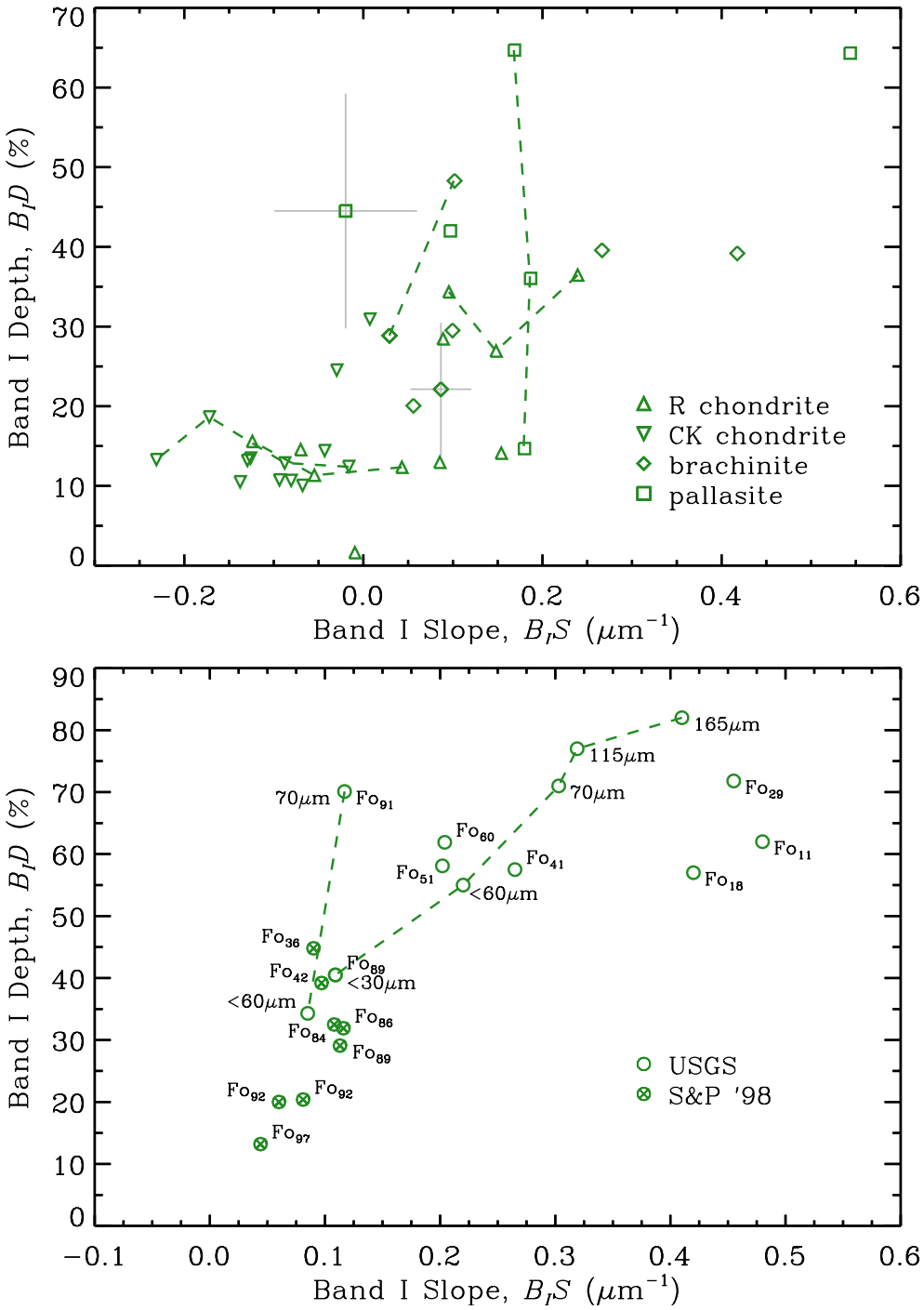

Figure 3.11: Spectral slope and band depth of olivine-rich meteorite groups (top) and terrestrial olivines (bottom). Lines connect spectral parameters of samples of similar origin.

Space Weathering Parameters

Several experimenters have succeeded at simulating the process(es) of space weathering on olivine in order to reproduce the resulting effects seen in reflectance spectra. Laboratory setups range from infrared (Gillis-Davis et al., 2017), visible (Sasaki et al., 2001; Kurahashi et al., 2002; Yang et al., 2017) and UV (Brunetto et al., 2006; Loeffler et al., 2016) laser irradiation as well as high-energy bombardment with various ion particles (Loeffler et al., 2009; Marchi et al., 2005). All of these works used terrestrial olivine samples — in fact, all but Yang et al. (2017) sourced from the same low-iron olivine (Fo_{91}) near the San Carlos Reservation in Arizona, USA. The results from applying the BAR-Ast algorithm on the irradiated samples are given in table 3.9 and their B_IS and B_ID values are plotted in figure 3.12.

These irradiated olivine samples initially show similar spectral slope and band depth variations to that of the set of meteorite and other terrestrial olivines in figure 3.11. Upon increasing irradiation exposure, large increases in spectral slope are observed, along with small decreases in the band depth; on average[7], the change in band depth per change in spectral slope is $\Delta B_ID/\Delta B_IS$ = -15.2%μm^{-1}. Only Sasaki et al. (2001) shows an anomalous increase in band depth at higher exposure. The Yang et al. (2017) samples show less spectral slope alteration at the same level of irradiation as the Sasaki et al. (2001) and Kurahashi et al. (2002) samples. A possible explanation for this discrepancy in spectral slope could come from the fact that Fo_{95} olivine was the subject of the Yang et al. (2017) experiments, and the lower FeO content may result in less pronounced spectral slope reddening compared to the San Carlos Olivine; irradiation experiments for systematically different Fo# are needed to test this idea. Band depth changes seem to cease above a cumulative exposure of 100–150 mJ, but noticeable spectral reddening continues to persist at energies exceeding 150 mJ.

Lastly, I analyze spectra from the experiment conducted by Kohout et al. (2014), in which controlled production of npFe^0 was achieved by heating of olivine samples under different oxidizing conditions. The resulting increases in B_IS and B_ID were similar to those of irradiated olivine samples, indicating that increasing amounts of npFe^0 were the direct cause of the spectral changes. Figure 3.13 shows these space weathering parameters as a

[7]Excluding the anomalous increase in band depth in Sasaki et al. (2001).

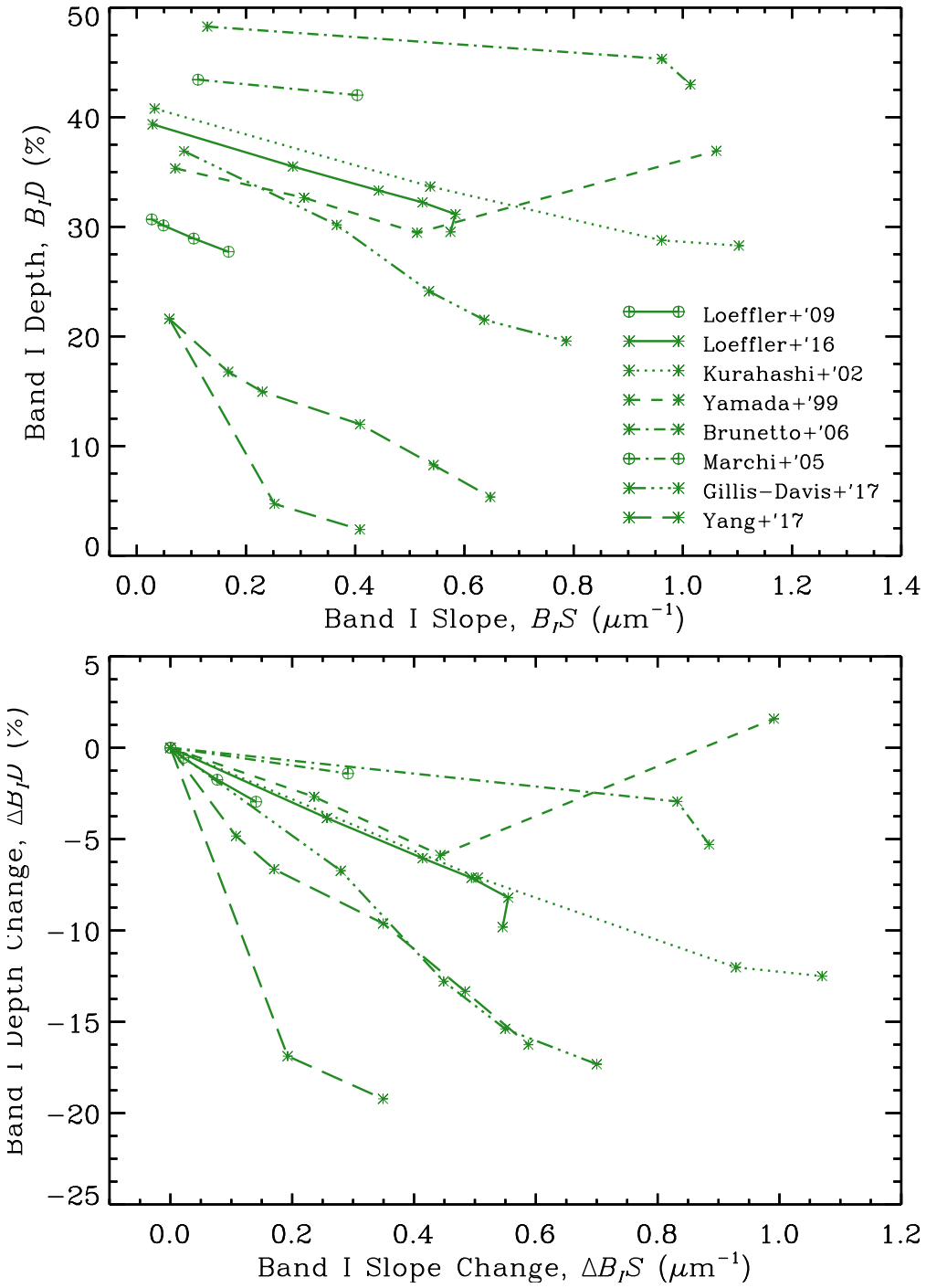

Figure 3.12: Space weathered band parameters of olivine samples. Solid lines represent the experiments led by M. Loeffler (circle with plus and asterisks for Loeffler et al. (2009) and Loeffler et al. (2016), respectively), dotted lines are from Kurahashi et al. (2002), short dash are from Yamada et al. (1999), dash-dot with asterisks are from Brunetto et al. (2006), dash-dot with circle with plus are from Marchi et al. (2005), and dash-dot-dot are from Gillis-Davis et al. (2017), and long dashes are from Yang et al. (2017).

Table 3.9: Band Parameters of Laser, Ion-irradiated, and Heated Terrestrial Olivine

Work	Fo#	Grain Size	Energy	B_IC (μm)	B_IS (μm^1)	B_ID (%)	$\Delta B_ID/\Delta B_IS$
Yamada et al. (1999)	91	$<$ 75 μm pellet	—	1.064	0.070	0.353	-13.2
			15 mJ	1.067	0.306	0.327	
			2x15 mJ	1.070	0.513	0.295	
			10x15 mJ	1.060	1.061	0.369	
Kurahashi et al. (2002)	91	$<$ 75 μm pellet	—	1.059	0.033	0.408	-12.0
			30 mJ	1.061	0.538	0.337	
			5x30 mJ	1.064	0.961	0.288	
			10x30 mJ	1.061	1.103	0.283	
Marchi et al. (2005)	91	100 – 200 μm	—	1.055	0.112	0.434	-4.8
			7 x 10^{15} Ar^+cm^{-2}	1.057	0.404	0.420	
Brunetto et al. (2006)	91	$\sim$ 200 μm	—	1.055	0.129	0.483	-4.9
			27 Jcm^{-2}	1.061	0.962	0.453	
			52 Jcm^{-2}	1.056	1.013	0.430	
Loeffler et al. (2016)	91	45 – 125 μm	—	1.054	0.029	0.394	-14.6
			1 pulse	1.054	0.286	0.355	
			4 pulses	1.056	0.443	0.333	
			7 pulses	1.057	0.523	0.322	
			25 pulses	1.057	0.584	0.312	
			99 pulses	1.057	0.574	0.295	
Gillis-Davis et al. (2017)	91	$<$ 75 μm pellet	—	1.055	0.087	0.369	-26.1
			12,000 shots	1.055	0.366	0.301	
			24,000 shots	1.057	0.535	0.241	
			36,000 shots	1.058	0.636	0.215	
			48,000 shots	1.058	0.787	0.196	
Yang et al. (2017)	95	$<$ 45 μm pellet	—	1.049	0.060	0.216	-25.5
			25 mJ	1.053	0.167	0.168	
			2x25 mJ	1.054	0.230	0.150	
			3x25 mJ	1.057	0.409	0.120	
			4x25 mJ	1.055	0.544	0.083	
			5x25 mJ	1.057	0.647	0.054	
			2x50 mJ	1.057	0.252	0.047	
			5x50 mJ	1.079	0.409	0.024	
Loeffler et al. (2009)	91	$<$ 45 μm pellet	—	1.052	0.027	0.307	-20.1
			1.5 x 10^{17} He	1.053	0.049	0.301	
			5.3 x 10^{17} He	1.054	0.104	0.289	
			25 x 10^{17} He	1.053	0.168	0.277	
			wt. % $npFe^0$				
Kohout et al. (2014)	93	10 – 80 μm	—	1.049	0.022	0.327	
			0.0075	1.049	0.144	0.284	
			0.011	1.052	0.204	0.245	
			0.013	1.058	0.235	0.297	
			0.015	1.052	0.326	0.249	
			0.023	1.052	0.357	0.194	
			0.049	1.058	0.308	0.126	
			0.059	1.052	0.463	0.123	
			0.12	1.069	0.533	0.069	

function of weight percent of npFe^0 in the heated sample. Both sets of data are shown with best-fit logarithmic functions, with the band depth data fit by using 1 $-B_ID$ as the dependent variable. These data show that both parameters exhibit most of the total change at the onset of npFe^0 formation. In section 3.8.1 I delve more into this observation.

Conclusions

In this section I have analyzed the depth change per change in spectral slope for pyroxene, HED, olivine, and ordinary chondrite samples. I use these average slopes of space weathering pathways to analyze the mineralogical effects on the spectral changes brought on by space weathering. Ordinary chondrites, which have Fo_{70-85} (Dunn et al., 2010a) and terrestrial olivines, which have $Fo_{>90}$, exhibit different space weathering paths, with greater depth per slope changes occuring among the ordinary chondrites with higher FeO. The two main lunar terrains — the Fe-rich basalt and Fe-poor anorthosite — show this same relationship Lucey et al. (2000); Nettles et al. (2011). The observed differences in space weathering pathways

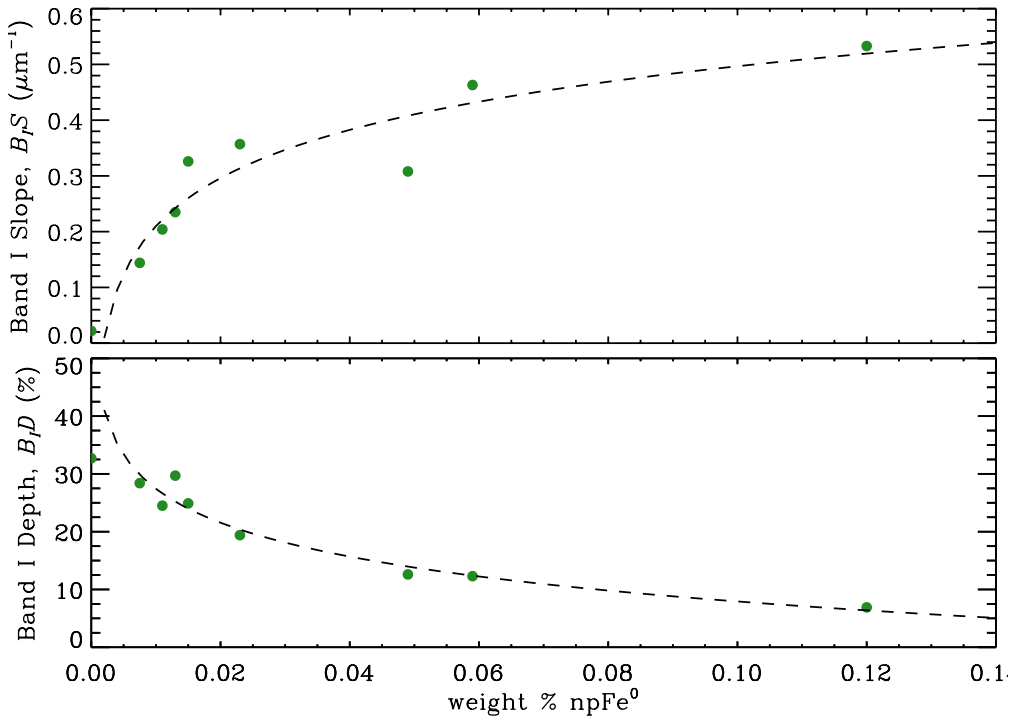

Figure 3.13: Measured B_IS (*top*) and B_ID (*bottom*) as a function of the weight percent of npFe^0, from Kohout et al. (2014). Dotted lines are the best-fit logarthmic functions to the points.

between olivine and pyroxene contradicts the idea that materials with higher relative olivine abundance exhibit greater space weathering. The irradiation experiments of Yamada et al. (1999) and Sasaki et al. (2001) show that greater spectral changes, particularly the spectral slope reddening, are exhibited more in olivine than pyroxene samples that were given the same dose of irradiation. Additionally, I show here that pyroxene samples showed more of a change in spectral slope and little decrease in band depth. I can conclude the following: 1) a sample with any amount of spectrally-identifiable olivine exhibits a greater sensitivity to space weathering processes regardless of the exact relative abundance to pyroxene and 2) the greater amount of FeO in olivine (Fa#= 100 - Fo#) will cause more band depth changes per change in spectral slope than in samples with higher Fo#.

3.4.4 The Asteroid Space Weathering Index

Given the information garnered from the space weathering band parameters, I proceed to formulate a single parameter that captures the degree of space weathering. This parameter is based off the separation, in spectral slope/band depth parameter space, from the appropriate meteorite analog of each compositional group. The "distance" measured is traced along the space weathering trend calculated for each compositional group. In order to do this, I establish a new coordinate basis: one coordinate parallel to the slope calculated for space weathering experiments, and the second that is aligned to the set of unweathered meteorite samples.

The zero-point, or "baseline", for unweathered band parameters of ordinary chondrites are established by fitting a line to all samples falling within the < 150 μm grain size bin. This bin is chosen since it contains an almost even distribution of all petrologic types. The line is fit such that band depth is the independent variable and spectral slope is the dependent variable. By removing the samples of different grain, sizes I avoid the complexity inherent to the correlation of petrologic type 3 and < 45 μm grain size bin that was just mentioned above. The cluster of BA asteroids appears to be simply shifted to the right (increase in spectral slope) from the HEDs, corroborating the laboratory irradiation experiments on terrestrial pyroxene samples. From the laser and ion-bombardment experiments, I have observed that changes in $B_I S$ and $B_I D$ are largest when first exposed to irradiation, and then changes

gradually become less great with increasing time/exposure. This relationship between the ever shrinking derivative with an increase in value is characteristic of a logarithmic function. I can conclude that space weathering measured for asteroids will not increase monotonically with irradiation dose, but instead is described by a logarithmic or power function.

Basis vectors for the space weathering coordinates are chosen such that one unit in the space weathered direction represents a change in spectral slope of 0.2 μm^{-1} and one unit in the orthogonal direction represents a change in band depth of 10%. figure 3.14 illustrates each coordinate transformation for each compositional group. The basis coordinates are combined to form a 2 x 2 matrix that represents a transformation from the space weathering coordinates to the original spectral slope and band depth parameters:

$$\begin{bmatrix} a & b \\ c & d \end{bmatrix} \begin{bmatrix} B_I S^* \\ B_I D \end{bmatrix} = \begin{bmatrix} SWI \\ BDI \end{bmatrix}, \tag{3.1}$$

where the coefficients in the leftmost matrix are given in table 3.10. This matrix is inverted to create the linear transformation equations for converting spectral slope and band depth to the space weathering coordinate system. The result of using the matrix equation in equation (3.1) is a rotation and shearing of the coordinate frame, but a shift in the $B_I S$ is necessary in order to align the vertical axis with the meteorites. The amount of shift for each composition is applied by adding the intercept (int) as such: $B_I S^* = B_I S + int$.

3.5 Results: Asteroids

Band parameters of each asteroid spectrum in my sample are given in table 3.11, table 3.12, and table 3.13 for S(IV), BA, and S(I) sub-types, respectively. Also given in all three

Table 3.10: Space weathering index coordinate transformation parameters.

	a	b	c	d	int
S(I)	4.60	-2.63	1.40	9.20	0.036
S(IV)	5.00	0.0035	2.55	10.0	-0.045

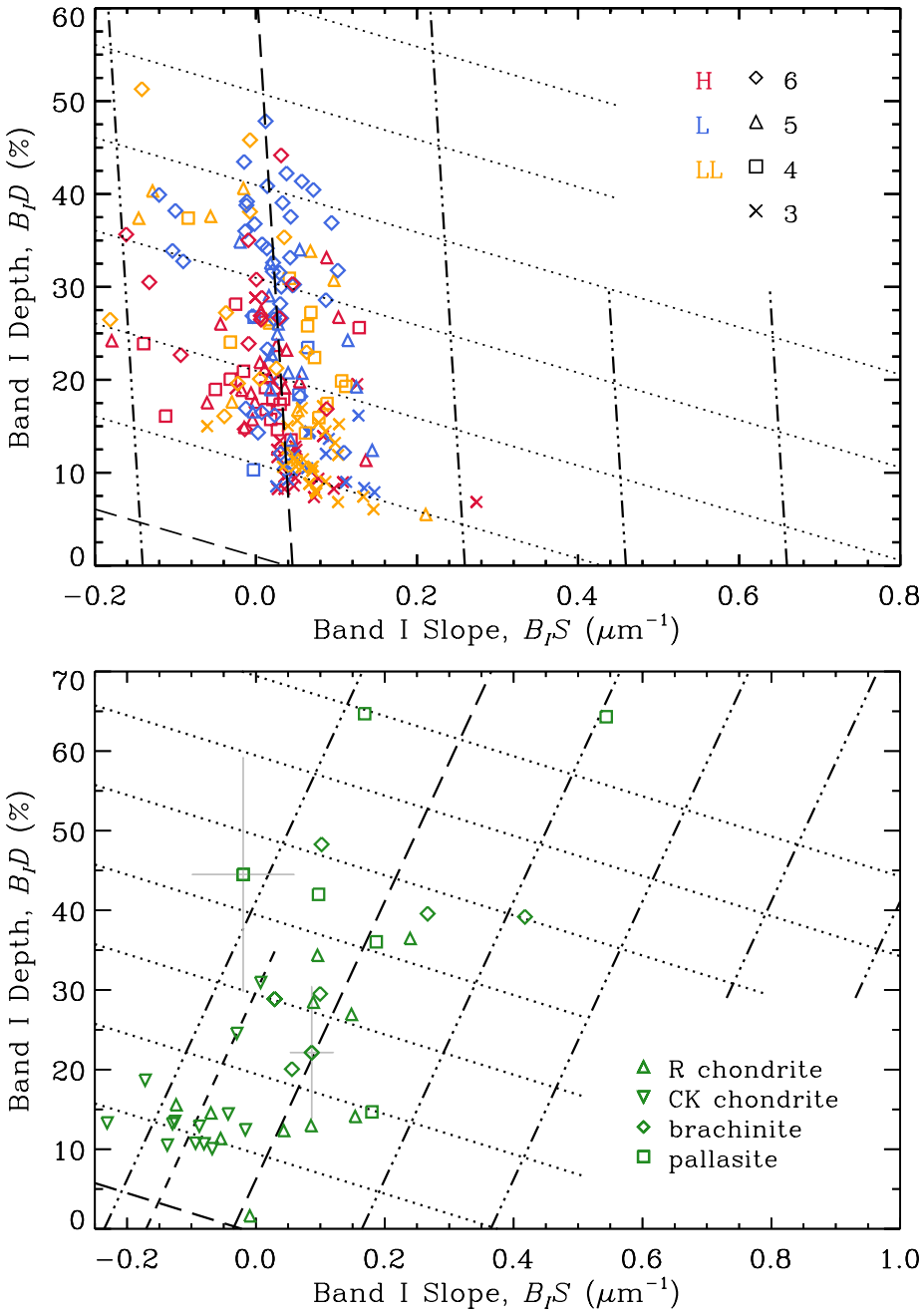

Figure 3.14: Definition of the *SWI* and *BDI* axes in B_IS vs. B_ID space. The top and bottom panels show the OC and olivine-rich samples, respectively.

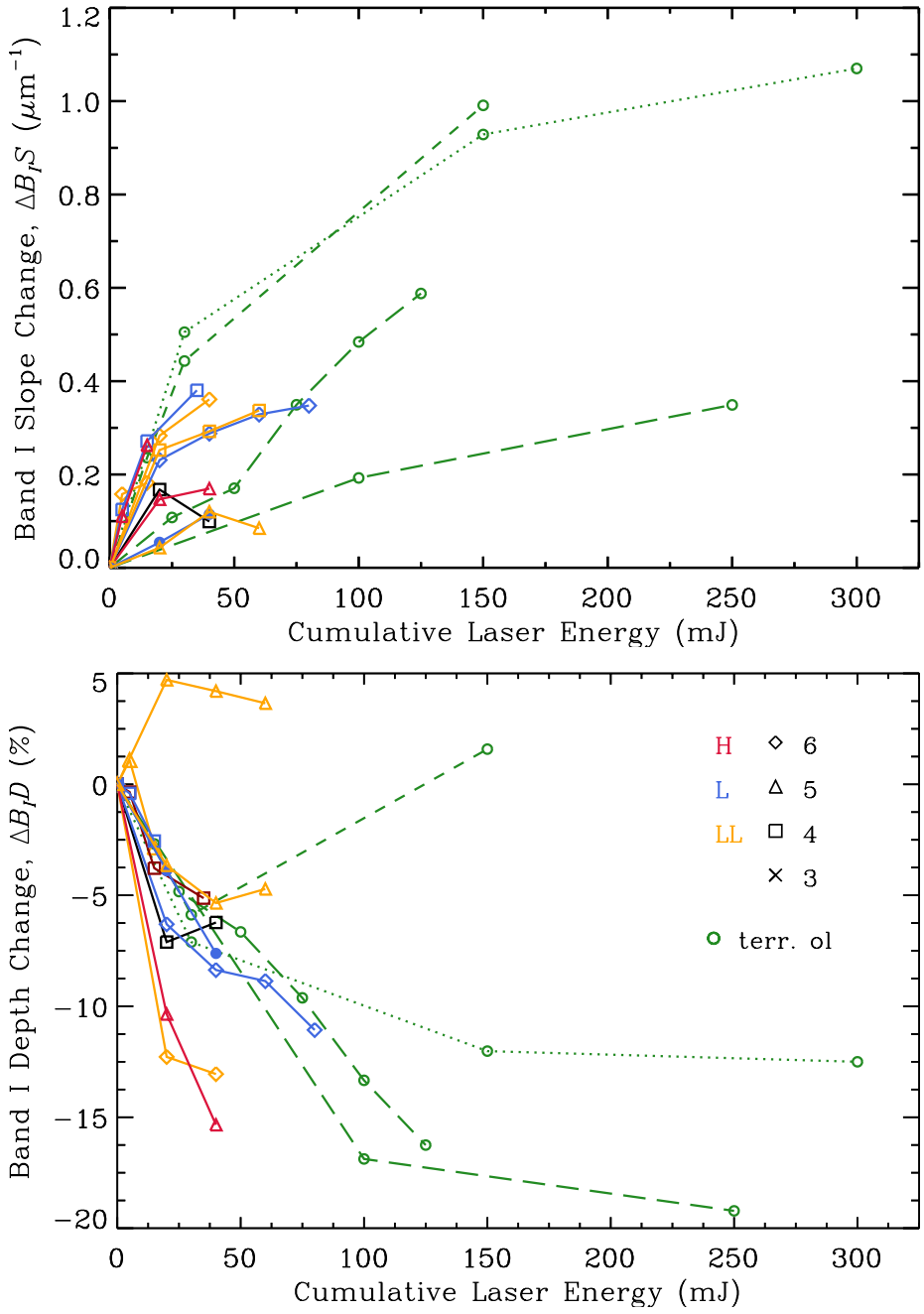

Figure 3.15: Change in $B_I S$ and $B_I D$ for olivine and ordinary chondrite samples as a function of laser energy.

Table 3.11: Band Parameters of S(IV) Asteroids

Object	Vis[a]	NIR[a]	tax[b]	met[c]	BIC[d]	BIS_{corr}[e]	BID_{corr}[f]	$BIIC$[d]	$BIIC_{corr}$[g]	BAR	BAR_{corr}[h]	R_{AU}[i]	$\alpha(^\circ)$[j]	T_c[k]
(3) Juno	s3os2	spex96	—	LL	0.952 ± 0.003	0.349 ± 0.002	0.100 ± 0.001	1.994	2.004 ± 0.008	0.793	0.751 ± 0.040	2.60	21.27	251
(3) Juno	smass1	spex96	—	LL	0.951 ± 0.002	0.358 ± 0.002	0.097 ± 0.001	1.994	2.004 ± 0.008	0.824	0.782 ± 0.041	2.60	21.27	251
(3) Juno	smass2	spex96	Sq	L	0.942 ± 0.004	0.279 ± 0.001	0.125 ± 0.001	1.994	2.004 ± 0.008	0.587	0.545 ± 0.030	2.60	21.27	251
(6) Hebe	smass1	spex67	—	H	0.930 ± 0.002	0.203 ± 0.002	0.095 ± 0.001	1.903	1.915 ± 0.030	0.784	0.734 ± 0.050	2.53	10.73	241
(6) Hebe	smass1	spex68	—	H	0.920 ± 0.001	0.277 ± 0.001	0.097 ± 0.001	1.915	1.928 ± 0.007	0.796	0.743 ± 0.020	2.64	13.73	236
(6) Hebe	smass2	spex67	S	L	0.931 ± 0.002	0.164 ± 0.002	0.110 ± 0.001	1.903	1.915 ± 0.029	0.614	0.564 ± 0.038	2.53	10.73	241
(6) Hebe	smass2	spex68	S	L	0.920 ± 0.001	0.232 ± 0.001	0.113 ± 0.001	1.915	1.928 ± 0.007	0.631	0.578 ± 0.015	2.64	13.73	236
(7) Iris	smass1	spex28	—	LL	0.950 ± 0.002	0.195 ± 0.001	0.087 ± 0.001	1.969	1.980 ± 0.009	0.565	0.518 ± 0.010	2.57	10.29	244
(7) Iris	smass2	spex28	S	L	0.942 ± 0.002	0.137 ± 0.001	0.112 ± 0.001	1.969	1.980 ± 0.009	0.426	0.379 ± 0.007	2.57	10.29	244
(11) Parthenope	smass2	spex47	Sq	L	0.945 ± 0.001	0.184 ± 0.001	0.105 ± 0.001	1.917	1.926 ± 0.009	0.280	0.240 ± 0.006	2.51	12.49	253
(14) Irene	as68	spex25	—	H	0.923 ± 0.001	0.262 ± 0.003	0.072 ± 0.001	1.920	1.932 ± 0.008	1.023	0.972 ± 0.027	2.74	20.98	239
(14) Irene	sawyer	spex25	—	H	0.924 ± 0.001	0.267 ± 0.001	0.070 ± 0.001	1.920	1.932 ± 0.008	1.063	1.013 ± 0.023	2.74	20.98	239
(14) Irene	sawyer	spex25	—	H	0.924 ± 0.001	0.271 ± 0.001	0.069 ± 0.001	1.920	1.932 ± 0.008	1.094	1.044 ± 0.024	2.74	20.98	239
(14) Irene	smass1	spex25	S	H	0.921 ± 0.001	0.235 ± 0.001	0.080 ± 0.001	1.920	1.932 ± 0.008	0.852	0.802 ± 0.018	2.74	20.98	239
(14) Irene	smass2	spex25	S	H	0.920 ± 0.001	0.214 ± 0.001	0.090 ± 0.001	1.920	1.932 ± 0.008	0.754	0.703 ± 0.015	2.74	20.98	239
(17) Thetis	smass2	spex96	S	H	0.916 ± 0.001	0.341 ± 0.002	0.093 ± 0.001	1.960	1.970 ± 0.006	1.280	1.237 ± 0.047	2.60	17.86	250
(17) Thetis	smass2	sunshine	S	H	0.920 ± 0.001	0.302 ± 0.002	0.096 ± 0.001	1.904	1.914 ± 0.009	0.979	0.937 ± 0.017	2.59	22.60	250
(17) Thetis	vilas	spex96	—	H	0.914 ± 0.001	0.336 ± 0.001	0.097 ± 0.001	1.960	1.970 ± 0.006	1.273	1.230 ± 0.050	2.60	17.86	250
(17) Thetis	vilas	sunshine	—	H	0.920 ± 0.001	0.304 ± 0.002	0.095 ± 0.001	1.904	1.914 ± 0.010	1.008	0.966 ± 0.018	2.59	22.60	250
(20) Massalia	sawyer	spex96	—	H	0.918 ± 0.001	0.320 ± 0.002	0.104 ± 0.001	1.969	1.977 ± 0.006	1.144	1.110 ± 0.047	2.16	25.84	262
(20) Massalia	sawyer	spex96	—	H	0.918 ± 0.001	0.326 ± 0.003	0.102 ± 0.001	1.969	1.977 ± 0.006	1.186	1.153 ± 0.049	2.16	25.84	262
(20) Massalia	sawyer	spex96	—	H	0.917 ± 0.001	0.322 ± 0.003	0.103 ± 0.001	1.969	1.977 ± 0.006	1.155	1.121 ± 0.048	2.16	25.84	262
(23) Thalia	s3os2	spex96	—	H/L	0.933 ± 0.002	0.321 ± 0.002	0.116 ± 0.001	1.938	1.941 ± 0.020	0.699	0.682 ± 0.059	2.02	11.70	284
(23) Thalia	smass2	spex96	S	L	0.935 ± 0.002	0.260 ± 0.002	0.135 ± 0.001	1.937	1.940 ± 0.020	0.537	0.520 ± 0.046	2.02	11.70	284
(25) Phocaea	s3os2	spex94	—	LL	0.961 ± 0.002	0.423 ± 0.002	0.128 ± 0.001	1.979	1.988 ± 0.006	0.657	0.617 ± 0.030	2.30	14.31	254
(25) Phocaea	smass1	spex94	—	LL	0.959 ± 0.001	0.405 ± 0.002	0.136 ± 0.001	1.979	1.988 ± 0.006	0.630	0.590 ± 0.029	2.30	14.31	254
(25) Phocaea	smass2	spex94	Sw	LL/L	0.950 ± 0.003	0.339 ± 0.002	0.156 ± 0.001	1.979	1.988 ± 0.006	0.514	0.474 ± 0.024	2.30	14.31	254
(26) Proserpina	smass2	spex92	S	LL	0.977 ± 0.022	0.212 ± 0.002	0.138 ± 0.001	1.915	1.928 ± 0.009	0.430	0.375 ± 0.056	2.69	21.50	233
(27) Euterpe	s3os2	spex31	—	LL	0.975 ± 0.003	0.331 ± 0.001	0.114 ± 0.001	1.957	1.968 ± 0.003	0.620	0.575 ± 0.005	2.46	7.69	246
(27) Euterpe	sawyer	spex31	—	LL	0.957 ± 0.002	0.328 ± 0.001	0.115 ± 0.001	1.957	1.968 ± 0.003	0.612	0.567 ± 0.005	2.46	7.69	246
(27) Euterpe	sawyer	spex31	—	LL	0.956 ± 0.001	0.331 ± 0.001	0.115 ± 0.001	1.957	1.968 ± 0.003	0.617	0.572 ± 0.005	2.46	7.69	246
(27) Euterpe	sawyer	spex31	—	LL	0.955 ± 0.001	0.310 ± 0.002	0.122 ± 0.001	1.957	1.968 ± 0.003	0.576	0.530 ± 0.005	2.46	7.69	246
(30) Urania	sawyer	spex92	—	LL	0.953 ± 0.003	0.330 ± 0.002	0.080 ± 0.001	1.916	1.925 ± 0.014	0.641	0.602 ± 0.067	2.34	5.32	254
(30) Urania	smass2	spex92	S	LL	0.964 ± 0.005	0.286 ± 0.002	0.095 ± 0.001	1.916	1.925 ± 0.014	0.497	0.458 ± 0.053	2.34	5.32	254
(32) Pomona	smass1	spex76	—	L	0.926 ± 0.001	0.279 ± 0.002	0.109 ± 0.001	1.904	1.918 ± 0.025	0.657	0.600 ± 0.049	2.77	11.67	231
(32) Pomona	smass2	spex76	S	L	0.921 ± 0.001	0.218 ± 0.002	0.131 ± 0.001	1.904	1.918 ± 0.026	0.504	0.447 ± 0.038	2.77	11.67	231

Table 3.11 — continued

Object	Vis[a]	NIR[a]	tax[b]	met[c]	BIC[d]	BIS_{corr}[e]	BID_{corr}[f]	$BIIC$[d]	$BIIC_{corr}$[g]	BAR	BAR_{corr}[h]	R_{AU}[i]	$\alpha(^\circ)$[j]	T_c[k]
(37) Fides	s3os2	spex94	—	L/H	0.929 ± 0.002	0.203 ± 0.002	0.080 ± 0.001	1.909	1.915 ± 0.013	0.667	0.638 ± 0.103	2.20	21.02	268
(37) Fides	smass2	spex94	S	L	0.931 ± 0.002	0.178 ± 0.002	0.092 ± 0.001	1.910	1.916 ± 0.014	0.562	0.533 ± 0.086	2.20	21.02	268
(43) Ariadne	s3os2	clark	—	LL	1.006 ± 0.010	0.275 ± 0.001	0.128 ± 0.001	1.979	1.983 ± 0.006	0.333	0.312 ± 0.008	1.91	27.00	278
(43) Ariadne	s3os2	spex48	—	LL	1.017 ± 0.001	0.290 ± 0.001	0.124 ± 0.001	1.943	1.955 ± 0.005	0.500	0.449 ± 0.007	2.57	21.22	240
(43) Ariadne	smass1	clark	—	LL	0.975 ± 0.008	0.222 ± 0.001	0.147 ± 0.001	1.979	1.983 ± 0.006	0.281	0.260 ± 0.007	1.91	27.00	278
(43) Ariadne	smass1	spex48	—	LL	1.024 ± 0.001	0.270 ± 0.001	0.130 ± 0.001	1.943	1.955 ± 0.005	0.455	0.405 ± 0.006	2.57	21.22	240
(43) Ariadne	smass2	clark	Sq	LL	0.983 ± 0.008	0.236 ± 0.001	0.142 ± 0.001	1.979	1.983 ± 0.006	0.290	0.269 ± 0.007	1.91	27.00	278
(43) Ariadne	smass2	spex48	Sq	LL	1.008 ± 0.005	0.247 ± 0.001	0.138 ± 0.001	1.943	1.955 ± 0.005	0.430	0.379 ± 0.006	2.57	21.22	240
(57) Mnemosyne	s3os2	spex92	—	H	0.926 ± 0.003	0.246 ± 0.004	0.100 ± 0.001	1.924	1.940 ± 0.011	1.056	0.993 ± 0.091	3.03	17.87	222
(57) Mnemosyne	smass2	spex92	S	H	0.929 ± 0.002	0.236 ± 0.004	0.102 ± 0.001	1.924	1.940 ± 0.011	0.984	0.920 ± 0.086	3.03	17.87	222
(61) Danae	smass2	spex94	S	L/H	0.921 ± 0.003	0.185 ± 0.003	0.118 ± 0.002	1.878	1.894 ± 0.027	0.698	0.635 ± 0.099	3.18	17.31	222
(63) Ausonia	sawyer	spex25	—	H	0.943 ± 0.001	0.317 ± 0.001	0.102 ± 0.001	1.943	1.952 ± 0.006	0.861	0.821 ± 0.013	2.31	8.69	254
(63) Ausonia	smass2	spex25	S	L	0.942 ± 0.002	0.259 ± 0.001	0.123 ± 0.001	1.943	1.952 ± 0.006	0.657	0.618 ± 0.010	2.31	8.69	254
(67) Asia	smass2	spex111	Sq	L	0.931 ± 0.001	0.093 ± 0.001	0.147 ± 0.001	1.922	1.927 ± 0.022	0.436	0.413 ± 0.051	1.98	20.07	276
(67) Asia	smass2	spex29	S	H	0.915 ± 0.001	0.205 ± 0.003	0.148 ± 0.001	1.909	1.917 ± 0.009	0.836	0.799 ± 0.042	2.27	22.57	258
(79) Eurynome	smass2	spex75	S	L	0.934 ± 0.002	0.180 ± 0.004	0.105 ± 0.002	1.877	1.884 ± 0.017	0.479	0.447 ± 0.080	2.12	26.25	263
(80) Sappho	smass2	EMMSpex	S	L	0.942 ± 0.004	0.230 ± 0.001	0.122 ± 0.001	1.921	1.934 ± 0.003	0.613	0.560 ± 0.007	2.60	6.05	236
(82) Alkmene	smass1	spex92	—	H	0.921 ± 0.001	0.252 ± 0.004	0.123 ± 0.001	1.888	1.906 ± 0.012	1.222	1.151 ± 0.105	3.33	15.64	212
(82) Alkmene	smass2	spex92	S	H	0.923 ± 0.002	0.170 ± 0.003	0.149 ± 0.002	1.888	1.906 ± 0.013	0.902	0.831 ± 0.080	3.33	15.64	212
(101) Helena	smass2	spex57	S	L/H	0.919 ± 0.001	0.195 ± 0.002	0.140 ± 0.001	1.870	1.883 ± 0.027	0.715	0.662 ± 0.025	2.82	9.81	235
(103) Hera	smass2	spex92	S	L	0.934 ± 0.003	0.207 ± 0.003	0.144 ± 0.002	1.933	1.943 ± 0.016	0.554	0.513 ± 0.066	2.48	20.59	251
(118) Peitho	smass2	spex102	S	H	0.910 ± 0.001	0.249 ± 0.003	0.140 ± 0.001	1.967	1.977 ± 0.024	0.911	0.870 ± 0.051	2.21	13.21	252
(119) Althaea	s3os2	spex92	—	LL	0.994 ± 0.033	0.463 ± 0.003	0.100 ± 0.001	1.956	1.971 ± 0.016	0.561	0.500 ± 0.057	2.86	20.76	226
(119) Althaea	smass2	spex92	Sw	L/LL	0.942 ± 0.015	0.348 ± 0.002	0.137 ± 0.001	1.956	1.971 ± 0.016	0.404	0.343 ± 0.043	2.86	20.76	226
(151) Abundantia	smass2	spex47	Sw	L	0.908 ± 0.001	0.417 ± 0.001	0.111 ± 0.001	1.962	1.974 ± 0.015	0.350	0.301 ± 0.014	2.56	22.03	240
(158) Koronis	smass1	spex94	S	L/H	0.937 ± 0.003	0.317 ± 0.003	0.101 ± 0.001	1.878	1.895 ± 0.019	0.671	0.601 ± 0.116	2.73	21.38	213
(158) Koronis	smass2	spex94	Sq	L	0.927 ± 0.002	0.172 ± 0.003	0.159 ± 0.001	1.878	1.895 ± 0.019	0.399	0.329 ± 0.072	2.73	21.38	213
(179) Klytaemnestra	smass2	clark09	S	H	0.915 ± 0.001	0.223 ± 0.002	0.130 ± 0.001	1.889	1.906 ± 0.016	1.081	1.012 ± 0.025	3.28	11.30	215
(180) Garumna	smass2	spex92	S	H	0.921 ± 0.001	0.148 ± 0.002	0.168 ± 0.001	1.865	1.880 ± 0.020	0.793	0.733 ± 0.042	3.18	7.83	226
(192) Nausikaa	smass2	spex50	Sw	LL	0.960 ± 0.004	0.357 ± 0.001	0.115 ± 0.001	1.962	1.978 ± 0.004	0.526	0.462 ± 0.008	3.00	11.42	221
(198) Ampella	smass2	feiberbeyer	S	H/L	0.907 ± 0.001	0.357 ± 0.003	0.119 ± 0.001	1.826	1.839 ± 0.011	0.771	0.716 ± 0.043	3.02	19.53	234
(208) Lacrimosa	smass2	spex101	Sq	L	0.924 ± 0.002	0.143 ± 0.002	0.141 ± 0.001	1.918	1.933 ± 0.033	0.364	0.303 ± 0.058	2.93	3.11	225
(264) Libussa	smass2	spex41	S	H	0.911 ± 0.001	0.263 ± 0.001	0.134 ± 0.001	1.945	1.959 ± 0.013	0.784	0.727 ± 0.017	3.00	19.42	231
(270) Anahita	s3os2	EMMSpex	—	L	0.933 ± 0.003	0.357 ± 0.001	0.104 ± 0.001	1.905	1.915 ± 0.018	0.687	0.643 ± 0.009	2.52	6.87	248
(288) Glauke	smass2	spex92	S	L	0.921 ± 0.002	0.086 ± 0.002	0.132 ± 0.001	1.964	1.974 ± 0.006	0.654	0.610 ± 0.045	2.60	0.85	248
(349) Dembowska	smass1	EMMSpex	—	H	0.937 ± 0.001	0.453 ± 0.001	0.257 ± 0.001	1.929	1.951 ± 0.001	0.935	0.848 ± 0.003	2.77	4.51	190
(349) Dembowska	smass2	EMMSpex	Srw	H	0.937 ± 0.001	0.455 ± 0.001	0.256 ± 0.001	1.929	1.951 ± 0.001	0.937	0.850 ± 0.003	2.77	4.51	190

Table 3.11 — continued

Object	Vis[a]	NIR[a]	tax[b]	met[c]	B_IC[d]	B_IS_{corr}[e]	B_ID_{corr}[f]	$B_{II}C$[d]	$B_{II}C_{corr}$[g]	BAR	BAR_{corr}[h]	R_{AU}[i]	$\alpha(^\circ)$[j]	T_c[k]
(371) Bohemia	smass1	spex92	S	L/H	0.926 ± 0.002	0.117 ± 0.002	0.149 ± 0.001	1.899	1.911 ± 0.010	0.707	0.658 ± 0.051	2.57	0.44	242
(371) Bohemia	smass2	spex92	S	H	0.925 ± 0.001	0.149 ± 0.002	0.134 ± 0.001	1.899	1.911 ± 0.010	0.811	0.763 ± 0.058	2.57	0.44	242
(376) Geometria	smass2	EMMSpex	Sw	H	0.937 ± 0.001	0.350 ± 0.002	0.122 ± 0.001	1.883	1.896 ± 0.001	0.755	0.703 ± 0.012	2.68	13.28	237
(389) Industria	smass2	spex94	S	H	0.912 ± 0.002	0.174 ± 0.002	0.106 ± 0.001	1.879	1.888 ± 0.015	0.889	0.851 ± 0.091	2.54	20.00	257
(391) Ingeborg	s3os2	EMMSpex	—	H/L	0.919 ± 0.001	0.380 ± 0.004	0.110 ± 0.001	1.897	1.957 ± 0.073	0.940	0.710 ± 0.090	2.88	13.17	227
(391) Ingeborg	smass2	EMMSpex	Sw	H/L	0.917 ± 0.011	0.378 ± 0.004	0.112 ± 0.003	1.900	1.960 ± 0.074	0.935	0.705 ± 0.089	2.88	13.17	233
(416) Vaticana	smass1	spex93	Sw	L/H	0.941 ± 0.006	0.452 ± 0.031	0.079 ± 0.005	1.911	1.927 ± 0.033	0.725	0.658 ± 0.170	3.40	16.73	218
(416) Vaticana	smass2	spex93	Sw	L	0.926 ± 0.005	0.404 ± 0.003	0.101 ± 0.001	1.912	1.928 ± 0.034	0.536	0.469 ± 0.085	3.40	16.73	218
(433) Eros	smassneo	spex101	Sw	LL	0.990 ± 0.005	0.348 ± 0.001	0.152 ± 0.001	1.996	1.993 ± 0.012	0.247	0.254 ± 0.021	1.49	42.72	334
(433) Eros	smassneo	spex102	Sw	LL	0.964 ± 0.004	0.346 ± 0.001	0.148 ± 0.001	1.984	1.978 ± 0.016	0.440	0.456 ± 0.016	1.38	45.46	328
(433) Eros	smassneo	spex103	Sqw	LL	0.980 ± 0.007	0.380 ± 0.002	0.153 ± 0.001	1.988	1.980 ± 0.022	0.356	0.380 ± 0.037	1.29	47.17	348
(433) Eros	smassneo	spex105	Sqw	LL	1.005 ± 0.028	0.534 ± 0.002	0.169 ± 0.001	1.987	1.975 ± 0.029	0.090	0.130 ± 0.028	1.14	43.66	370
(433) Eros	smassneo	spex15	Sw	LL/L	0.972 ± 0.028	0.351 ± 0.001	0.148 ± 0.001	1.969	1.971 ± 0.003	0.386	0.373 ± 0.008	1.77	34.89	289
(433) Eros	smassneo	spex16	Sw	LL	0.955 ± 0.001	0.269 ± 0.001	0.156 ± 0.001	1.963	1.964 ± 0.006	0.384	0.376 ± 0.006	1.69	21.84	296
(433) Eros	smassneo	spex17	Sw	LL	0.950 ± 0.001	0.254 ± 0.001	0.159 ± 0.001	1.966	1.966 ± 0.007	0.379	0.376 ± 0.005	1.62	12.62	302
(433) Eros	smassneo	spex201	Sw	LL	0.976 ± 0.019	0.333 ± 0.005	0.157 ± 0.003	1.922	1.924 ± 0.033	0.543	0.530 ± 0.057	1.78	32.14	288
(433) Eros	smassneo	spex223	Sw	LL	0.952 ± 0.002	0.312 ± 0.001	0.146 ± 0.001	1.973	1.972 ± 0.008	0.399	0.398 ± 0.011	1.60	36.75	304
(433) Eros	vilas	spex101	—	LL	1.010 ± 0.003	0.474 ± 0.002	0.112 ± 0.001	1.996	1.993 ± 0.012	0.344	0.351 ± 0.030	1.49	42.72	315
(433) Eros	vilas	spex102	—	LL	0.974 ± 0.005	0.443 ± 0.002	0.115 ± 0.001	1.984	1.978 ± 0.017	0.573	0.589 ± 0.022	1.38	45.46	328
(433) Eros	vilas	spex103	—	LL	0.991 ± 0.004	0.498 ± 0.002	0.117 ± 0.001	1.988	1.980 ± 0.023	0.477	0.501 ± 0.053	1.29	47.17	342
(433) Eros	vilas	spex105	—	LL	1.029 ± 0.004	0.671 ± 0.003	0.132 ± 0.001	1.986	1.974 ± 0.030	0.122	0.162 ± 0.040	1.14	43.66	362
(433) Eros	vilas	spex201	—	LL	1.007 ± 0.022	0.456 ± 0.006	0.119 ± 0.003	1.922	1.924 ± 0.034	0.753	0.739 ± 0.084	1.78	32.14	288
(433) Eros	vilas	spex223	—	LL	0.970 ± 0.003	0.417 ± 0.002	0.109 ± 0.001	1.973	1.972 ± 0.008	0.551	0.549 ± 0.017	1.60	36.75	304
(512) Taurinensis	smass1	spex32	—	LL	0.974 ± 0.003	0.376 ± 0.001	0.142 ± 0.001	2.002	2.005 ± 0.033	0.420	0.403 ± 0.007	1.84	29.96	284
(512) Taurinensis	smass2	spex32	—	LL	0.970 ± 0.004	0.271 ± 0.001	0.177 ± 0.001	2.003	2.006 ± 0.034	0.322	0.305 ± 0.006	1.84	29.96	284
(532) Herculina	sawyer	spex76	—	H/L	0.945 ± 0.002	0.244 ± 0.002	0.091 ± 0.001	1.954	1.970 ± 0.034	0.762	0.696 ± 0.037	2.99	7.56	218
(532) Herculina	smass2	spex76	—	L	0.931 ± 0.002	0.182 ± 0.001	0.115 ± 0.001	1.954	1.970 ± 0.034	0.582	0.515 ± 0.028	2.99	7.56	218
(584) Semiramis	smass2	spex65	—	LL	0.965 ± 0.004	0.298 ± 0.002	0.139 ± 0.001	1.946	1.945 ± 0.011	0.387	0.383 ± 0.035	1.93	9.56	303
(600) Musa	smass2	spex101	—	L	0.919 ± 0.001	0.204 ± 0.002	0.160 ± 0.001	1.895	1.909 ± 0.027	0.668	0.611 ± 0.041	2.69	15.30	231
(631) Philippina	smass1	spex101	—	L	0.926 ± 0.001	0.349 ± 0.002	0.114 ± 0.001	1.896	1.911 ± 0.021	0.566	0.503 ± 0.059	3.02	9.44	223
(631) Philippina	smass2	spex101	—	L	0.914 ± 0.001	0.208 ± 0.002	0.168 ± 0.001	1.896	1.911 ± 0.021	0.361	0.298 ± 0.039	3.02	9.44	223
(699) Hela	s3os2	spex35	—	H	0.930 ± 0.004	0.249 ± 0.006	0.097 ± 0.002	1.906	1.923 ± 0.036	0.958	0.890 ± 0.182	3.15	5.57	217
(699) Hela	smass2	spex35	—	L/H	0.912 ± 0.003	0.167 ± 0.005	0.137 ± 0.001	1.906	1.923 ± 0.037	0.712	0.644 ± 0.137	3.15	5.57	217
(714) Ulula	s3os2	feiberbeyer	—	H	0.924 ± 0.001	0.389 ± 0.005	0.078 ± 0.001	1.884	1.893 ± 0.002	1.387	1.347 ± 0.036	2.58	17.40	254
(720) Bohlinia	smass1	spex97	—	L	0.922 ± 0.002	0.132 ± 0.002	0.116 ± 0.001	1.839	1.855 ± 0.004	0.624	0.559 ± 0.063	2.86	15.68	221
(720) Bohlinia	smass2	spex97	—	L	0.918 ± 0.002	0.112 ± 0.002	0.123 ± 0.001	1.838	1.855 ± 0.004	0.545	0.481 ± 0.055	2.86	15.68	221
(793) Arizona	smass2	EMMSpex	—	H	0.921 ± 0.001	0.276 ± 0.003	0.169 ± 0.001	1.950	1.961 ± 0.007	1.076	1.028 ± 0.039	2.50	10.79	243

Table 3.11 — continued

Object	Vis[a]	NIR[a]	tax[b]	met[c]	BIC[d]	BIS_{corr}[e]	BID_{corr}[f]	$BIIC$[d]	$BIIC_{corr}$[g]	BAR	BAR_{corr}[h]	R_{AU}[i]	$\alpha(^\circ)$[j]	T_c[k]
(793) Arizona	smass2	spex92	—	H	0.918 ± 0.002	0.072 ± 0.004	0.143 ± 0.001	1.850	1.865 ± 0.009	1.115	1.055 ± 0.106	2.89	19.98	226
(808) Merxia	s3os2	spex92	—	H	0.918 ± 0.002	0.101 ± 0.002	0.196 ± 0.001	1.846	1.861 ± 0.006	0.795	0.735 ± 0.045	2.89	18.45	227
(808) Merxia	s3os2	sunshine04	—	L	0.891 ± 0.001	0.179 ± 0.002	0.192 ± 0.001	1.886	1.900 ± 0.014	0.606	0.548 ± 0.011	2.81	13.20	230
(808) Merxia	smass1	spex92	—	H	0.927 ± 0.002	0.297 ± 0.003	0.131 ± 0.001	1.846	1.861 ± 0.005	1.269	1.209 ± 0.067	2.89	18.45	227
(808) Merxia	smass1	sunshine04	—	H	0.908 ± 0.001	0.345 ± 0.002	0.136 ± 0.001	1.886	1.900 ± 0.013	0.884	0.827 ± 0.016	2.81	13.20	230
(847) Agnia	s3os2	sunshine04	—	L	0.922 ± 0.001	0.304 ± 0.002	0.156 ± 0.001	1.904	1.917 ± 0.008	0.515	0.461 ± 0.013	2.82	4.30	235
(847) Agnia	smass2	sunshine04	—	L	0.914 ± 0.001	0.251 ± 0.001	0.179 ± 0.001	1.904	1.917 ± 0.008	0.432	0.378 ± 0.011	2.82	4.30	235
(875) Nymphe	—	feiberbeyer	—	H/L	0.920 ± 0.012	0.194 ± 0.019	0.093 ± 0.009	1.954	1.961 ± 0.028	0.832	0.802 ± 0.378	2.20	23.80	267
(925) Alphonsina	smass2	spex102	—	H/L	0.920 ± 0.002	0.222 ± 0.003	0.116 ± 0.002	1.918	1.930 ± 0.033	0.832	0.781 ± 0.175	2.88	9.74	239
(1020) Arcadia	smass2	sunshine04	—	H/L	0.926 ± 0.003	0.306 ± 0.004	0.159 ± 0.002	1.891	1.901 ± 0.041	0.728	0.685 ± 0.052	2.74	12.20	250
(1036) Ganymed	smassneo	feiberbeyer	—	H	0.919 ± 0.001	0.215 ± 0.002	0.165 ± 0.001	1.872	1.888 ± 0.002	1.176	1.110 ± 0.019	3.08	10.80	219
(1036) Ganymed	smassneo	spex05	—	L	0.912 ± 0.002	0.153 ± 0.004	0.165 ± 0.001	1.830	1.851 ± 0.013	0.686	0.601 ± 0.041	3.97	4.95	193
(1036) Ganymed	smassneo	spex103	—	H/L	0.924 ± 0.002	0.124 ± 0.003	0.167 ± 0.002	1.935	1.929 ± 0.027	0.732	0.749 ± 0.095	1.37	7.40	329
(1036) Ganymed	smassneo	spex104	—	H	0.927 ± 0.001	0.140 ± 0.001	0.170 ± 0.001	1.934	1.929 ± 0.006	0.914	0.928 ± 0.027	1.40	2.35	325
(1036) Ganymed	smassneo	spex209	—	L/H	0.926 ± 0.002	0.346 ± 0.009	0.184 ± 0.002	1.904	1.913 ± 0.014	0.701	0.661 ± 0.079	2.29	20.41	254
(1036) Ganymed	smassneo	spex27	—	H	0.909 ± 0.001	0.271 ± 0.002	0.174 ± 0.001	1.859	1.877 ± 0.010	0.936	0.864 ± 0.023	3.34	10.46	211
(1036) Ganymed	smassneo	spex37	—	H	0.914 ± 0.001	0.151 ± 0.002	0.168 ± 0.001	1.859	1.881 ± 0.013	1.187	1.100 ± 0.054	4.09	5.96	190
(1036) Ganymed	smassneo	spex51	—	H	0.914 ± 0.001	0.272 ± 0.002	0.172 ± 0.001	1.876	1.892 ± 0.008	1.008	0.944 ± 0.022	3.01	15.18	222
(1036) Ganymed	smassneo	spex80	—	L/H	0.921 ± 0.004	0.225 ± 0.010	0.172 ± 0.004	1.872	1.894 ± 0.007	0.747	0.660 ± 0.211	4.07	13.12	191
(1036) Ganymed	vilas	feiberbeyer	—	H	0.922 ± 0.001	0.234 ± 0.002	0.160 ± 0.001	1.872	1.888 ± 0.002	1.248	1.183 ± 0.022	3.08	10.80	219
(1036) Ganymed	vilas	spex05	—	H/L	0.913 ± 0.001	0.199 ± 0.005	0.149 ± 0.001	1.830	1.851 ± 0.015	0.797	0.712 ± 0.052	3.97	4.95	193
(1036) Ganymed	vilas	spex103	—	H	0.926 ± 0.002	0.165 ± 0.004	0.152 ± 0.001	1.936	1.930 ± 0.028	0.851	0.868 ± 0.120	1.37	7.40	329
(1036) Ganymed	vilas	spex104	—	H	0.930 ± 0.001	0.180 ± 0.003	0.155 ± 0.001	1.934	1.929 ± 0.007	1.063	1.077 ± 0.035	1.40	2.35	325
(1036) Ganymed	vilas	spex209	—	H/L	0.927 ± 0.001	0.395 ± 0.011	0.172 ± 0.002	1.904	1.913 ± 0.015	0.765	0.725 ± 0.095	2.29	20.41	254
(1036) Ganymed	vilas	spex27	—	H	0.910 ± 0.001	0.317 ± 0.003	0.160 ± 0.001	1.859	1.877 ± 0.011	1.086	1.014 ± 0.030	3.34	10.46	211
(1036) Ganymed	vilas	spex37	—	H	0.915 ± 0.001	0.206 ± 0.004	0.149 ± 0.001	1.859	1.881 ± 0.014	1.462	1.375 ± 0.074	4.09	5.96	190
(1036) Ganymed	vilas	spex51	—	H	0.916 ± 0.001	0.323 ± 0.003	0.159 ± 0.001	1.876	1.892 ± 0.008	1.148	1.084 ± 0.028	3.01	15.18	222
(1036) Ganymed	vilas	spex80	—	H/L	0.919 ± 0.003	0.272 ± 0.012	0.159 ± 0.003	1.872	1.894 ± 0.007	0.846	0.759 ± 0.260	4.07	13.12	191
(1077) Campanula	s3os2	EMMSpex	—	H	0.923 ± 0.001	0.301 ± 0.002	0.099 ± 0.001	1.915	1.922 ± 0.010	1.142	1.111 ± 0.051	2.12	4.90	264
(1139) Atami	smass2	spex29	—	L	0.937 ± 0.005	0.257 ± 0.004	0.179 ± 0.002	1.951	1.962 ± 0.032	0.623	0.578 ± 0.061	2.43	20.80	247
(1140) Crimea	smass2	EMMSpex	—	LL	0.957 ± 0.008	0.582 ± 0.002	0.071 ± 0.001	1.986	1.997 ± 0.003	0.867	0.821 ± 0.021	2.48	21.30	244
(1152) Pawona	smass2	EMMSpex	—	LL/L	0.948 ± 0.002	0.549 ± 0.002	0.119 ± 0.001	1.890	1.900 ± 0.003	0.535	0.492 ± 0.011	2.38	1.94	249
(1443) Ruppina	—	EMMSpex	—	H/L	0.925 ± 0.002	0.270 ± 0.006	0.113 ± 0.002	1.904	1.918 ± 0.028	0.751	0.694 ± 0.079	2.76	1.03	232
(1565) Lemaitre	smass2	spex36	Sq	L	0.910 ± 0.006	0.166 ± 0.027	0.204 ± 0.005	1.801	1.815 ± 0.060	0.511	0.454 ± 0.929	2.79	11.69	230
(1577) Reiss	smass1	EMMSpex	—	LL	1.023 ± 0.023	0.348 ± 0.003	0.154 ± 0.001	1.903	1.913 ± 0.008	0.314	0.271 ± 0.037	2.36	10.98	250
(1620) Geographos	smassneo	reddy	Sq	LL	0.986 ± 0.006	0.064 ± 0.002	0.155 ± 0.001	1.941	1.930 ± 0.031	0.377	0.415 ± 0.017	1.16	12.00	357
(1620) Geographos	smassneo	spex03	S	LL	1.012 ± 0.018	0.192 ± 0.002	0.151 ± 0.001	1.975	1.970 ± 0.007	0.413	0.428 ± 0.019	1.39	16.67	326

Table 3.11 — continued

Object	Vis[a]	NIR[a]	tax[b]	met[c]	BIC[d]	BIS_{corr}[e]	BID_{corr}[f]	$BIIC$[d]	$BIIC_{corr}$[g]	BAR	BAR_{corr}[h]	R_{AU}[i]	$\alpha(^\circ)$[j]	T_c[k]
(1620) Geographos	smassneo	spex105	Sq	LL	1.004 ± 0.025	0.231 ± 0.004	0.160 ± 0.002	1.994	1.994 ± 0.018	0.288	0.284 ± 0.112	1.62	17.23	302
(1620) Geographos	smassneo	spex68	Sqw	LL	1.000 ± 0.005	0.269 ± 0.001	0.153 ± 0.001	2.019	2.005 ± 0.011	0.239	0.285 ± 0.013	1.10	36.90	368
(1627) Ivar	smassneo8	spex09	S	LL/L	0.952 ± 0.008	0.216 ± 0.003	0.180 ± 0.001	1.961	1.974 ± 0.024	0.784	0.731 ± 0.244	2.60	3.91	237
(1627) Ivar	smassneo8	spex118	Sqw	LL	0.975 ± 0.016	0.366 ± 0.004	0.177 ± 0.001	1.950	1.949 ± 0.019	0.367	0.367 ± 0.116	1.55	38.96	307
(1627) Ivar	smassneo8	spex73	Sqw	LL	0.960 ± 0.006	0.259 ± 0.002	0.149 ± 0.001	1.897	1.889 ± 0.059	0.212	0.237 ± 0.030	1.26	53.03	340
(1627) Ivar	smassneo8	spex74	Sw	LL	0.955 ± 0.004	0.279 ± 0.002	0.171 ± 0.001	1.968	1.967 ± 0.011	0.229	0.228 ± 0.036	1.57	31.30	305
(1627) Ivar	smassneo8	spex76	S	L/LL	0.945 ± 0.006	0.212 ± 0.002	0.172 ± 0.001	1.932	1.937 ± 0.064	0.377	0.355 ± 0.051	1.90	16.11	277
(1627) Ivar	smassneo8	spex77	Sr	LL	0.959 ± 0.010	0.337 ± 0.012	0.183 ± 0.002	1.954	1.962 ± 0.041	0.792	0.758 ± 0.281	2.14	26.92	261
(1627) Ivar	smassneo8	spex88	Sw	LL/L	0.950 ± 0.006	0.208 ± 0.002	0.182 ± 0.001	1.800	1.810 ± 0.007	0.254	0.210 ± 0.055	2.37	2.19	248
(1644) Rafita	—	EMMSpex	—	L/H	0.923 ± 0.002	0.228 ± 0.019	0.159 ± 0.006	1.869	1.879 ± 0.057	0.716	0.672 ± 0.416	2.41	6.66	248
(1644) Rafita	—	feiberbeyer	—	H	0.925 ± 0.003	0.474 ± 0.011	0.136 ± 0.003	1.886	1.899 ± 0.004	1.442	1.390 ± 0.127	2.63	20.02	237
(1660) Wood	s3os2	spex37	—	H	0.926 ± 0.002	0.325 ± 0.002	0.098 ± 0.001	1.971	1.975 ± 0.009	0.911	0.891 ± 0.049	2.09	26.56	281
(1660) Wood	smass2	spex37	S	L	0.907 ± 0.001	0.256 ± 0.002	0.132 ± 0.001	1.971	1.975 ± 0.009	0.660	0.641 ± 0.036	2.09	26.56	281
(1662) Hoffman	smass2	sunshine04	Sr	H	0.912 ± 0.002	0.277 ± 0.003	0.182 ± 0.002	1.852	1.869 ± 0.029	0.809	0.741 ± 0.048	3.18	8.10	216
(1685) Toro	s3os2	spex13	—	LL	1.028 ± 0.036	0.116 ± 0.005	0.119 ± 0.003	2.004	2.011 ± 0.080	0.402	0.371 ± 0.102	1.96	8.61	266
(1685) Toro	s3os2	spex215	—	LL	0.999 ± 0.004	0.132 ± 0.001	0.103 ± 0.001	2.027	2.016 ± 0.014	0.531	0.567 ± 0.016	1.11	53.65	354
(1685) Toro	s3os2	spex217	—	LL	1.008 ± 0.008	0.306 ± 0.011	0.136 ± 0.005	2.018	2.017 ± 0.120	0.460	0.459 ± 0.127	1.50	39.77	305
(1685) Toro	s3os2	spex37	—	LL	1.003 ± 0.021	0.236 ± 0.003	0.127 ± 0.002	1.998	2.001 ± 0.013	0.398	0.384 ± 0.072	1.69	22.09	287
(1802) Zhang Heng	—	EMMSpex	—	H	0.919 ± 0.002	0.330 ± 0.008	0.105 ± 0.002	1.926	1.940 ± 0.016	1.015	0.957 ± 0.193	2.91	6.67	230
(1858) Lobachevskij	smass2	sunshine08	S	H/L	0.919 ± 0.005	0.233 ± 0.008	0.062 ± 0.002	1.898	1.909 ± 0.032	0.862	0.817 ± 0.150	2.64	3.20	246
(1862) Apollo	smassneo8	spex47.1	Q	LL	0.992 ± 0.002	0.005 ± 0.002	0.224 ± 0.001	1.985	1.969 ± 0.010	0.224	0.278 ± 0.004	1.04	56.69	378
(1862) Apollo	smassneo8	spex47.2	Q	LL	0.988 ± 0.002	0.021 ± 0.002	0.221 ± 0.001	1.993	1.977 ± 0.008	0.256	0.310 ± 0.004	1.04	56.69	378
(1862) Apollo	smassneo8	spex48	Q	LL	0.959 ± 0.006	-0.004 ± 0.002	0.240 ± 0.001	2.018	2.006 ± 0.013	0.170	0.211 ± 0.016	1.13	23.3	362
(1864) Daedalus	smassneo	spex05	Q	LL	0.961 ± 0.009	-0.006 ± 0.004	0.200 ± 0.003	1.932	1.939 ± 0.073	0.317	0.284 ± 0.043	1.89	3.53	263
(1865) Cerberus	smassneo	spex75	S	L	0.934 ± 0.004	0.149 ± 0.004	0.151 ± 0.002	1.888	1.897 ± 0.054	0.420	0.381 ± 0.115	1.41	19.64	254
(1866) Sisyphus	smassneo	spex56	Sw	L	0.927 ± 0.001	0.245 ± 0.002	0.112 ± 0.001	1.954	1.934 ± 0.010	0.197	0.266 ± 0.026	0.98	66.06	399
(1866) Sisyphus	vilas1	spex56	—	L	0.934 ± 0.001	0.362 ± 0.002	0.073 ± 0.001	1.953	1.933 ± 0.009	0.281	0.350 ± 0.039	0.98	66.06	399
(1866) Sisyphus	vilas2	spex56	—	L	0.931 ± 0.001	0.327 ± 0.002	0.084 ± 0.001	1.954	1.934 ± 0.010	0.252	0.321 ± 0.035	0.98	66.06	399
(1916) Boreas	smassneo	spex07	Sw	LL	0.959 ± 0.002	0.403 ± 0.002	0.134 ± 0.001	1.975	1.967 ± 0.004	0.415	0.441 ± 0.008	1.27	38.25	341
(1917) Cuyo	smassneo	spex72	Sr	H	0.936 ± 0.014	0.180 ± 0.010	0.158 ± 0.005	1.849	1.843 ± 0.017	1.045	1.062 ± 0.193	1.37	47.45	329
(1943) Anteros	s3os2	spex09	—	LL/L	0.950 ± 0.022	0.379 ± 0.004	0.086 ± 0.002	1.974	1.970 ± 0.031	0.563	0.572 ± 0.097	1.46	14.36	319
(1943) Anteros	s3os2	spex103	—	LL	1.025 ± 0.020	0.292 ± 0.003	0.086 ± 0.001	1.985	1.988 ± 0.012	0.306	0.291 ± 0.163	1.80	16.54	287
(1943) Anteros	smassneo	spex09	—	LL/L	0.976 ± 0.032	0.374 ± 0.005	0.087 ± 0.002	1.974	1.970 ± 0.032	0.536	0.545 ± 0.094	1.46	14.36	319
(1943) Anteros	smassneo	spex103	—	LL	1.022 ± 0.010	0.288 ± 0.003	0.088 ± 0.001	1.985	1.988 ± 0.014	0.294	0.279 ± 0.166	1.80	16.54	287
(1980) Tezcatlipoca	s3os2	reddy	—	LL	0.956 ± 0.004	0.502 ± 0.004	0.141 ± 0.002	1.933	1.930 ± 0.007	0.810	0.818 ± 0.023	1.48	27.00	316
(1980) Tezcatlipoca	s3os2	spex55	—	LL	0.956 ± 0.002	0.476 ± 0.002	0.119 ± 0.001	1.987	1.976 ± 0.009	0.283	0.320 ± 0.031	1.17	54.62	356
(2042) Sitarski	smass2	sunshine04	—	H	0.919 ± 0.009	0.117 ± 0.005	0.184 ± 0.003	1.935	1.948 ± 0.049	0.891	0.837 ± 0.060	2.68	8.60	235

Table 3.11 — continued

Object	Vis[a]	NIR[a]	tax[b]	met[c]	B_IC[d]	B_IS_{corr}[e]	B_ID_{corr}[f]	$B_{II}C$[d]	$B_{II}C_{corr}$[g]	BAR	BAR_{corr}[h]	R_{AU}[i]	$\alpha(^\circ)$[j]	T_c[k]
(2062) Aten	smassneo	spex115	—	LL	0.962 ± 0.014	0.217 ± 0.006	0.214 ± 0.004	2.086	2.074 ± 0.048	0.414	0.454 ± 0.164	1.14	51.37	360
(2062) Aten	smassneo	spex206	—	LL/L	0.948 ± 0.003	-0.016 ± 0.004	0.177 ± 0.002	1.965	1.948 ± 0.052	0.309	0.366 ± 0.038	1.01	78.27	383
(2074) Shoemaker	s3os2	spex25	—	LL	0.959 ± 0.002	0.332 ± 0.001	0.227 ± 0.001	1.967	1.968 ± 0.004	0.352	0.345 ± 0.009	1.68	15.43	297
(2074) Shoemaker	smass1	spex25	—	LL	0.961 ± 0.001	0.478 ± 0.001	0.183 ± 0.001	1.967	1.968 ± 0.004	0.458	0.450 ± 0.012	1.68	15.43	297
(2078) Nanking	smass1	spex92	—	L/H	0.925 ± 0.001	0.144 ± 0.004	0.149 ± 0.001	1.910	1.918 ± 0.059	0.653	0.617 ± 0.299	2.23	4.73	258
(2078) Nanking	smassneo8	spex92	—	L/H	0.916 ± 0.004	0.125 ± 0.004	0.154 ± 0.001	1.910	1.918 ± 0.059	0.609	0.572 ± 0.283	2.23	4.73	258
(2089) Cetacea	smass2	feiberbeyer	—	L/H	0.918 ± 0.006	0.143 ± 0.004	0.150 ± 0.004	1.866	1.881 ± 0.035	0.675	0.615 ± 0.156	2.89	7.75	226
(2107) Ilmari	smass1	spex49	—	LL	0.967 ± 0.003	0.198 ± 0.003	0.120 ± 0.002	1.993	2.004 ± 0.177	0.371	0.325 ± 0.083	2.46	22.36	245
(2144) Marietta	—	EMMSpex	—	H	0.926 ± 0.002	0.227 ± 0.008	0.104 ± 0.003	1.869	1.884 ± 0.008	0.974	0.914 ± 0.150	2.90	2.72	226
(2335) James	smass2	spex45	—	L	0.920 ± 0.038	0.165 ± 0.005	0.164 ± 0.015	1.971	1.971 ± 0.017	0.522	0.519 ± 0.030	1.62	23.88	302
(2335) James	smass2	spex46	—	L	0.909 ± 0.039	0.164 ± 0.006	0.158 ± 0.017	1.941	1.939 ± 0.024	0.336	0.339 ± 0.056	1.53	23.81	311
(2340) Hathor	smassneo	spex203	—	LL	0.999 ± 0.026	0.021 ± 0.009	0.153 ± 0.004	1.991	1.975 ± 0.147	0.451	0.506 ± 0.704	1.02	56.42	381
(2504) Gaviola	smass2	sunshine04	—	H	0.924 ± 0.002	0.225 ± 0.005	0.158 ± 0.002	1.920	1.932 ± 0.020	1.072	1.023 ± 0.158	2.53	20.70	242
(2956) Yeomans	smass2	spex65	—	L	0.912 ± 0.001	0.129 ± 0.003	0.234 ± 0.001	1.955	1.971 ± 0.011	0.418	0.353 ± 0.116	3.01	4.80	220
(3066) McFadden	s3os2	feiberbeyer	—	H	0.927 ± 0.001	0.302 ± 0.002	0.088 ± 0.001	1.910	1.918 ± 0.008	0.993	0.957 ± 0.083	2.26	11.40	259
(3102) Krok	smassneo8	spex02	—	LL	1.002 ± 0.006	0.216 ± 0.003	0.188 ± 0.002	2.033	2.028 ± 0.023	0.494	0.510 ± 0.032	1.38	20.09	327
(3288) Seleucus	smassneo	spex67	—	LL	1.016 ± 0.010	0.489 ± 0.011	0.111 ± 0.004	1.981	1.980 ± 0.013	0.345	0.342 ± 0.097	1.61	10.02	303
(3288) Seleucus	smassneo	spex71	—	LL	1.022 ± 0.005	0.425 ± 0.006	0.084 ± 0.002	1.980	1.968 ± 0.023	0.364	0.403 ± 0.089	1.15	60.93	358
(3288) Seleucus	smassneo	spex99	—	LL	1.015 ± 0.005	0.423 ± 0.004	0.098 ± 0.002	2.025	2.013 ± 0.010	0.637	0.677 ± 0.046	1.14	57.03	361
(3352) McAuliffe	s3os2	spex103	—	H/L	0.945 ± 0.008	0.342 ± 0.006	0.149 ± 0.003	1.908	1.902 ± 0.019	0.667	0.685 ± 0.261	1.35	47.04	331
(3628) Boznemcova	smasneo	spex50	—	LL	1.003 ± 0.022	0.071 ± 0.012	0.392 ± 0.006	2.025	2.041 ± 0.021	0.717	0.653 ± 0.109	3.01	8.25	222
(3635) Kreutz	s3os2	spex47	—	H	0.928 ± 0.002	0.500 ± 0.005	0.144 ± 0.002	1.959	1.958 ± 0.033	1.221	1.220 ± 0.075	1.72	14.02	306
(3635) Kreutz	smass2	spex47	—	H	0.920 ± 0.002	0.347 ± 0.003	0.189 ± 0.001	1.956	1.955 ± 0.037	0.804	0.803 ± 0.052	1.72	14.02	306
(3637) O'Meara	—	feiberbeyer	—	H	0.926 ± 0.007	0.164 ± 0.050	0.132 ± 0.018	1.885	1.894 ± 0.010	0.972	0.932 ± 0.291	2.36	13.70	254
(3674) Erbisbuhl	smass1	spex92	—	L/H	0.927 ± 0.002	0.128 ± 0.003	0.143 ± 0.001	1.879	1.884 ± 0.041	0.681	0.658 ± 0.065	1.95	20.71	276
(3674) Erbisbuhl	smassneo8	spex92	—	L/H	0.927 ± 0.002	0.128 ± 0.003	0.143 ± 0.001	1.879	1.884 ± 0.041	0.681	0.658 ± 0.065	1.95	20.71	276
(3753) Cruithne	s3os2	spex17	—	L/LL	0.946 ± 0.006	0.257 ± 0.006	0.167 ± 0.003	1.882	1.876 ± 0.026	0.469	0.489 ± 0.057	1.34	47.21	332
(3753) Cruithne	s3os2	spex45	—	LL/L	0.950 ± 0.006	0.217 ± 0.004	0.161 ± 0.002	1.964	1.953 ± 0.019	0.463	0.498 ± 0.054	1.18	56.92	354
(3753) Cruithne	smassneo8	spex17	—	L	0.932 ± 0.004	0.146 ± 0.006	0.206 ± 0.002	1.881	1.875 ± 0.028	0.382	0.402 ± 0.049	1.34	47.21	332
(3753) Cruithne	smassneo8	spex45	—	L	0.938 ± 0.003	0.114 ± 0.003	0.200 ± 0.002	1.963	1.952 ± 0.020	0.370	0.405 ± 0.045	1.18	56.92	354
(3873) Roddy	s3os2	spex32	—	H	0.943 ± 0.005	0.193 ± 0.012	0.122 ± 0.006	1.999	2.006 ± 0.160	1.312	1.280 ± 0.405	2.13	27.82	264
(3873) Roddy	smass2	spex32	—	LL/L	0.961 ± 0.016	0.128 ± 0.011	0.128 ± 0.007	2.001	2.008 ± 0.162	1.029	0.997 ± 0.338	2.13	27.82	264
(4034) Vishnu	smassneo	spex119	—	LL/L	0.950 ± 0.012	-0.032 ± 0.009	0.214 ± 0.006	2.002	1.986 ± 0.091	0.257	0.312 ± 0.227	1.03	77.17	380
(4179) Toutatis	smass1	spex03	—	L	0.940 ± 0.001	0.169 ± 0.001	0.140 ± 0.001	1.974	1.970 ± 0.007	0.612	0.620 ± 0.016	1.46	2.11	318
(4179) Toutatis	smass1	spex115	—	LL	0.950 ± 0.001	0.328 ± 0.001	0.132 ± 0.001	1.985	1.969 ± 0.008	0.738	0.794 ± 0.022	1.02	47.14	382
(4179) Toutatis	smass1	spex116	—	LL/L	0.948 ± 0.002	0.215 ± 0.002	0.147 ± 0.001	2.011	2.000 ± 0.010	0.496	0.532 ± 0.045	1.18	8.94	355
(4179) Toutatis	smass1	spex30	—	LL	0.951 ± 0.001	0.248 ± 0.001	0.141 ± 0.001	1.987	1.973 ± 0.004	0.724	0.770 ± 0.006	1.09	26.74	369

Table 3.11 — continued

Object	Vis[a]	NIR[a]	tax[b]	met[c]	B_IC[d]	B_IS_{corr}[e]	B_ID_{corr}[f]	$B_{II}C$[d]	$B_{II}C_{corr}$[g]	BAR	BAR_{corr}[h]	R_{AU}[i]	$\alpha(^\circ)$[j]	T_c[k]
(4179) Toutatis	smass1	spex73	—	LL/L	0.950 ± 0.004	0.190 ± 0.002	0.152 ± 0.001	1.922	1.920 ± 0.018	0.283	0.285 ± 0.057	1.55	4.05	309
(4179) Toutatis	smass1	spex74	—	LL	0.955 ± 0.005	0.075 ± 0.002	0.096 ± 0.001	1.977	1.962 ± 0.013	0.589	0.640 ± 0.045	1.06	67.67	374
(4179) Toutatis	smassneo	reddy	—	L	0.944 ± 0.003	0.365 ± 0.003	0.157 ± 0.001	1.957	1.953 ± 0.050	0.012	0.022 ± 0.104	1.45	6.10	320
(4179) Toutatis	smassneo	spex03	—	L/H	0.941 ± 0.002	0.195 ± 0.001	0.129 ± 0.001	1.974	1.970 ± 0.007	0.664	0.673 ± 0.018	1.46	2.11	318
(4179) Toutatis	smassneo	spex116	—	LL	0.955 ± 0.002	0.235 ± 0.002	0.140 ± 0.001	2.011	2.000 ± 0.010	0.523	0.559 ± 0.048	1.18	8.94	355
(4179) Toutatis	smassneo	spex30	—	LL	0.953 ± 0.001	0.238 ± 0.001	0.144 ± 0.001	1.987	1.973 ± 0.004	0.704	0.750 ± 0.006	1.09	26.74	369
(4179) Toutatis	smassneo	spex73	—	LL	0.958 ± 0.003	0.223 ± 0.002	0.144 ± 0.002	1.922	1.920 ± 0.018	0.305	0.307 ± 0.063	1.55	4.05	309
(4179) Toutatis	smassneo	spex74	—	LL	0.964 ± 0.003	0.100 ± 0.002	0.089 ± 0.001	1.977	1.962 ± 0.013	0.629	0.679 ± 0.047	1.06	67.67	374
(4197) Toutatis	smassneo	spex115	—	LL	0.952 ± 0.002	0.350 ± 0.001	0.124 ± 0.001	1.985	1.969 ± 0.008	0.775	0.831 ± 0.024	1.02	47.14	382
(4197) Toutatis	smassneo	spex25	—	H	0.927 ± 0.002	0.108 ± 0.001	0.107 ± 0.001	1.962	1.953 ± 0.011	1.007	1.037 ± 0.030	1.24	42.27	346
(4341) Poseidon	smassneo	spex223	—	L/LL	0.946 ± 0.019	0.452 ± 0.028	0.263 ± 0.011	1.883	1.877 ± 0.012	0.467	0.485 ± 0.303	1.35	42.41	331
(4954) Eric	s3os2	reddy	—	H	0.935 ± 0.001	0.144 ± 0.001	0.114 ± 0.001	1.963	1.950 ± 0.002	0.945	0.990 ± 0.003	1.10	62.00	367
(4954) Eric	s3os2	spex61	—	H	0.922 ± 0.001	0.434 ± 0.003	0.112 ± 0.001	1.948	1.948 ± 0.021	1.060	1.053 ± 0.198	1.67	28.34	298
(4954) Eric	s3os2	spex64	—	H	0.923 ± 0.002	0.484 ± 0.004	0.111 ± 0.001	1.936	1.927 ± 0.016	1.326	1.355 ± 0.064	1.24	29.73	345
(4954) Eric	smassneo8	reddy	—	H	0.935 ± 0.001	0.145 ± 0.001	0.113 ± 0.001	1.963	1.950 ± 0.002	0.949	0.994 ± 0.003	1.10	62.00	367
(4954) Eric	smassneo8	spex61	—	L/H	0.918 ± 0.002	0.309 ± 0.002	0.153 ± 0.002	1.948	1.948 ± 0.022	0.653	0.646 ± 0.124	1.67	28.34	298
(4954) Eric	smassneo8	spex64	—	H	0.919 ± 0.001	0.355 ± 0.002	0.151 ± 0.001	1.936	1.927 ± 0.016	0.858	0.887 ± 0.040	1.24	29.73	345
(5143) Heracles	smass1	spex55	—	LL	1.019 ± 0.012	0.098 ± 0.003	0.193 ± 0.002	1.964	1.965 ± 0.027	0.262	0.254 ± 0.043	1.71	16.52	296
(5143) Heracles	smassneo	spex55	—	LL	1.006 ± 0.013	0.028 ± 0.003	0.221 ± 0.002	1.963	1.964 ± 0.030	0.219	0.211 ± 0.039	1.71	16.52	296
(5159) Burbine	smass2	spex201	—	L	0.935 ± 0.004	0.191 ± 0.005	0.148 ± 0.002	1.878	1.888 ± 0.072	0.364	0.322 ± 0.141	2.65	10.61	250
(5379) Abehiroshi	smass2	spex51	—	L	0.865 ± 0.119	0.200 ± 0.049	0.274 ± 0.028	1.961	1.946 ± 0.011	0.275	0.325 ± 0.049	1.27	8.62	374
(5392) Parker	smass2	spex95	—	H/L	0.929 ± 0.007	0.347 ± 0.007	0.141 ± 0.002	1.929	1.938 ± 0.008	0.863	0.826 ± 0.158	2.23	13.48	257
(5587) 1990 SB	smassneo	spex224	—	H/L	0.927 ± 0.002	0.130 ± 0.016	0.188 ± 0.003	1.955	1.963 ± 0.017	0.828	0.792 ± 0.221	2.41	17.15	258
(5626) 1991 FE	smassneo	spex84	—	H/L	0.925 ± 0.004	0.198 ± 0.005	0.117 ± 0.003	2.001	1.995 ± 0.090	0.885	0.902 ± 0.450	1.36	46.01	330
(5641) McCleese	smass2	spex42	—	L	0.898 ± 0.020	0.398 ± 0.012	0.178 ± 0.020	1.943	1.943 ± 0.019	0.241	0.237 ± 0.034	1.63	30.98	301
(5817) Robertfrazer	smass2	spex31	—	H	0.915 ± 0.001	0.195 ± 0.001	0.169 ± 0.001	1.960	1.962 ± 0.003	0.755	0.743 ± 0.009	1.75	19.85	291
(5836) 1993 MF	smassneo8	spex108	—	L/H	0.915 ± 0.004	0.069 ± 0.004	0.164 ± 0.003	1.926	1.930 ± 0.050	0.574	0.556 ± 0.262	1.86	3.61	282
(5836) 1993 MF	smassneo8	spex221	—	H	0.900 ± 0.002	0.304 ± 0.005	0.122 ± 0.002	1.882	1.871 ± 0.048	0.852	0.887 ± 0.060	1.19	58.00	353
(5840) Raybrown	smass2	sunshine08	—	LL/L	0.987 ± 0.135	0.050 ± 0.024	0.065 ± 0.076	2.007	2.015 ± 0.014	0.804	0.769 ± 0.169	2.51	2.50	260
(6455) 1992 HE	smassneo	spex107	—	LL	0.982 ± 0.011	0.271 ± 0.006	0.235 ± 0.003	1.940	1.945 ± 0.028	0.352	0.330 ± 0.074	1.57	22.98	277
(6455) 1992 HE	smassneo	spex19	—	L/LL	0.944 ± 0.005	0.411 ± 0.006	0.231 ± 0.002	1.956	1.951 ± 0.008	0.399	0.411 ± 0.016	1.16	13.53	323
(6585) O'Keefe	smass2	spex55	—	L/H	0.919 ± 0.003	0.170 ± 0.003	0.142 ± 0.002	1.911	1.909 ± 0.028	0.652	0.654 ± 0.081	1.54	25.95	310
(7088) 1992 AA	—	reddymc	—	LL	0.988 ± 0.005	0.205 ± 0.002	0.194 ± 0.001	1.959	1.951 ± 0.005	0.367	0.391 ± 0.009	1.29	18.60	339
(7336) 1989 RS_1	smasneo	spex93	—	LL	1.016 ± 0.008	-0.010 ± 0.003	0.234 ± 0.003	2.008	1.998 ± 0.015	0.292	0.325 ± 0.054	1.21	12.30	350
(7341) 1991 VK	smass1	spex103	—	LL	0.995 ± 0.005	0.211 ± 0.003	0.178 ± 0.001	1.982	1.975 ± 0.022	0.305	0.326 ± 0.082	1.32	24.66	334
(7341) 1991 VK	smass1	spex11	—	LL	0.998 ± 0.013	0.149 ± 0.009	0.166 ± 0.004	2.048	2.038 ± 0.066	0.572	0.606 ± 0.105	1.20	34.52	352
(7341) 1991 VK	smass1	spex223	—	LL	0.977 ± 0.004	0.212 ± 0.004	0.175 ± 0.002	2.069	2.062 ± 0.079	0.432	0.455 ± 0.055	1.31	27.04	336

Table 3.11 — continued

Object	Vis[a]	NIR[a]	tax[b]	met[c]	B_IC[d]	B_IS_{corr}[e]	B_ID_{corr}[f]	$B_{II}C$[d]	$B_{II}C_{corr}$[g]	BAR	BAR_{corr}[h]	R_{AU}[i]	$\alpha(^\circ)$[j]	T_c[k]
(7341) 1991 VK	smassneo	spex103	—	LL	0.987 ± 0.008	0.121 ± 0.002	0.210 ± 0.002	1.982	1.975 ± 0.025	0.243	0.264 ± 0.071	1.32	24.66	334
(7341) 1991 VK	smassneo	spex11	—	LL	0.983 ± 0.022	0.049 ± 0.008	0.202 ± 0.006	2.047	2.037 ± 0.072	0.445	0.478 ± 0.090	1.20	34.52	352
(7341) 1991 VK	smassneo	spex223	—	LL	0.969 ± 0.006	0.119 ± 0.004	0.209 ± 0.002	2.063	2.056 ± 0.084	0.345	0.367 ± 0.048	1.31	27.04	336
(7358) 1995 YA_3	smassneo	spex100	—	L	0.934 ± 0.009	0.041 ± 0.004	0.136 ± 0.003	1.944	1.947 ± 0.026	0.337	0.320 ± 0.096	1.84	1.09	284
(7482) 1994 PC_1	s3os2	spex72	—	LL	1.011 ± 0.009	0.277 ± 0.005	0.161 ± 0.003	1.916	1.914 ± 0.118	0.141	0.145 ± 0.412	1.52	20.00	312
(7482) 1994 PC_1	smassneo	spex72	—	LL	1.007 ± 0.008	0.185 ± 0.004	0.193 ± 0.003	1.915	1.913 ± 0.120	0.107	0.111 ± 0.330	1.52	20.00	312
(7822) 1991 CS	smassneo	spex216	—	H	0.918 ± 0.002	0.409 ± 0.003	0.146 ± 0.001	1.896	1.896 ± 0.014	0.915	0.908 ± 0.036	1.18	39.01	298
(8567) 1996 HW_1	reddy	spex104	—	LL	1.004 ± 0.009	0.351 ± 0.004	0.129 ± 0.002	1.980	1.974 ± 0.031	0.327	0.345 ± 0.151	1.36	39.93	330
(8567) 1996 HW_1	reddy	spex44	—	LL	1.006 ± 0.011	0.240 ± 0.004	0.119 ± 0.002	2.007	1.997 ± 0.014	0.390	0.425 ± 0.035	1.19	55.87	352
(8567) 1996 HW_1	reddy	spex48	—	LL	1.012 ± 0.017	0.324 ± 0.007	0.121 ± 0.004	2.059	2.049 ± 0.062	0.278	0.310 ± 0.126	1.21	53.15	349
(8567) 1996 HW_1	reddy	spex73	—	LL	1.010 ± 0.015	0.169 ± 0.004	0.125 ± 0.002	1.936	1.926 ± 0.039	0.315	0.347 ± 0.067	1.22	31.45	349
(8567) 1996 HW_1	reddy	spex74	—	LL	1.025 ± 0.005	0.189 ± 0.003	0.118 ± 0.001	2.005	1.993 ± 0.011	0.261	0.301 ± 0.029	1.15	23.99	360
(9400) 1994 TW_1	smassneo	spex106	—	L	0.925 ± 0.006	-0.066 ± 0.011	0.223 ± 0.004	1.913	1.922 ± 0.253	0.093	0.054 ± 0.412	2.27	2.02	255
(9400) 1994 TW_1	smassneo	spex215	—	L	0.918 ± 0.001	0.103 ± 0.002	0.201 ± 0.001	1.984	1.981 ± 0.016	0.629	0.634 ± 0.036	1.51	33.51	313
(10537) 1991 RY_{16}	moskovitz	moskovitz08	—	LL/L	0.949 ± 0.002	0.400 ± 0.008	0.379 ± 0.002	1.883	1.899 ± 0.008	1.093	1.030 ± 0.033	3.04	13.79	222
(10537) 1991 RY_{16}	moskovitz	moskovitz08	—	LL	0.960 ± 0.003	0.315 ± 0.008	0.389 ± 0.002	1.883	1.899 ± 0.008	1.026	0.962 ± 0.032	3.04	13.79	222
(11398) 1998 YP_{11}	smassneo8	reddy	—	H	0.931 ± 0.001	0.189 ± 0.003	0.167 ± 0.001	1.963	1.949 ± 0.004	1.265	1.311 ± 0.020	1.21	19.00	369
(11398) 1998 YP_{11}	smassneo8	spex68	—	H	0.926 ± 0.001	0.244 ± 0.002	0.158 ± 0.001	1.950	1.935 ± 0.009	0.706	0.758 ± 0.022	1.16	32.20	376
(11405) 1999 CV_3	smassneo8	reddy	—	LL/L	0.951 ± 0.007	0.131 ± 0.003	0.175 ± 0.002	1.979	1.975 ± 0.012	0.529	0.540 ± 0.012	1.44	14.00	321
(15745) 1991 PM_5	smassneo	spex82	—	H/L	0.941 ± 0.014	0.225 ± 0.008	0.084 ± 0.003	1.979	1.972 ± 0.140	0.892	0.913 ± 1.619	1.32	27.10	335
(16834) 1997 WU_{22}	smassneo	spex77	—	LL	1.007 ± 0.024	0.067 ± 0.009	0.097 ± 0.005	1.878	1.872 ± 0.114	1.545	1.564 ± 0.304	1.35	27.53	331
(16834) 1997 WU_{22}	smassneo	spex84	—	LL/L	0.954 ± 0.008	0.291 ± 0.004	0.125 ± 0.003	1.929	1.931 ± 0.074	0.396	0.385 ± 0.123	1.75	22.71	291
(16960) 1998 QS_{52}	smassneo	spex73	—	L	0.937 ± 0.003	-0.054 ± 0.004	0.160 ± 0.003	1.855	1.862 ± 0.022	0.488	0.458 ± 0.192	2.07	28.59	267
(16960) 1998 QS_{52}	smassneo	spex74	—	H	0.925 ± 0.001	-0.002 ± 0.003	0.157 ± 0.001	1.950	1.943 ± 0.036	0.796	0.817 ± 0.043	1.32	39.30	335
(18736) 1998 NU	smassneo	spex03	—	H/L	0.935 ± 0.002	0.388 ± 0.013	0.135 ± 0.004	1.987	1.977 ± 0.057	0.656	0.688 ± 0.044	1.21	49.44	349
(19356) 1997 GH_3	smassneo	spex03	—	LL/L	0.950 ± 0.003	0.096 ± 0.002	0.170 ± 0.001	1.990	1.977 ± 0.003	0.562	0.605 ± 0.018	1.12	35.11	364
(23183) 2000 OY_{21}	—	reddymc	—	LL	1.027 ± 0.014	0.159 ± 0.026	0.223 ± 0.010	2.112	2.104 ± 0.099	0.438	0.464 ± 0.094	1.27	33.60	341
(24475) 2000 VN_2	smassneo	spex05	—	LL	0.950 ± 0.002	0.356 ± 0.004	0.117 ± 0.002	1.905	1.903 ± 0.071	0.751	0.753 ± 0.052	1.54	24.12	310
(24475) 2000 VN_2	smassneo	spex105	—	LL	0.955 ± 0.002	0.335 ± 0.003	0.136 ± 0.001	1.990	1.988 ± 0.007	0.770	0.772 ± 0.078	1.54	24.12	310
(25143) Itokawa	sf36	binzel01	—	LL	0.998 ± 0.005	0.208 ± 0.002	0.155 ± 0.001	1.981	1.965 ± 0.006	0.322	0.379 ± 0.007	1.01	66.65	382
(32906) 1994 RH	smassneo	spex105	—	H	0.935 ± 0.002	0.250 ± 0.007	0.126 ± 0.003	1.940	1.934 ± 0.017	0.874	0.893 ± 0.131	1.35	34.20	331
(137032) 1998 UO_1	reddy	spex223	—	LL	0.961 ± 0.002	-0.081 ± 0.006	0.177 ± 0.003	1.942	1.929 ± 0.012	0.489	0.531 ± 0.043	1.13	61.60	363
(137032) 1998 UO_1	reddy	spex31	—	LL	0.956 ± 0.005	-0.003 ± 0.007	0.187 ± 0.003	1.997	1.983 ± 0.011	0.388	0.435 ± 0.022	1.08	63.30	370
(137032) 1998 UO_1	reddy	spex32	—	LL	0.956 ± 0.002	-0.055 ± 0.006	0.204 ± 0.003	2.129	2.124 ± 0.058	0.235	0.249 ± 0.037	1.40	24.10	325
(137032) 1998 UO_1	reddy	spex74	—	LL	0.974 ± 0.006	-0.024 ± 0.006	0.191 ± 0.003	2.007	1.992 ± 0.020	0.278	0.327 ± 0.027	1.07	52.00	373
(137062) 1998 WM	smassneo8	spex19	Sr	L/H	0.919 ± 0.003	0.380 ± 0.008	0.224 ± 0.003	1.984	1.983 ± 0.008	0.657	0.654 ± 0.082	1.60	18.10	304
(137126) 1999 CF_9	smassneo	spex124	Sq	L/H	0.918 ± 0.002	0.023 ± 0.003	0.186 ± 0.001	1.956	1.945 ± 0.063	0.578	0.615 ± 0.129	1.17	27.20	356

Table 3.11 — continued

Object	Vis[a]	NIR[a]	tax[b]	met[c]	B_IC[d]	B_IS_{corr}[e]	B_ID_{corr}[f]	$B_{II}C$[d]	$B_{II}C_{corr}$[g]	BAR	BAR_{corr}[h]	R_{AU}[i]	$\alpha(^\circ)$[j]	T_c[k]
(137799) 1999 YB	smassneo	spex103	S	LL	0.982 ± 0.022	0.138 ± 0.006	0.197 ± 0.004	1.910	1.905 ± 0.046	0.362	0.375 ± 0.193	1.42	2.60	323
(138254) 2000 FD_{61}	smassneo8	spex102	—	H	0.928 ± 0.001	0.148 ± 0.003	0.184 ± 0.001	1.954	1.968 ± 0.018	1.191	1.132 ± 0.063	2.85	16.00	228
(138258) 2000 GD_2	smassneo8	spex11	—	LL	1.012 ± 0.007	0.073 ± 0.006	0.177 ± 0.003	1.965	1.950 ± 0.036	0.501	0.551 ± 0.071	1.06	25.00	374
(138524) 2000 OJ_8	smassneo8	dm03	—	H/L	0.925 ± 0.004	0.119 ± 0.004	0.168 ± 0.003	1.914	1.899 ± 0.038	0.636	0.687 ± 0.176	1.06	26.85	374
(143678) 2003 SA_{224}	—	reddy	—	LL	0.977 ± 0.011	0.223 ± 0.006	0.144 ± 0.003	2.005	1.992 ± 0.010	0.406	0.449 ± 0.014	1.11	56.00	365
(143678) 2003 SA_{224}	—	reddymc	—	LL	0.978 ± 0.007	0.263 ± 0.005	0.191 ± 0.002	1.969	1.968 ± 0.030	0.440	0.437 ± 0.033	1.61	15.00	303
(159402) 1999 AP_{10}	reddy	spex84	—	LL	0.972 ± 0.017	0.361 ± 0.003	0.091 ± 0.002	1.955	1.944 ± 0.031	0.259	0.297 ± 0.079	1.16	19.35	357
(162142) 1998 VR	smassneo8	spex223	Sq	H	0.934 ± 0.011	0.118 ± 0.021	0.143 ± 0.007	2.030	2.018 ± 0.190	0.874	0.913 ± 0.170	1.15	27.78	358
(162781) 2000 XL_{44}	smassneo8	spex03	—	LL	1.004 ± 0.019	0.294 ± 0.008	0.154 ± 0.004	2.128	2.120 ± 0.034	0.783	0.809 ± 0.095	1.28	22.70	341
(163000) 2001 SW_{169}	spex212(vis)	spex73	—	LL/L	0.948 ± 0.025	0.293 ± 0.004	0.153 ± 0.003	1.940	1.930 ± 0.071	0.368	0.401 ± 0.340	1.20	12.70	351
(164400) 2001 SW_{169}	reddy	spex73	—	LL	0.980 ± 0.008	0.151 ± 0.004	0.195 ± 0.002	1.941	1.931 ± 0.033	0.325	0.358 ± 0.087	1.20	27.05	351
(200840) 2001 XN_{254}	smassneo8	spex12	—	L	0.947 ± 0.003	0.129 ± 0.004	0.119 ± 0.002	1.979	1.963 ± 0.008	0.558	0.612 ± 0.040	1.04	61.46	378
(216258) 2006 WH_1	—	reddy	—	LL	0.954 ± 0.003	-0.004 ± 0.015	0.206 ± 0.006	1.987	1.970 ± 0.015	0.460	0.517 ± 0.076	1.01	60.00	383

Notes. [a] Visible or near-infrared spectrum source.

[b] Bus-DeMeo taxonomic classification.

[c] Meteorite analog (H/L/LL), based on B_IC and BAR_{corr}.

[d] Band center wavelengths, given in μm.

[e] Band slope, given in μm^{-1} and corrected for phase angle.

[f] Band depth, given in % and corrected for temperature.

[g] $B_{II}C$, corrected for temperature.

[h] BAR corrected for temperature.

[i] Heliocentric distance of observation in AU.

[j] Solar phase angle of observation in degrees.

[k] Estimated color temperature (K) at the time of observation.

Table 3.12: Band Parameters of BA Asteroids

Object	Vis[a]	NIR[a]	tax[b] (met[c])	BIC^{d}	$BIC_{corr}{}^{d,e}$	BIS^{f}	BID^{g}	$BIIC^{d}$	$BIIC_{corr}{}^{d,h}$	BAR	$R_{\mathrm{AU}}{}^{i}$	$\alpha(^{\circ})^{j}$	$T_c{}^{k}$
(4) Vesta	smass1	moskovitz10	V (How)	0.928	0.931 ± 0.001	0.243 ± 0.001	0.343 ± 0.001	1.960	1.969 ± 0.001	1.982 ± 0.010	2.26	26	248
(4) Vesta	smass2	moskovitz10	V (How)	0.930	0.933 ± 0.001	0.232 ± 0.001	0.347 ± 0.001	1.960	1.969 ± 0.001	1.958 ± 0.010	2.26	26	248
(4) Vesta	smass1	reddymb	V (How)	0.931	0.935 ± 0.001	0.330 ± 0.001	0.347 ± 0.001	1.949	1.960 ± 0.002	1.855 ± 0.006	2.56	21	233
(4) Vesta	smass1	spex86	V (How)	0.922	0.925 ± 0.001	0.246 ± 0.004	0.338 ± 0.001	1.957	1.968 ± 0.006	1.668 ± 0.039	2.48	23	237
(4) Vesta	smass2	spex86	V (How)	0.929	0.933 ± 0.001	0.209 ± 0.004	0.354 ± 0.001	1.957	1.967 ± 0.006	1.569 ± 0.036	2.48	23	237
(809) Lundia	s3os2	moskovitz10	V (How)	0.935	0.936 ± 0.001	0.803 ± 0.002	0.491 ± 0.001	1.923	1.927 ± 0.002	1.932 ± 0.007	1.93	24	272
(956) Elisa	s3os2	moskovitz	V (How)	0.931	0.932 ± 0.001	0.728 ± 0.001	0.480 ± 0.001	1.942	1.944 ± 0.002	2.060 ± 0.005	1.85	17	287
(956) Elisa	s3os2	moskovitz	V (Di)	0.929	0.930 ± 0.001	0.794 ± 0.002	0.491 ± 0.001	1.905	1.907 ± 0.002	2.198 ± 0.012	1.85	30	287
(1468) Zomba	—	moskovitz	V (Eu)	0.944	0.945 ± 0.001	1.516 ± 0.045	0.354 ± 0.004	1.977	1.981 ± 0.006	2.961 ± 0.064	1.60	38	279
(1468) Zomba	—	moskovitz	V (How/Eu)	0.934	0.938 ± 0.001	0.729 ± 0.044	0.443 ± 0.006	1.978	1.991 ± 0.010	1.493 ± 0.075	2.51	13	223
(1929) Kollaa	smass1	moskovitz10	V (Eu)	0.938	0.942 ± 0.001	0.747 ± 0.003	0.464 ± 0.001	1.955	1.966 ± 0.005	1.867 ± 0.018	2.21	14	232
(1929) Kollaa	smass2	moskovitz10	V (Eu)	0.937	0.941 ± 0.001	0.692 ± 0.004	0.472 ± 0.001	1.955	1.966 ± 0.005	1.840 ± 0.017	2.21	14	232
(1981) Midas	smassneo	spex126	V (Eu)	0.942	0.943 ± 0.002	0.359 ± 0.005	0.471 ± 0.002	2.038	2.043 ± 0.020	1.734 ± 0.064	1.71	34	271
(2011) Veteraniya	—	hardersen15	V (How)	0.935	0.938 ± 0.001	0.590 ± 0.001	0.371 ± 0.001	1.921	1.930 ± 0.005	2.096 ± 0.001	2.04	8.0	242
(2045) Peking	smass2	moskovitz	V (How)	0.936	0.940 ± 0.001	0.657 ± 0.008	0.423 ± 0.002	1.929	1.939 ± 0.012	1.912 ± 0.031	2.48	27	238
(2371) Dimitrov	smass2	moskovitz10	V (Eu)	0.938	0.942 ± 0.001	0.803 ± 0.006	0.427 ± 0.001	1.992	2.005 ± 0.009	1.862 ± 0.060	2.47	20	221
(2442) Corbett	smass1	moskovitz10	V (How)	0.931	0.935 ± 0.001	0.545 ± 0.008	0.487 ± 0.002	1.933	1.943 ± 0.037	2.059 ± 0.025	2.25	7.8	239
(2511) Patterson	smass2	moskovitz10	V (How)	0.933	0.936 ± 0.001	0.594 ± 0.004	0.446 ± 0.001	1.958	1.967 ± 0.008	1.873 ± 0.015	2.23	21	244
(2566) Kirghizia	smass2	moskovitz10	V (How)	0.935	0.938 ± 0.001	0.425 ± 0.006	0.446 ± 0.002	1.929	1.939 ± 0.010	1.873 ± 0.029	2.41	10	241
(2579) Spartacus	smass2	moskovitz10	V (Eu)	0.943	0.947 ± 0.006	0.310 ± 0.009	0.487 ± 0.004	1.980	1.993 ± 0.027	1.297 ± 0.055	2.22	19	222
(2653) Principia	smass2	moskovitz	V (How)	0.932	0.935 ± 0.001	0.650 ± 0.010	0.506 ± 0.002	1.951	1.961 ± 0.012	1.868 ± 0.028	2.24	13	240
(2653) Principia	smass2	moskovitz	V (How)	0.931	0.934 ± 0.001	0.381 ± 0.004	0.475 ± 0.001	1.963	1.971 ± 0.007	1.712 ± 0.012	1.99	12	254
(2653) Principia	smass2	moskovitz	V (How)	0.937	0.939 ± 0.001	0.497 ± 0.005	0.500 ± 0.001	1.973	1.980 ± 0.005	1.735 ± 0.020	1.92	17	259
(2763) Jeans	smass2	moskovitz	V (Eu)	0.941	0.943 ± 0.001	0.484 ± 0.004	0.414 ± 0.001	1.985	1.991 ± 0.004	1.716 ± 0.011	2.24	13	263
(2763) Jeans	smass2	moskovitz	V (How)	0.938	0.939 ± 0.001	0.618 ± 0.002	0.418 ± 0.001	1.943	1.946 ± 0.002	1.571 ± 0.007	1.99	12	279
(2763) Jeans	smass2	moskovitz	V (Eu)	0.938	0.939 ± 0.001	0.704 ± 0.002	0.428 ± 0.001	2.000	2.002 ± 0.002	1.659 ± 0.007	1.92	17	284
(2851) Harbin	smass2	moskovitz	V (How/Di)	0.923	0.928 ± 0.001	0.424 ± 0.003	0.488 ± 0.001	1.910	1.923 ± 0.006	1.850 ± 0.012	2.42	8.7	223
(2851) Harbin	smass2	moskovitz	V (How/Di)	0.924	0.928 ± 0.001	0.552 ± 0.004	0.501 ± 0.001	1.930	1.943 ± 0.005	1.958 ± 0.012	2.34	16	226
(2912) Lapalma	smass2	EMMSpex	Vw (How/Di)	0.929	0.934 ± 0.001	0.866 ± 0.003	0.490 ± 0.001	1.929	1.944 ± 0.004	2.184 ± 0.017	2.43	11	213
(2912) Lapalma	smass2	moskovitz10	V (How)	0.931	0.935 ± 0.001	0.649 ± 0.003	0.507 ± 0.001	1.939	1.951 ± 0.003	1.890 ± 0.012	2.14	8.7	227
(3155) Lee	smass1	moskovitz	V (How/Di)	0.919	0.923 ± 0.001	0.552 ± 0.006	0.465 ± 0.001	1.920	1.933 ± 0.018	2.304 ± 0.058	2.56	8.4	221
(3155) Lee	smass2	moskovitz	V (How/Di)	0.920	0.925 ± 0.001	0.613 ± 0.006	0.454 ± 0.002	1.920	1.933 ± 0.017	2.310 ± 0.054	2.56	8.4	221
(3155) Lee	smass1	moskovitz	V (Di)	0.918	0.923 ± 0.001	0.661 ± 0.005	0.473 ± 0.001	1.892	1.904 ± 0.015	2.323 ± 0.032	2.43	7.9	227
(3155) Lee	smass2	moskovitz	V (Di)	0.919	0.923 ± 0.001	0.738 ± 0.006	0.463 ± 0.001	1.893	1.905 ± 0.016	2.331 ± 0.034	2.43	7.9	227
(3536) Schleicher	smass2	EMMSpex	V (Di)	0.929	0.932 ± 0.001	0.599 ± 0.007	0.383 ± 0.002	1.880	1.892 ± 0.013	2.061 ± 0.093	2.26	11	229
(3657) Ermolova	smass1	moskovitz10	V (Di)	0.935	0.940 ± 0.001	0.658 ± 0.003	0.474 ± 0.001	1.903	1.917 ± 0.003	2.044 ± 0.037	2.18	25	215

Table 3.12 — continued

Object	Vis[a]	NIR[a]	tax[b] (met[c])	B_IC[d]	B_IC_{corr}[d,e]	B_IS[f]	B_ID[g]	$B_{II}C$[d]	$B_{II}C_{corr}$[d,h]	BAR	R_{AU}[i]	$\alpha(^\circ)$[j]	T_c[k]
(3782) Celle	smass2	hardersen	V (Di)	0.928	0.932 ± 0.001	0.350 ± 0.001	0.441 ± 0.001	1.905	1.917 ± 0.001	1.893 ± 0.001	2.31	25	228
(3782) Celle	smass2	hardersen	V (Eu)	0.938	0.942 ± 0.001	0.327 ± 0.001	0.421 ± 0.001	1.952	1.964 ± 0.001	2.054 ± 0.001	2.31	25	228
(3782) Celle	smass2	moskovitz	V (How)	0.929	0.933 ± 0.001	0.403 ± 0.004	0.411 ± 0.001	1.937	1.948 ± 0.009	1.748 ± 0.023	2.19	13	234
(3867) Shiretoko	—	hardersen14	V (Eu)	0.947	0.949 ± 0.001	0.713 ± 0.001	0.449 ± 0.001	1.967	1.974 ± 0.001	1.195 ± 0.001	2.15	24	258
(4038) Kristina	smass1	moskovitz10	V (How)	0.922	0.920 ± 0.001	0.721 ± 0.003	0.291 ± 0.001	1.965	1.959 ± 0.003	2.503 ± 0.020	1.13	10	333
(4055) Magellan	s3os2	spex208	V (How)	0.932	0.933 ± 0.007	0.423 ± 0.018	0.506 ± 0.009	1.932	1.936 ± 0.006	1.840 ± 0.045	1.54	39	272
(4055) Magellan	smassneo8	spex208	V (How)	0.932	0.933 ± 0.002	0.306 ± 0.011	0.527 ± 0.003	1.932	1.936 ± 0.006	1.755 ± 0.029	1.54	39	272
(4055) Magellan	s3os2	spex38	V (Di)	0.965	0.968 ± 0.109	0.449 ± 0.102	0.443 ± 0.144	1.906	1.915 ± 0.006	2.454 ± 0.798	1.84	18	249
(4055) Magellan	smassneo8	spex38	V (Di)	0.924	0.927 ± 0.004	0.243 ± 0.006	0.525 ± 0.005	1.906	1.915 ± 0.006	2.021 ± 0.027	1.84	18	249
(4188) Kitezh	smass2	sunshine04	V (How/Eu)	0.936	0.939 ± 0.001	0.589 ± 0.004	0.417 ± 0.001	1.960	1.968 ± 0.006	1.821 ± 0.016	2.10	11	254
(4215) Kamo	smass1	moskovitz	V (How)	0.970	0.975 ± 0.120	0.430 ± 0.173	0.351 ± 0.128	1.907	1.921 ± 0.048	2.057 ± 0.755	2.52	17	213
(4215) Kamo	smass2	moskovitz	V (How)	0.951	0.956 ± 0.094	0.406 ± 0.121	0.380 ± 0.102	1.906	1.921 ± 0.048	1.831 ± 0.498	2.52	17	213
(4215) Kamo	smass1	moskovitz	V (How)	0.925	0.930 ± 0.005	0.304 ± 0.004	0.362 ± 0.005	1.972	1.986 ± 0.011	1.769 ± 0.038	2.51	3.2	214
(4215) Kamo	smass2	moskovitz	V (How)	0.925	0.929 ± 0.001	0.256 ± 0.003	0.373 ± 0.001	1.971	1.986 ± 0.012	1.663 ± 0.031	2.51	3.2	214
(4215) Kamo	smass1	moskovitz	V (How)	0.931	0.935 ± 0.001	0.372 ± 0.005	0.392 ± 0.002	1.936	1.949 ± 0.009	1.949 ± 0.045	2.29	10	224
(4215) Kamo	smass2	moskovitz	V (How)	0.930	0.934 ± 0.001	0.327 ± 0.004	0.401 ± 0.001	1.936	1.949 ± 0.010	1.848 ± 0.042	2.29	10	224
(4215) Kamo	smass1	moskovitz	V (How)	0.924	0.929 ± 0.001	0.570 ± 0.007	0.408 ± 0.002	1.947	1.962 ± 0.014	1.461 ± 0.082	2.55	7.9	212
(4215) Kamo	smass2	moskovitz	V (How)	0.925	0.930 ± 0.001	0.529 ± 0.007	0.418 ± 0.002	1.947	1.962 ± 0.014	1.395 ± 0.080	2.55	7.9	212
(4796) Lewis	smass2	moskovitz10	V (How)	0.934	0.938 ± 0.001	0.543 ± 0.006	0.486 ± 0.003	1.935	1.948 ± 0.026	1.993 ± 0.056	2.46	14	226
(5111) Jacliff	smass2	moskovitz10	V (How)	0.933	0.936 ± 0.054	0.464 ± 0.015	0.374 ± 0.055	1.954	1.963 ± 0.002	1.923 ± 0.282	2.06	7.3	245
(5235) Jean-Loup	—	hardersen14	V (Di)	0.931	0.935 ± 0.001	0.580 ± 0.001	0.486 ± 0.001	1.900	1.913 ± 0.001	1.920 ± 0.001	2.59	10	219
(5481) Kiuchi	s3os2	moskovitz10	V (How)	0.929	0.933 ± 0.002	0.734 ± 0.008	0.481 ± 0.002	1.953	1.964 ± 0.021	1.815 ± 0.057	2.37	11	230
(5498) Gustafsson	moskovitz	moskovitz10	V (Eu)	0.940	0.941 ± 0.001	0.817 ± 0.002	0.445 ± 0.001	1.958	1.962 ± 0.003	1.874 ± 0.007	1.92	7.8	276
(5604) 1992 FE	smassneo8	spex05	V (Di)	0.955	0.955 ± 0.102	0.226 ± 0.059	0.444 ± 0.131	1.937	1.937 ± 0.015	2.151 ± 0.634	1.26	30	297
(5604) 1992 FE	smassneo8	spex80	V (Di)	0.925	0.925 ± 0.002	0.391 ± 0.015	0.527 ± 0.005	1.895	1.896 ± 0.010	1.680 ± 0.085	1.29	37	294
(6611) 1993 VW	smassneo	spex40	V (How/Eu)	0.934	0.932 ± 0.001	0.173 ± 0.003	0.452 ± 0.001	1.982	1.977 ± 0.003	1.514 ± 0.007	1.15	27	330
(7889) 1994 LX	smassneo8	spex71	V (How/Di)	0.934	0.938 ± 0.003	0.232 ± 0.016	0.569 ± 0.003	1.913	1.922 ± 0.008	1.723 ± 0.046	1.65	25	241
(7889) 1994 LX	smassneo8	spex72	V (How/Di)	0.933	0.936 ± 0.003	0.104 ± 0.015	0.589 ± 0.003	1.912	1.922 ± 0.010	1.655 ± 0.050	1.69	22	238
(9147) Kourakuen	—	hardersen15	V (How)	0.937	0.940 ± 0.001	0.738 ± 0.010	0.411 ± 0.001	1.918	1.926 ± 0.001	2.189 ± 0.003	2.08	3.8	255
(9481) Menchu	moskovitz	moskovitz10	V (How/Di)	0.944	0.947 ± 0.001	0.285 ± 0.006	0.431 ± 0.002	1.905	1.915 ± 0.018	2.135 ± 0.080	2.48	6.2	243
(9553) Colas	—	hardersen15	V (Di)	0.927	0.929 ± 0.001	1.509 ± 0.001	0.450 ± 0.001	1.910	1.917 ± 0.001	2.875 ± 0.001	2.11	12	256
(9553) Colas	moskovitz	moskovitz10	V (Di)	0.934	0.936 ± 0.001	0.668 ± 0.003	0.511 ± 0.001	1.903	1.909 ± 0.004	2.141 ± 0.015	1.99	20	263
(15237) 1988 RL_6	—	hardersen15	V (Di)	0.924	0.927 ± 0.001	0.965 ± 0.001	0.393 ± 0.001	1.910	1.920 ± 0.001	2.410 ± 0.001	2.05	15	242
(15237) 1988 RL_6	—	hardersen15	V (How/Di)	0.925	0.928 ± 0.001	1.117 ± 0.001	0.383 ± 0.001	1.917	1.927 ± 0.001	2.586 ± 0.001	2.05	15	242
(17469) 1991 BT	—	hardersen14	V (Di)	0.927	0.931 ± 0.001	0.682 ± 0.001	0.515 ± 0.001	1.892	1.902 ± 0.001	2.270 ± 0.001	2.23	17	237
(26886) 1994 TJ_2	moskovitz	moskovitz10	V (Di)	0.938	0.940 ± 0.078	0.703 ± 0.050	0.487 ± 0.105	1.900	1.907 ± 0.013	2.544 ± 0.553	2.09	10	261
(27343) Deannashea	—	moskovitz10	V (How/Di)	0.924	0.926 ± 0.001	0.731 ± 0.018	0.554 ± 0.003	1.915	1.922 ± 0.005	2.031 ± 0.039	1.94	12	262

Table 3.12 — continued

Object	Vis[a]	NIR[a]	tax[b] (met[c])	B_IC[d]	B_IC_{corr}[d,e]	B_IS[f]	B_ID[g]	$B_{II}C$[d]	$B_{II}C_{corr}$[d,h]	BAR	R_{AU}[i]	$\alpha(^\circ)$[j]	T_c[k]
(29796) 1999 CW_{77}	—	hardersen14	V (Di)	0.932	0.936 ± 0.001	0.830 ± 0.001	0.506 ± 0.001	1.895	1.905 ± 0.001	2.335 ± 0.001	2.21	11	240
(30872) 1992 EM_{17}	—	hardersen14	V (Di)	0.936	0.940 ± 0.001	0.555 ± 0.001	0.359 ± 0.001	1.889	1.900 ± 0.001	1.869 ± 0.001	2.34	0.9	231
(31414) Rotarysusa	—	hardersen15	V (Di)	0.927	0.930 ± 0.001	0.838 ± 0.001	0.459 ± 0.001	1.897	1.905 ± 0.001	2.291 ± 0.001	1.96	0.2	254
(32940) 1995 UW_4	—	hardersen15	V (Di)	0.928	0.931 ± 0.001	1.290 ± 0.001	0.476 ± 0.001	1.892	1.901 ± 0.005	2.582 ± 0.001	1.89	10	247
(33881) 2000 JK_{66}	—	moskovitz10	V (Di)	0.934	0.935 ± 0.001	0.687 ± 0.015	0.534 ± 0.002	1.902	1.904 ± 0.005	1.970 ± 0.030	1.77	23	281
(36412) 2000 OP_{49}	—	moskovitz10	V (Eu)	0.947	0.950 ± 0.004	0.769 ± 0.056	0.475 ± 0.008	1.958	1.969 ± 0.014	2.024 ± 0.087	2.12	12	237
(38070) Redwine	moskovitz	moskovitz10	V (Eu)	0.941	0.943 ± 0.001	0.353 ± 0.006	0.412 ± 0.002	1.980	1.988 ± 0.014	1.800 ± 0.066	1.90	4.1	251
(68548) 2001 XR_{31}	—	spex204	V (How)	0.936	0.935 ± 0.020	0.347 ± 0.036	0.445 ± 0.024	1.965	1.964 ± 0.048	2.377 ± 0.183	1.22	1.9	305
(97276) 1999 XC_{143}	—	moskovitz10	V (Eu)	0.946	0.949 ± 0.002	0.270 ± 0.017	0.365 ± 0.004	1.996	2.005 ± 0.014	1.831 ± 0.065	2.05	2.4	247
(450894) 2008 BT18	—	reddy	V (Di)	0.928	0.926 ± 0.001	1.235 ± 0.013	0.614 ± 0.001	1.917	1.911 ± 0.010	1.968 ± 0.071	1.09	34	339

Notes. [a] Visible or near-infrared spectrum source.

[b] Bus-DeMeo taxonomic classification.

[c] Meteorite analog (How/Eu/Di), based on B_IC_{corr} and $B_{II}C_{corr}$.

[d] Band center wavelengths, given in μm.

[e] B_IC, corrected for temperature.

[f] Band slope, given in μm^{-1}.

[g] Band depth, given in %.

[h] $B_{II}C$, corrected for temperature.

[i] Heliocentric distance of observation in AU.

[j] Solar phase angle of observation in degrees.

[k] Estimated color temperature (K) at the time of observation.

Table 3.13: Band Parameters of S(I) Asteroids

Object	Vis[a]	NIR[a]	tax[b]	BIC[c]	ΔBIC[d]	BIC_{corr}[e]	BIS[f]	BID[g]	BAR	R_{AU}[h]	$\alpha(^\circ)$[i]	T_c[j]
Exhibits B_{II}												
(39) Laetitia	smass2	spex92	Sq	1.046	0.002	1.048 ± 0.005	0.255 ± 0.002	0.156 ± 0.001	0.386 ± 0.029	2.49	22	250
(39) Laetitia	smass1	spex92		1.051	0.002	1.052 ± 0.004	0.298 ± 0.002	0.142 ± 0.001	0.444 ± 0.033	2.49	22	250
(89) Julia	smass2	clark09	K	1.050	0.002	1.051 ± 0.004	0.235 ± 0.001	0.103 ± 0.001	0.209 ± 0.015	2.17	16	260
(89) Julia	s3os2	clark09		1.055	0.002	1.057 ± 0.004	0.277 ± 0.001	0.088 ± 0.001	0.260 ± 0.018	2.17	16	260
(113) Amalthea	smass2	spex87	Qw	1.044	0.002	1.047 ± 0.003	0.252 ± 0.003	0.302 ± 0.002	0.178 ± 0.027	2.27	15	247
(186) Celuta	smass2	clark09	K	1.049	0.002	1.051 ± 0.003	0.185 ± 0.002	0.107 ± 0.001	0.164 ± 0.029	2.71	17	242
(186) Celuta	smass1	clark09		1.046	0.002	1.048 ± 0.003	0.243 ± 0.002	0.087 ± 0.001	0.216 ± 0.037	2.71	17	242
(245) Vera	smass2	spex75	S	1.052	0.002	1.054 ± 0.004	0.160 ± 0.002	0.159 ± 0.001	0.375 ± 0.031	2.61	21	237
(245) Vera	smass1	spex75		1.053	0.002	1.055 ± 0.004	0.180 ± 0.002	0.152 ± 0.001	0.415 ± 0.034	2.61	21	237
(403) Cyane	smass2	spex93	S	1.038	0.003	1.041 ± 0.006	0.288 ± 0.001	0.152 ± 0.001	0.375 ± 0.027	2.88	18	233
(403) Cyane	s3os2	spex93		1.045	0.003	1.048 ± 0.003	0.336 ± 0.001	0.138 ± 0.001	0.438 ± 0.031	2.88	18	233
(446) Aeternitas	smass2	sunshine07	A	1.060	0.003	1.063 ± 0.001	0.606 ± 0.001	0.399 ± 0.001	0.063 ± 0.002	2.71	10	225
(446) Aeternitas	smass1	sunshine07		1.060	0.003	1.063 ± 0.001	0.639 ± 0.001	0.393 ± 0.001	0.064 ± 0.002	2.71	10	225
(562) Salome	—	EMMspex	K	1.074	0.003	1.077 ± 0.004	0.053 ± 0.002	0.061 ± 0.001	0.624 ± 0.148	3.27	12	205
(651) Antikleia	—	EMMspex	L	1.058	0.003	1.061 ± 0.001	0.143 ± 0.003	0.065 ± 0.001	0.980 ± 0.050	3.31	8.6	204
(661) Cloelia	smass2	clark2	K	1.056	0.003	1.059 ± 0.003	0.027 ± 0.001	0.062 ± 0.001	0.202 ± 0.042	2.93	8.3	227
(742) Edisona	smass2	clark2	K	1.053	0.003	1.056 ± 0.006	-0.018 ± 0.002	0.087 ± 0.002	0.385 ± 0.045	3.22	14	219
(863) Benkoela	smass2	spex76	A	1.051	0.004	1.055 ± 0.001	0.885 ± 0.002	0.380 ± 0.001	0.113 ± 0.011	3.16	18	185
(863) Benkoela	smass1	spex76		1.052	0.004	1.055 ± 0.001	0.973 ± 0.002	0.368 ± 0.001	0.121 ± 0.011	3.16	18	185
(863) Benkoela	smass2	sunshine07	A	1.055	0.004	1.059 ± 0.001	0.704 ± 0.001	0.380 ± 0.001	0.092 ± 0.003	3.18	7.6	184
(863) Benkoela	smass1	sunshine07		1.055	0.004	1.059 ± 0.001	0.840 ± 0.001	0.359 ± 0.001	0.100 ± 0.003	3.18	7.6	184
(876) Scott	—	EMMspex	L	1.066	0.003	1.069 ± 0.009	-0.022 ± 0.003	0.080 ± 0.002	-0.157 ± 0.132	3.03	19	228
(984) Gretia	smass2	spex92	Qw	1.049	0.003	1.053 ± 0.006	0.231 ± 0.005	0.358 ± 0.003	0.085 ± 0.047	3.17	18	204
(984) Gretia	smass2	sunshine07	Sa	1.046	0.003	1.048 ± 0.001	0.320 ± 0.001	0.316 ± 0.001	0.125 ± 0.002	2.51	9.6	229
(1536) Pielinen	—	EMMspex	Sq	1.037	0.003	1.039 ± 0.010	0.382 ± 0.009	0.136 ± 0.003	0.591 ± 0.094	2.48	7.5	230
(1723) Klemola	—	EMMspex	K	1.044	0.003	1.047 ± 0.006	0.320 ± 0.008	0.126 ± 0.003	0.099 ± 0.033	3.10	4.0	211
(1903) Adzhimushkaj	smass2	clark09	L	1.052	0.002	1.055 ± 0.004	0.001 ± 0.001	0.065 ± 0.001	0.405 ± 0.040	2.86	6.8	242
(1951) Lick	smass2	spex72	A	1.069	-0.002	1.068 ± 0.002	0.781 ± 0.003	0.438 ± 0.001	-0.024 ± 0.010	1.31	42	330
(2110) Moore-Sitterly	—	EMMspex	Sq	1.044	0.003	1.047 ± 0.006	0.320 ± 0.008	0.126 ± 0.003	0.559 ± 0.089	2.57	2.5	230
(2111) Tselina	—	EMMspex	L	1.096	0.003	1.099 ± 0.021	0.070 ± 0.003	0.054 ± 0.001	1.041 ± 0.118	3.16	16	206
(2501) Lohja	smass2	sunshine04	A	1.055	0.003	1.058 ± 0.001	0.749 ± 0.002	0.424 ± 0.001	0.036 ± 0.011	2.88	5.9	214
(3819) Robinson	smass2	spex84	Sa	1.057	0.003	1.059 ± 0.003	0.423 ± 0.003	0.395 ± 0.002	0.048 ± 0.018	2.41	4.9	233
(3819) Robinson	smass2	spex85	Sa	1.060	0.003	1.062 ± 0.002	0.344 ± 0.002	0.379 ± 0.001	0.111 ± 0.013	2.40	6.8	234
(3819) Robinson	smass2	sunshine07	Qw	1.056	0.003	1.059 ± 0.002	0.357 ± 0.002	0.391 ± 0.001	0.111 ± 0.013	2.63	12	223
(5131) 1990 BG	smassneo8	spex67	Q	1.020	0.001	1.022 ± 0.011	0.289 ± 0.010	0.239 ± 0.004	0.217 ± 0.032	1.90	14	267
(5131) 1990 BG	smassneo8	spex87	Q	1.040	-0.001	1.040 ± 0.003	0.401 ± 0.010	0.268 ± 0.003	0.187 ± 0.033	1.42	23	309
(5660) 1974 MA	smassneo	spex43		1.056	-0.001	1.055 ± 0.011	0.057 ± 0.004	0.267 ± 0.003	0.253 ± 0.035	1.32	37	320
(85989) 1999 JD_6	smassneo	spex92		1.077	-0.002	1.075 ± 0.013	0.081 ± 0.003	0.054 ± 0.002	0.611 ± 0.167	1.19	32	340

Table 3.13 — continued

Object	Vis[a]	NIR[a]	tax[b]	B_IC[c]	ΔB_IC[d]	B_IC_{corr}[e]	B_IS[f]	B_ID[g]	BAR	R_{AU}[h]	$\alpha(^\circ)$[i]	T_c[j]
No B_{II}												
(9) Metis	sawyer	smassir		1.082	0.002	1.084 ± 0.004	0.403 ± 0.002	0.101 ± 0.001	—	2.51	19	243
(9) Metis	s3os2	smassir		1.082	0.002	1.084 ± 0.003	0.405 ± 0.002	0.101 ± 0.001	—	2.51	19	243
(9) Metis	s3os2	spex75	K	1.084	0.001	1.086 ± 0.021	0.208 ± 0.004	0.091 ± 0.002	—	2.14	3.6	264
(9) Metis	sawyer	spex75	K	1.088	0.001	1.090 ± 0.034	0.228 ± 0.005	0.082 ± 0.003	—	2.14	3.6	264
(236) Honoria	smass2	smassir		1.279	0.003	1.281 ± 0.163	0.278 ± 0.045	0.098 ± 0.030	—	2.95	17	223
(236) Honoria	smass2	spex50	L	1.047	0.003	1.050 ± 0.002	0.220 ± 0.001	0.047 ± 0.001	—	3.20	3.4	214
(246) Asporina	smass2	smassir	A	1.100	0.003	1.103 ± 0.003	0.433 ± 0.002	0.308 ± 0.001	—	2.68	10	227
(246) Asporina	s3os2	smassir	A	1.106	0.003	1.109 ± 0.001	0.566 ± 0.003	0.279 ± 0.001	—	2.68	10	227
(246) Asporina	smass2	spex37	A	1.062	0.002	1.064 ± 0.001	0.428 ± 0.001	0.317 ± 0.001	—	2.43	10	238
(246) Asporina	s3os2	spex37	A	1.065	0.002	1.067 ± 0.001	0.577 ± 0.001	0.282 ± 0.001	—	2.43	10	238
(246) Asporina	smass2	sunshine07	A	1.065	0.002	1.067 ± 0.001	0.503 ± 0.001	0.295 ± 0.001	—	2.43	18	238
(246) Asporina	s3os2	sunshine07	A	1.066	0.002	1.068 ± 0.001	0.591 ± 0.001	0.276 ± 0.001	—	2.43	18	238
(289) Nenetta	smass2	sunshine07	A	1.070	0.002	1.072 ± 0.001	0.893 ± 0.001	0.484 ± 0.001	—	2.38	24	240
(289) Nenetta	smass1	sunshine07	A	1.071	0.002	1.073 ± 0.001	1.038 ± 0.002	0.467 ± 0.001	—	2.38	24	240
(354) Eleonora	smass2	dm02	A	1.060	0.003	1.063 ± 0.001	0.382 ± 0.002	0.271 ± 0.001	—	2.89	20	223
(354) Eleonora	s3os2	dm02	A	1.061	0.003	1.064 ± 0.001	0.435 ± 0.002	0.257 ± 0.001	—	2.89	20	223
(354) Eleonora	smass1	dm02	A	1.061	0.003	1.064 ± 0.001	0.437 ± 0.002	0.257 ± 0.001	—	2.89	20	223
(354) Eleonora	smass2	sunshine07	A	1.058	0.003	1.061 ± 0.001	0.609 ± 0.001	0.259 ± 0.001	—	2.91	20	222
(354) Eleonora	s3os2	sunshine07	A	1.060	0.003	1.063 ± 0.001	0.687 ± 0.001	0.243 ± 0.001	—	2.91	20	222
(354) Eleonora	smass1	sunshine07	A	1.059	0.003	1.062 ± 0.001	0.697 ± 0.001	0.241 ± 0.001	—	2.91	20	222
(1291) Phryne	—	EMMspex	L	1.108	0.003	1.111 ± 0.017	0.002 ± 0.003	0.053 ± 0.001	—	2.82	17	219
(1299) Mertona	—	EMMSpex	Sq	1.041	0.003	1.045 ± 0.002	0.158 ± 0.012	0.204 ± 0.004	—	3.08	11	209
(3199) Nefertiti	smassneo8	spex03		1.051	0.001	1.053 ± 0.004	0.174 ± 0.003	0.198 ± 0.002	—	1.61	25	266
(3199) Nefertiti	smassneo8	spex36	K	1.054	0.002	1.056 ± 0.005	0.190 ± 0.003	0.182 ± 0.002	—	1.78	3.5	253
(5261) Eureka	smass2	spex41	Sa	1.067	0.001	1.066 ± 0.005	0.223 ± 0.003	0.286 ± 0.002	—	1.54	4.9	302

Notes. [a] Visible or near-infrared spectrum source.

[b] Bus-DeMeo taxonomic classification.

[c] Band I center wavelength, given in μm.

[d] B_IC temperature correction factor.

[e] B_IC, corrected for temperature.

[f] Band I slope, given in μm^{-1}.

[g] Band I depth, given in %.

[h] Heliocentric distance of observation in AU.

[i] Solar phase angle of observation in degrees.

[j] Estimated color temperature (K) at the time of observation.

tables are the taxonomic classification of each spectrum and the assigned meteorite analog, if appropriate (see section 3.5.2 for further explanation). I do not explicitly list a meteorite analog for S(I) asteroids, but separate them into two groups based on the existence of B_{II} (those exhibiting B_{II} are likely associated with R chondrites; section 3.5.2). Also listed in the tables are the heliocentric distance ($R_{\rm AU}$), solar phase angle (α), and estimated color temperature (T_c) of the surface at the time of each spectral observation. As discussed in section 3.5.1, some band parameters are corrected for observing geometry or surface temperature. These corrected band parameters assure a more accurate comparison to spectra taken within laboratory setting and adjust for dependencies on observing circumstances, such as the solar phase angle.

3.5.1 Band Parameter Corrections

A handful of band parameters have been observed by previous works to vary based on non-compositional effects such as the observing geometry (i.e., solar phase angle) and surface temperature (next paragraph). The effect known as phase reddening, describing the increase in spectral slope with phase angle, has been shown to be insignifiant for observations for which $\alpha \lesssim 30°$. But, spectral slope corrections should be applied when an asteroid is observed at larger values. Spectral slope reddening has been studied for the compositional subgroups in this work: howardites, eucrites, and diogenites by Reddy et al. (2012), ordinary chondrites by Sanchez et al. (2012), and olivine-rich meteorites by Sanchez et al. (2014). While Sanchez et al. (2012) did not formally develop a formula for correcting spectral slope, I found that ordinary chondrite spectral slopes linearly increased for phase angles 50–90° and developed the following correction formula for $\alpha > 50°$ based on the data presented in that work: $BIS_{corr} = BIS - 0.005(\alpha - 50)$. The band depth of ordinary chondrite meteorites and S(IV) asteroids is also affected by the phase angle of observations. Using ordinary chondrite spectra Sanchez et al. (2012) found that band depths increase at a rate of 0.066%/degree, but using my asteroid band parameters I find a slightly different slope and instead use the following formula: $BID_{corr} = BID - 0.088 \times \alpha$. Other band parameters, such as both band centers and BAR have not been known to vary with phase angle for ordinary chondrites, but Reddy

et al. (2012) did find that the BAR of Vestian surface regolith was phase angle dependent and derived the following correction formula: $BAR_{corr} = BAR + 0.0292 \times \alpha$.

Both B_IC and $B_{II}C$ must be corrected for temperature effects in the HEDs and only B_IC must be corrected for the ordinary chondrite and olivine-rich meteorites. Sanchez et al. (2014) found an inverse temperature correlation also affects the BAR among ordinary chondrites, and Reddy et al. (2015) derived a temperature correction for B_ID using spectra from Hinrichs and Lucey (2002). These correction formulae are used here, unless otherwise noted, and can be found in Table 1 of Reddy et al. (2015).

Approximations for surface temperature are made here assuming that most of the observed reflected light originates from the hotter parts of the body (i.e., near the sub-solar point). I calculate the temperature by simply using the NEATM model's equilibrium temperature equation (1.1) and then using the empirically-derived relationship between it and the color temperature of the surface from section 2.5.2: $T_{ss} = 0.777 \times T_c^{1.063 \pm 0.005}$.

3.5.2 Mineralogy from Band Parameters

Since the pioneering work of Gaffey et al. (2002), much progress has been made in deriving modal mineralogies (relative mineral abundance) and mineral chemistry (e.g., Fo#) using estimates of the BAR and the locations of band centers. Mineral calibration formulas have been derived for each of the three compositional groups featured here. Using a suite of HED reflectance spectra, Burbine et al. (2007) developed equations that relate the band centers to the iron and calcium content in pyroxenes (Fs# and Wo#, respectively). The Dunn et al. (2010a) calibration equations for ordinary chondrites can be used to derive the iron content in olivine, Fa#, and pyroxene, Fs#, using band centers along with the relative abundance of olivine and pyroxene from the BAR. Reddy et al. (2011) improved upon the calibration begun by Sunshine and Pieters (1999) in an attempt to estimate the Fa# of the olivine in olivine-rich asteroids. Moving forward, I use these equations with caution, as further explained below.

Ordinary Chondrites

Building off other works (e.g., Cloutis et al., 1986; Burbine et al., 2003), Dunn et al. (2010a) developed equations that relate olivine and pyroxene mineral chemistry to spectral parameters of equilibrated ordinary chondrites. From using these equations, the Fa# and Fs# can be estimated from the B_IC and the relative olivine to pyroxene abundance can be estimated from the BAR. Unequilibrated ordinary chondrites represent the most pristine ordinary chondrite type, since the mineral chemistry of the chondrules has not thermodynamically equilibrated with the matrix the olivine and pyroxene distribution is not heterogeneous within the meteorite (Dodd et al., 1967); with increasing heat metamorphism, metallic Fe is transferred to silicate FeO, depending on the oxidation conditions (highest in LL and lowest in H; Rubin and Ma, 2017). These unequlibrated ordinary chchondrites (UOCs) thus have similar mineralogies and cannot be distinguished between one another as H, L, or LL but should be somewhat distinguishable using band parameters from the equilibrated ordinary chondrites (EOCs). Gietzen et al. (2012) utilize several techniques to relate an S-type spectrum to an unequilibrated ordinary chondrites, but leave some subjectivity in the process; they do remark that the UOC band parameters do plot in the S(IV) region defined by Gaffey et al. (1993), along with the EOCs.

Armed with the knowledge of past work, I utilize my vast dataset of band parameters in order to estimate the sub-type and petrologic type classification for my set of asteroids. I develop boundaries in band parameter space between compositional and petrologic types to distinguish between H, L, and LL-like asteroids. I find that using a cutoff of $BAR = 0.69$ to distinguish between the L and H chondrites and $B_IC = 0.95$ μm to distinguish the LL from the L chondrites. As seen in the right panel of figure 3.16, most of the unequilibrated (type < 4) ordinary chondrites overlap with the L chondrites. I thus take note that asteroids falling within the L subtype region defined here could actually be low petrologic types of any sub-group.

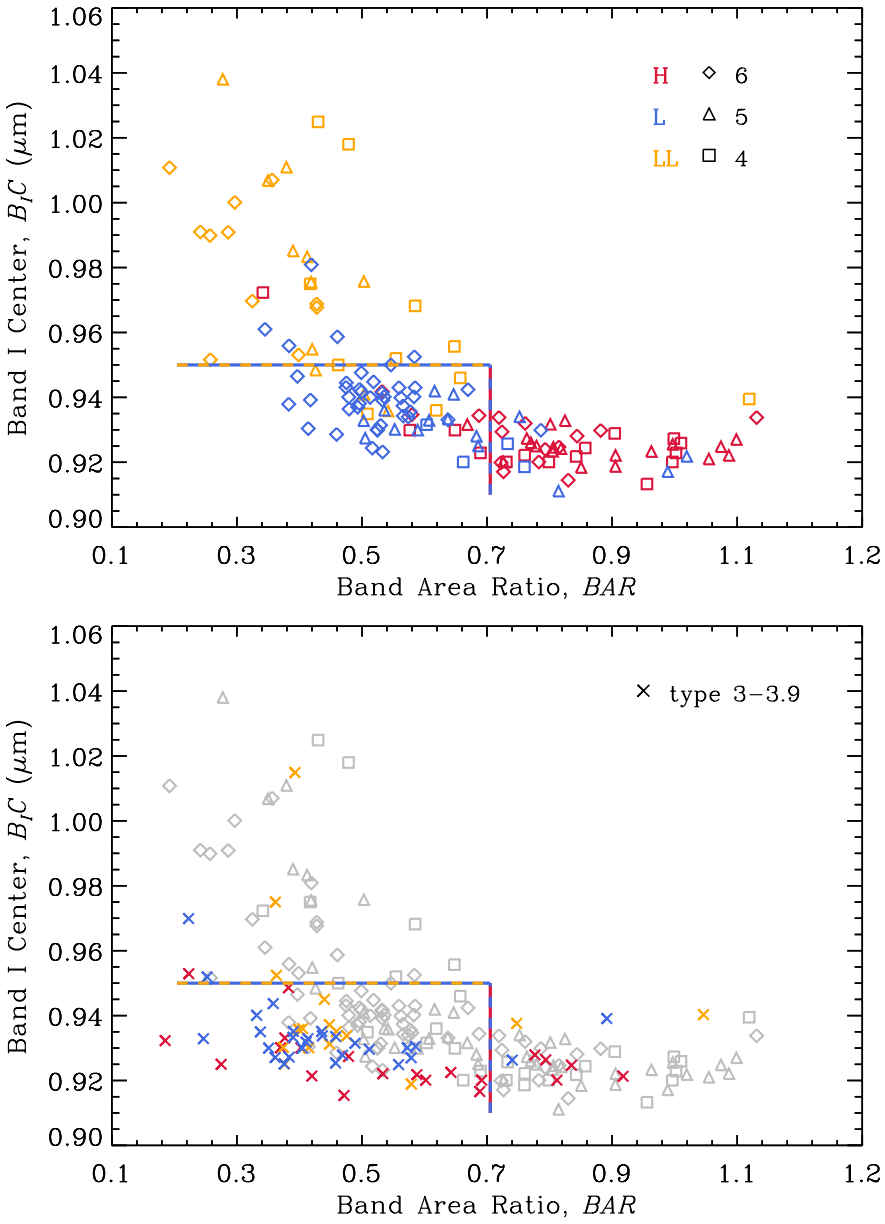

Figure 3.16: Equilibrated (*top*) and unequilibrated (*bottom*) ordinary chondrite BAR and B_IC values, grouped by sub-type. The vertical and horizontal lines show the cutoff values used to classify asteroids into their meteorite analog sub-type.

HEDs

As briefly noted in section 3.4.2, HED's often contain mulitple pyroxene species within a single meteorite sample (e.g., augite and enstatite; Burbine et al., 2001, 2018). The slow cooling process within a body of magma typically results in the crystallization and subsequent mixing of various mineral species. Additionally, the mineral chemistry of just a single pyroxene can vary freely between three oxide abundances (i.e., the FeO, MgO and CaO content; Klima et al., 2007, 2008, 2011). These two facts are indicative of how difficult it is to estimate, with substantial accuracy, the pyroxene chemistry of an asteroid from spectroscopic band parameters. However, directly comparing compositionally diagnostic band parameters — those unaffected by space weathering — of meteorite lab spectra with those from asteroid spectra provides a straightforward means of establishing a linkage. For example, both B_I and B_{II} band center measurements of HED meteorites have provided a useful means of discerning among the HEDs (Moskovitz et al., 2010). Eucrites show longer-wavelength absorptions (in both B_IC and $B_{II}C$) than diogenites (Burbine et al., 2001), with howardite band parameters positioned somewhere between.

Since characterization of a single pyroxene mineralogy for band parameters is very difficult, I take a conservative approach by classifying the BA asteroids into howardite, eucrite, and diogenite types. The top panel of figure 3.17 shows the B_IC and $B_{II}C$ for my sample of HED spectra, and my cutoff criteria for distinguishing between the three classes. Since a few polymict eucrite meteorites exist in the howardite region, I carefully classify those asteroids that fall within this cluster of meteorite points. Otherwise, in these cases of ambiguity, I classify samples that either do not neatly fall (i.e., if the 1σ error overlaps with another region) within each region or if the point falls within a cluster of points that contains a near 50/50 mix of two meteorite groups I ambiguously classify the asteroid as belonging to both groups.

Olivine-rich

Both B_I and B_{II} are apparent in R chondrite spectra, because olivine and pyroxene are both represented in their chondrules (Bischoff et al., 2011). Brachinites and pallasites, which

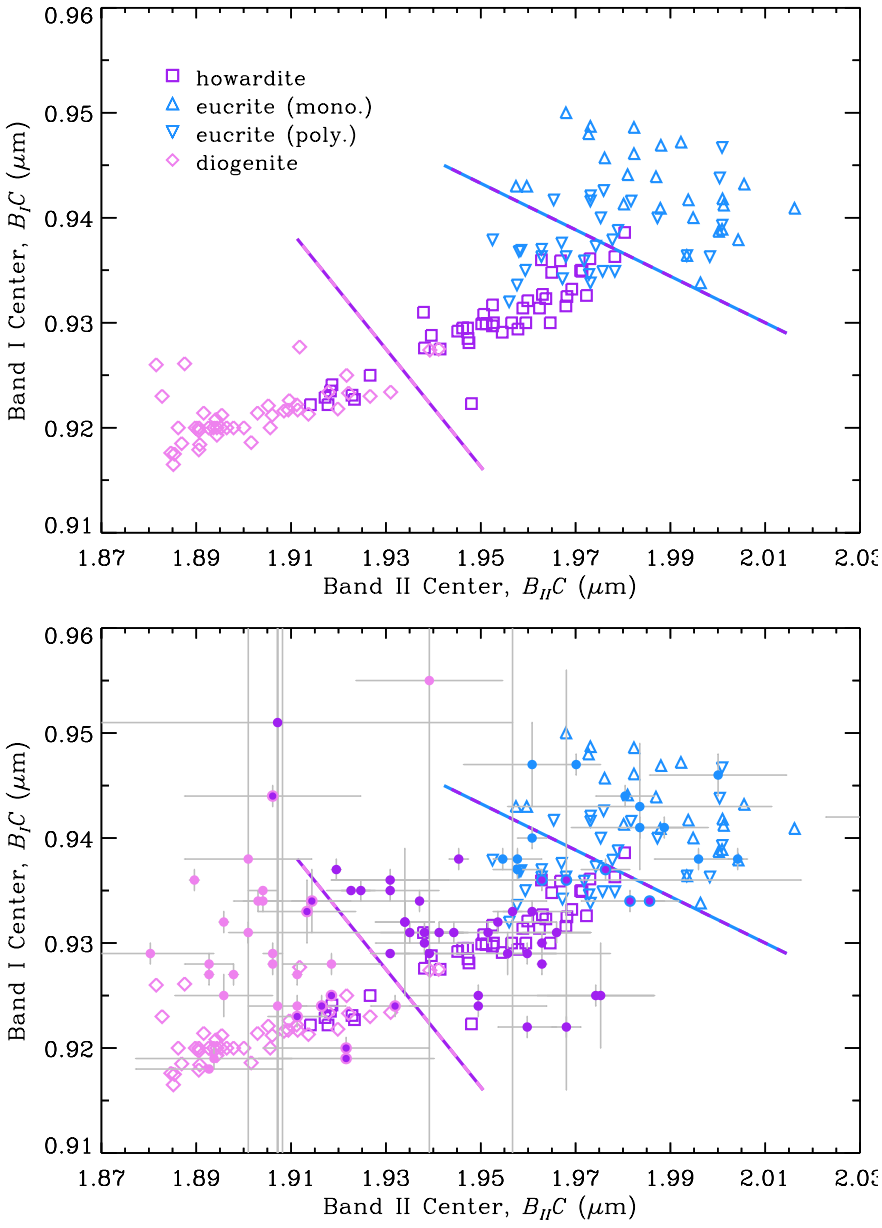

Figure 3.17: HED $B_{II}C$ and B_IC values and regions used to classify asteroid band parameters. The top panel shows only HED band centers, and the bottom panel depicts asteroid points (filled symbols) colored by the assigned meteorite analog. The multi-colored dashed lines separate the meteorite classification regions.

represent (respectively) partially and fully melted solar system material, only exhibit a B_I absorption due to a lack of substantial pyroxene. Therefore, following Sanchez et al. (2014) and Cloutis et al. (2015), I use the presence/absence of B_{II} to distinguish among asteroid spectra. Thus, if the asteroid spectrum exhibits a 2 μm feature, I associate it with the R chondrites, otherwise I relate it to either the brachinites, pallasites, or CK chondrites. The CK chondrites exhibit a characteristic rounded reflectance peak near 0.7 μm that contrasts with the sharp B_I blue edge of pallasite and brachinite meteorite spectra (Mothé-Diniz et al., 2008). So, along with having no discernable B_{II}, I identify CK chondrites as the meteorite analog for asteroid spectra with this rounded feature. Calibration tools, especially those developed by Sunshine et al. (2007) and Sanchez et al. (2014), exploit the relationship between the 1 μm band center and iron content of terrestrial olivines in order to estimate such mineralogic characteristics from an asteroid spectrum. Following this approach, the meteorite 1 μm band center and olivine chemistry are analyzed in order to search for an apparent relationship yet I find no such relationship exists across all the meteorite groups. The presence of chromite in brachinites and pallasites acts to alter the B_IC (Cloutis et al., 2015), thus complicating attempts to derive the olivine chemistry. Thus, I refrain from using the calibration equations from Sanchez et al. (2014) to estimate, e.g., FeO content in olivine.

3.6 Analysis: Space Weathering Index

I apply the matrix transformation equation (equation (3.1)) to S(I) and S(IV) asteroids to compute SWI and BDI for each individual asteroid spectrum. Standard errors from B_IS and B_ID are propagated through my calculations and reported for both parameters. For each object with more than one spectrum, I compute the averages of the calculated SWI and BDI values and report just a single value and update the 1σ error based on the dispersion between points. Figure 3.18 shows these indices calculated for S(I) and S(IV) asteroids.

Instead of estimating the individual degree of space weathering for each of the BA asteroids in my sample, I compare the mean space weathering band parameters to that computed for the HEDs. Unlike the OC and olivine-rich meteorites, the HEDs show a large spread in both B_IS and B_ID parameters that make it difficult to establish a well-constrained

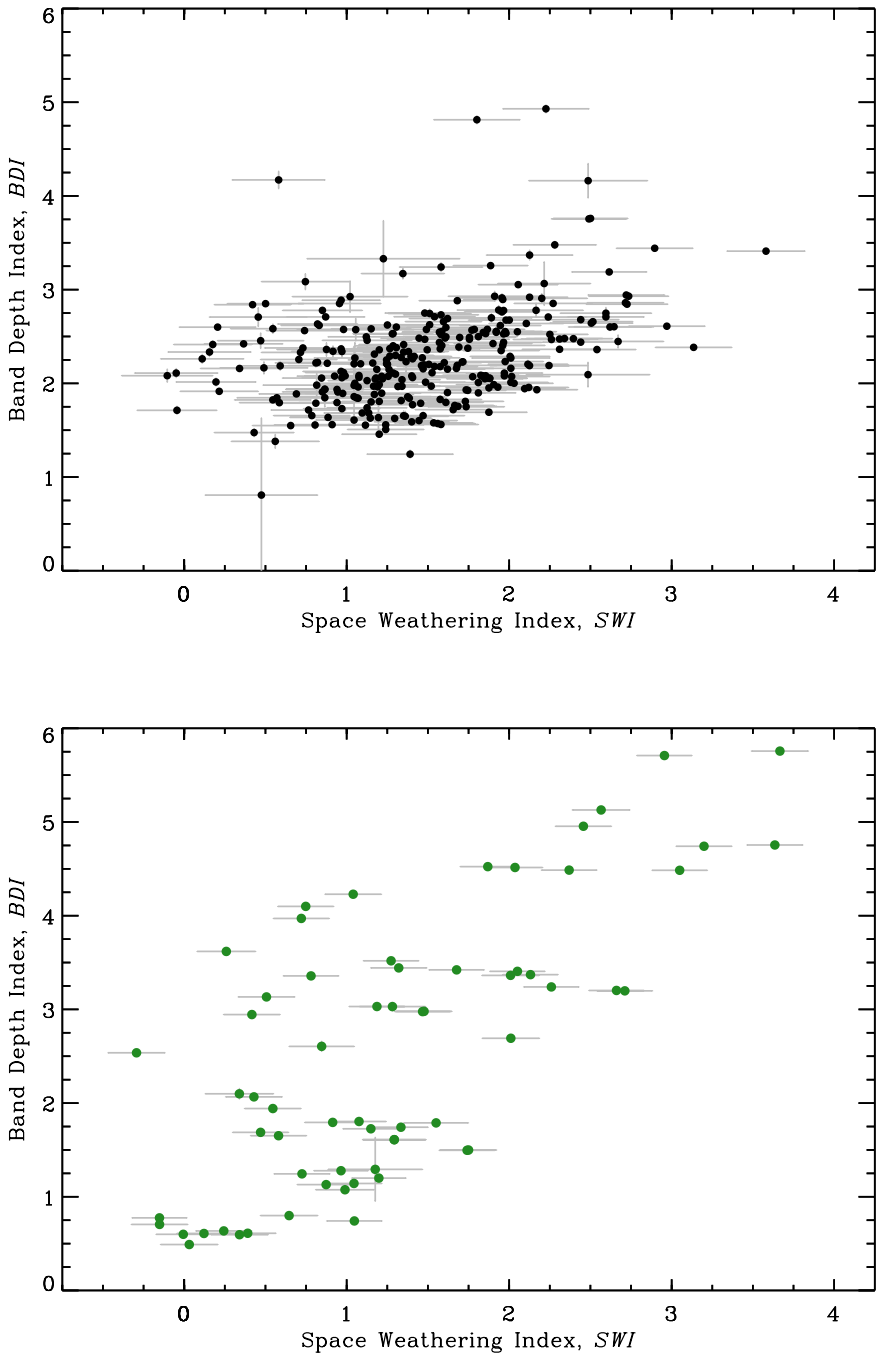

Figure 3.18: Space weathering band parameters transformed into *SWI* and *BDI* for S(IV) and S(I) asteroids in the top and bottom panels, respectively.

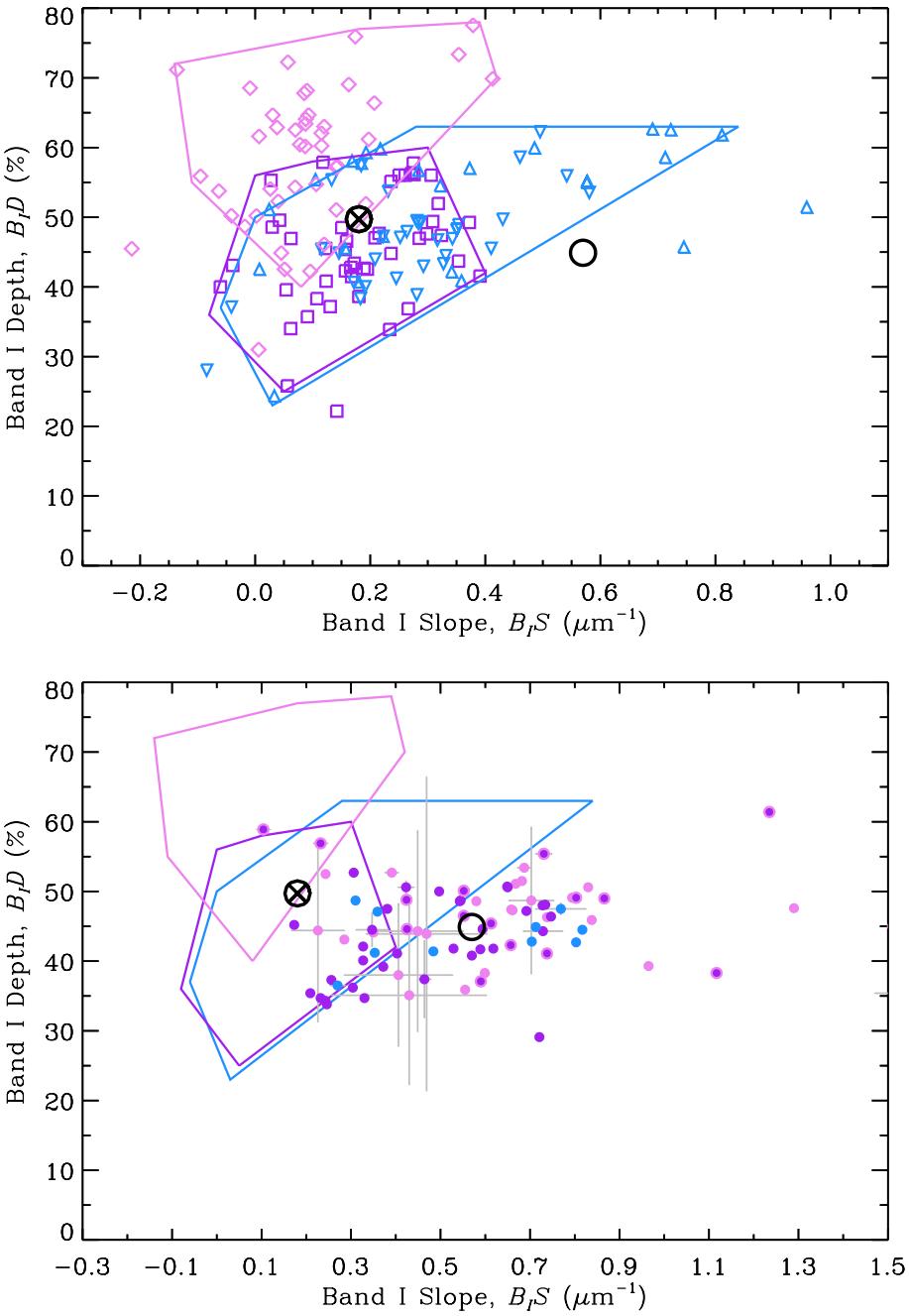

Figure 3.19: B_IS and B_ID for unweathered HEDs (top) and BA asteroids (bottom). The HEDs are outlined by sub-group in each panel and the circle with an 'X' shows the mean value of the whole sample of HEDs. The open circle shows the average B_IS and B_ID for the asteroids.

baseline for un-weathered parameters. Figure 3.19 shows B_IS and B_ID for HEDs and BA (V-type) asteroids and the mean values of the populations. The slope between the two mean points is calculated to be -12.4 $\%\mu m^{-1}$, which is remarkably close to the average value of slopes computed for the irradiated HED and pyroxene samples (-14.3 $\%\mu m^{-1}$). From the separation of these two points, I estimate the average extent of space weathering for my entire sample of BA asteroids to be $SWI = 1.84 \pm 1.04$.

The space weathering style of BA/V-type asteroids being mostly spectral reddening matches the results presented by Fulvio et al. (2016). Vesta, the HED parent body, exhibits a space weathering style unlike the reddening trend seen here in which an infall of carbonaceous material mainly darkens the surface (McCord et al., 2012). (Moskovitz et al., 2010) pointed out that V-types show spectral slopes that are, on average, larger than HED spectral slopes — although there is some overlap between the two distributions. The overlap is seen for V-type NEAs that exhibit low spectral slopes, compared to main-belt V-types (Fulvio et al., 2016) and within the range of HED spectral slopes. This result, also seen within our sample, is similar to that seen among Q and S-type NEAs, as studied by (Binzel et al., 2010). Therefore, V-type NEAs may also have experienced some degree of regolith freshening or even removal, as discussed in section 3.8.2.

3.6.1 Correlation Analysis

Here, I identify the potential effects of factors that influence the amount of space weathering seen among asteroids; such as the size, exposure to solar wind (per orbit), various orbital parameters, regolith grain size, and the surface age. For this analysis I exclusively use my sample of S(IV) asteroids, as they outnumber the BA and S(I) subsamples. Still, the *SWI* calculated for S(I) and BA asteroids provide useful ways to measure the average extent of space weathering for the Eos and Vesta families, respectively.

In my sample of 200+ S(IV) asteroids, a wide range of diameters, orbital parameters, grain sizes are represented, with several of objects belonging to a handful of asteroid families with a common surface age. Before I employ a multiple linear regression model with the *SWI* and the parameters listed above, I first perform separate correlation analyses on them in order to understand any potential co-variance that could be introduced in the model. A

calculation of the time-averaged proxy for the solar flux received by an object in a Keplarian orbit can be represented by:

$$\phi_{exp} = \frac{1}{a^2\sqrt{1-e^2}}, \tag{3.2}$$

where e is the orbital eccentricity and a is the orbital semimajor axis in AU. Here, I use *proper* orbital elements (a_p, e_p) when available, which are calculated to be stable over Gyr timescales (Knežević et al., 2002). Additionally, I include the geometric albedo, p_V, in my correlation analysis, since space weathering has also been shown to darken the lunar surface and laboratory samples, and the albedo of silicate regolith is affected by changing the grain size, with smaller particles increasing the brightness of a surface.

I hypothesize that p_V is correlated with the *SWI*, that smaller grain sizes increase the degree of space weathering, and longer solar wind exposure increases space weathering for main-belt objects. The results of the correlation calculations between all variable combinations, I found that the *SWI* is positively correlated with ϕ_{exp}, D_{eff}, and q, and negatively correlated with the grain size. It is interesting to note here that no correlation exists between p_V and *SWI*. I discuss this point further below and note that the albedos and grain sizes of my sample do have a statistically significant negative relationship with each other, which is consistent with Adams and Filice (1967).

3.6.2 Multivariate Regression

Here, I test a set of multivariate regression models in order to quantify the dependence that *SWI* has on the factors found to correlate with *SWI*: ϕ_{exp}, D_{eff}, and q. I pause, for now, on my analysis on the effect of grain size, since it would force me to severely limit the number of objects with which to fit the model. All three factors are included as independent variables in the multivariate regression model. Two sets of models are formulated: one in which co-linearity is accounted for between the independent variables and one in which they are treated as completely separate. The co-linearity is accounted for by multiplying pairs of the independent factors together and treating the product as another independent variable. Within each of these model sets, I also test whether or not a broken (segmented) fit is

more appropriate for each of the factors by using Davies Test (Davies, 2002) on each of the parameters.

Among this set of models, an influential factor that determined the quality of the fit was the inclusion of certain co-linear combinations between the independent variables. In a large number of these models, all three independent variables were shown to be statistically significant, and a breakpoint in q was necessary in providing a better fit to the data. I chose the model which accounted for the co-linearity between q and ϕ_{exp}, and q and D_{eff} as the preferred model. I find this particularly appropriate since the asteroids with the smallest perihelia are typically the smallest and also have smaller ϕ_{exp}. However, this leaves out co-linearity between D_{eff} and ϕ_{exp}, which I found to be an insignificant factor within all of the multivariate regression models, and redundant since, by the addition of the other two co-linear factors implicitly accounts for the co-linearity between these two. A summary of the best-fit coefficients is given in table 3.14 and figure 3.20 depicts the multi-linear model as a function of the independent variables.

It is possible that the SWI versus perihelia data are better fit by a polynomial function, rather than a segmented linear function. I tested many of these scenarios and found that using a $2nd$-degree polynomial was not sufficient at matching the low q objects, but a $3rd$-degree polynomial fits the data just as well as the segmented linear function. The addition of more orders within the polynomial function adds just as many terms (free parameters) as the segmented function. I choose the segmented linear fit as the preferred model, over the polynomial fits, as it offers a more straightforward interpretation for the decrease in degree of space weathering for low q objects. I would like to note that the location of the breakpoint shown in figure 3.20 is dependent on the assumption of a linear fit to these data. Non-linear functions, like the polynomial fits just mentioned, are able to fit the data without the need to be broken into segments. To check the amount of added potential uncertainty in the breakpoint, I modeled both $2nd$ and $3rd$-degree polynomials with breakpoints and found the location to be very consistent (within the 1σ range) with that of the linear model — although the uncertainty of the break in the latter was $\delta q_b = 0.167$.

Table 3.14: Multi-linear Model Coefficients and Parameters

Parameter	Estimate	1σ Uncertainty	p-value
intercept $[SWI]$	-0.813	$\pm$ 0.316	.011
q_b [AU]	0.960	$\pm$ 0.081	$<$.001
$log_{10}(D_{eff})^{\text{slope}}$	0.607	$\pm$ 0.279	.031
$1/\phi_{exp}^{\text{slope}}$	-0.356	$\pm$ 0.114	.002
q_{eff}^{slope} $(< q_b)$	3.004	$\pm$ 0.453	$<$.001
q_{eff}^{slope} $(> q_b)$	0.588	$\pm$ 0.359	.103
$(q/\phi_{exp})^{\text{slope}}$	0.058	$\pm$ 0.054	.284
$(q \times log_{10}(D_{eff}))^{\text{slope}}$	-0.229	$\pm$ 0.147	.122

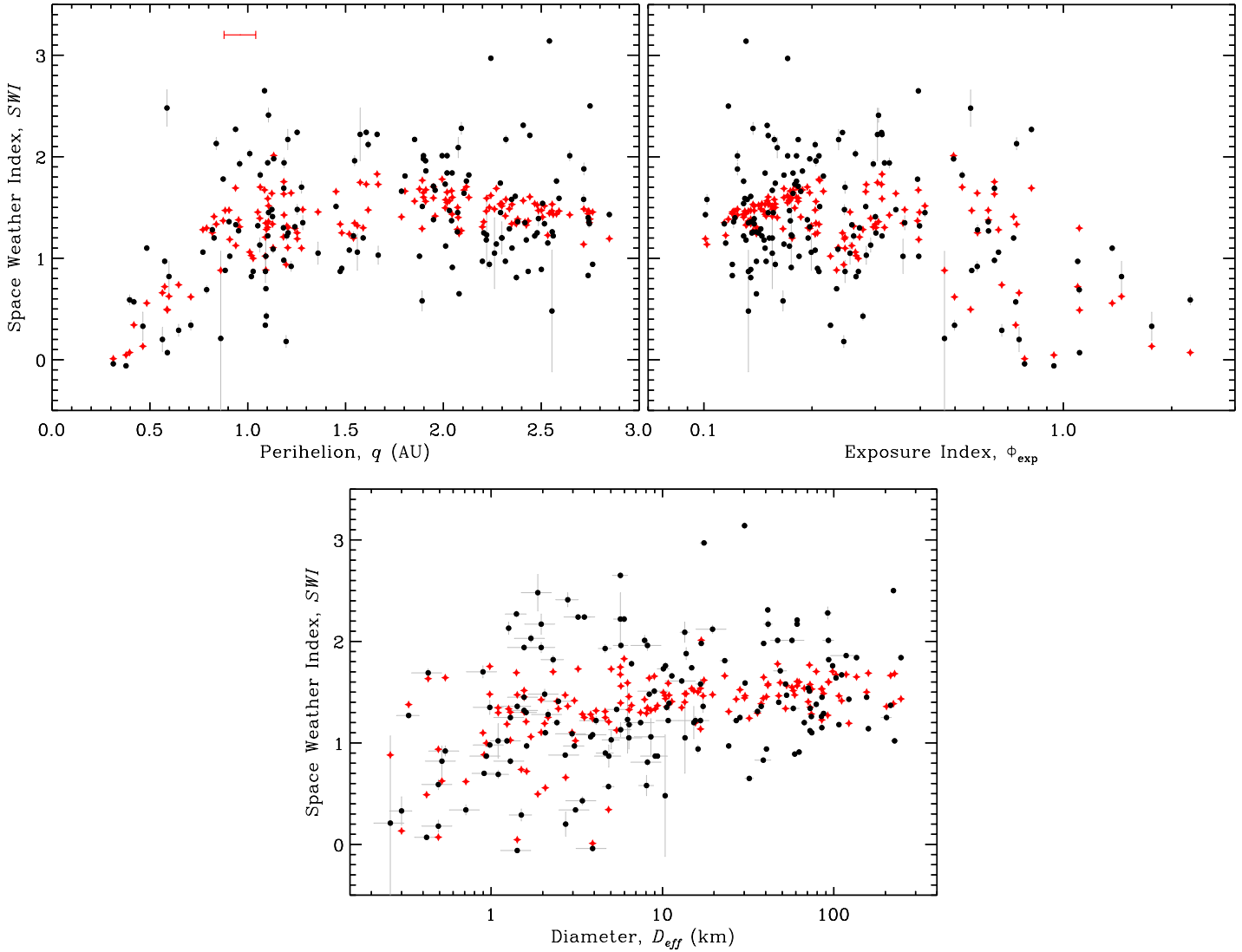

Figure 3.20: *SWI* values and as a function of q, ϕ_{exp}, and D_{eff}. Grey error bars represent 1σ uncertainty values and red stars show the best-fit multi-linear model described in the text.

3.6.3 Space Weathering Timescale

In my sample, no significant correlation could be found between family age and *SWI*, which is partly hampered by the relatively older ages of the families that are included. This lack of result is likely due to a short timescale in which space weathering alters the spectra and the fact that I do not account for solar wind flux. A more appropriate proxy for the dosage of solar wind particles is done by multiplying the exposure index by family age: $T_{exp} = \phi_{exp} \times T_{\rm age}$. This quantity represents the solar wind exposure, integrated over an orbit, at 1 AU from the Sun per Myr. To estimate a characteristic space weathering timescale I fit a power function to *SWI* and $\log_{10}(T_{exp})$. This choice is motivated by the observation that laboratory simulations of micrometeorite bombardment and/or solar wind irradiation indicate that changes in the band parameters ($B_I D$ and $B_I S$) are non-linearly dependent on both the irradiation dosage and npFe^0 abundance. The power function, $SWI = 1.39 \times T_{exp}^{0.57}$, proved to be the best-fit to the dataset. I considered fitting a logarithmic function to these data, but found it to provide a bad match to lower T_{exp} values, as the fit function overestimted the increase in *SWI* at smaller T_{exp}. This discrepancy between the quality of fit between logarithmic and power function might be best be explained by continual active resurfacing or gardening from small impacts occurring on the surface, which would result in a slower increase in *SWI* with T_{exp}.

A large variation in the *SWI* about the best-fit line is seen (figure 3.21) that may be due to the effect that grain size has on the spectral slope described in section 3.4.1. I also plot two offset lines from the best-fit trend at $\pm$ 0.5, in order to show the magnitude of the spread in *SWI*. The effect that grain size has on the *SWI* is discussed in detail below.

3.6.4 Grain Size and Albedo

As mentioned above, both p_V and grain size of the asteroids in my sample were uncorrelated with *SWI*. This is unexpected, as space weathering is the preferred explanation for the albedo variation observed for both lunar regolith and asteroids imaged by spacecraft. In figure 3.22 I plot both these parameters against *SWI* for closer inspection. The right panel shows that any positive or negative trend between *SWI* and p_V is not apparent. As seen in the left panel in figure 3.22, there is a dearth of asteroids having large grain sizes that are also highly space

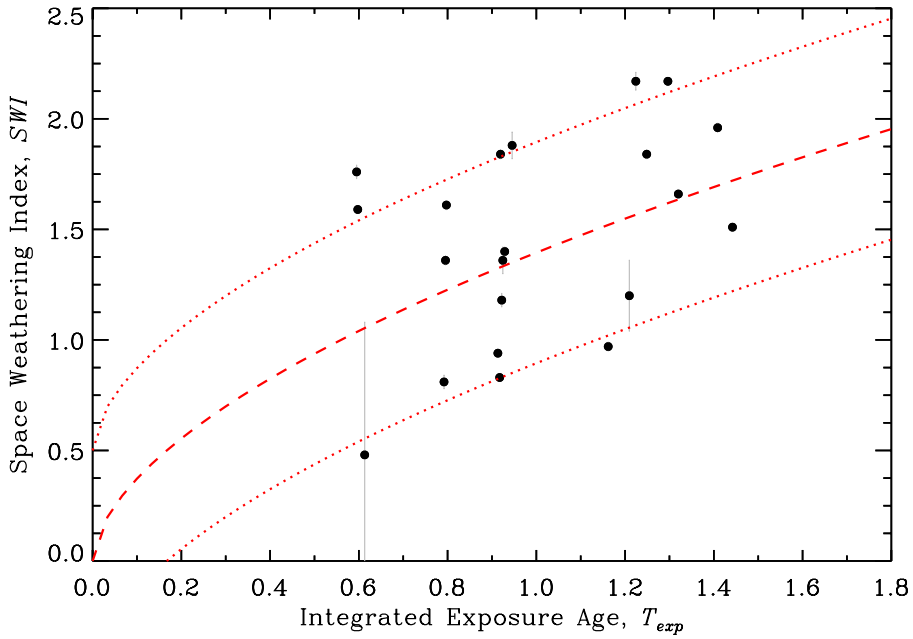

Figure 3.21: SWI as a function of the integrated exposure to the solar wind T_{exp}.

weathered. All the asteroids with larger characteristic grain sizes show low degrees of space weathering. On the other end of the grain size scale, a large variation in SWI is seen among the asteroids with more finer-grained regoliths. This variation in SWI is larger than what is expected from grain size alone. In section 3.4.1 I showed that a change in grain size by a factor of 10 can produce $B_I S$ changes on the order of 0.2 μm^{-1}, which is the same set value of $\Delta SWI = 1$. Therefore, this suggests that the variance in SWI of $\sim$3 seen in the left panel of figure 3.22 cannot fully be explained by grain size alone. Instead, the increase in SWI for smaller regolith grains could be a secondary effect from the enhanced scattering off space-weathered grains that contain more npFe^0.

3.7 Analysis: Band Depth Index

The band depth index, BDI, was constructed such that it is orthogonal to the SWI, and so is independent of space weathering. It can thus be used to study compositional trends and distributions among asteroid populations. To do so, I must first understand which characteristic(s) are captured by the BDI. In section 3.4.1, I showed how most of the variation

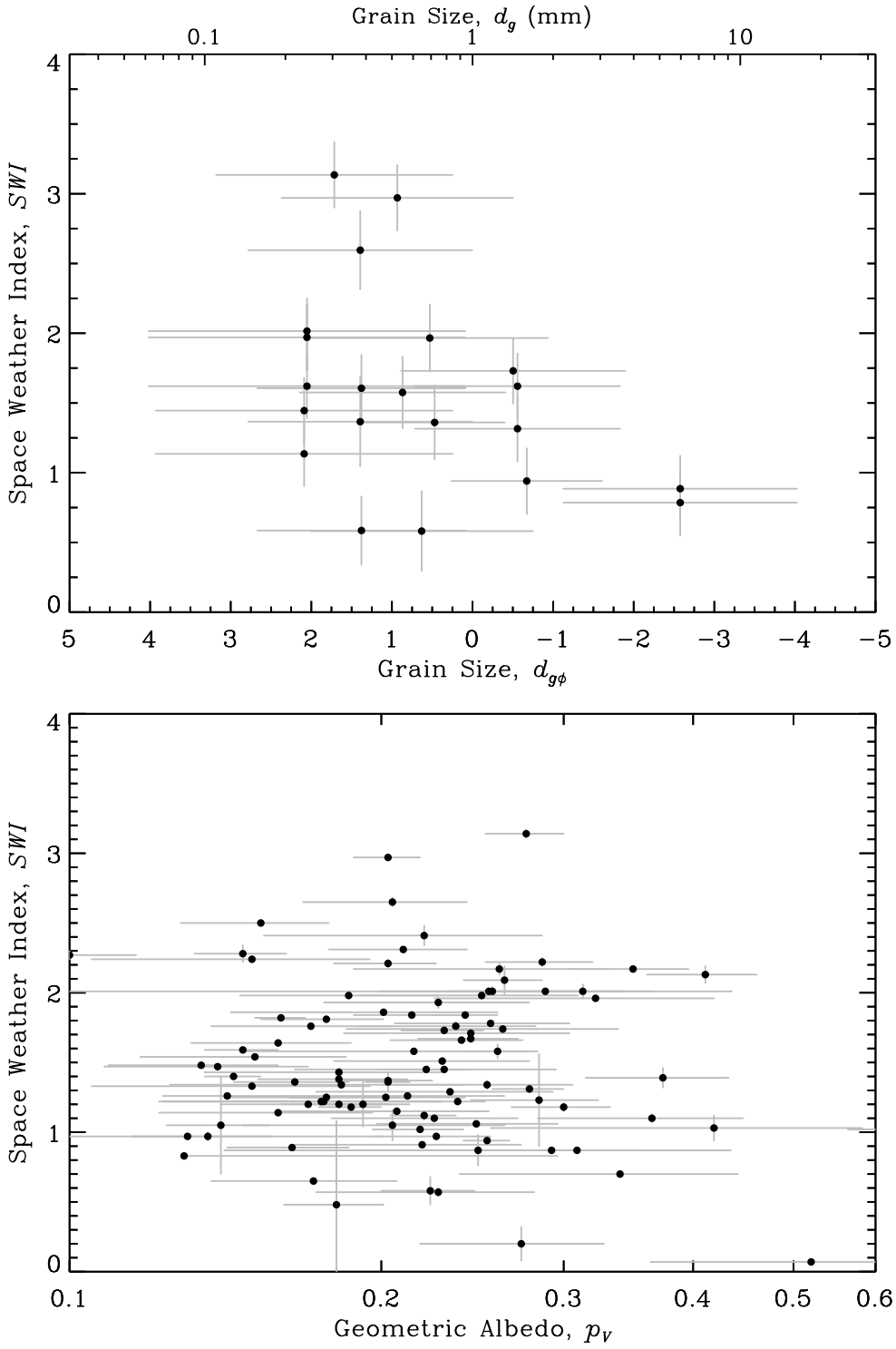

Figure 3.22: *SWI* as a function of regolith grain size (top) and albedo (bottom) for S(IV) asteroids. Grey bars show 1σ errors.

in ordinary chondrite band depth was controlled by the petrologic type — a scale that quantifies the amount of thermal alteration. Since the axis of the *BDI* is mostly in the direction of increased band depth and independent of the *SWI*, I can use it as a proxy for the petrologic type, knowing that it is independent of the spectral changes brought on by space weathering.

Interestingly, I found a strong relationship between asteroid size and the *BDI* for main-belt asteroids (figure 3.23), with a few outliers. This inverse correlation at large D_{eff} may be give clues as to the process by which thermal alteration has occurred in the early solar system. The largest objects in my sample exhibit the lowest *BDI* values, representing low thermal alteration, while main-belt asteroids of smaller sizes appear to have progressively larger *BDI*. This trend could indicate the exposure of more thermally metamorphosed material at depth for asteroids that have had material stripped off from impacts throughout their lifetime. It could also indicate that these smaller asteroids formed at an earlier time, compared to larger bodies, in which more radiogenic isotopes provided a heat source to cause greater thermal alteration. While this finding is interesting and requires more analysis, it is currently out of the scope of this work and should be re-investigated in future work.

Objects of Interest Three objects in particular, (349) Dembowska, (3628) Boznemcova, and (10537) 1991 RY_{16}, all exhibit very large *BDI* values, indicating that their surfaces are very likely comprised of highly metamorphosed (i.e., petrologic type of 5 or 6) ordinary chondrite material. The largest of the three, Dembowska ($D_{\mathit{eff}} \approx 223$ km), is likely to be the remnant of or an original primordial body that accreted shortly after the solar system began to form, while much of the abundant but short-lived radioisotope of the solar system had yet to decay. The other two are smaller than 10 km, and are probably the fragments off a larger asteroid or non-existent parent body who had been heated and metamorphosed to petrologic grade 6 (either at the surface or interior). The orbital locations of Dembowska, Boznemcova, and 1991 RY_{16} (2.93, 2.54, and 2.85 AU, respectively) means that they orbit the Sun near several different main-belt resonances with Jupiter: 7:3 at 2.95 AU, 3:1 at 2.5 AU, and 5:2 at 2.82 AU. Boznemcova, a rare O-type asteroid, is actually a member of a small group of asteroids that are orbitally-grouped by the resonance with Jupiter called

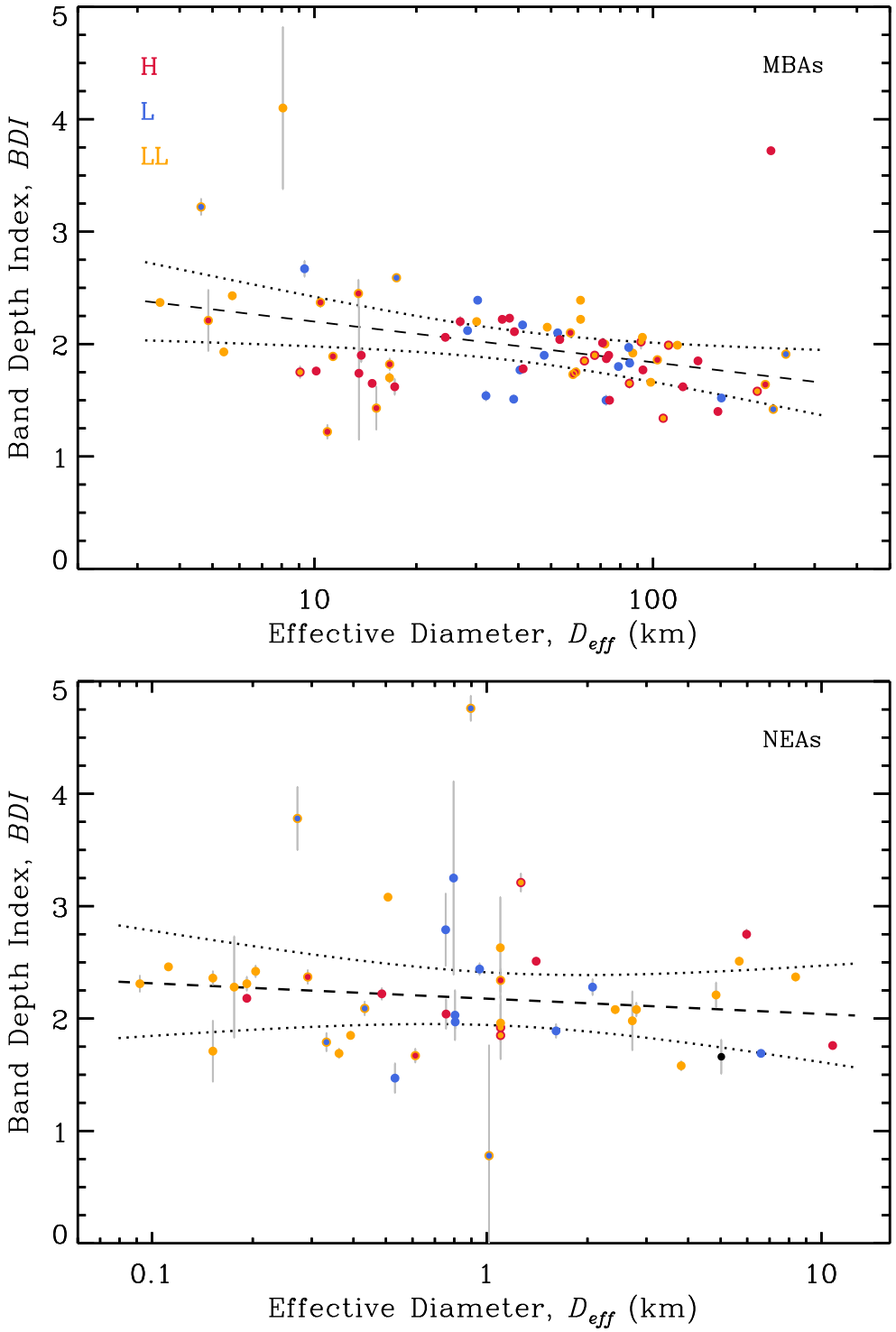

Figure 3.23: *BDI* as a function of D_{eff} for main-belt (top) and near-Earth (bottom) asteroids. Colors indicate the inferred meteorite analog, with two colors indicating ambiguity in the classification.

the Alinda group. (4179) Toutatis is another member of this group, and an NEA, which has a $BDI = 0.193$. Objects that enter the 5:2 resonance are most often placed into highly eccentric Jupiter-approaching, comet-like orbits, in which a collision with Jupiter is more likely (Farinella et al., 1994), so 1991 RY_{16} is likely not the origin of any meteorites found on Earth.

3.8 Discussion

3.8.1 Laboratory Simulations of Space Weathering

By analyzing meteorites and minerals irradiated in a laboratory setting, I have shown that the band parameter paths (in B_IS/B_ID space) of OCs, HEDs and olivines are statistically distinguishable. As is the case on the Moon, the FeO content of the material is the main factor in determining the space weathering pathway: greater FeO yields a greater decrease in band depth per change in spectral slope. Olivine content is not influential in determining the space weathering pathway; however terrestrial olivines exhibit greater sensitivity to irradiation than the other samples. The change in B_IS and B_ID as a function of the irradiation dose is non-linear, and is better described using a logarithmic function. This logarithmic response to irradiation dose may be due to a combination of effects. First, the growth of the $npFe^0$ is most likely non-linear, with most of the production occurring at the onset of irradiation. If this processes were to be thought of as a first-order chemical reaction in which metallic Fe, as the source reactant, is reduced then the logarithmic growth of the product ($npFe^0$) is exactly what is predicted. Secondly, the changes in B_IS and B_ID are certainly a non-linear function of the amount, or wt. %, of the $npFe^0$, since the calculation of the single-scattering albedo contains several non-linear, wavelength-dependent terms (Hapke, 1993, 2001).

My analysis of irradiation experiments in section 3.4.2 showed that B_IS increased while not much decrease in B_ID occurred. This result, combined with the significant overlap between BA asteroids and their meteorite analog limited my ability to constrain the degree of space weathering for individual asteroids. By analyzing the difference in average B_IS/B_ID band parameters, I was able to confirm that space weathering results in more reddening

for HEDs, compared to the OCs and olivine-rich samples, per unit decrease in $B_I D$. The slope in $B_I S$-$B_I D$ space between the average of unweathered HEDs and the average of BA asteroids (figure 3.19) is very similar to the average slope found for irradiated HEDs and pyroxene (figure 3.17), indicating that npFe^0 is the primary overall cause. However, on the surface of Vesta — the parent body of HEDs — variation in spectra and brightness are not related to the production of npFe^0 and instead are likely due to the addition of exogenous carbonaceous material from impacts (McCord et al., 2012), which is subsequently mixed in with host lithologies (Pieters et al., 2012).

3.8.2 Asteroid Parameters

Unexpectedly, no evidence for albedo correlation with *SWI* was detected, despite the fact that space weathering processes have been observed to darken mafic minerals and meteorite samples. This lack of albedo correlation could be explained by corresponding changes in grain size that do correlate the SWI and the albedo dependence on the grain size. As an asteroid surface physically weathers, regolith grains decrease in size, increasing the albedo (Adams and Filice, 1967), while space weathering continually darkens these grains — these two albedo-changing effects may effectively cancel each other out.

The model breakpoint between perihelion and *SWI* near Earth's orbit (i.e., figure 3.20) is consistent with the hypothesis that a "freshening" mechanism acts to reverse the effects of space weathering on these bodies. Asteroids with perihelia that approach the orbits of the terrestrial planets are more likely to pass within a few planetary radii (Morbidelli et al., 2000; Bottke et al., 2002). These asteroids likely have had surface resetting event via tidal interactions (Marchi et al., 2006b; Binzel et al., 2010; DeMeo et al., 2013), compared to objects with different perihelia (figure 3.20). If orbital evolution models can characterize the frequency and strength of these close encounters for individual objects, then estimates of the fraction of refreshed surface can be made. Alternatively, a coronal mass ejection (CME) — a high-energy release of plasma from the Sun — or thermal shock fracturing (a separate process from thermal fatigue) could act to freshen asteroid surfaces via mass loss. The kinetic energy of a CME drops off as the inverse-square distance from the Sun, thus I would expect low q asteroids to possess a greater chance of having regolith swept away from these

events over time. Thermal shock fracturing, which can eject small particles from asteroid surfaces, would also act to remove the effect of space weathering for low-q asteroids. The relative efficiency and operating timescale of each of these mechanisms is currently beyond the scope of this dissertation, but should be considered as freshening mechanisms in future space weathering studies.

Other alternative explanations for the low degree of space weathering observed for low perihelion asteroids are explored here. For example, the high temperature experienced closer to the Sun could anneal regolith grains, overpowering and erasing the spectral effects from solar wind bombardment. This seems unlikely, as Kohout et al. (2014) used a heating technique, rather than particle bombardment, to produce and grow npFe^0 in a reducing environment. Proximity to the Sun's powerful magnetic field could shield asteroids from high-energy cosmic rays, but this would only be a sufficient explanation for asteroids that were sourced interior to Earth, and is not a freshening mechanism. Solar tidal forces, while a theoretically-feasible explanation for a freshening mechanism, are unlikely to be of a greater magnitude than a tidal interaction via close encounter with a terrestrial planet such as Venus or Earth, due to the inverse cube dependency of tidal forces on the distance to the relevant body. Lastly, the YORP spin-up of asteroids could feasibly remove space weathered regolith from an asteroid surface. However, this would predict a correlation between the SWI and rotation period, which was considered in section 3.6.1 but did not produce a significant relationship.

Finally, I find that a power fit between the SWI and T_{exp} data to be more appropriate and consistent with most spectral changes occurring rapidly at the onset. This power fit is different from the suggestion by Vernazza et al. (2009) that space weathering operates as a two-tier process (rapid and slow) corresponding to ion irradiation and micrometeorite bombardment, respectively. Accounting for the fact that lab irradiation experiments show logarithmic changes in the space weathering band parameters, B_IS and B_ID, the power fit to these data appear to be more appropriate and do not require a two-step space weathering process.

3.8.3 Petrologic Variation

Internal heat within the ordinary chondrite parent body — produced via the decay of the ^{26}Al radioisotope during the early solar system — gave way to the higher petrologic types (above type 3) observed among the ordinary chondrites (Ghosh and McSween, 1998). Higher petrologic types are produced at the center of the parent body, as the heat buildup created greater temperatures, leaving the surface relatively unaltered. This "onion shell" model of the ordinary chondrite parent body is a likely explanation for the formation of various petrologic/metamorphic types seen in the meteorite record (∼2/3 of L are petrologic type 6 and ∼2/3 of H and LL are of petrologic types 5 or 6). Gietzen et al. (2012) predict that petrologic type 3 bodies should be common, since a catastrophic breakup of the parent body is needed in order to reveal the type 5 and 6 that were created deep in the interior. I showed in section 3.4.1 that the mean and variance of $B_I D$ was correlated with increasing petrologic type among ordinary chondrites, and in figure 3.20 I observed an inverse correlation between *BDI* and asteroid size. For 10–100 km main-belt asteroids, there exists an inverse trend between object D_{eff} and *BDI*, which is most likely due to the inclusion of higher-grade petrologic types on their surfaces.

Similar to the results presented here, Gaffey et al. (1993) reported an inverse trend between asteroid size and band depth for objects < 100 km — which they attributed to space weathering. But this diameter range does not align with the size transition at which asteroids are thought to young enough to have not shown evidence of space weathering (i.e., 5 km; Thomas et al., 2012). In the light of my results, I re-interpret the band depth and size relationship presented by Gaffey et al. (1993) as an indicator of changes in petrologic type, and not space weathering.

This onion shell parent body could have been subject to catastrophic impacts that redistribute and revealing higher grade petrologic types at the surface as it re-accumulates under self-gravity and forms a rubble-pile structure (Walsh, 2018). The spectral signature from the asteroid would resemble an average of the petrologic types that exist on the surface, complicating the interpretation of band parameters in this context. Small ($D_{eff} < 10$ km) have a much higher probability of being formed out of a collision (Bottke et al., 2005) which

implies that their surfaces are heavily processed and may explain the lack of any significant size correlation with BDI, for $D_{eff} < 10$ km. The near-Earth asteroids

Dunn et al. (2010b) presented evidence that petrologic type 3 OCs were metamorphosed in reduced conditions and show evidence of oxidation starting with type 4 samples. This oxidation and heating produces olivine at the expense of pyroxene (McSween and Labotka, 1993). This change in the olivine-to-pyroxene ratio is more pronounced among H chondrites and at higher temperatures (Dunn et al., 2010b). Thus, I would expect to observe higher relative olivine abundances for objects that are higher petrologic type. Unfortunately, the analyses in this chapter do not provide a means for estimating the petrologic type for every individual asteroid, but I highlight here the objects that have very large BDI and are likely a higher petrologic type: Dembowska, Boznemcova, and 1991 RY_{16}. According to my results, Dembowska resembles H chondrite material and has a $BAR \approx 0.849$. According to the measurements of (Dunn et al., 2010a), this BAR value is at the low end of other H chondrite meteorites, which indicates a higher olivine content within this sub-type. These mineralogical and petrologic indications for Dembowska are consistent with the meteoritical evidence that H chondrites experiencing heating have increased the relative olivine abundance relative to objects that experienced less heating. This analysis for Dembowska should be taken with caution as its classification as an H chondrite is dependent on spectroscopic band parameters, which form a continuum across ordinary chondrite sub-types (figure 3.16) and not discrete clusters, as shown by the calibration work by Dunn et al. (2010a).

3.8.4 Conclusions

I had hypothesized that the degree of space weathering is dependent on the amount of solar wind exposure and/or semimajor axis, corresponding to solar wind irradiation and micrometeoroid bombardment, respectively. Using the SWI as the dependent variable, the multiple linear regression analysis showed that the solar wind exposure index, size, and perihelion were statistically significant factors in determining the degree of space weathering. The result indicates that solar wind bombardment is the primary process by which space weathering progresses on silicate-bearing asteroids. The size dependence most likely indicates the time dependence on the degree of space weathering, as larger asteroids are statistically

older than smaller asteroids. The segmented linear relationship between perihelion and *SWI* — in particular the decrease in the degree of space weathering with decreasing perihelion — points to an likely freshening mechanism, as detailed further below in section 3.8.2. The degree of space weathering is also enhanced by the increase in surface area due to smaller regolith grains, as mentioned in section 3.6.4. From experimentation involving laboratory simulation of space weathering, I conclude that the amount of FeO in olivine, and not the relative abundance of olivine to pyroxene, determined the amount of decrease in band depth per unit change in spectral slope (section 3.8.1).

Conclusion

The surface of an average asteroid has evolved greatly through time through experiencing both mechanical breakdown, or disintegration, and simultaneously being bombarded by solar wind particles resulting in higher degree of space-weathering. This work has been as investigation into the factors and processes that determine the amount of weathering, through the use of a large dataset and sample sizes. A few main takeaway conclusions are given below.

There is a complex interplay between the dominant forces that break down asteroid surfaces (impact disintegration and thermal fatigue), those that retain the resulting regolith (gravity and cohesion), and those that remove and excavate and/or remove the regolith (impacts, centrifugal ejection, electrostatic levitation, and solar radiation pressure). Clearly, the gravitational and thermal environments and the mechanical properties of the asteroid are very influential underlying factors that are difficult or impossible to accurately measure for each asteroid without actually visiting an object. Given my results, I conclude that main-belt asteroids smaller than 1 km possess bare rock surfaces or, at least, very blocky regoliths consisting of rocks greater than a typical thermal skin depth for most asteroids, 6–14 mm (figure 2.11) and that loss mechanisms are the preferred explanation for this regolith structure.

Spectral type, or composition, likely plays a significant role in determining the regolith grain size. I demonstrate that Metal-rich asteroids have regoliths that are consistently comprised of large grains and, likely a large fractions of bare metal exposed at the surface. Similarly, E-type objects — which could contain a significant fraction of aubrite/enstatite achondrite parent bodies — exhibit larger regolith grain sizes than other objects at similar

sizes and rotation periods. The primitive P-type asteroids possess, on average, more fine-grained regoliths.

Near-Earth asteroids exhibit a complex relationship in relationship to the parameters that determine both how regolith is weathered and the effects of space weathering are exhibited. NEAs, which are often small, have regoliths that vary widely depending on object size, rotation period, and aphelion distance. Additionally, objects with perihelia interior to Earth's orbit show progressively less space weathering with decreasing perihelion distance.

The timescales for both mechanical and space weathering are short and on the order of $\lesssim 1$ Myr, meaning that surfaces older than this age will not evolve any further. It is not to say, however, that all asteroids older than this age will have similar regoliths and degree of space weathering — as the factors studied in this work provide a means of predicting the current state of regolith.

Bibliography

Adams, J. B. and Filice, A. L. (1967). Spectral Reflectance 0.4 to 2.0 microns of Silicate Rock Powders. *Journal of Geophysical Research*, 72(2):5705–5715. 152, 222, 232

Adams, J. B. and McCord, T. B. (1971). Optical properties of mineral separates, glass, and anorthositic fragments from Apollo mare samples. In *Lunar and Planetary Science Conference Proceedings*, volume 2, page 2183. 146

Alí-Lagoa, V., Lionni, L., Delbo', M., Gundlach, B., Blum, J., and Licandro, J. (2014). Thermophysical Properties of near-Earth Asteroid (341843) 2008 EV5 from WISE Data. *Astronomy and Astrophysics*, 561:A45. 8, 29, 33

Allen, D. A. (1970). Infrared Diameter of Vesta. *Nature*, 227:158–159. 8

Ammannito, E., Sanctis, M. C. D., Palomba, E., Longobardo, A., Mittlefehldt, D. W., McSween, H. Y., Marchi, S., Capria, M. T., Capaccioni, F., Frigeri, A., Pieters, C. M., Ruesch, O., Tosi, F., Zambon, F., Carraro, F., Fonte, S., Hiesinger, H., Magni, G., McFadden, L. A., Raymond, C. A., Russell, C. T., and Sunshine, J. M. (2013). Olivine in an unexpected location on Vesta's surface. *Nature*, 504:122–125. 185

Asada, N. (1985). Fine Fragments in High-Velocity Impact Experiments. *Journal of Geophysical Research*, 90(B14):12,445–12,453. 134

Bandfield, J. L., Ghent, R. R., Vasavada, A. R., Paige, D. A., Lawrence, S. J., and Robinson, M. S. (2011). Lunar surface rock abundance and regolith fines temperatures derived from LRO Diviner Radiometer data. *Journal of Geophysical Research*, 116:E00H02. 44

Basilevsky, A. T., Head, J. W., and Horz, F. (2013). Survival times of meter-sized boulders on the surface of the Moon. *Planetary and Space Science*, 89:118–126. 136

Basilevsky, A. T., Head, J. W., Horz, F., and Ramsley, K. (2015). Survival times of meter-sized rock boulders on the surface of airless bodies. *Planetary and Space Science*, 117:312–328. 136, 138

Bates, R. L. and Jackson, J. A. (1980). *Glossary of Geology*. American Geological Institute. 2

Beck, A. W. and McSween, Jr., H. Y. (2010). Diogenites as polymict breccias composed of orthopyroxenite and harzburgite. *Meteoritics & Planetary Science*, 45(5):850–872. 185

Beech, M., Coulson, I. M., Nie, W., and McCausland, P. (2009). The thermal and physical characteristics of the Gao-Guenie (H5) meteorite. *Planetary and Space Science*, 57:764–770. 97, 100

Bell, J. F., Izenberg, N. I., Lucey, P. G., Clark, B. E., Peterson, C., Gaffey, M. J., Joseph, J., Carcich, B., Harch, A., Bell, M. E., Warren, J., Martin, P. D., McFadden, L. A., Wellnitz, D., Murchie, S., Winter, M., Veverka, J., Thomas, P., Malin, M. S. R. M., and Cheng, A. (2002). Near-IR Reflectance Spectroscopy of 433 Eros from the NIS Instrument on the NEAR Mission: I. Low Phase Angle Observations. *Icarus*, 155:119–144. 147

Bendjoya, P. and Zappalá, V. (2002). Asteroid family identification. In Bottke, Jr., W. F., Cellino, A., Paolicchi, P., and Binzel, R. P., editors, *Asteroids III*. University of Arizona Press. 1

Binzel, R. P., Bus, S. J., Burbine, T. H., and Sunshine, J. M. (1996). Spectral properties of near-Earth asteroids: evidence for sources of ordinary chondrite meteorites. *Science*, 273:946–948. 3

Binzel, R. P., Morbidelli, A., Merouane, S., DeMeo, F. E., Birlan, M., Vernazza, P., Thomas, C. A., Rivkin, A. S., Bus, S. J., and Tokunaga, A. T. (2010). Earth encounters as the origin of fresh surfaces on near-Earth asteroids. *Nature*, 463:331–334. 147, 221, 232

Binzel, R. P., Rivkin, A. S., Stuart, J. S., Harris, A. W., Bus, S. J., and Burbine, T. H. (2004). Observed spectral properties of near-Earth objects: results for population distribution, source regions, and space weathering processes. *Icarus*, 170:259–294. 3, 152

Binzel, R. P., Thomas, C. A., DeMeo, F. E., Tokunaga, A., Rivkin, A. S., and Bus, S. J. (2006). The MIT-Hawaii-IRTF Joint Campaign for NEO Spectral Reconnaissance. In Mackwell, S. and Stansbery, E., editors, *37th Annual Lunar and Planetary Science Conference*, volume 37 of *Lunar and Planetary Science Conference*. Abstract #1491. 161

Bischoff, A., Scott, E. R. D., Metzler, K., and Goodrich, C. A. (2006). Nature and origins of meteoritic breccias. In Lauretta, D. S. and McSween, H. Y., editors, *Meteorites and the Early Solar System II*, pages 679–712. 108, 135

Bischoff, A., Vogel, N., and Roszjar, J. (2011). The Rumuruti chondrite group. *Chemie der Erde*, 71:101–133. 185, 216

Bodewits, D., Kelley, M. S., Li, J.-Y., Landsman, W. B., Besse, S., and A'Hearn, M. F. (2011). Collisional Excavation of Asteroid (596) Scheila. *Astrophysical Journal Letters*, 733:L3. 141

Bolin, B. T., Morbidelli, A., and Walsh, K. J. (2018). Size-dependent modification of asteroid family Yarkovsky V-shapes. *Astronomy & Astrophysics*, 611:A82. 129

Bottke, Jr., W. F., Brož, M., O'Brien, D. P., Bagatin, A. C., Morbidelli, A., and Marchi, S. (2015). The Collisional Evolution of the Main Asteroid Belt. In *Asteroids IV*. University of Arizona Press. 1

Bottke, Jr., W. F., Durda, D. D., Nesvorny, D., Jedicke, R., Morbidelli, A., Vokrouhlicky, D., and Levison, H. (2005). The fossilized size distribution of the main asteroid belt. *Icarus*, 175:111–140. 152, 234

Bottke, Jr., W. F., Morbidelli, A., Jedicke, R., Petit, J.-M., Levison, H. F., Michel, P., and Metcalfe, T. S. (2002). Debiased Orbital and Absolute Magnitude Distribution of the Near-Earth Objects. *Icarus*, 156:399–433. 232

Bottke, Jr., W. F., Nolan, M. C., Greenberg, R., and Kolvoord, R. A. (1994). Velocity Distributions Among Colliding Asteroids. *Icarus*, 107:255–268. 134

Bottke, Jr., W. F., Vokrouhlicky, D., Broz, M., Nesvorny, D., and Morbidelli, A. (2001). Dynamical Spreading of Asteroid Families by the Yarkovsky Effect. *Science*, 294:1693–1696. 129

Bottke, Jr., W. F., Vokrouhlicky, D., and Nesvorny, D. (2007). An asteroid breakup 160 Myr ago as the probable source of the K/T impactor. *Nature*, 449:48–53. 130

Bottke, Jr., W. F., Vokrouhlický, D., Rubincam, D. P., and Nesvorný, D. (2006). The Yarkovsky and YORP Effects: Implications for Asteroid Dynamics. *Annual Reviews of Earth and Planetary Science*, 34:157–91. 2, 142

Bowell, E., Hapke, B., Domingue, D., Lumme, K., Peltoniemi, J., and Harris, A. W. (1989). Application of Photometric Models to Asteroids. In Binzel, R. P., Gehrels, T., and Matthews, M. S., editors, *Asteroids II*, pages 524–556. University of Arizona Press. 9

Brent, R. P. (1973). *Algorithms for Minimization without Derivatives*. Prentice Hall, Englewood Cliffs, NJ. 20

Brož, M. and Vokrouhlický, D. (2008). Asteroid families in the first-order resonances with Jupiter. *Monthly Notices of the Royal Astronomical Society*, 390(2):715–732. 130

Broz, M., Morbidelli, A., Bottke Jr., W. F., Rozehnal, J., Vokrouhlicky, D., and Nesvorny, D. (2013). Constraining the cometary flux through the asteroid belt during the late heavy bombardment. *Astronomy & Astrophysics*, 551:A117. 130

Brunetto, R., Loeffler, M. J., Nesvorný, D., Sasaki, S., and Strazzulla, G. (2015). Asteroid surface alteration by space weathering processes. In *Asteroids IV*. University of Arizona Press. 3

Brunetto, R., Romano, F., Blanco, A., Fonti, S., Martino, M., Orofino, V., and Verrienti, C. (2006). Space weathering of silicates simulated by nanosecond pulse UV excimer laser. *Icarus*, 180:546–554. 150, 184, 190, 191, 192

Brunetto, R. and Strazzulla, G. (2005). Elastic collisions in ion irradiation experiments: A mechanism for space weathering of silicates. *Icarus*, 179:265–273. 150

Burbine, T. H. and Binzel, R. P. (2002). Small Main-Belt Asteroid Spectroscopic Survey in the Near-Infrared. *Icarus*, 159:468–499. 135

Burbine, T. H., Buchanan, P. C., and Binzel, R. P. (2007). Deriving Formulas from HED Spectra for Determining the Pyroxene Mineralogy of Vesta and Vestoids. In *Lunar and Planetary Science Conference #38*. Abstract #2117. 213

Burbine, T. H., Buchanan, P. C., Binzel, R. P., Bus, S. J., Hiroi, T., Hinrichs, J. L., Meibom, A., and McCoy, T. J. (2001). Vesta, Vestoids, and the howardite, eucrite, diogenite group: Relationships and the origin of spectral differences. *Meteoritics & Planetary Science*, 36:761–781. 216

Burbine, T. H., Buchanan, P. C., Klima, R. L., and Binzel, R. P. (2018). Can Formulas Derived from Pyroxene and/or HED Reflectance Spectra be Used to Determine the Mineralogies of V-Type NEAS? In *Lunar and Planetary Science Conference #49*. Abstract #2083. 216

Burbine, T. H., McCoy, T. J., Jaresowich, E., and Sunshine, J. M. (2003). Deriving asteroid mineralogies from reflectance spectra: Implications for the MUSES-C target asteroid. *Antarct. Meteorite Res.*, 16:185–195. 214

Burbine, T. H., McCoy, T. J., Meibom, A., Gladman, B., and Keil, K. (2002). Meteoritic parent bodies: Their number and identification. In Bottke, Jr., W. F., Cellino, A., Paolicchi, P., and Binzel, R. P., editors, *Asteroids III*. University of Arizona Press. 2

Burns, R. G. (1993). *Mineralogical Applications of Crystal Field Theory*. Cambridge Topics in Mineral Physics and Chemistry. Cambridge University Press, 2 edition. 153

Bus, S. J. and Binzel, R. P. (2002a). Phase II of the Small Main-Belt Asteroid Spectroscopic Survey: A Feature-Based Taxonomy. *Icarus*, 158:146–177. 161

Bus, S. J. and Binzel, R. P. (2002b). Phase II of the Small Main-Belt Asteroid Spectroscopic Survey: The Observations. *Icarus*, 158:106–145. 149

Bus, S. J., Vilas, F., and Barucci, M. A. (2002). Visible-wavelength spectroscopy of asteroids. In Bottke, Jr., W. F., Cellino, A., Paolicchi, P., and Binzel, R. P., editors, *Asteroids III*. University of Arizona Press. 1

Cadenhead, D. A. and Stetter, J. R. (1975). Specific gravities of lunar materials using helium pycnometry. In *Lunar and Planetary Science Conference Proceedings*, volume 6 of *Lunar and Planetary Science Conference Proceedings*, pages 3199–3206. 99

Capria, M. T., Tosi, F., Sanctis, M. C. D., Capaccioni, F., Ammannito, E., Frigeri, A., Zambon, F., Fonte, S., Palomba, E., Turrini, D., Titus, T. N., Schröder, S. E., Toplis, M., Li, J.-Y., Combe, J.-P., Raymond, C. A., and Russell, C. T. (2014). Vesta surface thermal properties map. *Geophysical Research Letters*, 41:1438–1443. 44

Carruba, V., Nesvorný, D., Aljbaae, S., Domingos, R. C., and Huaman, M. (2016). On the oldest asteroid families in the main belt. *Monthly Notices of the Royal Astronomical Society*, 458:3731–3738. 130

Chabot, N. L. and Haack, H. (2006). Evolution of Asteroidal Cores. In Lauretta, D. S. and McSween Jr., H. Y., editors, *Meteorites and the Early Solar System II*, pages 747–771. University of Arizona Press. 185

Chan, C. K. and Tien, C. L. (1973). Conductance of packed spheres in vacuum. *Journal of Heat Transfer*, 95:302–308. 102

Chapman, C. R. (1996). S-type asteroids, ordinary chondrites, and space weathering: The evidence from galileo's fly-bys of gaspra and ida. *Meteoritics & Planetary Science*, 31:699–725. 147

Cheng, A. F. (2002). Near earth asteroid rendezvous: Mission summary. In Bottke, Jr., W. F., Cellino, A., Paolicchi, P., and Binzel, R. P., editors, *Asteroids III*. University of Arizona Press. 2

Clark, B. E., Bus, S. J., Rivkin, A. S., McConnochie, T., Sanders, J., Shah, S., Hiroi, T., and Shepard, M. (2004). E-type asteroid spectroscopy and compositional modeling. *Journal of Geophysical Research*, 109:E02001. 158

Clark, B. E., Hapke, B., Pieters, C., and Britt, D. (2002). Asteroid Space Weathering and Regolith Evolution. In Bottke, Jr., W. F., Cellino, A., Paolicchi, P., and Binzel, R. P., editors, *Asteroids III*, pages 585–599. University of Arizona Press. 2, 152

Clark, B. E., Lucey, P., Helfenstein, P., Bell III, J. F., Peterson, C., Mcconnochie, J. V. T., Robinson, M. S., Bussey, B., Murchie, S. L., Izenberg, N. I., and Chapman, C. R. (2001).

Space weathering on Eros: Constraints from albedo and spectral measurements of Psyche crater. *Meteoritics & Planetary Science*, 36(12):1617–1637. 147

Cloutis, E. A., Gaffey, M. J., Jackowski, T. L., and Reed, K. L. (1986). Calibrations of phase abundance, composition, and particle size distribution for olivine-orthopyroxene mixtures from reflectance spectra. *Journal of Geophysical Research*, 91(B11):11,641–11,653. 153, 214

Cloutis, E. A., Sanchez, J. A., Reddy, V., Gaffey, M. J., Binzel, R. P., Burbine, T. H., Hardersen, P. S., Hiroi, T., Lucey, P. G., Sunshine, J. M., and Tait, K. T. (2015). Olivine–metal mixtures: Spectral reflectance properties and application to asteroid reflectance spectra. *Icarus*, 252:39–82. 188, 218

Conel, J. E. and Nash, D. B. (1970). Apollo 11 rocks spectral reflectance and albedo before/after proton irradiation and vitrification, investigating color differences for lunar surface dark and bright areas. In *Apollo 11 Lunar Science Conference*, 3rd, pages 2013–2023. 146

Consolmagno, G. J., Britt, D. T., and Macke, R. J. (2008). The Significance of Meteorite Density and Porosity. *Chemie der Erde*, 68:1–29. 101

Consolmagno, G. J., Schaefer, M. W., Schaefer, B. E., Britt, D. T., Macke, R. J., Nolan, M. C., and Howell, E. S. (2013). The measurement of meteorite heat capacity at low temperatures using liquid nitrogen vaporization. *Planetary and Space Science*, 87(146-156):146–156. 97, 100

Cremers, C. J. (1975). Thermophysical properties of Apollo 14 fines. *J. Geophys. Research*, 80:4466–4470. 44

Cushing, M. C., Vacca, W. D., and Rayner, J. T. (2004). Spextool: A Spectral Extraction Package for SpeX, a 0.8–5.5 Micron Cross-Dispersed Spectrograph. *Publications of the Astronomical Society of the Pacific*, 116(818):362–376. 155

Cutri, R. M., Wright, E. L., Conrow, T., Bauer, J., Benford, D., Brandenburg, H., Dailey, J., Eisenhardt, P. R. M., Evans, T., Fajardo-Acosta, S., Fowler, J., Gelino, C., Grillmair, C.,

Harbut, M., Hoffman, D., Jarrett, T., Kirkpatrick, J. D., Leisawitz, D., Liu, W., Mainzer, A., Marsh, K., Masci, F., McCallon, H., Padgett, D., Ressler, M. E., Royer, D., Skrutskie, M. F., Stanford, S. A., Wyatt, P. L., Tholen, D., Tsai, C.-W., Wachter, S., Wheelock, S. L., Yan, L., Alles, R., Beck, R., Grav, T., Masiero, J., McCollum, B., McGehee, P., Papin, M., and Wittman, M. (2012). Explanatory Supplement to the WISE All-Sky Data Release Products. http://wise2.ipac.caltech.edu/docs/release/allsky/expsup/. 32, 52

Davidsson, B. J. R. and Rickman, H. (2014). Surface roughness and three-dimensional heat conduction in thermophysical models. *Icarus*, 243:58–77. 7

Davidsson, B. J. R., Rickman, H., Bandfield, J. L., Groussin, O., Gutiérrez, P. J., Wilska, M., Capria, M. T., Emery, J. P., Helbert, J., Jorda, L., Maturilli, A., and Müeller, T. G. (2015). Interpretation of Thermal Emission I. The Effect of Roughness for Spatially Resolved Atmosphereless Bodies. *Icarus*, 252:1–21. 8

Davies, R. B. (2002). Hypothesis testing when a nuisance parameter is present only under the alternative: Linear model case. *Biometrika*, 89(2):484–489. 123, 223

Delbo', M., dell'Oro, A., Harris, A. W., Mottola, S., and Mueller, M. (2007). Thermal Inertia of near-Earth Asteroids and Implications for the Magnitude of the Yarkovsky Effect. *Icarus*, 190:236–249. 4

Delbo', M., Harris, A. W., Binzel, R. P., Pravec, P., and Davies, J. K. (2003). Keck Observations of near-Earth Asteroids in the Thermal Infrared. *Icarus*, 166:116–130. 8

Delbo', M., Libourel, G., Wilkerson, J., Murdoch, N., Michel, P., Ramesh, K. T., Ganino, C., Verati, C., and Marchi, S. (2014). Thermal fatigue as the origin of regolith on small asteroids. *Nature*, 508(7495):233–236. 47, 48, 137

Delbo', M., Mueller, M., Emery, J. P., Rozitis, B., and Capria, M. T. (2015). Asteroid Thermophysical Modeling. In Michel, P., DeMeo, F. E., and Bottke Jr., W. F., editors, *Asteroids IV*, pages 107–128. University of Arizona Press. 1, 4, 40, 45, 85, 88, 109

Delbo', M. and Tanga, P. (2009). Thermal Inertia of Main Belt Asteroids Smaller than 100 km from IRAS Data. *Planetary and Space Science*, 57:259–265. 11, 20, 29, 31

DeMeo, F. E., Alexander, C. M. O., Walsh, K. J., Chapman, C. R., and Binzel, R. P. (2015). The compositional structure of the asteroid belt. In *Asteroids IV*. University of Arizona Press. 1, 2

DeMeo, F. E., Binzel, R. P., and Lockhart, M. (2013). Mars encounters cause fresh surfaces on some near-Earth asteroids. *Icarus*, 227:112–122. 232

DeMeo, F. E., Binzel, R. P., Slivan, S. M., and Bus, S. J. (2009). An extension of the Bus asteroid taxonomy into the near-infrared. *Icarus*, 202:160–180. 1, 92, 93, 119, 149

DeMeo, F. E. and Carry, B. (2013). The taxonomic distribution of asteroids from multi-filter all-sky photometric surveys. *Icarus*, 226(1):723–741. 94, 126

DeMeo, F. E. and Carry, B. (2014). Solar System evolution from compositional mapping of the asteroid belt. *Nature*, 505:629–634. 94

Dodd, R. T., VanSchmus, W. R., and Koffman, D. M. (1967). A survey of the unequilibrated ordinary chondrites. *Geochimica et Cosmochimica Acta*, 31(6):921–934. 214

Dombard, A. J., Barnouin, O. S., Prockter, L. M., and Thomas, P. C. (2010). Boulders and ponds on the Asteroid 433 Eros. *Icarus*, 210:713–721. 144

Draper, N. R. and Smith, H. (1998). *Applied Regression Analysis*. John Wiley & Sons, Inc. 88

Duffard, R., Lazzaro, D., and DeLeón, J. (2005). Revisiting spectral parameters of silicate-bearing meteorites. *Meteoritics & Planetary Science*, 40(3):445–459. 178

Dullien, F. A. L. (1979). *Porous Media*. Academic Press. 103

Dunn, T. L., McCoy, T. J., Sunshine, J. M., and McSween Jr., H. Y. (2010a). A coordinated spectral, mineralogical, and compositional study of ordinary chondrites. *Icarus*, 208:789–797. 193, 213, 214, 235

Dunn, T. L., McSween, Jr., H. Y., McCoy, T. J., and Cressey, G. (2010b). Analysis of ordinary chondrites using powder x-ray diffraction: 2. applications to ordinary chondrite parent-body processes. *Meteoritics and Planetary Science*. 235

Ďurech, J. (2010). DAMIT: A Database of Asteroid Models. *Astronomy and Astrophysics*, 513:A46. 5, 22

Ďurech, J., Carry, B., Delbó, M., Kaasalainen, M., and Viikinkoski, M. (2015). Asteroid Models from Multiple Data Sources. In Michel, P., DeMeo, F. E., and Bottke, Jr., W. F., editors, *Asteroids IV*, pages 183–202. University of Arizona Press. 19, 31

Ďurech, J., Delbó, M., and Carry, B. (2012). Asteroid Models Derived from Thermal Infrared Data and Optical Lightcurves. In *Asteroids, Comets, Meteors (ACM) 2012*, LPI Contribution No. 1667. Lunar and Planetary Institute, Houston. Abstract #6118. 31

Ďurech, J., Delbo', M., Carry, B., Hanuš, J., and Alí-Lagoa, V. (2017). Asteroid Shapes and Thermal Properties from Combined Optical and Mid-Infrared Photometry Inversion. *Astronomy and Astrophysics*, 604:A27. 5, 12, 30, 31

Ďurech, J., Hanšs, J., Oszkiewicz, D., and Vanco, R. (2016). Asteroid models from the Lowell Photometric Database. *Astronomy & Astrophysics*, 587:A48. 91

Ďurech, J., Hanuš, J., Delbó, M., Alí-Lagoa, V., and Carry, B. (2014). Physical Properties of Asteroids Derived from a Novel Approach to Modeling of Optical Lightcurves and WISE Thermal Infrared Data. In *46th AAS/Division for Planetary Sciences Meeting*. Abstract #509.11. 19, 31

Dykhuis, M. J. and Greenberg, R. (2015). Collisional family structure within the Nysa–Polana complex. *Icarus*, 252:199–211. 130

Dykhuis, M. J., Molnar, L., Kooten, S. J. V., and Greenberg, R. (2014). Defining the Flora Family: Orbital Properties, Reflectance Properties and Age. *Icarus*, 243:111–128. 130

Emery, J. P., Fernández, Y. R., Kelley, M. S. P., Warden, K. T., Hergenrother, C., Lauretta, D. S., Drake, M. J., Campins, H., and Ziffer, J. (2014). Thermal Infrared Observations and Thermophysical Characterization and OSIRIS-REx Target Asteroid (101955) Bennu. *Icarus*, 234:17–35. 5, 30

Emery, J. P., Sprague, A. L., Witteborn, R. F., Colwell, J. E., Kozlowski, R. W. H., and Wooden, D. H. (1998). Mercury: Thermal Modeling and Mid-infrared (5–12 μm) Observations. *Icarus*, 136:104–123. 7, 15

Eppes, M.-C., Willis, A., Molaro, J., Abernathy, S., and Zhou, B. (2015). Cracks in Martian boulders exhibit preferred orientations that point to solar-induced thermal stress. *Nature Communications*, 6(6712). 137

Farinella, P. and Davis, D. R. (1992). Collision Rates and Impact Velocities in the Main Asteroid Belt. *Icarus*, 97:111–123. 134

Farinella, P., Froeschile, C., and Gonczi, R. (1994). Meteorite Delivery and Transport. *Symposium - International Astronomical Union*, 160:205–222. 231

Flynn, G. J., Consolmagno, G. J., Brown, P., and Macke, R. J. (2017). Physical properties of the stone meteorites: Implications for the properties of their parent bodies. *Chemie der Erde - Geochemistry*. 94, 97, 101

Frölich, C. (2009). Evidence of a Long-Term Trend in Total Solar Irradiance. *Astronomy and Astrophysics*, 501:L27–L30. 6

Fulvio, D., Brunetto, R., Vernazza, P., and Strazzulla, G. (2012). Space weathering of Vesta and V-type asteroids: new irradiation experiments on HED meteorites. *Astronomy & Astrophysics*, 537:L11. 150, 184

Fulvio, D., Perna, D., Ieva, S., Brunetto, R., Kanuchova, Z., Blanco, C., Strazzulla, G., and Dotto, E. (2016). Spectral characterization of v-type asteroids – i. space weathering effects and implications for v-type neas. *Monthly Notices of the Royal Astronomical Society*, 455:584–595. 221

Gaffey, M. J. (2001). Asteroids: Does space weathering matter? In *Lunar and Planetary Science Conference #32*. Lunar and Planetary Institute. Abstract #1587. 164

Gaffey, M. J. (2010). Space weathering and the interpretation of asteroid reflectance spectra. *Icarus*, 209:564–574. 150, 151

Gaffey, M. J., Bell, J. F., Brown, R. H., Burbine, T. H., Piatek, J. L., Reed, K. L., and Chaky, D. A. (1993). Mineralogical Variations Within the S-type Asteroid Class. *Icarus*, 106:573–602. 152, 153, 154, 214, 234

Gaffey, M. J., Cloutis, E. A., Kelley, M. S., and Reed, K. L. (2002). Mineralogy of Asteroids. In Bottke, Jr., W. F., Cellino, A., Paolicchi, P., and Binzel, R. P., editors, *Asteroids III*, pages 183–204. University of Arizona Press. 158, 213

Ghosh, A. and McSween, Jr., H. Y. (1998). A Thermal Model for the Differentiation of Asteroid 4 Vesta, Based on Radiogenic Heating. *Icarus*, 134(2). 234

Gietzen, K. M., Lacy, C. H. S., Ostrowski, D. R., and Sears, D. W. G. (2012). Irtf observations of s complex and other asteroids: Implications for surface compositions, the presence of clinopyroxenes, and their relationship to meteorites. *Meteoritics & Planetary Science*, 47:1789–1808. 214, 234

Gillis-Davis, J. J., Lucey, P. G., Bradley, J. P., Ishii, H. A., Kaluna, H. M., Misra, A., and Jr., H. C. C. (2017). Incremental laser space weathering of Allende reveals non-lunar like space weathering effects. *Icarus*, 286:1–14. 190, 191, 192

Gold, T. (1955). The Lunar Surface. *Monthly Notices of the Royal Astronomical Society*, 115:585–604. 146

Gould, B. A. (1855). On Peirce's Criterion for the Rejection of Doubtful Observations, with Tables for Facilitating its Application. *Astronomical Journal*, 4:81–87. 32, 52

Greenwood, R. C., Franchia, I. A., Kearsley, A. T., and O.Alard (2010). The relationship between CK and CV chondrites. *Geochimica et Cosmochimica Acta*, 74(5):1684–1705. 185

Guibout, V. and Scheeres, D. J. (2003). Stability of surface motion on a rotating ellipsoid. *Celestial Mechanics and Dynamical Astronomy*, 87(3):263–290. 142

Gundlach, B. and Blum, J. (2012). Outgassing of icy bodies in the Solar System – II. Heat transport in dry, porous surface dust layers. *Icarus*, 219:618–629. 102, 103

Gundlach, B. and Blum, J. (2013). A New Method to Determine the Grain Size of Planetary Regolith. *Icarus*, 223:479–492. 92, 102, 103, 108, 109

Hainaut, O. R., Boehnhardt, H., Snodgrass, C., Meech, K. J., Deller, J., Gillon, M., Jehin, E., Kuehrt, E., Lowry, S. C., Manfroid, J., Micheli, M., Mottola, S., Opitom, C., Vincent, J.-B., and Wainscoat, R. (2014). Continued activity in p/2013 p5 PANSTARRS. *Astronomy & Astrophysics*, 563:A75. 143

Hansen, O. L. (1977a). An Explanation of the Radiometric Method for Size and Albedo Determination. *Icarus*, 31:456–482. 15

Hansen, O. L. (1977b). On the Prograde Rotation of Asteroids. *Icarus*, 32:458–460. 12

Hanuš, J., Delbó, M., Ďurech, J., and Alí-Lagoa, V. (2015). Thermophysical Modeling of Asteroids from WISE Thermal Infrared Data – Significance of the Shape Model and the Pole Orientation Uncertainties. *Icarus*, 256:101–116. 5, 11, 29, 30, 31, 32, 33, 38

Hanuš, J., Delbo', M., Ďurech, J., and Alí-Lagoa, V. (2018). Thermophysical Modeling of Main-Belt Asteroids from WISE Thermal Data. *Icarus*, 309:297–337. 5, 11, 29, 33, 38, 39, 40, 41, 45, 85

Hanuš, J., Durech, J., Broz, M., Warner, B. D., Pilcher, F., Stephens, R., Oey, J., Bernasconi, L., Casulli, S., Behrend, R., Polishook, D., Henych, T., Lehky, M., Yoshida, F., and Ito, T. (2011). A study of asteroid pole-latitude distribution based on an extended set of shape models derived by the lightcurve inversion method. *Astronomy & Astrophysics*, 530:A134. 91

Hapke, B. (1984). Bidirectional Reflectance Spectroscopy 3. Correction for Macroscopic Roughness. *Icarus*, 59:41–59. 15, 73

Hapke, B. (1993). *Theory of Reflectance and Emittance Spectroscopy*. Cambridge University Press. 231

Hapke, B. (2001). Space weathering from Mercury to the asteroid belt. *Journal of Geophysical Research*, 106(5):10,039 – 10,073. 146, 150, 231

Hardersen, P. S., Reddy, V., Cloutis, E., Nowinski, M., Dievendorf, M., Genet, R. M., Becker, S., and Roberts, R. (2018). Basalt or not? near-infrared spectra, surface mineralogical estimates, and meteorite analogs for 33 vp-type asteroids. *The Astronomical Journal*, 156:11. 154

Harris, A. W. (1996). The Rotation Rates of Very Small Asteroids: Evidence for 'Rubble Pile' Structure. In *Lunar and Planetary Science Conference #27*, page 493. 142

Harris, A. W. (1998). A Thermal Model for Near-Earth Asteroids. *Icarus*, 131:291–301. 4, 6

Harris, A. W. (2005). The surface properties of small asteroids from thermal-infrared observations. *Proceedings of the International Astronomical Union*, pages 449–463. 24

Harris, A. W. and Davies, J. K. (1999). Physical Characteristics of Near-Earth Asteroids from Thermal Infrared Spectrophotometry. *Icarus*, 142:464–475. 8

Harris, A. W. and Drube, L. (2016). Thermal Tomography of Asteroid Surface Structure. *Astrophysical Journal*, 832:127. 11, 38, 88, 90

Harris, A. W. and Lagerros, J. S. V. (2002). Asteroids in the Thermal Infrared. In Bottke, Jr., W. F., Cellino, A., Paolicchi, P., and Binzel, R. P., editors, *Asteroids III*, pages 205–218. University of Arizona Press. 7

Hartmann, W. K. (1973). Ancient lunar mega-regolith and subsurface structure. *Icarus*, 18(4):634–636. 47

Hayne, P. O., Bandfield, J. L., Siegler, M. A., Vasavada, A. R., Ghent, R. R., Williams, J.-P., Greenhagen, B. T., Aharonson, O., Lucey, C. M. E. P. G., and Paige, D. A. (2017). Global Regolith Thermophysical Properties of the Moon From the Diviner Lunar Radiometer Experiment. *Journal of Geophysical Research: Planets*, 22:2371–2400. 44

Helfenstein, P., Veverka, J., Thomas, P. C., Simonelli, D. P., Lee, P., Klaasen, K., Johnson, T. V., Breneman, H., Head, J. W., Murchie, S., Fanale, F., Robinson, M., Clark, B., Granahan, J., Garbeil, H., McEwen, A. S., Kirk, R. L., Davies, M., Neukum, G., Mottola,

S., Wagner, R., Belton, M., Chapman, C., and Pilcher, C. (1994). Galileo Photometry of Asteroid 951 Gaspra. *Icarus*, 107:37–60. 147

Hinrichs, J. L. and Lucey, P. G. (2002). Temperature-dependent near-infrared spectral properties of minerals, meteorites, and lunar soil. *Icarus*, 155:169–180. 213

Hiroi, T., Abe, M., Kitazato, K., Abe, S., Clark, B. E., Sasaki, S., Ishiguro, M., and Barnouin-Jha, O. S. (2006). Developing space weathering on the asteroid 25143 Itokawa. *Nature*, 443:56–58. 147

Hiroi, T. and Sasaki, S. (2001). Importance of space weathering simulation products in compositional modeling of asteroids: 349 Dembowska and 446 Aeternitas as examples. *Meteoritics & Planetary Science*, 36:1587–1596. 150

Holsapple, K., Giblin, I., Housen, K., Nakamura, A., and Ryan, E. (2002). Asteroid Impacts: Laboratory Experiments and Scaling Laws. In Bottke, Jr., W. F., Cellino, A., Paolicchi, P., and Binzel, R. P., editors, *Asteroids III*, pages 443–462. University of Arizona Press. 134, 136

Hörz, F. and Schaal, R. B. (1981). Asteroidal agglutinate formation and implications for asteroidal surfaces. *Icarus*, 46(3):337–353. 108

Housen, K. R. and Holsapple, K. A. (2003). Impact cratering on porous asteroids. *Icarus*, 163:102–119. 47, 134

Housen, K. R. and Holsapple, K. A. (2011). Ejecta from impact craters. *Icarus*, 211:856–875. 134

Housen, K. R., Wilkening, L. L., Chapman, C. R., and Greenberg, R. (1979). Asteroidal Regoliths. *Icarus*, 39:317–351. 135

Hsieh, H. H., Yang, B., and Haghighipour, N. (2012). Optical and Dynamical Characterization of Comet-Like Main-Belt Asteroid (596) Scheila. *Astrophysical Journal*, 744(1):9. 141

Huss, G. R., Rubin, A. E., and Grossman, J. N. (2006). Thermal Metamorphism in Chondrites. In Lauretta, D. S. and McSween Jr., H. Y., editors, *Meteorites and the Early Solar System II*, pages 567–586. University of Arizona Press. 165

Ibrahim, E.-M. I. (2012). The Elastic Properties of Carbonaceous Chondrites. Master's thesis, University of Calgary. 99, 101

Ishiguro, M., Hanayama, H., Hasegawa, S., Sarugaku, Y., ichi Watanabe, J., Fujiwara, H., Terada, H., Hsieh, H. H., Vaubaillon, J. J., Kawai, N., Yanagisawa, K., Kuroda, D., Miyaji, T., Fukushima, H., Ohta, K., Hamanowa, H., Kim, J., Pyo, J., and Nakamura, A. M. (2011a). Interpretation of (596) Scheila's Triple Dust Tails. *Astrophysical Journal Letters*, 741(1):L24. 141

Ishiguro, M., Hanayama, H., Hasegawa, S., Sarugaku, Y., ichi Watanabe, J., Fujiwara, H., Terada, H., Hsieh, H. H., Vaubaillon, J. J., Kawai, N., Yanagisawa, K., Kuroda, D., Miyaji, T., Fukushima, H., Ohta, K., Hamanowa, H., Kim, J., Pyo, J., and Nakamura, A. M. (2011b). Observational Evidence for an Impact on the Main-Belt Asteroid (596) Scheila. *Astrophysical Journal Letters*, 740(1):L11. 141

Ishiguro, M., Hiroi, T., Tholen, D. J., Sasaki, S., Uedas, Y., Nimuras, T., Abe, M., Clark, B. E., Yamamoto, A., Yoshida, F., Nakamura, R., Hirata, N., Miyamoto, H., Yokota, Y., Hashimoto, T., Kubota, T., Nakamura, A. M., Gaskell, R. W., and Saito, J. (2007). Global mapping of the degree of space weathering on asteroid 25143 Itokawa by Hayabusa/AMICA observations. *Meteoritics & Planetary Science*, 42(10):1791–1800. 147

Jakosky, B. M. (1986). On the Thermal Properties of Martian Fines. *Icarus*, 66:117–124. 102

Jedicke, R., Nesvorný, D., Whiteley, R., Željko Ivezić, and Jurić, M. (2004). An age–colour relationship for main-belt S-complex asteroids. *Nature*, 429:275–277. 151

Jewitt, D. (2012). The Active Asteroids. *Astronomical Journal*, 143(3):66. 141, 142, 144

Jewitt, D., Agarwal, J., Weaver, H., Mutchler, M., and Larson, S. (2013). The Extraordinary Multi-Tailed Main-belt Comet P/2013 P5. *Astrophysical Journal Letters*, 778:L21. 142

Jewitt, D., Weaver, H., Agarwal, J., Mutchler, M., and Drahus, M. (2010). A recent disruption of the main-belt asteroid P/2010A2. *Nature*, 467:817–819. 141

Jewitt, D., Weaver, H., Mutchler, M., Larson, S., and Agarwal, J. (2011'). Hubble Space Telescope of Main-Belt Comet (596) Scheila. *Astrophysical Journal Letters*, 733:L4. 141

Johansen, A., Jacquet, E., Cuzzi, J. N., Morbidelli, A., and Gounelle, M. (2015). New paradigms for asteroid formation. In *Asteroids IV*. University of Arizona Press. 1

Johansen, A. and Lacerda, P. (2010). Prograde rotation of protoplanets by accretion of pebbles in a gaseous environment. *Monthly Notices of the Royal Astronomical Society*, 404:475–485. 91

Kaasalainen, M., Mottola, S., and Fulchignoni, M. (2002). Asteroid models from disk-integrated data. In Bottke, Jr., W. F., Cellino, A., Paolicchi, P., and Binzel, R. P., editors, *Asteroids III*, pages 139–150. University of Arizona Press. 1

Kanuchova, Z., Brunetto, R., Fulvio, D., and Strazzulla, G. (2015). Near-ultraviolet bluing after space weathering of silicates and meteorites. *Icarus*, 258:289–296. 175, 177

Kass, R. E. and Raftery, A. E. (1995). Bayes Factors. *Journal of the American Statistical Association*, 90(430):773–795. 123

Keil, K. (2014). Brachinite meteorites: Partial melt residues from an FeO-rich asteroid. *Chemie der Erde / Geochemistry*, 74:311–329. 185

Keller, L. P. and Clemett, S. J. (2001). Formation of nanophase iron in the lunar regolith. In *Lunar and Planetary Science Conference*, volume 32. 150

Klima, R. L., Dyar, M. D., and Pieters, C. M. (2011). Near-infrared spectra of clinopyroxenes: Effects of calcium content and crystal structure. *Meteoritics & Planetary Science*, 46(3):379–395. 216

Klima, R. L., Pieters, C. M., and Dyar, M. D. (2007). Spectroscopy of synthetic Mg-Fe pyroxenes I: Spin-allowed and spin-forbidden crystal field bands in the visible and near-infrared. *Meteoritics & Planetary Science*, 42(2):235–253. 216

Klima, R. L., Pieters, C. M., and Dyar, M. D. (2008). Characterization of the 1.2 μm M1 pyroxene band: Extracting cooling history from near-IR spectra of pyroxenes and pyroxene-dominated rocks. *Meteoritics & Planetary Science*, 43(10):1591–1604. 216

Knežević, Z., Lemaître, A., and Milani, A. (2002). The determination of asteroid proper elements. In Bottke, Jr., W. F., Cellino, A., Paolicchi, P., and Binzel, R. P., editors, *Asteroids III*, pages 603–612. University of Arizona Press. 222

Kohout, T., Čuda, J., Filip, J., Britt, D., Bradley, T., Tuček, J., Skála, R., Kletetschka, G., Kašlík, J., Malina, O., Šišková, K., and Zbořil, R. (2014). Space weathering simulations through controlled growth of iron nanoparticles on olivine. *Icarus*, 237:75–83. xiv, 150, 190, 192, 193, 233

Krumbein, W. C. and Aberdeen, E. J. (1937). The sediments of barataria bay [louisiana]. *Journal of Sedimentary Research*, 7:3–17. 109

Kryszczynska, A., Spina, A. L., Paolicchi, P., Harris, A. W., Breiter, S., and Pravec, P. (2007). New findings on asteroid spin-vector distributions. *Icarus*, 192:223–237. 91

Kurahashi, E., Yamanaka, C., Nakamura, K., and Sasaki, S. (2002). Laboratory simulation of space weathering: ESR measurements of nanophase metallic iron in laser-irradiated materials. *Earth, Planets, and Space*, 54:e5–e7. 190, 191, 192

Lagerros, J. S. V. (1996). Thermal Physics of Asteroids I. Effects of Shape, Heat Conduction and Beaming. *Astronomy and Astrophysics*, 310:1011–1020. 4, 12, 15, 31

Lagerros, J. S. V. (1997). Thermal Physics of Asteroids III. Irregular Shapes and Albedo Variegations. *Astronomy and Astrophysics*, 325:1226–1236. 30

Landsman, Z. A., Emery, J. P., Campins, H., Hanuš, J., Lim, L. F., and Cruikshank, D. P. (2018). Asteroid (16) psyche: Evidence for a silicate regolith from spitzer space telescope spectroscopy. *Icarus*, 304:58–73. 5

Lazzarin, M., Marchi, S., Moroz, L. V., Brunetto, R., Magrin, S., Paolicchi, P., and Strazzulla, G. (2006). Space Weathering in the Main Asteroid Belt: The Big Picture. *Astrophysical Journal*, 647:L179–L182. 150

Lazzaro, D., Angeli, C. A., Carvano, J. M., Mothé-Diniz, T., Duffard, R., and Florczak, M. (2004). S3OS2: the visible spectroscopic survey of 820 asteroids. *Icarus*, 172:179–220. 119, 161

Lebofsky, L. A. and Rieke, G. H. (1979). Thermal properties of 433 Eros. *Icarus*, 40:297–308. 8

Lebofsky, L. A., Sykes, M. V., Tedesco, E. F., Veeder, G. J., Matson, D. L., Brown, R. H., Gradie, J. C., Feierberg, M. A., and Rudy, R. J. (1986). A Refined 'Standard' Thermal Model for Asteroids Based on Observations of 1 Ceres and 2 Pallas. *Icarus*, 68:239–251. 4, 6

Lebofsky, L. A., Veeder, G. J., , Lebofsky, M. J., and Matson, D. L. (1978). Visual and radiometric photometry of 1580 Betulia. *Icarus*, 35:336–343. 4, 6

Ledbetter, H. M. and Reed, R. P. (1973). Elastic Properties of Metals and Alloys, I. Iron, Nickel, and Iron-Nickel Alloys. *Journal of Physical and Chemical Reference Data*, 2(3):531–618. 99, 101

Lee, P. (1996). Dust Levitation on Asteroids. *Icarus*, 124:181–194. 143

Lim, L. F., Emery, J. P., and Moskovitz, N. A. (2011). Mineralogy and Thermal Properties of V-type Asteroid 956 Elisa: Evidence for Diogenitic Material from the Spitzer IRS (5–35 μm) Spectrum. *Icarus*, 213:510–523. 8

Lindsay, S. S., Marchis, F., Emery, J. P., Enriquez, J. E., and Assafin, M. (2015). Classification and mineralogy of multiple asteroid systems from visible and near-infrared spectral data. *Icarus*, 247:53 – 70. 162

Loeffler, M. J., Dukes, C. A., and Baragiola, R. A. (2009). Irradiation of olivine by 4 keV He+: Simulation of space weathering by the solar wind. *Journal of Geophysical Research*, 114:E03003. 190, 191, 192

Loeffler, M. J., Dukes, C. A., Christoffersen, R., and Baragiola, R. A. (2016). Space weathering of silicates simulated by successive laser irradiation: In situ reflectance

measurements of Fo90, Fo99+, and SiO2. *Meteoritics & Planetary Science*, 51, 2:261–275. 190, 191, 192

Lord, S. D. (1992). A new software tool for computing Earth's atmospheric transmission of near- and far-infrared radiation. Technical Report 103957, NASA Technical Memorandum. 158

Lucey, P., Blewett, D. T., Taylor, G. J., and Hawke, B. R. (2000). Imaging of Lunar Surface Maturity. *Journal of Geophysical Research*, 105(8):20,377–20,386. 193

Lucey, P. G., Blewett, D. T., and Hawke, B. R. (1998). Mapping the FeO and TiO2 contentof the lunar surface with multispectralimagery. *Journal of Geophysical Research*, 103(2):3679–3699. 146

Macke, R. J. (2010). *Survey Of Meteorite Physical Properties Density, Porosity And Magnetic Susceptibility*. PhD thesis, University of Central Florida. 99, 101

MacLennan, E. M. and Emery, J. P. (2019). Thermophysical modeling of asteroid surfaces using ellipsoid shape models. *The Astronomical Journal*, 157(1):2. 4

Mainzer, A., Bauer, J., Grav, T., Masiero, J., Cutri, R. M., Dailey, J., Eisenhardt, P., McMillan, R. S., Wright, E., Walker, R., Jedicke, R., Spahr, T., Tholen, D., Alles, R., Beck, R., Brandenburg, H., Conrow, T., Evans, T., Fowler, J., Jarrett, T., Marsh, K., Masci, F., McCallon, H., Wheelock, S., Wittman, M., Wyatt, P., DeBaun, E., Elliott, G., Elsbury, D., Gautier, T., Gomillion, S., Leisawitz, D., Maleszewski, C., Micheli, M., and Wilkins, A. (2011a). PRELIMINARY RESULTS FROM NEOWISE: AN ENHANCEMENT TO THE WIDE-FIELD INFRARED SURVEY EXPLORERFOR SOLAR SYSTEM SCIENCE. *Astrophysical Journal*, 731:53. 5, 31, 52

Mainzer, A., Grav, T., Bauer, J., Masiero, J., McMillan, R. S., Cutri, R. M., Walker, R., Wright, E., Eisenhardt, P., Tholen, D. J., Spahr, T., Jedicke, R., Denneau, L., DeBaun, E., Elsbury, D., Gautier, T., Gomillion, S., Hand, E., Mo, W., Watkins, J., Wilkins, A., Bryngelson, G. L., Molina, A. D. P., Desai, S., Camus, M. G., Hidalgo,

S. L., Konstantopoulos, I., Larsen, J. A., Maleszewski, C., Malkan, M. A., Mauduit, J.-C., Mullan, B. L., Olszewski, E. W., Pforr, J., Saro, A., Scotti, J. V., and Wasserman, L. H. (2011b). NEOWISE Observations of near-Earth Objects: Preliminary Results. *The Astrophysical Journal*, 743:156. 7, 32, 38, 39, 85, 86, 104

Mainzer, A., Usui, F., and Trilling, D. E. (2015). Space-based thermal infrared studies of asteroids. In *Asteroids IV*. University of Arizona Press. 1

Marchi, S., Brunetto, R., Magrin, S., Lazzarin, M., and Gandolfi, D. (2005). Space weathering of near-Earth and main belt silicate-rich asteroids: observations and ion irradiation experiments. *Astronomy & Astrophysics*, 443:769–775. 150, 184, 190, 191, 192

Marchi, S., Magrin, S., Nesvorny, D., Paolicchi, P., and Lazzarin, M. (2006a). A spectral slope versus perihelion distance correlation for planet-crossing asteroids. *Monthly Notices of the Royal Astronomical Society*, 368:L39–L42. 151

Marchi, S., McSween, Jr., H. Y., O'Brien, D. P., Schenk, P., Sanctis, M. C. D., Gaskell, R., Jaumann, R., Mottola, S., Preusker, F., Raymonda, C. A., Roatsch, T., and Russell, C. T. (2012). The Violent Collisional History of Asteroid 4 Vesta. *Science*, 336(6082):690–694. 130

Marchi, S., Paolicchi, P., Lazzarin, M., and Magrin, S. (2006b). A General Spectral Slope-Exposure Relation for S-type main-belt and near-Earth Asteroids. *Astronomical Journal*, 131:1138–1141. 151, 232

Masiero, J. R., DeMeo, F. E., Kasuga, T., and Parker, A. H. (2015). Asteroid family physical properties. In *Asteroids IV*. University of Arizona Press. 2

Masiero, J. R., Mainzer, A. K., Grav, T., Bauer, J. M., Cutri, R. M., Dailey, J., Eisenhardt, P. R. M., McMillan, R. S., Spahr, T. B., Skrutskie, M. F., Tholen, D., Walker, R. G., Wright, E. L., DeBaun, E., Elsbury, D., Gautier, T., Gomillion, S., and Wilkins, A. (2011). Main Belt Asteroids with WISE/NEOWISE. I. Preliminary Albedos and Diameters. *The Astrophysical Journal*, 741:68–88. 7, 38, 39, 85, 86

Matter, A., Delbó, M., Carry, B., and Ligori, S. (2013). Evidence of a metal-rich surface for the asteroid (16) Psyche from interferometric observations in the thermal infrared. *Icarus*, 226:419–427. 45

Mazrouei, S., Daly, M. G., Barnouin, O. S., Ernst, C. M., and DeSouza, I. (2014). Block distributions on Itokawa. *Icarus*, 229:181–189. 44

McCord, T. B., Adams, J. B., and Johnson, T. V. (1970). Asteroid vesta: Spectral reflectivity and compositional implications. *Science*, 168:1445–1447. 175

McCord, T. B. and Johnson, T. V. (1970). Lunar spectral reflectivity (0.3 to 2.5 microns) and implications for remote mineralogical analysis. *Science*, 169:855–858. 146

McCord, T. B., Li, J., Combe, J., McSween, H. Y., Jaumann, R., Reddy, V., Tosi, F., Williams, D. A., Blewett, D. T., Turrini, D., Palomba, E., Pieters, C. M., Sanctis, M. C. D., Ammannito, E., Capria, M. T., Corre, L. L., Longobardo, A., Nathues, A., Mittlefehldt, D. W., Schröder, S. E., Hiesinger, H., Beck, A. W., Capaccioni, F., Carsenty, U., Keller, H. U., Denevi, B. W., Sunshine, J. M., Raymond, C. A., and Russell, C. T. (2012). Dark material on vesta from the infall of carbonaceous volatile-rich material. *Nature*, 491(7422):83–86. 221, 232

McFadden, L. A., Gaffey, M. J., and McCord, T. B. (1985). Near-earth asteroids: Possible sources from reflectance spectroscopy. *Science*, 229(4709):160–163. 3

McKay, D. S., Heiken, G., Basu, A., Blanford, G., Simon, S., Reedy, R., French, B. M., and Papike, J. (1991). The Lunar Regolith. In *Lunar Sourcebook*, pages 285–356. New York: Cambridge University Press. 44

McKay, D. S., Swindle, T. D., and Greenberg, R. (1989). Asteroidal regoliths - what we do not know. In Binzel, R. P., Gehrels, T., and Matthews, M. S., editors, *Asteroids II*, pages 617–642. University of Arizona Press. 135

McSween, Jr., H. Y., Binzel, R. P., de Sanctis, M. C., Ammannito, E., Prettyman, T. H., Beck, A. W., Reddy, V., Corre, L., Gaffey, M. J., McCord, T. B., Raymond, C. A.,

and Russell, C. T. (2013). Dawn; the vesta-hed connection; and the geologic context for eucrites, diogenites, and howardites. *Meteoritics and Planetary Science*, 48:2090–2104. 175, 178

McSween, Jr., H. Y. and Labotka, T. (1993). Oxidation during metamorphism of the ordinary chondrites. *Geochimica et Cosmochimica Acta*, 57(5):1105–1114. 235

McSween, Jr., H. Y., Lauretta, D. S., and Leshin, L. A. (2006). Recent advances in meteoritics and cosmochemistry. In Lauretta, D. S. and McSween, H. Y., editors, *Meteorites and the Early Solar System II*, pages 53–66. University of Arizona Press. 2

Michel, P., DeMeo, F. E., and Bottke, W. F. (2015). Asteroids: Recent advances and new perspectives. In *Asteroids IV*. University of Arizona Press. 1

Milani, A., Cellino, A., Knezevic, Z., Novakovic, B., Spoto, F., and Paolicchi, P. (2014). Asteroid families classification: Exploiting very large datasets. *Icarus*, 239:46–73. 130

Milani, A., Spoto, F., Knezevic, Z., Novakovic, B., and Tsirvoulis, G. (2015). Families classification including multiopposition asteroids. *Proceedings of the International Astronomical Union*, 10(S318):28–45. 130

Molaro, J. and Byrne, S. (2012). Rates of temperature change of airless landscapes and implications for thermal stress weathering. *Jounral of Geophysical Research*, 117:E10011. 47, 137, 138

Molaro, J. L., Byrne, S., and Langer, S. A. (2015). Grain-scale thermoelastic stresses and spatiotemporal temperature gradients on airless bodies, implications for rock breakdown. *Journal of Geophysical Research: Planets*, 120:255–277. 48, 137, 139

Molaro, J. L. and McKay, C. P. (2010). Processes controlling rapid†temperature variations on rock surfaces. *Earth Surface Processes Landforms*, 35:501–507. 137

Morbidelli, A., Bottke, Jr., W. F., Froeschlé, C., and Michel, P. (2002). Origin and evolution of near-earth objects. In Bottke, Jr., W. F., Cellino, A., Paolicchi, P., and Binzel, R. P., editors, *Asteroids III*. University of Arizona Press. 2

Morbidelli, A., Chambers, Lunine, J. I., Petit, J. M., Robert, F., Valsecch, G. B., and Cryr, K. E. (2000). Source regions and timescales for the delivery of water to the Earth. *Meteoritics & PIanetary Science*, 35:1309–1320. 232

Moroz, L. V., Fisenko, A. V., Semjonova, L. F., Pieters, C. M., and Korotaeva, N. N. (1996). Optical Effects of Regolith Processes on S-Asteroids as Simulated by Laser Shots on Ordinary Chondrite and Other Mafic Materials. *Icarus*, 122:366–382. 149, 150

Morris, R. V. (1978). The surface exposure (mature) of lunar soils: Some concept and Is/Feo compilation. In *Proceedings of the Lunar and Planetary Science Conference*, volume 9th, pages 2287–2297. 146

Morrison, D. (1973). Determination of Radii of Satellites and Asteroids from Radiometry and Photometry. *Icarus*, 19:1–14. 8

Morrison, D. (1977). Asteroid Sizes and Albedos. *Icarus*, 31:185–220. 12

Moskovitz, N. A., Willman, M., Burbine, T. H., Binzel, R. P., and Bus, S. J. (2010). A spectroscopic comparison of HED meteorites and V-type asteroids in the inner Main Belt. *Icarus*, 208:773–788. 154, 216, 221

Mothé-Diniz, T., Carvano, J., Bus, S., Duffard, R., and Burbine, T. (2008). Mineralogical analysis of the eos family from near-infrared spectra. *Icarus*, 195(1):277–294. 218

Mueller, M. (2007). *Surface Properties of Asteroids from Mid-Infrared Observations and Thermophysical Modeling*. PhD thesis, Freie Universitaet Berlin. 4, 8, 9, 21, 44

Mueller, M., Marchis, F., Emery, J. P., Harris, A. W., Mottola, S., Hestroffer, D., Berthier, J., and di Martino, M. (2010). Eclipsing binary Trojan asteroid Patroclus: Thermal inertia from Spitzer observations. *Icarus*, 205:505. 40, 88

Mueller, T. G. and Lagerros, J. S. V. (1998). Asteroids as far-infrared photometric standards for isophot. *Astronomy & Astrophysics*, 338:340–352. 44

Muinonen, K., Piironen, J., Shkuratov, Y. G., Ovcharenko, A., and Clark, B. E. (2002). Asteroid Photometric and Polarimetric Phase Effects. In Bottke, Jr., W. F., Cellino, A., Paolicchi, P., and Binzel, R. P., editors, *Asteroids III*. University of Arizona Press. 1

Müller, T. G., Ďurech, J., Ishiguro, M., Mueller, M., Krühler, T., Yang, H., Kim, M.-J., O'Rourke, L., Usui, F., Kiss, C., Altieri, B., Carry, B., Choi, Y.-J., Delbo, M., Emery, J. P., Greiner, J., Hasegawa, S., Hora, J. L., Knust, F., Kuroda, D., Osip, D., Rau, A., Rivkin, A., Schady, P., Thomas-Osip, J., Trilling, D., Urakawa, S., Vilenius, E., Weissman, P., and Zeidler, P. (2017). Hayabusa-2 mission target asteroid 162173 Ryugu (1999 JU3): Searching for the object's spin-axis orientation. *Astronomy & Astrophysics*, 599:A103. 5, 11

Müller, T. G., Hasegawa, S., and Usui, F. (2014). (25143) Itokawa: The Power of Radiometric Techniques for the Interpretation of Remote Thermal Observations in the Light of the Hayabusa Rendezvous Results. *Publications of the Astronomical Society of Japan*, 66:52. 5, 11, 12

Müller, T. G., O'Rourke, L., Barucci, A. M., Pál, A., Kiss, C., Zeidler, P., Altieri, González-Garcia, B. M., and Küppers, M. (2012). Physical Peroperties of OSIRIS-REx Target Asteroid (101955) 1999RQ36. *Astronomy and Astrophysics*, 548:A36. 12

Müller, T. G., Ďurech, J., Hasegawa, S., Abe, M., Kawakami, K., Kasuga, T., Kinoshita, D., Kuroda, D., Urakawa, S., Okumura, S., Sarugaku, Y., Miyasaka, S., Takagi, Y., Weissman, P. R., Choi, Y.-J., Larson, S., Yanagisawa, K., and Nagayama, S. (2011). Thermo-physical properties of 162173 (1993 JU3) a Potential Flyby and Rendezvous Target for Interplanetary Missions. *Astronomy and Astrophysics*, 525:A145. 5, 11, 12

Murchie, S., Robinson, M., Clark, B., Li, H., Thomas, P., Joseph, J., Bussey, B., Domingue, D., Veverka, J., Izenberg, N., and Chapman, C. (2002). Color Variations on Eros from NEAR Multispectral Imaging. *Icarus*, 155(1):145–168. 147

Murdoch, N., Sánchez, P., Schwartz, S. R., and Miyamoto, H. (2015). Asteroid Surface Geophysics. In Michel, P., DeMeo, F. E., and Bottke Jr., W. F., editors, *Asteroids IV*, pages 767–792. University of Arizona Press. 139

Myhrvold, N. (2016). Comparing NEO Search Telescopes. *Publications of the Astronomical Society of the Pacific*, 128:045004. 4, 6

Nakamura, A. and Fujiwara, A. (1991). Velocity Distribution of Fragments Formed ina Simulated Collisional Disruption. *Icarus*, 92:132–146. 134

Nakamura, A. M., Fujiwara, A., and Kadono, T. (1994). Velocity of finer fragments from impact. *Planetary and Space Science*, 42(13):1043–1052. 134

Nesvorný, D., Bottke, Jr., W. F., Dones, L., and Levison, H. F. (2002a). The recent breakup of an asteroid in the main-belt region. *Nature*, 417. 129

Nesvorný, D., Bottke, Jr., W. F., Levison, H. F., and Dones, L. (2003). Recent origin of the solar system dust bands. *Astrophysical Journal*, 591:486–497. 129

Nesvorný, D., Bottke Jr., W. F., Vokrouhlicky, D., Sykes, M., Lien, D. J., and Stansberry, J. (2008). Origin of the near-ecliptic circumsolar dust band. *Astrophysical Journal*, 679:L143. 130

Nesvorný, D., Broz, M., and Carruba, V. (2015). Identification and Dynamical Properties of Asteroid Families. In Michel, P., DeMeo, F. E., and Bottke Jr., W. F., editors, *Asteroids IV*, pages 297–321. University of Arizona Press. 1, 129, 130, 136

Nesvorný, D., Ferraz-Mello, S., Holman, M., and Morbidelli, A. (2002b). Regular and chaotic dynamics in the mean-motion resonances: Implications for the structure and evolution of the asteroid belt. In Bottke, Jr., W. F., Cellino, A., Paolicchi, P., and Binzel, R. P., editors, *Asteroids III*. University of Arizona Press. 2

Nesvorný, D., Jedicke, R., Whiteley, R. J., and Ivezic, Z. (2005). Evidence for asteroid space weathering from the Sloan Digital Sky Survey. *Icarus*, 173:132–152. 130, 151

Nesvorný, D., Vokrouhlicky, D., Morbidelli, A., and Bottke Jr., W. F. (2009). Asteroidal source of L chondrite meteorites. *Icarus*, 200:698–701. 130

Nettles, J. W., Staid, M., Besse, S., Boardman, J., Clark, R. N., Dhingra, D., Isaacson, P., Klima, R., Kramer, G., Pieters, C. M., and Taylor, L. A. (2011). Optical maturity

variation in lunar spectra as measured by Moon Mineralogy Mapper data. *Journal of Geophysical Research*, 116:E00G17. 193

Noble, S. K., Keller, L. P., and Pieters, C. M. (2005). Evidence of space weathering in regolith breccias i: Lunar regolith breccias. *Meteoritics & Planetary Science*, 40:397. 108, 151

Noble, S. K., Keller, L. P., and Pieters, C. M. (2010). Evidence of space weathering in regolith breccias II: Asteroidal regolith breccias. *Meteoritics & Planetary Science*, 45(12):2007–2015. 108

Noble, S. K., Pieters, C. M., and Keller, L. P. (2007). An experimental approach to understanding the optical effects of space weathering. *Icarus*, 192:629–642. 151

Noguchi, T., Kimura, M., Hashimoto, T., Konno, M., Nakamura, T., Zolensky, M. E., Okazaki, R., Tanaka, M., Tsuchiyama, A., Nakato, A., Ogami, T., Ishida, H., Sagae, R., Tsujimoto, S., Matsumoto, T., Matsuno, J., Fujimura, A., Abe, M., Yada, T., Mukai, T., Ueno, M., Shirai, T. O. K., and Ishibashi, Y. (2014). Space weathered rims found on the surfaces of the Itokawa dust particles. *Meteoritics and Planetary Science*, 49(2):188–214. 151

Opeil, C. P., Consolmagno, G. J., and Britt, D. T. (2010). The Thermal Conductivity of Meteorites: New Measurements and Analysis. *Icarus*, 208:449–454. 96, 97, 100, 101

Opeil, C. P., Consolmagno, G. J., Safarik, D. J., and Britt, D. T. (2012). Stony meteorite thermal properties and their relationship with meteorite chemical and physical states. *Meteoritics & Planetary Science*, 47(3):319–329. 96, 97, 100

Oszkiewicz, D. A., Muinonen, K., Bowell, E., Trilling, D., Penttilä, A., Pieniluoma, T., Wasserman, L. H., and Enga, M.-T. (2011). Online multi-parameter phase-curve fitting and application to a large corpus of asteroid photometric data. *Journal of Quantitative Spectroscopy & Radiative Transfer*, 112:1919–1929. 48

Peirce, B. (1852). Criterion for the Rejection of Doubtful Observations. *Astronomical Journal*, 2:161–163. 32, 52

Pieters, C. M., Ammannito, E., Blewett, D. T., Denevi, B. W., Sanctis, M. C. D., Gaffey, M. J., Corre, L. L., Li, J.-Y., Marchi, S., McCord, T. B., McFadden, L. A., Mittlefehldt, D. W., Nathues, A., Palmer, E., Reddy, V., Raymond, C. A., and Russell, C. T. (2012). Distinctive space weathering on vesta from regolith mixing processes. *Nature*, 491(7422):79–82. 232

Pieters, C. M. and Hiroi, T. (2004). Relab (reflectance experiment laboratory): A nasa multiuser spectroscopy facility. In *Lunar and Planetary Science Conference*. 161

Pieters, C. M. and Noble, S. K. (2016). Space weathering on airless bodies. *Journal of Geophysical Research: Planets*, 121:1865–1884. 146

Pieters, C. M., Taylor, L. A., Noble, S. K., Keller, L. P., Watson, B., Morris, R. V., Allen, C. C., McKay, D. S., and Wentworth, S. (2000). Space weathering on airless bodies: Resolving a mystery with lunar samples. *Meteoritics & Space Science*, 35:1101–1107. 146, 150

Piqueux, S. and Christensen, P. R. (2009). A model of thermal conductivity for planetary soils: 1. theory for unconsolidated soils. *Journal of Geophysical Research: Planets*, 114:E9. 102

Pravec, P., Harris, A., Vokrouhlický, D., Warner, B., Kušnirák, P., Hornoch, K., Pray, D., Higgins, D., Oey, J., Galád, A., Gajdoš, Š., Kornoš, L., Világi, J., Husárik, M., Krugly, Y., Shevchenko, V., Chiorny, V., Gaftonyuk, N., Cooney, W., Gross, J., Terrell, D., Stephens, R., Dyvig, R., Reddy, V., Ries, J., Colas, F., Lecacheux, J., Durkee, R., Masi, G., Koff, R., and Goncalves, R. (2008). Spin rate distribution of small asteroids. *Icarus*, 197(2):497–504. 143

Pravec, P. and Harris, A. W. (2000). Fast and Slow Rotation of Asteroids. *Icarus*, 148:12–20. 142

Pravec, P. and Harris, A. W. (2007). Binary Asteroid Population 1. Angular Momentum Content. *Icarus*, 190:250–259. 9

Pravec, P., Harris, A. W., and Michalowski, T. (2002). Asteroid rotations. In Bottke, Jr., W. F., Cellino, A., Paolicchi, P., and Binzel, R. P., editors, *Asteroids III*. University of Arizona Press. 2

Presley, M. A. (2010). Thermal conductivity measurements of particulate materials: 4. effect of bulk density for granular particles. *Jounral of Geophysical Research*, 115:E07003. 102

Presley, M. A. and Christansen, P. R. (1997). Thermal conductivity measurements of particulate materials: 2. results. *Journal of Geophysical Research*, 102(E3):6551–6566. 102

Presley, M. A. and Christansen, P. R. (2010). Thermal conductivity measurements of particulate materials: 5. effect of bulk density and particle shape. *Journal of Geophysical Research*, 115:E07004. 102

Presley, M. A. and Craddock, R. A. (2006). Thermal conductivity measurements of particulate materials: 3. natural samples and mixtures of particle sizes. *Journal of Geophysical Research*, 111:E09013. 102, 103, 108

Press, W. H., Teukolsky, S. A., Vetterling, W. T., and Flannery, B. P. (2007). *Numerical Recipes 3rd Edition*. Cambridge University Press. 20, 279, 280

Rayner, J. (2017). *SpeX Observing Manual*. NASA Infrared Telescope Facility, Institute for Astronomy, University of Hawaii, 4th edition. 155

Rayner, J. T., Toomey, D. W., Onaka, P. M., Denault, A. J., Stahlberger, W. E., Vacca, W. D., Cushing, M. C., and Wang, S. (2003). SpeX: A Medium-Resolution 0.8-5.5 micron Spectrograph and Imager for the NASA Infrared Telescope Facility. *Publications of the Astronomical Society of the Pacific*, 115(362). 155, 158

Reddy, V., Dunn, T. L., Thomas, C. A., Moskovitz, N. A., and Burbine, T. H. (2015). Mineralogy and Surface Composition of Asteroids. In Michel, P., DeMeo, F. E., and Bottke Jr., W. F., editors, *Asteroids IV*, pages 43–63. University of Arizona Press. 1, 3, 93, 213

Reddy, V., Nathues, A., J.Gaffey, M., and Schaeff, S. (2011). Mineralogical characterization of potential targets for the ASTEX mission scenario. *Planetary and Space Science*, 59:772–778. 213

Reddy, V., Sanchez, J. A., Nathues, A., Moskovitz, N. A., Li, J.-Y., Cloutis, E. A., Archer, K., Tucker, R. A., Gaffey, M. J., Mann, J. P., Sierks, H., and Schade, U. (2012). Photometric, spectral phase and temperature effects on 4 Vesta and HED meteorites: Implications for the Dawn mission. *Icarus*, 217:153–168. 212

Rivkin, A. S., Howell, E., Emery, J. P., and Sunshine, J. (2017). Evidence for OH or H2O on the Surface of 433 Eros and 1036 Ganymed. *Icarus*, 304:74–82. 38

Rivkin, A. S., Thomas, C. A., Trilling, D. E., therese Enga, M., and Grier, J. A. (2011). Ordinary chondrite-like colors in small Koronis family members. *Icarus*, 211:1294–1297. 152

Robinson, M. S., Thomas, P. C., Veverka, J., Murchie, S., and Carcich, B. (2001). The nature of ponded deposits on Eros. *Nature*, 413:396. 144

Robinson, M. S., Thomas, P. C., Veverka, J., Murchie, S. L., and Wilcox, B. B. (2002). The Geology of 433 Eros. *Meteoritics & Planetary Science*, 37:1651–1684. 44

Ross, S. M. (2003). Peirce's Criterion for the Elimination of Suspect Experimental Data. *Journal of Engineering Technology*, 20:38–41. 33

Rozitis, B. (2017). The Surface Roughness of (433) Eros as Measured by Thermal-Infrared Beaming. *Monthy Notices of the Royal Astronomical Society*, 464:915–923. 11, 12

Rozitis, B., Duddy, S. R., Green, S. F., and Lowry, S. C. (2013). A Thermophysical Analysis of the (1862) Apollo Yarkovsky and YORP Effects. *Astronomy and Astrophysics*, 555:A20. 30

Rozitis, B. and Green, S. F. (2011). Directional Characteristics of Thermal–Infrared Beaming from Atmosphereless Planetary Surfaces – A New Thermophysical Model. *Monthy Notices of the Royal Astronomical Society*, 415:2042–2062. 4, 7

Rozitis, B. and Green, S. F. (2013). The Influence of Global Self-Heating on the Yarkovsky and YORP Effects. *Monthy Notices of the Royal Astronomical Society*, 433:603–621. 29, 30

Rozitis, B. and Green, S. F. (2014). Physical Characterisation of near-Earth Asteroid (1620) Geographos: Reconciling Radar and Thermal-Infrared Observations. *Astronomy and Astrophysics*, 568:A43. 5, 30

Rozitis, B., Green, S. F., MacLennan, E., and Emery, J. P. (2018). Observing the Variation of Asteroid Thermal Inertia with Heliocentric Distance. *Monthly Notices of the Royal Astronomical Society*, 477(2):1782–1802. 5, 38, 40, 42, 45, 85, 87

Rozitis, B., MacLennan, E. M., and Emery, J. P. (2014). Cohesive forces prevent the rotational breakup of rubble-pile asteroid (29075) 1950 DA. *Nature*, 512:174. 5, 140

Rubin, A. E. and Ma, C. (2017). Meteoritic minerals and their origins. *Chemie der Erde*, 77:325–385. 214

Russell, H. N. (1916). On the Albedo of Planets and their Natural Satellites. *Astrophysical Journal*, 43(3):173–196. 9

Sanchez, J. A., Reddy, V., Kelley, M. S., Cloutis, E. A., Bottke Jr., W. F., Nesvorný, D., Lucas, M. P., Hardersen, P. S., Gaffey, M. J., Abell, P. A., and Corre, L. L. (2014). Olivine-dominated asteroids: Mineralogy and origin. *Icarus*, 228:288–300. 212, 213, 218

Sanchez, J. A., Reddy, V., Nathues, A., Cloutis, E. A., Mann, P., and Hiesinger, H. (2012). Phase reddening on near-Earth asteroids: Implications for mineralogical analysis, space weathering and taxonomic classification. *Icarus*, 220:36–50. 152, 212

Sasaki, S., Hiroi, T., Nakamura, K., Hamabe, Y., Kurahashi, E., and Yamada, M. (2002). Simulation of space weathering by nanosecond pulse laser heating: Dependence on mineral composition, weathering trend of asteroids and discovery of nanophase iron particles. *Advances in Space Research*, 29(5):783–788. 150

Sasaki, S., Kurahashi, E., and Nakamura, C. Y. K. (2003). Laboratory simulation of space weathering: Changes of optical properties and TEM/ESR confirmation of nanophase metallic iron. *Advances in Space Research*, 31(12):2537–2542. 150

Sasaki, S., Nakamura, K., Hamabe, Y., Kurahashi, E., and Hiroi, T. (2001). Production of iron nanoparticles by laser irradiation in a simulation of lunar-like space weathering. *Nature*, 410:555–557. 150, 190, 194

Scheeres, D. (2015). Landslides and mass shedding on spinning spheroidal asteroids. *Icarus*, 247:1–17. 142

Scheeres, D. J., Hartzell, C. M., Sańchez, P., and Swift, M. (2010). Scaling forces to asteroid surfaces: the role of cohesion. *Icarus*, 210:968–984. 139, 140, 141

Schröder, S., Keller, S. M. H. U., Raymond, C. A., and Russell, C. T. (2013). Resolved Photometry of Vesta Reveals Physical Properties of Crater Regolith. *Planetary and Space Science*, 85:198–213. 45

Scott, E. R. D., Keil, K., Goldstein, J. I., Asphaug, E., Bottke, Jr., W. F., and Moskovitz, N. A. (2015). Early impact history and dynamical origin of differentiated meteorites and asteroids. In *Asteroids IV*. University of Arizona Press. 2

Shestopalov, D. I., Golubeva, L. F., and Cloutis, E. A. (2013). Optical maturation of asteroid surfaces. *Icarus*, 225:781–793. 150

Simpson, E. H. (1951). The Interpretation of Interaction in Contingency Tables. *Journal of the Royal Statistical Society, Series B*, 13:238–241. 93

Snodgrass, C., Tubiana, C., Vincent, J.-B., Sierks, H., Hviid, S., Moissl, R., Boehnhardt, H., Barbieri, C., Koschny, D., Lamy, P., Rickman, H., Rodrigo, R., Carry, B., Lowry, S. C., Laird, R. J. M., Weissman, P. R., Fitzsimmons, A., Marchi, S., and the OSIRIS team (2010). A collision in 2009 as the origin of the debris trail of asteroid P/2010A2. *Nature*, 467:814–816. 141

Spencer, J. R. (1990). A Rough-Surface Thermophysical Model for Airless Planets. *Icarus*, 83:27–38. 4, 5, 7, 11, 15

Spencer, J. R., Lebofsky, L. A., and Sykes, M. V. (1989). Systematic Biases in Radiometric Diameter Determinations. *Icarus*, 78:337–354. 4, 7, 13, 14, 28, 85

Spina, A. L., Paolicchi, P., Kryszczynska, A., and Pravec, P. (2004). Retrograde spins of near-Earth asteroids from the Yarkovsky effect. *Nature*, 428:400. 91

Spoto, F., Milani, A., and Knežević, Z. (2015). Asteroid family ages. *Icarus*, 257:275–289. 130

Strazzulla, G., Dotto, E., Binzel, R., Brunetto, R., Barucci, M., Blanco, A., and Orofino, V. (2005). Spectral alteration of the meteorite epinal (h5) induced by heavy ion irradiation: a simulation of space weathering effects on near-earth asteroids. *Icarus*, 174(1):31–35. 175, 177

Sullivan, R., Greeley, R., Pappalardo, R., Asphaug, E., Moore, J. M., Morrison, D., Belton, M. J. S., Carr, M., Chapman, C. R., Geissler, P., Greenberg, R., Granahan, J., III, J. W. H., Kirk, R., McEwen, A., Lee, P., Thomas, P. C., and Veverka, J. (1996). Geology of 243 Ida. *Icarus*, 120(41):119–139. 147

Sullivan, R. J., Thomas, P. C., Murchie, S. L., and Robinson, M. S. (2002). Asteroid geology from galileo and near shoemaker data. In Bottke, Jr., W. F., Cellino, A., Paolicchi, P., and Binzel, R. P., editors, *Asteroids III*. University of Arizona Press. 2

Sunshine, J. M., Bus, S. J., Corrigan, C. M., McCoy, T. J., and Burbine, T. H. (2007). Olivine-dominated asteroids and meteorites: Distinguishing nebular and igneous histories. *Meteoritics & Planetary Science*, 42(2):155–170. 154, 218

Sunshine, J. M. and Pieters, C. M. (1999). Determining the composition of olivine from reflectance spectroscopy. *Journal of Geophysical Research*, 103(E3):13,675–13,68. 213

Swinbank, R. and Purser, R. J. (2006). Fibonacci Grids: A Novel Approach to Global Modelling. *Quarterly Journal of the Royal Meteorological Society*, 132:1769–1763. 20, 75

Szurgot, M., Wach, R. A., and Przylibski, T. A. (2012). Thermophysical Properties of the Soltmany Meteorite. *Meteorites*, 2(1-2):53–65. 97, 100, 101

Taylor, J. R. (1997). Rejection of data. In *An Introduction of Error Analysis*, pages 165–172. University Science Books. 33

Taylor, L. A., Pieters, C. M., Keller, L. P., Morris, R. V., McKay, D. S., Patchen, A., and Wentworth, S. (2001). The effects of space weathering on Apollo 17 mare soils: Petrographic and chemical characterization. *Meteoritics & Planetary Science*, 36:285–289. 146

Tholen, D. J. (1984). *Asteroid taxonomy from cluster analysis of photometry.* PhD thesis, University of Arizona. 92, 93, 119

Thomas, C. A., Emery, J. P., Trilling, D. E., Delbó, M., Hora, J. L., and Mueller, M. (2014). Physical characterization of Warm Spitzer-observed near-Earth objects. *Icarus*, 228:217–246. 120

Thomas, C. A., Rivkin, A. S., Trilling, D. E., therese Enga, M., and Grier, J. A. (2011). Space weathering of small Koronis family members. *Icarus*, 212:158–166. 152

Thomas, C. A., Trilling, D. E., and Rivkin, A. S. (2012). Space weathering of small Koronis family asteroids in the SDSS Moving Object Catalog. *Icarus*, 219:505–507. 152, 234

Thomas, P. C., Veverka, J., Robinson, M. S., and Murchie, S. (2001). Shoemaker crater as the source of most ejecta blocks on the asteroid 433 Eros. *Nature Letters*, 413:394–396. 134

Trilling, D. E., Mueller, M., Hora, J. L., Harris, A. W., Bhattacharya, B., Bottke, Jr., W. F., Chesley, S., Delbo', M., Emery, J. P., Fazio, G., Mainzer, A., Penprase, B., Smith, H. A., Spahr, T. B., Stansberry, J. A., and Thomas, C. A. (2010). ExploreNEOs. I. Description and First Results from the Warm Spitzer Near-Earth Object Survey. *Icarus*, 140:770–784. 7

Vasavada, A. R., Bandfield, J. L., Greenhagen, B. T., Hayne, P. O., Siegler, M. A., Williams, J.-P., and Paige, D. A. (2012). Lunar equatorial surface temperatures and regolith properties from the Diviner Lunar Radiometer Experiment. *Journal of Geophysical Research*, 117:E00H18. 44

Vasavada, A. R., Paige, D. A., and Wood, S. E. (1999). Near-surface temperatures on mercury and the moon and the stability of polar ice deposits. *Icarus*, 141(2):179–193. 38

Vernazza, P., Brunetto, R., Strazzulla, G., Fulchignoni, M., Rochette, P., Meyer-Vernet, N., and Zouganelis, I. (2006). Asteroid colors: a novel tool for magnetic field detection? The case of Vesta. *Astronomy & Astrophysics*, 451:L43–L46. 150, 184

Vernazza, P., nd A. Rossi, R. P. B., Fulchignoni, M., and Birlan, M. (2009). Solar wind as the origin of rapid reddening of asteroid surfaces. *Nature*, 458:993–995. 151, 233

Vernazza, P., Zanda, B., Binzel, R. P., Hiroi, T., DeMeo, F. E., Birlan, M., Hewins, R., Ricci, L., Barge, P., and Lockhart, M. (2014). Multiple and Fast: The Accretion of Ordinary Chondrite Parent Bodies. *Astrophysical Journal*, 791(2):120. 130

Veverka, J., Helfenstein, P., Lee, P., Thomas, P., McEwen, A., Belton, M., Klaasen, K., Johnson, T. V., Granahan, J., Fanale, F., Geissler, P., and III, J. W. H. (1996). Ida and Dactyl: Spectral Reflectance and Color Variations. *Icarus*, 120(37):66–76. 147

Vokrouhlický, D., Bottke, Jr., W. F., Chesley, S. R., Scheeres, D. J., and Statler, T. S. (2015). The yarkovsky and YORP effects. In *Asteroids IV*. University of Arizona Press. 2

Wach, R. A., Adamus, A., and Szurgot, M. (2013). Specific heat capacity of sołtmany and nwa 4560 meteorites. *Meteorit. Planet Sci.*, 48:5017. 97, 100

Walsh, K. J. (2018). Rubble pile asteroids. *Annual Review of Astronomy and Astrophysics*, 56(1):593–624. 234

Warner, B. D., Harris, A. W., and Pravec, P. (2009). The Asteroid Lightcurve Database. *Icarus*, 202:134–146. 48

Watson, K. (1964). *I. The thermal conductivity measurements of selected silicate powders in vacuum from 150o - 350oK, II. An interpretation of the moon's eclipse and lunation cooling as observed through Earth's atmosphere from 8-14 microns*. PhD thesis, California Institute of Technology. 102

Waza, T., Matsui, T., and Kani, K. (1985). Laboratory simulation of a planetesimal collision. 2. ejecta velocity distribution. *Journal of Geophysical Research*, 90(B2):1995. 134

Weisberg, M. K., McCoy, T. J., and Krot, A. N. (2006). Systematics and evaluation of meteorite classification. In Lauretta, D. S. and McSween Jr., H. Y., editors, *Meteorites and the Early Solar System II*. University of Arizona Press. 2

Welch, B. L. (1947). The Generalization of 'Student's' Problem When Several Different Population Variances are Involved. *Biometrika*, 34(1-2):28–35. 126

Wesselink, A. J. (1948). Heat conductivity and nature of the lunar surface material. *Bull. Astron. Inst. Netherlands*, 10:351–363. 44

Willman, M., Jedicke, R., Moskovitz, N., Nesvorný, D., Vokrouhlický, D., and Mothé-Diniz, T. (2010). Using the youngest asteroid clusters to constrain the space weathering and gardening rate on s-complex asteroids. *Icarus*, 208:758–772. 151

Willman, M., Jedicke, R., Nesvorný, D., Moskovitz, N., Ivezić, Ž., and Fevig, R. (2008). Redetermination of the space weathering rate using spectra of iannini asteroid family members. *Icarus*, 195:663–673. 151

Winter, D. F. and Saari, J. M. (1969). A particulate thermophysical model of the lunar soil. *The Astrophysical Journal*, 156:1135–1151. 44

Wolters, S. D. and Green, S. F. (2009). Investigation of systematic bias in radiometric diameter determination of near-earth asteroids: the night emission simulated thermal model (nestm). *Monthly Notices of the Royal Astronomical Society*, 400:204–218. 4, 6

Wolters, S. D., Rozitis, B., Duddy, S. R., Lowry, S. C., Green, S. F., Snodgrass, C., Hainaut, O. R., and Weissman, P. (2011). Physical characterization of low delta-V asteroid (175706) 1996 FG3. *Monthly Notices of the Royal Astronomical Society*, 418:1246–1257. 18, 21

Wright, E. (2007). Comparing the NEATM with a Rotating, Cratered Thermophysical Asteroid Model. http://arxiv.org/abs/astro-ph/0703085. 24

Wright, E. L., Eisenhardt, P. R. M., Mainzer, A. K., Ressler, M. E., Cutri, R. M., Jarrett, T., Kirkpatrick, J. D., Padgett, D., McMillan, R. S., Skrutskie, M., Stanford, S. A., Cohen, M., Walker, R. G., Mather, J. C., Leisawitz, D., Gautier, T. N., McLean, I., Benford, D., Lonsdale, C. J., Blain, A., Mendez, B., Irace, W. R., Duval, V., Liu, F., Royer, D., Heinrichsen, I., Howard, J., Shannon, M., Kendall, M., Walsh, A. L., Larsen, M., Cardon, J. G., Schick, S., Schwalm, M., Abid, M., Fabinsky, B., Naes, L., and Tsai, C.-W. (2010). The Wide-Field Infrared Survey Explorer (WISE): Mission Description and Initial On-Orbit Performance. *Astronomical Journal*, 140:1868–1881. 31, 32, 52

Xu, S., Binzel, R. P., Burbine, T. H., and Bus, S. J. (1995). Small Main-Belt Asteroid Spectroscopic Survey: Initial Results. *Icarus*, 115:1–35. 161

Yamada, M., Sasaki, S., Nagahara, H., Fujiwara, A., Hasegawa, S., Yano, H., Hiroi, T., Ohashi, H., and Otake, H. (1999). Simulation of space weathering of planet-forming materials: Nanosecond pulse laser irradiation and proton implantation on olivine and pyroxene samples. *Earth Planets Space*, 51:1255–1265. 150, 184, 191, 192, 194

Yang, Y., Zhang, H., Wang, Z., Yuan, Y., Li, S., Hsu, W., and Liu, C. (2017). Optical spectroscopic characterizations of laser irradiated olivine grains. *Astronomy and Astrophysics*, 597:A50. 190, 191, 192

Yomogida, K. and Matsui, T. (1983). Physical Properties of Ordinary Chondrites. *Journal of Geophysical Research*, 88, B11:9513–9533. 96, 100

Yoshikawa, M., Kawaguchi, J., Fujiwara, A., and Tsuchiyama, A. (2015). Hayabusa sample return mission. In *Asteroids IV*. University of Arizona Press. 2

Yu, Y., Michel, P., Hirabayashi, M., Schwartz, S. R., Zhang, Y., Richardson, D. C., and Liu, X. (2018). The dynamical complexity of surface mass shedding from a top-shaped asteroid near the critical spin limit. *The Astronomical Journal*, 156(2):59. 142

Yule, G. U. (1903). Notes on the Theory of Association of Attributes in Statistics. *Biometrika*, 2(2):121–134. 93

Zappala, V., Cellino, A., Farinella, P., and Knezevic, Z. (1990). Asteroid families. i - identification by hierarchical clustering and reliability assessment. *Astronomical Journal*, 100(6):2030. 129

Appendices

A TPM Numerical Techniques

The parameterized version of the time-dependent, one-dimensional heat diffusion equation is:

$$\frac{\partial T'(x',t')}{\partial t'} = \Theta \frac{\partial^2 T'(x',t')}{\partial x'^2} \tag{3}$$

where temperature, time and depth are parameterized into dimensionless form by: $T' = {}^{T}/_{T_{\rm eq}}$, $t' = {}^{t\omega}/_{\Theta}$, $x' = {}^{x}/_{l_s}$. To numerically solve the time-dependent one-dimensional heat diffusion equation we employ the Crank-Nicolson finite-difference approach (Press et al., 2007). Equation 3 is discretized into small finite elements with depth increments of $\delta x'$ and time increments of $\delta t'$. If T'^{n}_{j} is the temperature at time $t' = n\delta t'$ and depth $x' = j\delta x'$:

$$\frac{T'^{n+1}_{j} - T'^{n}_{j}}{\delta t'} = \frac{\Theta}{2} \frac{(T'^{n+1}_{j+1} - 2T'^{n+1}_{j} + T'^{n+1}_{j-1}) + (T'^{n}_{j+1} - 2T'^{n}_{j} + T'^{n}_{j-1})}{(\delta x')^2}. \tag{4}$$

Grouping the terms by time step gives:

$$T'^{n}_{j-1} + T'^{n}_{j}\left(\tfrac{2(\delta x')^2}{\Theta \delta t'} - 2\right) + T'^{n}_{j+1} = -T'^{n+1}_{j-1} + T'^{n+1}_{j}\left(\tfrac{2(\delta x')^2}{\Theta \delta t'} + 2\right) - T'^{n+1}_{j+1} \tag{5}$$

For N depth steps, a set of linear equations can be represented by the matrix equation:

$$\begin{bmatrix} a & -1 & 0 & \cdots & 0 \\ -1 & a & -1 & \ddots & \vdots \\ 0 & \ddots & \ddots & \ddots & 0 \\ \vdots & \ddots & -1 & a & -1 \\ 0 & \cdots & 0 & -1 & a \end{bmatrix} \begin{bmatrix} T'^{n}_{0} \\ T'^{n}_{1} \\ \vdots \\ T'^{n}_{N-1} \\ T'^{n}_{N} \end{bmatrix} = \begin{bmatrix} d_0 \\ d_1 \\ \vdots \\ d_{N-1} \\ d_N \end{bmatrix} \tag{6}$$

where $a = \frac{2(\delta x')^2}{\Theta \delta t'} + 2$ and $d_j = T'^{n+1}_{j-1} + T'^{n+1}_{j}\left(\frac{2(\delta x')^2}{\Theta \delta t'} - 2\right) + T'^{n}_{j+1}$ and the upper (surface) and lower boundary conditions implemented as such:

$$\left.\frac{dT'}{dx'}\right|_{surf} = \frac{1}{\delta x'}(T'^{n+1}_{1} - T'^{n+1}_{0}) \tag{7}$$

$$T'^{n}_{N} - T'^{n}_{N-1} = 0. \tag{8}$$

This system of equations is solved via the `tridag` routine provided in Press et al. (2007). We choose $\delta x' = l_s/5$ and calculate temperatures down to 10 l_s. The time steps, $\delta t'$, are varied such that for $\Theta = 0.055$ and 100 there are 1440 and 360 time steps per rotation, respectively. To establish whether temperature convergence has been reached for a particular latitude bin, we utilize an energy balance criterion to the latest rotation or ensure that the temperatures have not changed substantially from the previous rotation.

B Coordinate Transformation from a Sphere to Ellipsoidal Shape

A generalized ellipsoid with semi-axes $a \geq b \geq c$ is given in Cartesian coordinates $(\mathsf{x},\ \mathsf{y},\ \mathsf{z})$ by

$$\frac{\mathsf{x}^2}{\mathsf{a}^2} + \frac{\mathsf{y}^2}{\mathsf{b}^2} + \frac{\mathsf{z}^2}{\mathsf{c}^2} - 1 = 0, \tag{9}$$

and can be parameterized using body-centric coordinates, θ and ϕ, in the following way:

$$\mathsf{x} = \mathsf{a}\cos(\theta)\cos(\phi) \tag{10}$$

$$\mathsf{y} = \mathsf{b}\sin(\theta)\cos(\phi) \tag{11}$$

$$\mathsf{z} = \mathsf{c}\sin(\phi) \tag{12}$$

for $\theta \in [0, 2\pi)$ and $\phi \in [-\frac{\pi}{2}, \frac{\pi}{2}]$, the body-centric longitude and latitude, respectively. This chosen convention implies that an ellipsoid body rotates about the $+\mathsf{c}$-axis, in the $+\theta$ direction, as per the right-hand rule. The directional derivatives of the radius vector, $\mathbf{r} = \langle \mathsf{x},\ \mathsf{y},\ \mathsf{z} \rangle$, with respect to the body-centric coordinates can then be used to find the normal vector to the surface at every point:

$$\mathbf{R}_\theta \equiv \frac{\partial \mathbf{r}}{\partial \theta} = \langle -\mathsf{a}\sin(\theta)\cos(\phi), \mathsf{b}\cos(\theta)\cos(\phi), 0 \rangle \tag{13}$$

$$\mathbf{R}_\phi \equiv \frac{\partial \mathbf{r}}{\partial \theta} = \langle -\mathsf{a}\cos(\theta)\sin(\phi), -\mathsf{b}\sin(\theta)\sin(\phi), \mathsf{c}\cos(\phi) \rangle \tag{14}$$

$$\mathbf{n} = |\mathbf{R}_\theta \times \mathbf{R}_\phi| = \cos^2(\phi)\langle \mathsf{bc}\cos(\theta), \mathsf{ac}\sin(\theta), \mathsf{ab}\tan(\phi) \rangle \tag{15}$$

$$\|\mathbf{n}\| = \cos^2\phi\,[\,\mathsf{c}^2\,(\mathsf{a}^2\sin^2\phi + \mathsf{b}^2\cos^2\theta) + \mathsf{a}^2\mathsf{b}^2\tan^2\phi]^{1/2}. \tag{16}$$

An area element, (dA), on the ellipsoid surface can now be expressed as a function of the parameterized coordinates:

$$dA = \|\mathbf{n}\|\, d\theta\, d\phi = \cos^2\phi\,[\,\mathsf{c}^2\,(\mathsf{a}^2\sin^2\phi + \mathsf{b}^2\cos^2\theta) + \mathsf{a}^2\mathsf{b}^2\tan^2\phi]^{1/2} d\theta\, d\phi. \tag{17}$$

The surface-normal longitude, ϑ, is calculated by projecting the surface-normal vector onto the x–y plane and then taking the dot product with $\hat{\mathsf{x}}$:

$$\cos(\vartheta) = \frac{\cos^2\phi\,\langle \mathsf{bc}\cos\theta, \mathsf{ac}\sin\theta, 0\rangle}{\cos^2\phi\,[\,\mathsf{c}^2\,(\mathsf{a}^2\sin^2\phi + \mathsf{b}^2\cos^2\theta)]^{1/2}} \cdot \langle 1, 0, 0\rangle. \tag{18}$$

The surface-normal latitude, φ, is calculated by taking the dot product of the surface-normal vector and $\hat{\mathsf{z}}$:

$$\sin(\varphi) = \frac{\cos^2\phi\langle \mathsf{bc}\cos\theta, \mathsf{ac}\sin\theta, \mathsf{ab}\tan\phi\rangle}{\cos^2\phi\,[\,\mathsf{c}^2\,(\mathsf{a}^2\sin^2\phi + \mathsf{b}^2\cos^2\theta) + \mathsf{a}^2\mathsf{b}^2\tan^2\phi]^{1/2}} \cdot \langle 0, 0, 1\rangle. \tag{19}$$

Simplifying results in two transformation equations for converting body-centric coordinates to surface-normal coordinates:

$$\tan(\vartheta) = \left(\frac{\mathsf{a}}{\mathsf{b}}\right)\tan\theta \tag{20}$$

and

$$\tan(\varphi) = \left(\frac{\mathsf{ab}}{\mathsf{c}}\right)\frac{\tan(\phi)}{(\mathsf{a}^2\sin^2\theta + \mathsf{b}^2\sin^2\theta)^{1/2}}. \tag{21}$$

Vita

Eric Michael MacLennan was born and raised in Weymouth, Massachusetts – a suburb just a few miles south of Boston. Throughout his childhood he enjoyed playing outside, completing jigsaw puzzles, and watching Bill Nye, knowing that his Dad would soon be home from work. He was very active in youth soccer and baseball, even participating in an indoor soccer league during the winter. For a few years, he spent the summer months learning how to operate and race small sailboats – an activity that he continues to enjoy to this day. His passion for learning about science, especially the solar system, was always apparent. In second grade he challenged his teacher on the fact that Venus was the hottest planet, not Mercury. However, nobody could have guessed that he would later go on to research asteroids using thermal models.

Throughout his teenage years, Eric was a highly active member and leader in Troop 9 and by the time he achieved the rank of Eagle Scout in 2008, he set the troop record for total nights spent camping. He developed an enthusiasm for hiking and backpacking in the White Mountains of New Hampshire. During trips to the mountains, he would spent many nighttime hours looking up in hopes to catch a meteor streak across the sky. The summer before beginning college, Eric embarked on a coast-to-coast road trip with two of his best friends. They visited 26 states, at least 10 major U.S. cities, and over 11 national parks and landmarks in 18 days. This journey sparked a new enjoyment for travel and fueled ambitions to venture to many other faraway places.

Eric's undergraduate studies were conducted at Northern Arizona University in Flagstaff, Arizona. He treasured the dark skies and fresh air of the high desert and became devoted to his studies and fellowship with classmates. A few times Eric served in various official roles for both the Astronomy club and Society of Physics Students. His first experience in

Planetary Science research was studying possible extraterrestrial cave sites on Mars, through an internship with the United States Geological Survey in his $3rd$ year of study. The following summer, Eric was an intern student at the Institute for Astronomy where he studied active asteroids. Through this experience, and from working on a research project in the final year of his undergraduate work, Eric decided that he would pursue a PhD and continue researching small solar system bodies.